

*DTIC*

# JOURNAL OF FLUIDS AND STRUCTURES

Special Issue on  
Bluff Body Wakes and Vortex - Induced Vibrations  
edited by  
T. Leweke, P. W. Bearman and C. H. K. Williamson



ACADEMIC PRESS

A Harcourt Science and Technology Company

# JOURNAL OF FLUIDS AND STRUCTURES

## EDITOR

M. P. PAÏDOUSSIS

*Department of Mechanical Engineering, McGill University, 817 Sherbrooke St. W.,  
Montreal, Québec, Canada H3A 2K6 FAX: (514) 398 7365*

## ASSOCIATE EDITORS

P.W. BEARMAN *Department of Aeronautics, Imperial College of Science, Technology and Medicine, Prince Consort Road, London SW7 2BY, U.K.*

Y. T. CHEW *Department of Mechanical Engineering, The National University of Singapore, 10 Kent Ridge Crescent, Singapore 0511*

C. DALTON *Department of Mechanical Engineering, University of Houston, Houston, TX 77004, U.S.A.*

E. H. DOWELL *Dean's Office, School of Engineering, Duke University, Durham, NC 27706, U.S.A.*

R. EATOCK TAYLOR *Department of Engineering Science, University of Oxford, Parks Road, Oxford OX1 3PJ, U.K.*

P. P. FRIEDMANN *Department of Aerospace Engineering, University of Michigan, 3001 FXB Building, 1320 Beal Avenue, Ann Arbor, MI 48109-2140, U.S.A.*

J. M. R. GRAHAM *Department of Aeronautics, Imperial College of Science and Technology, Prince Consort Road, London SW7 2BY, U.K.*

J.-P. GRISVAL *ONERA/DDSS, B.P. No. 72, F-92322 Châtillon Cedex, France*

S. HAYAMA *Faculty of Engineering, Toyama Prefectural University, 5180 Kosugi-Machi, Toyama 939-03, Japan*

R. D. KAMM *Department of Mechanical Engineering, Massachusetts Institute of Technology, Rm 3-260, Cambridge, MA 02139, U.S.A.*

E. de LANGRE *Hydrodynamics Laboratory—LadHyx, Ecole Polytechnique 91128 Palaiseau, France*

M. MATSUMOTO *Department of Global Environment Engineering, Kyoto University, Sakyo-ku, Yoshida Honmachi, Kyoto 60601, Japan*

T. J. PEDLEY *Department of Appl. Mathematics & Theoretical Physics, University of Cambridge, Silver Street, Cambridge CB3 9EW, U.K.*

D. ROCKWELL *Department of Mechanical Engineering and Mechanics, 19 Memorial Drive West, Lehigh University, Bethlehem, PA 18015, U.S.A.*

R. H. SCANLAN *Department of Civil Engineering, Johns Hopkins University, 3400 North Charles Street, Baltimore, MD 21218, U.S.A.*

G. S. TRIANTAFYLLOU *The Lerich Institute, Steinman Hall 1M 9 Convent Avenue at 140th Street, The City College of New York, New York, NY 10031, U.S.A.*

D. S. WEAVER *Department of Mechanical Engineering, McMaster University, Hamilton, Ontario, Canada L8S 4L7*

C. H. K. WILLIAMSON *Sibley School of Mechanical & Aerospace Engineering, Upson Hall, Cornell University, Ithaca, NY 14853-7501, U.S.A.*

## EDITORS-AT-LARGE

E. J. CUI *Beijing Institute of Aerodynamics, PO Box 7215, Beijing 100074, People's Republic of China*

A. ROSHKO *Graduate Aeronautical Laboratories 105-50, California Institute of Technology, Pasadena, CA 91125, U.S.A.*

JOURNAL OF FLUIDS AND STRUCTURES: ISSN 0889-9746. Volume 15, 2001, published monthly except in Mar., Jun., Sep., Dec., total 8 issues by Academic Press at 32 Jamestown Road, London NW1 7BY, U.K. Annual worldwide subscription price including postage: £431. Buyers in Canada should add GST at the current rate of 7%. Subscription orders should be sent to: Journals Subscription Department, Harcourt Brace and Company Ltd., Foots Cray, High Street, Sidcup, Kent DA14 5HP, U.K. (Tel: 020-8308 5700). Send notices of changes of address to the publisher at least 6–8 weeks in advance, including both old and new address.

Academic Press Journals do not levy page charges.

Air freight and mailing in the U.S.A. c/o Mercury International Ltd, 365 Blair Road, Avenel, NJ 07001, U.S.A. Periodicals class postage paid at Rahway, NJ 07001, U.S.A.

U.S.A. POSTMASTERS: send changes of address to JOURNAL OF FLUIDS AND STRUCTURES, c/o Mercury International Ltd, 365 Blair Road, Avenel, NJ 07001, U.S.A.

Printed in U.K.

Copyright © 2001 by Academic Press. No part of this publication may be reproduced or transmitted in any form or by any means, electronic or mechanical, including photocopy, recording, or any information storage and retrieval system, without permission in writing from the Publisher. *Exceptions:* explicit permission from Academic Press is not required to reproduce a maximum of two figures or tables from an Academic Press article in another scientific or research publication provided that the material has not been credited to another source and that full credit to the Academic Press article is given. In addition, authors of work contained herein need not obtain permission in the following cases only: (1) to use their original figures or tables in their future works; (2) to make copies of their papers for use in their classroom teaching; and (3) to include their papers as part of their dissertations.

The appearance of the code at the bottom of the first page of a paper in this journal indicates the copyright owner's consent that copies of the paper may be made for personal or internal use or for the personal or internal use of specific clients in the USA. This consent is given on the condition, within the USA, that the copier pay the stated per-copy fee through the Copyright Clearance Center Inc., 222 Rosewood Drive, Danvers, MA 01923, U.S.A. for copying beyond that permitted by Sections 107 or 108 of the US Copyright Law. This consent does not extend to other kinds of copying, such as copying for general distribution, for advertising or promotional purposes, for creating new collective works, for resale or for copying or distributing copies outside the U.S.A.

## U.S. Government Rights License

This work relates to Department of the Navy  
Grant or Contract issued by Office of Naval  
Research (ONR) International Field Office-  
Europe. The United States Government has a  
royalty-free license throughout the world in all  
copyrightable material contained herein.



## Dedication of Proceedings to

PROFESSOR ANTHONY EDWARD PERRY

1937-2001

We would like to dedicate this Special Proceedings Issue to Professor Anthony Perry of Melbourne University, Australia. Tony has contributed with many well-known papers, several of them considered classics, to the fields of fluid mechanics and aerodynamics through both the experimental and theoretical approaches. He published extensively, and gave wonderfully original and entertaining presentations in studies of turbulence and structure-based modelling approaches, elegant use of scaling arguments, flow pattern topology, three-dimensional separation and vortex shedding processes. I still remember the first time I met Tony, as part of the great team of Tony and Chong, when they both turned up at a lunch party at Anatol Roshko's house in Pasadena, in the Fall of 1984. I had only just arrived at Caltech, and was not sure who was who in the world of fluid mechanics, but quickly realized Tony was one of the very best. What a wonderful experience it was to meet Tony and Min Chong and to go hiking with them in the hills behind Anatol's house. Tony's energy, joie de vivre and engaging sense of humour were infectious, and these aspects were always there through the intervening years. And so it was with the utmost pleasure that we welcomed Tony, and indeed Min Chong, as invited speakers to our IUTAM Conference in Carry-Le-Rouet in June 2000. We never suspected, based on the incredible level of noise, laughter, and liquid consumption at the "Australian table" at our conference banquet in the port of Marseille, that Tony would now not be with us. This volume of work is dedicated to the memory of a great scientist, and warm-hearted fellow.

CHARLES H. K. WILLIAMSON  
11 January 2001



Tony Perry at Trinity College, Cambridge (1999)

20011130 071

AQ F02-02-0261



**IUTAM Symposium on  
Bluff Body Wakes and Vortex-Induced Vibrations  
(BBVIV-2)**

Carry-Le-Rouet (near Marseille), France  
13–16 June 2000

**CHAIRMEN**

Peter W. Bearman	Imperial College, U.K.
Thomas Leweke	IRPHE/CNRS, France
Charles H. K. Williamson	Cornell University, U.S.A.

**INTERNATIONAL SCIENTIFIC COMMITTEE**

Morteza Gharib	California Institute of Technology, U.S.A.
Kerry Hourigan	Monash University, Australia
George E. Karniadakis	Brown University, U.S.A.
Masaru Kiya	Hokkaido University, Japan
Peter A. Monkewitz	EPF Lausanne, Switzerland
Christoffer Norberg	Lund Institute of Technology, Sweden
Michael P. Paidoussis	McGill University, Canada
Donald O. Rockwell	Lehigh University, U.S.A.
Michael S. Triantafyllou	Massachusetts Institute of Technology, U.S.A.
Tomomasa Tatsumi	International Institute for Advanced Studies, Japan

**LOCAL ORGANIZING COMMITTEE**

Thomas Leweke (Chairman)	IRPHE/CNRS, France
Stéphane Le Dizès	IRPHE/CNRS, France
Patrice Le Gal	IRPHE/CNRS, France
Michel Provansal	IRPHE/Université Aix-Marseille III, France

The Symposium was organized by the *Institut de Recherche sur les Phénomènes Hors Equilibre* (IRPHE), affiliated with the French *Centre National de la Recherche Scientifique* (CNRS), the *Université de Provence* (Aix-Marseille I), and the *Université de la Méditerranée* (Aix-Marseille II).

---

**IUTAM Symposium on  
Bluff Body Wakes and Vortex-Induced Vibrations**

**ACKNOWLEDGEMENT**

We are grateful for the enthusiastic support for this conference  
from the following sponsors:

*International Union of Theoretical and Applied Mechanics*

*European Commission*

Research Directorate-General, Human Potential Programme, High-Level  
Scientific Conferences, Contract no. HPCF-CT-1999-00099.

*United States Office of Naval Research*

Office of Naval Research, Arlington, VA, U.S.A.

Office of Naval Research International Field Office, London, U.K.

*Ministère de la Défense — Délégation Générale pour l'Armement (DGA)*

French Ministry of Defence — Procurement Agency

*Ministère de l'Education Nationale, de la Recherche et de la Technologie*

French Ministry of Education, Research, and Technology

*Centre National de la Recherche Scientifique (CNRS)*

French National Centre for Scientific Research

*Conseil Général des Bouches-du-Rhône* (Departmental Council)

*Conseil Régional Provence-Alpes-Côte d'Azur* (Regional Council)

*Université de Provence*

*Université de la Méditerranée*

## CORRIGENDUM

In Volume 15, numbers 3 and 4 of the *Journal of Fluids and Structures*, a Special Issue on Bluff Body Wakes and Vortex-Induced Vibrations, a misplacement of colour plate figures occurred. Figures 7 and 8 of both the articles by H. M. Blackburn, R. N. Govardhan & C. H. K. Williamson and D. Lucor, L. Imas & G. E. Karniadakis were transposed. These colour plates appear between pages 486-487 and pages 646-647 respectively in the printed copy, and should have appeared in the opposite position.

# REPORT DOCUMENTATION PAGE

Form Approved OMB No. 0704-0188

Public reporting burden for this collection of information is estimated to average 1 hour per response, including the time for reviewing instructions, searching existing data sources, gathering and maintaining the data needed, and completing and reviewing the collection of information. Send comments regarding this burden estimate or any other aspect of this collection of information, including suggestions for reducing this burden to Washington Headquarters Services, Directorate for Information Operations and Reports, 1215 Jefferson Davis Highway, Suite 1204, Arlington, VA 22202-4302, and to the Office of Management and Budget, Paperwork Reduction Project (0704-0188), Washington, DC 20503.

1. AGENCY USE ONLY (Leave blank)		2. REPORT DATE April/May 2001	3. REPORT TYPE AND DATES COVERED 13-16 June 2000 Final Report	
4. TITLE AND SUBTITLE IUTAM Symposium on Bluff Body Wakes and Vortex-Induced Vibrations 9BBVIV-2). Held in Carry-Le-Roeut, France on 13-16 June 2000.			5. FUNDING NUMBERS	
6. AUTHOR(S) T. Leweke, P.W. Bearman, C.H.K. Williamson, Editors				
7. PERFORMING ORGANIZATION NAME(S) AND ADDRESS(ES) Institut de Recherche sur les Phenomenes Hors Equilibre (IRPHE)			8. PERFORMING ORGANIZATION REPORT NUMBER  ISSN 0889-9746	
9. SPONSORING/MONITORING AGENCY NAME(S) AND ADDRESS(ES) Office of Naval Research, European Office PSC 802 Box 39 FPO AE 09499-0039			10. SPONSORING/MONITORING AGENCY REPORT NUMBER	
11. SUPPLEMENTARY NOTES Published as a Special Issue of the Journal of Fluids and Structures, Vol.15, No.3/4 (April/May 2000). Published by Academic Press, 32 Jamestown Road, London NW1 7BY UK. This work relates to Department of the Navy Grant issued by the Office of Naval Research International Field Office. The United States has a royalty free license throughout the world in all copyrightable material contained herein.				
12a. DISTRIBUTION/AVAILABILITY STATEMENT  Approved for Public Release; Distribution Unlimited. U.S. Government Rights License. All other rights reserved by the copyright holder.			12b. DISTRIBUTION CODE  A	
12. ABSTRACT (Maximum 200 words) This special issue of the Journal of Fluids and Structures is the proceedings of the 2 <sup>nd</sup> IUTAM Symposium on Bluff Body Wakes and Vortex-Induced Vibrations held at Carry-le-Rouet, France on 13-16 June 2000. Topical sessions included: wake fundamentals; vortex-induced vibrations, forced oscillations, sphere wakes, three-dimensional effects, three-dimensional instability, wake manipulation, wake control and flexible structures. A significant outcome of the meeting was the recognition of the advances being made by computational fluid dynamics (CFD).				
13. SUBJECT TERMS ONR, Foreign reports, Conference proceedings, Physics, Computational fluid dynamics,			15. NUMBER OF PAGES	
			16. PRICE CODE	
17. SECURITY CLASSIFICATION OF REPORT  UNCLASSIFIED	18. SECURITY CLASSIFICATION OF THIS PAGE  UNCLASSIFIED	19. SECURITY CLASSIFICATION OF ABSTRACT  UNCLASSIFIED	20. LIMITATION OF ABSTRACT  UL	

NSN 7540-01-280-5500

Standard Form 298 (Rev. 2-89)  
Prescribed by ANSI Std. Z39-18  
298-102

## CORRIGENDUM

In Volume 15, numbers 3 and 4 of the *Journal of Fluids and Structures*, a Special Issue on Bluff Body Wakes and Vortex-Induced Vibrations, a misplacement of colour plate figures occurred. Figures 7 and 8 of both the articles by H. M. Blackburn, R. N. Govardhan & C. H. K. Williamson and D. Lucor, L. Imas & G. E. Karniadakis were transposed. These colour plates appear between pages 486-487 and pages 646-647 respectively in the printed copy, and should have appeared in the opposite position.

## PREFACE

The present Special Issue makes up the Proceedings of the IUTAM Symposium on Bluff Body Wakes and Vortex-Induced Vibrations held at Carry-le-Rouet (near Marseille), France, 13–16 June 2000. This is the second conference on this subject in recent years, the first conference (BBVIV-1) having been held in Washington, DC, in June 1998; the Marseille conference was thus given the acronym BBVIV-2. The papers in this volume were selected by the Scientific Committee from amongst the oral presentations made at the Symposium. The Symposium itself attracted 100 participants from 18 countries and, apart from a few who were unable to be present, gathered together the most active researchers in the field. The scientific programme included 8 invited lectures, 38 oral presentations and 22 poster presentations. People responsible for the posters were given a few minutes each to make a short presentation on their work. A total of 91 abstracts had been received, and these were reviewed by the Scientific Committee and the Chairmen. It was agreed by all present that the general standard of the presentations and the scientific level achieved were high.

The complete set of abstracts, of both oral and poster presentations, were provided to all participants at the conference site. A detailed list of all presentations is included in a later section of these Proceedings. The topical sessions at the conference had the following titles:

- Wake Fundamentals (4 talks of 20 minutes, 6 poster presentations)
- Vortex-Induced Vibrations (6 talks, 2 posters)
- Forced Oscillations (3 talks, 5 posters)
- Sphere Wakes (5 talks, 3 posters)
- Three-dimensional Effects (4 talks)
- Three-dimensional Instability (4 talks)
- Wake Manipulation (3 talks, 3 posters)
- Wake Control (4 talks, 3 posters)
- Flexible Structures (5 talks)

One of the main purposes of the Symposium was to bring together people working on the wakes of fixed bluff bodies with those studying vortex-induced vibrations of bluff bodies. Papers on the wake structure of fixed bluff bodies were divided into two main areas: those dealing with two-dimensional shapes, or those with only small amounts of three-dimensionality, and those on spheres. Presentations were almost equally divided between experimental and computational work and several addressed the question of vortex shedding control, both passive and active. There were separate sessions on theoretical aspects with a number of presenters following the interesting non-linear model equation approach, showing that they were able to predict many of the physical features.

Vortex-induced vibration (VIV) is a subject that has been around for a long time, and key parameters include structural damping and mass ratio, i.e. the mass of the structure to the mass of displaced fluid. The flow can be studied by considering bluff bodies forced to oscillate, or elastically-mounted bluff bodies free to oscillate, and presentations on both approaches were given at the conference. Much is known about VIV of structures in air where mass ratios are high. Offshore oil production has stimulated an interest in large amplitude VIV for cylinders with mass ratios near unity. A number of new phenomena have been observed, including different modes of shedding, and distinct branches to the response curve of amplitude versus normalized velocity. For low mass ratios, the so-called “added mass component” provided by the fluid has a significant effect on oscillation frequency and is found to vary with normalized velocity, as might be expected. These findings provoked extensive and remarkably lively discussion at the conference on the meaning of “added

mass" and whether it should be considered in its ideal flow sense, or whether it should be defined as the component of the total fluid force in phase with acceleration.

A significant outcome of the meeting was the recognition of the advances being made by computational fluid dynamics (CFD). It was demonstrated that considerable insight can be provided by applying CFD to an idealized cylinder experiment with some combination of the mass, damping and stiffness equated to zero. Direct simulations of three-dimensional modes of shedding are now possible, and this prompted some discussion as to what role they play in determining the amplitude of VIV. Others argued that VIV imposes order on the wake and that two-dimensional codes should be adequate for predicting VIV, although at least one researcher showed that distinctly different VIV responses ensued, depending on whether a 2-D or 3-D direct simulation is used. An intriguing result, which was known before the symposium, but reaffirmed at the meeting, is that CFD codes are having great difficulty in predicting the maximum amplitude of oscillation when the combined mass and damping parameter is low. There was much speculation as to why this is. One researcher, using turbulence modelling, had found that the maximum response could be predicted if the flow speed in the computation was very slowly raised, as might happen in some of the experiments. Others, who had tried the same approach, could not attain large enough amplitudes. As the mass and damping tend to zero, the phase angle (by which the transverse fluid force leads the displacement) becomes extremely small, and to predict maximum amplitudes, this angle has to be found to a very high degree of accuracy.

Predicting maximum amplitude remains one of the challenges facing CFD specialists. In addition to those mentioned above, important new results were displayed on a number of other topics, including: sphere wakes, wakes of cylinders at or near a free surface, flow around multiple cylinders, and the extraction of energy from bluff body wakes.

It must be mentioned that much of the present stimulus for research on fixed bluff bodies over the last 10 years, and the strong resurgence of investigations into vortex-induced vibration over the last 5 years, have come from the focussed support program of the Ocean Engineering Division of the U.S. Office of Naval Research, monitored by Dr Tom Swain. Their support has provided a strong impetus for the two conferences on Bluff Body Wakes and Vortex-Induced Vibration (BBVIV-1 and BBVIV-2), and in both cases, the ONR have provided funds for publication and availability of the Proceedings.

This IUTAM Symposium was held in a resort hotel complex directly on the coast, which possessed a sufficient level of isolation to ensure that the scientific sessions were always very well attended. The hospitality and meals provided by the hotel were excellent, and they played a significant part in bringing the participants together for many interesting discussions. In the Chairman's final remarks of the conference, it was mentioned that the food was so superb and plentiful, that it gave new meaning to the expression "added mass", upon which so much debate had been focussed. Immense thanks are due to all those involved in the local organization of the event for setting up so many of the essential details for the success of the conference. One can say with confidence that everybody was able to leave the meeting with some new research ideas to follow up.

T. Leweke  
P. W. Bearman  
C. H. K. Williamson

Marseille, January 2001



## Opening Address

## FLUID MECHANICS IN THE COMING CENTURY

TOMOMASA TATSUMI

*IUTAM Bureau Member – International Institute for Advanced Studies, Kyoto, Japan*

**IUTAM.** The present Symposium on “Bluff Body Wakes and Vortex-Induced Vibrations” is one of the “IUTAM Symposia”, which are sponsored by the International Union of Theoretical and Applied Mechanics (IUTAM). Actually, this subject has been selected from many proposals made by various research groups in the world and adopted by the General Assembly of IUTAM. Another important activity of IUTAM is to organize the “International Congresses of Theoretical and Applied Mechanics” (ICTAM), which are held every 4 years in various cities in the world. The most recent ICTAM held in France was the 17th Congress in 1988, Grenoble, and one of the last was the 19th Congress held in 1996, Kyoto, Japan. Then, in the year of 2000, the 20th Congress was held in Chicago, U.S.A.

**Mechanics of Viscous Fluid.** The present century may be characterized by the great progress in mechanics of the “viscous fluid” governed by the Navier–Stokes equation. Until the last century, fluid mechanics has mostly been concerned with the “inviscid fluid”. Although the mathematical theory due to the Euler equation supplied us with useful mathematical results and elegant theorems for fluid motions, it often caused serious discrepancy from the physical reality such as functional singularities in the solutions and the d’Alembert’s paradox of vanishing drag for moving bodies. A big revolution has been achieved around the last turn of the century by two epoch-making works of O. Reynolds (1894) on “turbulent flows” and L. Prandtl (1904) on the “boundary layer”. The classification of the real viscous flows in terms of the magnitude of Reynolds number  $Re = UL/\nu$ ,  $U$  and  $L$  being the velocity and the length-scales of the flow and  $\nu$  the kinematic viscosity of the fluid, and introduction of suitable analytical and numerical methods for the corresponding magnitude of  $Re$ , enabled us to obtain mathematical solutions of the Navier–Stokes equation for almost all fluid flows of theoretical or practical significance.

**Mechanics of Turbulence.** An obvious exception from the above optimistic summary is “turbulent flows”, including the subject of the present Symposium. In spite of great advances in turbulence research during this Century initiated by the “statistical theory” of Sir Geoffrey Taylor (1935) and the “local equilibrium theory” of A.N. Kolmogorov (1941) and largely helped by the rapid progress in high-speed numerical computation, the theory is still lacking theoretical unity and much more works have to be done in the coming Century before the theory is accomplished as the “mechanics of turbulence”.

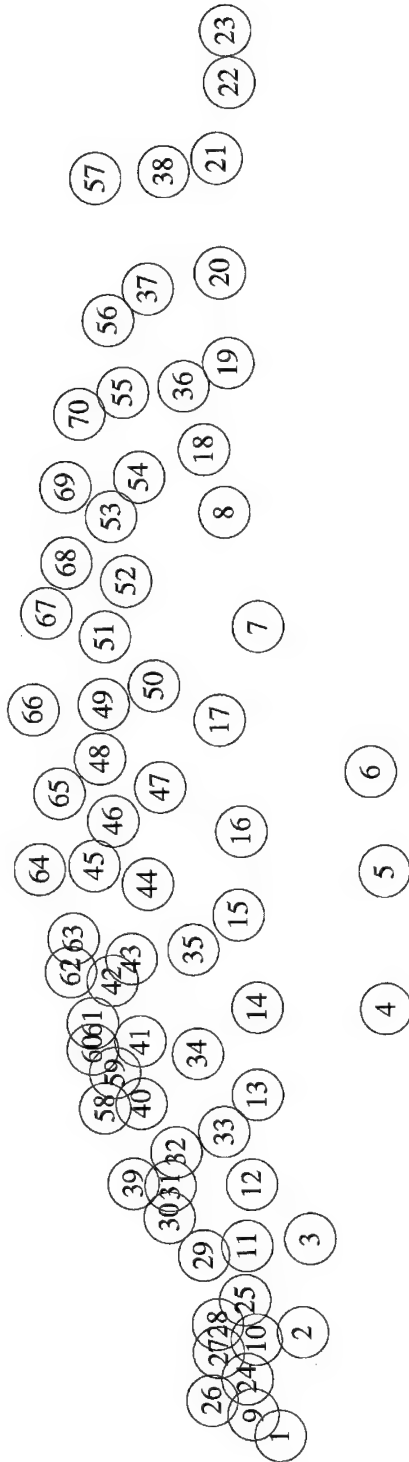
**Fluid Mechanics in the Coming Century.** The great success of mechanics of the “viscous fluid” developed during this century has resulted in a rich variety of engineering applications, including the subject of the present Symposium, “Bluff Body Wakes and Vortex-Induced Vibrations”. Such a tendency will be pushed even further toward the next century. The study of more “complex” fluid flows associated with thermal convection, combustion, phase change, chemical reaction, nuclear and thermo-nuclear reactions, which have already been included in applied fields of the present fluid mechanics, will certainly constitute the central part of the fluid mechanics in the coming century. The fluid dynamical problems may not be limited to engineering subjects, but they will be extended to fluid phenomena in other fields such as biological and life science, space and cosmic science, and environmental and energy technologies. Theoretically speaking, the enlargement of the subjects to huge scales such as environmental, global, planetary or even cosmical phenomena opens a novel

scope of fluid mechanics. Just like modern fluid mechanics has been largely supported by the developments in molecular physics of matter, the fluid mechanics of huge-scale phenomena must be built up on the theoretical basis of contemporary fluid mechanics of human scale. Even a brief survey as stated above may be sufficient to guarantee a rich and fascinating future for Fluid Mechanics in the coming century.

# IUTAM-BBVIV2 Group Photograph

- 16 June 2000 -





- 1 - Françoise BATAILLE 2 - Marianna BRAZA 3 - Iphigenia BRAZA 4 - Michael TRIANTAFYLLOU 5 - Charles WILLIAMSON 6 - George TRIANTAFYLLOU 7 - Tomomasa TATSUMI 8 - Marie Pierre CHAUVÉ 9 - Yong Tian CHEW 10 - Rupad DAREKAR 11 - Richard WILLDEN 12 - Masaru KIYA 13 - Charles DALTON 14 - Julio SORIA 15 - Min Seong CHONG 16 - Anthony PERRY 17 - Michael PAÏDOUSSIS 18 - David BEAL 19 - Raghuraman GOVARDHAN 20 - Valérie BLONDEAU 21 - Julio MENEHINI 22 - Hiroshi HIGUCHI 23 - Jean LEMAY 24 - Anne CROS 25 - Emmanuel VILLERMAUX 26 - Pierre ALBARÈDE 27 - ? 28 - Kerry HOURIGAN 29 - Olivier CADOT 30 - Christophe ELOY 31 - Lionel MATHELIN 32 - Peter MONKEWITZ 33 - John OWEN 34 - Hugh BLACKBURN 35 - Petros ANAGNOSTOPOULOS 36 - Patrice LE GAL 37 - Guido BURESTI 38 - Siao Chung LUO 39 - Lionel SCHOUVEILER 40 - Josie CARBERRY 41 - Brice VALLÈS 42 - Cesario SIQUEIRA 43 - David JEON 44 - Thomas GAUTHEROT 45 - Donald ROCKWELL 46 - Peter BEARMAN 47 - Albin SZEWCZYK 48 - Emmanuel GUILMINEAU 49 - An-Bang WANG 50 - Anatol ROSHKO 51 - Peter STANSBY 52 - Mohammad GHARIB 53 - Christoffer NORBERG 54 - Patrice MEUNIER 55 - John CHAPLIN 56 - Hayden MARCOLLO 57 - Thomas LEWEKE 58 - Benoît PIER 59 - Yves-Marie SCOLAN 60 - Ling QIAN 61 - Michel PROVANSAL 62 - Baoshan ZHU 63 - Stéphane ÉTIENNE 64 - Franz HOVER 65 - Sanjay MITTAL 66 - Bartosz PROTAS 67 - Anthony LEONARD 68 - Christoph BRÜCKER 69 - Maciej PODOLSKI 70 - Stéphane LE DIZÈS

## COMPLETE LIST OF PRESENTATIONS

## INVITED LECTURES

- Hourigan, K. & Thompson, M. C. (Australia) p. 387  
*Flow around elongated bodies: flow structure and resonance*
- Kiya, M., Mochizuki, O. & Ishikawa, H. (Japan) p. 399  
*Interaction between vortex rings and a separated shear layer: towards active control of separation zones*
- Leonard, A. (U.S.A.) p. 415  
*Flow-induced vibration of a circular cylinder: insights from computational experiments*
- Monkewitz, P. A. (Switzerland)  
*Modelling of vortex shedding from cylinders with span-wise non-uniformities*
- Perry, A. E. & Chong, M. S. (Australia) [1]  
*Interpretation of flow visualization*
- Rockwell, D. O. (U.S.A.) p. 427  
*Flow-structure interactions in presence of a free surface*
- Roshko, A. (U.S.A.) p. 415  
*Aspects of the classic VIV problem*
- Sarpkaya, T. (U.S.A.) [2]  
*Time-dependent flow about solid and perforated cylinders*

## SESSION: WAKE FUNDAMENTALS

- Buresti, G. & Lombardi, G. [3]  
*Characterization of the wake flow field of triangular prisms in cross-flow using wavelet-based techniques*
- Chaplin, J. R. & Teigen, P.  
*Drag on a vertical cylinder at a free surface*
- Le Gal, P., Nadim, A. & Thompson, M. p. 445  
*Forced response of the subcritical Landau equation: application to vortex shedding from a cylinder*
- Luo, S. C., Chew, Y. T. & Ng, Y. T. [4]  
*Hysteresis phenomenon in the galloping oscillation of a square cylinder*
- Norberg, C. p. 459  
*Flow around a circular cylinder: fluctuating lift*
- Pier, B. & Huerre, P. p. 471  
*Nonlinear frequency selection in wakes*
- Shuyang, C., Ozono, S. & Hirano, K. [5]  
*Vortex shedding from a circular cylinder placed in a linear shear flow at high Reynolds number*
- Villermaux, E.  
*On the Strouhal-Reynolds dependence in the Bénard-Kármán problem*
- Wang, A.-B., Trávníček, Z. & Wu, M.-H. [6]  
*Oblique and parallel vortex shedding of a heated circular cylinder at low Reynolds number*
- Weiss, J., Lecordier, J. C., Godard, G. & Paranthoën, P.  
*Dispersion of heat from a line source located in the near wake of a circular cylinder at low Reynolds number*

## SESSION: VORTEX-INDUCED VIBRATIONS

- Blackburn, H. M., Govardhan, R. & Williamson, C. H. K. p. 481  
*A complementary numerical and physical investigation of vortex-induced vibration*
- Etienne, S. & Scolan, Y.-M. [7]  
*Vortex shedding and induced vibrations of multiple cylinders at arbitrary Reynolds numbers*
- Gharib, M. R. & Leonard, A. p. 533  
*Vortex-induced vibration, mass ratio effects and introducing effective stiffness*
- Govardhan, R. & Williamson, C. H. K. p. 489  
*Response and vortex formation modes of an elastically-mounted cylinder at high and low mass-damping*
- Guilmineau, E. & Queutey, P.  
*Dynamics simulation of a hydroelastic structure with very low mass and damping*
- Hover, F. S. & Triantafyllou, M. S. p. 503  
*Free vibrations of a cylinder with upstream wake interference*
- Kamemoto, K. & Zhu, B.  
*Oscillation characteristics of a circular cylinder in a uniform flow with intermittent touching to a close structure*
- Stansby, P. K. & Rainey, R. C. T. p. 513  
*On the big dynamic response of a rotating cylinder in a current*

## SESSION: FORCED OSCILLATIONS

- Anagnostopoulos, P. [8]  
*Numerical visualization of aperiodic vortex structures in the wake of a transversely excited cylinder*
- Carberry, J., Sheridan, J. & Rockwell, D. p. 523  
*Forces and wake modes of an oscillating cylinder*
- Chew, Y. T., Luo, S. C. & Guo, T. [9]  
*A new formula for in-line force calculation of oscillatory flow past a circular cylinder*
- Choi, H. & Choi, S. [10]  
*Effect of periodic rotary oscillation on flow past a circular cylinder*
- Jarza, A. & Podolski, M. [11]  
*Random and periodical velocity fluctuations in vortex formation region behind cylinder in lock-on regime*
- Jeon, D. & Gharib, M. p. 533  
*On circular cylinders undergoing two-degree-of-freedom forced motions*
- Qian, L. & Vezza, M.  
*Development of a vorticity based method for studying bluff body flow problems*
- Rodriguez, O. & Pruvost, J. [12]  
*Wakes of an oscillating cylinder*

## SESSION: SPHERE WAKES

- Brücker, C. p. 543  
*Spatio-temporal reconstruction of the unsteady wake of axi-symmetric bluff bodies via time-recording DPIV*

- Bouchet, G., Dušek, J., Ghidersa, B. & Woehl, P. [13]  
*Axisymmetry breaking in the wake of a fixed and a free falling sphere*
- Jauvtis, N., Govardhan, R. & Williamson, C. H. K. p. 555  
*Vortex-induced vibrations of a sphere*
- Johansson, P. & George, W. K.  
*Application of equilibrium similarity analysis on the axisymmetric wake*
- Kiura, T. & Higuchi, H.  
*Knuckleball aerodynamics: passive alteration of three-dimensional wake-structure interactions*
- Michalski, C., Schouveiler, L. & Provansal, M. p. 565  
*Periodic wakes of spheres and low aspect ratio cylinders*
- Park, J., Choi, H. & Jeon, W.  
*Active control of flow over a sphere for drag reduction using electro-magnetic actuators*
- Thompson, M. C., Leweke, T. & Provansal, M. p. 575  
*Dynamics of sphere wake transition*

## SESSION: THREE-DIMENSIONAL EFFECTS

- Andersson, H. I., Jenssen, C. B. & Vallès, B. [14]  
*Oblique vortex shedding behind tapered cylinders*
- Darekar, R. M. & Sherwin, S. J. p. 587  
*Flow past a bluff body with a wavy separation line*
- Higuchi, H. & Hiramoto, R.  
*Wake interactions behind a non-parallel pair of circular cylinders*
- Owen, J. C., Bearman, P. W. & Szewczyk, A. A. p. 597  
*The influence of streamwise vorticity on von Kármán vortex shedding*

## SESSION: THREE-DIMENSIONAL INSTABILITY

- Braza, M. [15]  
*Successive mode changes in 3D transition to turbulence in the wake of circular cylinder by means of DNS.*
- Cadot, O. [16]  
*Viscoelastic effects on the two- and three-dimensional structure of the wake of a cylinder*
- Siqueira, C. L. R., Meneghini, J. R. & Saltara, F. [17]  
*Three-dimensional simulation of the flow past a circular cylinder at low Reynolds numbers*
- Thompson, M. C., Leweke, T. & Williamson, C. H. K. p. 575  
*Transition in bluff body wakes: is the initial transition elliptic?*

## SESSION: WAKE MANIPULATION

- Beal, D. N., Techet, A. H., Hover, F. S., Yue, D. K. P. & Triantafyllou, M. S.  
*Vortex modulation by an oscillating foil*
- Bouak, F. & Lemay, J.  
*Flow around two circular cylinders in crossflow: simultaneous measurements and analysis of unsteady lift and drag forces*
- Bruneau, C.-H. & Mortazavi, I.  
*Passive control of flows past an obstacle using porous media*

- Dalton, C., Xu, Y. & Owen, J. C. p. 617  
*The suppression of the oscillating lift due to vortex shedding at moderate Reynolds numbers for a circular cylinder*
- Flatschart, R. B., Meneghini, J. R. & Saltara, F.  
*Numerical simulation of flow interference between four cylinders in various arrangements*
- Lalanne, L., Le Guer, Y. & Creff, R. [18]  
*Experiments on the passive control of a confined jet impinging a heated bluff body*

## SESSION: WAKE CONTROL

- Amitay, M. & Glezer, A.  
*Flow control on bluff bodies using synthetic jet technology*
- Koumoutsakos, P. & Milano, M.  
*Active control algorithms for cylinder drag minimization*
- Mathelin, L., Bataille, F., Brillant, G. & Lallemand, A. [19]  
*Blowing impact on the wake of a circular cylinder*
- Mittal, S. [20]  
*Finite element computation of flows past circular cylinder*
- Panchapakesan, N. R., Bulbeck, J. & Soria, J. [21]  
*Control of square trailing edge wake flow*
- Posdziech, O. & Grundmann, R. [22]  
*Electromagnetic control of flow around an infinitely long cylinder in the transition regime*
- Protas, B. & Styczek, A.  
*Optimal feedback control of the cylinder wake*

## SESSION: FLEXIBLE STRUCTURES

- Allen, J. & Smits, A. p. 629  
*Energy harvesting eel*
- Kirby, R. M. & Karniadakis, G. E.  
*Flow past a bluff body with a rigid and a flexible splitter plate*
- Lucor, D. & Karniadakis, G. E. p. 641  
*Vortex dislocations, vortex splits and forces distribution in flows past bluff bodies*
- Pesce, C. P., Fajarra, A. L. C., Flemming, F. & Williamson, C. H. K. p. 651  
*Vortex-induced vibrations of a flexible cantilever*
- Willden, R. H. J. & Graham, J. M. R. p. 659  
*Numerical prediction of VIV on long flexible circular cylinders*

## REFERENCES

- [1] PERRY, A. E. & CHONG, M. S. 2000 Interpretation of flow visualization. In *Flow Visualization: Techniques and Examples* (eds A. J. Smits & T. T. Lim). London: Imperial College Press.
- [2] SARPKEYA, T. 2001 Hydrodynamic damping and quasi-coherent structures at large Stokes numbers. *Journal of Fluids and Structures* **15** (to appear).
- [3] BURESTI, G. & LOMBARDI, G. 1999 Application of continuous wavelet transforms to the analysis of experimental turbulent velocity signals. In *Proceedings of the 1st International Symposium on Turbulence and Shear Flow Phenomena*, pp. 767–772. Santa Barbara, CA, U.S.A.
- [4] LUO, S. C., YAZDANI, M. G., CHEW, Y. T. & LEE, T. S. 1994 Effects of incidence and afterbody shape on flow past bluff cylinders. *Journal of Wind Engineering and Industrial Aerodynamics* **53**, 375–399.



- 
- [5] OZONO, S. 1999 Flow control of vortex shedding by a short splitter plate asymmetrically arranged downstream of a cylinder. *Physics of Fluids* **11**, 2928–2934.
- [6] WANG, A.-B., TRÁVNÍČEK, Z. & CHIA, K.-C. 2000 On the relationship of effective Reynolds number and Strouhal number for the laminar vortex shedding of a heated circular cylinder. *Physics of Fluids* **12**, 1401–1410.
- [7] ETIENNE, S., SCOLAN, Y.-M. & MOLIN, B. 1999 Numerical study of flow around an array of circular cylinders at high Reynolds number. In *Proceedings of the 7th International Conference on Numerical Ship Hydrodynamics*. Nantes.
- [8] ANAGNOSTOPOULOS, P. 2000 Numerical study of the flow past a cylinder excited transversely to the incident stream. *Journal of Fluids and Structures* **14**, 819–882.
- [9] PAN, L. S., CHEW, Y. T. & LIU, G. R. 2001 A general formula for calculating forces acting on a 2-D arbitrary body in any incompressible flows. *Journal of Fluids and Structures* **15** (to appear).
- [10] KANG, S., CHOI, H. & LEE, S. 1999 Laminar flow past a rotating circular cylinder. *Physics of Fluids* **11**, 3312–3321.
- [11] JARŻA, A. & TARNOWSKI, T. 1999 Turbulent flow around circular cylinder in oscillatory inlet conditions. *Transactions of the IFFM* **105**, 3–16.
- [12] RODRIGUEZ, O. 1997 Experimental analysis of the wake instabilities of an oscillating cylinder near synchronisation: influence of the amplitude parameter. In: *Proceedings of the 7th International Offshore and Polar Engineering Conference — Vol. III*, pp. 694–701. Golden, CO: International Society of Offshore and Polar Engineers.
- [13] GHIDERSA, B. & DUŠEK, J. 2000 Breaking of axisymmetry and onset of unsteadiness in the wake of a sphere. *Journal of Fluid Mechanics* **423**, 33–69.
- [14] VALLÈS, B., ANDERSSON, H. I. & JENSSSEN, C. B. 2001 Oblique vortex shedding behind tapered cylinders. *Journal of Fluids and Structures* (submitted).
- [15] PERSILLON, H. & BRAZA, M. 1998 Physical analysis of the transition to turbulence in the wake of a circular cylinder by three-dimensional Navier–Stokes simulation. *Journal of Fluid Mechanics* **365**, 23–88.
- [16] CADOT, O. & KUMAR, S. 2000 Experimental characterization of viscoelastic effects on two- and three-dimensional shear instabilities. *Journal of Fluid Mechanics* **416**, 151–172.
- [17] SIQUEIRA, C. L. R., MENEGHINI, J. R. & SALTARA, F. 2000 Three-dimensional simulation of the flow about an oscillating circular cylinder at low Reynolds numbers. In *Proceedings of the 2000 ASME Fluids Engineering Division Summer Meeting*. New York: American Society of Mechanical Engineers.
- [18] LALANNE, L., LE GUER, Y. & CREFF, R. 2001 Dynamics of a bifurcating flow within an open heated cavity. *International Journal of Thermal Sciences* (to appear).
- [19] MATHELIN, L., BATAILLE, F. & LALLEMAND, A. 2001 Near wake of a circular cylinder submitted to blowing. Part II: boundary layers evolution. *International Journal of Heat and Mass Transfer* (to appear).
- [20] MITTAL, S. & KUMAR, V. 1999 Finite element study of vortex-induced cross-flow and in-line oscillations of a circular cylinder at low Reynolds numbers. *International Journal for Numerical Methods in Fluids* **31**, 1087–1120.
- [21] PANCHAPAKESAN, N. R. & SORIA, J. 1999 Separation control using surface oscillations — some preliminary results. In *Proceedings of the 2nd Australian Conference on Laser Diagnostics in Fluid Mechanics and Combustion*. Melbourne.
- [22] POSDZIECH, O. & GRUNDMANN, R. 2001 Electromagnetic control of seawater flows around circular cylinders. *European Journal of Mechanics B/Fluids* (submitted).



## SELF-SUSTAINED OSCILLATIONS IN FLOWS AROUND LONG BLUNT PLATES

K. HOURIGAN, M. C. THOMPSON AND B. T. TAN

*Fluids Laboratory for Aeronautical and Industrial Research (FLAIR)  
Department of Mechanical Engineering, Monash University  
Clayton, 3800, Australia*

(Received 10 September 2000, and in final form 10 November 2000)

The presence of flow separation from both leading and trailing edges of elongated bluff bodies leads to vortex interactions and resonances not observed in shorter bodies such as circular and square cylinders. Stepwise behaviour in the Strouhal number with increasing plate chord-to-thickness ratio has been observed for long bodies in a number of different situations: natural shedding, under transverse forcing, and with excited duct modes. In the present study, an investigation is made of the predicted unforced laminar flow around long plates (up to chord,  $c$ , to thickness,  $t$ , ratio  $c/t = 16$ ). The two main types of plate geometry considered are rectangular plates and plates with an aerodynamic leading edge. The rectangular plate represents a geometrical extension of the normal flat and square plates. The aerodynamic leading-edge plate is a natural precursor to the rectangular plate because the vortex shedding is only from the trailing edge. The natural flow around rectangular plates is of greater complexity due to the interaction between the leading- and trailing-edge shedding. The previously neglected influence of the trailing-edge vortex shedding is found to play an important role in the stepwise progression of the Strouhal number with chord-to-thickness ratio. In addition, the formation of three-dimensional patterns in the boundary layer along the plate and in the trailing-edge wake is predicted. The predicted boundary layer hairpin vortices are compared with previous observations and the predicted streamwise modes in the wake are compared with those found in the case of circular cylinders.

© 2001 Academic Press

### 1. INTRODUCTION

THE FLOW around elongated bluff bodies, even of simple geometries such as rectangular plates, can result in a number of different local instabilities. Moreover, the complexity of the flow is increased as a result of interaction between upstream and downstream flow structures and the interaction of flow and solid structures. These interactions can lead to global instabilities arising in the flow. In this paper, we explore some of the different two- and three-dimensional instabilities that occur in flow around two-dimensional blunt plates at relatively low Reynolds number.

Instability in the wake is present in most bluff bodies above a critical Reynolds number. With long bluff bodies, it is possible for the flow to separate at the leading edge and reattach while shedding large-scale vortices. A detailed investigation into the nature of this separated and reattaching flow is found in Cherry *et al.* (1984). Two instabilities are involved: the Kelvin–Helmholtz instability present in the shear layer; and the instability causing the large-scale shedding. In combination, there is a weak flapping of the shear layer and an irregularity of shedding. Experiments by Soria *et al.* (1993) used long rectangular plates to isolate any trailing edge effects. The separating and reattaching flow was shown to be

predominantly convectively unstable and receptive to a broad range of frequencies. The weak flapping of the shear layer without external perturbation could be the result of regions of local absolute instabilities.

Another type of global instability occurs when a local convective instability interacts with a solid boundary downstream. Disturbances from the object downstream propagate upstream to complete a feedback loop. For a rectangular plate, this phenomenon is observed when the shear layer from the leading edge is influenced by the trailing edge. This type of instability is similar to when jet or mixing layers impinge on some downstream geometry, for example a bluff body, wall or sharp edge. A comprehensive review is found in Rockwell & Naudascher (1979). The concept of global instability was associated with these sorts of flows by Rockwell (1990).

The flow around rectangular plates in the absence of any external forcing has been studied previously both experimentally and numerically (Nakamura *et al.* 1991; Ohya *et al.* 1992). The vortex shedding from the leading edge of the plate generally locked to a single frequency at low Reynolds numbers [up to  $Re \sim 3000$ , Nakamura *et al.* (1991)]. This instability was thought to rely on the interaction of the leading-edge vortices with the trailing edge to generate a pressure pulse. This pulse locks the leading-edge shedding and completes the feedback loop. The pressure pulse is relatively weak and therefore this locked response is restricted to low Reynolds numbers and only a limited range of chord-to-thickness ratios. It was initially classified as an impinging shear layer (ISL) instability by Nakamura & Nakashima (1986) and Nakamura *et al.* (1991) because in some cases (where the chord-to-thickness ratios were low), the shear layer directly interacted with the trailing edge; this has similarities with the instability in cavity flows. Later studies (Naudascher & Wang 1993; Hourigan *et al.* 1993; Naudascher & Rockwell 1994; Mills *et al.* 1995; Mills 1998; Tan *et al.* 1998) preferred the description impinging leading-edge vortex (ILEV) instability because it better describes the process wherein leading-edge vortices are shed, convected downstream and then interact with the trailing edge. A result of this instability is the occurrence of distinct integer shedding modes (denoted by  $n$ , the number of pairs of vortices distributed along the plate at any time). Observationally, as the plate chord-to-thickness ratio is increased, the Strouhal number of vortex shedding based on chord ( $St_c$ ) shows a stepwise response with each subsequent step corresponding to a higher shedding mode.

In the studies undertaken previously on the natural shedding modes for elongated plates, the presence of trailing-edge vortex shedding was generally not observed or included in discussions. In the case of Ohya *et al.* (1992) where it was observed, the trailing-edge shedding was not considered to be part of the feedback loop but merely led to contamination of the downstream wake. The present study approaches the problem of natural shedding modes from a different perspective in order to establish the importance of trailing-edge shedding to the self-sustained oscillations. As a starting point, the case of a blunt plate with an aerodynamic leading edge is investigated numerically to understand the trailing-edge shedding in the absence of upstream vortex interference. Then, the two-dimensional flow around rectangular plates is studied with a view to understanding the role of the leading-edge vortices in interfering with the trailing-edge shedding and the occurrence of frequency stepping. Finally, some predictions are undertaken to confirm the continued presence of trailing-edge vortex shedding and the locking of the vortex shedding when extended to three dimensions. In addition, the formation of three-dimensional patterns in the boundary layer along the plate, and in the trailing-edge wake, are investigated. The boundary layer hairpin vortical structures are compared with those from the experiments of Sasaki & Kiya (1991) and the predicted streamwise modes in the wake are compared with those found in the case of circular cylinders (Williamson 1988; Thompson *et al.* 1996; Barkley & Henderson 1996).

## 2. NUMERICAL METHOD

The wake of a fixed circular cylinder has been well characterised over the transition region (Reynolds number ranging from 180 to 300). Following the pioneering numerical work of Karniadakis & Triantafyllou (1992), Thompson *et al.* (1994, 1996) first predicted the wavelengths of both wake Modes, A and B, and validated those against the rigorous measurements of Williamson (1988). The spectral-element method used in that study was employed in the current study. The spectral-element method is a high-order finite-element approach. Within each element, the nodes correspond to Gauss-Lobatto points and Gauss-Legendre-Lobatto quadrature is used to approximate the integrations over elements resulting from the application of the Galerkin finite-element method to the Navier-Stokes equations. For high-order elements, this approach is far more economical than equispaced nodes, while still maintaining the spectral convergence rate.

The time-stepping method used was a classical three-step approach described by Karniadakis *et al.* (1991). In the spanwise direction for the three-dimensional predictions, a Fourier expansion was used, resulting in the equations decoupling for each Fourier mode.

The conditions applied at the boundaries of the computational domain were: (i) no slip on the plate; (ii) zero normal velocity derivative at the outflow boundary; and (iii) on the side and inflow boundary, the velocity was taken as uniform in the horizontal direction. A typical computational mesh displaying the macro-elements employed for the elliptical leading-edge plate is shown in Figure 1.

Before the detailed investigation into the flow around long plates was undertaken, some preliminary simulations were performed to determine an adequate domain size and resolution. For flow around bluff bodies, the predictions of surface pressure can be significantly altered if the boundaries are too close to the body (Barkley & Henderson 1996). The two-dimensional simulations were intended to produce quantitative predictions of base pressure and forces on the plate and therefore some preliminary simulations were performed to determine an adequate domain size. The resolution was confirmed to be adequate (to within 2%) by performing simulations with higher spatial and temporal resolution.

## 3. RESULTS AND DISCUSSION

Figure 2 shows schematics of the long plates studied together with their associated flow features. The flow around plates with only trailing-edge vortex shedding was investigated as a precursor to the study of flows around rectangular plates.

### 3.1. FLOW AROUND ELLIPTICAL LEADING-EDGE PLATES

The shedding frequency predicted by the simulation was compared with the results obtained experimentally by Eisenlohr & Eckelmann (1988). Simulations were performed for a plate with  $c/t = 7.5$  between  $Re = 200$  and  $700$ ; the leading edge was semi-elliptical with a 5:1 axes ratio. The shedding frequency was extracted from the base pressure trace, which in all these cases asymptoted to a periodic state.

Eisenlohr & Eckelmann (1988) found a correlation between the reduced shedding frequency ( $F_r$ ) and the Reynolds number ( $Re_r$ ) if the characteristic length was taken as the plate thickness plus twice the displacement thickness at the trailing edge. The simulations were in good agreement with these results (see Figure 3). The plots show that the rate of increase of  $F_r$  with  $Re_r$  is visually indistinguishable between the predictions and experiments. The predicted  $F_r$  at all but the lowest Reynolds number simulated were within the range of experimental uncertainty. This demonstrated that the simulation was able to

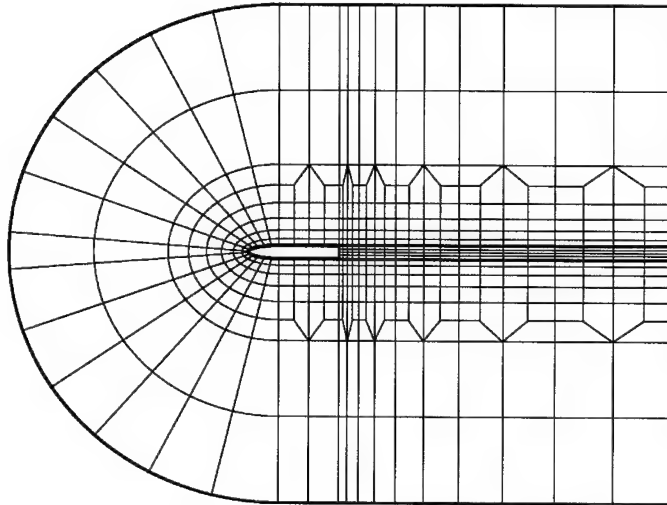


Figure 1. The computational mesh showing the macro-elements for an elliptical leading-edge plate with  $c/t = 7.5$ .

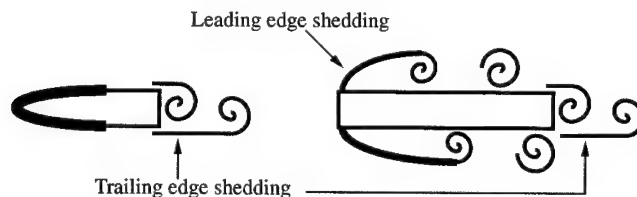


Figure 2. A sketch of the vortical flow structures for flow past an elliptical leading-edge plate and a rectangular plate.

capture most of the experimental trends; differences may have been due to the much longer plates and higher Reynolds numbers (resulting in three dimensionality) used in the experiments.

### 3.2. LEADING- AND TRAILING-EDGE SHEDDING: RECTANGULAR PLATES

#### 3.2.1. Simulation results

Several simulations were performed to study the effect of Reynolds number. Flow around plates with chord-to-thickness ratios of  $c/t = 3$  and 10 were simulated at  $Re = 300, 400$  and 500. All simulations with  $c/t = 3$  locked to the first shedding mode ( $n = 1$ ) while at  $c/t = 10$ , the flow locked to the third shedding mode ( $n = 3$ ) when  $Re = 300$  and 400. At  $Re = 400$ , there were small fluctuations between periods in the base pressure trace and at  $Re = 500$ , the flow no longer locked to a particular shedding mode; there were several frequencies present in the base pressure trace. When the flow was locked to a particular mode, varying the Reynolds number had only a small influence on the shedding frequency (i.e., less than 10%). Nakamura *et al.* (1991) also found that the shedding frequency was independent of Reynolds number when this mechanism locked the flow. The base pressure trace showed that the mean and standard deviation increased with Reynolds number for all cases where

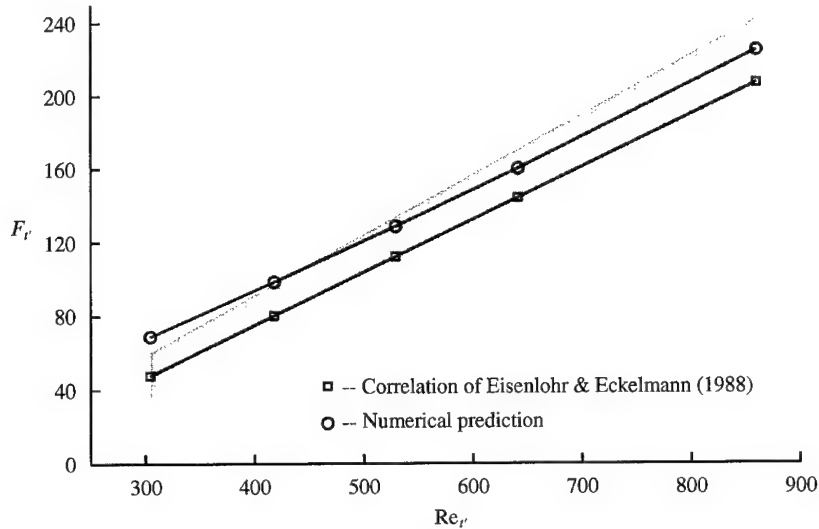


Figure 3. A plot of the nondimensional shedding frequency,  $F_v$ , as a function of the Reynolds number  $Re_v$  for the flow around an elliptical leading-edge plate with  $c/t = 7.5$ . The correlation obtained from experiments by Eisenlohr & Eckelmann (1988) is plotted for comparison. The shaded region is indicative of the spread in the experimental data.

the flow was locked. There was a drop in the mean and standard deviation when the Reynolds number was increased and the flow no longer locked to a shedding mode.

Next, the chord-to-thickness ratio was systematically varied in unit increments from  $c/t = 3$  to 16 at  $Re = 400$ . The flow locked to a shedding mode for each  $c/t$  between 3 and 10 and also at  $c/t = 13$ . Vorticity plots in Figure 4 show that for  $c/t = 3-5$ , the vortex shedding locked to  $n = 1$ ; for  $c/t = 6-8$ , it locked to  $n = 2$ ; for  $c/t = 9$  and 10, it locked to  $n = 3$ ; and for  $c/t = 13$ , it locked to  $n = 4$ . The Strouhal number based on chord approximately corresponds to  $St_c = 0.55n$  for all these cases. The factor 0.55 represents the mean convection velocity, normalized by the free-stream velocity, of the vortices along the plate. The base pressure trace in Figure 5 shows a higher level of fluctuation between periods towards the higher chord-to-thickness ratio end of each shedding mode. The spectrum taken from the base pressure trace when  $c/t = 11$  (not locked) was found to contain three frequencies, one corresponding to the  $n = 3$  shedding mode, another to a frequency that was in the middle of the  $n = 2$  and 3 shedding mode, plus a third corresponding to the nonlinear interaction between these two modes.

The effect of the global instability is also seen in the variation of the base pressure and forces on the plate (see Figure 6). The mean base suction and drag forces are generally higher at the lower  $c/t$  end of the step and decrease with  $c/t$ . This trend continues even to chord-to-thickness ratios that no longer lock to a single frequency. The standard deviation of lift coefficient varies approximately in inverse proportion to  $c/t$ .

Animations of the predicted pressure fields show that the large stepwise changes in the base pressure as the plate chord-to-thickness ratio is increased are due to the return of strong trailing-edge vortex shedding. With increasing chord-to-thickness ratio, the leading-edge vortices are increasingly diffused by the time they reach the trailing edge. When the flow is strongly locked, the leading-edge vortices move almost parallel to the plate into the wake. The dominant fluctuation in pressure at the trailing edge is due to the intense formation and shedding of trailing-edge vortices. An instantaneous plot of the pressure field of the locked flow for  $c/t = 10$  is shown in Figure 7. At the trailing edge, more intense

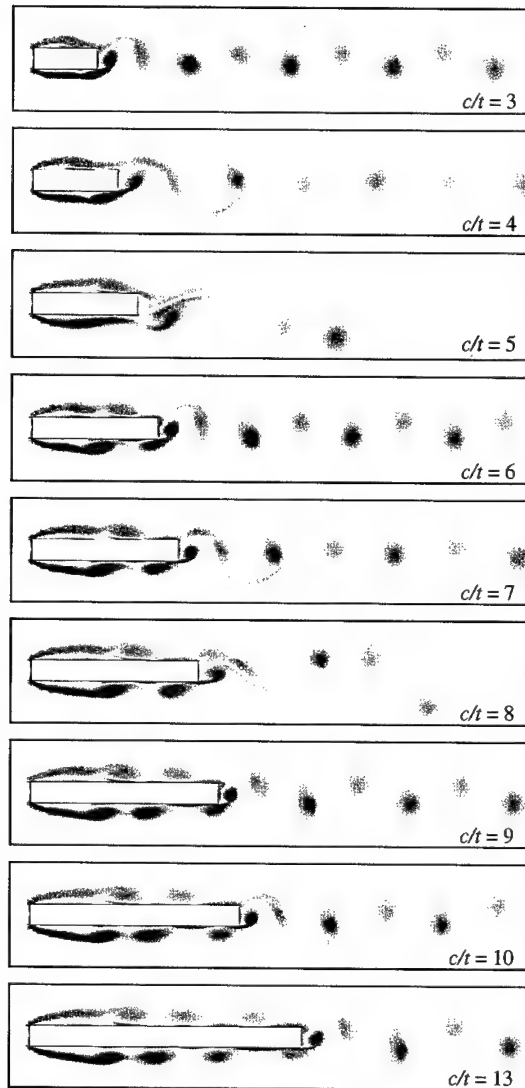


Figure 4. Vorticity plots of flow around rectangular plates at  $Re = 400$  taken at approximately the same phase in the shedding cycle for the various chord-to-thickness ratios.

structures are seen to be forming and shedding while the more diffuse leading-edge vortices pass over the top and are merged further downstream. For all the chord-to-thickness ratios, the trailing-edge vortex shedding provided the strong pressure fluctuations at the trailing edge while the leading-edge vortices sometimes acted to frustrate the regularity of this shedding.

### 3.2.2. On the controlling mechanism

Previous studies and classification associated with the flow around long rectangular plates did not include the important role of shedding from the trailing edge (Nakamura *et al.* 1991; Ozono *et al.* 1992; Naudascher & Wang 1993). In the current simulations, although weak

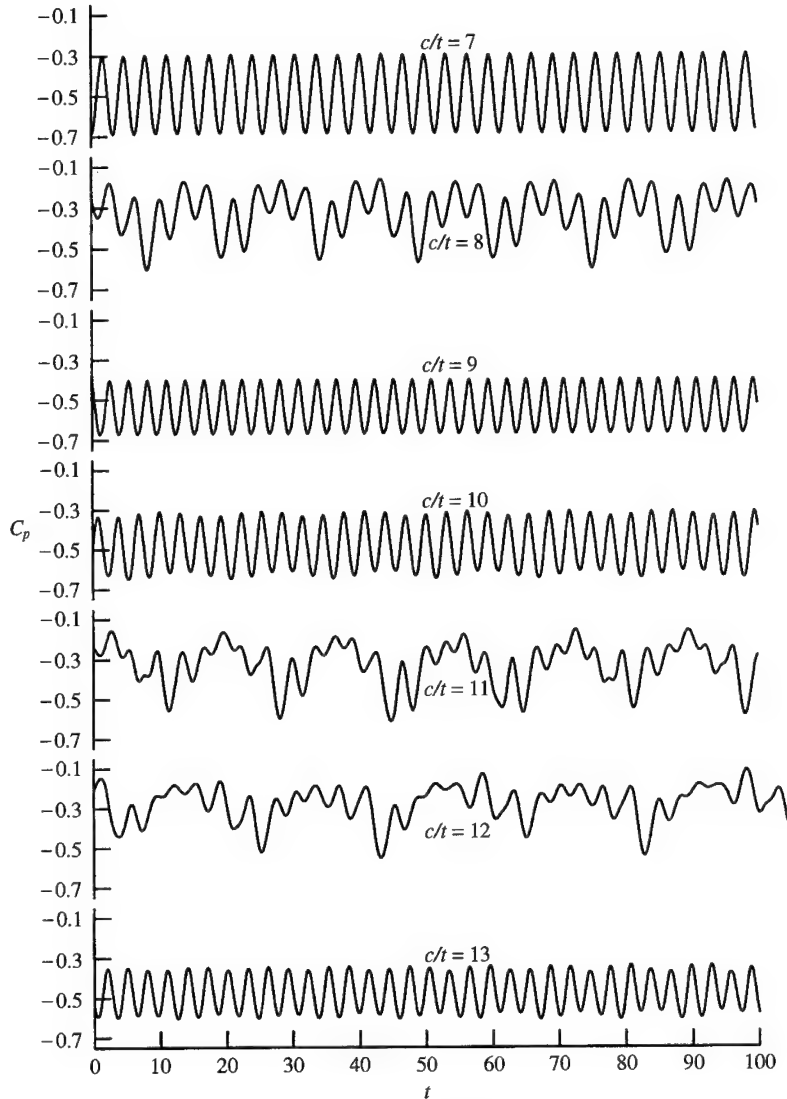


Figure 5. A sample of 100 time units of the base pressure coefficient,  $C_p$ , trace for flow around rectangular plates at different chord-to-thickness ratios at  $Re = 400$ .

pressure fluctuations would occur when the leading-edge vortices pass the trailing edge, strong base shedding is also observed leading to more significant pressure fluctuations. This is seen in the large mean and fluctuating components in base pressure. A description of the different feedback processes for bluff bodies is shown in Figure 8. For short bodies, the leading-edge shear layer can impinge directly on the trailing edge. For longer bodies, vortices are shed from the shear layer at the leading edge. These vortices convect along the plate and interact with the trailing edge. For bodies with streamlined trailing edges [for example, the  $\vdash$  section and a wide variety of bluff bodies such as cylinders and square sections fitted with splitter plates (Nakamura 1996)], the leading-edge vortices generate a pressure pulse as they pass the trailing edge. However, for the bodies with bluff trailing edges as in the present case, the leading-edge vortices interact with the shedding at the



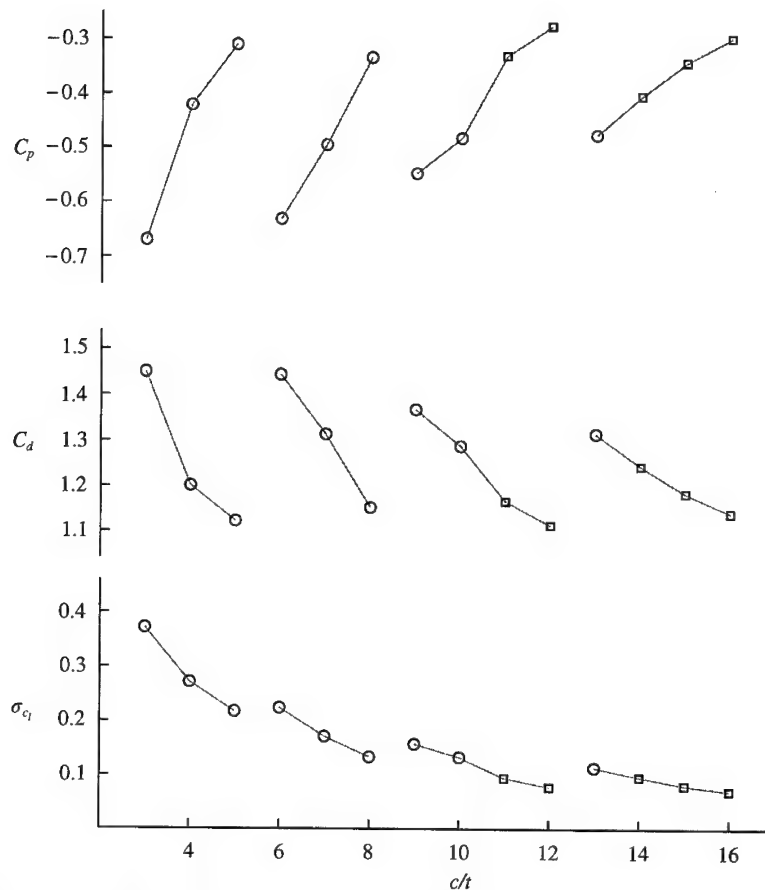


Figure 6. Mean base pressure coefficient,  $C_p$ , mean drag coefficient,  $C_d$ , and standard deviation of lift coefficient,  $\sigma_{C_l}$ , as a function of the chord-to-thickness ratio for flow around rectangular plates at  $Re = 400$ . The circular symbols represent cases where the flow shows an association with a particular shedding mode while the squares represent the cases where the flow is not strictly locked to any one shedding mode.

trailing edge. That is, trailing-edge vortices can only form between the passing of leading-edge vortices. Vortices at the trailing edge form from the redeveloped thin boundary layer between vortices, in a manner similar to their formation for the elliptical leading-edge case. The leading-edge vortices punctuate the redeveloped boundary layer and restrict the phases at which trailing-edge shedding can occur. The pressure pulse from the vigorous base shedding then feeds back upstream and controls the leading-edge shedding. The global instability in this case, therefore, consists of a combination of impinging leading-edge vortex shedding (ILEV) and trailing-edge vortex shedding (TEVS).

### 3.3. THREE-DIMENSIONAL SIMULATIONS

A limited number of three-dimensional flow simulations were performed to study the transitional states for flow around elliptical leading-edge and rectangular plates. The Reynolds numbers in these simulations were chosen to be slightly in excess of the values at which transition from two- to three-dimensional flow occurs. In the aerodynamic leading-edge plate case, the transition in the wake was examined. The spanwise instability of leading-edge vortices was the focus in simulations involving rectangular plates. The nature

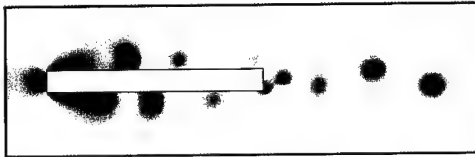


Figure 7. Instantaneous pressure field for a plate with  $c/t = 10$ . Blue indicates lower pressure, generally indicative of vortex structures, and red higher pressure.

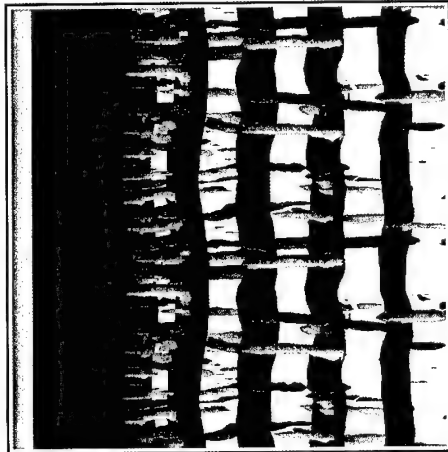
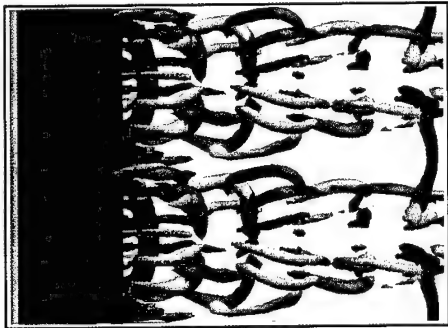


Figure 9. Isosurface plots for predicted flow (left to right) past an elliptical leading-edge plate with  $c/t = 2.5$  for  $Re = 300$  (top) and  $Re = 380$  (bottom). The nondimensionalized values of the kinematic pressure (blue) are  $-0.25$  (top) and  $-0.20$  (bottom), and the streamwise vorticity (red and gray)  $\pm 1.0$  (top) and  $\pm 1.2$  (bottom).

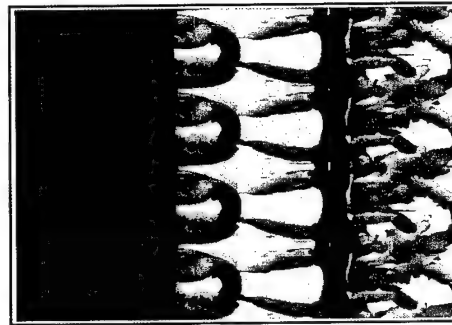


Figure 10. Isosurface plot for predicted flow (left to right) around a rectangular plate with  $c/t = 13$  at  $Re = 350$  viewed from the top. The normalized value of the isosurface of kinematic pressure is at  $-0.15$  and the values of the streamwise vorticity are at  $\pm 0.8$ . Note that the simulated spanwise domain has been doubled for this visualization (and also for Figure 9).

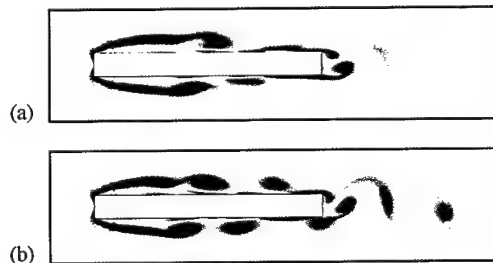


Figure 11. Vorticity plots of flow past a rectangular plate with  $c/t = 10$  and  $Re = 350$ . The top plot, (a), shows span-averaged vorticity from a three-dimensional simulation. The bottom plot, (b), shows the corresponding vorticity field from a two-dimensional simulation. Opposite-signed vorticity is coloured red and blue.

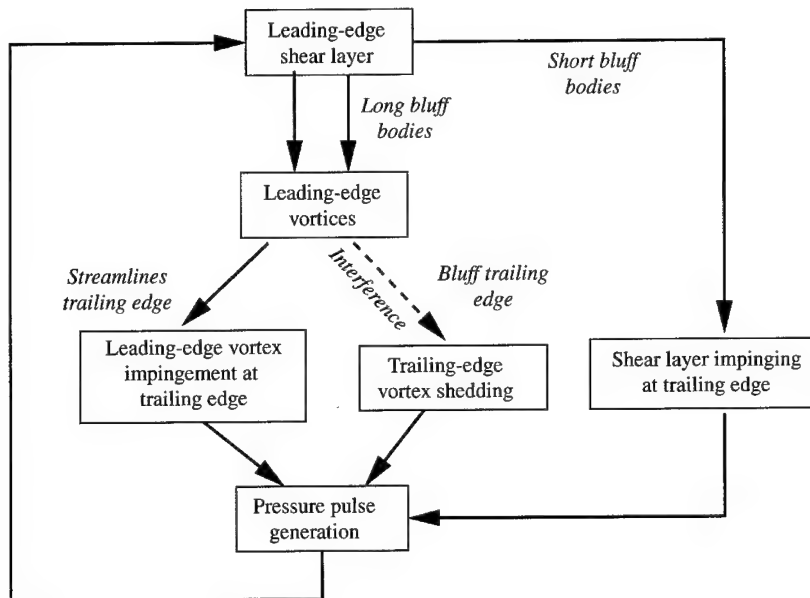


Figure 8. Schematic of feedback loops of locked vortex shedding for blunt leading-edge plates with either blunt or streamlined trailing edges.

of the technique used here enforced periodic boundary conditions on the spanwise boundaries. This allowed only discrete spanwise wavelengths (which is more restrictive for instabilities of longer wavelengths) to be captured.

### 3.3.1. Elliptical leading-edge plates

Simulations were performed for the flow around elliptical leading-edge plates with a 5:1 axes ratio and ratios of  $c/t = 7.5$  and  $2.5$ . Two spanwise wake shedding modes were observed similar to Modes A and B for a circular cylinder (Williamson 1988). The spanwise wavelengths in the current simulations were generally larger for these plates possibly due to the thicker boundary layers near the trailing edge and the resulting vortices being more diffused.

Simulations with  $c/t = 2.5$  have captured the two shedding modes in the transition process. The simulation captured a long wavelength flow structure at  $Re = 300$  with topology consistent with Mode A shedding (see Figure 9). As only one wavelength of this flow structure was captured within the domain ( $2\pi t$ ), there is some uncertainty as to which is the most unstable wavelength. There are smaller wavelengths that develop in certain shedding cycles. This could be either a competition between shedding modes or a result of the restrictive domain. At  $Re = 350$ , Mode A shedding is suppressed and the presence of some (streamwise vortical) flow structures consistent with Mode B shedding is apparent. The wavelength of these structures is uncertain because they are sporadic and not uniform across the span. When the Reynolds number is increased to  $Re = 380$ , these structures become more intense and more regular (also see Figure 9). These flow structures have a spanwise wavelength of approximately  $0.8t$ . The simulations were able to capture three-dimensional vortical structures with topology similar to Mode A at  $Re = 500$  and  $c/t = 7.5$ .

### 3.3.2. Rectangular plates

The flows around rectangular plates with  $c/t = 6, 10$  and  $13$  were simulated at  $Re = 350$  and  $400$ . No boundary layer spanwise instability was observed in the simulations with  $c/t = 6$ . Flow structures similar to those classified as Pattern B by Sasaki & Kiya (1991) were observed when  $c/t = 10$  and  $13$  at both  $Re = 350$  (see Figure 10) and  $400$ . These were hairpin-like structures arranged in a staggered manner on both sides of the plate. In all cases, two wavelengths were captured in the domain and therefore the spanwise wavelength was approximately  $3t$ . (Again, because of the discrete Fourier mode description, there is some uncertainty in this estimate.) The streamwise wavelengths were approximately  $3t$  when  $c/t = 10$  and  $4t$  when  $c/t = 13$ . Both the streamwise and spanwise wavelengths are within the range of experimental uncertainty of those observed experimentally (Sasaki & Kiya 1991). Pattern A shedding (vortices aligned) has been more difficult to capture, possibly due to the shorter plate lengths employed in the simulations.

### 3.3.3. Comparison with two-dimensional simulations

In this section, several flow characteristics of the two- and three-dimensional simulations are compared. A motivation for this is to demonstrate that the two-dimensional simulations are semi-quantitatively correct even when the flow has undergone transition. The case considered here is the flow past a rectangular plate with  $c/t = 10$  and  $Re = 350$ . The computational domain and resolution on a two-dimensional plane was identical in both cases. The Strouhal numbers,  $St$ , in the two- and three-dimensional cases were  $St = 0.170$  and  $0.174$ , respectively. Figure 11 shows a comparison of the two-dimensional flow structures between the two- and three-dimensional simulations. The three-dimensional simulation is reduced to a two-dimensional plane by averaging across the span. The vorticity plots clearly show that both cases are locked to the third,  $n = 3$ , shedding mode. The main difference between the plots is the more diffuse leading-edge vortices in the three-dimensional case. Importantly, from the point of view of the controlling mechanism, as for the two-dimensional simulation, strong base shedding is also observed with trailing-edge vortices seen to form from the redeveloped boundary layer between the passing of leading-edge vortices.

## 4. CONCLUSIONS

A series of simulations of flows around blunt plates have been undertaken to test the hypothesis that the trailing-edge shedding plays an important role in the self-sustained oscillations observed in flows around rectangular plates. First, the flow around plates of different chord-to-thickness ratios, with elliptical leading and square trailing edges, was studied. No leading-edge vortex shedding was present and strong periodic trailing-edge shedding was found with frequency in line with previous observations. Next, the flow around rectangular plates of various chord-to-thickness ratios was investigated. Self-sustained oscillations were found to occur which, for most chord-to-thickness ratios, were strictly periodic. Distinct vortex shedding from both the leading and trailing edges was observed. It is concluded that the preferred frequency of oscillation (i.e., both leading- and trailing-edge shedding) is that of the trailing-edge shedding. However, the leading-edge vortices punctuate the redeveloped boundary layer on the plate surface from which the trailing-edge vortices form. As the plate chord-to-thickness ratio is increased, this results in a gradual decrease in the possible trailing-edge shedding frequency until the preferred frequency is again possible; at this stage, the frequency undergoes a step change. The three-dimensional simulations show three-dimensional structures forming both along the

plate surface and in the wake. The spanwise-averaged flow, however, shows a distribution of structures similar to the two-dimensional flow, including strong trailing-edge vortex shedding. Pattern B vortical structures along the plate, and Modes A and B structures in the wake, each similar to those observed previously experimentally, have been captured by the simulations.

In some other flows where there is an absence of trailing-edge vortex shedding, the mechanism leading to self-sustained oscillations may in fact be the feedback loop generated by the impinging shear layer or the impinging leading-edge vortices. Although neglected in previous studies of flows around rectangular plates, it would appear that the trailing-edge shedding is a powerful influence on the self-sustained oscillations observed at lower Reynolds numbers. It is concluded in these cases that the global instability is a combination of the impinging shear layer instability (ILEV) and the trailing-edge vortex shedding instability (TEVS).

### ACKNOWLEDGEMENTS

The Australian Research Council is thanked for supporting these studies through Small and Large Grants. Mr Tan Boon Thong acknowledges the support of a Monash Graduate Scholarship and an International Postgraduate Research Scholarship.

### REFERENCES

- BARKLEY, D. & HENDERSON, R. D. 1996 Three-dimensional Floquet stability analysis of the wake of a circular cylinder. *Journal of Fluid Mechanics* **322**, 215–241.
- CHERRY, N. J., HILLIER, R. & LATOUR, M. E. M. P. 1984 Unsteady measurements in a separated and reattaching flow. *Journal of Fluid Mechanics* **144**, 13–46.
- EISENLOHR, H. & ECKELMANN, H. 1988 Observations in the laminar wake of a thin flat plate with a blunt trailing edge. In *Proceedings of the Conference on Experimental Heat Transfer, Fluid Mechanics and Thermodynamics* (eds R. K. Shah, E. N. Ganic & K. T. Yang), pp. 264–268, 4–9 September, Dubrovnik, Yugoslavia.
- HOURIGAN, K., MILLS, R., THOMPSON, M. C., SHERIDAN, J., DILIN, P. & WELSH, M. C. 1993 Base pressure coefficients for flows around rectangular plates. *Journal of Wind Engineering and Industrial Aerodynamics* **49**, 311–318.
- KARNIADAKIS, G. E., ISRAELI, M. & ORSZAG, S. A. 1991 High-order splitting methods for the incompressible Navier–Stokes equations. *Journal of Computational Physics* **97**, 414–443.
- KARNIADAKIS, G. E. & TRIANTAFYLLOU, G. S. 1992 Three-dimensional dynamics and transition to turbulence in the wake of bluff objects. *Journal of Fluid Mechanics* **238**, 1–30.
- MILLS, R., SHERIDAN, J., HOURIGAN, K. & WELSH, M. C. 1995 The mechanism controlling vortex shedding from rectangular bluff bodies. In *Proceedings of the 12th Australasian Fluid Mechanics Conference* (ed. R. W. Bilger), pp. 227–230, 10–15 December, Sydney, Australia.
- MILLS, R. H. 1998 Vortex interaction in flows over bluff bodies. Ph.D. Dissertation, Department of Mechanical Engineering, Monash University, Melbourne, Australia.
- NAKAMURA, Y. 1996 Vortex shedding from bluff bodies with splitter plates. *Journal of Fluids and Structures* **10**, 147–158.
- NAKAMURA, Y., OHYA, Y. & TSURUTA, H. 1991 Experiments on vortex shedding from flat plates with square leading and trailing edges. *Journal of Fluid Mechanics* **222**, 437–447.
- NAKAMURA, Y. & NAKASHIMA, M. 1986 Vortex excitation of prisms with elongated rectangular, H and  $\vdash$  cross-sections. *Journal of Fluid Mechanics* **163**, 149–169.
- NAUDASCHER, E. & ROCKWELL, D. 1994 *Flow-Induced Vibrations: An Engineering Guide*. Rotterdam: A. A. Balkema.
- NAUDASCHER, E. & WANG, Y. 1993 Flow-induced vibration of prismatic bodies and grids of prisms. *Journal of Fluids and Structures* **7**, 341–373.
- OHYA, Y., NAKAMURA, Y., OZONO, S., TSURUTA, H. & NAKAYAMA, R. 1992 A numerical study of vortex shedding from flat plates with square leading and trailing edges. *Journal of Fluid Mechanics* **236**, 445–460.

- OZONO, S., OHYA, Y., NAKAMURA, Y. & NAKAYAMA, R. 1992 Stepwise increase in the Strouhal number for flows around flat plates. *International Journal of Numerical Methods in Fluids* **15**, 1025–1036.
- ROCKWELL, D. 1990 Active control of globally-unstable separated flows. In *Proceedings of the ASME Symposium on Unsteady Flows*, 3–9 June, Toronto, Canada.
- ROCKWELL, D. & NAUDASCHER, E. 1979 Self-sustained oscillations of impinging free shear layers. *Annual Review of Fluid Mechanics* **11**, 67–94.
- SASAKI, K. & KIYA, M. 1991 Three-dimensional vortex structure in a leading-edge separation bubble at moderate Reynolds numbers. *ASME Journal of Fluids Engineering* **113**, 405–410.
- SORIA, J., SHERIDAN, J. & WU, J. 1993 Spatial evolution of the separated shear layer from a square leading-edge plate. *Journal of Wind Engineering and Industrial Aerodynamics* **49**, 237–246.
- TAN, B. T., THOMPSON, M. C. & HOURIGAN, K. 1998 Flow around long rectangular plates under cross-flow perturbations. *International Journal of Fluid Dynamics* (<http://elecpress.monash.edu.au/IJFD>) **2**, Article 1.
- THOMPSON, M. C., HOURIGAN, K. & SHERIDAN, J. 1994 Three-dimensional instabilities in the wake of a circular cylinder. In *Proceedings of the International Colloquium on Jets, Wakes and Shear Layers*, 18–20 April, Melbourne, Australia.
- THOMPSON, M. C., HOURIGAN, K. & SHERIDAN, J. 1996 Three-dimensional instabilities in the wake of a circular cylinder. *Experimental and Thermal Fluid Science* **12**, 190–196.
- WILLIAMSON, C. H. K. 1988 The existence of two stages in the transition to three-dimensionality of a cylinder wake. *Physics of Fluids* **31**, 3165–3168.

## INTERACTION BETWEEN VORTEX RINGS AND A SEPARATED SHEAR LAYER: TOWARDS ACTIVE CONTROL OF SEPARATION ZONES

M. KIYA, O. MOCHIZUKI AND H. ISHIKAWA

*Graduate School of Engineering, Hokkaido University  
Sapporo, 060-8628, Japan*

(Received 29 August 2000, and in final form 14 November 2000)

The separation zone of an inclined flat plate was reduced by bombarding rolling-up vortices in the separated shear layer with a chain of vortex rings introduced from the side of the main flow. The reduction was realized because a compact and strong vortex is successively formed near the leading edge, transporting high-momentum fluid of the main flow towards the surface. Momentum defect in the near wake, which serves as a measure of effectiveness of reduction in the separation zone and can be approximately interpreted as the drag of the plate, generally decreases with increasing frequency of introduction of the rings  $F$  and their circulation  $\Gamma$ , saturating at sufficiently large values of  $F$  and  $\Gamma$ . The momentum defect appears to attain a minimum at a particular frequency  $Fc/U_\infty \approx 4$ , where  $c$  is the length of the plate and  $U_\infty$  is the main-flow velocity. This frequency can be interpreted as the fundamental frequency of the shedding-type instability of the separated flow. Efficiency, which is defined as decrease in loss of power in the wake divided by the power required to generate the vortex rings, attains a maximum approximately at the same frequency  $Fc/U_\infty \approx 4$ , and at a particular value of the circulation  $\Gamma/U_\infty c \approx 0.32$ , which is approximately 1.6 times the circulation of the shear-layer vortices in the region of interaction. Thus, the steady jet which corresponds to  $F = \infty$  is not the best choice in terms of the efficiency.

© 2001 Academic Press

### 1. INTRODUCTION

ACTIVE CONTROL OF SEPARATED FLOWS around bluff bodies has been made by acoustic wave, suction or blowing, oscillating flaps, moving surfaces, etc. These methods, except the control by acoustic wave, employ actuators installed inside or on the surface of the body. This is not always possible in engineering applications. For example, blades of axial-flow compressors or blowers are not usually thick enough to install such actuators. Active control of separated flow around the blades is of vital importance to improve off-design performance of turbomachinery.

This paper presents a novel method to solve the above problem. In this method self-travelling vortices such as vortex rings or vortex pairs are introduced into separated shear layers from outside to reduce the separation zone. Figures 1 and 2 are flow visualizations which demonstrate the interaction between the external vortices and rolling-up vortices in a separated shear layer (Kiya *et al.*, 1986). Note that the vortex ring and the vortex pair in these figures are introduced from the low-velocity side of the shear layer. The interaction appears to generate rolling-up vortices which are larger than those in the undisturbed shear layer.

The interaction between rolling-up vortices in a plane mixing layer and a vortex pair was studied by numerical simulations to understand essential aspects of the vortex interaction

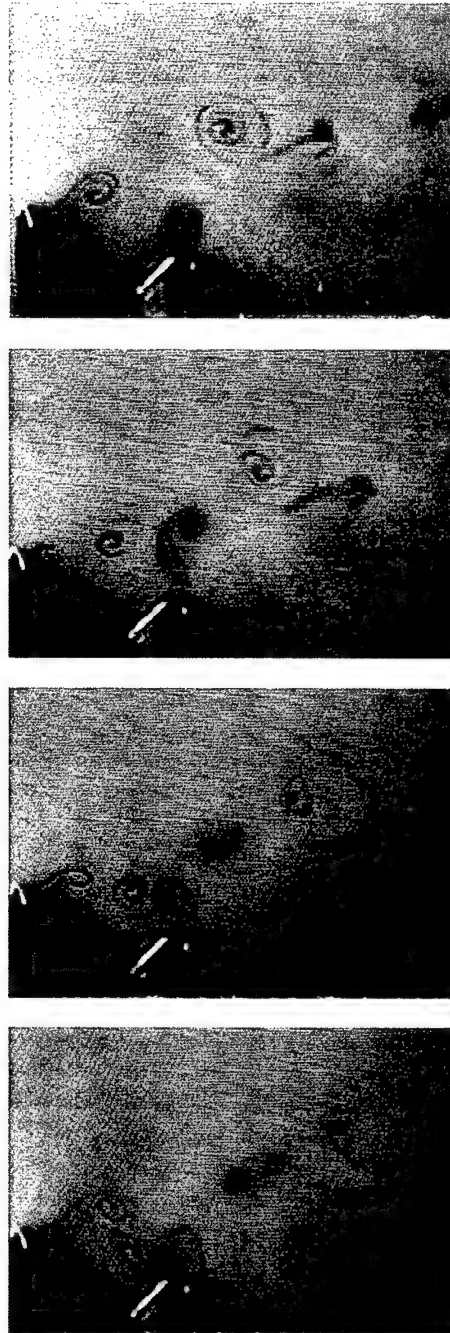


Figure 1. Interaction between a vortex pair and shear-layer vortices (Kiya *et al.*, 1986). Flow is from left to right. Main-flow velocity  $U_\infty = 2.8$  cm/s, height of normal plate  $h = 4.3$  cm, circulation of the vortex pair  $\Gamma_{vp}/(U_\infty h) \approx 0.78$ , circulation of the shear-layer vortices  $\Gamma_{sh}/(U_\infty h) \approx 0.50$  and Reynolds number  $U_\infty h/\nu = 1.2 \times 10^5$ . The time interval between two consecutive photographs is 0.5 s.

(Kiya *et al.* 1999). This two-dimensional interaction induces larger vortices than those in the undisturbed mixing layer, yielding a significant increase of momentum thickness and entrainment rate. Moreover, vortex pairs whose circulation is larger than approximately 2.5



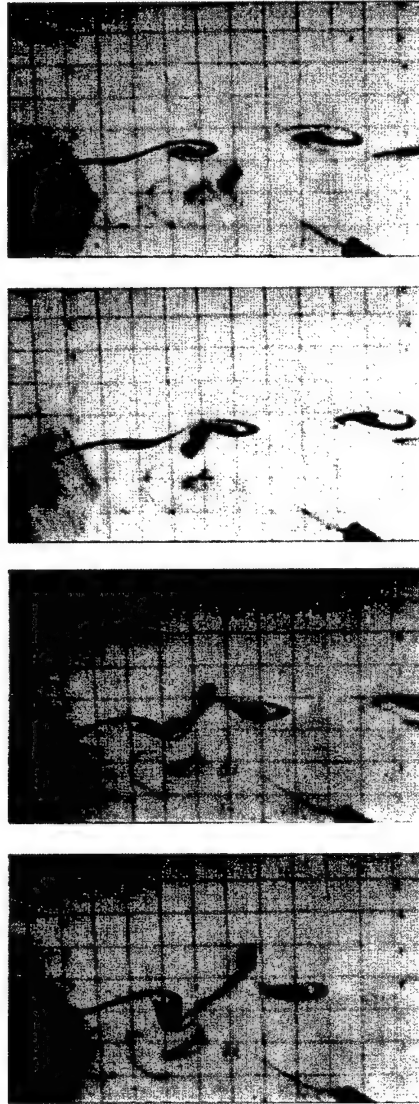


Figure 2. Interaction between a vortex ring and shear-layer vortices (Kiya *et al.*, 1986). Flow is from left to right.  $U_{\infty} = 3.0$  cm/s,  $h = 4.3$  cm, circulation of the vortex ring  $\Gamma_{vr}/(U_{\infty}h) \approx 0.58$ ,  $\Gamma_{sh}/(U_{\infty}h) \approx 0.85$ . The time interval between two consecutive photographs is 0.25 s.

times the circulation of the mixing-layer vortex pass through the mixing layer, leaving more or less the same effect on the mixing-layer vortices.

A problem of using a vortex pair for the control is that it has a mode of instability (Lewke *et al.* 1996), which degenerates the vortex pair to a series of vortex rings. Thus, in engineering applications, the external vortices should be vortex rings. Interaction between vortex rings and shear-layer vortices was studied experimentally by Kiya *et al.* (1986) and Maekawa & Nishioka (1992) and numerically by Kiya & Ishii (1988) and Ishikawa *et al.* (2000). In the Ishikawa *et al.* (2000) simulations, a vortex ring of radius  $R$  and core radius of  $0.155R$  interacts with a rectilinear vortex tube of the same core radius; the Reynolds number based on the diameter  $2R$  and the initial convection velocity of the vortex ring is 300. The

simulations revealed that the vortex ring passes through the vortex tube if the circulation of the vortex ring is approximately 1.5 times the circulation of the vortex filament.

In this paper, vortex rings were introduced into the separated shear layer of an inclined flat plate to reduce the height of the separation zone. A reduction in the height is expected to be accompanied by lower drag and higher lift, and lower level of fluctuating components of these forces. Trajectories of vortex rings ejected into the main flow are shown to have a similarity for different parameters associated with generation of the vortex rings (Suzuki *et al.* 1999), and this similarity was used to introduce the vortex rings into the separated shear layer near the leading edge. Circulation of the vortex rings  $\Gamma$  and frequency of its introduction (shooting frequency)  $F$  were changed to obtain conditions of the greatest reduction in the separation zone. Momentum defect in the near wake of the plate is employed as a measure of effectiveness of the control. Moreover, the mechanism of the reduction is discussed in terms of phase-averaged flow visualizations and phase-averaged velocity distributions.

## 2. EXPERIMENTAL APPARATUS AND METHOD

Experiments were performed in a low-speed, open-return wind tunnel with a 40.0 cm high, 20.0 cm wide and 90.0 cm long working section. The flow was introduced into the working section through a bell entrance of 1:12.6 contraction. The time-mean velocity in the tunnel was uniform within  $\pm 2\%$  in the cross section where the leading edge of a model plate is to be located except the boundary layers on the tunnel walls. The free-stream turbulence intensity was 0.7%.

Vortex rings were produced through a circular orifice of diameter  $d = 5.0$  mm, which were bored through the top wall of the tunnel in the mid-span plane. This orifice was connected to a woofer through a chamber. In the second part of the experiments, which will be described in Section 3.3, two orifices of the same dimensions were added  $6.0d$  apart, on both sides of the above-mentioned orifice; all the five orifices were arranged along a line normal to the main-flow direction, being connected to the woofer through the same chamber. Thus, five vortex rings of the same circulation and dimensions were generated simultaneously.

The woofer was driven by square-wave input from a power unit. The square wave had a period of  $2t_b$ ; in the first half of the period the woofer was in the phase of ejection flow through the orifice, while in the second half the woofer was in the suction phase.

Circulation of the vortex ring generated during one period was obtained in the following way. The cylindrical coordinate  $(\xi, \sigma, \varphi)$ , whose origin is at the centre of the orifice, is defined such that  $\xi$  is the longitudinal distance,  $\sigma$  is the radial distance, and  $\varphi$  is the azimuthal angle about the axis  $\sigma = 0$ . Assuming that the flow in the plane of the orifice is axisymmetric, circulation shed per unit time from the edge of the orifice is given by

$$\frac{d\Gamma}{dt} = \int_{d/2-\delta}^{d/2} \omega_\varphi u_\xi d\sigma, \quad (1)$$

where  $\delta$  is the thickness of the shear layer,  $\omega_\varphi = \partial u_\sigma / \partial \xi - \partial u_\xi / \partial \sigma$  is the azimuthal component of vorticity, and  $u_\xi$  and  $u_\sigma$  are the velocity components in the  $\xi$  and  $\sigma$  directions. The first term in  $\omega_\varphi$  is much smaller than the second term, so that we obtain  $\omega_\varphi u_\xi = -u_\xi(\partial u_\xi / \partial \sigma)$ . Thus, noting that the flow in the suction phase had no contribution to circulation, the circulation of the vortex ring generated during one period of motion of the woofer can be evaluated from

$$\Gamma = \frac{1}{2} \int_0^{t_b} [V_j(t)]^2 dt, \quad (2)$$

where  $V_j(t)$  is the longitudinal velocity component at the edge of the shear layer in the plane of the orifice.

An inclined flat plate of length  $c = 100$  mm was made from an acrylic resin plate of 2.0 mm in thickness, having the semicircular leading and trailing edges. This form of the leading edge was employed to reduce the receptivity of the acoustic wave generated by the motion of the woofer. It is possible that the receptivity might influence the rolling up of the

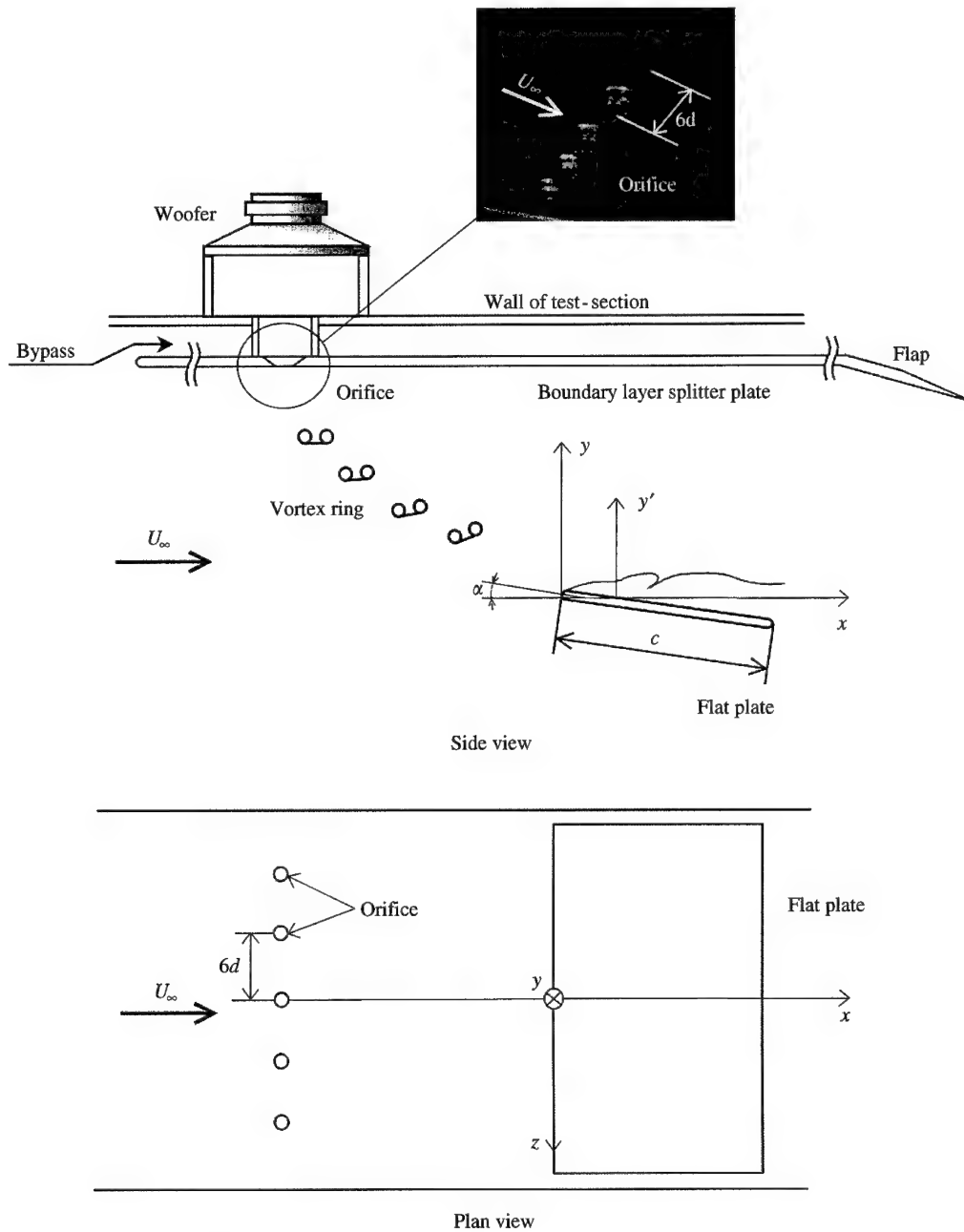


Figure 3. Flow configuration and definition of coordinate system for active control of separation zone of an inclined flat plate by impinging vortex rings.

separated shear layer, making it difficult to differentiate its effects on the separation zone from those of the vortex rings. The plate was fixed at an attack angle  $\alpha = 10^\circ$ , at which the flow separated from the leading edge to reattach to the surface near the trailing edge.

Figure 3 illustrates the flow configuration, and definition of the  $(x, y, z)$  coordinate system and symbols. The  $x$ -axis is in the direction of main flow of velocity  $U_\infty$ ,  $y$  is vertically upward, and  $z$  is in the spanwise direction, the origin being at the leading edge. The distance from the suction surface along the  $y$ -axis is denoted by  $y'$ . The instantaneous velocity components in the  $xy$ -plane and in the  $x$ -direction are denoted by  $q$  and  $u$ , respectively. The leading edge of the plate was located  $15.0d$  below and  $25.0d$  downstream of the centre of the orifice from which the vortex rings were generated.

The velocities were measured by a constant-temperature hot-wire anemometer and a Laser-Doppler velocimeter (LDV). A single hot-wire probe of  $5\text{ }\mu\text{m}$  diameter and working length of  $1\text{ mm}$ , which was parallel to the  $z$ -axis, was used, so that this probe measured the velocity component in the  $(x, y)$  plane  $q$ , whose time-mean value and r.m.s. fluctuations are denoted by  $\bar{q}$  and  $q'$ , respectively. The LDV measured the longitudinal component  $u$ , whose time-mean value is denoted by  $\bar{u}$ .

The vortex rings and their interaction with the separated shear layer were visualized by a smoke-wire technique. Smoke wires were tungsten wires of  $0.1\text{ mm}$  diameter with kinks at intervals of  $2d$ . Flow-visualization photographs were taken in synchronization with fixed phases of generation of the vortex rings.

Reynolds number  $Re (= U_\infty c/\nu, \nu$  being the kinematic viscosity) was 8300. The main-flow velocity was  $1.25\text{ m/s}$ . The frequency of introduction of the vortex rings to the separated shear layer  $F$  was varied in the range of  $Fc/U_\infty = 0\text{--}12$ , while circulation of the vortex rings was in the range of  $\Gamma/(U_\infty c) = 0.20\text{--}0.66$ . Circulation of shear-layer vortices with which the vortex rings interacted,  $\Gamma_{sh}$ , was  $\Gamma_{sh}/(U_\infty c) = 0.21$ , as described in Section 3.1.

### 3. RESULTS AND DISCUSSION

#### 3.1. UNDISTURBED FLOW

Figure 4 shows the flow pattern visualized by smoke particles, the distributions of the time-mean velocities  $\bar{q}$  and  $\bar{u}$  and the r.m.s. velocity fluctuation  $q'$  on the suction side of the plate. The flow separates from the leading edge to form a separation zone. The distributions of  $\bar{u}$  measured by the LDV indicate the reverse flow near the surface. In the reverse-flow region, the distributions of  $\bar{q}$  measured by the hot-wire probe has a definite plateau. The plateau is generated by the rectification of the velocity signal  $u$  in the reverse-flow region. Near a position of  $u = 0$ , the hot-wire signal is expected to attain a broad minimum because the rectification yields a higher signal between this position and the surface. The broad minimum looks like a plateau. It may be noted that the hot-wire signal is not zero at the position of  $u = 0$  due to effects of natural convection and the turbulent velocity component along the probe. Thus, in this paper the plateau is interpreted as an indication of reverse flow. On the basis of this interpretation, the separated shear layer appears to reattach on the surface near the trailing edge. This is partially supported by the fact that the distribution of  $\bar{u}$  in the near wake at  $x/c = 1.14$  indicates no reverse-flow region.

Circulation of rolling-up vortices in the undisturbed shear layer  $\Gamma_{sh}$  can be estimated on the basis of the velocity at the edge of the shear layer  $U_s (= 1.27U_\infty$  at  $U_\infty = 1.25\text{ m/s}$ ) and the fundamental frequency of Kelvin-Helmholtz instability  $f_{KH} = 50\text{ Hz}$ , which was measured at  $x/c = 0.4$ . As seen in Figure 4, the rolling-up vortex in the shear layer first appears between  $x/c = 0.3$  and  $0.4$ . The longitudinal distance between rolling-up vortices near the

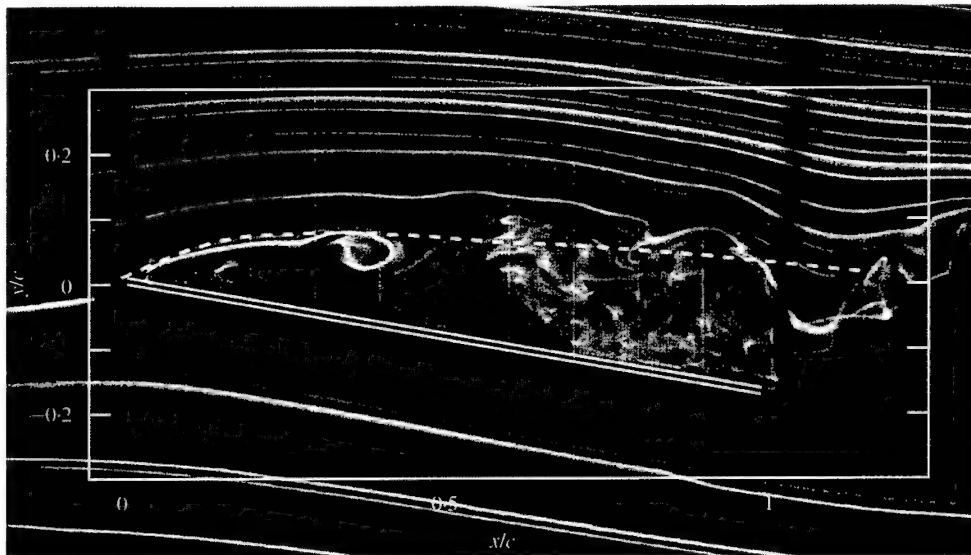
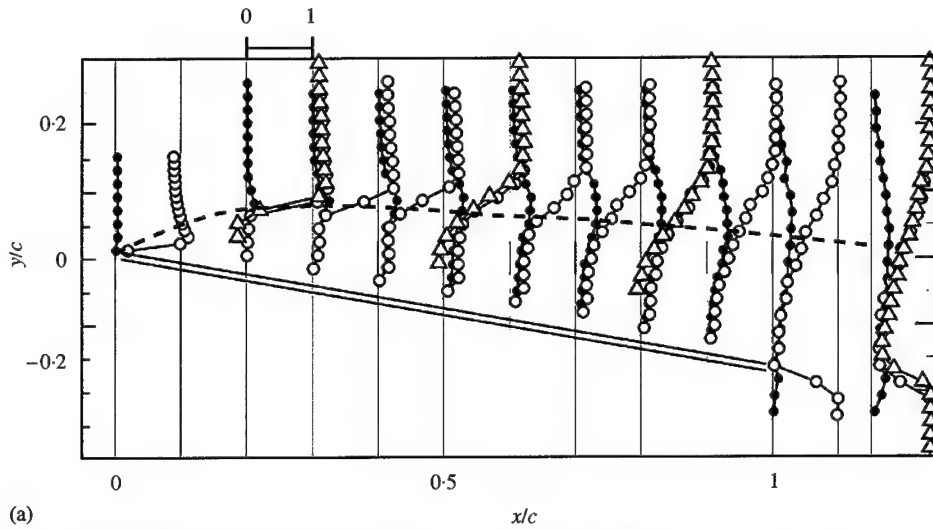


Figure 4. (a) Distributions of time-mean velocities  $\bar{q}$  and  $\bar{u}$ , and r.m.s. velocity fluctuation  $q'$ , and (b) smoke-wire flow visualization for undisturbed separation zone.  $\alpha = 10^\circ$  and  $Re = 8300$ .  $\circ$ ,  $\bar{q}/U_\infty$ ;  $\triangle$ ,  $\bar{u}/U_\infty$ ;  $\bullet$ ,  $q'/U_\infty$ . The broken line shows the centre of the shear layer. The scale of the velocities is shown on top of (a).

leading edge (which will be referred to as KH vortices) is estimated as  $\lambda_{KH} = (U_s/2)/f_{KH} (= 0.16c)$ , with the reasonable assumption that the rolling-up vortices are convected by the velocity  $U_s/2$ . Circulation of the shear layer vortices can be estimated as  $U_s$  times this wavelength, that is,  $\Gamma_{sh}/(U_\infty c) = 0.21$ .

### 3.2. EFFECTS OF VORTEX RINGS ON SEPERATED FLOW

In order to demonstrate the effects of vortex rings on the shear layer, phase-averaged flow visualizations and distributions of phase-averaged velocity  $\bar{q}$  are presented in Figures 5 and 6

for the shooting frequency of  $Fc/U_\infty = 0.80$ . The vortex rings were generated only from the central orifice; the flow visualizations and the velocity measurements were made in the mid-span plane. The phase averaging was made on the basis of waveform of input to the woofer. For convenience the phase  $\phi = 0$  is defined as the instant at which the centre of a vortex ring arrives at the leading edge of the airfoil, while the phase  $\phi = 2\pi$  is the instant at which the next vortex ring arrives at the same position. The velocity distributions and the flow visualizations are shown with the interval of  $\Delta\phi = \pi/3$ . It may be noted that each photograph of Figure 5 is the superposition of 20 realizations; the centre of the vortex ring is indicated by solid triangles on the longitudinal and horizontal scales. The phase-averaged velocity distributions are also the superposition of 20 realizations. It is also worth noting that position of the vortex rings was much clearer in each flow realization than that in the phase-averaged visualization.

The flow patterns in Figure 5 demonstrate the process of interaction between the shear layer and the vortex ring. The vortex ring impinges on the shear layer near the leading edge at  $\phi = \pi/3$ , generating a compact rolling-up vortex whose centre is at  $x/c \approx 2.5$  for  $\phi = 2\pi/3$  [Figure 5(c)]. This compact vortex eliminates the reverse flow on its downstream side to reduce the instantaneous length of the separation zone, as seen from the velocity profile at  $x/c = 0.4$ , by transporting high-momentum fluid of the main flow towards the surface. At the same time, the centre of the shear layer  $y_c$ , which is the  $y$  position of maximum of  $q'$ , shifts towards the surface, yielding a dip in the plot of  $y_c$  against  $x$ .

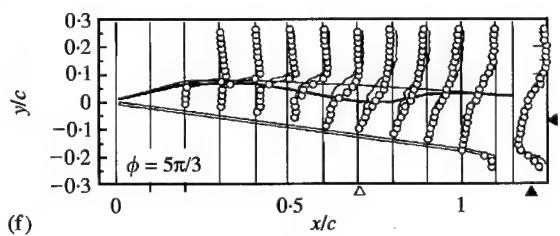
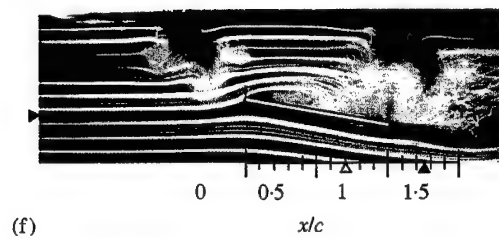
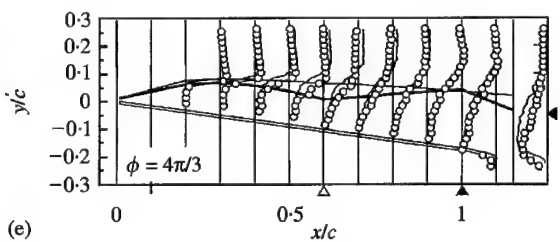
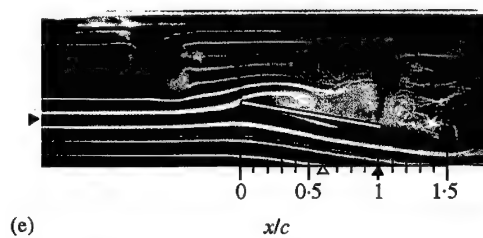
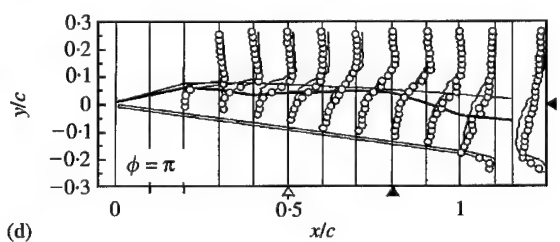
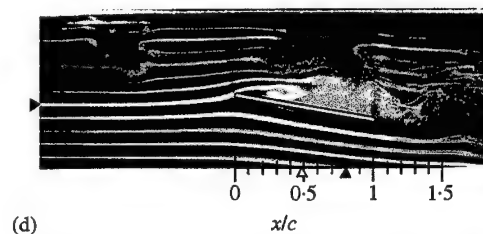
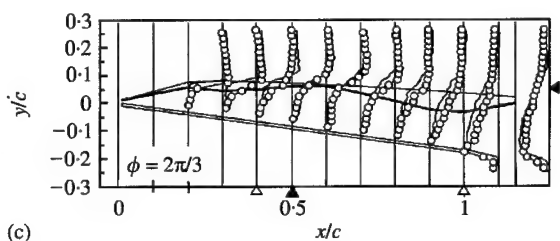
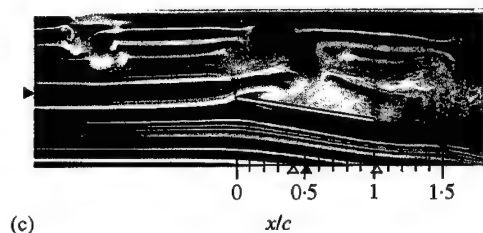
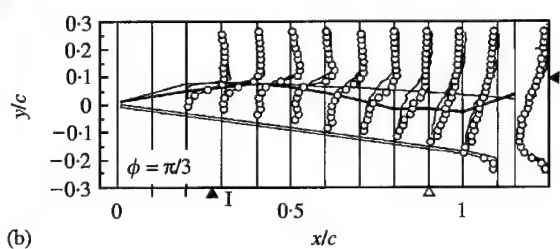
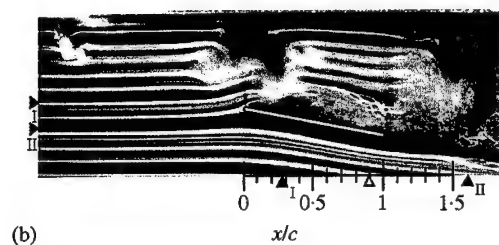
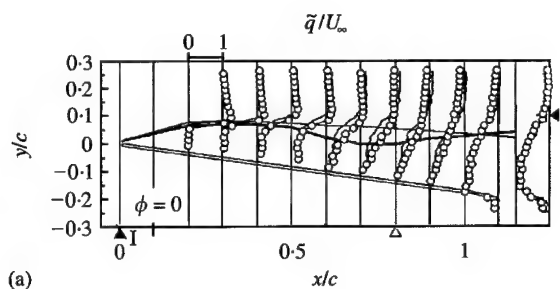
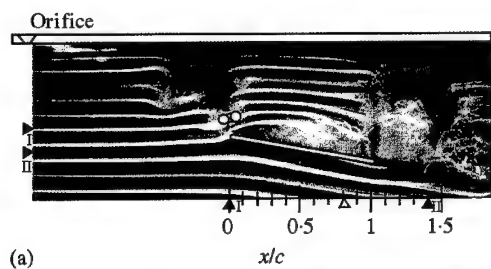
This compact vortex grows in size downstream to make the shear layer reattach at a position  $x/c \approx 0.5 - 0.6$  at  $\phi = \pi$  [Figure 5(d)]. The  $x$  coordinate of the reattachment position is indicated by the open triangle. As the interaction zone moves downstream, the reattachment position and the dip of  $y_c$  also move downstream. At the last phase  $\phi = 5\pi/3$  [Figure 5(f)], the reattachment position the dip are located further downstream at  $x/c \approx 0.7$ ; the next vortex ring is approaching the leading edge to yield the same pattern as that at  $\phi = 0$ .

It is worth noting that the motion of the dip is preceded by the motion of the vortex ring (Figure 6). The convection velocity of the dip is estimated to be approximately  $0.50 U_s$ , while the convection velocity of the vortex ring is estimated to be  $0.91 U_s$ . This means that the dip is actually caused by the local enhancement of rolling-up of the shear layer by the interaction with the vortex ring. This also suggests that the longitudinal motion of the vortex rings are affected by its self-induced velocity because the vortex rings travel downstream along the suction surface.

Effects of the shooting frequency  $F$  on distributions of the time-mean and r.m.s. velocities are shown in Figure 7 for two shooting frequencies  $Fc/U_\infty = 0.80$  and  $5.6$ . The ratio of circulation is in the range of  $\Gamma/\Gamma_{sh} = 2.5-3.6$ , so that, in view of the numerical simulations (Kiya *et al.*, 1999; Ishikawa *et al.*, 2000), the vortex rings are expected to pass through the shear layer. Figure 7 also indicates that the separated shear layer approaches the suction

Figure 5. Flow visualization of the separated flow affected by the impinging vortex rings for  $Fc/U_\infty = 0.80$  and  $\Gamma/(U_\infty c) = 0.67$ . Flow is from left to right. Phase is  $\phi = 0$  in (a) and  $\phi = 5\pi/3$  in (f) with the same interval of  $\pi/3$  between successive snapshots. The phase-averaged reattachment position is indicated by the open triangles. Coordinates of position of the vortex rings are denoted by the solid triangles on the  $x$ - and  $y$ -axes.

Figure 6. Phase-averaged velocity distributions  $\bar{q}$  in the separated flow affected by the impinging vortex rings for  $Fc/U_\infty = 0.80$  and  $\Gamma/(U_\infty c) = 0.67$ . Flow is from left to right. Phase is  $\phi = 0$  in (a) and  $\phi = 5\pi/3$  in (f) with the same interval of  $\pi/3$  between successive snapshots. The phase-averaged reattachment position is indicated by the open triangles. Coordinates of the position of the vortex rings are denoted by the solid triangles on the  $x$ - and  $y$ -axes. Thin solid lines indicate the distributions of the time-averaged velocity  $\bar{q}$  in the undisturbed shear layer, while the thick solid lines show the centre of the shear layer affected by the vortex rings.



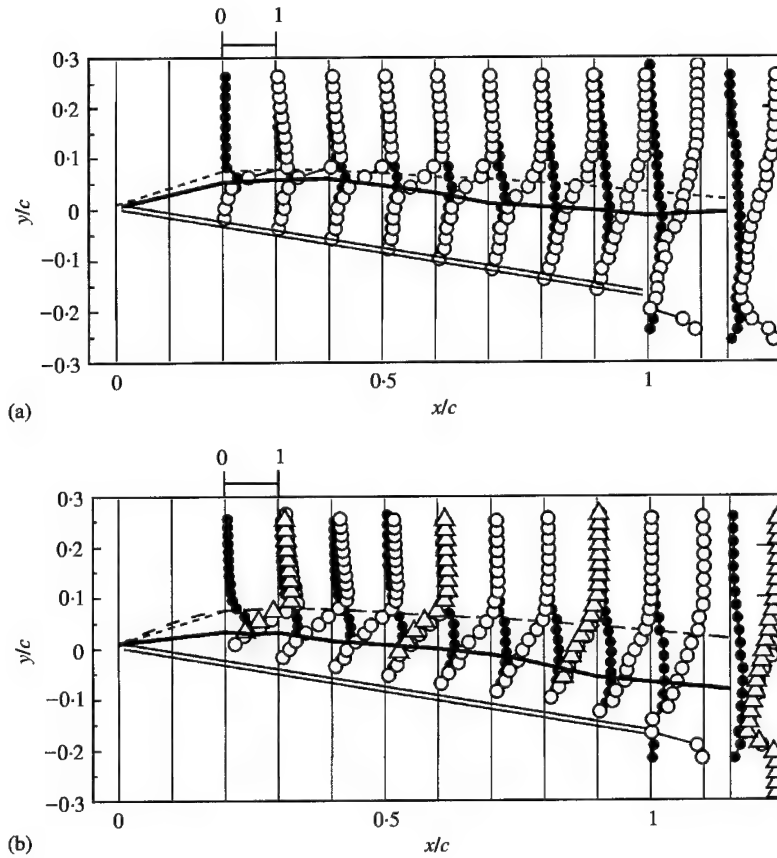


Figure 7. Effects of the impinging vortex rings on the separated flow around the inclined flat plate for (a)  $Fc/U_\infty = 0.80$ ,  $\Gamma/(U_\infty c) = 0.73$  and (b)  $Fc/U_\infty = 5.6$ ,  $\Gamma/(U_\infty c) = 0.50$ :  $\Delta$ ,  $\bar{u}/U_\infty$ ;  $\circ$ ,  $\bar{q}/U_\infty$ ;  $\bullet$ ,  $q'/U_\infty$ . The scale of the velocities is shown on top of (a) and (b).

surface as the frequency  $F$  increases. Especially, at the frequency  $Fc/U_\infty = 5.6$ , the separation zone is likely to be suppressed.

Effects of the frequency  $F$  on time histories of the instantaneous velocity  $q$  in the shear layer are shown in Figure 8. The time histories are measured at a fixed position  $(x/c, y'/c) = (0.5, 0.13)$ , which is approximately the centre of the undisturbed shear layer. For example, the time history for  $Fc/U_\infty = 0.80$  is periodic; its time-mean value is approximately 68% greater than that for the undisturbed shear layer. This increase is due to the above-mentioned shift of the shear layer towards the suction surface. The time at which a peak of  $q$  appears corresponds to the phase  $\phi$  at which the dip of the centre of the shear layer  $y_c$  locates right at the longitudinal position of  $x/c = 0.5$  (Figure 6).

As the frequency  $F$  increases further up to  $Fc/U_\infty = 5.2$ , the time-mean value of  $q$  increases to attain a value almost equal to  $U_\infty$  (Figure 8). At the same time, the time history of  $q$  for this frequency is random, containing no periodic component corresponding to the frequency  $F$ . Thus, at sufficiently high shooting frequencies  $F$ , the effects of the vortex rings are expected to be the same as those of the steady round jet of the same momentum. On the other hand, at a low frequency  $Fc/U_\infty = 0.08$ , the time-mean value of  $q$  is the same as that



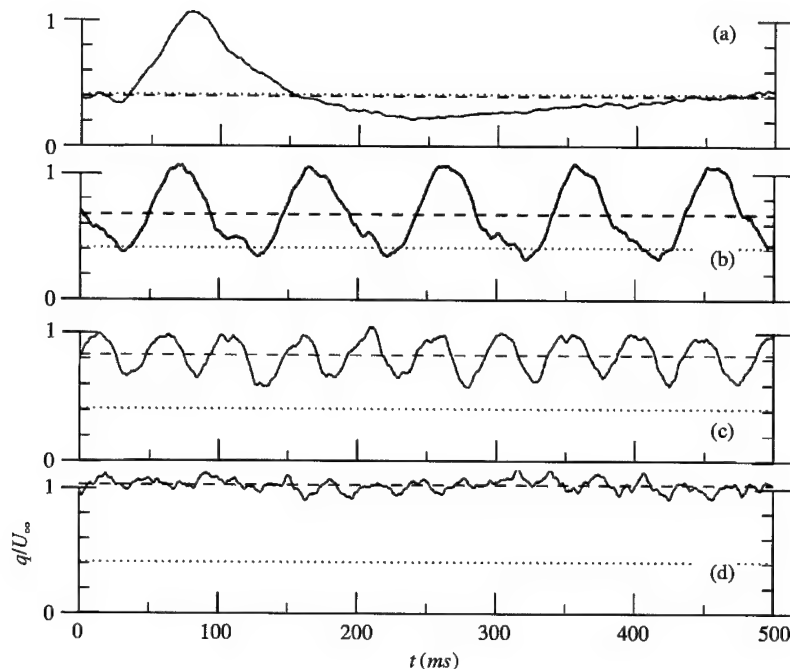


Figure 8. Time histories of velocity  $q$  in the shear layer at  $(x/c = 0.5, y'/c = 0.13)$  for different shooting frequencies  $F$ : (a)  $Fc/U_\infty = 0.08$ ; (b)  $Fc/U_\infty = 0.80$ ; (c)  $Fc/U_\infty = 1.60$ ; (d)  $Fc/U_\infty = 5.20$ .  $\Gamma/(U_\infty c) = 0.67$ . The broken lines are the time-mean velocity  $\bar{q}$ , while the dotted lines is the time-mean velocity  $\bar{q}$  at the same position in the undisturbed shear layer.

for the undisturbed flow, so that the vortex rings introduced at this frequency have an insignificant effect on the separated shear layer.

### 3.3. MOMENTUM DEFECT IN THE NEAR WAKE

The previous results are for the vortex rings generated from a single orifice whose centre is at mid-span, the measurements having been made in the mid-span plane. In the following, results will be presented for the vortex rings simultaneously generated from the five orifices arranged in the spanwise direction with the distance  $6d$ , as described in Section 2, in order to have fairly two-dimensional interaction between the vortex rings and the shear layer. The distance of  $6d$  was employed because the time-mean velocity contours in the  $yz$ -plane, for the single orifice, were two-dimensional in the near wake within the spanwise distance of  $\pm 3d$ . The velocity contours in the  $yz$ -plane for the simultaneously generated five vortex rings were found to be fairly two-dimensional at  $x/c = 1.15$  (Suzuki *et al.*, 1999).

A measure of effects of the vortex rings impinging on the separated flow is the drag acting on the inclined plate. In the present study the drag was evaluated in terms of the momentum defect in the near wake of the plate, neglecting the contribution of pressure. High momentum defect in the near wake is associated with low pressure there, so that high momentum defect implies high drag. The momentum defect  $M$  is defined by

$$M = \int \rho \bar{u} (U_\infty - \bar{u}) dy, \quad (3)$$

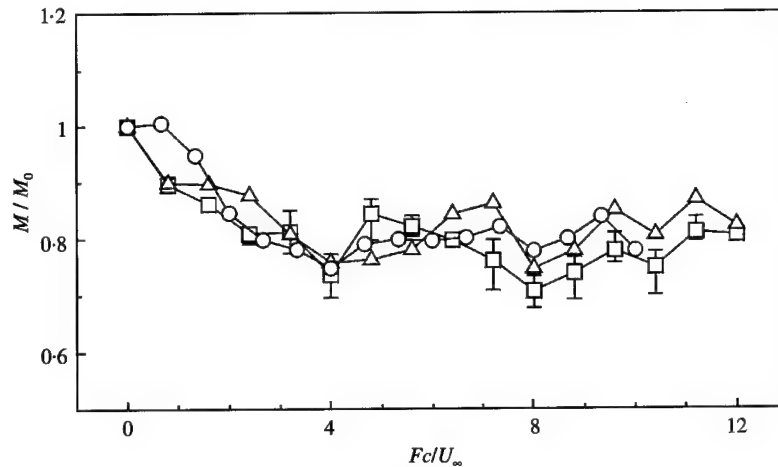


Figure 9. Momentum defect  $M$  versus the shooting frequency  $F$  for vortex rings issuing from five orifices arranged in the spanwise direction with a distance of  $6.0d$ :  $\circ$ ,  $\Gamma/(U_\infty c) = 0.23$ ;  $\Delta$ ,  $\Gamma/(U_\infty c) = 0.29$ ;  $\square$ ,  $\Gamma/(U_\infty c) = 0.36$ .

where  $\rho$  is the density of fluid. Figure 9 shows the momentum defect  $M$  in the mid-span plane at  $x/c = 1.15$ , divided by its value of the undisturbed flow  $M_0$ , as a function of the shooting frequency  $F$ . The momentum defect initially decreases with increasing  $F$  to attain a fairly constant value of  $M/M_0 = 0.8$  for  $Fc/U_\infty > 4.0$ . However, a perusal of Figure 9 reveals that the momentum defect attains a definite minimum at  $Fc/U_\infty \approx 4.0$ . This is the same even when the main-flow velocity has been changed by the factor of 2, as shown in Figure 10.

The particular frequency  $Fc/U_\infty = 4.0$  can be explained as follows. Periodic forcing of stalled flow around two-dimensional airfoils yields a particular forcing frequency,  $F_p$ , at which the lift attains a maximum (Hsiao *et al.*, 1989; Bar-Sever 1989; Zaman & McKinzie 1991; Zaman 1992). The drag is also expected to attain a minimum value at the same frequency because the height of the separated zone becomes minimum. This frequency when normalized in the form  $F_p c/U_\infty$  is in a range of 3–4 (Zaman & McKinzie 1991; Zaman 1992), 1–3 (Hsiao *et al.*, 1989) and 2 (Bar-Sever 1989), being of the same order as the above-mentioned frequency  $Fc/U_\infty = 4$ . At high Reynolds numbers the frequency  $F_p$  is much lower than the fundamental frequency of Kelvin–Helmholtz (K–H) instability in the separated shear layer  $F_{KH}$  (Zaman 1992). Nishioka *et al.* (1990) found that the forcing by acoustic waves of low amplitude amplifies the fundamental mode of the linear instability, whereas high amplitude forcing amplifies the mode of much lower frequency. The primary mechanism is likely to be the shedding-type instability (Nishioka *et al.*, 1990; Sigurdson 1995) whose frequency scales with the height of the separation zone and the velocity at the separation edge  $U_s$ . The mechanism is also interpreted as the impinging-type instability (Nakamura & Nakashima 1986; Kiya *et al.*, 1997).

At sufficiently low Reynolds numbers the frequency of the shedding-type instability is perhaps of the same order as that of the K–H instability because vortices rolled-up by the K–H instability can be shed downstream without further merging. This is probably the case in the present experiment at  $Re = 8300$  because the frequency  $Fc/U_\infty = 4$  happens to be that of the K–H frequency at  $x/c = 0.4$ . A similar relation is observed between the frequency of the shear layer instability and that of the column-type instability of a round jet (Ho & Huerre 1984).

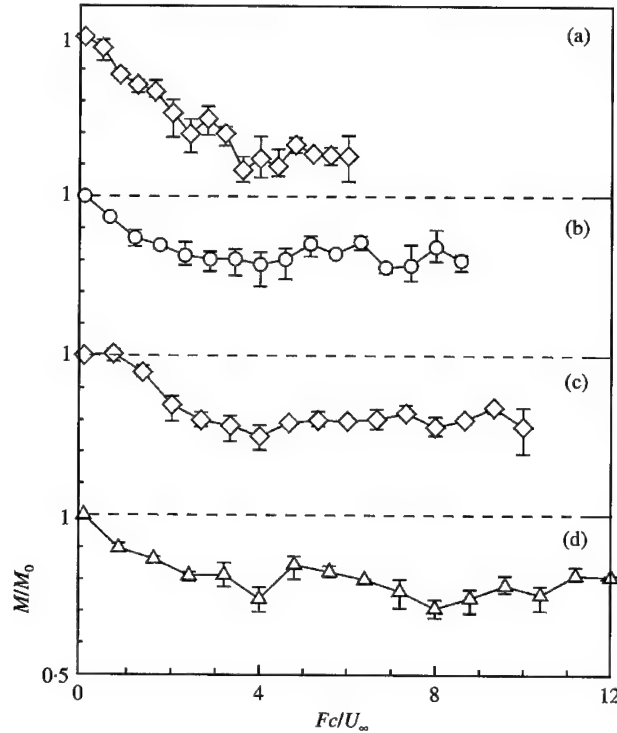


Figure 10. Momentum defect  $M$  versus the shooting frequency  $F$  at (a)  $Re = 16600$ ,  $\Gamma/(U_\infty c) = 0.34$ ; (b)  $Re = 11600$ ,  $\Gamma/(U_\infty c) = 0.48$ ; (c)  $Re = 100000$ ,  $\Gamma/(U_\infty c) = 0.56$ ; (d)  $Re = 8300$ ,  $\Gamma/(U_\infty c) = 0.67$  for the vortex rings issuing from five orifices.

At the optimum frequency  $Fc/U_\infty = 4$ , the distance between the centre of the consecutive interaction zones is approximately  $0.16c$  because the convection velocity of the interaction zone is  $0.51U_s (= 0.65U_\infty)$ . The diameter of the vortex ring is approximately  $1.5d (= 0.075c)$ , so that the interaction zone is just sufficient to accommodate one vortex ring.

As mentioned before, the momentum defect becomes fairly constant at the shooting frequencies in the range of  $Fc/U_\infty > 4.0$  (Figure 9). At these frequencies there is no inherent instability in the shear layer to be enhanced by the interaction with the vortex rings. The primary mechanism for the constant value of  $M$  should be attributed to an increase in the longitudinal momentum due to the vortex rings. The momentum of the vortex rings is basically in the normal ( $y$ ) direction but this is converted to the longitudinal momentum by their impingement on the surface.

Effects of circulation of the vortex rings on  $M$  are shown in Figure 11. The momentum defect decreases with increasing circulation  $\Gamma$  but is likely to become constant at sufficiently high values of  $\Gamma$ . The latter is probably because such vortex rings pass through the separated shear layer, leaving more or similar effects on the rolling up of the shear layer, as suggested by the numerical simulations (Kiya *et al.*, 1999; Ishikawa *et al.*, 2000).

It may be noted here that, for signal vortex rings, the momentum defect decreased with increasing frequency  $F$  (not shown), attaining a fairly constant value of  $M/M_0 = 0.8$  for  $Fc/U_\infty > 6$ . This is the same as in the case of arrays of vortex rings. The main difference is that no significant minimum appeared at  $Fc/U_\infty \approx 4.0$  for the single vortex rings. This is probably because the single vortex rings modified only a limited spanwise region of the

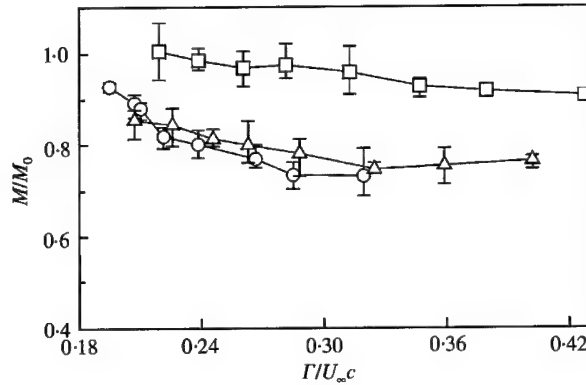


Figure 11. Momentum defect  $M$  versus circulation of the vortex rings issuing from five orifices: □,  $Fc/U_\infty = 0.80$ ; △,  $Fc/U_\infty = 4.0$ ; ○,  $Fc/U_\infty = 8.0$ .

rolling-up vortices in the shear layer, which were otherwise fairly two-dimensional, and thus the two-dimensional shedding-type instability was not enhanced.

### 3.4. EFFICIENCY OF SEPARATION CONTROL BY VORTEX RINGS

Loss of power by the drag acting on the plate is the drag multiplied by the main-flow velocity. The drag of the plate is reduced by the impinging vortex rings; this reduction is accompanied by a reduction in loss of power  $\Delta W$ . Thus, the efficiency of control can be evaluated by  $\eta = \Delta W/W_{vr}$ , where  $W_{vr}$  is the power of generation of the vortex ring. The kinetic energy of the vortex ring  $K_{vr}$  is given by

$$K_{vr} = \frac{1}{2} \rho A_0 \int_0^{t_b} [V(t)]^3 dt, \quad (4)$$

where  $A_0 = \pi d^2/4$  is the area of the orifice. The vortex ring is generated with frequency  $F$  and the number of the vortex rings per unit length of the span is  $1/(6d)$ . Thus the power, per unit length, of generation of the vortex rings is  $W_{vr} = (F/6d)K_{vr}$ . On the other hand, the reduction in loss of power per unit length by the control is given by  $\Delta W = U_\infty(M_0 - M)$ .

The efficiency  $\eta$  is shown in Figure 12 as a function of the normalized frequency  $Fc/U_\infty$  and circulation  $\Gamma/(U_\infty c)$ . It is noteworthy that a maximum of  $\eta$  appears at a frequency centred around  $Fc/U_\infty \approx 4$ . Thus the steady round jet, which corresponds to  $Fc/U_\infty = \infty$ , is not the best choice for the control in terms of the efficiency. Moreover, the efficiency attains a maximum at a particular value of  $\Gamma/(U_\infty c) \approx 0.32$ , which is approximately 1.5 times that of shear layer vortices. It is worth noting that the value of this ratio is equal to the critical value for which a vortex ring passes through a rectilinear vortex tube (Ishikawa *et al.*, 2000).

## 4. CONCLUSION

In this paper, vortex rings were successively introduced into the separated shear layer of an inclined flat plate to reduce the spatial extent of the separation zone. The circulation and frequency of successive introduction of the vortex rings were changed to examine their effects on the reduction of the separation zone. The main results of this study may be

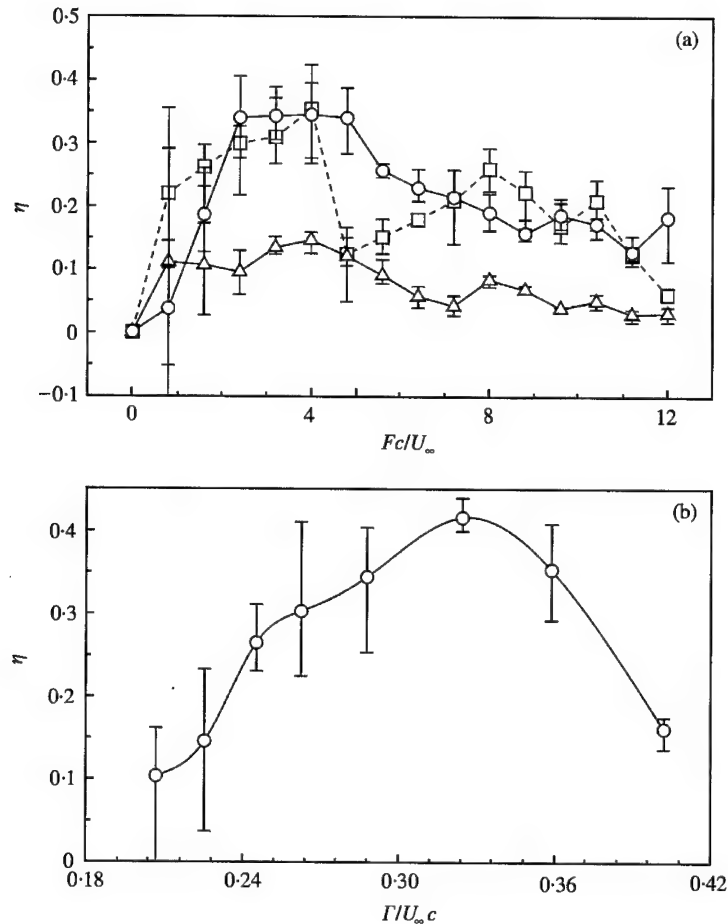


Figure 12. Efficiency of the active control of separation zone  $\eta$  versus (a) the shooting frequency  $F$  and (b) the circulation of the vortex rings  $\Gamma$  at  $Fc/U_\infty = 4.0$ :  $\triangle$ ,  $\Gamma/(U_\infty c) = 0.22$ ;  $\circ$ ,  $\Gamma/(U_\infty c) = 0.27$ ;  $\square$ ,  $\Gamma/(U_\infty c) = 0.32$ .

summarized as follows.

(i) The separation zone can be reduced by a chain of vortex rings impinging on the shear layer. This is because a compact and strong vortex is successively formed near the leading edge to transport high-momentum fluid of the main flow towards the surface.

(ii) The momentum defect in the near wake of the plate, which is approximately proportional to the drag, is introduced as a measure of effectiveness of active control by the impinging vortex rings. The momentum defect decreases with increasing frequency of introduction of the vortex rings  $F$ , saturating at frequencies greater than  $Fc/U_\infty \approx 4$ . At this particular frequency, the momentum defect appears to attain a minimum value. This optimum frequency is of the order as the frequency at which the lift attains a maximum by periodic forcing of stalled flow around airfoils, suggesting that the impinging vortex rings enhance the shedding-type instability of the separated flow.

(iii) In the present experiment at Reynolds number of 8300, the optimum frequency happens to be approximately equal to the fundamental frequency of Kelvin-Helmholtz instability of the separated shear layer. At higher Reynolds numbers, the optimum frequency  $Fc/U_\infty \approx 4$  is expected to be much lower than the Kelvin-Helmholtz frequency.

(iv) There exists a particular value of circulation of the vortex rings beyond which the momentum defect attains a constant value. This is because such vortex rings pass through the separated shear layer, leaving more or less the same effects on the rolling up of the shear layer.

(v) The efficiency of reduction of the separation zone attains a broad maximum approximately at the frequency  $Fc/U_\infty = 4$  and at a particular value of circulation of the vortex ring. The former implies that the steady round jet is not the best choice for the control in terms of efficiency.

### ACKNOWLEDGEMENTS

The authors express their sincere thanks to Mr Toshiyuki Sampo for his help in the construction of the experimental apparatus. This study was financially supported by the Grant-in-Aid for Scientific Research from the Ministry of Education, Science and Culture, Japan (Category (A)(2), No. 11305016).

### REFERENCES

- BAR-SEVER, A. 1989 Separation control on an airfoil by periodic forcing. *AIAA Journal* **27**, 820–821.
- HSIAO, F., LIU, C., SHYU, J. & WANG, M. 1989 Control of wall-separated flow by internal acoustic excitation. *AIAA Paper* 89-0974.
- HO, C.-M. & HUERRE, P. 1984 Perturbed free shear layers. *Annual Review of Fluid Mechanics* **16**, 365–424.
- ISHIKAWA, H., IZAWA, S. & KIYA, M. 2000 Lagrangian LES and vortex dynamics of forced unsteady jets and colliding vortices. In *Advances in Turbulence VIII* (eds C. Topazo *et al.*), pp. 825–828. Barcelona: International Center for Numerical Methods in Engineering.
- KIYA, M. & ISHII, H. 1988 Vortex dynamics simulation of interacting vortex rings and filaments. *Fluid Dynamics Research* **3**, 197–202.
- KIYA, M., OHYAMA, M. & HUNT, J. C. R. 1986 Vortex pairs and rings interacting with shear-layer vortices. *Journal of Fluid Mechanics* **172**, 1–15.
- KIYA, M., SHIMIZU, M. & MOCHIZUKI, O. 1997 Sinusoidal forcing of a turbulent separation bubble. *Journal of Fluid Mechanics* **342**, 119–139.
- KIYA, M., TAKEO, H., MOCHIZUKI, O. & KUDO, D. 1999 Simulating vortex pairs interacting with mixing-layer vortices. *Fluid Dynamics Research* **24**, 61–79.
- LEWEKE, T., MILLER, G. D. & WILLIAMSON, C. H. K. 1996 Instability in trailing vortices in the temporal development of vortex pairs. In *Advances in Turbulence VI* (eds S. Gavrilakis *et al.*), pp. 361–364. Dordrecht: Kluwer Academic Publishers.
- MAEKAWA, H. & NISHIOKA, T. 1992 Control of mixing layer developing structures using a vortex ring. *Transactions of JSME* **58**, 2659–2666 (in Japanese).
- NAKAMURA, Y. & NAKASHIMA, M. 1986 Vortex excitation of prisms with elongated rectangular, H and  $\vdash$  cross sections. *Journal of Fluid Mechanics* **163**, 149–169.
- NISHIOKA, M., ARAI, M. & YOSHIDA, S. 1990 Control of flow separation by acoustic excitation. *AIAA Journal* **28**, 1905–1915.
- SIGURDSON, L. W. 1995 The structure and control of a turbulent reattaching flow. *Journal of Fluid Mechanics* **289**, 139–165.
- SUZUKI, N., MOCHIZUKI, O. & KIYA, M. 1999 A pulsating round jet ejected into cross flow. In *Proceedings of International Conference on Fluid Engineering I - The JSME Centennial Grand Congress*, pp. 129–134. Tokyo: The Japan Society of Mechanical Engineers.
- ZAMAN, K. B. M. Q. 1992 Effect of acoustic excitation on stalled flows over an airfoil. *AIAA Journal* **30**, 1492–1499.
- ZAMAN, K. B. M. Q. & MCKENZIE, D. J. 1991 Control of laminar separation over airfoils by acoustic excitation. *AIAA Journal* **29**, 1075–1083.

## ASPECTS OF FLOW-INDUCED VIBRATION

A. LEONARD AND A. ROSHKO

*Graduate Aeronautical Laboratories, California Institute of Technology  
Pasadena, CA 91125, U.S.A.*

(Received 20 September 2000, and in final form 22 November 2000)

Phenomena associated with flow-induced transverse oscillation of an elastically mounted body are considered. The use of a recently introduced parameter that combines the effect of mass and elasticity—effective elasticity—is exploited to demonstrate the predictive value of the new approach and to provide insights into solution branching, the maximum amplitude of vibration, and modeling.

© 2001 Academic Press

### 1. INTRODUCTION

IN SHIELDS, LEONARD & ROSHKO (2001), henceforth SLR, results of numerical simulations were presented for vortex-induced vibration of a circular cylinder vibrating transversely in a two-dimensional flow at Reynolds number  $Re = 100$ . The single value of  $Re$  together with zero value for the system damping ( $b = 0$ ) were chosen, thus reducing the number of independent variables to two, namely the mass  $m$  and the spring constant  $k$ . It was found that, in a great majority of the cases, the response was essentially sinusoidal. In this situation, at frequency  $f = \omega/2\pi$ , the spring force,  $ky$ , and inertial force,  $m\omega^2 y$ , are continually in opposition, and their net effect can be represented by the “effective” elasticity,  $k_{\text{eff}}^* \equiv k^* - m^*\omega^{*2}$ . The notation  $(\cdot)^*$  indicates nondimensional forms,

$$k^* \equiv k/\frac{1}{2} \rho U_\infty^2, \quad m^* \equiv m/\frac{1}{2} \rho D^2, \quad \omega^* \equiv \omega D/U_\infty \quad \text{and} \quad A^* \equiv A/D, \quad (1)$$

where  $\rho$  and  $U_\infty$  are flow density and velocity, respectively, and  $D$  is the cylinder diameter, i.e., the scaled time is  $t^* = tU_\infty/D$  rather than the traditional  $\tau \equiv t\omega_n$ , where  $\omega_n = (k/m)^{1/2}$ . Scaling with flow variables instead of the mechanical ones leads to the single-variable formulation, which gives a unified solution as function of  $k_{\text{eff}}^*$ . In the traditional formulation,  $m^*$  is an independent parameter and the mechanical frequency  $\omega_n$  appears in the “reduced velocity”,  $U_R \equiv U_\infty/\omega_n D$ , that is usually adopted as the primary variable. It may also be written  $U_R = 1/\omega_n^*$ . In Figure 1, we show the results of numerical simulations for the response of the system  $A^*$  and  $f^* = \omega^*/2\pi$  versus  $k_{\text{eff}}^*$ . The simulations are those reported in SLR and more recent ones by L. Barba (private communication).

The advantage of a universal solution in terms of a single parameter,  $k_{\text{eff}}^*$ , is that it is not necessary to make an experimental (computational) run for each value of  $m^*$ . On the other hand, the effect of mechanical parameters is hidden in the solution. For example, the phenomena of “lock-in” and of multiple branches which are observed in the conventional coordinates are not obvious. One of the main objectives of this paper is to elucidate the connection between these phenomena and our unified description.

The universal solution includes the transverse force (“lift”) on the cylinder which, for sinusoidal motion, can be expressed as  $F_y = C_L \frac{1}{2} \rho U_\infty^2 D \sin \omega t$ . The coefficient  $C_L$  may be of

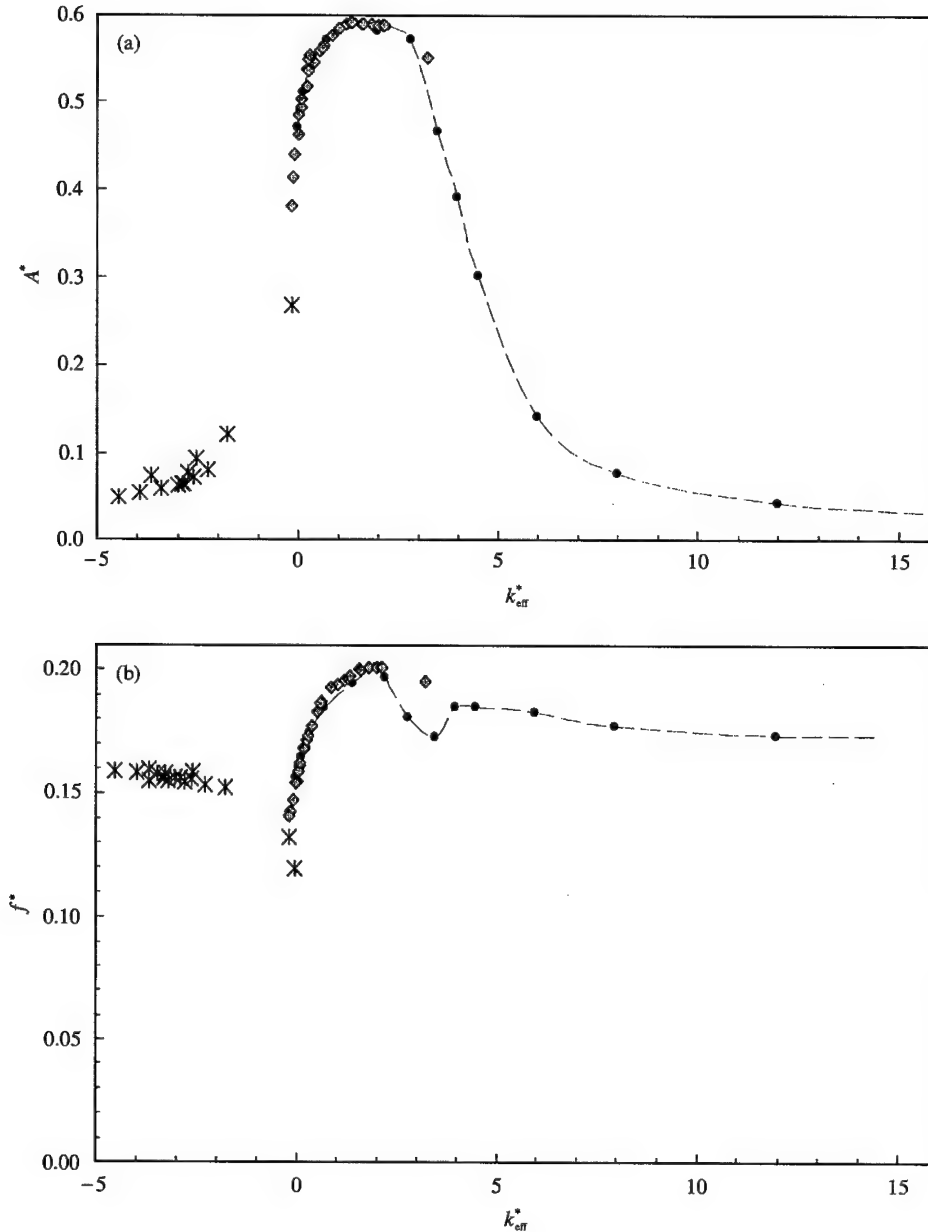


Figure 1. Response for undamped systems, with and without inertia, plotted against effective elasticity: (a) amplitude  $A^*$ ; (b) frequency  $f^*$ . Notation: —●—, DS '98; ◇, LB '99; × LB '00. Numerical simulations of SLR (DS '98) and L. Barba (private communication, LB '99; '00).

interest for modeling. In SLR, the transverse force was decomposed into two components,  $C_L = C_{Lw} + C_{La}$ , where  $C_{Lw}$  is the “wake” force due to the effect of all the vorticity in the boundary layer and wake, while  $C_{La}$  is the “added-mass” force induced by the acceleration of the cylinder. The latter is easily computed for a given frequency and amplitude, i.e.,  $C_{La} = \frac{1}{2} \pi \omega^2 A^*$ . Because of continuing controversy about the applicability of the classical result for the added mass contribution to the fluid force, we present a review in the



appendix. More difficult to understand is the total cross-force  $C_L$  and its component  $C_{Lw}$ . For example, it is counter-intuitive that  $C_L = 0$  at the synchronization condition  $f = f_n$ , at which condition, then,  $C_{Lw} = -C_{La}$ . These aspects of the transverse force are described in Sections 2 and 3, while the branching solutions associated with the universal solution are discussed in Section 4.

## 2. SYNCHRONIZATION AND LOCK-IN

The two terms, synchronization and lock-in, are often used synonymously but in SLR it was shown that, for zero damping and sinusoidal motion, synchronization ( $f = f_n$ ) occurs at only one condition,  $k_{\text{eff}}^* = 0$ . This follows from

$$k_{\text{eff}}^* = k^* - m^* \omega^{*2} = m^*(\omega_n^{*2} - \omega^{*2}), \quad (2)$$

which can be rewritten to show

$$\omega^{*2} = \omega_n^{*2} - k_{\text{eff}}^*/m^*. \quad (3)$$

That is, for nonzero values of  $k_{\text{eff}}^*$ ,  $\omega$  only approaches  $\omega_n$  asymptotically when  $m^* \gg 1$ . Indeed, it is from experiments in air (Feng 1968), for which  $m^* \sim 10^3$ , that the traditional knowledge of "lock-in" developed. (Note, in equation (2), that in the range of high-amplitude response,  $\omega_n^* = U_R^{-1} \sim 1$  and  $k_{\text{eff}}^* < 3$ .) On the other hand, it was from experiments in water [e.g., Khalak & Williamson (1997), Gharib *et al.* (1997), 1998, Gharib (1999)], for which  $m^* \sim 1 - 10$ , that the notion of "absence of lock-in" developed. In such cases, the plot of  $f/f_n$  is an increasing function of  $U_R$  which crosses the ordinate  $f/f_n = 1$  at  $U_R \approx 1.0$ . Those values of  $U_R$  for synchronization, at  $\text{Re} \sim 10^3 - 10^4$ , are remarkably close to the value from the universal solution  $f^*(k_{\text{eff}}^*)$  at  $\text{Re} = 100$ ; that is,  $f_n^* = f^*(0) = 0.156$ , from which  $U_R = (2\pi f_n^*)^{-1} = 1.02$ .

It is also noteworthy that for large values of  $m^*$ , for which the synchronization value of  $U_R$  cannot be readily identified, as noted above, the value  $U_R \approx 1.0$  is the point at which a jump in amplitude is observed from an upper to a lower branch, as  $U_R$  is increasing. In some cases (Feng 1968; Brika & Laneville 1993), the jump is hysteretic, i.e., a jump from a lower to an upper branch, for decreasing  $U_R$ , is not observed. In other cases (Khalak & Williamson 1999), the jumps are intermittent rather than hysteretic, perhaps depending on the mass-damping parameter  $m^*\zeta$  ( $= \frac{1}{2} U_R b^*$ ). The connection with synchronization may be found in the equation of motion which, for zero damping and sinusoidal motion, as explained above, reduces to

$$(-m^* \omega^{*2} + k^*)A^* = k_{\text{eff}}^* A^* = C_L. \quad (4)$$

Thus,  $C_L = m^*(\omega_n^{*2} - \omega^{*2})A^*$  is changing sign, i.e., phase, at synchronization. From the investigations in air ( $m^* \gg 1$ ), it is known that at the hysteretic jump there is a phase change ( $\pi$ ) in vortex shedding. Further discussion on branching is in Section 4.

## 3. AMPLITUDE AND CROSS-FORCE

To associate the amplitude of vibration  $A^*$  with the transverse force coefficient  $C_L$  can be misleading. Thus, for a stationary cylinder,  $A^* = 0$  and  $C_L = 1.30$  while for a cylinder vibrating at high amplitude  $C_L$  may have the value zero (at  $k_{\text{eff}}^* = 0$ , where  $A^* = 0.47$ !) Figure 2(a) shows the overall relation between  $C_L$  and  $A^*$ . The components of  $C_L$ , i.e., the added-mass component  $C_{La}$  and the wake component  $C_{Lw}$ , are shown in Figures 2(b) and 2(c), respectively. Clearly, the relations are not simple. The plot for the wake force is especially interesting, showing a large change of  $C_{Lw}$ , from negative to positive values, at

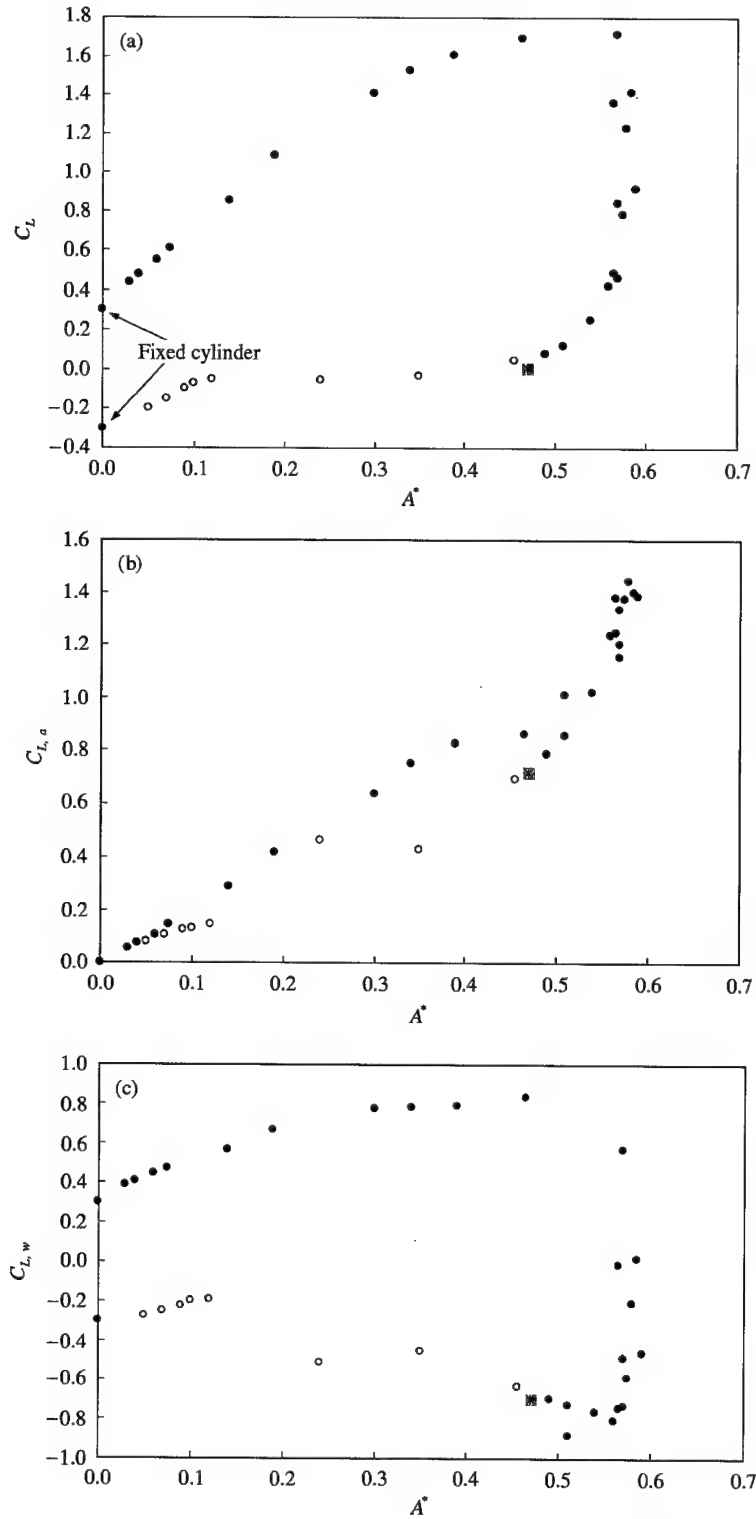


Figure 2. Components of the lift coefficient,  $C_L = C_{La} + C_{Lw}$ : (a)  $C_L$ ; (b)  $C_{La}$ ; (c)  $C_{Lw}$ . Notation:  $\circ$   $k_{eff}^* < 0$ ;  $\bullet$   $k_{eff}^* > 0$ ;  $\blacksquare$ ,  $k_{eff}^* = 0$ . Numerical simulations of SLR.

nearly constant amplitude,  $A^* \approx 0.58$ . Surprisingly, as noted in SLR, that change is accompanied by barely perceptible change in the pattern of separation and vortical structure in the wake.

#### 4. BRANCHING OF SOLUTIONS

In this section, we discuss the discontinuous or branching behavior often observed when following the amplitude of the response as the reduced velocity is varied continuously; see, e.g., Khalak & Williamson (1999). In particular, we show how this behavior is connected to our unified description.

As shown in Figure 1, the frequency,  $f^*$ , and amplitude,  $A^*$ , of the response will depend only on the effective stiffness,  $k_{\text{eff}}^* = k^* - m^*\omega^{*2}$ , the nondimensional damping,  $b^*$ , and the Reynolds number,  $\text{Re}$ , i.e.,

$$f^* = f^*(k_{\text{eff}}^*, b^*, \text{Re}), \quad A^* = A^*(k_{\text{eff}}^*, b^*, \text{Re}), \quad (5, 6)$$

assuming that the motion is nearly sinusoidal. Given the functions (5) and (6), consider now determining the response for a given experiment. For a fixed mechanical and fluid system,  $m^*$  is fixed but  $k^*$ ,  $b^*$ , and  $\text{Re}$  vary as the freestream velocity,  $U_\infty$ , varies. If we then also fix  $U_\infty$ , then we need only to solve equation (5) implicitly for  $f^*$  or  $\omega^{*2} = 4\pi^2 f^{*2}$ . To do so let

$$\omega^{*2} = F(k_{\text{eff}}^*, b^*, \text{Re}). \quad (7)$$

Then

$$k_{\text{eff}}^* = k^* - m^*\omega^{*2} = k^* - m^*F(k_{\text{eff}}^*, b, \text{Re}). \quad (8)$$

Thus

$$m^*F(k_{\text{eff}}^*, b^*, \text{Re}) + k_{\text{eff}}^* = k^* = \frac{m^*}{U_R^2}, \quad (9)$$

and so  $k_{\text{eff}}^*$  may be determined from (9) and then  $f^*$  or  $\omega^{*2}$  may be found from equations (5) or (7), respectively, and  $A^*$  from (6). (An alternative procedure to do this inversion was presented in SLR in which one begins with chosen  $m^*$  and  $k_{\text{eff}}^*$  and then determines the corresponding  $A^*$ ,  $f^*$  and  $U_R$ . However, using this method it is not convenient to demonstrate branching behavior and one also has accuracy problems at large  $m^*$  as discussed by SLR.)

However, equation (9) may produce multiple solutions for  $k_{\text{eff}}^*$ . Consider the data produced by computational experiments of SLR for  $b^* = 0$  and  $\text{Re} = 100$ . Using the results shown in Figure 1, we show in Figure 3 the left-hand side of equation (9) versus  $k_{\text{eff}}^*$  for the case  $m^* = 2$ . Note that, in this case, any value of  $U_R$  will produce a unique value  $k_{\text{eff}}^*$ , i.e., no multiple solutions. On the other hand, as  $m^*$  increases the importance of the nonlinear (in  $k_{\text{eff}}^*$ ) first term on the left-hand side of equation (9) increases. For example the case  $m^* = 28$  is shown in Figure 4. Note that in the range  $36 \leq m^*/U_R^2 \leq 46$  or  $0.78 \leq U_R \leq 0.88$  three solutions may be possible. As illustrated in the figure, the one corresponding to the largest  $k_{\text{eff}}^*$  would have the lowest amplitude [see Figure 1(a)] and therefore belong to the "lower" branch and the smallest  $k_{\text{eff}}^*$  would correspond to the highest amplitude or "upper" branch. A third or intermediate solution could possibly fall in the range  $2 \leq k_{\text{eff}}^* \leq 4$  but it is approximately within this range that the response has been found to be nonsinusoidal as indicated in the figure. Branching for this case ( $m^* = 28$ ) is seen to occur also in the range  $16 \leq m^*/U_R^2 \leq 25$  or  $1.06 \leq U_R \leq 1.32$  and corresponds to the branching discussed in Section 3, connected with the condition  $k_{\text{eff}}^* \approx 0$ . In this regime the largest solution for

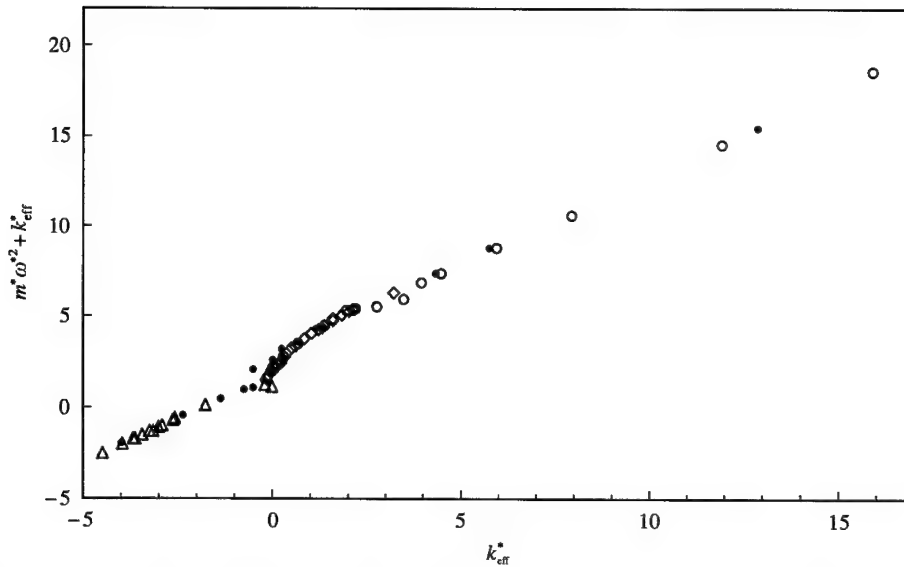


Figure 3.  $m^* \omega^{*2} + k_{eff}^*$  or  $m^*/U_R^2$  plotted against effective elasticity for the case  $m^* = 2.0$ :  $\circ$ , DS,  $m = 0$ ;  $\bullet$ , DS,  $m \neq 0$ ;  $\diamond$ , LB '99;  $\triangle$ , LB '00. Numerical simulations of SLR and L. Barba (private communication).

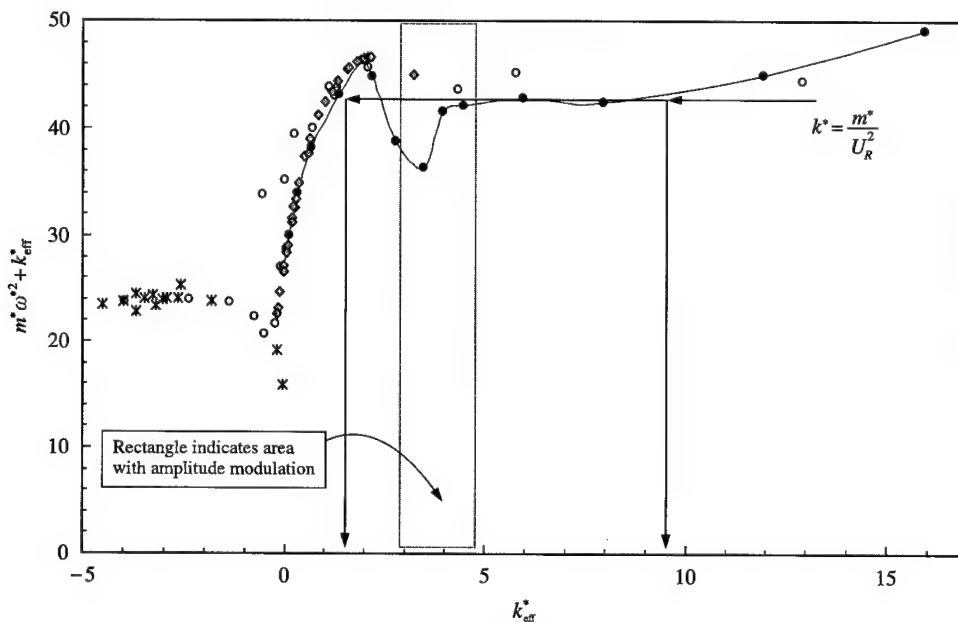


Figure 4.  $m^* \omega^{*2} + k_{eff}^*$  or  $m^*/U_R^2$  plotted against effective elasticity for the case  $m^* = 28.0$ :  $\circ$ , DS,  $m = 0$ ;  $\bullet$ , DS,  $m \neq 0$ ;  $\diamond$ , LB '99;  $\triangle$ , LB '00. Numerical simulations of SLR and L. Barba (private communication).

$k_{eff}^*$  (i.e.,  $k_{eff}^* \approx 0$ ) would correspond to the largest amplitude  $A^*$  while the intermediate solution for  $k_{eff}^*$  would yield, in general, a significantly smaller amplitude. A third solution also exists for a larger negative value of  $k_{eff}^*$ , because the left-hand side of equation (9) tends to  $k_{eff}^*$  as  $k_{eff}^*$  becomes large negative, but the corresponding amplitude would be even smaller.

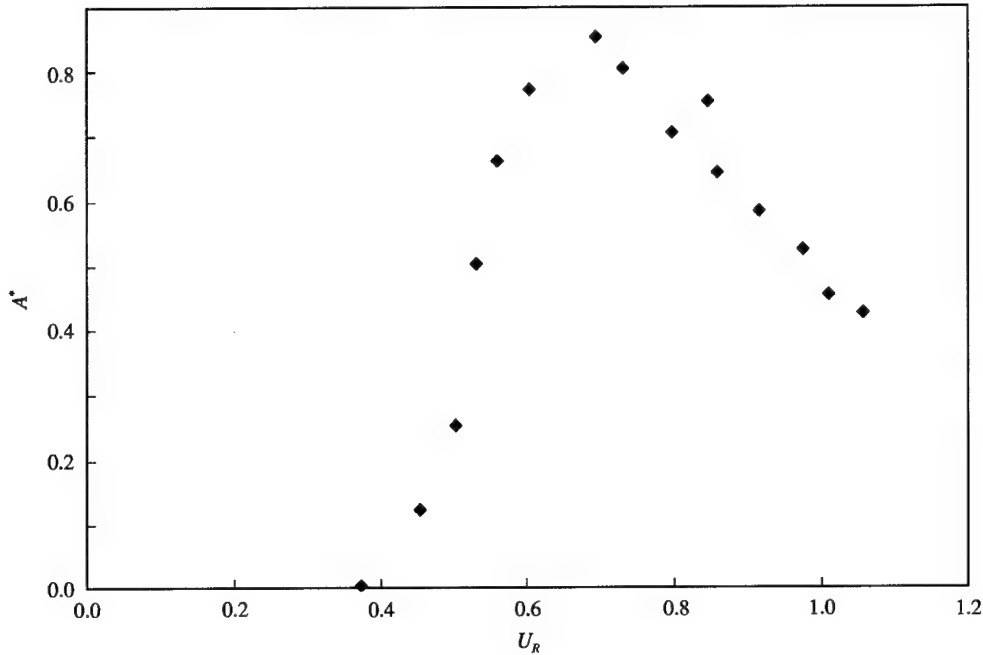


Figure 5. Amplitude plotted against reduced velocity for  $m^* = 2.1$ . From the value  $U_R = 1$ :  $b^* = 0.31$ ,  $k^* = m^*$ , and  $Re = 32 \times 10^3$ . Experiments of Gharib (1999).

This type of discontinuous or branching behavior is also found in the laboratory experiments of Gharib (1999), depending on the value of  $m^*$ . In Figure 5, we show the response  $A^*$  versus  $U_R$ , for the case  $m^* = 2.1$ .  $A^*$  appears to vary smoothly, in agreement with the behavior inferred for the computational case,  $m^* = 2$ , from Figure 3. However, a different result occurs for the case  $m^* = 28$ , as shown in Figure 6. Note the nearly discontinuous behavior at  $U_R \approx 0.86$  and possible branching near  $U_R \approx 1.05$ . The source of this behavior is clear when we consider the variation of  $m^*F(k_{eff}^*, b^*, Re) + k_{eff}^*$  as a function of  $k_{eff}^*$  for this data, shown in Figure 7. The jump in amplitude at  $U_R \approx 0.86$  is a consequence of the flatness of the curve in the range  $4 \leq k_{eff}^* \leq 6$  and the fact that  $A^*$  is a rapidly varying function of  $k_{eff}^*$  in this range (see Figure 8). The drop to low  $A^*$  at  $U_R \approx 1.05$  is simply the change in solution branch as  $m^*/U_R^2$  decreases through the value  $\approx 25$ .

In the laboratory experiments (fixed  $m^*$  but  $U_R$  variable) some variation in  $b^*$  and  $Re$  takes place because  $b^* \sim U_R^{-1}$  and  $Re \sim U_R$ . [For the case  $m^* = 2.1$  above,  $b^* = 0.31$  and  $Re = 32 \times 10^3$  at  $U_R = 1$  and, for the case  $m^* = 28$ ,  $b^* = 0.39$  and  $Re = 23 \times 10^3$  at  $U_R = 1$  (Gharib 1999).] Thus, the data shown in Figure 7 are not at fixed  $b^*$  and  $Re$ , but include some variation in both parameters while the data of Figures 3 and 4 are at fixed  $b^* = 0$  and  $Re = 100$ . Of course, equation (9) is valid in either case but its use in the case of varying  $b^*$  and  $Re$  may require some additional iteration.

## 5. REMARKS

We have developed further insights into the phenomena of flow-induced vibration by exploiting a unified description of the response of the system, presented in a recent paper by SLR. In this approach, the effective elasticity,  $k_{eff}^*$ , and damping,  $b^*$ , replace three traditional

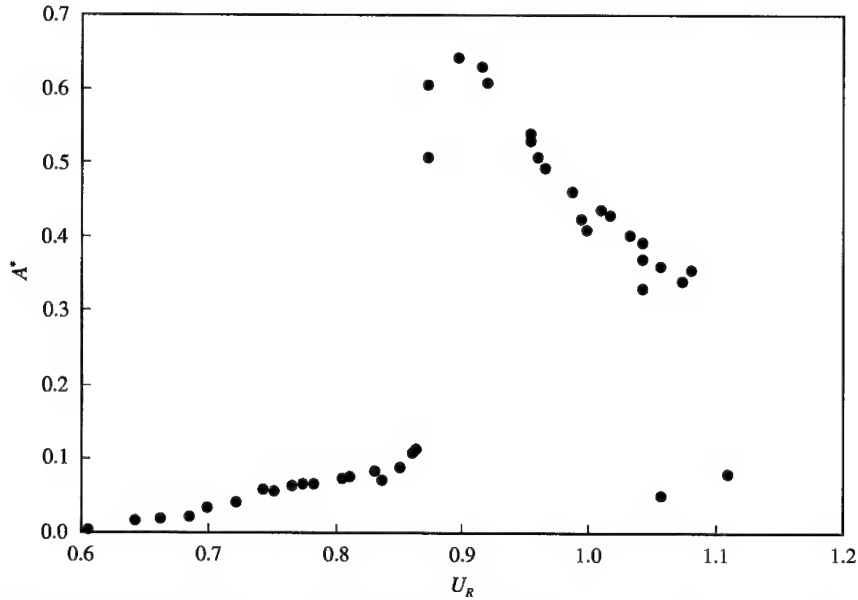


Figure 6. Amplitude plotted against reduced velocity for  $m^* = 28.0$ . For the value  $U_R = 1$ ,  $b^* = 0.39$ ,  $k^* = m^*$ , and  $Re = 23 \times 10^3$ . Experiments of Gharib (1999).

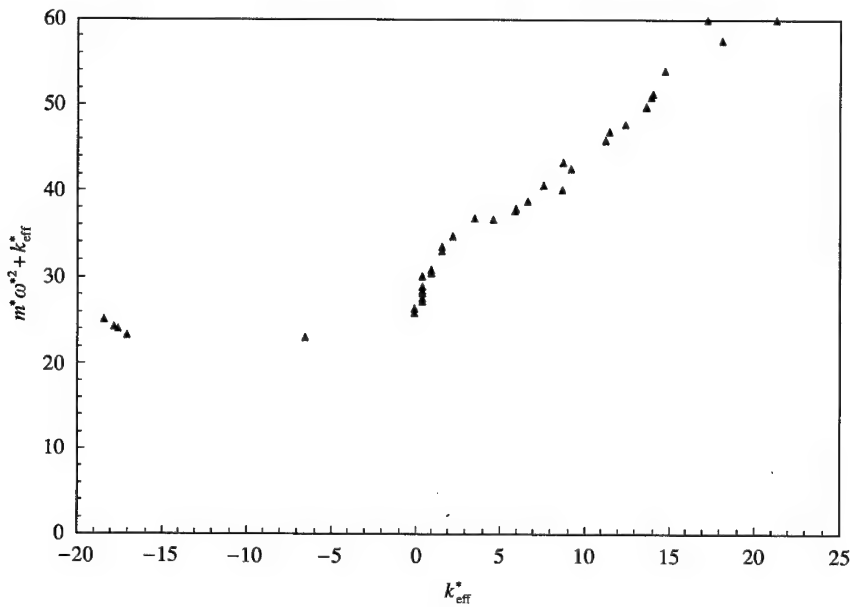


Figure 7.  $m^*\omega^{*2} + k_{\text{eff}}^*$  or  $m^*/U_R^2$  plotted against effective elasticity for the case  $m^* = 28.0$ . Same experiment as in Figure 6.

parameters, mass ratio,  $m^*$ , reduced velocity,  $U_R$ , and mass damping,  $m^*\zeta$  for transverse oscillations of an elastically mounted body. Body geometry and Reynolds number remain as additional parameters in either case.

As noted in SLR, the results of a traditional experiment performed at a given  $m^*$  may be used to predict the results for other  $m^*$ . This is so because, in a given experiment in which

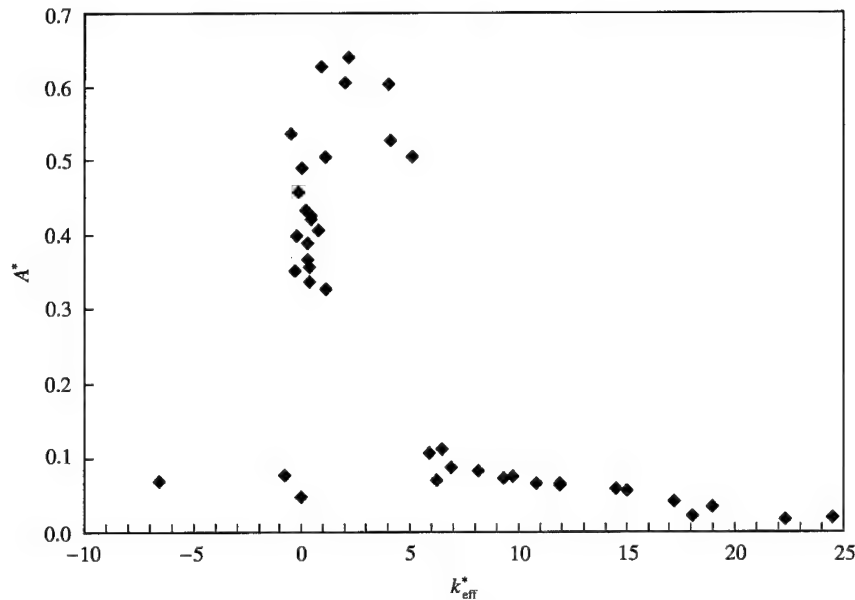


Figure 8. Amplitude plotted against effective elasticity for  $m^* = 28.0$ . Same experiment as in Figure 6.

$U_R$  is varied, the unifying parameter

$$k_{\text{eff}}^* = k^* - m^* \omega^{*2} = m^* / U_R^2 = m^* \omega^{*2} \quad (10)$$

also takes on all values of interest. In particular, we have shown that the branching of solutions, often observed in traditional experiments, is a consequence of the response frequency dependence on  $k_{\text{eff}}^*$ , which itself is dependent on the response frequency. For the limited computational and experimental data we have considered in this paper branching behavior is predicted and observed to occur only at higher  $m^*$ . The response,  $A^*$  versus  $U_R$ , is smooth at low  $m^*$ . This result appears to be at odds with the branching observed by Khalak & Williamson (1997) for  $m^* = 2.4(\pi/2) = 3.7$  but could be due to effects of Reynolds number.

The possibility of formulating a unified description of the response, in terms of one parameter,  $k_{\text{eff}}^*$ , was facilitated by setting the damping  $b^*$  equal to zero in the numerical simulations, thereby ensuring that the spring and inertial forces are in line. A few simulations (in SLR) over a range of finite  $b^*$  show, not surprisingly, that amplitude is reduced ( $dA^*/db^* \simeq -0.3$  for  $b^* \ll 1$ ). Thus, the maximum value of amplitude for the unified solution,  $A^* = 0.59$  [Figure 1(a)], must be the maximum value for any combination of parameters, at  $\text{Re} = 100$ !

The relation of  $b^*$  to the conventional damping coefficient  $\zeta$  is given by  $b^* = 2m^*\zeta/U_R$ , i.e., it is equal to about twice the "mass-damping parameter"  $m^*\zeta$  (since  $U_R \sim 1$ ) that has been used to determine maximum values of amplitude, starting with investigations by Griffin & Ramberg (1982). Indeed,  $A^* \rightarrow A_{\text{max}}^*$  for  $b^* \rightarrow 0$ , as found by those and other investigators. The maximum value of amplitude, however, depends on Reynolds number. This is evident from the result of Khalak & Williamson (1997, 1999) and of Gharib (1999); values of  $A^*$  as high as 1.2 have been observed.

Among the issues that need further investigation is that of modeling vortex-induced vibration. It seems that modeling efforts could benefit by considering the unified description

presented in this paper and SLR. But it will still be a challenging task given, e.g., the counter-intuitive relation between amplitude and transverse force coefficient discussed above. Another item that needs further consideration is nonsinusoidal response and how such a response might be considered within the framework of the unified description. As noted above, aperiodic behavior does occur under certain conditions. In the computational study, for example, the response becomes modulated in what would be the range,  $3 < k_{\text{eff}}^* < 5$ .

### ACKNOWLEDGEMENTS

Thanks to Ms Lorena Barba for providing the results of her numerical simulations prior to publication and for her assistance in preparing the figures. We have also benefited greatly from interactions with Dr Mohammad Gharib and with Prof. Morteza Gharib. This work has been supported by ONR Grant #N00014-94-1-0793.

### REFERENCES

- BRIKA, D. & LANEVILLE, A. 1993 Vortex-induced vibrations of a long flexible circular cylinder. *Journal of Fluid Mechanics* **250**, 481–508.
- FENG, C. C. 1968 The measurement of vortex-induced effects in flow past stationary and oscillating circular and D-section cylinders. M.A.Sc. thesis, University of British Columbia, Vancouver, BC, Canada.
- GHARIB, M. R. 1999 Vortex-induced vibration, absence of lock-in and fluid force deduction. Ph.D. Thesis, California Institute of Technology, Pasadena, CA, U.S.A.
- GHARIB, M. R., LEONARD, A., GHARIB, M. & ROSKO, A. 1998 The absence of lock-in and the role of mass ratio. In *Proceedings of the 1998 Conference on Bluff-Body Wakes and Vortex-Induced Vibration* (eds P. W. Bearman and C. H. K. Williamson), Paper No. 24. Ithaca, NY: Cornell University.
- GHARIB, M. R., SHIELS, D., GHARIB, M., LEONARD, A. & ROSKO, A. 1997 Exploration of flow-induced vibration at low mass and damping. In *Proceedings of Fourth International Symposium on Fluid-Structure Interaction, Aeroelasticity, Flow-Induced Vibration, and Noise* (eds M. P. Paidoussis *et al.*), Vol. 1, pp. 75–81. New York: ASME.
- GRIFFIN, O. M. & RAMBERG, S. E. 1982 Some recent studies of vortex shedding with application to marine tubulars and risers. *ASME Journal of Energy Research and Technology* **104**, 2–13.
- KHALAK, A. & WILLIAMSON, C. H. K. 1997 Fluid forces and dynamics of a hydroelastic structure with very low mass and damping. *Journal of Fluids and Structures* **11**, 973–982.
- KHALAK, A. & WILLIAMSON, C. H. K. 1999 Motions, forces and mode transitions in vortex-induced vibrations at low mass-damping. *Journal of Fluids and Structures* **13**, 813–851.
- KOUMOUTSAKOS, P. & LEONARD, A. 1995 High-resolution simulations of the flow around an impulsively started cylinder using vortex methods. *Journal of Fluid Mechanics* **296**, 1–38.
- SHIELS, D., 1998 Simulation of controlled bluff body flow with a viscous vortex method. Ph.D. thesis, California Institute of Technology, Pasadena, CA, U.S.A.
- SHIELS, D., LEONARD, A. & ROSKO, A. 2001 Flow-induced vibration of a circular cylinder at limiting structural parameters. *Journal of Fluids and Structures* **15**, 3–21.

### APPENDIX: ADDED MASS

The “apparent” or “added mass” of an accelerating body is equal to the reactive force which the body exerts on the fluid in which it is immersed divided by the acceleration. Alternatively, it is equal to the impulse given to the fluid during an incremental change of body velocity divided by that incremental velocity. For the circle (cylinder in two-dimensional flow) or sphere, the impulse is aligned with the velocity change, but not in general, and then the ratio of impulse to velocity, i.e., the apparent mass, is a tensor quantity. These properties are well known from textbook derivations which are usually obtained for irrotational flow



and so it is not as well known that the resulting definitions are applicable more generally, e.g., in separated flows such as those that occur in problems of flow-induced vibration. As a result, empirical relations are sometimes introduced into models, unnecessarily. This assertion perhaps becomes obvious on noting that, in incompressible flow, an incremental velocity  $\Delta V$  instantaneously generates a potential velocity field, proportional to  $\Delta V$ , which is superimposed on the existing velocity field, whatever that may be, and that is why the conventional derivation based on irrotational flow is successful. But an alternative derivation, which addresses the vorticity field explicitly, may be more convincing. Here, we derive the result specifically for a circular cylinder.

The force  $F_b$  on the cylinder in two-dimensional flow can be calculated from the following relation (Koumoutsakos & Leonard 1995):

$$\mathbf{F}_b = \rho \frac{d}{dt} \int_{\text{fluid}} \boldsymbol{\omega} \times \mathbf{x} dA + \rho A_B \frac{d\mathbf{U}}{dt}. \quad (\text{A.1})$$

[In equation (21) of Koumoutsakos & Leonard, the sign of the first term is incorrect.] Using polar coordinates  $(r, \theta)$ , with origin at the center of the circle and  $\theta$  measured from the direction of acceleration,  $dV/dt$ , the force  $F$  in that direction is

$$F = \frac{d}{dt} \int_a^\infty \int_0^{2\pi} r \omega_z \sin \theta r dr d\theta + \rho \pi a^2 \frac{dV}{dt}. \quad (\text{A.2})$$

Vorticity is found only in the boundary layer and wake of the body. Unsteadiness of that vorticity results in unsteadiness of  $F$ , even if the body is stationary. However, independently, during acceleration *new* vorticity is generated at the surface of the body, and instantaneously creates a potential velocity field as noted above; its contribution to the force integral is the only contribution connected with the body acceleration and it uniquely defines the added mass. This contribution to the integral in equation (A.2) may be evaluated by noting that the new vorticity is contained in a singular layer whose strength  $\gamma(\theta) = \lim_{\delta \rightarrow 0} \int_a^{a+\delta} r^2 \omega_z dr = \lim_{\delta \rightarrow 0} \int r^2 (-\partial u_\theta / \partial r) dr = a^2 (-2\Delta V \sin \theta)$ . The last term in parenthesis is the velocity along the cylinder surface (i.e., at the edge of the singular vorticity layer) due to an incremental velocity  $\Delta V$  of the cylinder. Using this in equation (A.2) to complete the evaluation of the integral, we get

$$F = -2\rho\pi a^2 \frac{dV}{dt} + \rho\pi a^2 \frac{dV}{dt} = -\rho\pi a^2 \frac{dV}{dt}. \quad (\text{A.3})$$

(Note that for a stationary body [ $U_b = 0$  in equation (A.1)] in an accelerating stream, the result will be  $F = -2\rho\pi a^2 dV/dt$ .)

## QUANTITATIVE IMAGING OF THE WAKE OF A CYLINDER IN A STEADY CURRENT AND FREE-SURFACE WAVES

D. ROCKWELL, J.-C. LIN, O. CETINER, K. DOWNES AND Y. YANG

*Department of Mechanical Engineering and Mechanics, 354 Packard Laboratory  
19 Memorial Drive West, Lehigh University, Bethlehem, PA 18015, U.S.A.*

(Received 4 September 2000, and in final form 6 November 2000)

The technique of high-image-density particle image velocimetry (PIV) can lead to instantaneous, global representations of the wake of a cylinder in a steady current and free-surface waves. Approaches to characterizing the complex patterns of the wake are described for several classes of experimental systems. Emphasis is on imaging in different planes, with the aim of providing insight into the quasi-two- and three-dimensional features of the near-wake.

© 2001 Academic Press

### 1. INTRODUCTION

DURING THE PAST DECADE, application of particle image velocimetry to the wakes of cylinders has yielded quantitative insight in a wide variety of investigations. They are described in works edited by Eckelmann *et al.* (1992) and Bearman & Williamson (1998), and the conference abstracts provided by Bearman *et al.* (2000). Further overviews are given by Rockwell (1998, 2000).

High-image-density particle image velocimetry, based on film as a recording medium, was employed in the investigations summarized by Rockwell *et al.* (1993). Representative images therein illustrate both the quasi-two- and three-dimensional features of the near-wakes of cylinders. More recent studies that employed film-based systems have focused on the issues of: Reynolds number sensitivity of the near-wake vortex patterns (Lin *et al.* 1995); simultaneous existence of small- and large-scale concentrations of vorticity in the near-wake (Chyu & Rockwell 1996a; Sheridan *et al.* 1997); timing of initially-shed concentrations of vorticity in relation to oscillations of the cylinder (Gu *et al.* 1994; Sheridan *et al.* 1998); three-dimensional structure of the near-wake of a stationary cylinder (Lin *et al.* 1996b; Chyu & Rockwell 1996b; Brede *et al.* 1996) and an oscillating cylinder (Towfighi & Rockwell 1994; Gu & Rockwell 1995); control of the near-wake by three-dimensional fluid injection (Lin *et al.* 1995) and interaction between stationary and deformed free-surfaces with the near-wakes of stationary and oscillating cylinders (Lin *et al.* 1996a; Sheridan *et al.* 1997). The consequence of spatial resolution of the image acquisition system on interpretation of small- and large-scale vortex interactions in the near-wake region is assessed by Lin & Rockwell (1997).

Recent investigations that employ the digital version of particle image velocimetry (DPIV) have provided substantial insight into the near-wake structure of a cylinder. The three-dimensional features of the wake from a stationary cylinder were addressed by Wu *et al.* (1994, 1996). More recently, the emphasis of most investigations has been on

quasi-two-dimensional patterns of the near-wake structure of a stationary and an oscillating cylinder. This series of investigations includes: the wake system from arrangements of cylinders (Sumner *et al.* 1998, 2000); the wake from an accelerating cylinder (Noca *et al.* 1998, 1999); wakes from oscillating cylinders (Techet & Triantafyllou 1998; Atsavapranee *et al.* 1998); the wake structure from a cylinder in orbital motion (Williamson *et al.* 1998); and the two- and three-dimensional wake from a stationary cylinder in presence of a free-surface (Lang & Gharib 1998).

In nearly all of the foregoing investigations, presentations of patterns of instantaneous velocity and vorticity, as well as phase- or time-averaged representations of them, has been a primary goal. Of course, once quantitative images are attained, a range of possibilities for interpretation become available, as described by Rockwell (2000). For example, employment of topological concepts based on critical point theory, a snapshot version of proper orthogonal decomposition (POD), as well as a variety of other approaches can be invoked. Furthermore, direct links to a range of theoretical, vorticity-based models can be attained. These models represent concepts of: convective instabilities of the near-wake; forces on the cylinder in relation to patterns of velocity and vorticity; generation of acoustic power in coupled wake-resonator systems; and the onset of critical states in swirling flows.

Of all of these conceptual frameworks for interpreting PIV images, the most relevant to our present considerations is the relationship between the forces on the cylinder and the space-time imaging of the cylinder wake, for either a stationary or an oscillating cylinder. For the situation where the vorticity is confined to the field of view during the process of vortex shedding, Lin & Rockwell (1996) and Zhu *et al.* (2000) have employed the vorticity moment concept described, for example, by Lighthill (1986) to determine either the unsteady forces or the time integral of the unsteady forces acting on a cylinder. In fact, the theoretical concept advocated by Wu (1981) and Lighthill (1986) has been further developed by Noca (1996) and Noca *et al.* (1997), with the aim of accounting for all of the previously generated vorticity that is not contained within the field of view of the PIV imaging system. In essence, this involves a control volume approach. Unal *et al.* (1997) developed a control volume technique based on momentum concepts and, in a parallel and complementary investigation, Noca (1997) and Noca *et al.* (1999) arrive at a different, but presumably, equivalent momentum-based control volume expression. More recently, Noca *et al.* (1999) provide a critical assessment of various control volume representations and, in addition, formulate a type of flux equation that requires knowledge of only the parameters along the boundary of the control surface. Application of particle image velocimetry (PIV) to the assessment of forces on a cylinder clearly involves a number of limitations, as described in the foregoing citations. Irrespective of the degree of approximation, however, links to theoretical concepts have clearly been established, thereby allowing more meaningful interpretation of quantitative images.

The wake from a cylinder can take on a variety of forms, depending upon the nature of the incident current (steady flow), the wave motion, or a combination of them. By now it is well known that even for the comparatively simple system of a stationary cylinder in a current, the near-wake exhibits a range of possible states. When a stationary, vertical cylinder is immersed in a wave, one expects particularly complex states of the wake, due to the elliptical particle trajectories of the wave motion and their variation along the span of the cylinder. Furthermore, elastic or controlled oscillation of the cylinder can further modify the nature of the wake. Interpretation of these representative wake patterns in relation to the loading on the cylinder can be guided by the conceptual frameworks outlined by Wu (1981) and Lighthill (1986). Central to this interpretation, of course, is a quantitative knowledge of the wake structure, preferably in terms of vorticity.

The present aim is to describe selected imaging configurations and representative images that address complex features of the near-wakes of cylinders. An overview of experimental approaches and generic features of imaging systems is followed by descriptions of arrangements that allow simultaneous orthogonal views and dual views of the near-wake.

## 2. OVERVIEW OF EXPERIMENTAL APPROACHES

All of the investigations herein employ one of a variety of continuous wave Argon-ion lasers as an illumination source, either a rotating, multi-faceted polygon mirror or an oscillating flat mirror to induce rapid scanning of the laser beam, and one of several types of 35 mm film (motor-driven) cameras for image acquisition.

An Argon-ion laser, with a maximum power rating between 5 and 25 W, generated a continuous beam of approximately 1 mm diameter. This beam then impinged upon either the rotating or oscillating mirror, which scanned the laser across the region of interest. For both types of mirror systems, the aim was to provide relatively high-intensity illumination from a continuous laser source. The effective pulse rate of the illumination was dictated by the laser-scanning rate. A major advantage of laser scanning is that the total power of the laser beam illuminates each particle as it sweeps across the flow. Moreover, generation of multiple-pulsed images of particles is easily achieved by adjusting the scanning rate relative to the shutter speed of the camera. A further virtue of this scanning illumination technique is that qualitative patterns of particles can be continuously observed in the plane of the laser sheet immediately prior to and during acquisition of PIV images. This approach allows effective monitoring of the overall features of the flow. A disadvantage of the laser scanning approach is an effective reduction in illumination time of each particle at higher scanning frequency, which is required at higher values of flow velocity. In addition, the retrace time of the oscillating mirror, whereby the beam traces back to its initial position during each scanning cycle, or splitting of the beam at the edge of a polygon (multi-faceted) rotating mirror, can result in a reduction of the effective duty cycle of the scanning laser beam if the system is not properly designed (Rockwell *et al.* 1993). For the investigations described herein, the rotating polygon mirror had either 8, 48 or 72 facets. It was controlled externally by an analog system in order to maintain the revolution rate to within an accuracy of 0.1%. In effect, the typical scanning rate of the laser beam across the plane of interest using the polygon mirror ranged from approximately 100 to 700 cycles/s. Alternately, an oscillating mirror was employed. It was mounted on a galvanometer scanner, which was externally controlled by a driver unit. This arrangement is effective for lower scanning rates, extending up to approximately 100 Hz; such scanning rates are required at lower values of velocity. Over this range of operation, the oscillating mirror system is preferred to the rotating polygon mirror, which yields significant uncertainty of the laser-scanning rate at low values of mirror rotation rate. For the experimental configurations described herein, the oscillating mirror is preferred over the rotating mirror for certain end views, i.e., crossflow planes.

For all of the present experiments, the flow was seeded with metallic coated, hollow plastic spheres having a nominal diameter of 12–14  $\mu\text{m}$ . The required number of particles can be estimated *a priori*. The relevant image density parameter, originally defined by Adrian & Yao (1984), is  $N_I = C\Delta z_0 A_I/M$ , in which  $C$  is the mean number of particles per unit volume, and  $\Delta z_0$  is the thickness of the laser sheet. The interrogation cell employed for evaluation of the velocity vector has an area of  $A_I/M$  on the plane of the laser sheet. If  $N_I \gg 1$ , there is a high probability of finding many particle images in the interrogation cell. For the present experiments, the representative interrogation area was 0.5 mm<sup>2</sup>, the thickness of the laser sheet was approximately 1 mm, and values of magnification ranged from

1:6 to 1:11. The interrogation volume contained approximately 30–60 particle images, which substantially exceeds the high image density criterion.

Multiple-pulsed illumination was attained by maintaining the camera shutter open during three to five scans of the laser beam across the plane of interest. Keane & Adrian (1990, 1991) undertook theoretical and numerical analyses to assess the performance criteria of multiple- versus double-pulsed systems, as well as other features of PIV approaches employing autocorrelation techniques. As pointed out by Adrian (1991), a four-pulse single exposure that contains  $N_I$  particles yields a self-correlation peak of height  $4N_I$ , a first correlation peak of height  $3N_I$  and so on. The overall performance is essentially equivalent to that of a double-pulse image pattern obtained from  $3N_I$  particles at the same time spacing  $\Delta t$ .

The multiply-pulsed patterns of particle images were recorded on high-resolution 35 film. It provides an effective pixel size, as calculated from one-half of the line pairs per millimeter, of  $5\text{ }\mu\text{m} \times 5\text{ }\mu\text{m}$ , and an effective format of  $7000 \times 4800$  pixels or, equivalently, a total of  $33.6 \times 10^6$  pixels. This concept of pixel equivalents for a film-based format relative to the pixel format of video/digital camera systems is assessed by Adrian (1995). It is crucial that the 35 mm negatives are digitized at sufficiently high resolution. For the present experiments, the digitizing process was executed at 125 pixels/mm.

Several types of motor-driven 35 mm cameras were employed to acquire sequential images of the flow. Depending upon the time scale of the flow event, which was relatively slow in the water systems described herein, it was possible to attain adequate temporal resolution to allow reconstruction of cinema sequences. Standard, motor-driven 35 mm cameras had framing rates in the range of approximately 5–10 frames/s. In addition, a specially designed framing camera allowed acquisition of images at a rate of 60 frames/s. This system is the basis of the cinema PIV approach described in detail by Lin & Rockwell (1994, 1999). It provides an effective transfer rate of  $2 \times 10^9$  equivalent pixels/s.

For all camera systems, an image-shifting mirror was located immediately in front of the lens system. While the camera shutter was open, the mirror was subjected to a prescribed rate of rotation by a galvanometer scanner. This image shifting, in essence, provides a constant bias displacement to all particle images, which is removed following the interrogation procedure to evaluate the velocity field. Such a bias is necessary in order to preclude directional ambiguity in regions of negative or reverse flow. In the present investigations, the typical dimensions of the bias mirror were  $50\text{ mm} \times 30\text{ mm} \times 1\text{ mm}$ . Full details of the bias mirror concept are described by Adrian (1986). In order to ensure that the motion of the bias mirror does not distort the pattern of particle images, it should be operated within a specific range of parameters. If caution is not exercised, systematic distortions of the patterns of particle images may arise, as described by Oschwald *et al.* (1995), Lee *et al.* (1996) and Raffel & Kompenhans (1995). The latter two groups of investigators propose techniques to correct for systematic errors.

Irrespective of the type of image acquisition system, it is important to consider the paraxial recording criterion. Let  $x_{\text{max}}$  represent the maximum in-plane location of a particle measured from the centerline of the camera lens, and  $d_o$  the object distance; the ratio  $x_{\text{max}}/d_o$  should be minimized (Lourenco & Whiffen 1986; Adrian 1991). This condition ensures that the consequences of out-of-plane motion are small when determining the velocity field from in-plane measurements.

In addition to the foregoing considerations, Keane & Adrian (1990, 1991) show, via theoretical concepts and numerical simulations, that the best overall performance of a double-pulsed imaging system is attained when: (i) the in-plane displacement of a particle is less than one-fourth the width of the measuring volume (cell); (ii) the out-of-plane displacement of a particle is less than one-fourth the thickness of the laser sheet; and (iii) the

velocity variation over the measuring volume is less than 20% of the characteristic velocity within the volume. Criterion (ii) is particularly important for end view measurements, i.e., measurements in the crossflow plane of a highly three-dimensional flow. Design of the imaging systems described herein aimed to satisfy these criteria.

In the following, three different classes of PIV arrangements are considered: (i) an orthogonal view system, which allows simultaneous acquisition of images in orthogonal laser sheets; (ii) a dual view system, which provides simultaneous acquisition of images in two adjacent fields of view in the same plane for cases where the region of interest has a very high aspect ratio; and (iii) a dual view system, which also involves adjacent fields of view, but with the aim to preclude blind areas, or shadow effects, due to use of a long object distance in presence of a stationary or oscillating body.

### 3. ORTHOGONAL VIEW SYSTEM FOR THREE-DIMENSIONAL FLOWS

The objective of this class of imaging is to acquire space-time representations of the flow in two orthogonal views, i.e., in two planes oriented perpendicular to each other. This approach allows simultaneous characterization of the quasi-two- and three-dimensional structure of the flow. An important physical issue is the degree to which motion of the body attenuates large-scale three dimensionality, and whether the nature of small-scale spanwise three dimensionality is attenuated, or even enhanced, by the body motion. This issue is generic to oscillating bodies undergoing not only transverse motion, but also in-line and orbital motions relative to an incident, steady current. The nature of the three-dimensional structure from a stationary cylinder has been the subject of intense investigation as reviewed by Williamson (1996b), who describes numerical, theoretical and experimental investigations. For our present purposes, selected experimental studies are of interest. Remarkable insight has been provided by the visualization studies of Hama (1957), Gerrard (1978) and Williamson (1988, 1992, 1996a). Corresponding application of particle image velocimetry to characterize patterns of instantaneous velocity, streamlines and vorticity were initially undertaken along the span of the stationary cylinder, and at a transverse location corresponding to the outer edge of the wake, by Rockwell *et al.* (1993) and Wu *et al.* (1994, 1996). Subsequent studies of Chyu & Rockwell (1996b), Lin *et al.* (1996b) and Brede *et al.* (1996) used space-time imaging to determine patterns of velocity and vorticity across the entire crossflow plane in the near-wake. To date, the quantitative patterns of streamwise vorticity in the near-wake of a cylinder undergoing transverse oscillations have not been characterized.

A schematic of an orthogonal view system is given in Figure 1. It involves a single laser beam and two rotating polygon (multi-faceted) mirrors, as well as two bias mirror-camera units. Details of this arrangement and its application to a variety of oscillating cylinder systems are given by Cetiner & Rockwell (2000). A major challenge of orthogonal laser sheet PIV is the interference of one laser sheet with imaging in the other sheet. For example, if one attempts to obtain patterns of particle images in the side view, the high intensity of the end view laser sheet intersects the side view sheet. This intersection makes it impossible to attain adequately resolved particle images over a significant region of the field of view. To circumvent this difficulty, it is desired to shut off the illumination of the end view sheet when imaging in the side view, and conversely. This is accomplished by employing a Pockels cell arrangement, as indicated in Figure 1. The Pockels cell rapidly switches the laser beam from its colinear (throughput) mode to its deflected mode. In doing so, the beam is shifted from a position that generates a side view laser sheet, which is eventually transmitted to camera 1, to an end view laser sheet, which is recorded by camera 2.

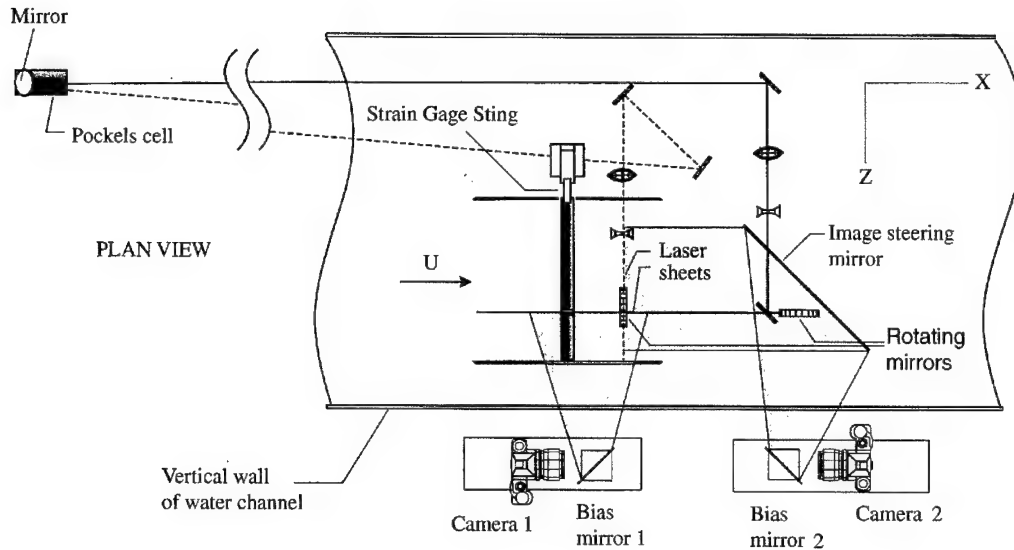


Figure 1. Schematic of arrangement for space-time imaging in two orthogonal views which are defined by two laser sheets. A single laser generates the laser sheets via deflection of the laser beam through a Pockels cell.

More specifically, the end view of the laser sheet was generated as follows. The beam from the Pockels cell was deflected at an angle as represented by the circular mirror arrangement on the side of the Pockels cell. This deflected mode is designated by the dashed line. The beam eventually impinged upon two successive steering mirrors. It was then transmitted through a series of focusing optics and eventually impinged upon the rotating mirror that generated a scanning laser beam over a plane orthogonal to the incident flow  $U$ . The field of the end view of the laser sheet is designated by the gray shaded area. The pattern of particle images was transmitted to the bias mirror 2, then reflected to the back of camera 2. An analogous concept was employed for the side view. The entire system comprising the Pockels cell and the camera-bias mirror units 1 and 2 were controlled by a laboratory microcomputer. The time delay between the throughput and deflected laser beam modes of the Pockels cell was approximately 70 ms. This laser switching arrangement thereby provides multiplexing of the side and end view image acquisition. Such multiplexing allows a space-time reconstruction in the two orthogonal views, whereby the image sequence is essentially synchronized, with the aforementioned time delay. The values of magnification of cameras 1 and 2 were 1:6 and 1:7.8. The fields of view in the side and end views were, respectively, 206 mm  $\times$  133 mm and 223 mm  $\times$  164 mm. Typically, a total of 6111 and 4720 velocity vectors were obtained for the side and end views, respectively. Representative excerpts from the synchronized sequences of side and end view images of vorticity are exhibited in Figure 2 for the case of a cylinder undergoing transverse oscillations at a value of  $A/D = 0.96$ , in which  $A$  is the amplitude of the cylinder motion, and  $D$  is the cylinder diameter. The Reynolds number is  $Re = 1238$ . It is evident that projections of streamwise vorticity exhibited in the end view sequence can have substantial values of peak vorticity and circulation. In fact, the peak values of these vorticity concentrations are of the order of  $13 \text{ s}^{-1}$  in comparison with representative concentrations in the side view having  $30 \text{ s}^{-1}$ . It is therefore apparent that cross-stream oscillations can effectively attenuate larger modes of

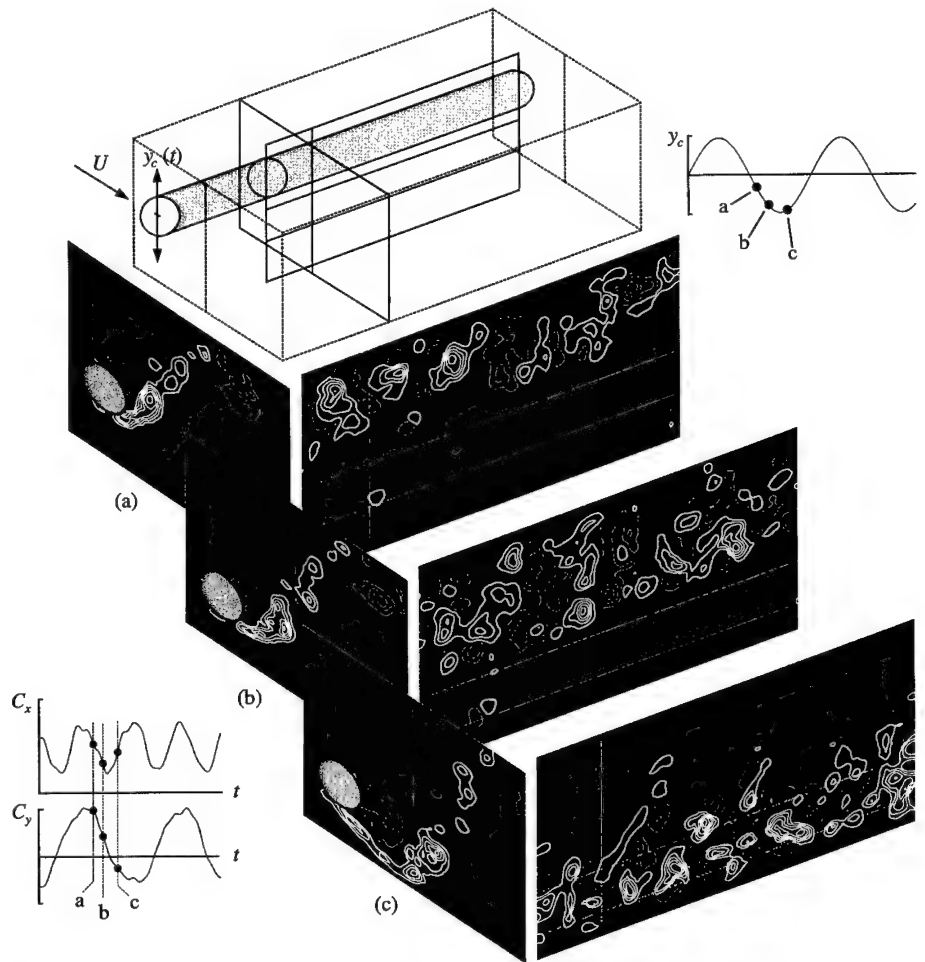


Figure 2. Space-time imaging in orthogonal views of vortex formation from an oscillating cylinder.

spanwise three dimensionality, but, in fact, are associated with pronounced concentrations of small-scale streamwise vorticity.

#### 4. DUAL VIEW SYSTEM FOR FLOW REGIONS WITH HIGH ASPECT RATIO

The overall goal of this type of quantitative imaging is to provide instantaneous views of the flow structure over, for example, the entire spanwise extent of a cylinder having a relatively large length-to-diameter ratio. It is, of course, desired to maintain adequate spatial resolution, in order to characterize the evolution of patterns of instantaneous velocity and vorticity in the near-wake. A representative configuration is a long vertical cylinder in a wave tank. The present aim is to characterize the variations of the direction of transverse vortex shedding along the span of the cylinder. Such a variation is an indicator of the spanwise coherence of vortex shedding, and thereby the transverse force on the cylinder. It is well known that time-dependent variations of the transverse force on a vertical cylinder in a wave can exhibit substantial modulations. The issue is to what degree such modulations can be associated with spontaneous transformation between states of three-dimensionality.



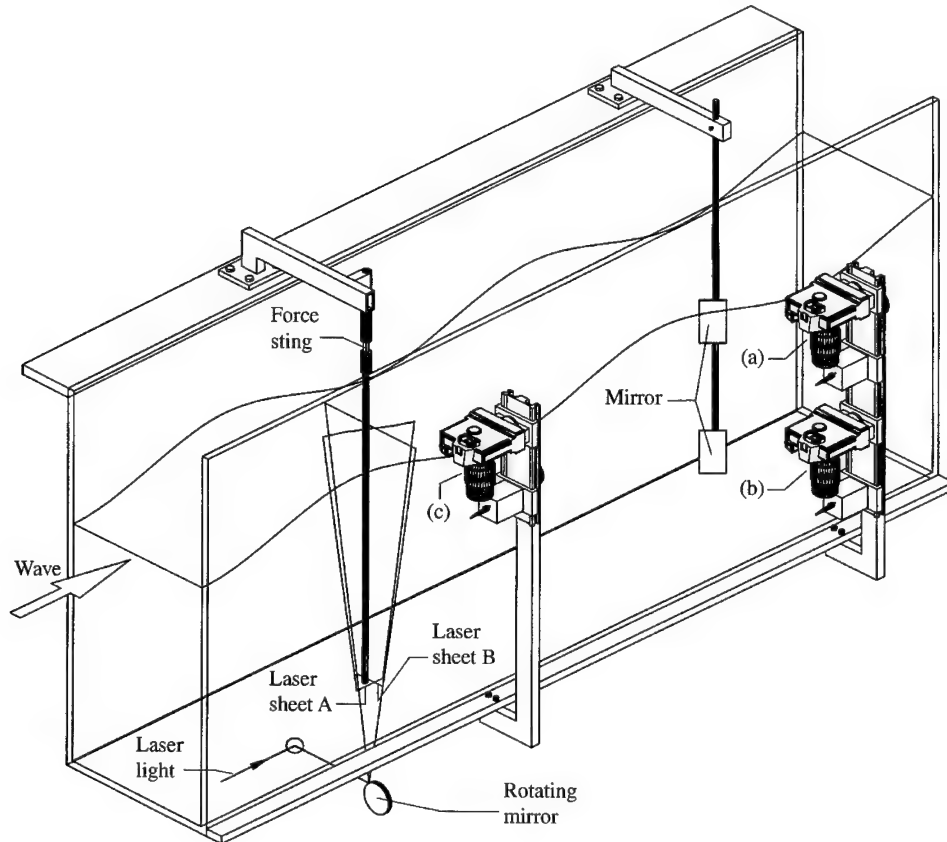


Figure 3. Schematic of experimental system illustrating wave tank, laser sheets, and orientations and arrangements of cameras employed for high-image-density particle image velocimetry.

For the particular case of a cylinder subjected to unidirectional oscillations in quiescent fluid or, conversely, a stationary cylinder in a flow undergoing unidirectional oscillations, Honji (1981), Sarpkaya (1986), and Tatsumo & Bearman (1990) have effectively characterized the patterns of spanwise-periodic three dimensionality using qualitative visualization. These studies vividly show that the spanwise wavelength of these patterns can range from approximately one cylinder diameter to several cylinder diameters. Furthermore, in the experiments of Obasaju *et al.* (1988), particle visualization taken simultaneously at two cross-sections along the span of the cylinder clearly suggests the existence of three dimensionality. With regard to numerical simulations of such three-dimensionality, the recent investigation of Duetsch *et al.* (1998) shows well-defined, spanwise periodic structure along the cylinder. The present emphasis is on the case of an actual free surface wave incident upon a vertical cylinder. The orbital particle trajectories of the wave, along with the different boundary conditions at the free surface and bottom (solid) surface of the wave tank are expected to significantly alter the nature of the three-dimensionality. Characterization of the spanwise structure of the near-wake, either for the aforementioned case of unidirectional flow or cylinder motion, or orbital motion of an actual wave, has not yet been pursued using high-image-density particle image velocimetry.

An overview of the imaging system, in conjunction with the wave tank, is given in Figure 3. Of principal interest for our present considerations is the PIV imaging technique.

Complete details of this approach, as well as descriptions of corresponding shadowgraph and force measurement techniques, are given by Yang, Lin & Rockwell (2000). The wave tank was custom-designed in order to allow optical access on all three sides. It is constructed of high-quality one-half inch glass suspended in a metal frame. As indicated in Figure 3, cameras (a) and (b) are employed for the dual end view, and camera (c) for a side view. Emphasis herein is on laser sheet orientation B, which is orthogonal to the direction of wave propagation. The location and orientation of the multi-faceted rotating mirror (48 facets) that generates this laser sheet is indicated beneath the wave tank. The plane of laser sheet B is located at a distance of 5 mm from the surface of the cylinder, which has a diameter of  $D = 12.7$  mm. Two small mirrors were located a distance of 1190 mm away from the centerline of the cylinder. Each of these mirrors had dimensions of 64 mm  $\times$  114 mm; they reflected the images from the upper and lower regions of the cylinder to the bias mirrors of each of the mirror-camera systems (a) and (b). The total distance from the plane of the laser sheet B to the image steering mirror within the wave tank, then to the bias mirror, and through the lens of the camera to the camera back was 1580 mm. For each of the cameras (a) and (b), the value of magnification was  $M = 1:11$ . The field of view in the plane of the laser sheet was 264 mm  $\times$  396 mm. Considering both of the adjacent images together, a total of approximately 12 000 velocity vectors were obtained. Both cameras (a) and (b), and their respective bias mirrors, were synchronized using a laboratory microcomputer. The fields of view of the images acquired by cameras (a) and (a) were adjusted such that they overlapped by  $2D$  in the plane of the laser sheet. This approach allowed acquisition of two instantaneous images covering the entire span of the cylinder of submerged length  $L = 700$  mm and aspect ratio  $L/D = 55$ .

A representative pattern of instantaneous velocity vectors in the crossflow plane is illustrated in the left image of Figure 4. It is evident that, at this instant, the velocity vectors have a substantial vertical component in the region beneath the free surface due to the orbital-like motion of the incident wave. Of particular interest herein is the manner in which the transverse (horizontal) velocity component varies along the span of the cylinder. As confirmed by independent vorticity measurements, the direction of the local transverse velocity corresponds to the direction of the vortex formation in the wake of the cylinder. When a given pattern of vortices forms, it sweeps fluid in a preferred direction from the base of the cylinder. Contours of constant transverse (horizontal) velocity are indicated in the right image of Figure 4. It is evident that these contours take on a quasi-periodic variation along the span of the cylinder. They have a longer wavelength between successive zero crossings at locations immediately beneath the free surface, where the orbital trajectory of the incident wave has a significant vertical component. On the other hand, this distance between zero crossings is relatively small near the bottom of the cylinder, where the incident wave is essentially unidirectional. Other admissible patterns of the near-wake, as well as aspects related to the measurement of the instantaneous transverse and in-line forces, are described by Yang & Rockwell (2000).

## 5. DUAL VIEW SYSTEM FOR FLOWS CONTAINING LONG BODIES ALONG THE AXIS OF VIEW

A cylinder in a wave gives rise to patterns of vortex formation that exist over the entire region about the periphery of the cylinder. That is, the vorticity concentrations are not swept away from the cylinder by a steady current. A single camera cannot adequately capture the features of the flow field surrounding the cylinder when the distance from the end of the cylinder to the cross-section of interest is relatively large, especially for the case where elastic oscillations occur. This situation arises for the case of a long vertical cylinder

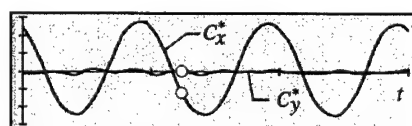
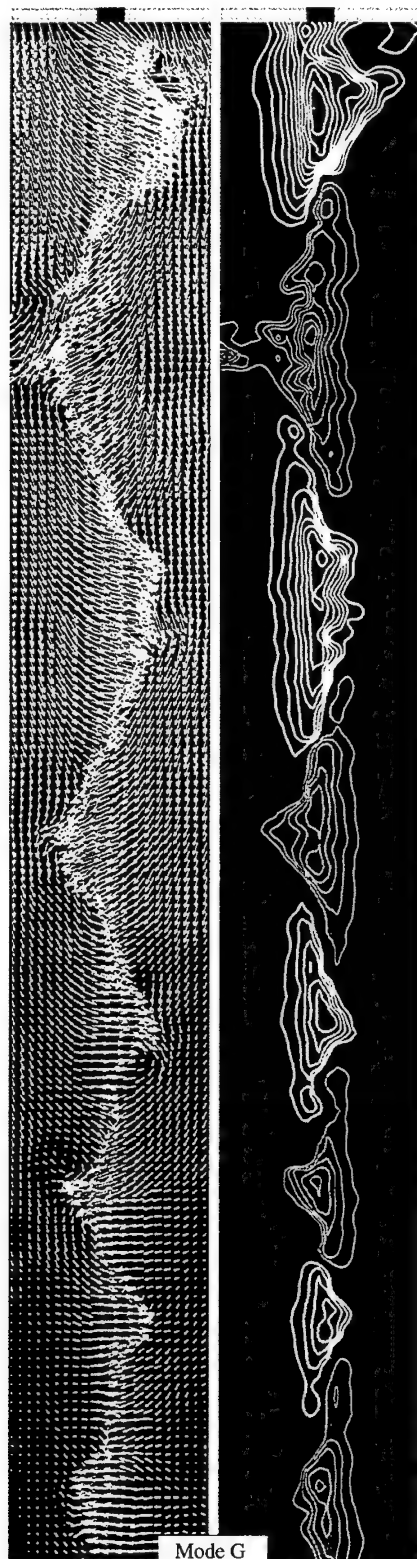


Figure 4. Patterns of instantaneous velocity determined from PIV measurements in laser sheet B in Figure 3. The left image shows patterns of velocity vectors, while the right image exhibits contours of constant horizontal velocity. Thick and thin white lines represent, respectively, positive (rightward) and negative (leftward) horizontal velocity. These patterns of velocity indicate the local direction of transverse vortex shedding in the near-wake of the cylinder. Value of Keulegan-Carpenter number is  $KC = 10$ .

in a wave tank. Quantitative imaging in a horizontal plane immediately beneath the free-surface must be accomplished through the bottom of the wave tank, due to refraction effects associated with the undulating free surface.

Major issues are the manner of generation of vorticity concentrations from the oscillating cylinder and the rate of decay of quasi-two-dimensional concentrations in the wave field. The physics of vortex formation from an oscillating, cantilevered vertical cylinder in a wave has been characterized by Borthwick & Herbert (1988) and Kaye (1989). They employed qualitative visualization to observe patterns of vortex formation at the free surface. Interpretation of this type of vortex formation, based on quantitative imaging, has yet to be undertaken. In doing so, it is necessary to account for the instantaneous relative velocity of the wave with respect to the cylinder when making an assessment of the instantaneous patterns of vorticity, which, in turn, are intimately related to not only the cylinder trajectory, but also to the forces on the cylinder.

Figure 5 shows side and plan views of the elastically mounted cylinder system. In essence, the vertical cylinder was attached to a lightweight hover plate, which remained suspended above a system of approximately 300 mini-jets that emanated from the top surface of a circular air plenum in the form of a donut. Four springs were employed to provide the desired stiffness. The system stiffness is essentially invariant in the circumferential direction. The cylinder is made of hollow Plexiglas in order to minimize its mass. At one section of the cylinder, a nonrefractive window, similar to that in Figure 1, is employed to allow illumination about the entire periphery of the cylinder. A horizontal laser sheet was generated immediately beneath the free surface of the wave by employing a long rectangular beam steering mirror. This mirror had dimensions of 610 mm  $\times$  102 mm. The scanning laser beam from the multi-faceted polygon mirror was reflected from this first-surface mirror at an angle of 90°, thereby forming the horizontal, scanning laser sheet. The scanning rate was 180 c/s. Two camera-bias mirror systems were employed for image acquisition, as indicated in Figure 5. The centerlines of the lenses of the two-camera system were displaced from each other by a distance of 140 mm. This spacing was found to be optimal for viewing the complete field about the periphery of the cylinder. The distance from the plane of the laser sheet to the back of each camera was 1180 mm. Both camera-bias mirror systems were synchronized using the laboratory microcomputer. Taking the images of the two cameras together, the field of view was 262 mm  $\times$  314 mm in the physical plane of the laser sheet. A total of 1650 velocity vectors were typically acquired in each camera view, giving a total of approximately 3000 vectors, excluding duplicate vectors in the region of image overlap.

Figure 6 shows a representative pattern of vorticity concentrations, along with the trajectory of the cylinder, which has the form resembling the outline of a "butterfly" pattern. The instant of image acquisition corresponds to the solid symbol 1 on the trajectory. At this instant, the cylinder is undergoing the initial phase of its transverse motion across the wave tank. The symbol  $U$  represents the instantaneous wave velocity,  $V_c$  is the cylinder velocity, and  $V_R$  is the relative velocity of the wave with respect to the cylinder. Vorticity concentrations C and A were shed during previous portions of the trajectory and concentrations B are in the process of formation from the surface of the cylinder. A full description of the admissible patterns of vortex formation, in relation to the instantaneous values of  $V_R$ , is given by Downes & Rockwell (2000).

## 6. CONCLUDING REMARKS

The approaches of high-image-density particle image velocimetry described herein hopefully will serve as a stimulus for further efforts, not only for the wake of a circular cylinder, but also for a broader range of flow systems that involve generation of unsteady separated

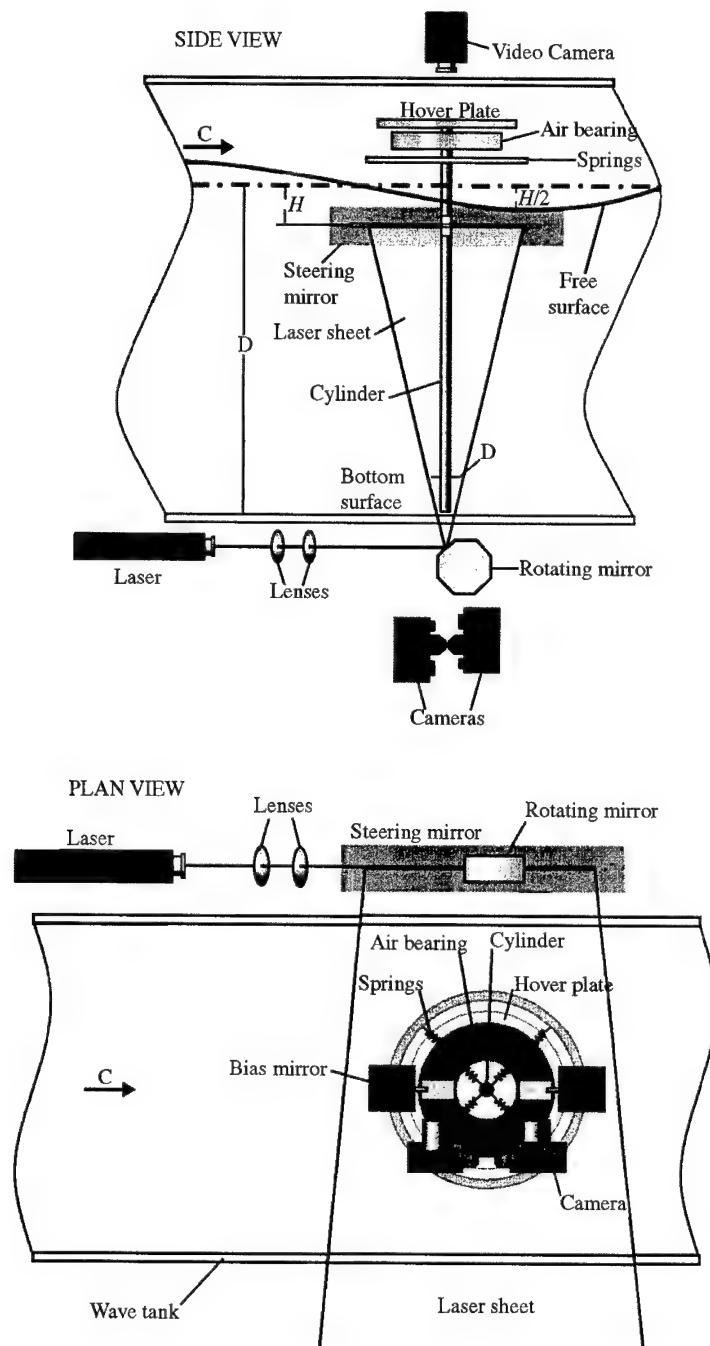


Figure 5. Schematics illustrating plan and side views of elastically mounted cylinder in conjunction with laser illumination for high-image-density particle image velocimetry. The plan view is upwards through the bottom of the wave tank.

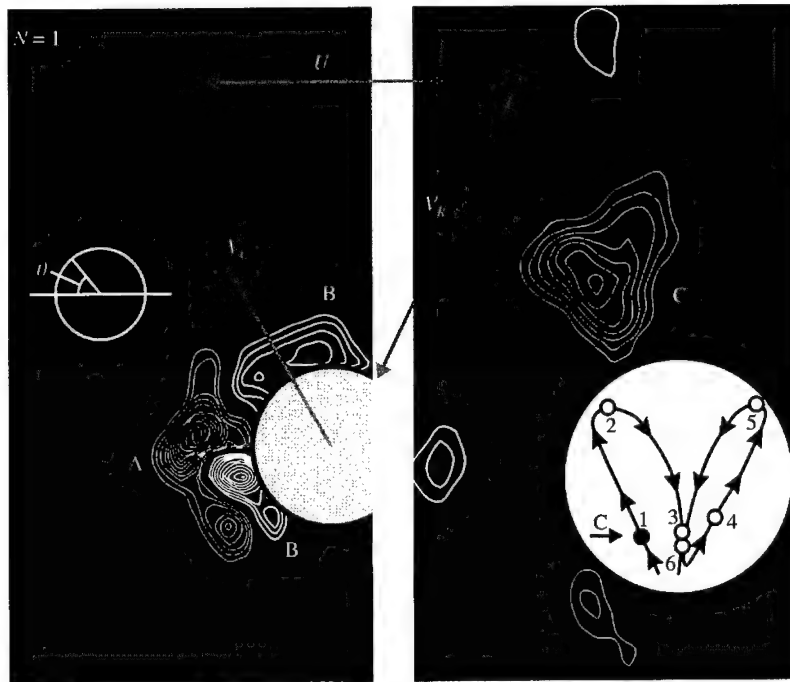


Figure 6. Patterns of positive (thick line) and negative (thin line) vorticity from a cylinder undergoing oscillations in a "butterfly" trajectory, as indicated in the inset. The location of the cylinder corresponds to point 1, which is designated by the black dot. Minimum vorticity level is  $\omega_{\min} = 5 \text{ s}^{-1}$  and incremental vorticity is  $\Delta\omega = 2.5 \text{ s}^{-1}$ . Velocity vectors correspond to:  $V_c$  = velocity of the cylinder;  $U$  = particle velocity of undisturbed region of wave adjacent to cylinder; and  $V_R$  = relative particle velocity of wave with respect to the cylinder.

flow in conjunction with unsteady loading, vibration, and noise. These methods are intended to serve as a complement to measurements of unsteady forces and surface pressures, though certain information on the surface loading can be estimated directly from this type of quantitative imaging, provided that the near-wake can be approximated as two-dimensional. Irrespective of the complexity of the wake structure, this type of imaging is also intended to provide guidance for development of corresponding numerical simulations.

The first two approaches, which involve imaging in orthogonal planes and in dual planes located adjacent to each other, aim to define the critical features of spanwise three-dimensionality, both for stationary and oscillating bodies. Although a full volume representation has not been addressed, acquisition of a space-time sequence of such images can lead to construction of a pseudo-volume representation, which can provide further insight into the three dimensionality of the wake. Furthermore, both of these approaches directly yield patterns of instantaneous velocity and vorticity over a defined plane. Using a sequence of images, it is possible to calculate, for example, the spanwise spatial correlation or the cross-spectral density in a direction parallel to the axis of the cylinder. Such calculations could be coupled with classical, time-averaged spanwise correlations of surface pressure, as well as measurement of forces. This type of comparison can provide insight into the physics related to traditional measurements of surface loading.

The third approach described herein involves imaging in dual planes, with emphasis on the quasi-two-dimensional features of the cylinder wake. It involves synchronized

acquisition of two images, which cover the entire periphery of an oscillating body, and aims to overcome the occurrence of blind regions or shadows due to blockage of the cylinder. This issue is particularly important for oscillatory flows past a stationary body, or conversely an oscillating body in quiescent fluid, both in absence of a steady current. Knowledge of the patterns of vorticity in the entire domain about the body, as a function of time, can provide insight into the rate of decay of peak vorticity and circulation of individual vorticity concentrations in either a unidirectional oscillatory flow or an inherently three-dimensional wave field.

All of the foregoing approaches are under continuous development. Part of this effort involves their implementation for digital camera systems. Rapid advances in both spatial and temporal resolution of image acquisition systems are expected in coming years.

### ACKNOWLEDGEMENTS

Primary support for this research program was provided by the Office of Naval Research Grant No. N00014-94-1-0185, P00007, monitored by Dr Thomas Swaan. In addition, supplemental support was provided by the Office of Naval Research Grant Nos. N00014-98-1-0817 and N00014-99-1-0581, AFOSR Grant No. F49620-99-1-0011 and NSF Grant CTS-9803734. The authors gratefully acknowledge this financial support.

### REFERENCES

- ADRIAN, R. J. 1986 Image-shifting technique to resolve directional ambiguity in double-pulsed velocimetry. *Applied Optics* **25**, 3855–3858.
- ADRIAN, R. J. 1991 Particle-imaging techniques for experimental fluid mechanics. *Annual Review of Fluid Mechanics* **23**, 361–304.
- ADRIAN, R. J. 1995 Limiting resolution of particle image velocimetry for turbulent flow. In *Advances in Turbulence Research—1995* (ed. M. J. Lee), pp. 1–19. Pohang, Korea: Turbulence Research Association.
- ADRIAN, R. J. & YAO, C.-S. 1984 Development of pulsed laser velocimetry (PLV) for measurement of turbulent flow. In *Proceedings of the Ninth Symposium on Turbulence* (eds X. Reed, G. Patterson & J. Zakin), pp. 170–186. Rolla, MO: University of Missouri.
- ATSAVAPRANEE, P., BENAROYA, H. & WEI, T. 1998 Vortex dynamics in the near-wake of a freely-oscillating cylinder. In *Proceedings of the 1998 Conference on Bluff-Body Wakes and Vortex-Induced Vibration* (eds P. W. Bearman & C. H. K. Williamson), Paper No. 5. Ithaca, NY: Cornell University.
- BEARMAN, P. W. & WILLIAMSON, C. H. K. (eds) 1998 *Advances in Understanding of Bluff Body Wakes*. "Forum" at the 1998 ASME Fluids Engineering Division Summer Meeting, Washington, DC, 21–25 June.
- BEARMAN, P. W., LEWEKE, T. & WILLIAMSON, C. H. K. (eds) 2000 *IUTAM Symposium on Bluff Body Wakes and Vortex-Induced Vibrations (BBVIV2)*, Book of Abstracts, 13–16 June, Marseille, France.
- BORTHWICK, A. G. L. & HERBERT, D. M. 1988 Loading and response of a small diameter flexibly mounted cylinder in waves. *Journal of Fluids and Structures* **2**, 479–501.
- BREDE, M., ECKELMANN, H. & ROCKWELL, D. 1996 On secondary vortices in the cylinder wake. *Physics of Fluids* **8**, 2117–2124.
- CETINER, O. & ROCKWELL, D. 2000 Near-wake structure of an oscillating cylinder: Imaging in orthogonal planes (in preparation).
- CHYU, C.-K. & ROCKWELL, D. 1996a Near-wake structure of an oscillating cylinder: effect of controlled shear-layer vortices. *Journal of Fluid Mechanics* **322**, 21–49.
- CHYU, C.-K. & ROCKWELL, D. 1996b Evolution of patterns of streamwise vorticity in the turbulent near-wake of a circular cylinder. *Journal of Fluid Mechanics* **320**, 117–137.

- DOWNES, K. & ROCKWELL, D. 2000 Oscillations of a vertical elastically-mounted cylinder in a wave: imaging of vortex patterns (in preparation).
- DUETSCH, H., DURST, F., BECKER, S. & LIENHART, H. 1998 Low-Reynolds-number flow around an oscillating circular cylinder at low Keulegan-Carpenter numbers. *Journal of Fluid Mechanics* **360**, 249–271.
- ECKELMANN, H., GRAHAM, J. M. R., HUERRE, P. & MONKEWITZ, P. A. (eds) 1992 *Bluff Body Wakes, Dynamics and Instabilities*. Berlin: Springer-Verlag.
- GERRARD, J. H. 1978 The wakes of cylindrical bluff bodies at low Reynolds number. *Philosophical Transactions of the Royal Society (London) A* **288**, 351–382.
- GU, W., CHYU, C. & ROCKWELL, D. 1994 Timing of vortex formation from an oscillating cylinder. *Physics of Fluids* **6**, 3677–3682.
- GU, W. & ROCKWELL, D. 1995 Flow structure from an oscillating cylinder with a localized nonuniformity: patterns of coherent vorticity concentrations. *Physics of Fluids* **7**, 993–998.
- HAMA, F. R. 1957 Three-dimensional vortex pattern behind a circular cylinder. *Journal of Aeronautical Science* **24**, 156–158.
- HONJI, H. 1981 Streaked flow around an oscillating circular cylinder. *Journal of Fluid Mechanics* **107**, 509–520.
- KAYE, D. 1989 Oscillation of a vertical cylinder in waves. Ph.D. dissertation, University of Cambridge, Cambridge, U.K.
- KEANE, R. D. & ADRIAN, R. J. 1990 Optimization of particle image velocimeters. Part I: double pulsed systems. *Measurement Science and Technology* **1**, 1202–1215.
- KEANE, R. D. & ADRIAN, R. J. 1991 Optimization of particle image velocimeters: Part II: multiple pulsed systems. *Measurement Science and Technology* **2**, 963–974.
- LANG, A. W. & GHARIB, M. 1998 On the effects of surface contamination in the wake of surface-piercing cylinder. In *Proceedings of the 1998 Conference on Bluff-Body Wakes and Vortex-Induced Vibrations* (eds P. W. Bearman & C. H. K. Williamson), Paper No. 28. Ithaca, NY: Cornell University.
- LEE, S. D., CHUNG, S. H. & KIHM, K. D. 1996 Suggestive correctional methods for PIV image biasing caused by a rotating mirror system. *Experiments in Fluids* **21**, 201–208.
- LIGHTHILL, J. 1986 Fundamentals concerning wave loading on offshore structures. *Journal of Fluid Mechanics* **173**, 667–681.
- LIN, J.-C. & ROCKWELL, D. 1994 Cinematographic system for high-image-density particle image velocimetry. *Experiments in Fluids* **17**, 110–118.
- LIN, J.-C. & ROCKWELL, D. 1996 Force identification by vorticity fields: techniques based on flow imaging. *Journal of Fluids and Structures* **10**, 663–668.
- LIN, J.-C. & ROCKWELL, D. 1997 Quantitative interpretation of vortices from a cylinder oscillating in quiescent fluid. *Experiments in Fluids* **23**, 99–104.
- LIN, J.-C. & ROCKWELL, D. 1999 Cinema PIV and its application to impinging vortex systems. *ASME Journal of Fluids Engineering* **121**, 720–724.
- LIN, J.-C., SHERIDAN, J. & ROCKWELL, D. 1996a Near-wake of a perturbed, horizontal cylinder at a free-surface. *Physics of Fluids* **8**, 2107–2116.
- LIN, J.-C., TOWFIGHI, J. & ROCKWELL, D. 1995 Near-wake of a circular cylinder: control by steady and unsteady surface injection. *Journal of Fluids and Structures* **9**, 659–669.
- LIN, J.-C., VOROBIEFF, P. & ROCKWELL, D. 1996b Space-time imaging of a turbulent near-wake by high-image-density particle image cinematography. *Physics of Fluids* **8**, 555–564.
- LOURENCO, L. M. & WHIFFEN, M. C. 1986 Laser speckle methods in fluid dynamics applications. In *Laser Anemometry and Fluid Mechanics—II* (eds R. Adrian, D. Durão, F. Durst, H. Mishina & J. Whitelaw), pp. 51–68. Lisbon: Ladoan-Inst. Super. Tec.
- NOCA, F. 1996 On the evaluation of instantaneous fluid-dynamic forces on a bluff body. GALCIT Report FM96-5, California Institute of Technology, Pasadena, CA, U.S.A.
- NOCA, F. 1997 On the evaluation of time-dependent fluid dynamic forces on bluff bodies. Ph.D. dissertation, California Institute of Technology, Pasadena, CA, U.S.A.
- NOCA, F., SHIELDS, D. & JEON, D. 1997 Measuring instantaneous fluid dynamic forces on bodies using only velocity field and their derivatives. *Journal of Fluids and Structures* **11**, 345–350.



- NOCA, F., PARK, H. G. & GHARIB, M. 1998 Vortex formation length of a circular cylinder ( $300 < Re < 4,000$ ) using DPIV. In *Proceedings of the 1998 Conference on Bluff-Body Wakes and Vortex-Induced Vibration* (eds P. W. Bearman & C. H. K. Williamson), Paper No. 46. Ithaca, NY: Cornell University.
- NOCA, F., SHIELS, D. & JEON, D. 1999 A comparison of methods for evaluating time-dependent fluid dynamic forces on bodies, using only velocity fields and their derivatives. *Journal of Fluids and Structures* **13**, 551–578.
- OBASAJU, E. D., BEARMAN, P. W. & GRAHAM, J. M. R. 1988 A study of forces, circulation and vortex patterns around a circular cylinder in oscillating flow. *Journal of Fluid Mechanics* **196**, 467–494.
- OSCHWALD, M., BECHLE, S. & WELKE, S. 1995 Systematic errors in PIV by realizing velocity offsets with the rotating mirror method. *Experiments in Fluids* **18**, 329–334.
- RAFFEL, M. & KOMPENHANS, J. 1995 Theoretical and experimental aspects of image-shifting by means of a rotating mirror system for particle image velocimetry. *Measurement, Science and Technology* **6**, 795–808.
- ROCKWELL, D. 1998 Quantitative imaging of flow–structure interactions. In *Thirteenth Australasian Fluid Mechanics Conference* (eds M. C. Thompson & K. Hourigan), pp. 707–711. Melbourne, Australia: Monash University.
- ROCKWELL, D. 2001 Imaging of unsteady separated flows: global approaches to new insight. Special Issue of *Experiments in Fluids* (in press).
- ROCKWELL, D., MAGNESS, C., TOWFIGHI, J., AKIN, O. & CORCORAN, T. 1993 High image-density particle image velocimetry using laser scanning techniques. *Experiments in Fluids* **14**, 181–192.
- SARPKAYA, T. 1986 Force on a circular cylinder in viscous oscillatory flow at low Keulegan–Carpenter numbers. *Journal of Fluid Mechanics* **165**, 61–71.
- SHERIDAN, J., LIN, J.-C. & ROCKWELL, D. 1997 Flow past a cylinder close to a free-surface. *Journal of Fluid Mechanics* **330**, 1–30.
- SHERIDAN, J., CARBERRY, J., LIN, J.-C. & ROCKWELL, D. 1998 On the near-wake topology of an oscillating cylinder. *Journal of Fluids and Structures* **12**, 215–220.
- SUMNER, D., PRICE, S. J. & PAÏDOUSSIS, M. P. 1998 Investigation of side-by-side circular cylinders in steady cross-flow, by particle image velocimetry. In *Proceedings of the Conference on Bluff-Body Wakes and Vortex-Induced Vibration* (eds P. W. Bearman & C. H. K. Williamson), Paper No. 37. Ithaca, NY: Cornell University.
- SUMNER, D., PRICE, S. J. & PAÏDOUSSIS, M. P. 2000 Flow-pattern identification for two staggered circular cylinders in cross-flow. *Journal of Fluid Mechanics* **411**, 263–303.
- TATSUMO, M. & BEARMAN, P. W. 1990 A visual study of the flow around an oscillating circular cylinder at low Keulegan–Carpenter numbers and low Stokes numbers. *Journal of Fluid Mechanics* **211**, 157–182.
- TECHET, A. H. & TRIANTAFYLLOU, M. S. 1998 The evolution of a ‘hybrid’ shedding mode. In *Proceedings of the 1998 Conference on Bluff-Body Wakes and Vortex-Induced Vibration* (eds P. W. Bearman & C. H. K. Williamson), Paper No. 4. Ithaca, NY: Cornell University.
- TOWFIGHI, J. & ROCKWELL, D. 1994 Flow structure from an oscillating nonuniform cylinder: generation of patterned vorticity concentrations. *Physics of Fluids* **6**, 531–536.
- UNAL, M. F., LIN, J.-C. & ROCKWELL, D. 1997 Force prediction by PIV imaging: a momentum-based approach. *Journal of Fluids and Structures* **11**, 965–971.
- WILLIAMSON, C. H. K. 1988 The existence of two stages in the transition to three-dimensionality of a cylinder wake. *Physics of Fluids* **31**, 3165–3168.
- WILLIAMSON, C. H. K. 1992 The natural and forced formation of spot-like dislocations in the transition of a wake. *Journal of Fluid Mechanics* **243**, 393–441.
- WILLIAMSON, C. H. K. 1996a Three-dimensional wake transition. *Journal of Fluid Mechanics* **328**, 345–408.
- WILLIAMSON, C. H. K. 1996b Vortex dynamics in the cylinder wake. *Annual Review of Fluid Mechanics* **28**, 477–539.
- WILLIAMSON, C. H. K., HESS, P., PETER, M. & GOVARDHAN, R. 1998 Fluid loading and vortex dynamics for a body in elliptic orbits. In *Proceedings of the Conference on Bluff-Body Wakes and Vortex-Induced Vibration* (eds P. W. Bearman & C. H. K. Williamson), Manuscript No. 18. Ithaca, NY: Cornell University.

- WU, J. C. 1981 Theory for aerodynamic force and moment in viscous flows. *AIAA Journal* **19**, 432–441.
- WU, J., SHERIDAN, J., HOURIGAN, K., WELSH, M. C. & THOMPSON, M. 1994 Longitudinal vortex structures in a cylinder wake. *Physics of Fluids* **6**, 2883–2885.
- WU, J., SHERIDAN, J., WELSH, M. C. & HOURIGAN, K. 1996 Three-dimensional vortex structures in a cylinder wake. *Journal of Fluid Mechanics* **312**, 201–222.
- YANG, Y., & ROCKWELL, D. 2000 Vertical cylinder in a wave: patterns of spanwise vortex formation and loading. Submitted to *Journal of Fluid Mechanics*.
- ZHU, Q., LIN, J.-C., UNAL, M. F. & ROCKWELL, D. 2000 Motion of a cylinder adjacent to a free-surface: flow patterns and loading. *Experiments in Fluids* **28**, 559–575.



## HYSTERESIS IN THE FORCED STUART-LANDAU EQUATION: APPLICATION TO VORTEX SHEDDING FROM AN OSCILLATING CYLINDER

P. LE GAL

*Institut de Recherche sur les Phénomènes hors Equilibre  
49, rue Frédéric Joliot-Curie, B.P. 146, F-13384 Marseille, Cedex 13, France*

A. NADIM

*Department of Aerospace and Mechanical Engineering, Boston University  
Boston, MA 02215, U.S.A.*

AND

M. THOMPSON

*Department of Mechanical Engineering, Monash University  
Clayton, VIC 3800, Australia*

(Received 3 October 2000, and in final form 6 November 2000)

The complex Stuart–Landau equation models a prototypical Hopf bifurcation in which, when the control parameter exceeds a critical value, the null solution bifurcates into a finite amplitude time-periodic solution. We study the response of this equation to time-harmonic forcing in the subcritical regime (i.e., before the bifurcation). We show that when a second parameter in the Stuart–Landau equation passes a critical value, a portion of the solution surface as a function of forcing frequency and amplitude becomes multivalued. For instance, at a fixed forcing amplitude, one finds a well-defined range of frequencies over which two stable periodic responses may coexist, having different amplitudes. We apply this result to predict the behaviour of the wake downstream of an oscillating cylinder, and compare the predictions with experimental and computational observations of such a wake.

© 2001 Academic Press

### 1. INTRODUCTION

THE COMPLEX STUART-LANDAU EQUATION has been widely used to model the shedding of vortices in the two-dimensional wake of a cylinder at low Reynolds numbers. Specifically, the different coefficients of the model have been measured from experiments (Sreenivasan *et al.* 1986; Provansal *et al.* 1987; Schumm *et al.* 1994; Albarède & Provansal 1995) and from numerical simulations (Dušek *et al.* 1994). Two-dimensional flows past a laterally oscillating cylinder have also been the subject of extensive research. In particular, the experiments of Bishop & Hassan (1964) have clearly shown jumps and hysteresis loops in the resonance curves for the amplitude and the phase of the vortex shedding. These resonances appear for particular excitation frequencies, and Stansby (1976) has shown the existence of resonant horns where the wake is locked to the cross-flow oscillation of the cylinder. Different modes of vortex shedding can be associated with these lockings (Williamson & Roshko 1988); in particular, the classical Bénard–von Kármán wake can be excited among other nonsymmetric wakes. Visualization of moderate Reynolds number

forced wakes shows a jump in the phase of the vortex shedding when the frequency of the excitation passes through the resonance frequency (Ongoren & Rockwell 1988). The different phase lags between the laterally oscillating cylinder and the vortex shedding have been associated with a competition between several mechanisms of vorticity generation (Blackburn & Henderson 1999).

The present study is devoted to the theoretical analysis of the response of the forced Landau equation and to the comparison of its predictions with experiments and numerical simulations. We focus our attention on the subcritical regime, where the periodic solution is damped when it is not excited. To our knowledge, the only attempt at modelling the periodically forced wake by a forced Landau equation below the threshold has been by Provansal *et al.* (1987). In this case, the forcing term which is added to the model is a simple harmonic term, having a given amplitude and frequency. Above the threshold, additional third-order terms are involved in the amplitude equation associated with the forced Hopf bifurcation (Walgraef 1997). The solution is much more intricate in this case with the possibility of the appearance of higher-order resonances and biperiodic behaviour. A complete mathematical analysis of the different possibilities has been provided by Gambaudo (1985). In addition, numerical solutions of the forced Stuart–Landau equation in the supercritical regime have been obtained (Olinger 1993) to establish that its underlying dynamics are similar to those of the circle map.

In our work, we restrict our analysis to the subcritical regime of the Stuart–Landau equation where locking is expected (Gambaudo 1985). We find that, due to the cubic nonlinearity of the Landau equation, the resonance curve can exhibit a hysteresis loop in a certain range of parameters. This behaviour is similar to the response of a forced harmonic mechanical pendulum (Landau & Lifshitz 1976). We then compare our predictions against experiments and numerical simulations. In both cases, we study the two-dimensional wake of a circular cylinder subject to cross-flow oscillations. Although the predicted resonance below the Bénard–von Kármán threshold is observed, no evidence of hysteretic behaviour has yet been seen in the experiments and computations.

## 2. THE FORCED STUART–LANDAU EQUATION

The complex Stuart–Landau equation with time-periodic forcing is given by

$$\frac{dA}{dt} = (a_R + ia_I)A - \ell_R(1 + ic)|A|^2A + Fe^{i\omega t}, \quad (1)$$

in which  $A$  is a complex-valued function of time  $t$  and the parameters  $a_R, a_I, \ell_R$  ( $\ell_R > 0$ ) and  $c$  are all real. The last term in this equation represents the forcing. We take the forcing amplitude  $F$  and frequency  $\omega$  to be real.

In the absence of forcing, equation (1) represents the normal form of the Hopf bifurcation which occurs at the critical value of the parameter  $a_R = 0$ . For  $a_R < 0$ , the null solution  $A = 0$  is a stable solution of the unforced equation. For  $a_R > 0$ , this base state loses its stability and the solution settles down to a time-periodic state with constant amplitude  $|A| = (a_R/\ell_R)^{1/2}$ , orbiting the origin in the complex plane with angular velocity  $a_I - a_R c$ . Note that parameter  $\ell_R$  is taken to be positive. The time-scale for the transient approach to this final periodic state is given by  $a_R^{-1}$ .

In order to investigate the forced response of the system, we first non-dimensionalize equation (1) so as to minimize the total number of parameters that need to be studied. Using the natural scales of the system which are evident in the supercritical solution just discussed,

and subtracting the constant rotation imparted by parameter  $a_I$ , we define the following dimensionless (primed) variables:

$$t' \equiv |a_R| t, \quad (2)$$

$$A'(t') \equiv (\ell_R/|a_R|)^{1/2} A(t) e^{-ia_I t}, \quad (3)$$

$$F' \equiv |a_R|^{-1} (\ell_R/|a_R|)^{1/2} F, \quad (4)$$

$$\omega' \equiv (\omega - a_I)/|a_R|. \quad (5)$$

Upon substitution into equation (1) we obtain

$$\frac{dA'}{dt'} = \text{sgn}(a_R) A' - (1 + ic) |A'|^2 A' + F' e^{i\omega' t'},$$

in which  $\text{sgn}(a_R)$  is the sign of the Hopf bifurcation parameter  $a_R$ . In what follows, we shall focus our attention on the forced response of the subcritical state  $a_R < 0$ . This corresponds to the vortex shedding experiments and simulations which are also being reported in Sections 3 and 4 of this paper. The supercritical case exhibits a much richer (and more difficult to analyse) variety of solutions; see Gambaudo (1985) for a detailed discussion. Considering the subcritical case  $a_R < 0$  only, we rewrite the last equation and drop the primes from all the variables for clarity to obtain

$$\frac{dA}{dt} = -A - (1 + ic) |A|^2 A + F e^{i\omega t}. \quad (6)$$

Three real dimensionless parameters,  $c$ ,  $F$  and  $\omega$ , entirely determine the solution  $A(t)$ . Parameter  $c$  is an intrinsic property of the unforced system; for the supercritical state, it would determine the frequency of the solution after the Hopf bifurcation. Parameters  $F$  and  $\omega$  are simply the amplitude and reduced frequency of the time-periodic forcing. In the following, we restrict our attention to the case  $F > 0$ . The case of negative  $F$  is identical, but with a corresponding sign change in  $A$  (i.e., with a phase difference of  $\pi$ ).

## 2.1. PHASE-LOCKED SOLUTION

To obtain two real equations from the complex equation (6), we first write  $A(t)$  in the form

$$A(t) = \rho(t) e^{i\phi(t)},$$

where  $\rho(t) = |A(t)|$  is the real and nonnegative amplitude of the complex function  $A$  and  $\phi(t)$  is its phase (also real). Substitution into equation (6) results in the pair of equations

$$\dot{\rho}/\rho = -1 - \rho^2 + (F/\rho) \cos(\omega t - \phi), \quad (7)$$

$$\dot{\phi} = -c\rho^2 + (F/\rho) \sin(\omega t - \phi), \quad (8)$$

in which the overdot represents the time derivative. We now seek a solution of constant magnitude whose phase is locked with the forcing, lagging behind it with constant angle  $\phi_o$ . In other words, we seek a solution of the form  $\rho = \rho_o$  and  $\phi = \omega t - \phi_o$ , where  $\rho_o$  and  $\phi_o$  are constants. Such a solution would have to satisfy

$$0 = -1 - \rho_o^2 + (F/\rho_o) \cos \phi_o, \quad (9)$$

$$\omega = -c\rho_o^2 + (F/\rho_o) \sin \phi_o. \quad (10)$$

Upon elimination of  $\phi_o$  between equations (9) and (10) (by collecting the trigonometric terms on one side, squaring and adding the two equations), a single algebraic equation for the amplitude  $\rho_o$  is readily obtained. Upon defining  $x \equiv \rho_o^2$ , this equation reads

$$x[(1+x)^2 + (\omega + cx)^2] = F^2, \quad (11)$$

which is cubic in  $x$ , with its solution depending on the three parameters,  $c$ ,  $F$  and  $\omega$ , of the original system. Of course, the only solutions which are acceptable are real and non-negative. Furthermore, once a solution  $x = \rho_o^2$  has been found, the phase-lag  $\phi_o$  can always be obtained by solving

$$\tan \phi_o = \frac{\omega + cx}{1 + x}. \quad (12)$$

Being a cubic equation with real coefficients, equation (11) may have up to three real solutions, depending upon the parameters of the system. The parameter ranges for which three real and positive solutions exist are of particular interest, since they suggest the possibility of having multiple states of the system under identical forcing conditions. Fortunately, equation (11) is simple enough that a complete analysis as a function of the three independent parameters  $c$ ,  $F$  and  $\omega$  is possible; this is what we now attempt.

Denote the left-hand side of equation (11) by  $g(x; c, \omega)$ , i.e.,

$$g(x; c, \omega) \equiv x[(1+x)^2 + (\omega + cx)^2]. \quad (13)$$

The amplitude of the phase-locked solution is thus obtained from the positive solutions  $x$  to  $g(x) = F^2$ . Graphically, this can be achieved by plotting the function  $g(x)$  (for a given set of parameters  $c$  and  $\omega$ ) over positive  $x$  and considering the intersections of this graph with horizontal lines which are drawn at height  $F^2$  above the  $x$ -axis. As it turns out, the cubic function  $g(x)$  [which is asymptotic to  $(1 + \omega^2)x$  for small  $x$  and to  $(1 + c^2)x^3$  for large  $x$ ] can only have one of the two forms depicted in Figure 1. Namely, over the positive range of  $x$ , the function  $g(x)$  is either monotonically increasing, as depicted in Figure 1(a), or it goes through a local maximum and minimum prior to increasing indefinitely as  $x$  increases, as drawn in Figure 1(b). In the latter case, there is clearly a pair of values,  $F_{\min}$  and  $F_{\max}$ , such that for  $F_{\min} < F < F_{\max}$ , the equation  $g(x) = F^2$  admits three positive solution for  $x$ .

To identify the region of the  $(c, \omega)$  parameter space within which the function  $g(x; c, \omega)$  has a shape similar to that in Figure 1(b), let us find the position of the local maximum and minimum of  $g(x)$ . These are found by setting

$$\frac{\partial g}{\partial x} = 3(1 + c^2)x^2 + 4(1 + c\omega)x + (1 + \omega^2) = 0. \quad (14)$$

As such, the local extrema are located at

$$x_{\pm} = \frac{-2(1 + c\omega) \pm \sqrt{4(1 + c\omega)^2 - 3(1 + c^2)(1 + \omega^2)}}{3(1 + c^2)}. \quad (15)$$

Evidently, in order that both  $x_-$  and  $x_+$  be positive, i.e. to have a local maximum and minimum in  $g(x)$  over positive  $x$ , we must require that

$$-2(1 + c\omega) > 0, \quad (16)$$

$$4(1 + c\omega)^2 - 3(1 + c^2)(1 + \omega^2) > 0. \quad (17)$$

Condition (16) requires  $c\omega < -1$  which means that  $\omega$  and  $c$  must be of different signs and the magnitude of  $\omega$  must be larger than  $|c|^{-1}$ . Simultaneously, condition (17) must be met.

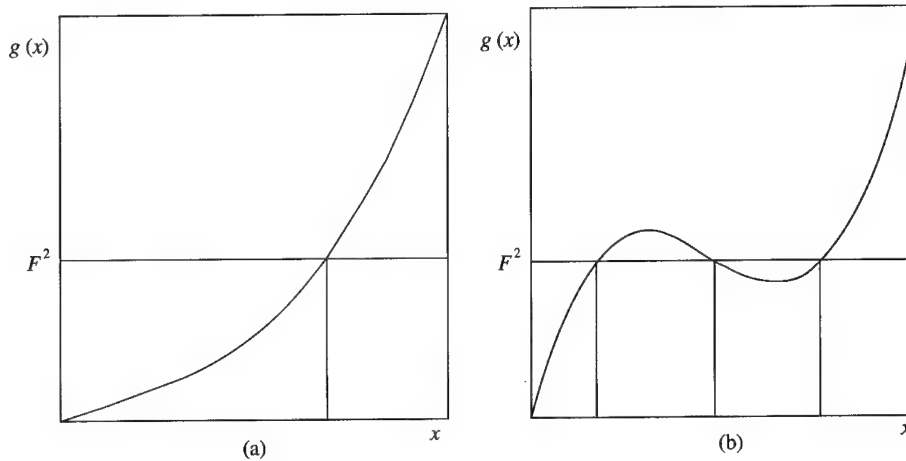


Figure 1. Possible shapes of the cubic function  $g(x)$ : (a) single solution to  $g(x) = F^2$ ; (b) multiple solutions to  $g(x) = F^2$ .

The latter can be written as a quadratic function of  $\omega$  in the form

$$(c^2 - 3)\omega^2 + 8c\omega + (1 - 3c^2) > 0. \quad (18)$$

To analyse the parameter space further, we now restrict our attention to the case  $c < 0$ . There are two reasons for doing so. First, parameter  $c$  for cylinder wakes is known to be negative. Secondly, since parameters  $c$  and  $\omega$  appear throughout the above only in the forms  $\omega^2$ ,  $c^2$  and  $c\omega$ , any statement which is true for a given pair of values  $(c, \omega)$  is also true for the pair  $(-c, -\omega)$ . Therefore, the behaviour for positive  $c$  can be directly inferred from the results obtained for  $c < 0$ .

Based upon condition (16), for  $c < 0$ , multivalued solutions to  $g(x) = F^2$  can only exist if  $\omega > 0$ . So, let us now consider the left-hand side (lhs) of condition (18) for positive  $\omega$ . The coefficient of  $\omega^2$  determines whether the parabola obtained when this lhs is plotted against positive  $\omega$  points upward or downward. There are three possibilities to explore: (i) When the coefficient  $(c^2 - 3)$  is negative, i.e., for  $-\sqrt{3} < c < 0$ , the lhs of equation (18) monotonically decreases from  $(1 - 3c^2)$  to  $-\infty$ , as  $\omega$  goes from 0 to  $\infty$ . Even if this lhs starts out being positive at  $\omega = 0$  [which is the case when  $(1 - 3c^2) > 0$ ], it will eventually become negative as  $\omega$  gets larger. Recalling that condition (16) required the magnitude of  $\omega$  to exceed  $|c|^{-1}$  in order to have multivalued solutions, it is easy to show that in this case, conditions (16) and (18) cannot be simultaneously satisfied and the solution to  $g(x) = F^2$  is always single-valued. (ii) When the coefficient  $(c^2 - 3)$  vanishes, i.e., when  $c = -\sqrt{3}$ , the lhs of equation (18) becomes a straight line when plotted against  $\omega$ , and it is always negative for positive values of  $\omega$ . Therefore, condition (18) cannot be satisfied and the solution to  $g(x) = F^2$  remains single-valued. (iii) Finally, when the coefficient  $(c^2 - 3)$  is positive, i.e., when  $c < -\sqrt{3}$ , the lhs of equation (18) starts out negative at  $\omega = 0$ , but it will eventually cross zero and remain positive as  $\omega$  increases. Hence, condition (18) will be met for  $\omega$  larger than a critical value (which is a root of the lhs, given explicitly below). In that range of  $\omega$ , the first condition which required that  $\omega > |c|^{-1}$  is also satisfied and, therefore, multivalued solutions to  $g(x) = F^2$  can exist.

These results can be summarized as follows. In order for the cubic equation  $g(x; c, \omega) = F^2$  to admit multivalued solutions for  $x$ , parameter  $c$  must satisfy  $c < -\sqrt{3}$  and  $\omega$  must be

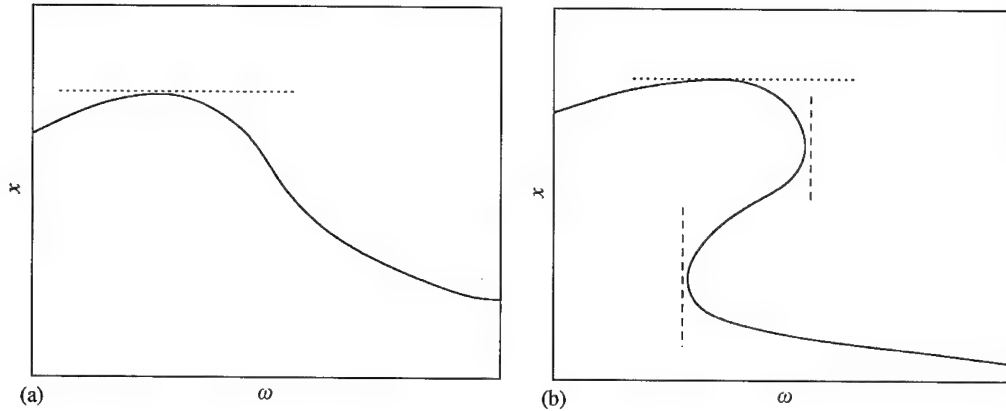


Figure 2. The frequency-response curves,  $x$  versus  $\omega$ : (a) single-valued case, (b) multivalued case.

larger than the positive root (in  $\omega$ ) of the lhs of equation (18), i.e.,

$$c < -\sqrt{3} \quad \text{and} \quad \omega > \omega_{\text{crit}} \equiv \frac{\sqrt{3}c - 1}{c + \sqrt{3}}. \quad (19)$$

For any  $(c, \omega)$  which satisfy conditions (19), the graph of the function  $g(x)$  resembles Figure 1(b). There will then exist the pair of values

$$F_{\min} = \sqrt{g(x_+; c, \omega)} \quad \text{and} \quad F_{\max} = \sqrt{g(x_-; c, \omega)} \quad (20)$$

with  $x_{\pm}$  given by equation (15), such that for  $F_{\min} < F < F_{\max}$ , the equation  $g(x; c, \omega) = F^2$  possesses three positive solutions for the amplitude  $x = \rho_o^2$ . At exactly the critical value  $\omega = \omega_{\text{crit}}$ , i.e., just before multivalued solutions emerge, the corresponding critical forcing amplitude is given by

$$F_{\text{crit}}^2 = \frac{-8}{3\sqrt{3}} \frac{(c^2 + 1)}{(c + \sqrt{3})^3}.$$

## 2.2. RESONANCE

For a fixed forcing amplitude  $F$ , as the forcing frequency  $\omega$  varies, the amplitude  $\rho_o = \sqrt{x}$  of the phase-locked solution also varies. The graph obtained by plotting the response of the system (characterized by  $\rho_o$  or  $x$ ) as a function of the forcing frequency  $\omega$  is the frequency-response curve. Note that under the conditions described above, this curve may be multivalued over a certain range of frequencies. Let us now consider the problem of finding the forcing frequency at which the response has its largest amplitude. We define this as “resonance” for our nonlinear oscillator.

Equation (11) can be thought of as providing an implicit solution for the response  $x$  as a function of frequency  $\omega$  for a fixed value of the forcing amplitude  $F$ . Typically, the frequency-response curves which result may resemble those in Figure 2, depicted here under the conditions when the solution is single-valued, [Figure 2(a)], or multivalued [Figure 2(b)].

In either case, the maximum in the curve (resonance) is obtained by finding the frequency at which the derivative  $\partial x / \partial \omega$  vanishes. Given the implicit solution  $g(x; c, \omega) = F^2$ , for



constant values of parameters  $c$  and  $F$ , this derivative is found to be

$$\frac{\partial x}{\partial \omega} = - \frac{\partial g / \partial \omega}{\partial g / \partial x}. \quad (21)$$

The numerator  $\partial g / \partial \omega$  is simply given by  $2x(\omega + cx)$ , indicating that resonance occurs when  $\omega = -cx$ . Therefore, at resonance, equation (11) reduces to

$$x_{\text{res}}(1 + x_{\text{res}})^2 = F^2. \quad (22)$$

Once the solution  $x_{\text{res}}(F)$  to this equation is obtained, the resonance frequency as a function of forcing amplitude is given by

$$\omega_{\text{res}}(F) = -c x_{\text{res}}(F). \quad (23)$$

For large  $F$  the solution behaves as  $x_{\text{res}} \sim F^{2/3}$ , whereas for small  $F$  its behaviour is like  $x_{\text{res}} \sim F^2$ . More generally, the solution to the cubic equation (22) is given by

$$x_{\text{res}}(F) = \frac{1}{6} W^{1/3} + \frac{2}{3} W^{-1/3} - \frac{2}{3}, \quad (24)$$

where

$$W \equiv 8 + 108F^2 + 12(12F^2 + 81F^4)^{1/2}. \quad (25)$$

As such, for a fixed  $c$ , there is a well-defined resonance curve in the  $(\omega, F)$ -plane over which resonance occurs and the amplitude  $\rho_o$  of the solution is a maximum. An explicit graph of this curve for a typical value of  $c$  will be presented in a later subsection.

Since at resonance,  $\omega + cx = 0$ , the phase-lag of the resonant solution is found from equation (12) to be  $\phi_o = 0$  provided we take  $F > 0$ ; note that besides satisfying (12), the phase-lag must also be consistent with  $(F/\rho_o) \sin \phi_o = \omega + cx$  and  $(F/\rho_o) \cos \phi_o = 1 + x$ . Upon recalling that in the Stuart-Landau equation, the function  $A$  can be thought of as being proportional to “velocity” rather than “displacement”, this behaviour is seen to be consistent with standard linear oscillators for which the displacement lags the forcing by a phase of  $\pi/2$  while the velocity and the forcing are in phase at resonance.

We also make the observation that the points at which the denominator in equation (21) vanishes are where the derivative of the frequency-response curve becomes infinite. These points are identified by the vertical dashed lines in Figure 2(b). Evidently, having two such points is a prerequisite for having a range of frequencies over which the solution is triple-valued. The vanishing of this denominator is precisely the condition we posed earlier [cf. equation (14)] to locate a local maximum and minimum of  $g(x)$  over positive  $x$ . It is also possible to demonstrate that in the multivalued frequency-response curve, [Figure 2(b)] the portion of the curve connecting the two turning points (tangent to the dashed vertical curves) is unstable, whereas the upper and lower segments of this curve are stable.

### 2.3. RESULTS FOR $c = -3$

The small dimensionless parameter  $c$  in the Stuart-Landau equation describing the wakes of cylinders has been measured for cylinders of different aspect ratios. For an aspect ratio of 10, its value turns out to be approximately  $c = -3$  (Albarède *et al.* 1995; Peschard 1995). The experimental portion of this work deals with subcritical uniform flow past a cylinder of aspect ratio 10; therefore, let us consider more precisely the nature of the solution at  $c = -3$ .

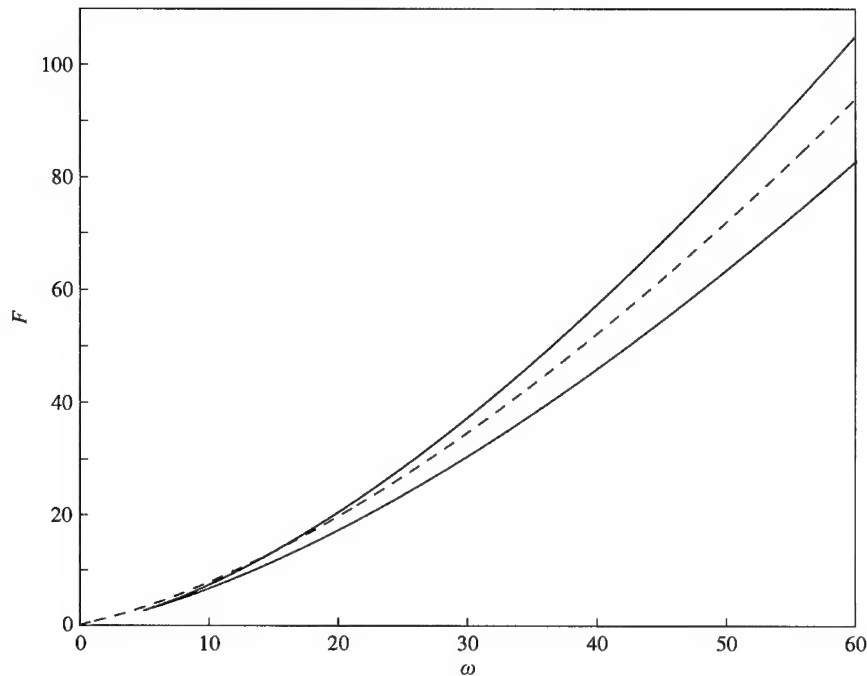


Figure 3. The minimum and maximum values of  $F$  (solid lines) which bound the region in which the solution is multivalued for  $c = -3$ . The dashed line represents the resonance curve at  $c = -3$ .

Since this value of  $c$  is less than the critical value  $-\sqrt{3}$ , we know that for large enough frequencies, we will always have a window of forcing amplitudes over which multivalued solutions exist. The critical value  $\omega_{\text{crit}}$  which needs to be exceeded is given by equation (19) and turns out to be  $\omega_{\text{crit}} \approx 4.8868$ . The corresponding critical value of the forcing at this point turns out to be  $F_{\text{crit}} \approx 2.7482$ . For any  $\omega$  larger than  $\omega_{\text{crit}}$ , there exist lower and upper bounds  $F_{\text{min}}$  and  $F_{\text{max}}$ , given by equation (20), such that for values of  $F$  which are in between, the solution surface is multivalued. In the  $(\omega, F)$ -plane, we can trace out the two curves which provide the bounds on  $F$  as a function of  $\omega$ . We have done this in Figure 3 for  $c = -3$ . The two solid lines which form a cusp at the critical point  $(\omega_{\text{crit}}, F_{\text{crit}}) = (4.8868, 2.7482)$  in this figure represent these bounds.

Also in Figure 3, we have traced out the resonance curve given by equations (22), (23) and (25), for the case  $c = -3$ . The resonance curve enters the multivalued region as  $\omega$  and  $F$  increase and remains there. That is, the maximum point in Figure 2(b) lies somewhere in between the two turning points with infinite slopes (when  $\omega$  and  $F$  are large enough). Lastly, we show in Figure 4, the solution surface itself ( $\rho_o = \sqrt{x}$  versus  $\omega$  and  $F$ ) for  $c = -3$  obtained by plotting a family of solutions at different frequencies as the forcing amplitude is varied. It is clear that surface is folded and above the region bounded by the solid curves in Figure 3, the solution is triple-valued. Of the three solutions, those with the largest and smallest amplitudes are stable while the one in the middle is unstable.

### 3. EXPERIMENTAL OBSERVATIONS

As explained before, the parameter  $c$  is a constant which characterizes the limit cycle which appears at the Hopf bifurcation. For the Bénard–von Kármán wake, it has been measured

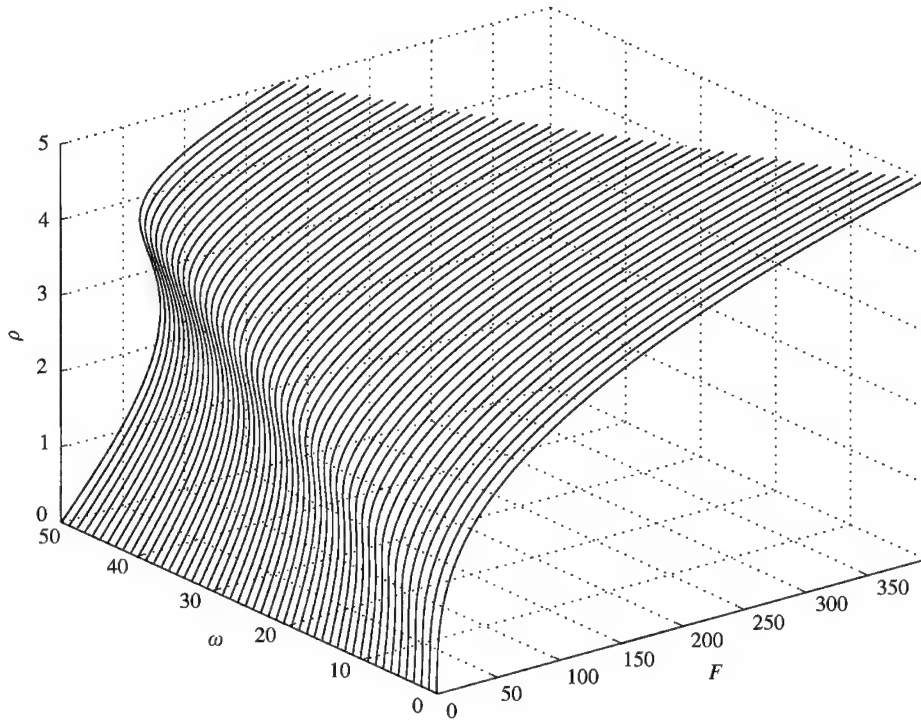


Figure 4. The solution surface  $\rho_o(\omega, F)$  at  $c = -3$ .

both experimentally and numerically. However, this value varies with the aspect ratio of the cylinder that generates the wake. In our experiments, the cylinder has a diameter of 2 mm and a length of 20 mm, giving an aspect ratio of 10 which, according to Peschard (1995) and Albarède *et al.* (1995) gives a value for  $c$  close to  $-3$ . In this case, the critical Reynolds number for the appearance of the vortex street is about 70. The flow is generated in a water tunnel and the cylinder is mounted on a support which can oscillate at a given frequency by the use of an electric motor. In this study, only visual observations will be reported. These visualizations are made by oxidation of a tin wire. As predicted by our theoretical analysis, a strong resonance is seen when the forcing frequency is close to the natural frequency of the wake. Figure 5 presents snapshots of the wake for different cross-flow oscillation frequencies and for a Reynolds number equal to 60. On these images, the amplitude of the cylinder oscillation is 3 mm (the corresponding nondimensional value for  $F$  is not known *a priori* because we do not know how much energy is actually transmitted to the wake when oscillating the cylinder). The resonance phenomenon is clearly evidenced by the shedding of strong vortices when the excitation frequency approaches a value close to 1 Hz. In the figure caption, we also indicate the values of the non-dimensional frequency calculated using the expected parameters of the Landau equation [see Peschard (1995), Olinger (1993)]. Scanning the forcing frequency up and down does not reveal (at least visually) any hysteretic behaviour. More experiments would seem to be necessary to confirm this apparent deviation from the Landau model prediction. Let us note in particular that the strong spatial deformation of the wake, as it is visualized in Figure 5, is not taken into account in the model. This effect might be avoided when applying a very weak forcing very close to the threshold where the receptivity of the wake is large.

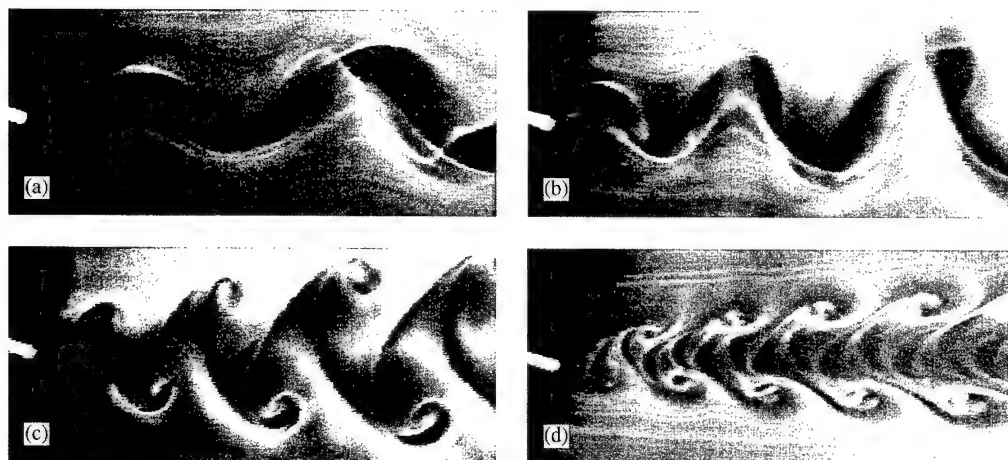


Figure 5. Visualization of the wake at  $Re = 60$  for different exciting frequencies: (a) 0.52 Hz ( $\omega = -10$ ); (b) 0.70 Hz ( $\omega = -7$ ); (c) 0.95 Hz ( $\omega = -2.4$ ); (d) 1.4 Hz ( $\omega = 5.6$ ).

#### 4 NUMERICAL SIMULATIONS

Two-dimensional numerical simulations were also undertaken to explore the frequency response. These were done with a spectral-element code described in Thompson *et al.* (1996), which employs a similar method to that used to examine the unforced post-transition behaviour in Dušek *et al.* (1994). Initial runs were performed to verify the chosen domain size and mesh point distribution and density were adequate.

The system was forced by applying an oscillating cross-flow velocity at the inlet and side boundaries of the domain, i.e., at the inlet and side boundaries  $\mathbf{u} = (1, (B/\omega) \sin(\omega t))$ . The cross-flow amplitude is divided by  $\omega$  to maintain a constant acceleration forcing amplitude as dictated by the Landau model. It is thus expected that there is a linear relationship between  $B$  and  $F$  regardless of frequency. Note that in the numerical simulations, the governing equations are rendered dimensionless using the diameter of the cylinder as the length scale and the ratio of that diameter to the uniform flow velocity as the time scale.

Initially, runs were performed to determine the values of the critical parameters in the Landau model. Simulations at  $Re = 50, 48$  and  $45$ , the first two starting from the two-dimensional steady flow and the last from the time-periodic flow at  $Re = 48$ , allowed the transition Reynolds number to be determined as  $Re_{crit} = 46.7$  from interpolation of the measured growth rates. The dimensionless Landau constant was also evaluated for  $Re = 50$  and  $48$  by determining the difference between the frequency of oscillation in the linear regime and at saturation. As in Dušek *et al.* (1994), the response was monitored by the vertical velocity at various points in the domain. For these two cases, the Landau constant was determined to be  $c(Re = 50) = -2.52$  and  $c(Re = 48) = -2.78$ . Thus, it is less than the critical value of  $c_{crit} = -\sqrt{3}$  from the theoretical analysis [equation (19)] in this paper and consistent with estimates from Dušek *et al.* (1994). To examine the response in the subcritical regime, simulations were performed at  $Re = 44$ . At this Reynolds number, the model parameters (scaled with the time-scale mentioned above) can be estimated by extrapolation to be  $a_I = 0.3648$ ,  $a_R = -0.0057$ ,  $c = -3.3$  and  $l_R = 0.32$ . Again, the critical parameter is the Landau constant,  $c$ , which indicates that the system should be hysteretic if the forcing is above a critical value. The frequency response was determined numerically by fixing the forcing level and stepping up from one forcing frequency to another after the

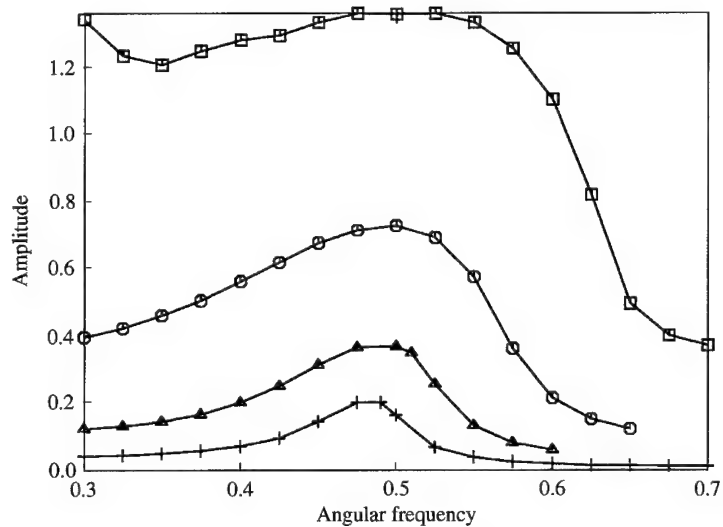


Figure 6. Numerical resonance curves for forcing amplitudes ( $B$ ) of 0.01 (crosses), 0.03 (triangles), 0.10 (circles) and 0.30 (squares). The Reynolds number is 44. The curves show the amplitude of the vertical velocity component on the centreline 4 radii downstream of the cylinder centre.

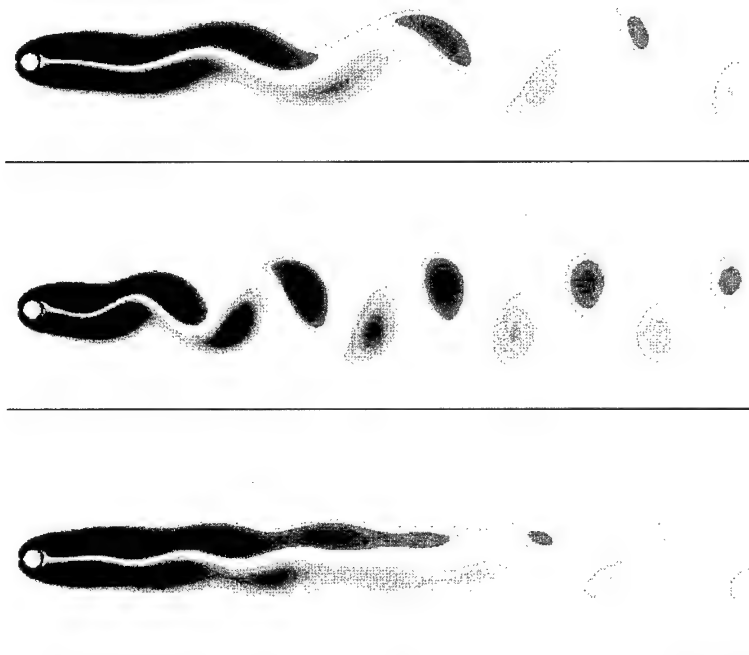


Figure 7. Vorticity plots of the oscillating wake. The forcing amplitude is set to 0.01. The centre plot shows the response at close to the optimal forcing frequency. The top and bottom plots show the wake for forcing frequencies 25% below and 25% above the resonant frequency, respectively.

periodic asymptotic solution had been reached. This response is shown in Figure 6 for forcing amplitude  $B = 0.01, 0.03, 0.10$  and  $0.30$ . These curves show the amplitude of the vertical velocity component at a point 4 radii downstream from the cylinder centre on the

symmetry axis. The nonlinear shift of the maxima, as predicted by equation (23) and observed in the experiments, is visible. Note that the sign of this deviation (here towards higher frequencies) is opposite to that of parameter  $c$  in agreement with predictions. Although the shift is in the right direction, it does not show the expected quadratic behaviour predicted by equation (23) for low forcing amplitudes.

Figure 7 shows the wake vorticity pattern corresponding to forcing (from top to bottom) at 25% below, equal to, and 25% above the resonant frequency. The asymmetry of the response—characteristic of the presence of odd terms in the dynamical system—is again evident through these visualizations; however, no hysteresis is observed.

## 5. CONCLUSION

The mismatch between both the experimental and numerical results, and the theoretical analysis, is surprising. The study of Dušek *et al.* (1994) indicates that the post-transition behaviour obeys the unforced Landau equation to a high degree of accuracy. One possible explanation is that higher-order terms in the Landau equation are not necessarily small and may contribute to the saturated behaviour. This is suggested by the failure of the numerical frequency–response curves to conform to the predictions of equation (23). If quintic and higher-order terms cannot be neglected in equation (1), they will cause deviations from the current predictions; preliminary numerical studies indicate that the predicted hysteresis can easily be destroyed by the additions of such terms. Moreover, the value of  $c$  in the numerical simulations was estimated indirectly based on the observed amplitude and frequency at saturation; hence it relies on the higher-order terms being negligible.

Because the scaled critical value of  $F$  only depends on  $c$ , equations (3) and (4) suggest that the dimensional critical forcing and the response amplitude both approach zero as the Reynolds number approaches the transition value. In turn, this means that close to the critical Reynolds number there should be some range of forcing for which high-order terms can be neglected and hysteresis will occur, provided  $c < -\sqrt{3}$ . The numerical results suggest that this range may be very small. Unfortunately, close to the transition Reynolds number, and for very small forcing amplitudes, it takes many cycles for the transient response to decay and hence it is difficult to explore this region numerically. We are currently attempting to obtain direct measures of the critical parameters of the Landau model to further refine the predicted behaviour (if necessary including the effects of higher-order terms). It will then be possible to better test the validity of the model by careful comparisons with the numerical frequency–response curves. These results will be reported elsewhere.

## REFERENCES

- ALBARÈDE, P. & PROVANSAL, M. 1995 Quasi-periodic cylinder wakes and the Ginzburg–Landau model. *Journal of Fluid Mechanics* **291**, 191–222.
- BISHOP, R. E. D. & HASSAN, A. Y. 1964 The lift and drag forces on a circular cylinder oscillating in a flowing fluid. *Philosophical Transactions of the Royal Society (London)* A **227**, 51–75.
- BLACKBURN, H. M. & HENDERSON, R. D. 1999 A study of two-dimensional flow past an oscillating cylinder. *Journal of Fluid Mechanics* **385**, 255–286.
- DUŠEK, J., LE GAL, P. & FRAUNÉ, P. 1994 A numerical and theoretical study of the first Hopf bifurcation in a cylinder wake. *Journal of Fluid Mechanics* **264**, 59–80.
- GAMBAUDO, J. M. 1985 Perturbation of a Hopf bifurcation by an external time-periodic forcing. *Journal of Differential Equations* **57**, 172–199.
- LANDAU, L. D. & LIFSHITZ, E. M. 1976 *Mechanics*, 3rd edition. Oxford: Pergamon Press.

- OLINGER, D. J. 1993 A low-dimensional model for chaos in open fluid flows. *Physics of Fluids A* **5**, 1947–1951.
- ONGOREN, A. & ROCKWELL, D. 1988 Flow structure from an oscillating cylinder. Part 1. Mechanisms of phase shift and recovery in the near wake. *Journal of Fluid Mechanics* **191**, 197–223.
- PESCHARD, I. 1995 De l'oscillateur aux sillages couplés. Ph.D. Thesis, Université de la Méditerranée, Marseille, France.
- PROVANSAL, M., MATHIS, C. & BOYER, L. 1987 Bénard–von Kármán instability: transient and forced regimes. *Journal of Fluid Mechanics* **182**, 1–22.
- SCHUMM, M., BERGER, E. & MONKEWITZ, P. A. 1994 Self-excited oscillations in the wake of two-dimensional bluff bodies and their control. *Journal of Fluid Mechanics* **271**, 17–53.
- STANSBY, P. K. 1976 The locking-on vortex shedding due to the cross-stream vibration of circular cylinders in uniform and shear flows. *Journal of Fluid Mechanics* **74**, 641–655.
- SREENIVASAN, K. R., STRYKOWSKI, P. J. & OLINGER, D. J. 1986 Hopf bifurcation, Landau equation, and vortex shedding behind circular cylinders. In *Proceedings of the Forum on Unsteady Flow Separation* (ed. K. N. Ghia). FED-Vol. 52, pp. 1–13, New York: ASME.
- THOMPSON, M. C., HOURIGAN, K. & SHERIDAN, J. 1996 Three-dimensional instabilities in the wake of a circular cylinder. *Experimental Thermal and Fluid Science* **12**, 190–196.
- WALGRAEF, D. 1997 *Spatio-Temporal Pattern Formation: with Examples from Physics, Chemistry and Materials Science*. Berlin: Springer Verlag.
- WILLIAMSON, C. H. K. & ROSHKO, A. 1988 Vortex formation in the wake of an oscillating cylinder. *Journal of Fluids and Structures* **2**, 355–381.



## FLOW AROUND A CIRCULAR CYLINDER: ASPECTS OF FLUCTUATING LIFT

C. NORBERG

*Department of Heat and Power Engineering, Lund Institute of Technology  
P.O. Box 118, S-22100 Lund, Sweden*

(Received 1 September 2000, and in final form 15 November 2000)

The paper is concerned with some aspects of the fluctuating lift acting on a stationary circular cylinder in cross flow, in particular effects of Reynolds number in the nominal case of a large-aspect-ratio cylinder at small to vanishing blockage and free-stream turbulence, respectively. The Reynolds number range covered is from about  $Re = 47$ – $2.2 \times 10^5$ , i.e., from the onset of vortex shedding up to the point where a subsequent increase in  $Re$  gives a rapid fall in the mean drag coefficient, the all-familiar drag crisis. A review of 2-D numerical simulations suggests that the r.m.s. lift coefficient ( $C_{L'}$ ) within the laminar shedding regime can be approximated as  $\sqrt{\varepsilon/30 + \varepsilon^2/90}$ , where  $\varepsilon = (Re - 47)/47$ . For all Reynolds numbers above the inception of three-dimensional flow instabilities, i.e., for  $Re > (160\text{--}190)$ , the near-wake flow is supposed to be partially correlated along the span. The lift fluctuations on a finite (spanwise) length of the cylinder are then not only dependent on the sectional lift variations but also on the spanwise correlation of the lift-related flow. At around  $Re = 230$ , which is the approximate onset  $Re$  for mode B instability, the one-sided spanwise correlation length ( $\Lambda$ ) is about twice the wavelength of the most unstable mode A instability,  $\Lambda/d \approx 7$ . Up to  $Re = 260\text{--}300$  the spanwise correlation increases dramatically, the indicated peak value being  $\Lambda/d \approx 30$ . From 3-D numerical simulations, the corresponding  $C_{L'}$  is approximately 0.5, which coincidentally is about the same value as found experimentally just before the rapid fall when entering the critical regime. Dramatic variations of both sectional  $C_{L'}$  and  $\Lambda/d$  occur within the range  $Re \approx 0.3 \times 10^3$ – $2.2 \times 10^5$ . For instance, at around  $Re = 1.6 \times 10^3$  a local minimum of about  $C_{L'} = 0.045$  is indicated, at  $Re \approx 16 \times 10^3$  the corresponding  $C_{L'}$ -value is ten times higher. At  $Re = 5.1 \times 10^3$  there is a peak in spanwise correlation,  $\Lambda/d \approx 15$ .

© 2001 Academic Press

### 1. INTRODUCTION

THE FLOW AROUND A CIRCULAR CYLINDER has been the subject of intense research in the past, mostly by experiments but also by using numerical simulation. The flow situation is of relevance for many practical applications, e.g. offshore risers, bridge piers, periscopes, chimneys, towers, masts, stays, cables, antennae and wires. During the last 15 years there has been an accelerating interest in bluff body wakes, in particular so for the wake flow generated by the circular cylinder. Important findings and developments have been made, especially with regards to three-dimensional effects, physical and theoretical modelling, flow instabilities, numerical simulation and flow control, see Williamson (1996a).

A perspective outlook on bluff body flows in general and flow around circular cylinders in particular is presented in Roshko (1993). Despite the above findings, some of which have been made after the publication of Roshko's outlook paper, it seems that still "the problem of bluff body flow remains almost entirely in the empirical, descriptive realm of knowledge" (Roshko 1993). Roshko, a modern pioneer in this field, also wrote: "Finally, we must keep in mind the basic problem, to find suitable models for the forces on bluff bodies"



(Roshko 1993). However, there is no modelling of fluctuating lift to be found in this work. Such modelling needs to take into proper account the supposedly subtle aspects of inherently three-dimensional, transitional and lift-related flow features present in the near-wake. At present, at least for turbulent shedding conditions, we do not even have a conceptual description of these intriguing flow features. The present work should be seen primarily as an attempt to find a better representation of lift-related quantities, as a function of the Reynolds number. Hopefully, this attempt can stimulate later modelling efforts.

Under nominal conditions and when present, the fluctuating lift is dominated by the actions from the periodic phenomenon called vortex shedding, the principal source of cross-stream flow-induced vibration and acoustic emissions (Blevins 1990). The fluctuating lift is due mainly to the fluctuating pressures acting on the surface of the cylinder (Drescher 1956; Kwon & Choi 1996) and except for the rearmost part of the cylinder the pressure fluctuation energy is concentrated to a band around the mean shedding frequency  $f_s$  (Sonneville 1976). The alternate periodic shedding causes the pressure fluctuations at around  $f_s$  to be essentially out-of-phase between the upper and lower side of the cylinder (Gerrard 1961), i.e., the lift fluctuation energy is concentrated to a band around  $f_s$ . The amplitudes of fluctuating drag, which are significantly smaller than the fluctuating lift (Bouak & Lemay 1998; Posdziech & Grundmann 2000), are dominated by fluctuating pressures which are in-phase between the upper and lower side of the cylinder, which in turn are concentrated to very low frequencies and to a band around two times  $f_s$  (Sonneville 1976). The Strouhal number, the nondimensional shedding frequency, is defined as  $St = f_s d/U$ , where  $d$  is the cylinder diameter and  $U$  is the (assumed constant) oncoming free-stream velocity. The Reynolds number in the assumed incompressible flow is defined as  $Re = \rho U d/\mu$ , where  $\rho$  is the density and  $\mu$  is the dynamic viscosity of the fluid. All fluid properties are assumed to be constant.

The nominal case under consideration is flow around a nonvibrating cylinder with negligible effects of surface roughness, with a large enough aspect ratio  $\ell/d$  and with suitable end conditions (Williamson 1989) at vanishing or very small solid blockage ratios (wall confinement) and free stream turbulence, respectively. These additional factors have all been shown to have an influence on the flow in general and on the fluctuating lift in particular, see, e.g., Farell (1981) and Blevins (1990) and references cited therein. In this work, the Reynolds number range of principal interest is from  $Re \simeq 47$  to  $\simeq 2 \times 10^5$ , i.e., from the onset of vortex shedding up to the end of the subcritical regime where there is a rapid decrease in mean drag coefficient with increasing  $Re$ , the so-called drag crisis. For higher  $Re$ , see Farell (1981) and Ribeiro (1992).

The r.m.s. (root-mean-square) lift coefficient is defined as

$$C_{L'} = \frac{2L'}{\rho U^2 d \ell_c}, \quad (1)$$

where  $L'$  is the r.m.s. of lift fluctuations acting on a spanwise segment of length  $\ell_c$ . The *sectional* r.m.s. lift coefficient is the r.m.s. lift coefficient for which the segment length is vanishingly small ( $\ell_c/d \rightarrow 0$ ). The sectional lift can thus be seen as lift per unit span. The *total* lift fluctuations are defined as those acting on the whole cylinder length exposed to flow ( $\ell_c = \ell$ ). The fluctuating lift on a finite cylinder segment is dependent on the degree of three dimensionality in the shedding flow close to the cylinder. One measure of this three dimensionality is the span-wise or axial correlation length scaled with the diameter,  $\Lambda/d$  (Blake 1986). The scarceness of data for this quantity is even larger than for the r.m.s. lift coefficient (Ribeiro 1992). A near-wake spanwise correlation study is presented in Norberg (2000), extending down to  $Re = 230$  and using hot wire anemometry. Knowledge of

spanwise correlation also has a great significance for vortex-induced sound generation (Æolian tones) and for the important question of the necessary spanwise computational dimension to capture significant flow-dynamic features in three-dimensional (3-D) numerical simulations.

In almost every fluid mechanics textbook there is a graph for the circular cylinder in cross-flow, showing the variation of mean drag coefficient  $C_D$  versus  $Re$ . Since the extensive measurements of Wieselsberger (1921) and Roshko (1961), the general appearance of this graph is unaltered. Corresponding graphs for the r.m.s. lift coefficient,  $C_L$ , versus  $Re$ , are much more indefinite, despite the various compilations that have been presented, e.g., see Morkovin (1964), Blevins (1990) and Ribeiro (1992). For a continuous flow situation the very first measurement of fluctuating lift was carried out by Drescher (1956). Since then, a vast amount of data has been gathered. However, when plotting out all r.m.s. lift coefficients as a function of Reynolds number the picture becomes increasingly scattered and inconclusive. It is also evident from such a plot that almost all measured  $C_L$ -data is restricted to  $Re > 6 \times 10^3$ . However, in 1992, the author presented experimental data on the sectional r.m.s. lift coefficient for Reynolds numbers between 720 and  $2 \times 10^5$  (Norberg 1993). Many further results, and extensive experimental details, are contained in a comprehensive companion paper (Norberg 2000).

The main objective of this work is to make an overview of the fluctuating lift acting on a circular cylinder, especially regarding the influence of Reynolds number and the relation between fluctuating lift and flow features in the near-wake region.

## 2. SUMMARY OF RESULTS ON LIFT-RELATED QUANTITIES

Compilation graphs on  $St$ ,  $C_L$  and  $\Lambda/d$  versus  $Re$  are shown in Figures 1, 2 and 3. Solid lines refer to empirical functions as presented in Norberg (2000). As with all empirical functions they are open for re-evaluation when more data has been collected.

The shaded region in Figure 1 corresponds to the bandwidth ( $-3$  dB) of the shedding peak frequency (Norberg 1993). Smoke-wire flow visualizations (Norberg 1992, 1993) reveal

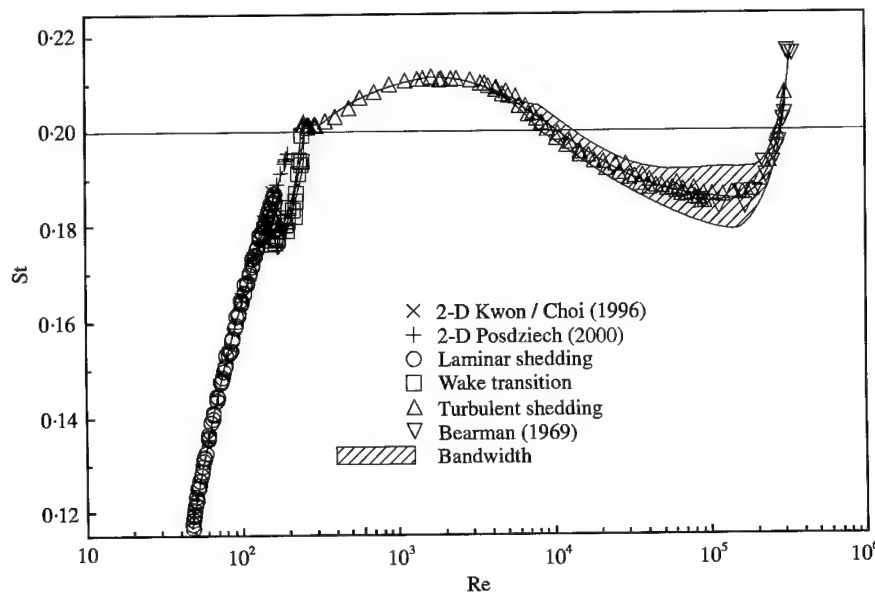


Figure 1. Strouhal number versus Reynolds number.

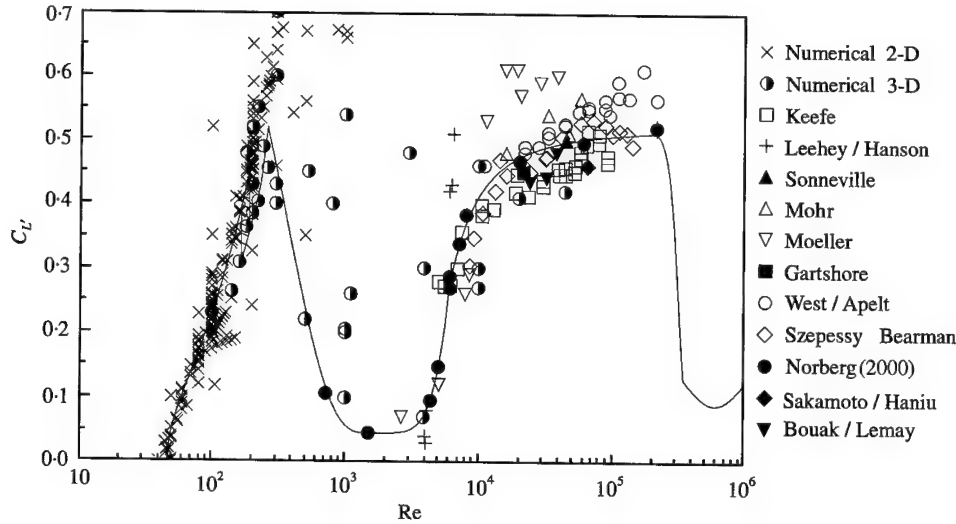


Figure 2. R.m.s. lift coefficient versus Reynolds number.

that the change-over to a low-quality shedding at  $Re \simeq 5.1 \times 10^3$  is associated with a transitional change in the three dimensionality of near-wake vortex shedding, more specifically with an increasing degree of spanwise waviness of primary vortices and by the (somewhat later) inception of naturally occurring and random-positioned vortex dislocations, also see Prasad & Williamson (1997b).

The experimental lift data in Figure 2 only contains sectional or near-sectional lift coefficients ( $\ell_c/d \leq 1$ ). A summary of previous laboratory measurements of both sectional and total lift fluctuations, for  $Re < 3 \times 10^5$ , is found in Norberg (2000), where tables summarizing previous results on fluctuating lift from 2-D and 3-D numerical simulations are also provided. As evident from Figure 2 dramatic variations in  $C_{L'}$  occur at turbulent shedding conditions. Corresponding variations in Strouhal number (Figure 1) are much more gentle.

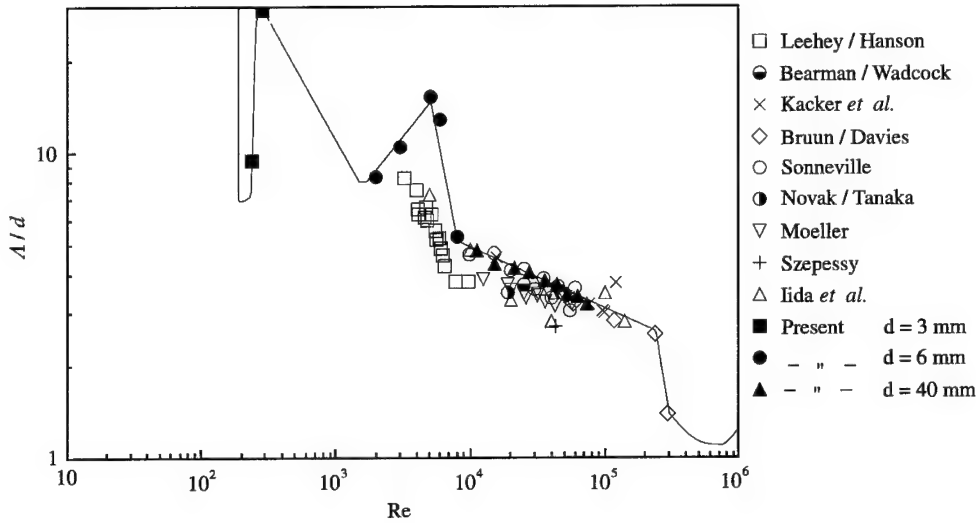
For turbulent shedding conditions (approximately  $Re > 260$ ) and with increasing  $Re$  there is a general downward trend in  $\Lambda/d$  versus  $Re$ , see Figure 3. However, a local maximum occurs at  $Re \simeq 5 \times 10^3$ , previously noted by Norberg (1987), which coincides with the Reynolds number with inception of low-spectral-quality shedding (Figure 1).

### 3. FLUCTUATING LIFT AND SPANWISE CORRELATION

Assuming spanwise flow homogeneity, the ratio,  $\gamma_L$ , between r.m.s. lift on a finite length  $\ell_c$  and sectional r.m.s. lift times  $\ell_c$  is (Kacker *et al.* 1974)

$$\gamma_L = \frac{1}{\ell_c} \left[ 2 \int_0^{\ell_c} (\ell_c - s) R_{LL}(s) ds \right]^{1/2}, \quad (2)$$

where  $R_{LL}(s)$  is the correlation coefficient, at zero time delay, between sectional lift forces separated a spanwise distance  $s$ . Since lift is dominated by actions of surface wall pressures, an accurate approximation for  $R_{LL}$  is the lift correlation based on sectional pressure forces. As discussed in Ribeiro (1992), also see Sonnevile (1976) and Moeller (1982), the correlation coefficient,  $R_{pp}(s)$ , between fluctuating wall pressures along the generator at  $\varphi = 90^\circ$  (the

Figure 3. Spanwise correlation length versus  $Re$ .

mean stagnation line at  $\varphi = 0^\circ$ ) or between fluctuating velocities along a generator close to the separated shear layers but not too far from the cylinder,  $R_{uu}(s)$ , can also provide a reasonable estimate for  $R_{LL}$ , i.e.,  $R_{LL}(s) \approx R_{pp}(s) \approx R_{uu}(s)$ . With a known or estimated correlation function  $R_{LL}$ , equation (2) can be used to convert the finite section r.m.s. lift coefficient to the sectional r.m.s. lift coefficient. "Present" results in Figure 3 were obtained using  $R_{LL} \approx R_{uu}$ , see Norberg (2000).

The one-sided spanwise correlation length  $\Lambda$  and the centroid of spanwise correlation  $\sigma$ , related to the fluctuating lift, are defined as (Blake 1986)

$$\Lambda = \int_0^\infty R_{LL}(s) ds, \quad \sigma = \Lambda^{-1} \int_0^\infty s R_{LL}(s) ds. \quad (3, 4)$$

At large separations and for turbulent shedding conditions  $R_{LL}$  is expected to vanish,  $R_{LL}(s \rightarrow \infty) = 0$ . In reality, the upper limits in equations (3) and (4) have to be finite and for convenience, neglecting effects of end disturbances, they can be set to the full length of the cylinder. A neglect of end disturbances implies a sufficiently large aspect ratio, and under such circumstances and when the segment length  $\ell_c$  equals the full length  $\ell$  in equation (2) the lift ratio becomes (Keefe 1961)

$$\hat{\gamma}_L = \ell^{-1} \sqrt{2\Lambda(\ell - \sigma)}. \quad (5)$$

This is the ratio between the total r.m.s. lift coefficient and its sectional counterpart (Keefe 1961). Naturally,  $\hat{\gamma}_L$  equals unity in fully correlated flow ( $\Lambda = \ell$ ,  $\sigma = \ell/2$ ). For turbulent shedding conditions the centroid appears to be of the same magnitude as the correlation length (Leehey & Hanson 1971; Norberg 2000). The exponential drop,  $R_{LL} = \exp(-s/\Lambda)$ , which seems to work well as a model function for  $Re > 8 \times 10^3$  (Norberg 2000), gives  $\sigma = \Lambda$ . For a sufficiently long cylinder and for partially correlated conditions the lift ratio becomes proportional to  $\sqrt{\Lambda/\ell}$ . Eventually, with increasing aspect ratio  $\ell/d$ , the r.m.s. lift coefficient based on the fluctuating lift acting on the full length of the cylinder goes to zero, the total r.m.s. lift being proportional to  $\sqrt{\ell/d}$ .

#### 4. FINAL REMARKS—FACTS AND SPECULATION

##### 4.1. LAMINAR SHEDDING

Onset of vortex shedding occurs at  $Re = Re_c \simeq 47$  (Provansal *et al.* 1987; Norberg, 1994). Obviously,  $Re_c$  is also the onset of fluctuating lift. The onset can be characterized as a supercritical Hopf bifurcation which as well as the resulting stable two-dimensional periodic shedding close to onset can be described by the Stuart–Landau equation (Provansal *et al.* 1987). A supercritical parameter may be defined:

$$\varepsilon = \frac{Re - Re_c}{Re_c}. \quad (6)$$

As suggested from the Stuart–Landau equation, at least close to the onset, the limit-cycle amplitude of periodic velocity fluctuations in the flow is proportional to  $\varepsilon^{1/2}$  (Schumm *et al.* 1994). Although not fully established as a theoretical fact, it seems that the sectional lift amplitude is linearly related to velocity fluctuations close to the cylinder. For laminar shedding the lift fluctuations are virtually indistinguishable from a sinusoidal variation (Kwon & Choi 1996). Consequently and to leading order, a square-root dependency for the r.m.s. lift coefficient versus  $Re$  is expected,  $C_{L'} \propto \varepsilon^{1/2}$ . Results from 2-D simulations within the laminar shedding regime, e.g. Posdziech & Grundmann (2000), support this initial square-root dependency. For higher Reynolds numbers a gradual change to a linear variation is indicated. Based on published 2-D simulation data for  $Re \leq 200$ , see Norberg (2000), the following approximate formula is suggested ( $Re_c = 47$ ):

$$C_{L'} = \sqrt{\varepsilon/30 + \varepsilon^2/90}. \quad (7)$$

In summary, the r.m.s. lift coefficient increases rapidly within the laminar shedding regime. At the highest attainable Reynolds number for two-dimensional flow,  $Re \simeq 190$ , the r.m.s. lift coefficient is  $C_{L'} = 0.45$  (Posdziech & Grundmann 2000).

##### 4.2. WAKE TRANSITION

Following Williamson (1996a), the natural wake transition follows the sequence (2-D  $\rightarrow$  A\*  $\rightarrow$  B). Mode A\* is a highly disturbed flow state comprising a mix between mode A instability structures and large-scale dislocations (Williamson 1992). For obvious reasons the change from 2-D to A\* involves a dramatic decrease in the spanwise correlation of velocity fluctuations in the wake. It also involves a significant drop in shedding frequency and its associated spectral quality (Norberg 1987; Williamson 1988, 1996b). The sectional r.m.s. lift coefficient is expected to decrease in this process (Zhang *et al.* 1995). Measurements in Norberg (2000) indicate for  $Re = 230$  a spanwise correlation length of about 7 diameters, which is about twice the wavelength of the most unstable mode A instability (Barkley & Henderson 1996). As shown in Norberg (1994) a relatively weak influence of the necessary aspect ratio to obtain independent global results is indicated for the range  $Re \simeq 165$ –230. This suggests a rather low spanwise correlation for this initial, A\*-dominated part of the wake transition regime, also see Roshko (1954). Within flow state A\* and with increasing  $Re$  both Strouhal number (Williamson 1996a) and r.m.s. lift coefficient (Zhang *et al.* 1995) increases.

Mode B instability involves the generation of rib-like streamwise vortices with a spanwise wavelength slightly less than one diameter. With the inception of mode B ( $Re \approx 230$ ), mode A being in a declining phase, there is a stabilization on the near-wake vortex shedding (Williamson 1996b). With a subsequent increase in  $Re$ , mode B gradually becomes the

dominant 3-D wake feature (Williamson 1996b), and during this process the spanwise correlation is expected to increase. As shown in Williamson (1996b), the shedding flow at  $Re \simeq 260$  exhibits a remarkable high spanwise coherence. Experiments in Norberg (2000) indicate a spanwise correlation length of about 9.5 diameters at  $Re = 240$  rising to a maximum of about 30 diameters at  $Re = 260$ –300. The high  $A/d$  is in conformity with the very large aspect ratios which are needed for independent results at around these Reynolds numbers (Norberg 1994).

After the inception of mode B and with an increase in  $Re$ , the r.m.s. lift coefficient continues to increase (Zhang *et al.* 1995). However, based on the simulations by Zhang *et al.* there seems to be a local maximum reached for  $C_L$  at around the same point where there is a peak in base suction (Williamson & Roshko 1990; Norberg 1994), which also coincides with the re-introduction of an extremely high spectral quality of the shedding frequency, at  $Re \simeq 260$  (Norberg 1987).

#### 4.3. TURBULENT SHEDDING

Based on previous measurements, e.g. Roshko (1954), Bloor (1964), Gerrard (1978), Norberg (1987), Unal & Rockwell (1988) and Williamson (1996b), the transition to turbulence in the wake reaches the vortex formation region somewhere within  $Re \simeq 260$ –300. Turbulent shedding conditions prevail for all higher  $Re$ . In vortex shedding flows, the actual point or streamwise position of wake transition is meaningful only in the time-averaged sense, given that there is a workable definition of “transition to turbulence”. However, at these rather low Reynolds numbers, such a definition has not yet been given and consequently there are no precise quantitative results reported. A complication is that the wake transition at these  $Re$  appears linked to multiple and strongly interacting wake instabilities (Morkovin 1964; Williamson 1996b). At higher  $Re$  the transition appears to be more distinct and rapid, with a stronger linkage to specific subfields, e.g. see Bloor (1964).

As from the onset of turbulent shedding and with increasing  $Re$  there seems to be an increasing disorder in the fine-scale three dimensionalities associated with the secondary and essentially streamwise-oriented vortices of type mode B (Williamson 1996a). As shown in Brede *et al.* (1996) the normalized circulation of the secondary mode B vortices (scaling with  $Ud$ ) increases by as much as 50% in between  $Re \simeq 300$  and 500 (which is their highest attainable  $Re$ ). This increase in secondary (essentially streamwise) circulation occurs probably at the expense of the primary (essentially spanwise) circulation associated with the roll-up of the von Kármán vortices (Mansy *et al.* 1994). Consequently, since the alternate roll-up is closely related to fluctuating lift,  $C_L$  drops with increasing  $Re$ .

The indicated spanwise correlation length at  $Re = 1.6 \times 10^3$  is approximately 8 cylinder diameters while the corresponding local minimum of the sectional r.m.s. lift coefficient is only  $C_L \simeq 0.045$  (Norberg 2000). It is to be noted that from about  $Re = 270$ –1400 the total r.m.s. lift force on a large-aspect-ratio cylinder, proportional to  $C_L \times Re^2 \times \sqrt{A/d}$  [equations (1) and (5)], is indicated to be approximately constant. It seems appropriate to classify this remarkable behaviour (and the subsequent very low r.m.s. lift coefficient at  $Re \simeq 1.6 \times 10^3$ ) as a *lift crisis*. The suggested variations for  $C_L$  and  $A/d$  (Norberg 2000) indicate that the corresponding increase in free-stream velocity with a factor of about 5 ( $1400/270 = 5.2$ ) will only cause a  $\pm 15\%$  variation in the total r.m.s. lift acting on the cylinder! As a perspective, the total mean drag increases by about a factor 600 ( $C_D \approx 1$ ).

Within the initial part of the turbulent shedding regime, up to about  $Re = 5 \times 10^3$ , the streamwise position of wake transition appears to be rather fixed with respect to the cylinder, although being upstream of the mean position of wake closure (Bloor 1964). It

seems, at these  $Re$ , that the transition to turbulence in the wake is not due to a shear-layer instability; if so, the position ought to be moving towards the cylinder with increasing Reynolds number. Instead, it is suggested that the wake transition has its origin in the near-wake development of the rib-like secondary vortices of mode B type. As such, a rib-like vortex structure is swept across the wake centre line, being on the upstream side of its associated von Kármán vortex within the connecting braid shear layer inside the formation region (Bays-Muchmore & Ahmed 1993; Brede *et al.* 1996; Lin *et al.* 1996), there will be a rapid stretching of the structure itself which, in connection with possible interactions with the primary roll-up, leads to a rapid breakdown into small-scale turbulence. However, it seems that the mode B vortices also have some sort of a timing or regulating role for the vortex shedding process. As from about  $Re = 260\text{--}5.1 \times 10^3$ , the spectral quality of the shedding frequency is extremely high (Norberg 1987). The stabilization of the shedding frequency for the circular cylinder may be related to a feedback mechanism in between the rib-like vortices, the developing von Kármán vortices and ultimately with the separation process, causing small but regulating undulations of the separation line.

The subsequent increase in  $C_L$  from about  $Re = 1.6 \times 10^3$  seems to coincide with the point where shear-layer vortices show up as important ingredients in the near wake (Prasad & Williamson 1997a). The shear-layer vortices will introduce additional shear stresses to the near wake and to balance this (Roshko 1993) the formation region shrinks and the base suction increases (Linke 1931; Bloor 1964; Norberg 1994, 1998). Consequently, the sectional  $C_L$  increases, at first rather slow but then at an increasing rate, especially within  $Re = 5 \times 10^3$  to  $7 \times 10^3$  (Figure 2). A local maximum in  $A/d$  occurs at  $Re = 5.1 \times 10^3$ ,  $A/d \approx 15$ . At this point, a change-over in the wake transitional process is suggested; below  $Re \approx 5 \times 10^3$ , the (mean position of) transition to turbulence occurs at some near-constant distance upstream of the (mean) wake closure, the transition being triggered by actions of secondary vortices of type mode B; for higher  $Re$  the transition instead is primarily governed by a Kelvin-Helmholtz instability mechanism within the separated shear layers, at a (mean) position which thereafter is moving upstream with increasing  $Re$ . At the critical  $Re$  the two (mean) streamwise positions coincide causing a resonance-like behaviour, presumably in-between spanwise length scales of mode B vortices and shear-layer vortices (Norberg 1998). For  $Re > 5 \times 10^3$ , due to the change-over in the position of wake transition, the harmony between the mode B vortices and the roll-up of von Kármán vortices is lost, and this causes more and more disruptions to the vortex shedding process, e.g. a significant spanwise undulation of developing von Kármán vortices, a characteristic lift amplitude modulation and a spectral broadening of the shedding peak frequency. Occasionally, these disruptions lead to random-positioned vortex dislocations, along the span and within the vortex formation region. During such events the local sectional lift amplitude is very low.

The change-over from the "high-quality" shedding mode displaying a fairly regular vortex shedding with only minor spanwise undulation of the developing von Kármán vortices to the "low-quality" shedding mode displaying significant spanwise undulations and occasional but characteristic vortex dislocations appears to be fully completed at  $Re \approx 8 \times 10^3$  (Norberg 1993, 1998). At  $Re \approx 10^4$  the transition in the separated shear layers has reached a mean position corresponding to just above the base point of the cylinder (Linke 1931; Bloor 1964; Norberg 1998). As from about this  $Re$  the variations of  $C_L$  and  $A/d$  with increasing  $Re$  slow down (Figures 2 and 3), the probable reason being the diminishing relative importance of the actual position of wake transition on the global flow development. At  $Re \approx 1.6 \times 10^5$ , due to the closeness of transition in the separated shear layers, the first signs of a reattachment behaviour becomes visible in the measured r.m.s. pressure distributions, at  $\varphi \approx 105^\circ$  (Norberg 1993). With a subsequent increase in  $Re$ , the build-up to a fully reattached flow continues, the position of laminar separation moves

downstream, the wake narrows and the Strouhal number increases, and finally at  $Re \approx 2.3 \times 10^5$  there is a rapid fall in both  $C_D$  and  $C_L$  when entering the critical regime.

### DEDICATION

This paper is submitted in honour of the outstanding achievements, insightful publications and contributions in this field over the last 50 years made by Professor Anatol Roshko (California Institute of Technology, Pasadena, U.S.A.). At the last day of the IUTAM Symposium related to these proceedings (16 June 2000), Professor Roshko mentioned that the first time he "dipped" the hot wire into the shedding wake was in August 1950. The publication "On the development of turbulent wakes from vortex streets" was published 4 years later (Roshko 1954). Among other things this classic work contains the Roshko relation for the  $St-Re$  variation within the laminar shedding regime, as Roshko refers to as the stable range. This relation, which has resisted the ravages of time, was not verified until 1987 when the author presented his thesis work (Norberg 1987).

### ACKNOWLEDGEMENTS

The author would like to express his sincere thanks to Peter Bearman (U.K.), Charles Williamson (U.S.A.) and Thomas Leweke (France) for their support and helpful advice.

### REFERENCES

- BARKLEY, D. & HENDERSON, R. D. 1996 Three-dimensional Floquet stability analysis of the wake of a circular cylinder. *Journal of Fluid Mechanics* **322**, 215–241.
- BAYS-MUCHMORE, B. & AHMED, A. 1993 On streamwise vortices in turbulent wakes of cylinders. *Physics of Fluids A* **5**, 387–392.
- BEARMAN, P. W. 1969 On vortex shedding from a circular cylinder in the critical Reynolds number regime. *Journal of Fluid Mechanics* **37**, 577–585.
- BEARMAN, P. W. & WADCOCK, A. J. 1973 The interaction between a pair of circular cylinders normal to a stream. *Journal of Fluid Mechanics* **61**, 499–511.
- BLAKE, W. K. 1986 *Mechanics of Flow-Induced Sound and Vibration*, Vol. 1, London: Academic Press.
- BLEVINS, R. D. 1990 *Flow-Induced Vibration*, 2nd edition. New York: Van Nostrand Reinhold.
- BLOOR, M. S. 1964 The transition to turbulence in the wake of a circular cylinder. *Journal of Fluid Mechanics* **19**, 290–304.
- BOUAK, F. & LEMAY, J. 1998 Passive control of the aerodynamic forces acting on a circular cylinder. *Experimental Thermal and Fluid Sciences* **16**, 112–121.
- BREDE, M., ECKELMANN, H. & ROCKWELL, D. 1996 On secondary vortices in the cylinder wake. *Physics of Fluids* **8**, 2117–2124.
- BRUUN, H. H. & DAVIES, P. O. A. L. 1975 An experimental investigation of the unsteady pressure forces on a circular cylinder in a turbulent cross flow. *Journal of Sound and Vibration* **40**, 535–559.
- DRESCHER, H. 1956 Messung der auf querangeströmte Zylinder ausgeübten zeitlich veränderten Drücke. *Zeitschrift für Flugwissenschaften und Weltraumforschung* **4**, 17–21.
- FARELL, C. 1981 Flow around fixed circular cylinders: Fluctuating loads. *ASCE Journal of the Engineering Mechanics Division* **107**, 565–587.
- GARTSHORE, I. S. 1984 Some effects of upstream turbulence on the unsteady lift forces imposed on prismatic two dimensional bodies. *ASME Journal of Fluids Engineering* **106**, 418–424.
- GERRARD, J. H. 1961 An experimental investigation of the oscillating lift and drag of a circular cylinder shedding turbulent vortices. *Journal of Fluid Mechanics* **11**, 244–256.
- GERRARD, J. H. 1978 The wakes of cylindrical bluff bodies at low Reynolds number. *Philosophical Transactions Royal Society (London) A* **288**, 351–382.
- IIDA, A., OTAGURO, T., KATO, C. & FUJITA, H. 1997 Prediction of aerodynamic sound spectra from a circular cylinder. In *Proceedings of the 5th Triennial International Symposium on Fluid Control, Measurement and Visualization (FLUCOME '97)*, Hayama, Japan, Vol. 1, pp. 126–131.



- KACKER, S. C., PENNINGTON, B. & HILL, R. S. 1974 Fluctuating lift coefficient for a circular cylinder in cross flow. *Journal Mechanical Engineering Science* **16**, 215–224.
- KEEFE, R. T. 1961 An investigation of the fluctuating forces acting on a stationary circular cylinder in a subsonic stream, and of the associated sound field. Report No. 76, Institute of Aerophysics, University of Toronto (UTIA).
- KWON, K. & CHOI, H. 1996 Control of laminar vortex shedding behind a circular cylinder. *Physics of Fluids* **8**, 479–486.
- LEEHEY, P. & HANSON, C. E. 1971 Aeolian tones associated with resonated vibration. *Journal of Sound and Vibration* **13**, 465–483.
- LIN, J. C., VOROBIEFF, P. & ROCKWELL, D. 1996 Space-time imaging of a turbulent near-wake by high-image-density particle image cinematography. *Physics of Fluids* **8**, 555–564.
- LINKE, W. 1931 Neue Messungen zur Aerodynamik des Zylinders, insbesondere seines reinen Reibungswiderstandes. *Physikalische Zeitschrift* **32**, 900–914.
- MANSY, H., YANG, P. M. & WILLIAMS, D. R. 1994 Quantitative measurements of three-dimensional structures in the wake of a circular cylinder. *Journal of Fluid Mechanics* **270**, 277–296.
- MOELLER, M. J. 1982 Measurement of unsteady forces on a circular cylinder in cross flow at subcritical Reynolds numbers. Ph.D. Dissertation, Massachusetts Institute of Technology, Cambridge, MA, U.S.A.
- MOHR, K. H. 1981 Messungen instationärer Drucke bei Queranströmung von Kreiszyklindern unter Berücksichtigung fluidelastischer Effekte. Ph.D. Dissertation, KFA Jülich, Germany. Report Jul-1732.
- MORKOVIN, M. V. 1964 Flow around circular cylinder—a kaleidoscope of challenging fluid phenomena. In *Proceedings of the Symposium on Fully Separated Flows, Philadelphia* (ed. A. G. Hansen), pp. 102–118, New York: ASME.
- NORBERG, C. 1987 Effects of Reynolds number and a low-intensity freestream turbulence on the flow around a circular cylinder. Publication 87/2, Department of Applied Thermodynamics and Fluid Mechanics, Chalmers University of Technology, Gothenburg, Sweden.
- NORBERG, C. 1992 An experimental study of the flow around cylinders joined with a step in the diameter. In *Proceedings of the 11th Australasian Fluid Mechanics Conference, Hobart, Australia* (eds M. R. Davis & G. J. Walker), Vol. 1, pp. 507–510.
- NORBERG, C. 1993 Pressure forces on a circular cylinder in cross flow. In *Bluff-Body Wakes, Dynamics and Instabilities* (eds H. Eckelmann, J. M. R. Graham, P. Huerre, P. A. Monkewitz), pp. 275–278, Berlin: Springer-Verlag.
- NORBERG, C. 1994 An experimental investigation of the flow around a circular cylinder: influence of aspect ratio. *Journal of Fluid Mechanics* **258**, 287–316.
- NORBERG, C. 1998 LDV-measurements in the near wake of a circular cylinder. In *Proceedings of the 1998 Conference on Bluff Body Wakes and Vortex-Induced Vibration, Washington, DC, USA* (eds P. W. Bearman & C. H. K. Williamson), pp. 1–12, Ithaca, NY: Cornell University.
- NORBERG, C. 2000 Flow around a circular cylinder: fluctuating lift. *Journal of Fluids and Structures* (submitted).
- NOVAK, M. & TANAKA, H. 1977 Pressure correlations on a vibrating cylinder. In *Proceedings of the 4th International Conference on Wind Effects on Buildings and Structures, Heathrow, U.K.* (ed. K. J. Eaton), pp. 227–232, Cambridge: Cambridge University Press.
- POSDZIECH, O. & GRUNDMANN, R. 2000 A systematic approach to the numerical calculation of fundamental quantities of the two-dimensional flow over a circular cylinder. *Journal of Fluids and Structures* (submitted).
- PRASAD, A. & WILLIAMSON, C. H. K. 1997a The instability of the shear layer separating from a bluff body. *Journal of Fluid Mechanics* **333**, 375–402.
- PRASAD, A. & WILLIAMSON, C. H. K. 1997b Three-dimensional effects in turbulent bluff-body wakes. *Journal of Fluid Mechanics* **343**, 235–265.
- PROVANSAL, M., MATHIS, C. & BOYER, L. 1987 Bénard-von Kármán instability: transient and forced regimes. *Journal of Fluid Mechanics* **182**, 1–22.
- RIBEIRO, J. L. D. 1992 Fluctuating lift and its spanwise correlation on a circular cylinder in a smooth and in a turbulent flow: a critical review. *Journal of Wind Engineering and Industrial Aerodynamics* **40**, 179–198.
- ROSHKO, A. 1954 On the development of turbulent wakes from vortex streets. NACA Report 1191, National Advisory Committee for Aeronautics, Washington, DC, U.S.A.
- ROSHKO, A. 1961 Experiments on the flow past a circular cylinder at very high Reynolds number. *Journal of Fluid Mechanics* **10**, 345–356.

- ROSHKO, A. 1993 Perspectives on bluff body aerodynamics. *Journal of Wind Engineering and Industrial Aerodynamics* **49**, 79–100.
- SAKAMOTO, H. & HANIU, H. 1994 Optimum suppression of fluid forces acting on a circular cylinder. *ASME Journal of Fluids Engineering* **116**, 221–227.
- SCHUMM, M., BERGER, E. & MONKEWITZ, P. A. 1994 Self-excited oscillations in the wake of two-dimensional bluff bodies and their control. *Journal of Fluid Mechanics* **271**, 17–53.
- SONNEVILLE, P. 1976 Étude de la structure tridimensionnelle des écoulements autour d'un cylindre circulaire. Bulletin de la Direction des Etudes et Recherches, Série A, No. 3-1976, Electricité de France.
- SZEPESSY, S. 1994 On the spanwise correlation of vortex shedding from a circular cylinder at high subcritical Reynolds number. *Physics of Fluids* **6**, 2406–2416.
- SZEPESSY, S. & BEARMAN, P. W. 1992 Aspect ratio and end plate effects on vortex shedding from a circular cylinder. *Journal of Fluid Mechanics* **234**, 191–217.
- UNAL, M. F. & ROCKWELL, D. 1988 On vortex formation from a cylinder. Part 1. The initial instability. *Journal of Fluid Mechanics* **190**, 491–512.
- WEST, G. S. & APELT, C. J. 1993 Measurements of fluctuating pressures and forces on a circular cylinder in the Reynolds number range  $10^4$  to  $2.5 \times 10^5$ . *Journal of Fluids and Structures* **7**, 227–244.
- WIESELSBERGER, C. 1921 Neuere Feststellungen über die Gesetze des Flüssigkeits- und Luftwiderstandes. *Physikalische Zeitschrift* **22**, 321–328.
- WILLIAMSON, C. H. K. 1988 The existence of two stages in the transition to three-dimensionality of a cylinder wake. *Physics of Fluids* **31**, 3165–3168.
- WILLIAMSON, C. H. K. 1989 Oblique and parallel modes of vortex shedding in the wake of a circular cylinder at low Reynolds numbers. *Journal of Fluid Mechanics* **206**, 579–627.
- WILLIAMSON, C. H. K. 1992 The natural and forced formation of spot-like “vortex dislocations” in the transition of a wake. *Journal of Fluid Mechanics* **243**, 393–441.
- WILLIAMSON, C. H. K. 1996a Vortex dynamics in the cylinder wake. *Annual Review of Fluid Mechanics* **28**, 477–539.
- WILLIAMSON, C. H. K. 1996b Three-dimensional wake transition. *Journal of Fluid Mechanics* **328**, 345–407.
- WILLIAMSON, C. H. K. & ROSHKO, A. 1990 Measurements of base pressure in the wake of a cylinder at low Reynolds numbers. *Zeitschrift für Flugwissenschaften und Weltraumforschung* **14**, 38–46.
- ZHANG, H. Q., FEY, U., NOACK, B. R., KÖNIG, M. & ECKELMANN, H. 1995 On the transition of the cylinder wake. *Physics of Fluids* **7**, 779–793.

## NONLINEAR SYNCHRONIZATION IN OPEN FLOWS

B. PIER\* AND P. HUERRE

*Laboratoire d'Hydrodynamique (LadHyX), CNRS – École Polytechnique  
F-91128 Palaiseau Cedex, France*

(Received 14 September 2000, and in final form 7 November 2000)

The selection criteria governing finite-amplitude synchronized oscillating states are discussed for model systems and real wake flows in a domain of infinite streamwise extent. Two types of nonlinear global modes are possible: *hat* modes with overall smoothly varying amplitude and *elephant* modes with a sharp front. The vortex street in wake flows is of elephant type, as observed in direct numerical simulations of a real spatially developing wake. Furthermore, the elephant frequency selection criterion is in excellent agreement with the numerically determined vortex shedding frequency.

© 2001 Academic Press

### 1. INTRODUCTION

A VARIETY OF OPEN FLOWS may sustain globally synchronized oscillations. Wakes behind bluff-bodies are well known [for a review see Williamson (1996)] to undergo a transition to a periodic vortex shedding régime at moderate Reynolds numbers. Experimentally and numerically, the features of a globally synchronized vortex street are now well documented [e.g., Provansal *et al.* (1987), Hammond & Redekopp (1997)]. However, the selected frequency of the global structure has not been theoretically predicted in the framework of hydrodynamic stability theory. The aim of the present paper is to discuss recent progress made in the identification of resonance mechanisms which are responsible for global synchronization in spatially developing flows. We restrict here our attention to one-dimensional complex Ginzburg–Landau (CGL) equations with spatially varying coefficients in an infinite domain and to two-dimensional spatially developing wake flows governed by the Navier–Stokes (NS) equations. The paper is mainly based on the recent dissertation of Pier (1999) and the corresponding publications by Pier & Huerre (1996), Pier *et al.* (1998), Pier *et al.* (2001) and Pier & Huerre (2001). For a general background on the hydrodynamic stability theory of spatially developing flows, the reader is referred to the review articles and tutorial presentations of Huerre & Monkewitz (1990), Huerre & Rossi (1998) and Huerre (2000). A brief summary of relevant issues is given below.

The existence of self-sustained oscillations in shear flows is closely related to the transition from *convective* to *absolute instability* (Briggs 1964; Bers 1983). In convectively unstable (CU) systems, the basic flow carries growing perturbations away in the downstream direction, and the system eventually returns to its unperturbed state. Hence, if a flow changes from local stability to convective instability, only its transient response to perturbations is affected. In a locally stable configuration all perturbations are damped, whereas in a CU basic flow they grow in the downstream direction. In the latter configuration, perturbations eventually leave the domain of interest: in the long term, the flow is globally

\*Present address: Department of Applied Mathematics and Theoretical Physics, University of Cambridge, Silver Street, Cambridge CB3 9EW, UK. E-mail: [b.pier@damtp.cam.ac.uk](mailto:b.pier@damtp.cam.ac.uk).

stable and it may only be kept out of equilibrium if perturbations are continuously entering the inflow boundary. Thus, CU flows may be interpreted as *amplifiers* since perturbations entering the inlet grow along the stream until they leave the system at the outlet.

In contrast, transition from convective to absolute instability drastically changes the dynamical behaviour. In absolutely unstable (AU) systems, instabilities grow *in situ* and survive for all times. A self-sustained nontrivial state may therefore be observed without external input. Thus, as far as the long term asymptotic behaviour is concerned, transition from local stability to convective instability proves irrelevant, whereas transition from convective to absolute instability plays a crucial rôle.

The above-mentioned instability properties are defined for infinite and spatially homogenous systems. Since real flows develop in the streamwise direction, stable, CU and AU domains may coexist as the local properties vary along the stream. Under the assumption that the streamwise variations be small on a typical instability length scale, the previous definitions still apply locally at each streamwise station. In wake flows at moderate Reynolds numbers, which are of particular interest to readers of this Special Issue, the transient régime leads to a stationary time-periodic state; the flow globally behaves as an *oscillator*. Characteristics such as spatial structure and global frequency become intrinsic to the flow: They are selected in the bulk and largely independent of inflow conditions.

The following questions then arise. (i) Under which conditions does global instability occur? Does global instability coincide with the onset of local absolute instability or is an AU domain of finite extent required? (ii) In the case of globally synchronized oscillations, how is the global frequency determined? Which part of the flow acts as a wave maker? (iii) How is the global behaviour affected by nonlinearities? Are finite-amplitude oscillations governed by linear or nonlinear selection criteria? What is the importance of the mean flow correction generated by nonlinear interactions?

In the following, these issues are preferentially addressed in the context of streamwise developing flows in an *infinite domain*, whether in the form of CGL model equations or real wakes. In the latter instance, we solely consider wakes produced by a velocity deficit introduced at some streamwise station and boldly set aside the wake producing body. This assumption is in marked contrast with the recent investigations by Couairon & Chomaz (1997, 1999a, b) of nonlinear global modes governed by one-dimensional CGL model equations in *semi-infinite domains*. In this case, global mode onset takes place whenever a front succeeds in propagating upstream against the advecting flow, thereby getting pinned at the upstream boundary point. This precisely takes place when transition from convective to absolute instability occurs at the upstream boundary. Furthermore, Couairon & Chomaz (1999b) have derived scaling laws for the global mode characteristic length scale and its streamwise shape near onset which are in excellent agreement with experimental and numerical studies of vortex shedding behind bluff bodies by Goujon-Durand *et al.* (1994) and Zielinska & Wesfreid (1995). Such a scenario is also supported by the direct numerical simulations of the nonlinear impulse response in parallel wakes conducted by Delbende & Chomaz (1998): although the impulse response is of finite amplitude, its upstream edge is governed by linear dynamics.

## 2. SCALE SEPARATION

The theoretical formulation underlying all global mode analyses, whether linear or nonlinear, essentially relies on the assumption of *slow streamwise variations* of instability properties. This hypothesis is required if one is to establish a specific relationship between global behaviour and local properties.

At an intuitive level of understanding, in open systems the mean flow introduces a preferred streamwise direction along which the entire dynamics develops. Let  $x$  denote the streamwise distance, increasing from the inlet to the outlet. The coordinate  $x$  appears both as a *variable* in streamwise derivative operators related to the instability properties and as a *parameter* to account for the streamwise evolution of the basic flow. If  $\lambda$  denotes a typical instability length scale and  $L$  the streamwise evolution length scale of the basic flow, weak inhomogeneity is characterized by the small parameter

$$\varepsilon \equiv \frac{\lambda}{L} \ll 1. \quad (1)$$

Under assumption (1), the parametric streamwise dependence of the dynamics only occurs through the slow coordinate  $X = \varepsilon x$ . At leading order, the slow parameter  $X$  may be considered independent of the fast variable  $x$ . Local instability characteristics are then retrieved by freezing  $X$  in the governing equations and studying the equivalent homogenous system in the infinite domain  $-\infty < x < +\infty$ . Hence the fast evolving local dynamics is slaved to the slow evolution of the basic flow. This technique is fully justified by resorting to the method of multiple scales (Crighton & Gaster 1976; Bender & Orszag 1978).

### 3. MODEL FLOWS AND REAL FLOWS

The global behaviour of spatially developing flows has typically been studied in the context of the one-dimensional CGL model or the complete two-dimensional Navier-Stokes (NS) equations.

The spatially inhomogenous Ginzburg-Landau evolution equation for a complex field  $\psi(x, t)$  may conveniently be written as

$$\begin{aligned} i \frac{\partial \psi}{\partial t} = & \left( \omega_0(X) + \frac{1}{2} \omega_{kk}(X) k_0(X)^2 \right) \psi + i \omega_{kk}(X) k_0(X) \frac{\partial \psi}{\partial x} \\ & - \frac{1}{2} \omega_{kk}(X) \frac{\partial^2 \psi}{\partial x^2} + \gamma(X) |\psi|^2 \psi, \end{aligned} \quad (2)$$

where  $\omega_0$  and  $k_0$  denote the absolute frequency and wavenumber, respectively,  $\omega_{kk}$  the second derivative of the frequency with respect to wavenumber. The choice  $\gamma_i \equiv \text{Im } \gamma < 0$  ensures that nonlinearities are stabilizing everywhere. All complex coefficients of equation (2) depend on  $X = \varepsilon x$  to enforce assumption (1) of weak spatial inhomogeneity.

For two-dimensional incompressible flows, the total streamfunction  $\Psi(x, y, t)$  is governed by the nondimensional vorticity equation

$$\left( \frac{\partial}{\partial t} + \frac{\partial \Psi}{\partial y} \frac{\partial}{\partial x} - \frac{\partial \Psi}{\partial x} \frac{\partial}{\partial y} \right) \Delta \Psi = \frac{1}{\text{Re}} \Delta^2 \Psi, \quad (3)$$

where  $y$  denotes the cross-stream coordinate and  $\text{Re}$  the Reynolds number. Real flows fulfill the assumption of slow streamwise development in high Reynolds number situations, and the inhomogeneity parameter then reads

$$\varepsilon = \frac{1}{\text{Re}}. \quad (4)$$

When  $\varepsilon \ll 1$ , the leading-order time-independent basic flow resulting from (3) obeys the Prandtl boundary-layer equation

$$\left( \frac{\partial \Psi}{\partial y} \frac{\partial}{\partial X} - \frac{\partial \Psi}{\partial X} \frac{\partial}{\partial y} \right) \frac{\partial \Psi}{\partial y} = - \frac{dP}{dX} + \frac{\partial^3 \Psi}{\partial y^3}, \quad (5)$$

where the streamwise pressure gradient  $dP/dX$  arises as an integration constant. Basic streamwise and cross-stream velocity components are then obtained as  $U(y; X) = \partial \Psi / \partial y$  and  $V(y; X) = -\varepsilon \partial \Psi / \partial X$ , respectively. Decomposition of the total streamfunction into basic field and finite-amplitude perturbations according to  $\Psi(x, y, t) = \int_0^y U(\eta; X) d\eta + \psi(x, y, t)$  yields the governing vorticity equation for  $\psi(x, y, t)$  as

$$\left( \frac{\partial}{\partial t} + U(y; X) \frac{\partial}{\partial x} \right) \Delta \psi - \frac{\partial^2 U}{\partial y^2}(y; X) \frac{\partial \psi}{\partial x} + \left( \frac{\partial \psi}{\partial y} \frac{\partial}{\partial x} - \frac{\partial \psi}{\partial x} \frac{\partial}{\partial y} \right) \Delta \psi = \frac{1}{\text{Re}} \Delta^2 \psi. \quad (6)$$

Although real flows are two dimensional, there is only one slow streamwise coordinate  $X$  that accounts for the evolution of local instability properties as described by a local dispersion relation. The study of two-dimensional flows is more complex since cross-stream eigenfunctions have to be computed; however, the analysis of CGL or NS global modes proceeds in exactly the same manner since all the fast evolving features are slaved to  $X$ .

Note that in the CGL model (2) any variations of the complex coefficients with  $X$  may be considered. In the hydrodynamic context (6) however, the basic flow  $U(y; X)$  governed by (5) is uniquely determined by the inlet velocity profile, say  $U(y; X = 0)$ , and the streamwise pressure distribution  $P(X)$  for  $X > 0$ . In a self-consistent formulation, the velocity profiles  $U(y; X)$  appearing as coefficients in (6) cannot be arbitrarily specified. In the present analysis, a coflowing wake profile is chosen for  $U(y; X = 0)$  and the pressure field  $P(X)$  is then carefully tailored so that the essential features of experimental wake flows are reproduced. In this procedure, a "synthetic wake" is thereby generated without requiring the presence of a solid obstacle [cf. Figure 2(a)]!

#### 4. LINEAR RESONANCE CRITERION

In a strictly linear framework, theoretically consistent results have first been derived by Chomaz *et al.* (1991) for the linear version of model (2) and by Monkewitz *et al.* (1993) for the linear version of the vorticity equation (6). The essential physical property is the complex local absolute frequency  $\omega_0(X)$  defined in classical fashion (Briggs 1964; Bers 1983) by imposing a zero group velocity condition on the *local linear dispersion relation*

$$\omega = \Omega^l(k, X). \quad (7)$$

The form of the CGL model (2) already displays its dependence on  $\omega_0(X)$ , whereas for real flows the dispersion relation (7) is derived by solving the Orr–Sommerfeld equation applied to the velocity profiles  $U(y; X)$  prevailing at each station  $X$ .

The criterion for linear global instability is then based on the variations of  $\omega_0(X)$  and states that the complex frequency  $\omega_s^l$  of a self-sustained linear global mode is given by the saddle-point condition

$$\frac{d\omega_0}{dX}(X_s^l) = 0 \quad \text{and} \quad \omega_s^l = \omega_0(X_s^l), \quad (8)$$

where it is understood that  $\omega_0(X)$  has been analytically continued in the complex  $X$ -plane. In general, the saddle point  $X_s^l$  does not occur on the real axis, and linear global instability characterized by  $\text{Im } \omega_s^l > 0$  requires an AU region of *finite extent* in the slow variable  $X$ . Thus, in the linear framework, absolute instability is a prerequisite for global instability. However, it is not a sufficient condition: Linear global modes are observed to decay in time for AU domains of finite but small extent in  $X$ , which may correspond to very large AU domains in terms of  $x$ .

The typical shape of a linear CGL global mode is sketched in Figure 1(a). Note that, in general, maximum amplitude occurs downstream of  $\text{Re } X_s^l$ .

## 5. NONLINEAR RESONANCE CRITERIA

A weakly nonlinear approach (Le Dizès *et al.* 1993) conducted close to the onset of global instability specified by  $\text{Im } \omega_s^l = 0$  has proven that the bifurcation analysis is ill-behaved and suggested that only a fully nonlinear theory is appropriate. In the nonlinear framework, two types of finite-amplitude oscillating states have been identified for the inhomogenous CGL equation in infinite media: *soft* or *hat* (Pier & Huerre 1996) and *steep* or *elephant* (Pier *et al.* 1998) *nonlinear global modes* [cf. Figure 1(b,c)]. Their selection criteria are obtained from the local linear and nonlinear dispersion relations, as summarized below.

The *local nonlinear dispersion relation* is defined via a temporal evolution problem in the following way. Consider a homogenous medium obtained by freezing  $X$  at a prescribed value. An unstable spatially periodic perturbation of *real* wavenumber  $k$  grows according to  $\Omega_i^l(k, X) > 0$  until its amplitude reaches a finite level. Due to stabilizing nonlinearities, a fully nonlinear wavetrain is generated with spatial periodicity imposed by the initial wavenumber. Its frequency, measured for each  $k$ , then yields the nonlinear dispersion relation

$$\omega = \Omega^l(k, X). \quad (9)$$

Whereas the local linear dispersion relation (7) yields a *complex* frequency for any *complex* wavenumber, the nonlinear dispersion relation (9) is defined only for *real* wavenumbers  $k$  associated with a positive growth rate  $\Omega_i^l(k, X) > 0$  and it necessarily yields *real* frequencies. For the CGL model (2), nonlinear wave-trains are finite-amplitude harmonic waves of the form  $\text{Re } e^{i(kx - \omega t)}$  and (9) reads  $\omega = \text{Im}(\gamma^*(X) \Omega^l(k, X)) / \text{Im} \gamma^*(X)$ . Computation of (9) for real flows, however, requires a numerical integration as discussed by Pier & Huerre (2000).

Hat global modes [Figure 1(b); Pier & Huerre 1996] have an overall smoothly varying amplitude, and their real frequency  $\omega_s^{nl}$  is selected at a saddle-point  $X_s^{nl}$  of the nonlinear dispersion relation according to

$$\frac{\partial \Omega^{nl}}{\partial X}(X_s^{nl}, k_s^{nl}) = \frac{\partial \Omega^{nl}}{\partial k}(X_s^{nl}, k_s^{nl}) = 0 \quad \text{and} \quad \omega_s^{nl} = \Omega^{nl}(k_s^{nl}, X_s^{nl}). \quad (10)$$

Elephant global modes [Figure 1(c); Pier *et al.* 1998] are characterized by a sharp front governed by the Dee & Langer (1983) marginal stability criterion and located at the upstream transition station  $X^{ca}$  between CU and AU regions. The entire structure is tuned to the front frequency given by the corresponding real absolute frequency

$$\omega_0^{ca} = \omega_0(X^{ca}) \quad \text{with} \quad \text{Im } \omega_0(X^{ca}) = 0. \quad (11)$$

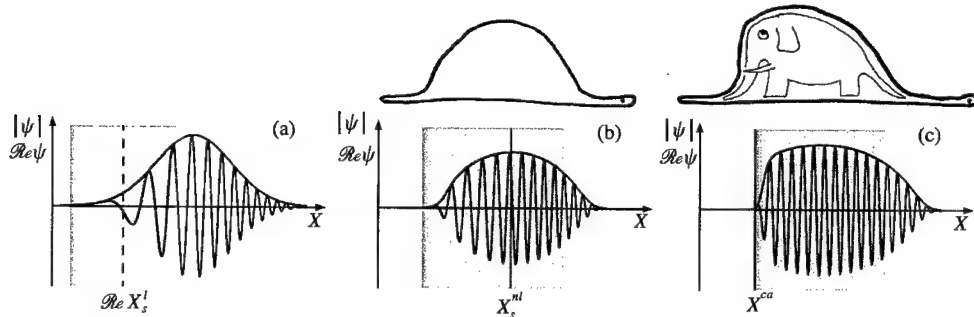


Figure 1. Shapes of CGL global modes. Shaded regions indicate extent of AU domain. (a) Linear global mode. (b) Nonlinear soft global mode or hat mode. (c) Nonlinear steep global mode or elephant mode. The names “hat” and “elephant” have been chosen in reference to Saint-Exupéry (1946).

The detailed analysis of the transition scenarios between the unperturbed state and either type of nonlinear global mode reveals (Pier 1999, Pier *et al.* 2001) that the two nonlinear resonance criteria (10, 11) are mutually exclusive and that the appropriate global bifurcation parameter is the maximum absolute growth rate over the entire medium  $\omega_{0,i}^{\max} \equiv \max \omega_{0,i}(X)$ . Nonlinear global modes exist whenever an AU region is present ( $\omega_{0,i}^{\max} > 0$ ). At transition ( $\omega_{0,i}^{\max} = 0$ ) an elephant mode is always selected. Hat modes exist further above threshold and are more readily obtained in systems where the basic advection velocity is weak. Absolute instability is therefore a *necessary and sufficient* condition for the existence of self-sustained *nonlinear* structures. This is in contrast with the results of Section 4: Local absolute instability is only a necessary condition for the existence of amplified *linear* global modes.

## 6. FINITE-AMPLITUDE VORTEX STREET AS AN ELEPHANT MODE

The generalization of the above nonlinear theory to real flows governed by the Navier–Stokes equations has been conducted by Pier (1999) and Pier & Huerre (2001).

In order to obtain unambiguous results that can be compared with the theory, the basic flow has to strictly comply with the condition of weak streamwise nonuniformity. Bluff body wakes display a recirculation bubble near the obstacle which violates this assumption. The “synthetic wakes” governed by the Prandtl boundary-layer equation (5) all avoid this difficulty. In the example represented in Figure 2(a) for  $Re = 100$ , the pressure gradient has been selected to be mildly adverse in order to produce a central AU region (displayed in gray), which is an essential feature of real wakes.

Direct numerical simulations of the temporal evolution of this basic flow [see Pier & Huerre (2001) for details] leads to a finite-amplitude vortex shedding régime [Figure 2(b)] tuned at a well-defined global frequency  $\omega_g = 0.186 \pm 0.002$ . This vortex street is made up of wave-trains which slowly deform while travelling downstream: such structures are locally periodic and their  $(x, t)$ -dependence solely occurs via a phase function with only slow streamwise variations. Hence the multiple-scale formalism (Bender & Orszag 1978) applies and the global structure may be analysed in terms of local linear and nonlinear waves.

In the upstream domain ( $x < 25$ ), the basic flow is seen to remain unperturbed: small-amplitude wave-trains prevail in this linear region. Further downstream, nonlinear travelling waves develop and completely mask the underlying basic wake flow. In order to



establish that the nonlinear globally synchronized state [Figure 2(b)] follows the elephant resonance criterion (11), its numerically determined features are now compared with predictions based on the local linear and nonlinear instability analyses of the basic flow [Figure 2(a)].

The computation of the local linear dispersion relation (7) via the Orr–Sommerfeld equation reveals an AU domain extending over the streamwise interval  $24 < x < 55$  (gray regions in Figure 2). The real absolute frequency prevailing at its upstream boundary  $x^{ca} = 24$  reads  $\omega_0^{ca} = 0.190$ . The nonlinear resonance criterion (11) therefore accurately predicts the vortex shedding frequency, unlike the linear criterion (8) which yields  $\omega_s^l = 0.143 + 0.008i$ .

The local nonlinear dispersion relation (9) is illustrated in Figure 2(c) by isofrequency contours in the linearly unstable domain of the  $(X, k)$ -plane. These contours precisely define the nonlinear spatial branches  $k^{nl}(X, \omega)$  obtained by solving the nonlinear dispersion relation (9) at a given frequency. A global mode synchronized at the frequency  $\omega_0^{ca}$  is expected to follow the spatial branch  $k^{nl}(X, \omega_0^{ca})$  represented by a thick dashed curve. The local wave number of the numerically computed spatially developing vortex street [Figure 2(b)] is represented by a thick solid curve in the same sketch and it is seen to closely follow the path predicted by the elephant global mode structure.

*The finite-amplitude vortex street is thus described by a nonlinear elephant global mode. This theory not only accurately predicts the vortex shedding frequency but also the spatial structure of the downstream developing vortex street.*

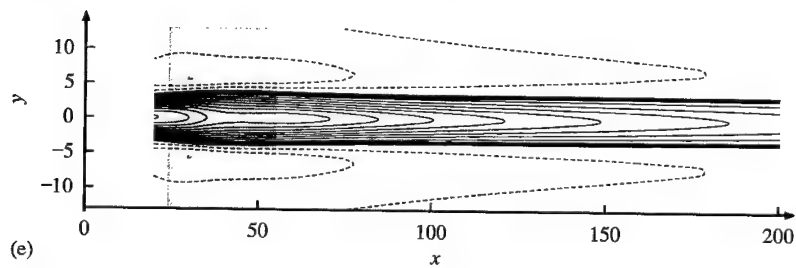
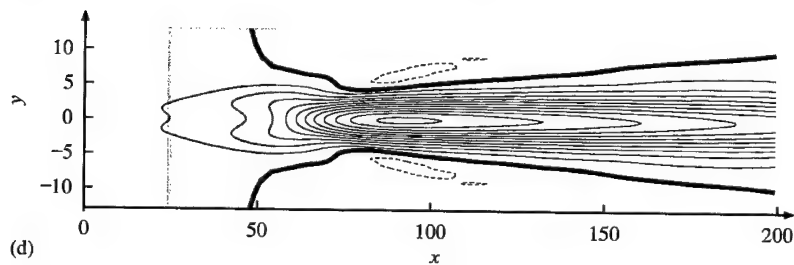
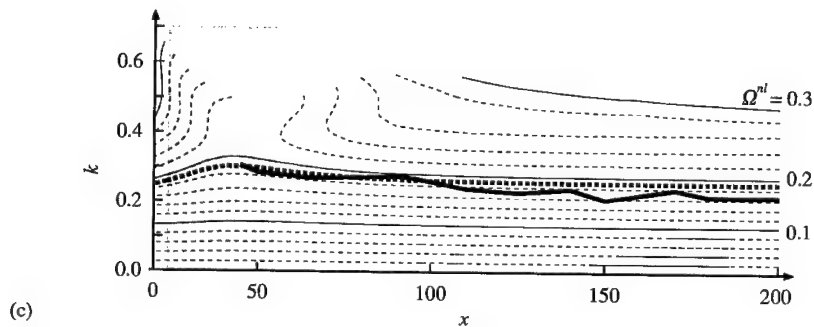
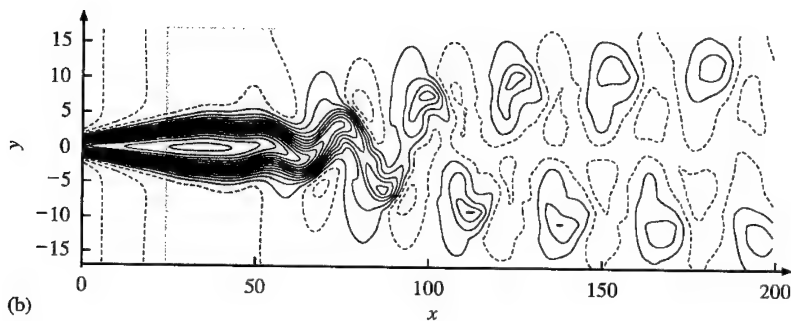
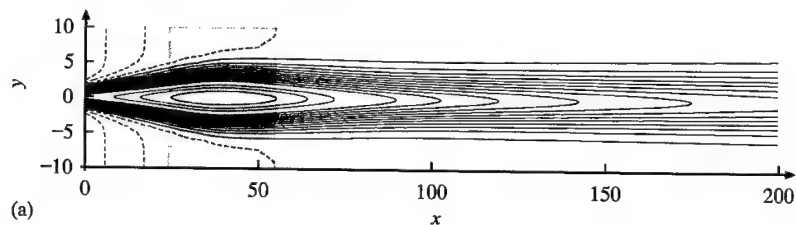
The mean-flow correction, which is absent in CGL models, is specific to real shear flows. Indeed, nonlinear quadratic interactions in the NS equations generate a time-independent mean-flow component as well as higher harmonics. In the fully developed vortex shedding régime, the total mean flow then results from the superposition of the basic flow [Figure 2(a)] and the mean-flow correction [Figure 2(d)]. According to Figure 2(d), the mean-flow correction tends to fill up the velocity deficit in the wake. It is instructive to compare the results of direct numerical simulations with those emerging from a temporal evolution problem pertaining to a parallel wake frozen at a prescribed  $X$  station and perturbed with a spatially periodic wave of wavenumber  $k^{nl}(X, \omega_0^{ca})$ . Via this procedure, a finite-amplitude wave-train is obtained for large time, the frequency of which is precisely  $\omega_0^{ca}$ . Local mean-flow corrections are thereby computed for each station  $X$ , which may be pieced together to generate a spatially evolving mean correction field as displayed in Figure 2(e). The agreement between direct numerical simulation [Figure 2(d)] and local predictions [Figure 2(e)] is less satisfactory than for the unsteady part of the flow field [Figure 2(c)]. Whereas in the limit of vanishing inhomogeneity, the local analysis predicts a mean-flow correction of almost constant cross-stream width, the width of the mean flow in the direct numerical simulation is seen to increase with downstream distance. The mean-flow correction field is generated in the central shear region by nonlinear interactions and slowly diffuses on a viscous scale into the outer cross-stream direction. This diffusion process takes place in time [Figure 2(e)] or along the stream [Figure 2(d)], and there is no obvious relationship between these two situations.

## 7. CONCLUSIONS

We are now in a position to answer the questions listed in the introductory section.

1. In a strictly linear approximation global instability in general requires an AU region of finite extent, whereas *nonlinear global instability takes place as soon as local absolute instability arises at some point in the flow*. When nonlinearities are present, the linear

resonance criterion (8) becomes irrelevant. It is the existence of a transition point from convective to absolute instability which is crucial in the establishment of a self-sustained nonlinear state.



Note that the *real* cylinder wake becomes absolutely unstable at  $Re \sim 25$ , whereas onset of vortex shedding occurs only for  $Re \sim 46$ . This discrepancy is presumably due to a violation of the assumption of slow spatial development in the neighborhood of the obstacle.

2. The complex frequency of a linear global mode [Figure 1(a)] is obtained at a saddle point  $X_s^l$  of  $\omega_0(X)$  analytically continued in the complex  $X$ -plane see (8). Due to this continuation procedure, no frequency generating location may be identified in physical space; note however, that the region of maximum absolute growth rate plays an essential part. In contrast, the global frequency of nonlinear global modes [Figure 1(b, c)] is selected at a specific location: either the saddle point  $X_s^{nl}$  of the nonlinear dispersion relation (10) or the upstream boundary  $X^{ca}$  of the AU region (11). These nonlinear resonance criteria are purely local in the sense that only the properties of the system at these stations are involved. In the case of wake flows, the vortex street is triggered by a front structure at  $X^{ca}$  which acts as a source and imposes its frequency to the entire flow.

3. The selection mechanisms pertaining to hat and elephant nonlinear global modes are markedly distinct. The hat frequency selection criterion (10) involves a saddle point of the nonlinear dispersion relation (9) in the bulk of the finite-amplitude region [Figure 1(b)]. Elephant modes [Figure 1(c)] are selected by a front located at the upstream boundary of the AU domain; finite amplitude wave-trains develop downstream of this location. Since the elephant frequency selection criterion (11) only involves the linear dispersion relation, this variety of *nonlinear global* mode is surprisingly governed by a *local linear* criterion.

Finite-amplitude vortex shedding in wakes generates a mean-flow correction comparable in magnitude to the basic flow. Nonlinearities thus completely modify the underlying basic flow which becomes unobservable unless one artificially kills the perturbations by imposing for example a symmetry condition.

The comparison between the results of direct numerical simulations and locally computed nonlinear wave-trains has demonstrated the validity of a *linear* and *nonlinear* analyses based on a scale separation assumption. The theory has led to the identification of two varieties of global modes: elephants and hats. The vortex street has been shown to be of elephant type with a front located at the convective-absolute instability transition point imposing its frequency to the entire flow. There remains to determine a real flow that sustains a global mode of hat type. Rayleigh-Bénard convection in the presence of a horizontally varying temperature difference or Taylor-Couette flow between rotating coaxial cylinders with a varying gap may be good candidates for such a situation since there is no basic advection.

#### REFERENCES

- BENDER, C. M. & ORSZAG, S. A. 1978 *Advanced Mathematical Methods for Scientists and Engineers*. New York: McGraw-Hill.

Figure 2. Intrinsic synchronization of spatially developing wake flow at  $Re = 100$ . Shaded regions indicate extent of AU domain. (a) Streamwise velocity isolines of unperturbed basic wake flow. (b) Snapshot of total streamwise velocity isolines in periodic vortex shedding régime. (a, b) Dashed lines represent the levels 0.95, 0.90, 0.85 above the outlet free-stream velocity; solid lines pertain to the levels 0.80, ..., 0.10. (c) Isofrequency contours of the nonlinear dispersion relation  $\Omega''(k, X)$  in the linearly unstable domain of the  $(X, k)$ -plane. Thin solid contours are separated by  $\delta\Omega = 0.1$ , thin dashed contours by  $\delta\Omega = 0.02$ . Predicted nonlinear spatial branch  $k^w(X, \omega_0^w)$  of global frequency  $\omega_0^w = 0.19$  is represented by thick dashed curve. Observed local wave number in (b) follows path indicated by thick solid line. (d) Mean streamwise velocity correction of vortex street sketched in (b). (e) Mean streamwise velocity correction of local nonlinear wave-trains of wavenumber  $k^w(X, \omega_0^w)$ . (d, e) Thick line separates regions of positive (0.05, 0.10, ... solid lines) and negative (-0.05, -0.10, ... dashed line) levels.

- BERS, A. 1983 Space-time evolution of plasma instabilities — absolute and convective. In *Handbook of Plasma Physics* (eds M. N. Rosenbluth & R. Z. Sagdeev), pp. 451–517, Amsterdam: North-Holland.
- BRIGGS, R. J. 1964 *Electron-Stream Interaction with Plasmas*. Cambridge, MA: MIT Press.
- CHOMAZ, J.-M., HUERRE, P. & REDEKOPP, L. G. 1991 A frequency selection criterion in spatially developing flows. *Studies in Applied Mathematics* **84**, 119–144.
- COUAIRO, A. & CHOMAZ, J.-M. 1997 Absolute and convective instabilities, front velocities and global modes in nonlinear systems. *Physica D* **108**, 236–276.
- COUAIRO, A. & CHOMAZ, J.-M. 1999a Primary and secondary nonlinear global instability. *Physica D* **132**, 428–456.
- COUAIRO, A. & CHOMAZ, J.-M. 1999b Fully nonlinear global modes in slowly varying flows. *Physics of Fluids* **11**, 3688–3703.
- CRIGHTON, D. & GASTER, M. 1976 Stability of slowly diverging jet flow. *Journal of Fluid Mechanics* **77**, 397–413.
- DEE, G. & LANGER, J. S. 1983 Propagating pattern selection. *Physical Review Letters* **50**, 383–386.
- DELBENDE, I. & CHOMAZ, J.-M. 1998 Nonlinear convective/absolute instabilities in parallel two-dimensional wakes. *Physics of Fluids* **10**, 2724–2736.
- GOUJON-DURAND, S., JENFFER, P. & WESFREID, J. E. 1994 Downstream evolution of the Bénard–von Kármán instability. *Physical Review E* **50**, 308–313.
- HAMMOND, D. & REDEKOPP, L. 1997 Global dynamics of symmetric and asymmetric wakes. *Journal of Fluid Mechanics* **331**, 231–260.
- HUERRE, P. 2000 Open shear flow instabilities. *Perspectives in Fluid Dynamics* (eds G. K. Batchelor, H. K. Moffatt & M. G. Worster), Cambridge: Cambridge University Press.
- HUERRE, P. & MONKEWITZ, P. A. 1990 Local and global instabilities in spatially developing flows. *Annual Review of Fluid Mechanics* **22**, 473–537.
- HUERRE, P. & ROSSI, M. 1998 Hydrodynamic instabilities in open flows. In *Hydrodynamics and Nonlinear Instabilities* (eds C. Godrèche & P. Manneville), pp. 81–294, Cambridge: Cambridge University Press.
- LE DIZÈS, S., HUERRE, P., CHOMAZ, J.-M. & MONKEWITZ, P. A. 1993 Nonlinear stability analysis of slowly-diverging flows: limitations of the weakly nonlinear approach. In *Bluff-Body Wakes, Dynamics and Instabilities* (eds H. Eckelmann, J. M. R. Graham, P. Huerre & P. A. Monkewitz), pp. 147–152, Berlin: Springer.
- MONKEWITZ, P. A., HUERRE, P. & CHOMAZ, J.-M. 1993 Global linear stability analysis of weakly non-parallel shear flows. *Journal of Fluid Mechanics* **251**, 1–20.
- PIER, B. 1999 Comportement non linéaire synchronisé dans les écoulements cisailés. Ph.D. Dissertation, École polytechnique, Palaiseau, France.
- PIER, B. & HUERRE, P. 1996 Fully nonlinear global modes in spatially developing media. *Physica D* **97**, 206–222.
- PIER, B. & HUERRE, P. 2000 Nonlinear self-sustained structures and fronts in wake flows. *Journal of Fluid Mechanics* (in press).
- PIER, B., HUERRE, P. & CHOMAZ, J.-M. 2001 Bifurcation to fully nonlinear synchronized structures in slowly varying media. *Physica D* **148**, 49–96.
- PIER, B., HUERRE, P., CHOMAZ, J.-M. & COUAIRO, A. 1998 Steep nonlinear global modes in spatially developing media. *Physics of Fluids* **10**, 2433–2435.
- PROVANSAL, M., MATHIS, C. & BOYER, L. 1987 Bénard–von Kármán instability: transient and forced regimes. *Journal of Fluid Mechanics* **182**, 1–22.
- SAINT-EXUPÉRY, A. DE 1946 *Le Petit Prince*. Paris: Gallimard.
- WILLIAMSON, C. H. K. 1996 Vortex dynamics in the cylinder wake. *Annual Review of Fluid Mechanics* **28**, 477–539.
- ZIELINSKA, B. J. A. & WESFREID, J. E. 1995 On the spatial structure of global modes in wake flow. *Physics of Fluids* **7**, 1418–1424.



## A COMPLEMENTARY NUMERICAL AND PHYSICAL INVESTIGATION OF VORTEX-INDUCED VIBRATION

H. M. BLACKBURN

*CSIRO Building Construction and Engineering, P.O. Box 56  
Highett, VIC 3190, Australia*

R. N. GOVARDHAN AND C. H. K. WILLIAMSON

*Mechanical and Aerospace Engineering  
Upson Hall, Cornell University, Ithaca, NY 14853, U.S.A.*

(Received 15 September 2000, and in final form 23 October 2000)

Results are presented from low Reynolds number experimental investigations of vortex-induced vibration and comparison is made with results from corresponding two- and three-dimensional direct numerical simulations. It is shown that three-dimensional simulations are required to reproduce the response envelope observed experimentally. Phase-averaged contours of span-wise vorticity demonstrate the presence of the 2P shedding mode on the lower response branch in both the experimental and three-dimensional simulation results.

© 2001 Academic Press

### 1. INTRODUCTION

A NUMBER OF FUNDAMENTAL STUDIES of the vortex-induced vibration of slender cylindrical structures in cross flow have been published over the last decade. Recent experiments [e.g., Khalak & Williamson (1999)] have extended the early works, such as that of Feng (1968), while numerical simulations have also started to make inroads at the lower end of the Reynolds number spectrum. Despite the quantity of experimental and numerical activity, there has been no published study in which it has been attempted to match parameters between the two domains. In this work, our aim is to increase understanding of the problem by comparing results from water-tunnel experiments with those from two- and three-dimensional direct numerical simulations, in which Reynolds numbers and mechanical dynamic parameters such as cylinder mass and damping ratios are the same for both the experiments and the simulations.

### 2. EXPERIMENTAL METHOD

Figure 1 shows a diagram of the experimental equipment. The set-up uses a cylinder that is cantilevered from an air-bearing sled through a bi-axial force transducer. A position transducer is attached to the sled, and a spring suspension system provides central restoring forces to the cylinder-sled assembly. The bearings are mounted above a water channel; the cylinder pierces the water surface and can translate cross-flow on its bearings. The free end of the cylinder had an end plate located close to the lower wall of the water channel. DPIV measurements of two components of the velocity field can be obtained using laser-sheet

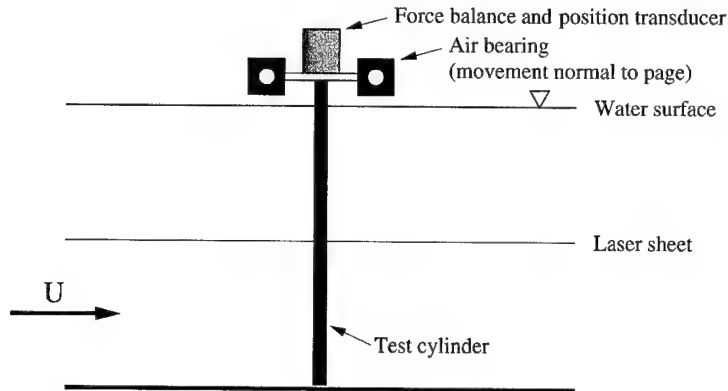


Figure 1. Diagram of experimental set-up in water tunnel working section.

lighting that is parallel to the water surface, and image capture can be conditioned on cylinder position. More detailed descriptions of the experimental apparatus may be found in Khalak & Williamson (1997) and Govardhan & Williamson (2000).

In running the experiments, the cylinder, spring rate and damping were kept constant, and the reduced velocity was varied by changing the flow speed, hence the Reynolds number varied with reduced velocity. The submerged depth of the cylinder had an aspect ratio (length/diameter) of  $L/D = 26.7:1$ . The cylinder mass ratio  $m^* = 4m/\rho\pi D^2 = 50.8$ , where  $m$  is the sprung mass per unit length of submerged cylinder depth, and  $\rho$  is the density of water. The damping ratio, derived from the free-vibration decay rate in air,  $\zeta = 0.0024$ , giving a mass-damping parameter  $m^*\zeta = 0.122$  (cf. Feng 1968, where  $m^*\zeta \approx 0.25$ ). A reference Reynolds number is  $Re = UD/\nu = 556$  at a reduced velocity  $V_r = UT_n/D = 5.00$ , where  $U$  is the average free-stream flow speed,  $T_n$  is the free-vibration natural frequency in air and  $\nu$  is the kinematic viscosity of water.

Although good response amplitude data could be obtained, difficulty was experienced in obtaining reliable force and DPIV measurements at the Reynolds numbers used in these experiments. For purposes of comparison with the three-dimensional simulation results, we have included force and vorticity data obtained at somewhat higher Reynolds numbers ( $Re \approx 1250$  at peak response amplitude) and mass damping ( $m^*\zeta = 0.251$ , similar to that used by Feng), as described in more detail in Govardhan & William (2000, 2001).

### 3. SIMULATION METHOD

The simulation method and its numerical implementation using a spectral element–Fourier spatial discretisation has been previously documented in Blackburn & Karniadakis (1993) and Blackburn & Henderson (1996, 1999). The incompressible Navier–Stokes equations are solved in an accelerating reference frame, and this simulation is coupled to that for a set of first-order ODEs that describe the motion of the cylinder in response to the forces exerted on it by the fluid. The reference frame acceleration, and velocity boundary conditions on the outer edge of the flow domain, are set according to the values obtained by simulating the response of the cylinder. This method allows simulation of the rigid-body response of a freely oscillating cylinder without the overheads associated with distortion of the mesh to accommodate motion of the cylinder within the domain.

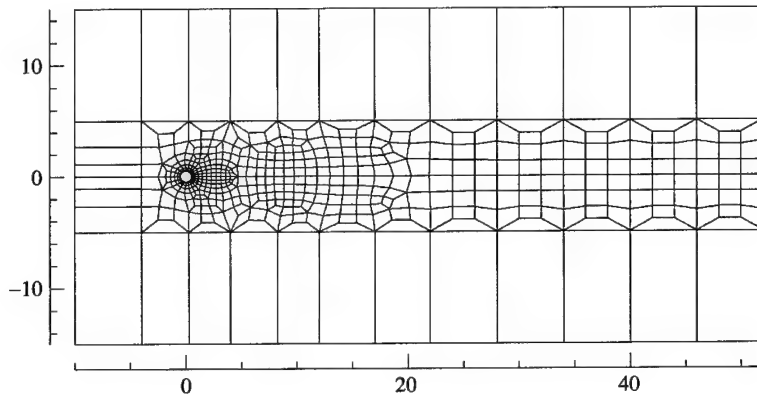


Figure 2. Computational mesh, showing element boundaries; dimensions are based on cylinder diameter.

The computational mesh is shown in Figure 2. For three-dimensional simulations, Fourier expansions are used in the cylinder-axis direction; the two-dimensional projection of the three-dimensional mesh is identical to that used for the two-dimensional simulations. The mesh shown has 502 elements, and 10th-order Gauss-Lobatto-Legendre-based two-dimensional Lagrange shape functions were used for the in-plane spatial discretization. This was found to be adequate for 4-figure convergence of integral measures of the two-dimensional simulation results [see the similar and related tests presented in Blackburn & Henderson (1999)]. The dynamic equations are integrated in time using a second-order operator-splitting scheme.

For all the results presented here, the axial extent of the three-dimensional domain was  $3.28D$ , with 24 planes of data. While the axial extent and resolution are both lower than desirable, the size was limited by computer memory and simulation time constraints. The three-dimensional simulations required approximately 2 GB of memory and 12 CPU-hours per motion cycle when run on an NEC SX-4 computer (peak speed approximately 2 GFLOPS/processor). Typical runs used 4–6 CPUs.

Reynolds numbers and dimensionless dynamic parameters in the simulations were chosen to match those in the experimental set-up, as described in Section 2. It should be noted that, even with this degree of matching, cylinder-end boundary conditions differ between the experiments and the simulations, since with the adoption of Fourier expansions the flow is assumed periodic in the axial direction for the simulations.

#### 4. RESPONSE AMPLITUDE RESULTS

A compilation of experimental and simulated cross-flow response amplitudes is presented in Figure 3. The average peak dimensionless amplitude  $A^* = \bar{y}_{\max}/D$ , while the reduced velocity  $V_r = UT_n/D$  is normalized by an appropriate representative Strouhal number for a fixed cylinder  $St = f_v D/U$  to form  $StV_r$ . This normalization of reduced velocities has been carried out because of the disparity of two- and three-dimensional Strouhal numbers at these Reynolds numbers: for the two-dimensional results,  $St = 0.225$  (Blackburn & Henderson 1999), while for both the simulated three-dimensional and experimental results,  $St = 0.205$ , where both values are appropriate for a Reynolds number  $Re \sim 500$  (Norberg 1994).

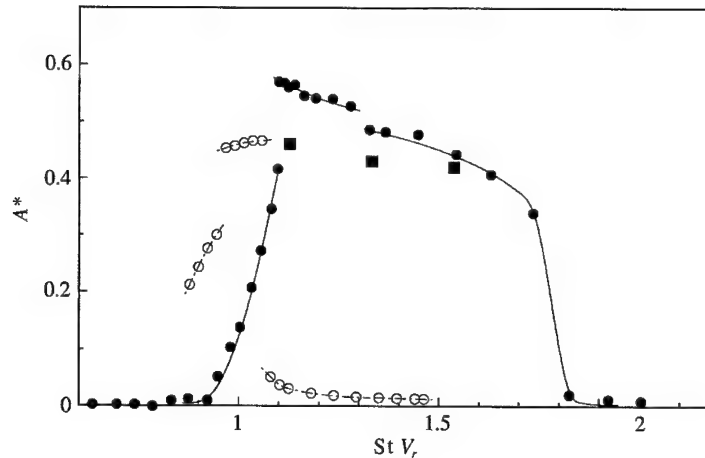


Figure 3. Dimensionless average peak response amplitude  $A^*$  as a function of  $St V_r$ : ●, experimental results; ■, three-dimensional simulations; ○, two-dimensional simulations.

#### 4.1. EXPERIMENTAL

Turning first to the experimental results, the response envelope exhibits three distinct branches, similar to results previously presented for higher Reynolds numbers and lower mass-damping values by Khalak & Williamson (1997, 1999). The two highest amplitude branches, the “upper” and “lower” branches here are less separated in amplitude than for the previous results, which is thought likely to be a result both of Reynolds number and mass-damping effects.

#### 4.2. THREE-DIMENSIONAL SIMULATIONS

The three-dimensional simulations were carried out for reduced velocities chosen to place them near the highest observed amplitudes on the upper and lower response branches ( $St V_r = 1.13, 1.33$  and  $1.58$ ). The response amplitudes, while similar to the experimental results, are somewhat smaller, which is thought likely to be a consequence of the restricted axial periodic length of the computational domain ( $3.28D$ ), and, less significantly, to the differences in end conditions. The difference in amplitudes for the three values of  $St V_r$  does, however, mimic the experimentally observed behaviour, with the highest amplitude occurring at the lowest reduced velocity.

#### 4.3. TWO-DIMENSIONAL SIMULATIONS

Given the high demand on computer resources made by the three-dimensional simulations, it is obviously of interest to compare the results for the two-dimensional simulations with the experiments and the three-dimensional simulations. The two-dimensional results were obtained using small decrements of  $U$  between each run. It is apparent from an examination of Figure 3 that, although the peak response observed for the two-dimensional simulations is similar to the higher of the three-dimensional results, the computed results are substantially different from the experimental measurements in terms of the  $St V_r$  location and extent of the peak response branch. It is interesting to note that the general form and position of the response amplitude diagram is similar to that observed for two-dimensional simulations



at  $Re = 250$ ,  $m^*\zeta = 0.127$  — see Figure 2 in Blackburn & Henderson (1996), allowing for variation in  $T_n$  as opposed to  $U$ , which reverses orientation on the abscissa.

Of the three response branches observed in the two-dimensional results, only the lowest amplitude branch was associated with conventional periodic Kármán-mode vortex shedding (with period close to that for a fixed cylinder at corresponding Reynolds number). On the high-response branch, the time trace of response amplitude was very nearly sinusoidal for all simulations, with a frequency near the structural natural frequency; however, only for the very highest amplitude did the lift-response phase plane plot approach a closed limit cycle with periodic vortex shedding. In this case, however, the wake, although periodic, did not exhibit Kármán-mode shedding — see related unconventional but periodic wake modes presented in Blackburn & Henderson (1999). Another significant feature of results on this branch is that they all possessed a time-average wake that was asymmetric about the cylinder centreline, with a time-mean coefficient of lift. On the low  $St_V$  branch with moderate response amplitudes, peak values of both the cross-flow response and force varied significantly over long time scales.

## 5. FORCES AND CROSS-FLOW RESPONSE

In this section, we present an analysis of force and displacement time-series from the three-dimensional simulation at  $St_V = 1.33$ , obtained after sufficient simulation time had elapsed for these to approach a statistically steady state. Results collected over 20 motion cycles are presented — this simulation was also used to collect the phase-averaged results to be described in Section 6.

Figure 4 shows time-series of coefficients of drag and lift, and also of dimensionless cross-flow response amplitude  $\alpha = y(t)/D$ , presented as functions of normalized time  $t/T_n$ .

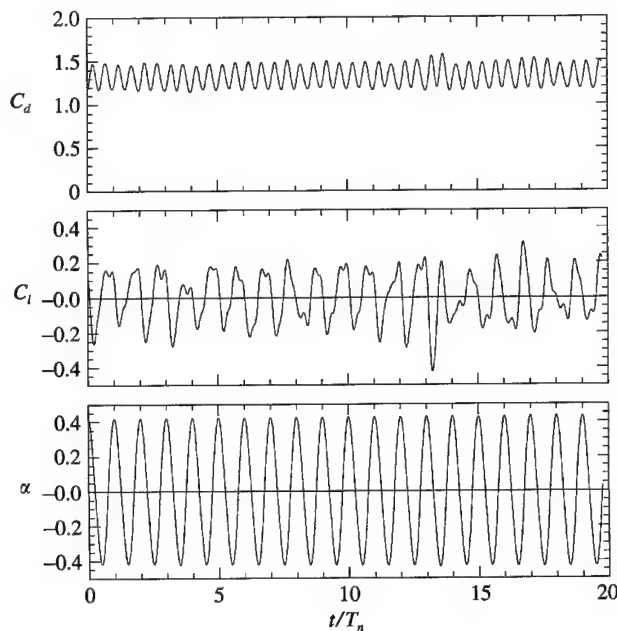


Figure 4. Time-series of coefficients of drag and lift ( $C_d$ ,  $C_l$ ), and dimensionless response amplitude  $\alpha$  for the three-dimensional simulation at  $St_V = 1.33$ .

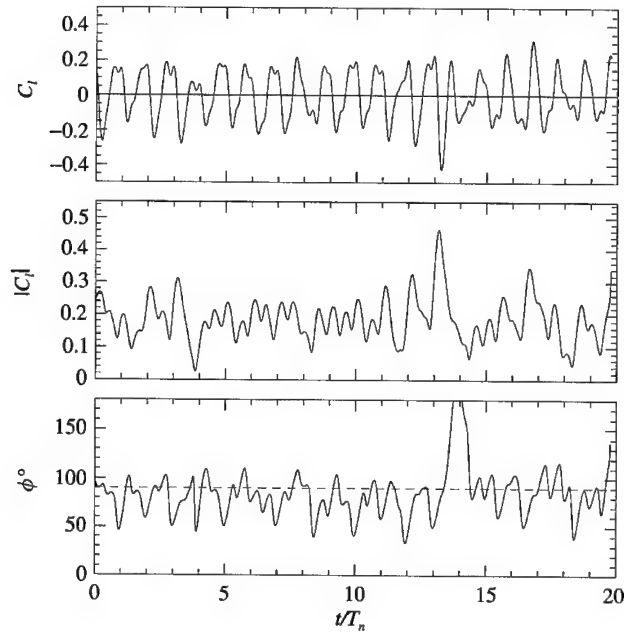


Figure 5. Time-series of lift coefficient, its instantaneous magnitude and phase angle in relation to cross-flow displacement for the three-dimensional simulations.

The time-mean coefficient of drag,  $\bar{C}_d = 1.32$ , and the standard deviation of coefficient of lift  $C_l' = 0.14$ . Note the typical “double-peaked” nature of the  $C_l$  waveform. Despite the quite large variability in the lift force, the cross-flow response stayed nearly sinusoidal in form, as the lift force magnitude is relatively small in comparison to the mechanical restoring force for the spring-mounted cylinder.

Since simulated damping forces are present, there must on average be work done on the cylinder by the lift force; for this to be true the time-average phase angle between the lift force and cylinder displacement must lie in the range  $0$ – $180^\circ$ . In Figure 5, we present time series of the coefficient of lift, together with its instantaneous magnitude and phase angle in relation to cross-flow displacement, computed using the Hilbert transform (Schumm *et al.* 1994; Blackburn & Melbourne 1997). Apart from a single large excursion near  $t/T_n = 14$ , the phase angle  $\phi$  remained near  $90^\circ$ , with average value  $\bar{\phi} = 84^\circ$ .

The average work done on the cylinder by lift forces can also be assessed by examining the area enclosed by a phase-plane plot of  $C_l$  versus  $\alpha$  (Blackburn & Henderson 1999). In Figure 6(a) we show the phase-plane plot for the data presented in Figure 4. On the  $C_l$  versus  $\alpha$  trajectory, the sense of traverse is clockwise, as it must be for a transfer of energy from the fluid to the cylinder. The two largest excursions from the average trajectory correspond to the largest positive and negative peaks in the  $C_l$  time-series, while the wave-shaped form of the average trajectory is related to the double-peaked characteristic of the  $C_l$  time-series. In Figure 6(b) we present the phase-plane plot from the related set of experiments described in Govardhan & Williamson (2000): this set of data is for  $StV_r = 1.27$ , and it can be seen to have a similar nature (and peak amplitude) to that for the current simulations, although the form is more stable over time — however, since the mass-damping value is higher than for the present work, the enclosed area in Figure 6(b) is greater than that in Figure 6(a).

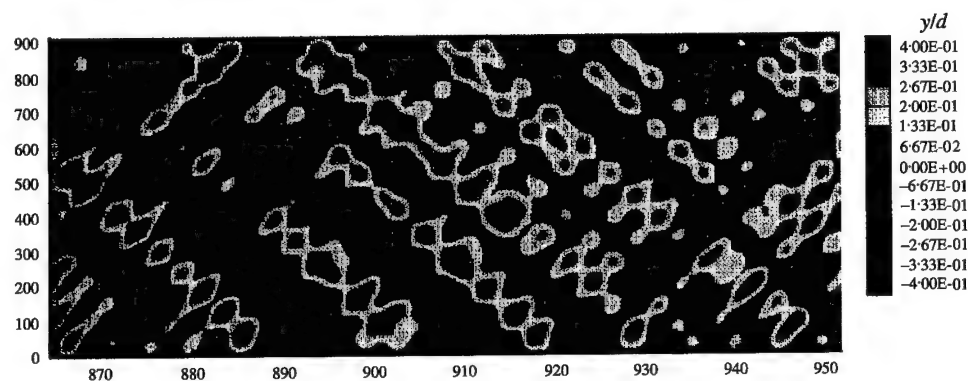


Figure 7. Time-history of the distribution of crossflow displacement along the span. A mixed standing-traveling wave pattern prevails, unlike the linear shear case.

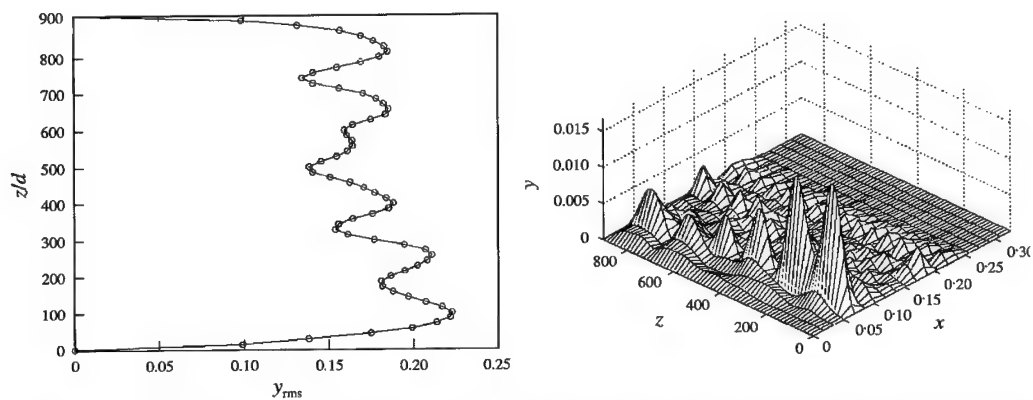


Figure 8. (a) Crossflow displacement (r.m.s. values) along the span (normalized with the cylinder diameter). (b) Corresponding spectrum showing the (nondimensional) frequency response (range: 0–0.3) along the span. The frequency is normalized with the maximum inflow velocity (x-axis: frequency nondimensionalized with maximum velocity; y-axis: power spectral density; z-axis: span of the cylinder).

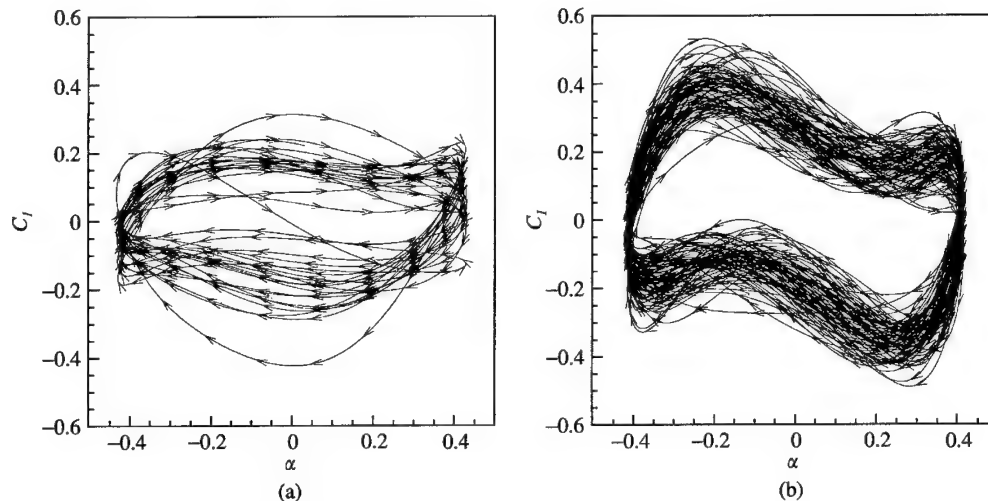


Figure 6. Phase-plane plot of  $C_l$  versus  $\alpha$ ; the area enclosed by the average trajectory is representative of the average work transfer per motion cycle between the fluid and the cylinder. (a) Data from three-dimensional simulation at  $StV_r = 1.33$ ; (b) data from a set of experiments at higher Reynolds number but  $StV_r = 1.27$  with a similar response amplitude (Govardhan & Williamson 2000).

## 6. VORTEX SHEDDING MODES

Now we turn to an examination of the topology of the wake for the three-dimensional simulation at  $StV_r = 1.33$ . In Figure 7 we show a plot of instantaneous isosurfaces of pressure and streamwise vorticity. Note that, especially in the near-wake, there is intense turbulent activity, which is particularly evident in the vorticity isosurfaces — isosurfaces of spanwise directed vorticity, or of vorticity magnitude, show similar disorganization.

In order to find the coherent structure of the near-wake, we have used a phase-averaging approach related to that adopted by Cantwell & Coles (1983). Estimates of the ensemble-average velocity field are computed from averages taken at four phases of the motion cycle — since the motion is very nearly periodic it is appropriate to use the cross-flow motion amplitude as a conditioning signal. From the simulations used to produce the data shown in Figure 4 we have collected 20 velocity field averages at each of the four phases:  $t/T_n = 0.0$  (maximum negative displacement),  $t/T_n = 0.25$  (maximum positive velocity), etc. For each of these four average fields we compute the vorticity, then its spanwise average.

Contours of span- and phase-averaged spanwise vorticity for each of the four phases are presented in Figure 8. For purposes of comparison, we have also shown contours of phase-averaged spanwise vorticity computed from the DPIV data of Govardhan & Williamson (2000), measured at  $StV_r = 1.27$  — the overall similarity of these two sets of results is immediately apparent despite some differences in detail. It is evident that in each half motion cycle, the shear layer from one side of the cylinder rolls up into two distinct concentrations of vorticity as it leaves the near-wake region. As they evolve downstream, the four regions of concentrated vorticity form into pairs of counter-rotating vortex couples, one on each side of the wake.

## 7. DISCUSSION AND CONCLUSIONS

This work represents the first direct comparison between numerical and physical experiments in vortex-induced vibration, in which both fluid and mechanical dynamic parameters

have been matched. There have been some operational problems on both sides, related to the difficulties in obtaining high Reynolds number values in the simulations, on the one hand, and low values in experiments, on the other; however, the results are encouraging.

A significant outcome is that it appears that, at least in the absence of a turbulence model, two-dimensional simulations are inadequate for the task of predicting the full nature both of the response envelope and of vortex shedding mechanics, even at these low Reynolds numbers. This finding is likely to hold both for free and forced cylinder oscillations. Whether the difference between two- and three-dimensional dynamics is caused by effects in the very near-wake produced by turbulence in the vortex formation region, or perhaps by feedback from changed conditions further downstream as the streamwise roller structures evident in Figure 7 enhance the transfer of free-stream momentum into the centre of the wake, is a matter open for further investigation.

Another significant outcome is that, for the first time in a set of simulation results, we have clear evidence (Figure 8) of the 2P shedding mode first reported in Williamson & Roshko (1988). The double-peaked form of the lift time-series exhibited in Figures 4 and 5 and the characteristic shape of the average  $C_l$  versus  $\alpha$  trajectory shown in Figure 6 are both likely to be related to the shedding of four concentrated regions of vorticity per motion cycle, although the relationship remains to be examined in detail. On the evidence of the smaller excursions from the average trajectory shown in Figure 6(b), when compared to those in Figure 6(a), it appears that the 2P shedding mode may become better established as the Reynolds number increases.

#### REFERENCES

- BLACKBURN, H. M. & HENDERSON, R. D. 1996 Lock-in behaviour in simulated vortex-induced vibration. *Experimental Thermal and Fluid Science* **12**, 184–189.
- BLACKBURN, H. M. & HENDERSON, R. D. 1999 A study of two-dimensional flow past an oscillating cylinder. *Journal of Fluid Mechanics* **385**, 255–286.
- BLACKBURN, H. M. & KARNIADAKIS, G. E. 1993 Two- and three-dimensional simulations of vortex-induced vibration of a circular cylinder. In *Proceedings of the Third (1993) International Offshore and Polar Engineering Conference, Singapore*, Vol. III, pp. 715–720, Golden, CA, U.S.A.: ISOPE.
- BLACKBURN, H. M. & MELBOURNE, W. H. 1997 Sectional lift forces for an oscillating cylinder in smooth and turbulent flows. *Journal of Fluids and Structures* **11**, 413–431.
- CANTWELL, B. J. & COLES, D. 1983 An experimental study of entrainment and transport in the turbulent near wake of a circular cylinder. *Journal of Fluid Mechanics* **136**, 321–374.
- FENG, C. C. 1968 The measurement of vortex-induced effects in flow past stationary and oscillating circular and D-section cylinders. Master's Thesis, University of British Columbia, Vancouver, BC, Canada.
- GOVARDHAN, R. N. & WILLIAMSON, C. H. K. 2001 Mean and fluctuating velocity fields in the wake of a freely vibrating cylinder. *Journal of Fluids and Structures* **15**, xxx–xxx.
- GOVARDHAN, R. & WILLIAMSON, C. H. K. 2000 Modes of vortex formation and frequency response of a freely vibrating cylinder. *Journal of Fluid Mechanics* **420**, 85–130.
- KHALAK, A. & WILLIAMSON, C. H. K. 1997 Fluid forces and dynamics of a hydroelastic structure with very low mass and damping. *Journal of Fluids and Structures* **11**, 973–982.
- KHALAK, A. & WILLIAMSON, C. H. K. 1999 Motions, forces and mode transitions in vortex-induced vibrations at low mass-damping. *Journal of Fluids and Structures* **13**, 813–851.
- NORBERG, C. 1994 An experimental investigation of the flow around a circular cylinder: influence of aspect ratio. *Journal of Fluid Mechanics* **258**, 287–316.
- SCHUMM, M., BERGER, E. & MONKEWITZ, P. A. 1994 Self-excited oscillations in the wake of two-dimensional bluff bodies and their control. *Journal of Fluid Mechanics* **271**, 17–53.
- WILLIAMSON, C. H. K. & ROSHKO, A. 1988 Vortex formation in the wake of an oscillating cylinder. *Journal of Fluids and Structures* **2**, 355–381.



## MEAN AND FLUCTUATING VELOCITY FIELDS IN THE WAKE OF A FREELY-VIBRATING CYLINDER

R. GOVARDHAN AND C. H. K. WILLIAMSON

*Sibley School of Mechanical and Aerospace Engineering, Upson Hall  
Cornell University, Ithaca, NY 14853–7501, U.S.A.*

(Received 7 September 2000, and in final form 7 November 2000)

In the present work, we study the wake velocity field of an elastically mounted rigid cylinder oscillating transverse to a fluid flow, using DPIV measurements. It is shown that there are large qualitative changes in these velocity fields, depending on the mode of cylinder oscillation. In particular, the characteristic “recirculation bubble”, usually seen in the mean velocity field behind the nonoscillating cylinder, is found to be present in the case of the ‘2S’ wake formation mode, yet is completely absent for the ‘2P’ mode. For the ‘2P’ mode, we find instead the appearance of a pair of counter-rotating vortices of opposite sign to what is expected, causing a downstream-oriented jet-type flow close to the cylinder, which in turn results in a ‘double-wake’ type velocity profile. Measurements of both the total Reynolds stresses, and the periodic stresses evaluated using phase-averaged velocity data, show that more than 90% of the total stresses are due to the repeatable large-scale coherent structures in the wake, when the body is vibrating. Periodic stresses make up only about 60% of the total stresses, in the case of the stationary body. Interestingly, for the fixed body, the periodic stresses remain relatively unchanged between our experiments ( $Re = 3900$ ) and those of Cantwell & Coles, at  $Re = 140\,000$ , although the total stresses are significantly increased at the larger  $Re$ . Our experimental evaluation of Reynolds stress is stimulated by the need for such data in developing turbulence modelling of these flows, as well as to enable detailed comparison with direct numerical simulations.

© 2001 Academic Press

### 1. INTRODUCTION

THE PROBLEM OF VORTEX-INDUCED VIBRATION OF A CYLINDER, in particular the case where a rigid circular cylinder is elastically mounted and constrained to oscillate transversely to a free stream, has been well-studied in the literature, as may be seen from the comprehensive reviews of Sarpkaya (1979), Bearman (1984) and Parkinson (1989). However, apart from the early work of Griffin (1971) where selected wake velocity profiles were measured at low  $Re \approx 200$ , from forced transverse oscillations of the cylinder, there have been no detailed investigations of the mean and fluctuating wake velocity fields for such a transversely oscillating cylinder. It should be mentioned here that the motivation for the present study of the wake velocity field, over a range of Reynolds numbers,  $Re = 3000$ – $4000$ , comes from Stansby & Apsley (2000) and from Peter Stansby, Julio Meneghini and Hugh Blackburn (private communications), who are using turbulence modelling to predict the behaviour of an elastically mounted cylinder at high  $Re$ , and for which detailed experimental measurements of the velocity field are useful to validate the modelling procedure.

The amplitude response ( $A^* = A/D = \text{amplitude/diameter}$ ) of such an elastically mounted cylinder shows two distinctly different types of behaviours, depending on whether one has a high or low combined mass-damping parameter ( $m^*\zeta$ ), as shown in Khalak & Williamson (1999) and Govardhan & Williamson (2000). [The mass ratio,  $m^* = (\text{mass of$

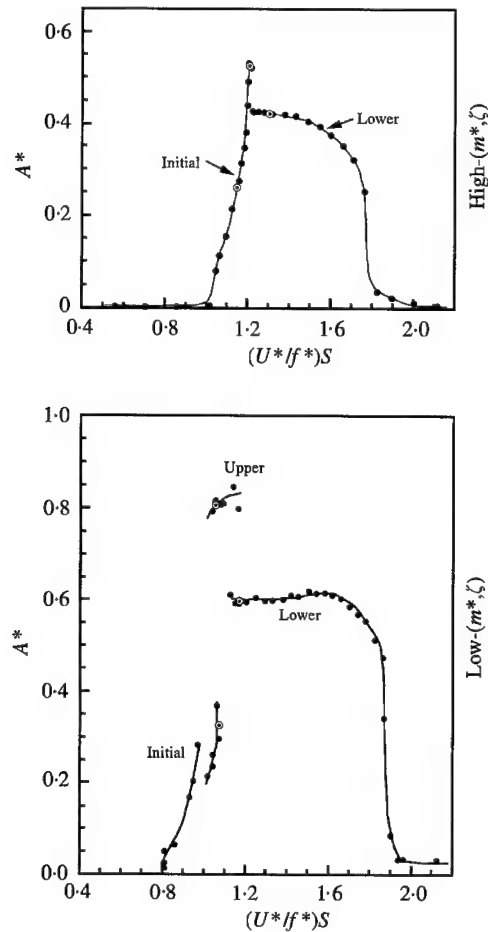


Figure 1. Amplitude response ( $A^* = A/D$ ) of the elastically mounted cylinder as a function of flow speed. In the classical high- $(m^*\zeta)$  case, only 2 response branches ('Initial' & 'Lower') are seen, whereas in the low- $(m^*\zeta)$  case, a further higher amplitude 'Upper' branch of response is also observed. The flow speed parameter  $(U^*/f^*)S = (f_{vo}/f)$ , where  $f_{vo}$  is the stationary body shedding frequency, and  $f$  is the actual cylinder oscillation frequency. Mass-damping values for the two response plots shown are  $(m^* + C_A)\zeta = 0.251$  (High) and  $(m^* + C_A)\zeta = 0.013$  (Low), while the corresponding mass ratios are  $m^* = 320$  and  $m^* = 8.63$ , respectively. ●, Present response data; ○, location where the wake velocity field is measured.

oscillating structure)/(displaced mass of fluid); and the damping ratio  $\zeta$  = structural damping/critical damping.] In the classical high- $(m^*\zeta)$  case, an 'Initial' and 'Lower' amplitude branch are separated by a discontinuous mode transition. However, in the case of low- $(m^*\zeta)$ , a further higher amplitude 'Upper' branch of response appears, and there exist three response branches, as shown in Figure 1. There are therefore two mode transitions in this case. The existence of, not one, but two mode transitions at low- $(m^*\zeta)$ , and their relationship with the forces and wake vortex dynamics, is studied in detail by simultaneous force, displacement and vorticity measurements for a freely vibrating cylinder in Govardhan & Williamson (2000). The present study of the wake velocity fields is related to work reported there.

Vorticity contours corresponding to the different response branches at low- $(m^*\zeta)$  shown in Figure 2, indicate that the Initial branch is associated with the 2S wake mode, while both

the Upper and Lower branches correspond to the 2P-mode; '2S' indicating 2 Single vortices formed per cycle, and '2P' meaning 2 Pairs of vortices formed per cycle, as defined by Williamson & Roshko (1988) based on their forced oscillation experiments. As may be seen from Figure 2, the strengths of the two vortices of each vortex pair are quite unequal in the Upper branch, but are roughly equal in the Lower branch. In the case of forced vibration, the 2S and 2P modes have also been shown using PIV by Carberry *et al.* (2001) for the forced transverse vibration of a circular cylinder, and these modes are also observed from forced oscillations of a tapered cylinder by Techet *et al.* (1998). At high values of the mass ratio, flow visualization of the wake of a freely vibrating wire also indicated a 2S and 2P mode, as shown by Brika & Laneville (1993).

In the present work, we study the mean and fluctuating velocity fields in the wake of a freely oscillating circular cylinder, at  $Re = 3000$ – $4000$ , corresponding to each of the three response branches at low- $(m^*\zeta)$ , namely the Initial, Upper and Lower branches. For comparison, a stationary cylinder case at approximately similar Reynolds numbers ( $Re = 3900$ ) is also studied.

## 2. EXPERIMENTAL DETAILS

The present experiments were conducted using a hydroelastic facility, which is described in Khalak & Williamson (1999), in conjunction with the Cornell-ONR Water Channel. The hydroelastic facility comprises a carriage mounted on air-bearings situated above the channel test section, which allow a vertical cylinder in the fluid to move transverse to the free-stream. The turbulence level in the test section of the Water Channel was less than 0.9%, in the  $0.381\text{ m} \times 0.508\text{ m}$  cross section, over the range of free-stream velocities  $U$  ( $0.04$ – $0.32\text{ m s}^{-1}$ ) used in this study. The test cylinder had a diameter of  $0.0381\text{ m}$ , and a length-diameter ratio of 10.

For the purpose of employing DPIV, the flow was seeded with  $14\text{ }\mu\text{m}$  silver-coated glass spheres, which were illuminated by a sheet of laser light from a 5 W continuous Argon ion laser. Images of the particles were captured using a high-resolution CCD Kodak Megaplug (1008  $\times$  1018 pixels) camera. Pairs of particle images were analysed using cross-correlation of sub-images, our implementation of which is described in more detail in Govardhan & Williamson (2000), and resulted in a set of 3600 vectors ( $60 \times 60$ ) for a typical velocity field. Each of the mean and fluctuating velocity fields shown in the paper have been obtained from about 300 such DPIV velocity fields.

The origin of the co-ordinate system is fixed at the centre of the cylinder, at zero flow speed. The  $x$ -axis is downstream, the  $y$ -axis is perpendicular to the flow direction and to the cylinder axis (defined as transverse), and the  $z$ -axis lies along the axis of the cylinder. The velocity components along the  $\{x, y, z\}$  axes are denoted as  $\{u, v, w\}$ , respectively, and the freestream velocity is denoted as  $U$ . The Reynolds number, normalized velocity ( $U^* = U/f_N D$ ), and oscillation amplitude ( $A^* = A/D$ ) corresponding to each of the three cylinder response modes studied are: Initial ( $Re \approx 3000$ ,  $U^* = 5.18$ ,  $A^* = 0.33$ ); Upper ( $Re \approx 3100$ ,  $U^* = 5.33$ ,  $A^* = 0.81$ ); Lower ( $Re \approx 3700$ ,  $U^* = 6.40$ ,  $A^* = 0.60$ ).

## 3. MEAN VELOCITY FIELDS

Although the mean velocity field in the wake of a stationary cylinder has been extensively studied, relatively little is known about the velocity field in the wake of a transversely oscillating cylinder. The only detailed investigation of the velocity field (in the form of a set of velocity profiles) to our knowledge, was conducted by Griffin (1971), for the forced



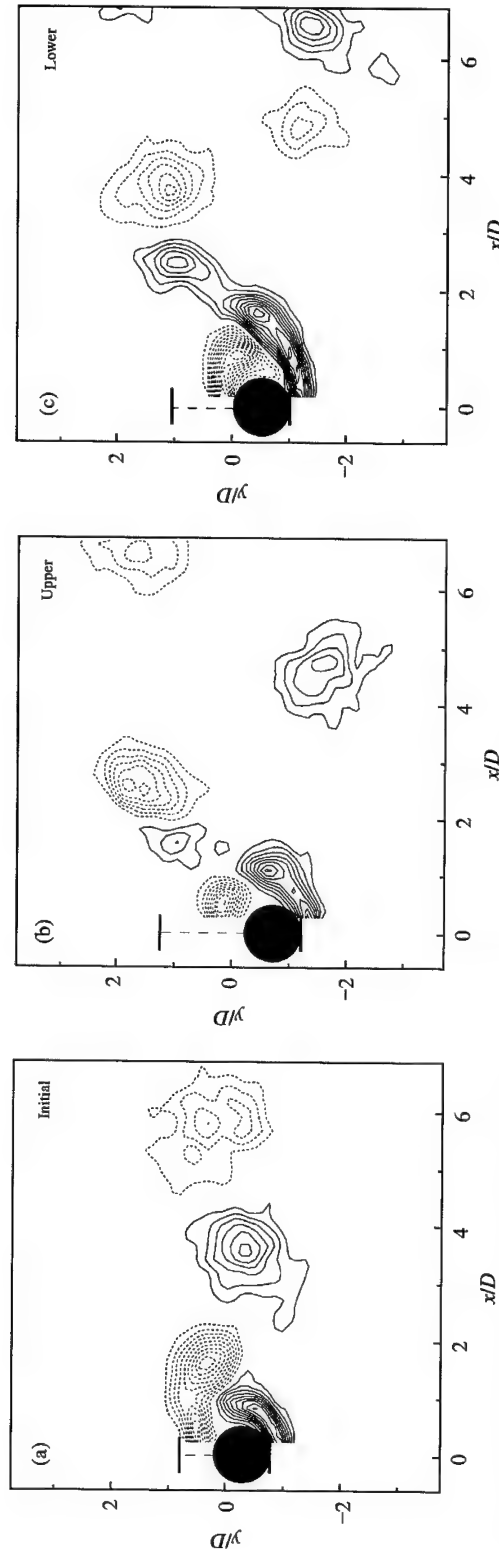


Figure 2. Vortex formation modes in the different response branches. (a) Initial branch - 2S; (b) Upper branch - 2P; (c) Lower branch - 2P. In the Upper branch case, there are two vortex pairs formed per cycle, although the second vortex of each pair is much weaker than the first vortex, and decays rapidly. The Initial, Upper, and Lower branch cases shown, in this and subsequent figures, correspond with data points marked as  $\odot$  in the low- $(m^*\zeta)$  amplitude response plot in Figure 1. Vorticity contours levels shown are separated by  $\Delta\omega D/U = 0.4$ . Solid contour lines denote anticlockwise vorticity and dashed lines are for clockwise vorticity. (a)  $Re \approx 3000$ ,  $U^* = U/f_N D = 5.18$ ,  $A^* = 0.33$ ; (b)  $Re \approx 3100$ ,  $U^* = 5.39$ ,  $A^* = 0.81$ ; (c)  $Re \approx 3700$ ,  $U^* = 6.40$ ,  $A^* = 0.60$ .

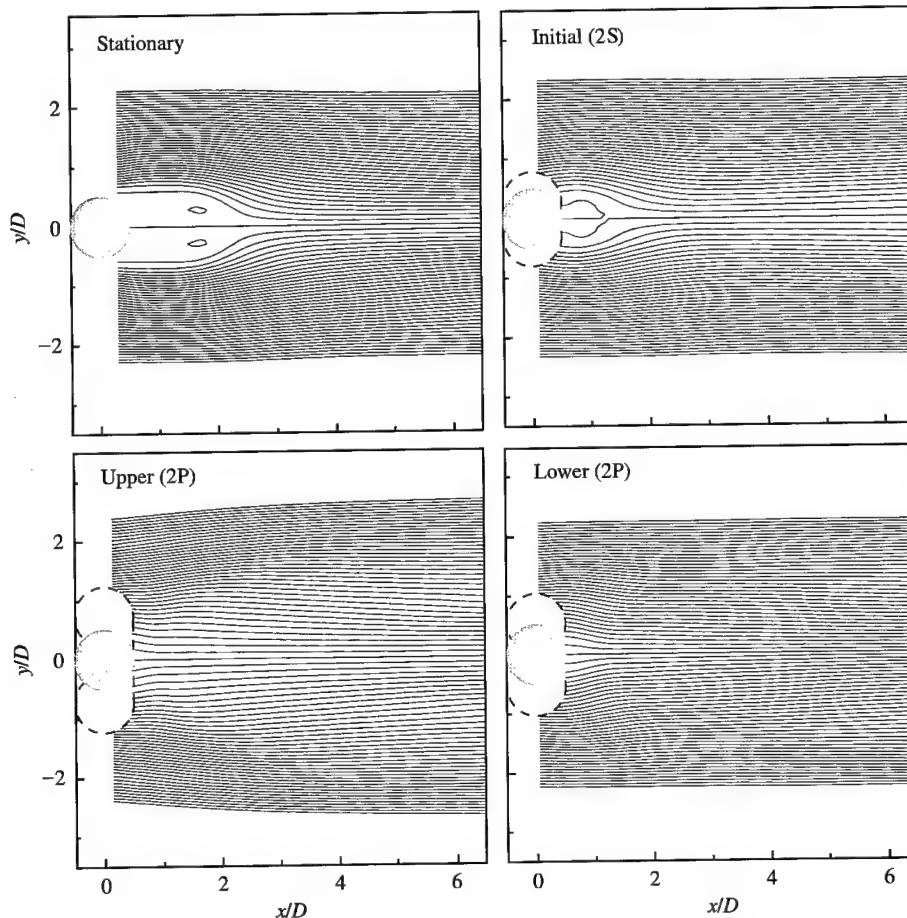


Figure 3. Streamlines for the mean velocity field indicating the disappearance of the "recirculation bubble" in the Upper and Lower branches which correspond to the 2P-mode.  $Re = 3900$  for the stationary cylinder case shown here and in later figures.

vibration of a cylinder at low  $Re \approx 200$ . He found that the formation length, defined as the location along the wake centreline where velocity fluctuations reach a maximum, reduced to half the value found for a stationary cylinder. It is expected that a similar reduction in size of the mean "recirculation bubble" will ensue when a body vibrates. At higher  $Re$  as in the present study ( $Re = 3000-4000$ ), one might expect large deviations in the mean velocity field for the 2P-mode as compared with the wake of the 2S-mode, where the vortices are arranged as in a Kármán vortex street.

The streamlines for the mean velocity field corresponding to the Initial branch (2S-mode) in Figure 3, show the presence of a "recirculation bubble", as in the stationary cylinder case. The effect of body vibration, for the 2S-mode, is to markedly shorten the bubble, which is consistent with the reduced "formation length" for an oscillating body found by Griffin (1971). Interestingly, this "recirculation bubble" disappears for the Upper and Lower response branches that are associated with the 2P-mode, as may be seen in Figure 3.

The mean vorticity field, shown in Figure 4, for the Lower branch (2P-mode) shows the presence of a pair of counter-rotating vortices of opposite sign to what one might expect in a wake, in contrast to the Initial branch (2S-mode) case. The jet flow induced by this vortex

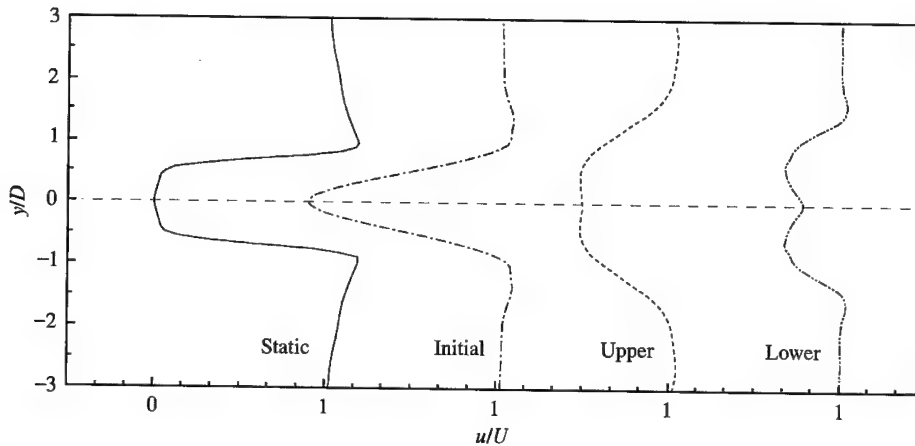


Figure 5. Streamwise velocity profiles at  $x/D = 1.25$ . In the Lower branch (2P-mode), the velocity profile takes on the appearance of a 'double-wake' profile, due to the jet flow induced by the presence of counter-rotating vortices of opposite sign to what is expected in the wake.

pair, gives the streamwise mean velocity profile a 'double-wake' type appearance, as may be seen in Figure 5. It should be mentioned here that this type of 'double-wake' profile was observed by Koochesfahani (1989) for a mode of vortex formation downstream of a pitching airfoil, which is equivalent to the present 2P-mode. In the Upper branch (unequal 2P-mode) case, the mean vortex pair is again present in the mean vorticity field, although in this case it is rather weaker than for the Lower branch case, hence the 'double-wake' profile is only just discernible. The mean vortex pair, in the case of the 2P-modes found here, may be interpreted as due to vorticity being drawn across the wake, to form the second vortex in each pair of the 2P-mode. It has a sign of vorticity opposite to the classical wake vorticity. The detailed formation of the 2P-mode is described further in Govardhan & Williamson (2000).

#### 4. FLUCTUATING VELOCITY FIELDS

We present, in this section, global mean Reynolds stresses in the wake, for the stationary cylinder as well as for the oscillating cylinder in each of the three branches of response, namely the Initial, Upper and Lower branches. In each case, the total Reynolds stress, computed from a large number of instantaneous DPIV velocity fields, as well as the periodic component of the Reynolds stress, calculated from phase-averaged velocity data as in Cantwell & Coles (1983), is shown. In the present work, the phase averaging of the velocity data is performed using the lift force signal as the reference, for the stationary cylinder, and using the cylinder displacement signal as a reference, for the oscillating cylinder cases. The set of instantaneous velocity fields obtained are divided into 30 different sub-groups, each sub-group corresponding to a certain phase of cylinder motion (or lift force), and the velocity fields within each sub-group are averaged. The periodic Reynolds stress is calculated from the resulting 30 phase-averaged velocity fields.

As discussed by Cantwell & Coles (1983), based on Reynolds & Hussain (1972), a flow variable  $s(t)$  in the near wake can be viewed formally as a combination of a global mean component  $\bar{s}$ , a periodic mean component  $\tilde{s}$  (which depends on the phase  $\theta$  during a cycle), and a random component  $s'(t)$ . By definition, the total variable  $s(t)$  is then the sum

$$s(t) = \bar{s} + \tilde{s}(\theta) + s'(t). \quad (1)$$

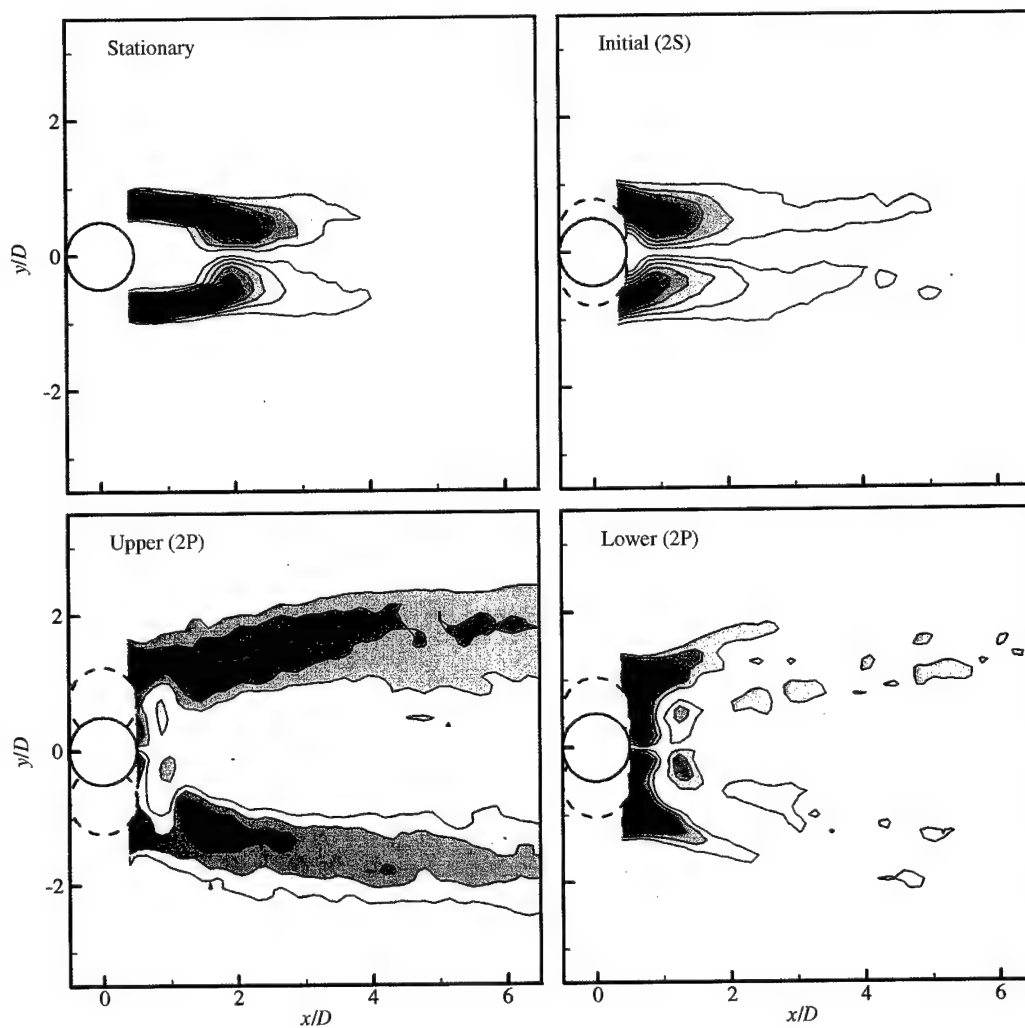


Figure 4. Mean vorticity fields showing the presence behind the cylinder of a pair of counter-rotating vortices of opposite sign to what is expected in a wake, for the Upper and Lower response branches, which correspond to the 2P-mode. Vorticity contours levels shown are  $\omega D/U = \pm 0.4, \pm 0.8, \pm 1.2 \dots$  (for stationary cylinder and Initial branch), and  $\omega D/U = \pm 0.2, \pm 0.4, \pm 0.8 \dots$  (for the Upper and Lower branches).

TABLE 1  
Peak Reynolds stress in the wake of a stationary circular cylinder

(a) Total Reynolds stress		$(\overline{u''u''}/U^2)$	$(\overline{v''v''}/U^2)$	$(\overline{u''v''}/U^2)$
Cantwell & Coles (1983)	Re = 140 000	0.22	0.43	0.12
Present	Re = 3900	0.11	0.23	0.085
(b) Periodic part of Reynolds stress		$(\overline{\tilde{u}\tilde{u}}/U^2)$	$(\overline{\tilde{v}\tilde{v}}/U^2)$	$(\overline{\tilde{u}\tilde{v}}/U^2)$
Cantwell & Coles (1983)	Re = 140 000	0.08	0.23	0.05
Present	Re = 3900	0.065	0.18	0.06

The global mean  $\bar{s}$ , may be obtained by averaging over all the instantaneous velocity fields. On the other hand, in order to obtain the periodic mean  $\tilde{s}(\theta)$ , we need to average the data at constant phase of vortex shedding ( $\theta$ ), as in Cantwell & Coles (1983). Following the notation used in Cantwell & Coles (1983), the periodic component ( $\tilde{s}$ ) may then be defined as

$$\tilde{s}(\theta) = \langle s \rangle_\theta - \bar{s}, \quad (2)$$

where  $\langle s \rangle_\theta$  is the mean of  $s$  at a particular phase  $\theta$ . In the present work, we also introduce the additional notation,  $s''(t)$ , as the total fluctuation, defined by

$$s''(t) = s(t) - \bar{s} = \tilde{s}(\theta) + s'(t). \quad (3)$$

If  $s(t)$  is the streamwise velocity component  $u(t)$ , then the total streamwise Reynolds normal stress ( $\overline{u''u''}$ ) would have two components; the periodic component  $\overline{\tilde{u}\tilde{u}}$ , due to the repeatable large-scale coherent structures in the wake, and the random component  $\overline{u'u'}$ , due to the random small-scale turbulence, as discussed in Cantwell & Coles (1983) and shown below:

$$\overline{u''u''} = \overline{\tilde{u}\tilde{u}} + \overline{u'u'}$$

Total = Periodic + Random

The peak value of the total streamwise Reynolds stress for the stationary cylinder, at our  $Re \approx 3900$ , is about  $(\overline{u''u''}/U^2) \approx 0.11$ , as may be seen from Figure 6. As one might expect, this value is substantially smaller than the peak value of  $(\overline{u''u''}/U^2) \approx 0.22$  found in the much higher  $Re$  ( $Re = 140\,000$ ) experiments of Cantwell & Coles (1983). However, if instead we now compare the peak periodic stress, we find interestingly that their values are quite similar, 0.065 and 0.08, respectively. In fact, comparison of the peak values of each of the other Reynolds stresses between the two widely different Reynolds numbers, also shown in Table 1, indicates that in each case, the peak periodic components are very nearly the same, although the peak total Reynolds stress is significantly larger for the higher  $Re$  experiments. This suggests that the repeatable large-scale coherent structures, responsible for the periodic part of the Reynolds stresses, are quite similar over the range of  $Re$  from 3900 to 140 000. Therefore, the increase in Reynolds stresses over this range of  $Re$  seems to be principally due to the random component. We suggest that this is fed by the increasing strength of the Kelvin–Helmholtz instability of the separating shear layer, as  $Re$  increases in this “Shear Layer instability regime”, defined in the review of Williamson (1996), and first studied by Schiller & Linke (1933); see also Roshko’s (1993) review.

For the stationary cylinder case, at our  $Re = 3900$ , the maximum total stress  $(\overline{u''u''}/U^2)$  is about 0.11, while the periodic stress  $(\overline{\tilde{u}\tilde{u}}/U^2) \approx 0.065$ , indicating that in this case the periodic

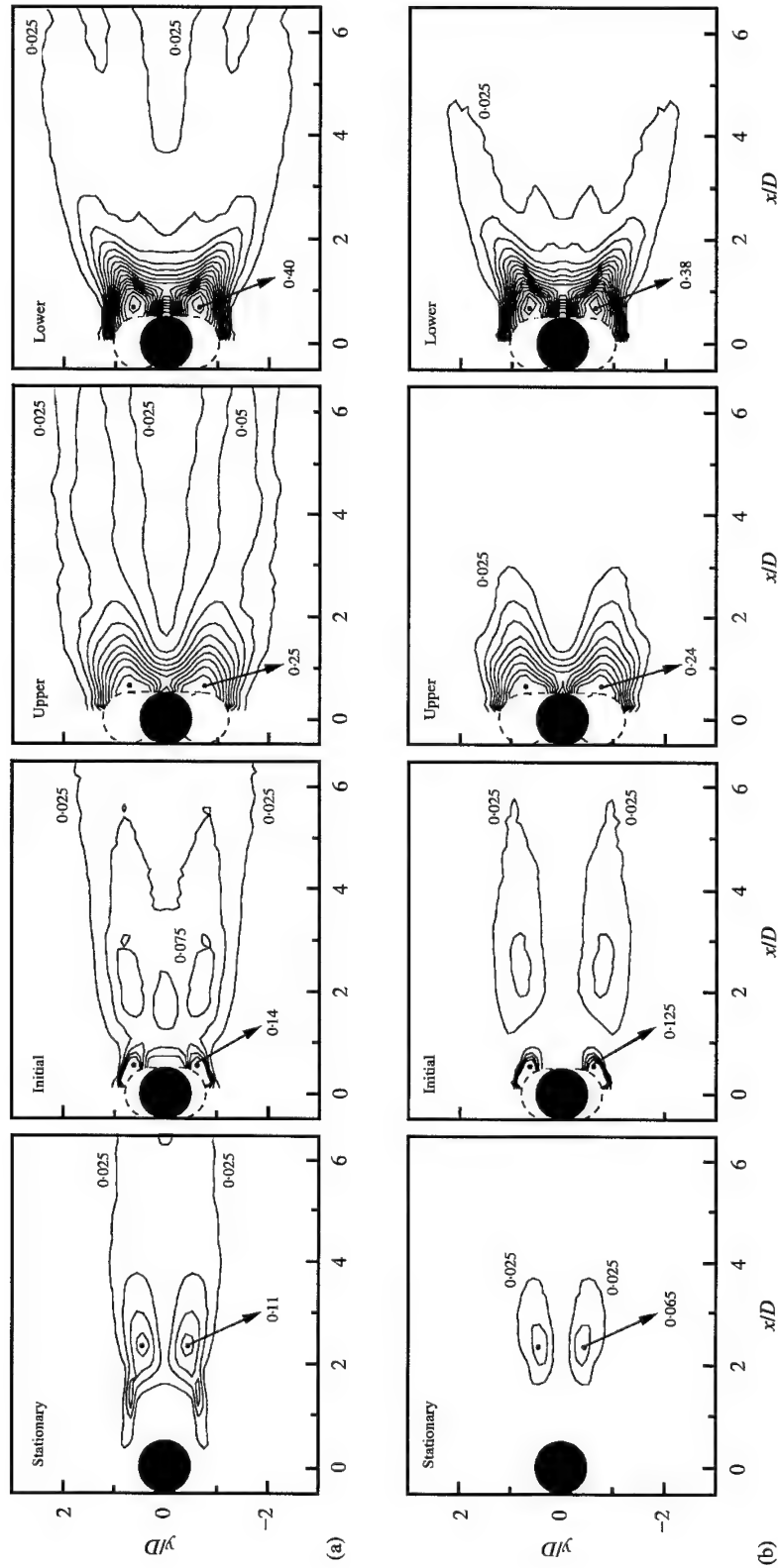


Figure 6. Contours of (a) total  $\overline{(u''u'')/U^2}$  and (b) periodic component  $\overline{(\tilde{u}\tilde{u})/U^2}$  of the global mean streamwise Reynolds normal stress. The total Reynolds stress is calculated from a large number of instantaneous velocity fields, while the periodic part of the Reynolds stress is calculated from phase-averaged velocity data. Contours shown are separated by  $0.025$  for all cases.  $\bullet$ , location of the maximum value of the Reynolds stress.

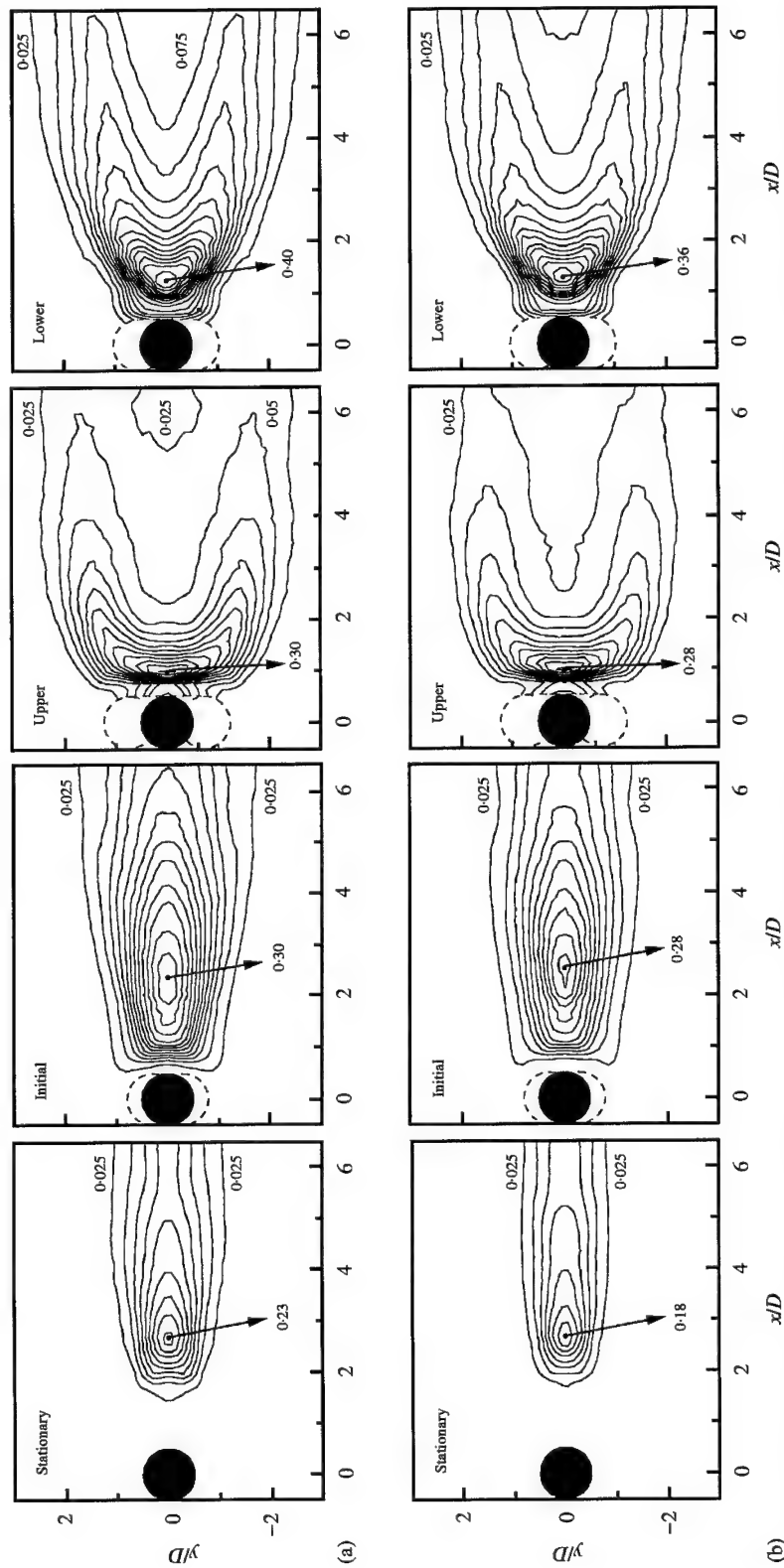


Figure 7. Contours of (a) total  $(\overline{v''v''}/U^2)$  and (b) periodic component  $(\overline{v''v''}/U^2)$  of the global mean crossflow Reynolds normal stress. Contours shown are separated by 0.025 for all the cases. ●, location of the maximum value of the Reynolds stress.

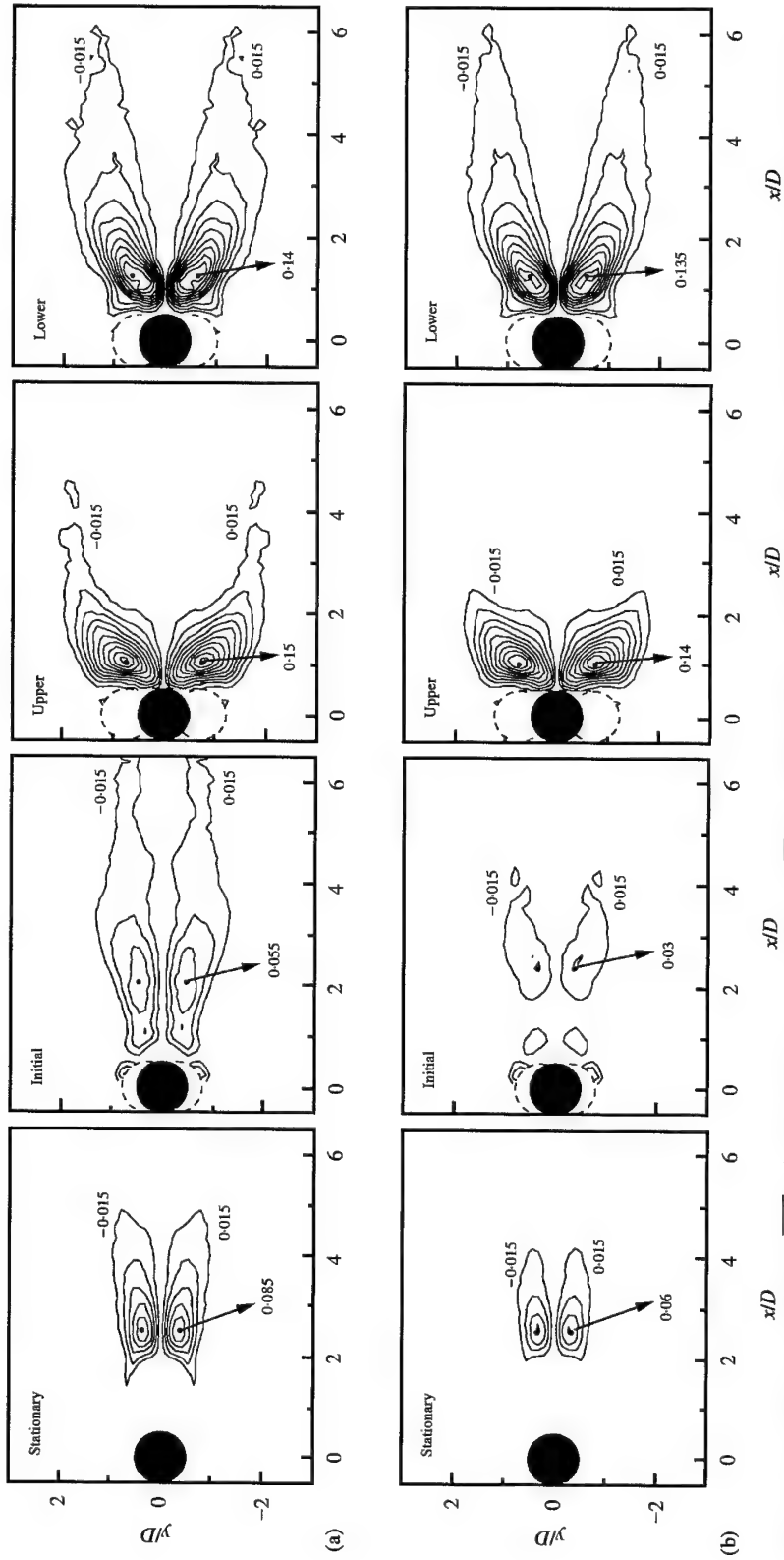


Figure 8. Contours of (a) total  $(\overline{u''v''}/U^2)$  and (b) periodic component  $(\overline{u''v''}/U^2)$  of the global mean Reynolds shear stress. Contours shown are separated by 0.015 for all the cases. ●, location of the maximum value of the Reynolds stress.



TABLE 2  
Peak periodic Reynolds stress ( $\overline{\tilde{s}s}$ ) as a percentage of peak total Reynolds stress ( $\overline{s''s''}$ )

	Stationary (%)	Initial (%)	Upper (%)	Lower (%)
$(\overline{\tilde{u}u}/\overline{u''u''})$	59	89	96	95
$(\overline{\tilde{v}v}/\overline{v''v''})$	78	93	93	90
$(\overline{\tilde{u}v}/\overline{u''v''})$	71	55	93	96

TABLE 3  
Vortex formation length ( $l_f$ )

	Stationary	Initial	Upper	Lower
$(l_f/D)_{\text{closure point}}$	2.27	1.46	—	—
$(l_f/D)_{\text{location of max } \overline{u''u''}}$	2.33	0.55	0.64	0.68

part is approximately 60% of the total Reynolds stress. In Table 2, we present percentages for the ratios of periodic to total stress, for the three different Reynolds stresses, and corresponding to each of the three cylinder response branches as well as for the stationary cylinder (see Figures 6–8). A striking feature of Table 2, is the increase in percentages for the oscillating cylinder cases, to about 90% or greater, in contrast to the approximately 70% level for the stationary cylinder. This would indicate that for the oscillating cylinder, nearly all the total Reynolds stress comes from the large-scale periodic dynamics of the flow. The above point, combined with the fact that these large-scale periodic coherent structures seem to be relatively independent of  $Re$ , as noted previously in comparison to Cantwell & Coles (1983), would indicate that the Reynolds stresses measured in the present work, for the oscillating cylinder at  $Re = 3000$ – $4000$ , would be quite representative also of much higher Reynolds numbers; a point that could be useful in modelling these problems. [It may be noted in Table 2, that unlike all the other cases, the percentage of the periodic shearing stress ( $\overline{\tilde{u}v}/U^2$ ) in the Initial branch, is quite small, about 55% of the total shearing stress. The reason for the low value in this particular case is not known at present.]

The numerical values of the peak periodic stress, and indeed the peak total stress, can be considerably larger for an oscillating cylinder, compared to the stationary cylinder, as may be seen from Figures 6–8. In particular, the largest increase in periodic stress appears to be for the Lower branch of cylinder response, which corresponds to the 2P-mode, where  $(\overline{\tilde{u}u}/U^2)_{\text{max}}$  increases by 485%,  $(\overline{\tilde{v}v}/U^2)_{\text{max}}$  increases by 100%, and  $(\overline{\tilde{u}v}/U^2)_{\text{max}}$  increases by 125%, compared to the stationary cylinder values, which seem to be relatively independent of  $Re$ . This large increase in the periodic Reynolds stresses in the Lower branch is consistent with the large increase (of about 200%) in the total circulation that is shed into the large-scale vortices, as discussed in Govardhan & Williamson (2000). The increased vortex circulation corresponds with the large increase in fluctuating lift (by a factor of 6), and in mean drag (by a factor of 5), as shown in Khalak & Williamson (1997).

We shall now briefly look at the “formation length” for the oscillating cylinder. Contour plots of the total streamwise Reynolds stress ( $\overline{u''u''}$ ) in the wake, shown in Figure 6, indicate that the location of the maximum value of  $\overline{u''u''}$  gets closer to the cylinder when it vibrates, compared to the stationary cylinder, consistent with the observations of Griffin (1971), and with our earlier observation of a reduction in the size of the recirculation bubble. The formation length ( $l_f$ ) has been defined in many ways as discussed recently by Noca *et al.*

(1998) and by Norberg (1998). In Table 3, we show values of  $l_f$  calculated from the 'closure point' ( $\bar{u}/U = 0$  on wake centreline), and from the streamwise location of maximum  $\overline{u''u''}$  in the wake; in each case  $l_f$  is measured from the cylinder axis. It can be seen that  $l_f$  (computed in either of the two ways) is considerably reduced for the oscillating cylinder compared to the stationary cylinder. However, at the present  $Re = 3000$ – $4000$ , the reduction in  $l_f$  is substantially greater than that observed by Griffin at  $Re \approx 200$ . In fact, it is interesting to note that one cannot define  $l_f$  based on the closure point for the Upper and Lower branches, as there is no recirculation bubble in these cases. The formation length can however still be calculated based on the streamwise location of maximum  $\overline{u''u''}$  in the wake, which gives values of  $l_f/D \approx 0.6$ , which is substantially lower than the smallest values of  $l_f/D \approx 1.6$  reported by Griffin at  $Re \approx 200$ .

## 5. CONCLUSIONS

In this work, we study the wake velocity field of an elastically mounted rigid cylinder that is constrained to move transverse to the free stream, using DPIV measurements.

The measured mean velocity fields indicate that the characteristic "recirculation bubble", usually seen in the mean velocity field behind the nonoscillating cylinder, is present in the case of the '2S' wake formation mode, but is completely absent for the 2P-mode. For the '2P' mode, we find instead the appearance of a pair of counterrotating vortices of opposite sign to what is expected, causing a downstream oriented jet-type flow close to the cylinder, which in turn results in a 'double-wake' type velocity profile.

We evaluate the total Reynolds stresses, and the periodic component of stress, computed from phase-averaged velocity data, for the stationary cylinder as well as for the oscillating cylinder in each of the three response branches, namely the Initial, Upper and Lower branches. Comparison of the stationary cylinder peak stresses, at  $Re = 3900$ , with the data of Cantwell & Coles (1983), at much higher  $Re$  ( $Re = 140\,000$ ), indicate that although the total Reynolds stresses are significantly larger at the higher Reynolds numbers, the periodic component of stress is quite similar in both cases. This suggests that the repeatable large-scale coherent structures, responsible for the periodic part of the Reynolds stresses, are quite similar over the wide range of  $Re$  from 3900 to 140 000. In the case of the oscillating cylinder, typically more than 90% of the total Reynolds stresses are due to these repeatable large-scale coherent structures. The above facts suggest that the Reynolds stresses obtained in the present work, at  $Re \approx 3900$  for the oscillating cylinder, would be quite representative also of much higher  $Re$  cases; a point that could be useful in modelling these problems.

Reynolds stresses at different constant phases of vortex shedding, corresponding to each of the three cylinder response modes, have also been computed, but are not included in this paper, for brevity.

## ACKNOWLEDGEMENTS

The support from the Ocean Engineering Division of O.N.R., monitored by Dr. Tom Swean, is gratefully acknowledged (O.N.R. Contract Nos. N00014-94-1-1197 and N00014-95-1-0332).

## REFERENCES

- BEARMAN, P. W. 1984 Vortex shedding from oscillating bluff bodies. *Annual Review of Fluid Mechanics* **16**, 195–222.

- BRIKA, D. & LANEVILLE, A. 1993 Vortex-induced vibrations of a long flexible circular cylinder. *Journal of Fluid Mechanics* **250**, 481–508.
- CANTWELL, C. & COLES, D. 1983 An experimental study of entrainment and transport in the turbulent near wake of a circular cylinder. *Journal of Fluid Mechanics* **136**, 321–374.
- CARBERRY, J., SHERIDAN, J. & ROCKWELL, D. 2001 Forces and wake modes of an oscillating cylinder. *Journal of Fluids and Structures* **15**, 523–532.
- GOVARDHAN, R. & WILLIAMSON, C. H. K. 2000 Modes of vortex formation and frequency response of a freely-vibrating cylinder. *Journal of Fluid Mechanics* **420**, 85–130.
- GRIFFIN, O. M. 1971 The unsteady wake of an oscillating cylinder at low Reynolds number. *Journal of Applied Mechanics* **38**, 729–738.
- KHALAK, A. & WILLIAMSON, C. H. K. 1997 Fluid forces and dynamics of a hydroelastic structure with very low mass and damping. *Journal of Fluids and Structures* **11**, 973–982.
- KHALAK, A. & WILLIAMSON, C. H. K. 1999 Motions, forces and mode transitions in vortex-induced vibrations at low mass-damping. *Journal of Fluids and Structures* **13**, 813–851.
- KOOCHESFAHANI, M. M. 1989 Vortical patterns in the wake of an oscillating airfoil. *AIAA Journal* **27**, 1200–1205.
- NOCA, F., PARK, H. G. & GHARIB, M. 1998 Vortex formation length of a circular cylinder ( $300 < Re < 4000$ ) using DPIV. In *Proceedings of the 1998 Conference on Bluff Body Wakes and Vortex-Induced Vibration*, Washington DC (eds P. W. Bearman & C. H. K. Williamson), Paper No. 46, Ithaca, NY: Cornell University.
- NORBERG, C., 1998 LDV-measurements in the near wake of a circular cylinder. In *Proceedings of the 1998 Conference on Bluff Body Wakes and Vortex-Induced Vibration* (eds P. W. Bearman & C. H. K. Williamson), Paper No. 42, Ithaca, NY: Cornell University.
- PARKINSON, G. 1989 Phenomena and modelling of flow-induced vibrations of bluff bodies. *Progress in Aerospace Sciences* **26**, 169–224.
- ROSHKO, A. 1993 Perspectives on bluff body aerodynamics. *Journal of Wind Engineering and Industrial Aerodynamics* **49**, 79.
- REYNOLDS, W. C. & HUSSAIN, A. K. M. F. 1972 The mechanics of an organized wave in turbulent shear flow. Part 3. Theoretical models and comparisons with experiments. *Journal of Fluid Mechanics* **54**, 263–288.
- SARPKAYA, T. 1979 Vortex-induced oscillations. *Journal of Applied Mechanics* **46**, 241–258.
- SCHILLER, L. & LINKE, W. 1933 Pressure and frictional resistance of a cylinder at Reynolds numbers 5000 to 40,000. NACA TM 715.
- STANSBY, P. K. & APSLEY, D. D. 2000 Flow around cylinders: modelling, dynamic response, arrays. In *Proceedings of the Workshop on Vortex-Induced Vibrations of Offshore Structures* (eds C. P. Pesce, C. A. Martins, J. R. Meneghini & J. A. P. Aranha), pp. 32–34, São Paulo, Brazil: Universidade de São Paulo.
- TECHET, A. H., HOVER, F. S., & TRIANTAFYLLOU, M. S. 1998 Vortical patterns behind a tapered cylinder oscillating transversely to a uniform flow. *Journal of Fluid Mechanics* **363**, 79–96.
- WILLIAMSON, C. H. K. 1996 Vortex dynamics in the cylinder wake. *Annual Review of Fluid Mechanics* **28**, 477–539.
- WILLIAMSON, C. H. K. & ROSHKO, A. 1988 Vortex formation in the wake of an oscillating cylinder. *Journal of Fluids and Structures* **2**, 355–381.



## GALLOPING RESPONSE OF A CYLINDER WITH UPSTREAM WAKE INTERFERENCE

F. S. HOVER AND M. S. TRIANTAFYLLOU

*Department of Ocean Engineering, Massachusetts Institute of Technology  
77 Massachusetts Avenue, Cambridge, MA 02139, U.S.A.*

(Received 3 September 2000, and in final form 15 November 2000)

A compliantly-mounted rigid cylinder was towed at  $Re = 3 \times 10^4$ , 4.75 diameters behind a stationary leading cylinder of the same size. An in-line configuration and a 12-degree staggered arrangement each produced large-amplitude galloping responses, and an upward extension of the frequency lock-in range to a reduced velocity of at least 17. The frequency lock-in begins at nearly the same free-stream reduced velocity as a single cylinder, while a large phase change in the lift force occurs at higher reduced velocities, which can be extrapolated from the single-cylinder lock-in point. Force spectra indicate that shedding from the upstream cylinder is completely unaffected by motions of the trailing cylinder. Furthermore, the motion-coupled peaks suggest that only one lift force cycle and one or two drag force cycles occur per oscillation, the latter depending on the offset.

© 2001 Academic Press

### 1. INTRODUCTION

THE WAKE INTERACTION of parallel cylinders arises in many applications, including arrays of offshore risers and moorings, and power transmission lines. For nonoscillating cylinders, a number of distinct flow regimes exist, which depend on the separation distance  $S$  (Zdravkovich & Pridden 1977; Igarashi 1981). Small separation distances ( $S/D < 2$ ) limit the reattachment of the leading cylinder's shear layer to the trailing one, and can lead to bistable gap flows. Quasi-steady recirculation cells, with coupled vortex formation, occur for larger separation distances ( $2 < S/D < 4$ ), and, finally, vortex roll-up from the leading cylinder occurs for  $S/D > 4$ , where coupling is diminished. For the case of forced vibrations of two tandem cylinders, a wake lock-in exists for the extreme motion phase angles of zero and  $180^\circ$ , and lock-in of the wake to the motion occurs over a dramatically expanded region of amplitude and frequency, for small  $S$  (Mahir & Rockwell 1996).

In tests where both cylinders are compliantly-mounted, large-amplitude vibrations of both cylinders can occur when the separation is about  $5-7D$ , and at least for lateral offsets up to  $1.5D$  (Zdravkovich 1985). The vibrations are limited to a specific range of reduced velocities, typically beginning at lower values than for a single cylinder.

Bokaian & Geoola (1984) considered the case of a fixed leading cylinder, and a compliantly-mounted trailing cylinder. They report both vortex-resonance regions, i.e., motion occurring only over a specific range of reduced velocity, and galloping instabilities, where motions persist for high reduced velocities. These two types of responses can occur independently or coalesce, depending on the separation distance. Vortex resonance occurs alone for  $S/D > 3$ , for both the in-line case and with offsets of one diameter. In other tests at much higher Reynolds number, galloping is suggested for  $S/D < 7$ , diminishing as the vortex-induced vibration is recovered for large  $S/D$  (Brika & Laneville 1999).

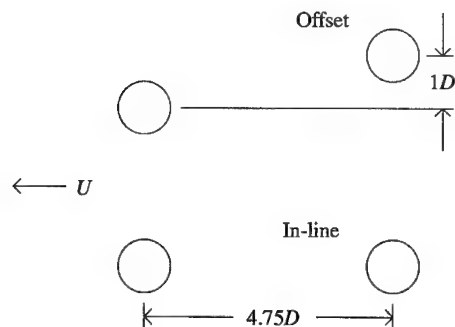


Figure 1. Configurations for the in-line and offset VIV tests.

The tandem arrangement of two cylinders in mid-proximity ( $S/D = 5-10$ ) creates a reduced natural shedding frequency, with comparison to a single cylinder. When one cylinder vibrates freely, however, the wake frequency behind the leading cylinder is unaffected by the trailing cylinder. The wake of the trailing cylinder still exhibits a lower Strouhal frequency, consistent with reduced mean flow calculations, until it reaches lock-in conditions. Hence, on a reduced-velocity scale employing free-stream velocity, frequency lock-in occurs at a higher value than for a single cylinder (Brika & Laneville 1999).

In order to bridge some of these results, we consider here a compliantly-mounted rigid circular cylinder in the wake of a stationary fixed cylinder of the same diameter. Locations for the trailing cylinder are 4.75 diameters downstream (tandem), and 4.75 diameters downstream, with a lateral offset of one diameter (relative angle  $12^\circ$ ); see Figure 1. These locations are near Zdravkovich's point of maximum response, and near the edge of the wake interference zone, respectively.

## 2. APPARATUS AND EXPERIMENTAL SETUP

Tests were conducted at the MIT Testing Tank facility, a  $30 \times 2.5 \times 1.2$  m still-water towing tank. We used rigid aluminum cylinders with diameter  $D = 7.62$  cm and span  $L = 200$  cm, moving at constant speed horizontally; the downstream cylinder oscillates transversely to the flow (in the vertical direction). A view of the device from inside the tank is given in Figure 2. The cylinders terminate with 0.2 cm gaps onto 31 cm diameter end-plates at each end. The downstream cylinder is supported by a pair of three-axis piezoelectric load cells, which in turn attach to a heaving structure that also supports the end-plates. This assembly is positioned using a lead screw with 30 cm travel, driven by a brushless servomotor. The uniform tow velocity for the tests corresponds with  $Re = 3.05 \times 10^4$ .

We employed a robotic force-feedback loop as described in Hover *et al.* (1998). In this system, dynamic lift force measurements are injected into a real-time simulation of a compliant structure, whose output drives the servomotor reference trajectory, and ultimately the physical cylinder. The functional result is a cylinder that appears to be compliantly mounted, even though its position is controlled very accurately with a servomotor. In the present experiments, the simulated compliance consisted of a simple mass and spring. The simulation mass  $M$  and stiffness  $K$  can be arbitrarily specified by the user, thus allowing the variation of nominal reduced velocity  $V_m = 2\pi U/\omega_n D$  at constant Reynolds number. Here,  $U$  represents the steady towing speed of the carriage, and  $\omega_n = \sqrt{K/M}$  is the undamped natural frequency of the virtual structure.

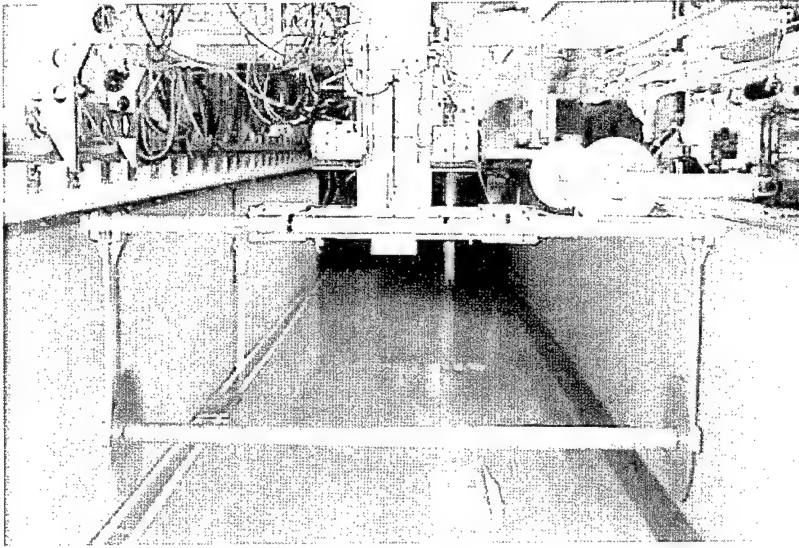


Figure 2. The testing apparatus installed at the MIT Towing Tank, showing one 2 m cylinder, with end-plates and lower yoke assembly. Photo viewpoint is inside the tank.

Intrinsic in the feedback loop is a correction for the component of measured force that is due to the inertia in the material test cylinder; this mass is effectively replaced with  $M$ . The data in the current work were obtained with the nondimensional mass ratio  $m^* = 4M/\rho\pi D^2 L = 3.0$ , and an effective damping ratio of about 4%. The nonzero damping ratio is an artifact of the closed-loop control system, which imposes some phase loss to achieve smooth operation.

The following coefficients are calculated for each test: (i) average 1/10th-highest amplitude/diameter ratio  $A/D_{1/10}$ , with excursions taken from the mean position; (ii) mean drag coefficient,  $\text{mean}(C_d)$ ; (iii) fluctuating drag coefficient  $\text{std}(C_d)$ , the standard deviation of the drag signal; (iv) total lift coefficient amplitude  $C_l = 2|F|/\rho DLU^2$ , constructed as the Euclidean norm of components in phase with vibration velocity and position; (v) phase angle  $\phi$ , between the oscillating lift force and the imposed motion, computed as an arctangent of the lift coefficients in phase with velocity and position.

### 3. AMPLITUDE, DRAG, AND LIFT COEFFICIENTS

We give the amplitudes and force coefficients in Figure 3, and the phase angle in Figure 4. In each figure, the calculated value is plotted against nominal reduced velocity for three configurations: (a) in-line, (b) offset, and (c) single cylinder.

The case of a single cylinder is provided for comparison with previously published results, and reflects a number of typical characteristics. First, as  $V_m$  increases, the amplitude ratio approaches unity, then drops to a short plateau with  $A/D \approx 0.75$ , and then a longer plateau at  $A/D \approx 0.50$ , before dropping again in the range of  $V_m = 9-11$ . This type of  $A/D$  response envelope, i.e. localized on the  $V_m$ -axis, is termed vortex resonance in the sequel. The highest-amplitude part of the curve correlates with a steady drag coefficient of about 3.0, and the main plateau matches the zero-motion drag coefficient of 1.25. A similar dependence can be observed for the fluctuating component of drag, as well as lift coefficient magnitude.

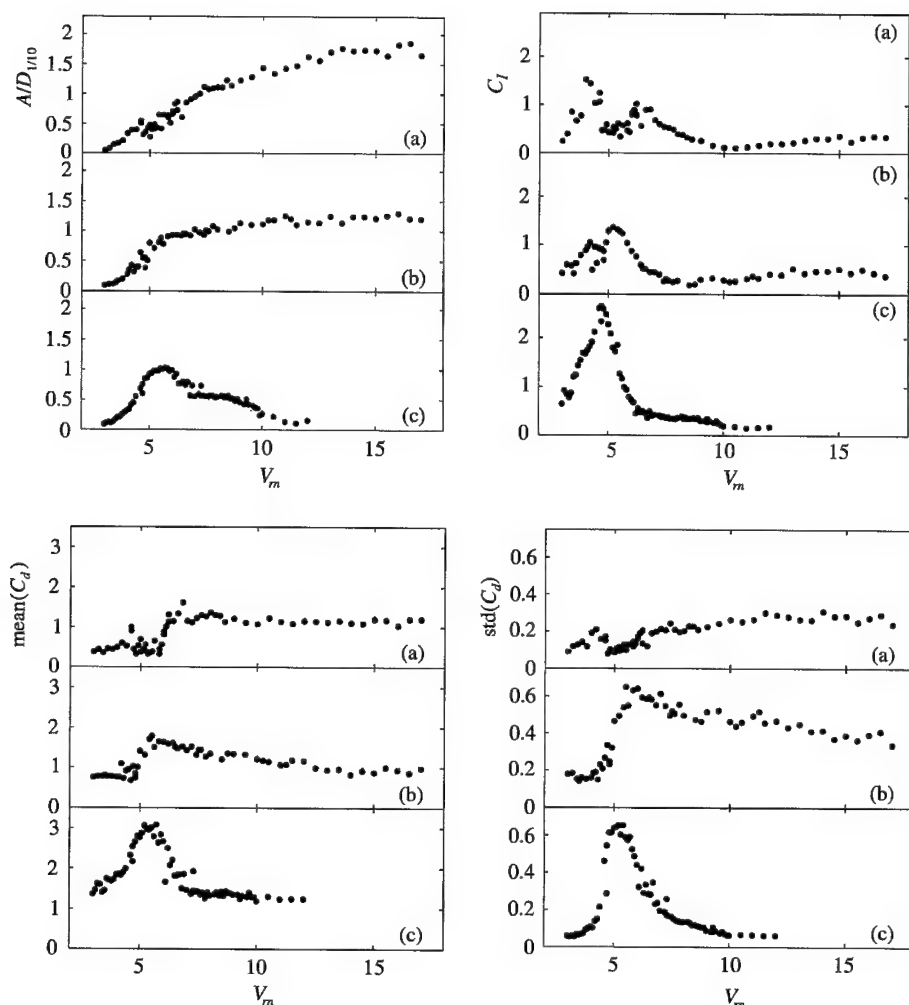


Figure 3. Average one-tenth highest amplitude of motion (upper left), mean drag coefficient (lower left), fluctuating lift coefficient (upper right), and fluctuating drag coefficient (lower right), as functions of  $V_m$ : (a) in-line; (b) offset; (c) single cylinder.

The phase angle for the single cylinder in free-vibration undergoes a rapid transition from near zero to near  $180^\circ$ , near  $V_m = 6.0$ ; this event generally marks a mode change from “2S” - to “2P”-type vortex shedding, evident in forced and free vibrations (Williamson & Roshko 1988; Brika & Laneville 1993). The phase points near  $90^\circ$ , amid the transition, result from averaging the phase calculated at each end of the cylinder. In this regime, we often observe one large-amplitude end force with  $0^\circ$  phasing, and one small-amplitude end force with  $180^\circ$  phasing.

For both configurations involving interference, galloping occurs, without any clear signatures of vortex resonance; the growth of motion with  $V_m$  is largely monotonic. Amplitude ratios become very high, reaching 1.9 in the in-line case and 1.3 in the offset case. It is likely that larger amplitudes could also occur at higher velocities.

Steady drag coefficients for the in-line and offset cases with no vibration, i.e. low  $V_m$ , are 0.35 and 0.80, respectively. These values are in reasonable agreement with Zdravkovich

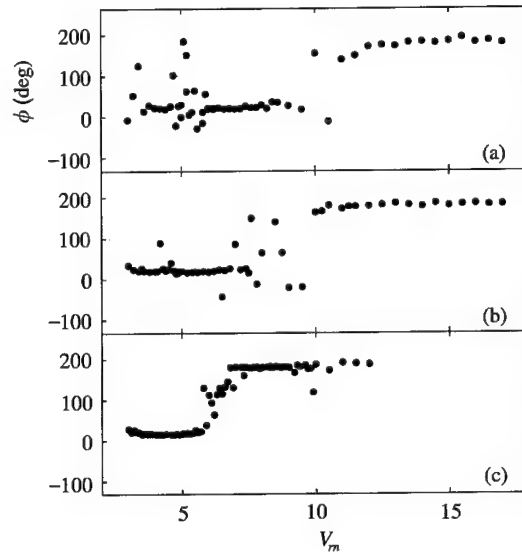


Figure 4. Lift coefficient phase  $\phi$  as a function of  $V_m$ : (a) in-line; (b) offset; (c) single cylinder.

& Pridden (1977), and also with the mean wake analysis described by Huse (1992), for which trailing cylinder  $C_d$  values of 0.49 and 0.83 are generated from a base  $C_d$  of 1.2. For the in-line case, the mean drag jumps from 0.35 to about 1.2, at  $V_m \approx 6$ , although some scatter exists. In contrast, the offset case has  $C_d$  increasing to about 1.8 at  $V_m \approx 5$ , before a gradual descent to about 1.0 at the higher  $V_m$ . Roughly speaking, these upward jumps in mean  $C_d$  for both configurations correspond to regimes of highly irregular amplitude ratios.

Fluctuating drag for the offset case reaches the same maximum value as the single cylinder, although at a slightly higher  $V_m$ , and then declines gradually to a value near 0.4, markedly higher than the single cylinder. When the trailing cylinder is in-line, values are much lower overall, and a local minimum at  $V_m \approx 5.5$  is in the same area of scattered amplitudes noted above.

Peak lift coefficients  $C_l$  for the interference cases are much lower than for the single cylinder, and both curves have an area of low value, again roughly in the regime of scattered amplitudes. Noteworthy is the fact that each lift coefficient has the nature of a vortex resonance, in the sense that it decays at high velocities. Phase angle, however, indicates that the main transition occurs well away from the usual range of  $V_m$ . The in-line configuration changes phase at  $V_m = 9-11$ , while it changes over a larger range,  $V_m = 7-10$ , for the offset case. Several effects are likely. The in-line cylinder arrangement imposes a reduced mean flow on the trailing cylinder, while in the offset case, the trailing cylinder can additionally emerge from the wake periodically, and is therefore exposed to higher velocities. Further discussion of phase variation is given in Section 5.

Interestingly, no unique features in any of the other coefficient plots (Figure 3) signal the phase change with wake interference. For the single cylinder, amplitude and mean drag both drop dramatically through the phase change.

#### 4. SPECTRAL DESCRIPTION OF RESPONSES

In Figures 5-7 are plotted the spectral content of the displacement, and lift and drag forces. Each set of Fourier transform magnitudes has arbitrary scaling, and these are overlaid on



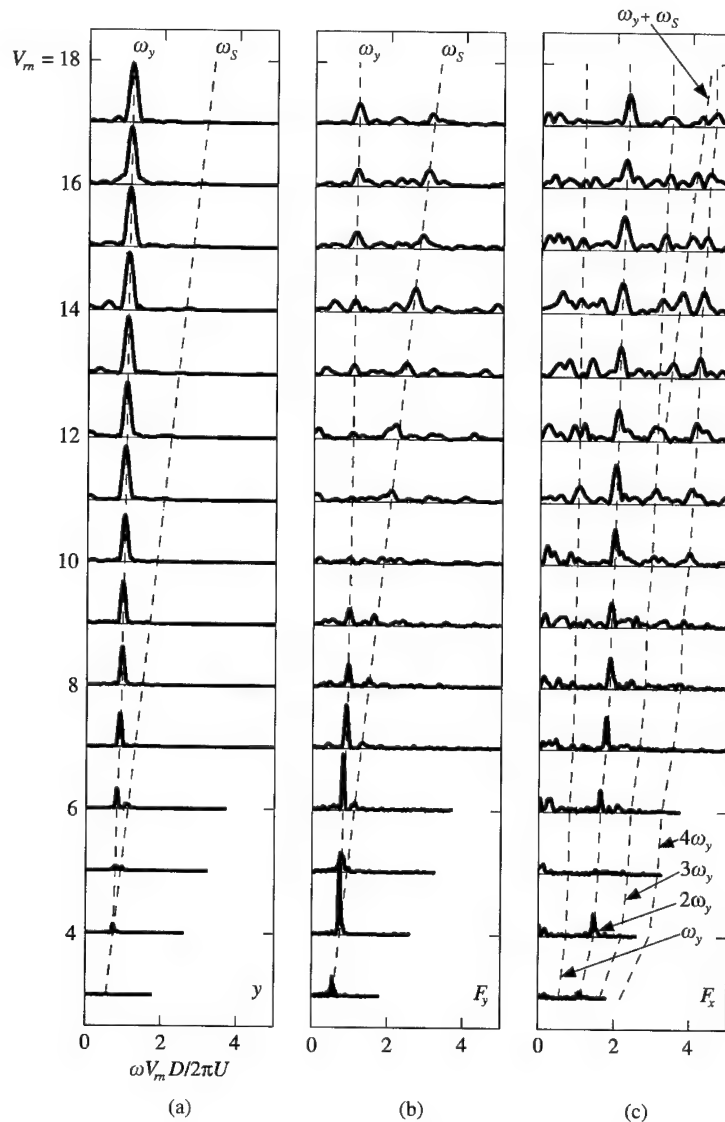


Figure 5. (a) Displacement and (b, c) force spectra of a cylinder centered 4.75D behind a stationary leading cylinder.

a vertical  $V_m$ -axis. The horizontal axis carries normalized frequency, scaled so that unity corresponds with the undamped natural frequency of the structure. Dashed lines are also given in each subplot, which follow the evolution of various peaks. Spectral peaks widen at the higher reduced velocities, but this is only a remnant of the frequency nondimensionalization, since all of the tests were performed at the same physical velocity.

In Figure 7 (single cylinder), the lines classify features in the following ways. The displacement ( $y$ ) and lift ( $F_y$ ) peaks follow the single-cylinder shedding frequency  $\omega_S$  ( $St = 0.185$ ) at low  $V_m$ , and lock on to the structural mode  $\omega_n$  at around  $V_m = 6.5$ . The locked-in nondimensional frequency  $\omega_y/\omega_n \approx 1.15$  is typical for tests with  $m^* = 3$ , where negative added mass significantly increases the net natural frequency. Lift force spectra track the motion spectra closely, becoming quite small for  $V_m > 10$ . The fluctuating drag

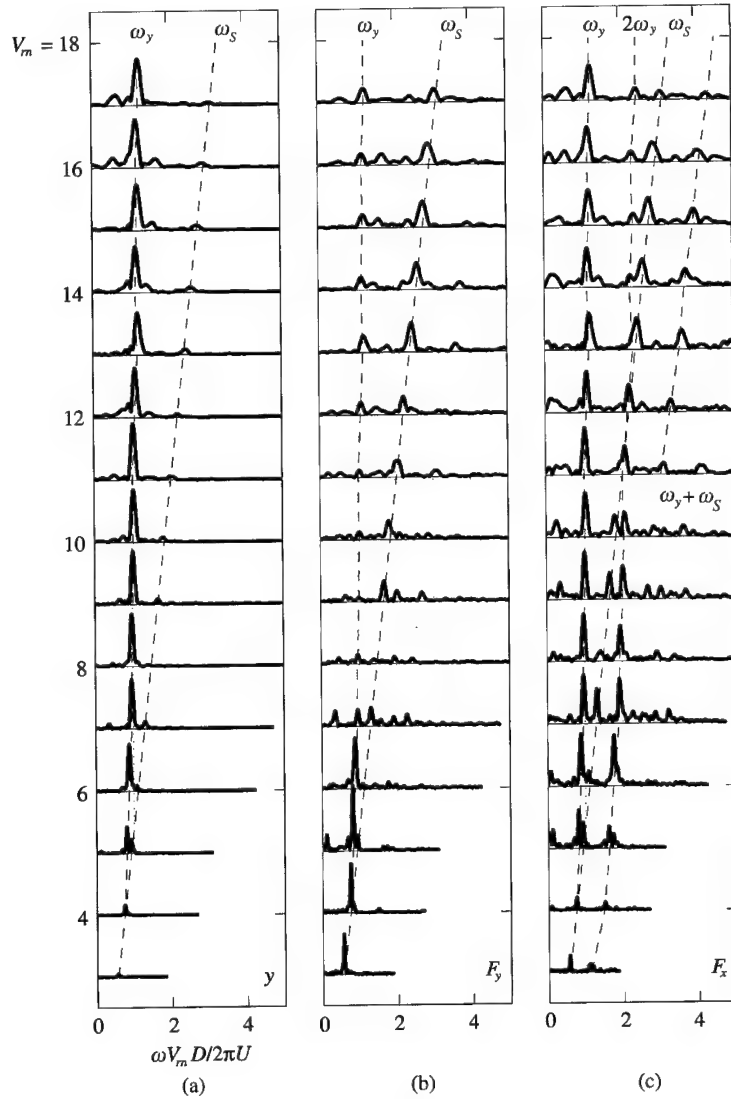


Figure 6. (a) Displacement and (b, c) force spectra of a cylinder located  $4.75D$  behind a stationary leading cylinder, with a one-diameter lateral offset.

force ( $F_x$ ) is significant only near the onset of lock-in, and the peak here follows the second harmonic of  $\omega_y$ . The lift and drag forces thus indicate the simplest modes of VIV, involving 2S and 2P types of wake.

For the in-line experiments of Figure 5, oscillations are narrow-banded, and occur near and just above  $\omega_n$ ; the amplitude  $A/D_{1/10}$  grows throughout the range of reduced velocity. Lift has very significant components at both the frequency of motion  $\omega_y$  and at  $\omega_S$ , especially for high  $V_m$ . The shedding frequency plotted here is the *same* as that for the single cylinder, and therefore likely relates to the incoming wake. Below the phase change at  $V_m \simeq 10$ , the lift force is primarily at  $\omega_y$ ; above the phase change,  $\omega_S$  dominates for a short while, before a peak at  $\omega_y$  grows to similar magnitude. The phase transition occurs at a  $V_m$  where the lift force peaks are broad-banded and small.

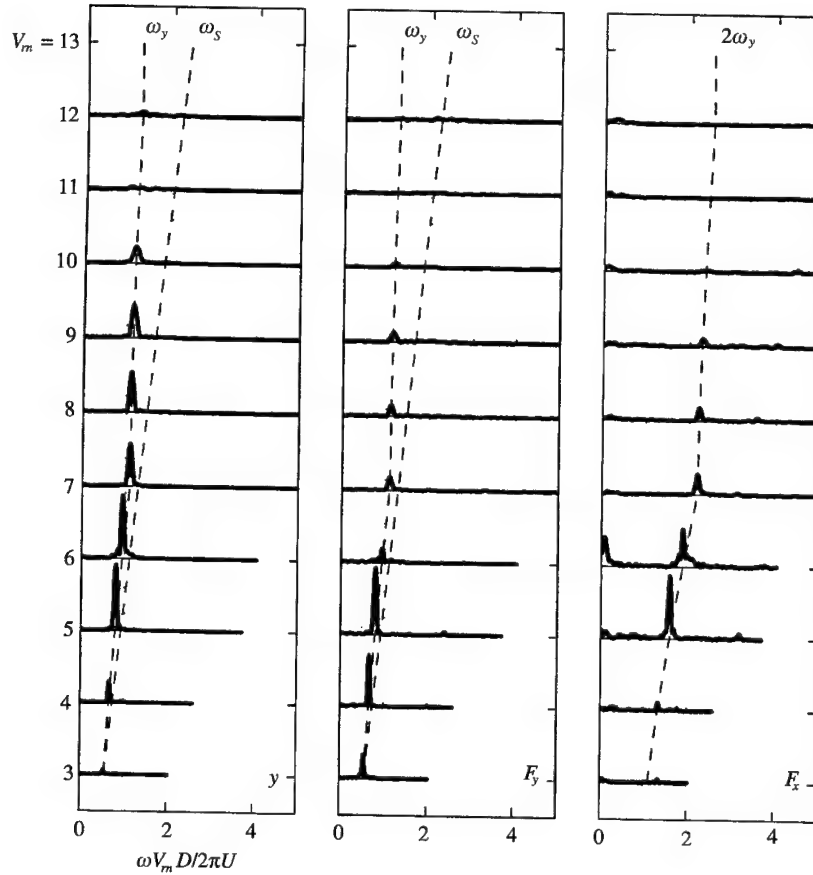


Figure 7. Displacement and force spectra of a single cylinder.

The drag signals present at least four traceable frequency peaks. The dominant force occurs at  $2\omega_y$ , but there are also harmonics at  $3\omega_y$  and  $4\omega_y$ . Additionally, we see significant energy at  $\omega_y + \omega_s$ , for  $V_m > 11$ , above the phase change. Other harmonics may be present as well, although they do not appear to be as repeatable.

When the trailing cylinder is moved to the offset position, the main frequency of motion is still centered just above the structural mode. Lift has a strong component at the shedding rate throughout the range of  $V_m$ , although a component at  $\omega_y$  intensifies at high  $V_m$ , as for the in-line case. Drag has a dominant component at  $\omega_y$ , and a significant second harmonic. We observe fluctuating drag at  $\omega_s$  and  $\omega_y + \omega_s$  also, the latter for the highest range of  $V_m$ .

## 5. DISCUSSION

Both of the wake-interference systems considered show strong galloping, in the sense that vibrations occur for a wide range of reduced velocities, and seem to increase with  $V_m$ . The result pertains to a separation distance smaller than that of Brika & Laneville (1999), whose data arguably points to galloping below  $S/D = 7$ . With regard to the other studies, we employed a much higher Reynolds number than Bokaian & Geoola (1984). High wake sensitivity to Re has in fact been noted for tandem stationary cylinders, but in somewhat

TABLE 1  
Physical parameters of some wake-interference VIV studies

Reference	Response	$Re/10^4$	$L/D$	Blockage ratio	$S_c$	$m^*$
Zdravkovich (1985)*	VR	1-8	11.7	0.042	23	1126
Bokaian & Geoola (1984)†	VR	0.06-0.6	18.1	0.053	1.07	8.42
Brika & Laneville (1999)†	VR, G	0.51-2.75	52.7	0.018	0.78	$\approx 1000$
Current study†	G	3.2	26.3	0.045	0.95	3.0

\* Leading cylinder compliantly mounted. VR: vortex resonance; G: galloping.

† Leading cylinder stationary.

closer proximity (Igarashi 1981). Compliance of the leading cylinder remains a dominant factor in the response; Zdravkovich (1985) observed vortex resonance in the same geometry. Table 1 lists these references, along with some of the physical parameters from the experiments for comparison.

Contrasting with Brika & Laneville (1999), the traceable effect of lower mean velocity on the rear cylinder is not so much an increase in the free-stream  $V_{rn}$  at which motion starts, but rather on the location of the phase change. An extrapolation of phase change location from single-cylinder tests can be made using the same mean wake analysis as for the drag coefficient in Section 3 (Huse 1992). In terms of the drag coefficients, the corrected reduced velocity for a feature occurring at  $V_{rn}^*$ , in free-stream conditions, is

$$V_{rn}^* [\text{mean}(C_d)^{\text{free}}/\text{mean}(C_d)^{\text{wake}}]^{1/2},$$

where the superscript “free” indicates exposure to the free-stream velocity, and “wake” indicates wake flow conditions. Since phase passes through  $90^\circ$  at  $V_{rn} \approx 6.5$  for the single cylinder, we then have the estimates  $V_{rn} \approx 10.2$  for the in-line wake, and for the offset wake  $V_{rn} \approx 7.8$ . These values are in good agreement with Figure 4, and suggest that the primary mechanism for  $V_{rn}$ -dependent phase change stays remarkably intact in the wake. On the other hand, the trailing cylinders begin to oscillate at the same free-stream  $V_{rn}$  as a single cylinder, and at identical frequencies. With respect to a *local*  $V_{rn}$  scale, the trailing cylinder locks to the structural mode quite early, by  $V_{rn} = 3.8$  for the in-line case. Thus, a phase change and frequency locking to the structural mode cannot both define lock-in in the usual sense: wake interference causes these events to occur independently.

Despite the variation of reduced velocity that marks the lift phase change, the component frequencies of lift evolve largely as expected. There are two main peaks at high  $V_{rn}$ :  $\omega_s$ , associated with the stationary leading cylinder, and another  $\omega_y \approx \omega_n$ , associated with the primary motion near the structural mode. First, we may observe that no reduction of  $\omega_s$  is evident; the same value,  $St = 0.185$ , matches peaks throughout, for every configuration. Thus, the normal shedding mechanism from the leading cylinder is completely unaffected by even the large-scale motions of the trailing cylinder.

With regard to the second component of lift, the drag spectra in the in-line configuration indicate motion-coupled forcing consistent with two or four symmetric vortices per cycle. The existence of a smaller third harmonic of  $\omega_y$  probably pertains to an odd symmetry such that some forcing cycles may be sporadic. Nonetheless, the typical mechanisms for motion-coupled shedding seem to be present. For the offset case, drag peaks occurring at  $\omega_s$  correlate with one out of two shed vortices from the leading cylinder reaching the rear cylinder, or at least a significant imbalance in the pressure force from the pair. Note that, in the

corresponding lift spectra, we cannot discern directly whether one or two incoming vortices per cycle cause lift, since they may now act on the same side of the trailing, offset cylinder. The dominant motion-coupled peak in drag near  $\omega_y$  similarly indicates that the loading has a large asymmetry, especially at high  $V_m$ .

## 6. CONCLUSIONS

Lightly-damped cylinders in free vibrations  $4.75D$  behind a stationary cylinder are capable of large-scale galloping, helping fill-in a gap between similar tests at larger spacing ratios, and the case of dually compliant cylinders. Frequency lock-in occurs at a low reduced velocity and remains through  $V_m = 17$ , but the phase change, which typically accompanies frequency lock-in, occurs at higher speeds. This phase change is of the same nature as for single-cylinder tests, and suggests the same fundamental mode transition.

The spectra of the rear cylinder lift and drag forces allow a plausible description of a simple motion-coupled forcing superimposed with a stable wake from the leading cylinder. The former component in the in-line case indicates two or four symmetric vortices per cycle throughout the range of  $V_m$ ; for the offset cylinder, a one-sided loading is evident. We plan DPIV and anemometry tests to verify these observations.

## ACKNOWLEDGEMENTS

We thank Mr F. Gillebo for helping to perform some of the tests and processing. This work is funded by the Office of Naval Research (Ocean Engineering Division), under grant no. N00014-95-1-0106, monitored by Dr T. F. Swann, Jr.

## REFERENCES

- BOKAIAN, A. & GEOOLA, F. 1984 Wake-induced galloping of two interfering circular cylinders. *Journal of Fluid Mechanics* **146**, 383–415.
- BRIKA, D. & LANEVILLE, A. 1993 Vortex-induced vibrations of a long flexible cylinder. *Journal of Fluid Mechanics* **250**, 481–508.
- BRIKA, D. & LANEVILLE, A. 1999 The flow interaction between a stationary cylinder and a downstream flexible cylinder. *Journal of Fluids and Structures* **13**, 579–606.
- HOVER, F. S., TECHET, A. H. & TRIANTAFYLLOU, M. S. 1998 Forces on oscillating uniform and tapered cylinders in crossflow. *Journal of Fluid Mechanics* **363**, 97–114.
- HUSE, E. 1992 Current force on individual elements of riser arrays. In *Proceedings second International Offshore and Polar Engineering Conference* (ed. J. Chung). San Francisco: ISOPE.
- IGARASHI, T. 1981 Characteristics of the flow around two circular cylinders arranged in tandem (First report). *Bulletin of the Japanese Society of Mechanical Engineers* **24**, 323–331.
- MAHIR, N. & ROCKWELL, D. 1996 Vortex formation from a forced system of two cylinders. Part 1: tandem arrangement. *Journal of Fluids and Structures* **10**, 473–489.
- WILLIAMSON, C. H. K. & ROSHKO, A. 1988 Vortex formation in the wake of an oscillating cylinder. *Journal of Fluids and Structures* **2**, 355–381.
- ZDRAVKOVICH, M. M. 1985 Flow induced oscillations of two interfering circular cylinders. *Journal of Sound and Vibration* **101**, 511–521.
- ZDRAVKOVICH, M. M. & PRIDGEN, D. L. 1977 Interference between two circular cylinders; series of unexpected discontinuities. *Journal of Industrial Aerodynamics* **2**, 255–270.



## A CFD STUDY OF THE DYNAMIC RESPONSE OF A ROTATING CYLINDER IN A CURRENT

P. K. STANSBY

*Department of Civil and Construction Engineering, UMIST  
Manchester M60 1QD, U.K.*

AND

R. C. T. RAINEY†

*Centre for Nonlinear Dynamics, University College London  
Gower Street, London WC1E 6BT, U.K.*

(Received 28 September 2000, and in final form 15 November 2000)

A new form of dynamic response for a flexibly mounted, rotating cylinder in a current, as observed in experiments, has been investigated through 2-D, laminar CFD. Orbital response of opposite rotation to that of the cylinder and with amplitudes of several diameters can occur with a maximum at  $\alpha = 0.3$ , where  $\alpha$  is the ratio of current velocity to rotation speed of the cylinder surface. Instantaneous flows and forces for this  $\alpha$  value are related to those for a nonresponding cylinder but it is shown that the forcing is far from quasi-steady and is due to rapidly changing wake structures during part of a cycle.

© 2001 Academic Press

### 1. INTRODUCTION

FOR DEEP-WATER offshore oil exploration, the possibility of using a drillstring without an outer casing is of operational interest. It poses the hydrodynamic problem of a flexibly mounted rotating cylinder in a current. To investigate this, simple experiments with a lightly damped rotating cylinder in a current and computational fluid dynamics (CFD) have been undertaken.

A new form of orbital response was observed in the experiments. It is mainly dependent on the ratio,  $\alpha$ , of current velocity,  $U_{\text{cur}}$ , to cylinder surface velocity,  $U_{\text{rot}}$ , and the reduced velocity,  $V_r = U_{\text{cur}}/f_n D$ , where  $f_n$  is the natural frequency in water and  $D$  is the diameter. Low-frequency response with an amplitude of several diameters can occur with  $0.25 < \alpha < 0.5$ , the orbital rotation being of opposite sense to the cylinder rotation, and high-frequency response of small amplitude, with orbital rotation of the same sense, may be superimposed, becoming more noticeable as  $\alpha$  decreases. Elementary potential-flow analysis consistently predicts that there will be two natural periods of orbital oscillation: one larger than the structural natural period and one smaller. This analysis combined with empirical estimates of the Magnus force gave approximate predictions of the oscillation frequencies observed. The analysis does not, however, explain the origin of the hydrodynamic mechanisms causing the response to occur. In order to understand this, a 2-D

† Also with W. S. Atkins Ltd., Berkshire House, 171 High Holborn, London WC1V 7AA, U.K.

computational study has been undertaken where streamline and vorticity plots may be related to response and force time histories. Such numerical simulation is now quite reliable for unsteady, laminar flow which, in 2-D, may be undertaken on modern workstations. The finite-volume code of Lien & Leschziner (1994) has been adapted for cylinder flows (Cobbin *et al.* 1998) and further modified to allow dynamic response by modifying the outer boundary conditions to define the velocity relative to the cylinder and the pressure gradient with the effect of relative flow acceleration. The resulting computed force includes a Froude-Krylov component which must be subtracted to correspond with the force in the experimental conditions. Values of mass, damping and natural frequency typical of the practical situation are chosen: the cylinder mass is given a relative density of 2.83, the logarithmic decrement of damping  $\delta = 0.01$  and  $V_r = 14$ . A Reynolds number  $Re_{cur} = U_{cur} D/\nu = 200$  ( $\nu$  is kinematic viscosity) was chosen for the dynamic simulations as this is approximately the largest value (for nonrotating cylinders) which allows 2-D flow, before 3-D effects appear. This is an order of magnitude lower than that in the experiments which is an order of magnitude lower than in the offshore problem.

The mass-spring-damper system defining the displacements with two degrees of freedom,  $x$  and  $y$ , is given by

$$\begin{aligned}\ddot{x} + 2c\omega_n \dot{x} + \omega_n^2 x - 2c\omega\omega_n y &= F_x/m, \\ \ddot{y} + 2c\omega_n \dot{y} + \omega_n^2 y + 2c\omega\omega_n x &= F_y/m,\end{aligned}\quad (1)$$

where  $m$  is the mass per unit length,  $F_x$ ,  $F_y$  are forces per unit length in the  $x$ - and  $y$ -directions,  $\omega$  is the angular rotation (clockwise) speed of the cylinder,  $\omega_n$  and  $c$  are the structural natural frequency and damping ratio in vacuo/air (although the value of  $f_n$  in water is used to define  $V_r$ ). Note the additional cross-coupling effect due to cylinder rotation (Bishop 1959).

It is the intention of this note to summarize some of the CFD results which give insight into the origin of the response where it is a maximum. Further detailed description, including experiments, potential-flow analysis and CFD, will be given in Stansby & Rainey (2001).

## 2. RESULTS

It is first important to know how the flow around a rotating cylinder which is not responding depends on  $\alpha$ . Figure 1 shows streamline plots with  $Re_{cur} = 200$  and  $\alpha = 0.2, 0.25, 0.3, 0.5$  and  $1.0$ . For  $\alpha = 0.2$ , the stagnation point is detached from the cylinder surface (and on the  $y$ -axis); the streamlines are similar to those of a point vortex in a uniform stream. For  $\alpha = 0.25$  the stagnation point has moved closer the cylinder surface and a steady wake has started to form with  $\alpha = 0.3$ . Note that the stagnation point never actually reaches the surface due to the surface velocity. For  $\alpha = 0.5$ , the wake has increased in size but remains attached, fluctuating slightly about a mean position. For  $\alpha = 1$ , vortex shedding has become established, generating fluctuating lift and drag forces as shown in Figure 1(f). The dependence of these flows on  $\alpha$  is consistent with the early experimental visualisations shown in Prandtl & Tietjens (1934).

Computed variations of mean lift and drag with  $\alpha$  are shown in Figure 2 with  $Re_{cur} = 200$  and  $10^3$ , where drag coefficient is defined in the usual way,  $C_D = \text{drag}/(0.5 \rho U_{cur}^2 D)$ , and lift coefficient is defined as the fraction of the inviscid Magnus force,  $c_L = \text{lift}/(\rho U_{cur} \Gamma)$  where  $\Gamma = \pi D U_{rot}$  and  $\rho$  is water density. From the present computations, for small  $\alpha$ ,  $C_D$  is very small and  $c_L \rightarrow 1$  as  $\alpha \rightarrow 0$ , in agreement with the theoretical (asymptotic) analysis of Moore (1957).

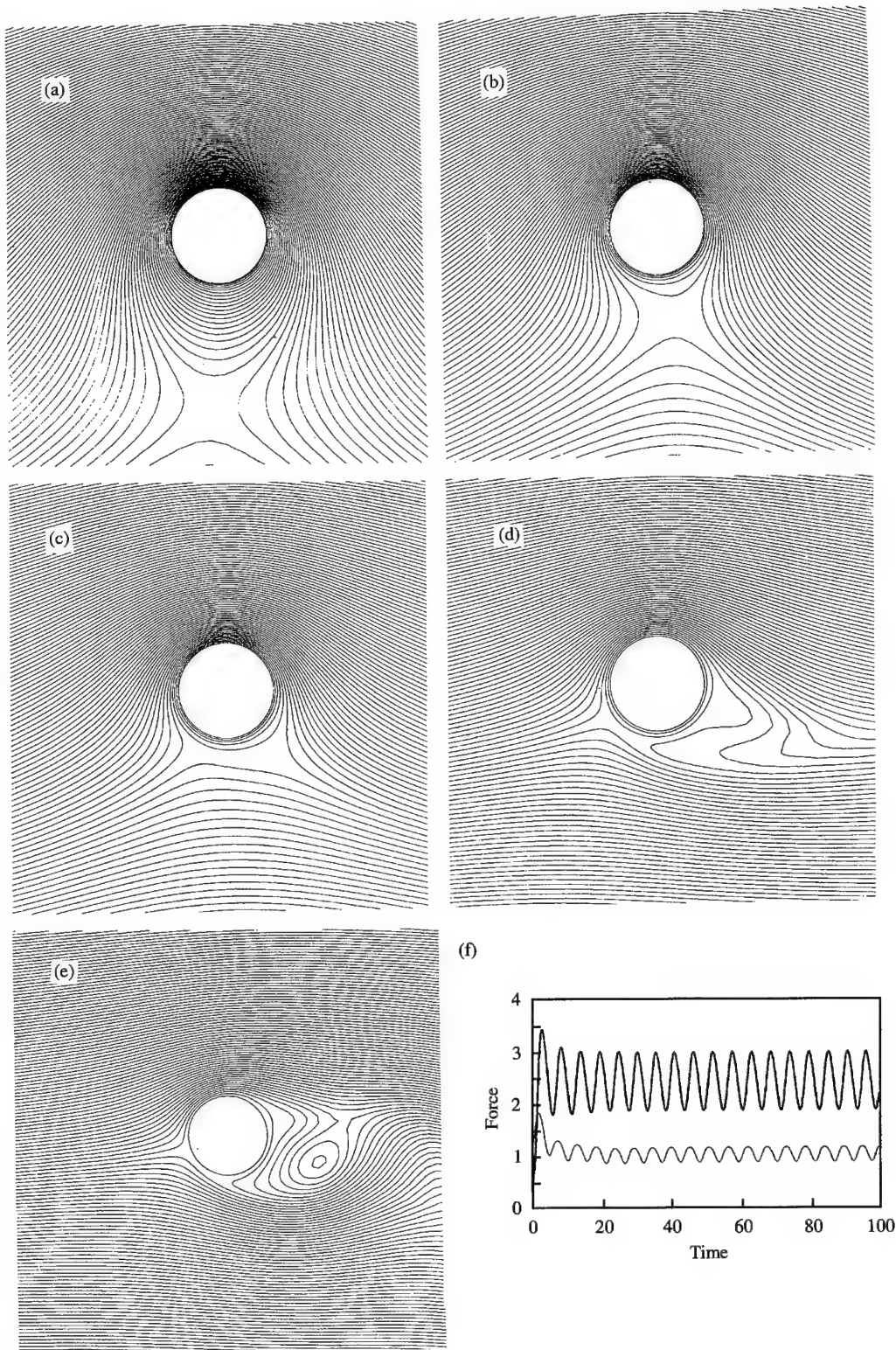


Figure 1. Computed streamline plots for a nonresponding rotating cylinder with  $Re_{cur} = 200$ : (a)  $\alpha = 0.2$ , (b)  $\alpha = 0.25$ , (c)  $\alpha = 0.3$ , (d)  $\alpha = 0.5$ , (e)  $\alpha = 1.0$ ; (f) lift and drag force variation with time for  $\alpha = 1.0$  (force normalized by  $\rho U_{rot}^2 D/2$ ). Flow is from left to right.



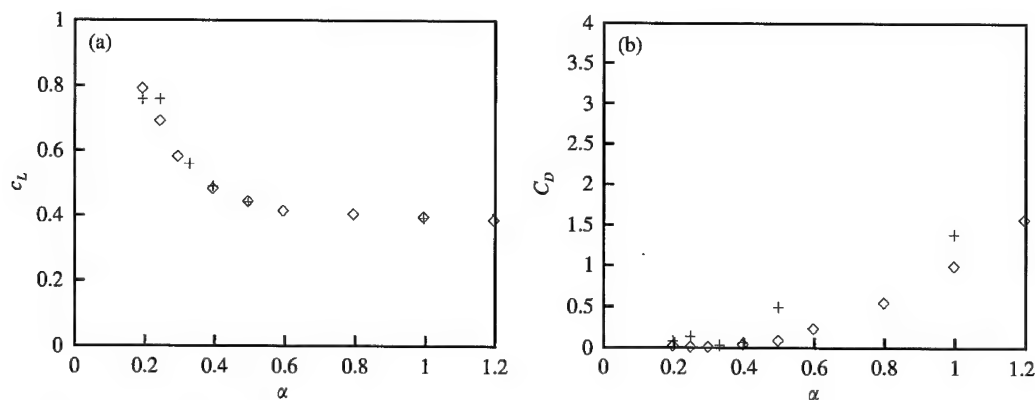


Figure 2. Computed mean force coefficients for a fixed rotating cylinder. (a)  $c_L$  variation with  $\alpha$ :  $\diamond$ ,  $\text{Re}_{\text{cur}} = 200$ ;  $+$ ,  $\text{Re}_{\text{cur}} = 10^3$ . (b)  $C_D$  variation with  $\alpha$ ; notation as in (a).

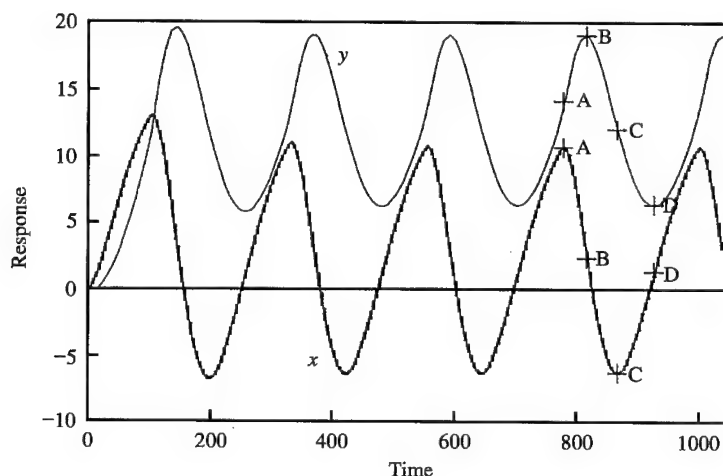
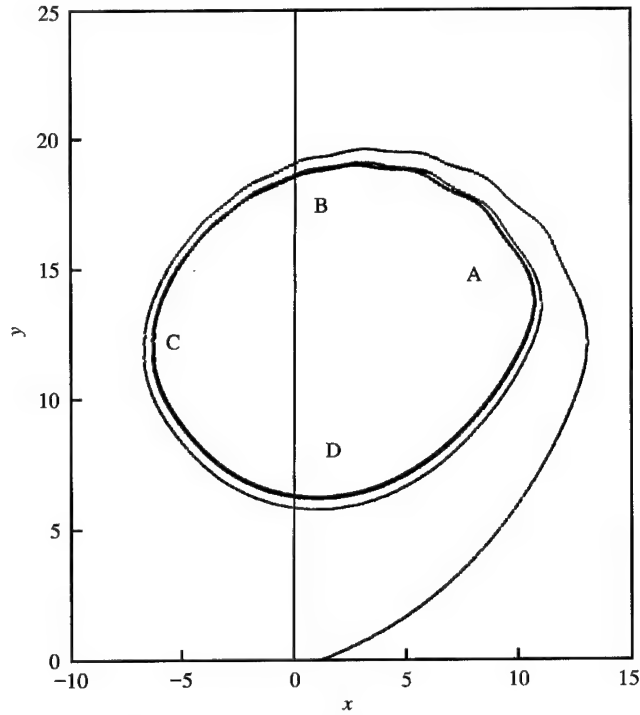
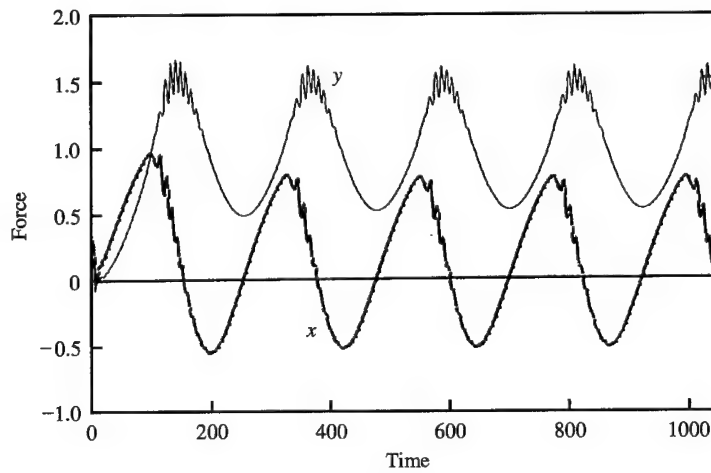


Figure 3. Variation of  $y/D$  and  $x/D$  with  $(tU_{\text{rot}}/D)$  for  $\bar{\alpha} = 0.3$  and  $V_r = 14$ .

When the cylinder is free to respond (for  $tU_{\text{rot}}/D > 5$ ) with the parameters defined above,  $x$ - and  $y$ -response variations with time are shown in Figure 3 with the corresponding  $y$  versus  $x$  plot in Figure 4, showing the orbital nature of the response and some small-amplitude, high-frequency effects. The anticlockwise, large orbital response is of opposite rotation to the clockwise cylinder rotation and the small, high-frequency response is of the same rotation. Points of maximum and minimum  $x$ -response are denoted by A and C and of maximum and minimum  $y$ -response by B and D. Time variations of force in the  $x$ - and  $y$ -directions,  $F_x$  and  $F_y$ , are shown in Figure 5 and can be seen to be in phase with response. The high-frequency force fluctuations are associated with the high-frequency response between A and C.

The "instantaneous"  $c_L$  and  $\alpha$  due to flow relative to the cylinder are of interest to determine whether quasi-steady assumptions are of value. It is well known, for example, that the flow-induced oscillation known as galloping, resulting from the variation of lift with angle of incidence for noncircular sections, is a quasi-steady phenomenon. Since  $\alpha$  is now an instantaneous value  $\bar{\alpha}$  is now used to define  $U_{\text{cur}}/U_{\text{rot}}$ . Instantaneous lift and drag coefficients and  $\alpha$  are based on the relative onset velocities:  $u_{\text{rel}} = U_{\text{cur}} - \dot{x}$ ,  $v_{\text{rel}} = -\dot{y}$ , so


 Figure 4. Variations of computed  $y$  responses with  $x$ , both normalized by  $D$ .

 Figure 5. Variations of  $x$ - and  $y$ -forces with time ( $tU_{\text{rot}}/D$ ). Force is normalized by  $\rho U_{\text{rot}}^2 D/2$ .

that the angle of incidence  $\theta = \tan^{-1} (v_{\text{rel}}/u_{\text{rel}})$  and velocity magnitude  $U = \sqrt{u_{\text{rel}}^2 + v_{\text{rel}}^2}$  gives an instantaneous  $\alpha = U/U_{\text{rot}}$ . The corresponding lift and drag forces transverse to and in line with the instantaneous onset velocity are given by

$$\begin{aligned} F_L &= F_y \cos \theta - F_x \sin \theta, \\ F_D &= F_x \cos \theta + F_y \sin \theta. \end{aligned} \quad (2)$$

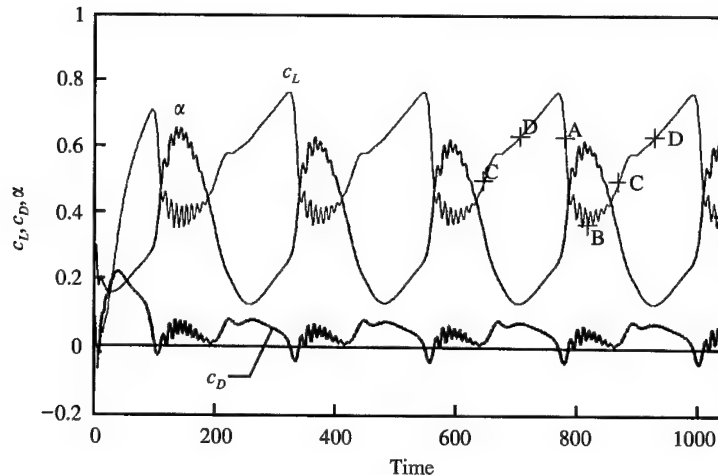


Figure 6. Variations of instantaneous  $c_L$ ,  $c_D$  and  $\alpha$  with time ( $tU_{rot}/D$ ) for  $\bar{\alpha} = 0.3$  and  $V_r = 14.0$ .

Lift is then normalized so that instantaneous  $c_L = F_L/(\rho U \Gamma)$  and  $c_D$  (as distinct from  $C_D$ ) is normalized in the same way for comparison with  $c_L$ . Variations of  $c_L$ ,  $c_D$ , and  $\alpha$  with time are shown in Figure 6 and points A–D are marked on the  $c_L$  curve.

From Figure 6 it is clear that a rapid increase in  $\alpha$  around time A coincides with a rapid decrease in  $c_L$ . Corresponding streamline and vorticity patterns (for flow relative to the cylinder) are shown in Figure 7 for times  $tU_{rot}/D = 780, 785, 790$  and  $795$ . For “small”  $\alpha$ , corresponding to times between C ( $tU_{rot}/D = 647$ ), and A ( $tU_{rot}/D = 782$ ), the stagnation point is well below the cylinder, typical of a nonresponding cylinder with  $\alpha < 0.25$ . As  $\alpha$  increases rapidly through time A, the stagnation point moves upwards towards the cylinder and an attached wake starts to form soon after time A, at about time 785. By time 790 a wake has formed, associated with a marked decrease in  $c_L$ . With high  $\alpha$  values around time B the attached wake fluctuates rapidly about some slowly varying position and this is responsible for the high-frequency components in the force variation, the period being about  $9D/U_{rot}$ . By time C the wake is about to collapse and the stagnation point move away from the cylinder as the cycle is completed.

Plots of  $c_L$  against  $\alpha$  are shown in Figure 8 with positions A–D marked. These are plotted for the second half of the time-series where the motion has become periodic. It can be seen that the gradient is generally negative and periodic dynamic response is associated with a pronounced hysteresis loop. It is interesting to see that the high-frequency behaviour is quite repeatable from one cycle to another. The  $c_L$  versus  $\alpha$  curve effectively defines the response since  $c_D$  is small in relation to  $c_L$ . Unfortunately, the curve is quite complex and different for each value of  $\bar{\alpha}$  [shown in Stansby & Rainey (2001)]. The variation of  $c_L$  with  $\alpha$  in a cycle is thus far removed from the mean  $c_L$  versus  $\alpha$  variation for a nonresponding cylinder.

It should be mentioned that these computations are extremely time-consuming. The high-frequency flow structures need to be resolved requiring a small time step while the slow oscillations require long times to cover several cycles. The above run required 4–5 days of computation time (each) on a modern workstation (Dec Alpha 600). A mesh with  $80 \times 80$  nodes was used with an inner radial mesh spacing of  $\sqrt{2\nu\Delta t}$ , where  $\Delta t$  is time step (the diffusion length scale), and an outer boundary at  $20D$ . A time step given by  $\Delta t U_{rot}/D = 0.05$  was used. Using a  $120 \times 120$  mesh with an outer boundary at greater distances showed convergence almost of within plotting accuracy.

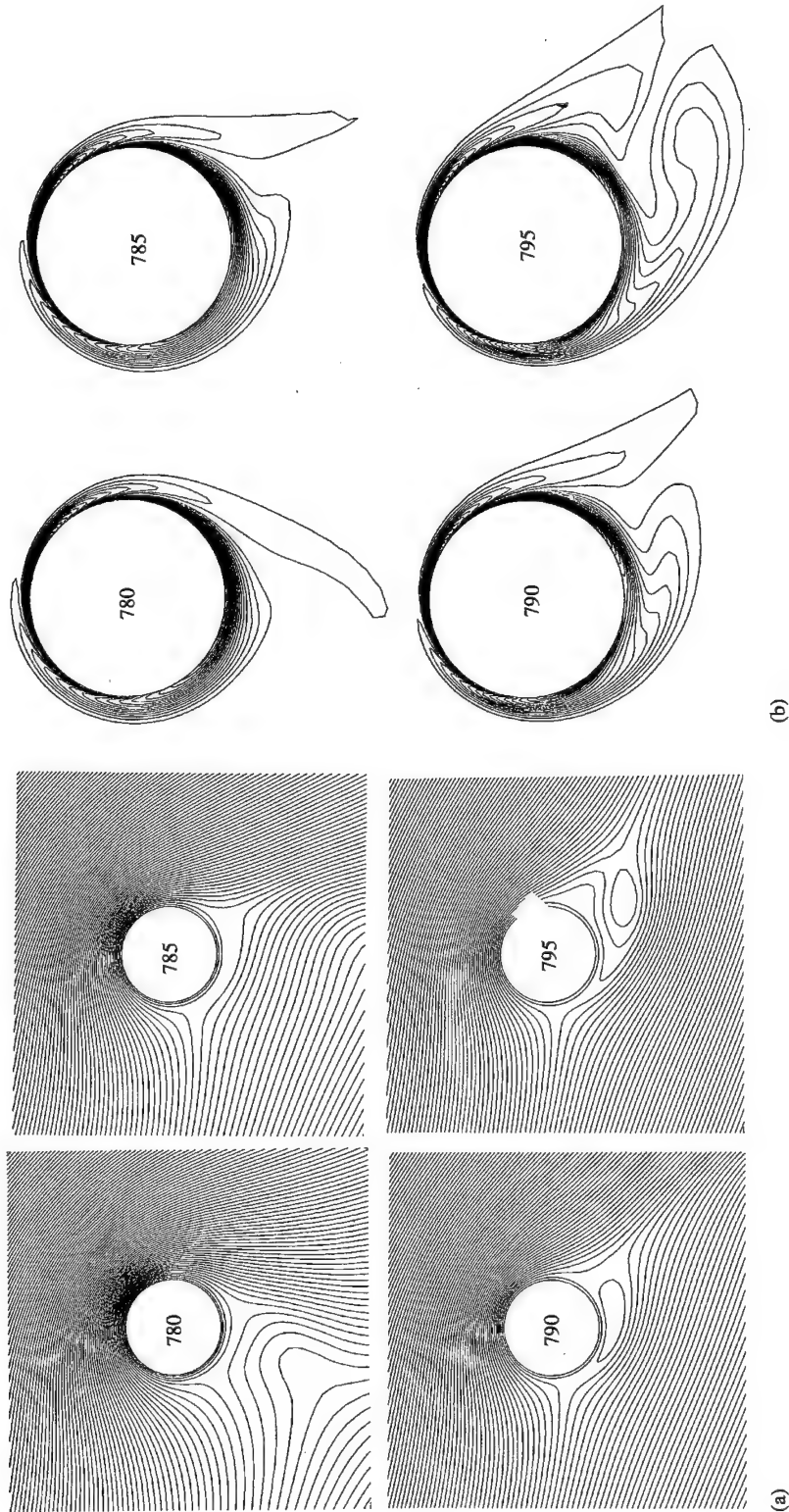


Figure 7. (a) Streamline plots at  $tU_{\infty}/D = 780, 785, 790$  and  $795$  (as marked on the figure). The flow is relative to the cylinder. (b) Vorticity plots for (a).

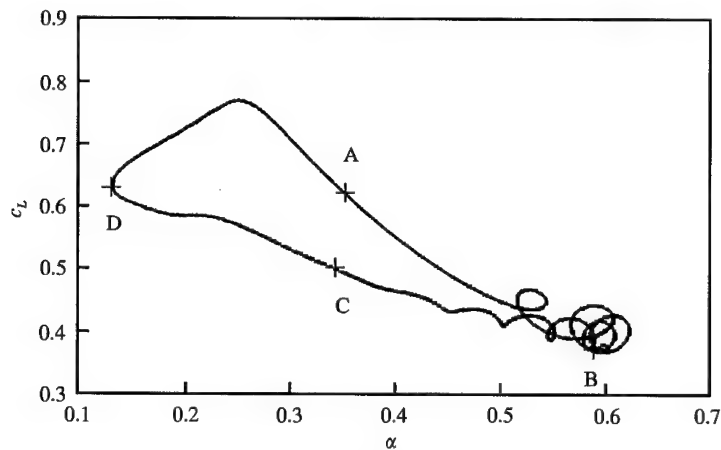


Figure 8. Plots of instantaneous  $c_L$  against  $\alpha$ .

### 3. CONCLUSIONS

The large orbital response of opposite rotation to that of the cylinder, observed in experiments, has been qualitatively reproduced by CFD for laminar 2-D flow. Maximum response occurs with  $\bar{\alpha} = 0.3$  and results for this case with  $V_r = 14$  are shown to aid understanding of the hydrodynamic mechanisms causing response. The response and force are shown to be in phase, and there is a rapid decrease in “instantaneous” lift coefficient  $c_L$  associated with rapid movement of the stagnation point towards the cylinder, causing wake formation. This is associated with a rapid increase in instantaneous  $\alpha$ . As the cycle progresses, wake formation eventually ceases and the stagnation point moves away from the cylinder;  $\alpha$  decreases and  $c_L$  increases until the dramatic changes noted above are repeated. There is some similarity with flows for a nonresponding cylinder at different (constant)  $\bar{\alpha}$  values. However, the plot of  $c_L$  versus  $\alpha$  shows that the forcing is far from quasi-steady with pronounced hysteresis. High-frequency, small-amplitude response is superimposed for part of the cycle; both the low- and high-frequency responses are consistent with elementary potential-flow analysis. A more general description and analysis is given in Stansby & Rainey (2001).

### ACKNOWLEDGEMENTS

This work was supported on a contract from Conoco (US) while the first author was at the Victoria University of Manchester.

### REFERENCES

- BISHOP, R. E. D. 1959 The vibration of rotating shafts. *IMechE. Journal of Mechanical Engineering Sciences* **1**, 50–65.
- COBBIN, A. M., STANSBY, P. K. & LESCHZNER, M. A. 1998 Modelling oscillatory flow around a cylinder using a RANS scheme. In *Proceedings of the ASME Conference on Offshore Mechanics and Arctic Engineering*, Lisbon.
- LIEN, F. S. & LESCHZNER, M. A. 1994 A general non-orthogonal finite-volume algorithm for turbulent flows at all speeds incorporating second-moment closure. Part 1. Numerical implementation. *Computational Methods in Applied Mechanics and Engineering* **114**, 123–148.

- MOORE, D. W. 1957 The flow past a rapidly rotating circular cylinder in a uniform stream. *Journal of Fluid Mechanics* **2**, 541–550.
- PRANDTL, L. & TIETJENS, O. G. 1934 *Applied Hydro- and Aeromechanics*. New York: McGraw Hill.
- STANSBY, P. K. & RAINEY, R. C. T. 2001 On the orbital response of a rotating cylinder in a current. *Journal of Fluid Mechanics* (in press).



## FORCES AND WAKE MODES OF AN OSCILLATING CYLINDER

J. CARBERRY, J. SHERIDAN

*Department of Mechanical Engineering, Monash University  
Clayton, 3800, Australia*

AND

D. ROCKWELL

*Department of Mechanical Engineering and Mechanics, Lehigh University  
Bethlehem, PA 18015, U.S.A.*

(Received 31 August 2000, and in final form 27 November 2000)

This investigation considers the wake states of a cylinder subjected to forced oscillations at frequencies close to the Karman frequency. Two distinctly different wake states are observed. The emphasis is on the transition between these states, which is characterized in terms of the lift force on the cylinder and the instantaneous patterns of vortex structures in the near-wake. As the frequency of oscillation increases, there is simultaneously an abrupt jump in the lift force and a change in the mode of vortex shedding. The jump in the lift force involves a sharp increase in the magnitude of the lift coefficient and a phase shift of the order  $180^\circ$ . The corresponding mode change involves an alteration in both the timing of the vortex initially shed from the cylinder and the overall pattern of vortices in the near-wake. Whilst previously these changes have been observed individually in separate forced vibration investigations, we show conclusive evidence that these two events are intrinsically linked. Moreover, for a narrow band of frequencies, a self-excited transition is possible, where the wake state changes while the cylinder oscillates at a constant frequency.

© 2001 Academic Press

### 1. INTRODUCTION

FLOW PAST A STATIONARY CYLINDER results in organized vortex shedding at a characteristic frequency  $f_o$ . Controlled excitation of the cylinder at frequencies  $f_e$ , close to the frequency  $f_o$  of the natural instability, results in significant changes in both the wake structure and the forces on the cylinder.

The interaction of a flow field and an oscillating cylinder has received extensive investigation. An early study by Bishop & Hassan (1963) found that, as  $f_e/f_o$  increased through unity, the lift force showed a sharp increase in amplitude and a phase “jump” of close to  $180^\circ$ . Similar changes in the lift force have been observed by a number of researchers including Sarpkaya (1995), Gopalkrishnan (1993) and Staubli (1993). Separate studies have shown that there are also significant changes in the vortex patterns of the near-wake around  $f_e/f_o = 1$ ; these investigations have focussed on either qualitative or quantitative visualization. Williamson & Roshko (1988), in their extensive mapping of vortex shedding modes, observed a change in the mode of vortex shedding from 2P to 2S. Changes in the wake have also been described in terms of the timing of the initially formed vortex: Ongoren & Rockwell (1988) and Gu *et al.* (1994) found that as  $f_e/f_o$  increased there was a systematic

shortening of the wake, until at a critical  $f_e/f_o$  close to unity, there was an abrupt change in the sign of the initial vortex. This change in timing is related to an alteration of the near-wake topology. Furthermore, the near-wake of an oscillating cylinder is directly analogous to the wake from the thick trailing edge of a plate. Staubli & Rockwell (1989) and Lotfy & Rockwell (1993) have defined a change in timing of the initially shed vortex similar to that of the foregoing cases of the wake from a circular cylinder.

A link between the wake mode and forces on the cylinder was established numerically by Blackburn & Henderson (1999). They found that a change of the lift force on the oscillating cylinder was associated with a change in the timing of the initially shed vortex. However, they did not observe the 2P mode of vortex shedding described by Williamson & Roshko (1988). This may have been due to their simulation being two-dimensional, and also at a low amplitude of oscillation and Reynolds number. They also found that, for a given  $f_e/f_o$ , the wake could exhibit two different states and that these states were not always stable. Staubli & Rockwell (1989) show that, for controlled oscillations of the thick trailing edge of a plate, there is a relationship between the switch in timing of the initially shed vortex and an abrupt change in the phase and magnitude of the lift force determined from pressure measurements.

Both the jump in the properties of the lift force and the change in either the mode of vortex shedding or the sign of the initial vortex, have been observed over a wide range of Reynolds numbers and oscillation amplitudes. While the finer details of these changes may vary with flow parameters such as  $Re$  and  $A/D$ , the abrupt changes described above appear to be a robust feature of these flows. The present work is an experimental investigation of the link between changes in the wake of an oscillating cylinder and the forces on the cylinder. In particular, we focus on patterns of vorticity and their relationship to the amplitude and phase of the unsteady lift.

An interesting aspect of the forced oscillation of a cylinder is how it relates to self-excited vibration induced by vortex shedding. Recently, the elastically mounted cylinder has received considerable attention, particularly for cases with low mass damping. As the reduced velocity is varied, there are abrupt changes in the amplitude of oscillation and the phase of the lift force. These features have allowed the flow to be categorized into different branches, as presented by Khalak & Williamson (1999). Brika & Laneville (1993) found that, as their long vibrating cable moved from the initial branch to the lower branch, there appeared to be a corresponding change in the mode of vortex shedding from 2S to 2P. More recently Govardhan & Williamson (2000) have presented evidence that, as the reduced velocity decreases (analogous to an increase in  $f_e/f_o$ ), the movement of the flow state from the upper or lower branch to the initial branch corresponds to a change in the mode of vortex shedding from 2P to 2S, and a change in the phase of the vortex lift force. They also observed a change in the timing of vortex shedding and therefore a change in the sign of the initially formed vortex. The changes in the forces and wake modes in vortex-induced vibrations appear to have many features in common with the simplified case where the cylinder oscillations are forced.

## 2. EXPERIMENTAL METHOD

The experiments were performed in a free-surface water channel at Lehigh University. The working section had a width of 914 mm, depth 609 mm and was 4928 mm long. The free-stream velocity  $U$  was  $0.090 \text{ m s}^{-1}$  with a turbulence level of less than 0.1%. A schematic of the experimental apparatus is shown in Figure 1. The 317.5 mm long cylinder had a diameter  $D$  of 25.4 mm giving an aspect ratio of 12.5. The Reynolds number based on  $U$  and  $D$  was  $2.3 \times 10^3$  and the Kármán frequency,  $f_o$ , of vortex formation from the corresponding stationary cylinder was 0.748 Hz. A high-resolution stepper motor system



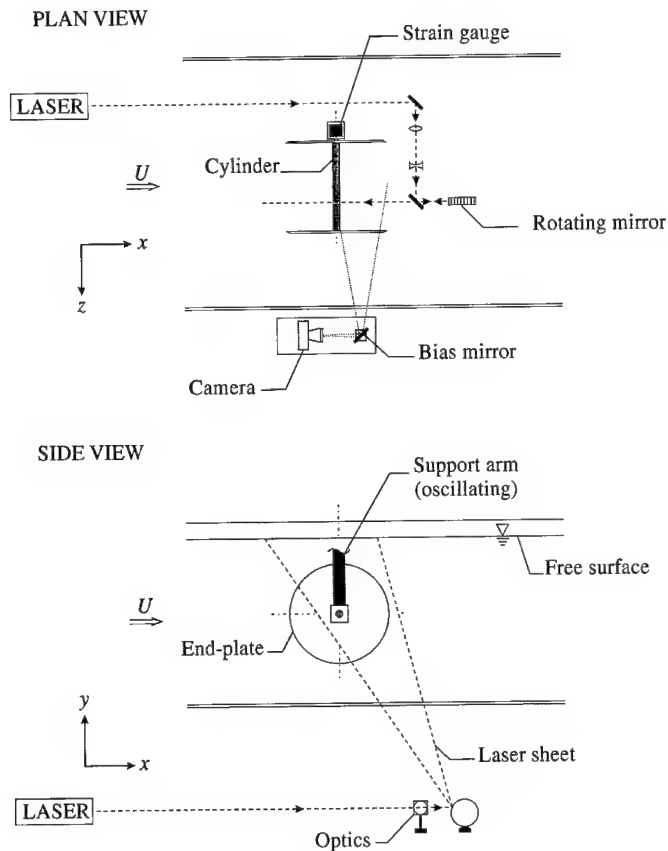


Figure 1. Schematic of experimental system.

was used to oscillate the cylinder transverse to the free stream such that its vertical motion was given by

$$y(t) = A \sin(2\pi f_e t), \quad (1)$$

where  $A$  is the amplitude of oscillation and  $f_e$  is the frequency of oscillation.

The amplitude of the oscillations was held constant at  $A/D = 0.5$ , while the frequency was varied over the range  $0.5 \leq f_e/f_o \leq 1.4$ . For each value of  $f_e/f_o$ , the cylinder started oscillations from rest at  $t = 0$ , corresponding to the beginning of the force traces. Following each experiment, the cylinder remained stationary in the free stream for a time equivalent to more than 500 Kármán cycles.

A cross-section of the flow was illuminated by a laser sheet, as shown in Figure 1. A transparent laser window incorporated into the cylinder allowed the laser to illuminate the flow on the opposite side of the cylinder. The velocity field around the cylinder was measured using a laser scanning version of high-image-density particle image velocimetry, described by Rockwell *et al.* (1993). The images were recorded on high-resolution 35 mm film and digitised at 106 pixels/mm. The velocity field was calculated by employing a single-frame cross-correlation technique. An interrogation window of  $90 \times 90$  pixels and overlap ratio of 0.50 resulted in a velocity field with 3700 vectors.

The span-averaged forces on the cylinder were measured using strain gauges in a full Wheatstone bridge configuration. For each experiment 5000 data points were sampled at

a Nyquist frequency of 6.25 Hz. The inertia forces due to the vertical acceleration of the cylinder were calculated and subtracted from the lift force. For the range of frequencies studied, the wake was "locked-on" to the cylinder oscillation and the dominant frequency in the lift forces was  $f_e$ . Thus, the lift force can be approximated by a sinusoidal function:

$$\text{Lift}(t) \approx (\frac{1}{2} \rho U^2 D L) C_L \sin(2\pi f_e t + \phi_{\text{lift}}), \quad (2)$$

where  $C_L$  is the amplitude of the lift coefficient and  $\phi_{\text{lift}}$  is the phase with respect to the cylinder displacement,  $y(t)$ . Both  $C_L$  and  $\phi_{\text{lift}}$  were calculated in the time domain using data points corresponding to more than 400 cylinder oscillations.

### 3. RESULTS AND DISCUSSION

#### 3.1. RELATION OF LIFT FORCES TO WAKE MODES

The amplitude and phase of the lift coefficient are shown as a function of  $f_e/f_o$  in Figure 2(a). At low values of  $f_e/f_o$ , the lift force has a small amplitude and is approximately out-of-phase

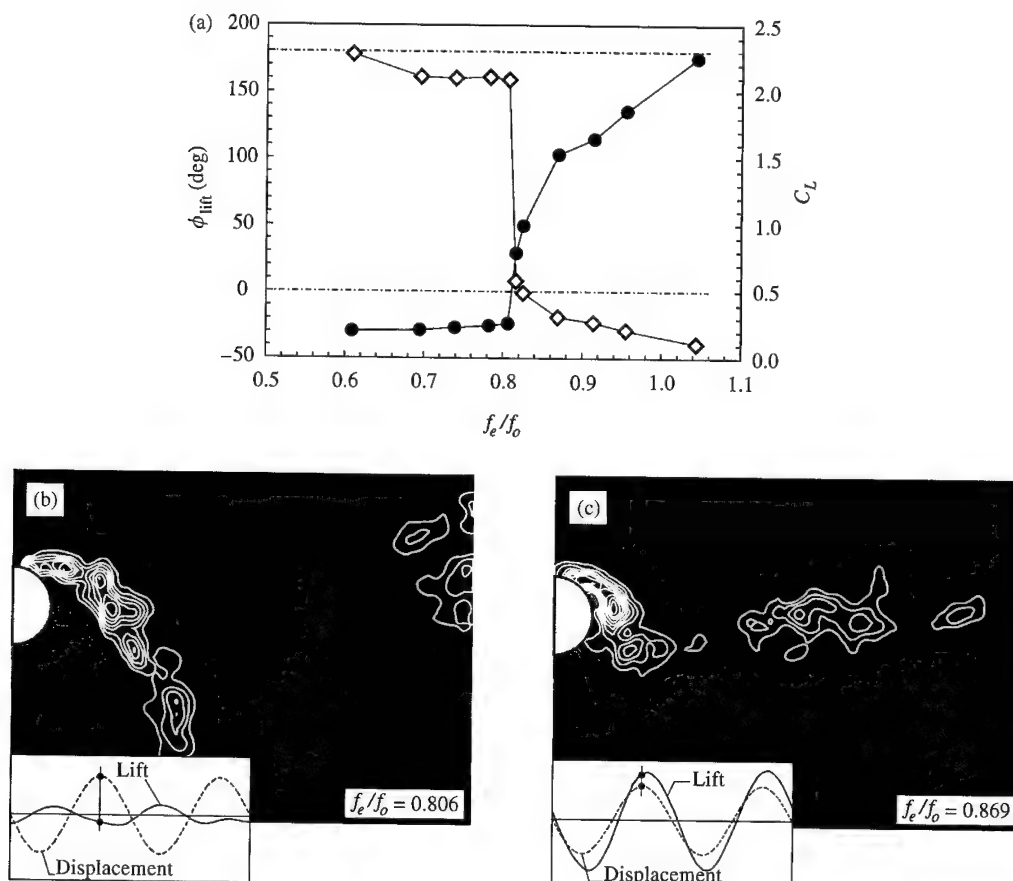


Figure 2. (a) Lift phase,  $\phi_{\text{lift}}$ , and amplitude of the lift coefficient  $C_L$  as a function of frequency ratio  $f_e/f_o$ , in which  $f_e$  is the excitation frequency and  $f_o$  is the Kármán frequency:  $\diamond$ , lift phase;  $\bullet$ ,  $C_L$ . Instantaneous vorticity fields are shown in (b) and (c). The time trace inserts show the instantaneous lift and displacement, where the timing of the image acquisition is indicated by a small circle.

with the cylinder displacement,  $y$ . As  $f_e/f_o$  increases, the lift properties do not vary significantly until  $f_e/f_o = 0.81$ . At this value, there is simultaneously an abrupt increase in  $C_L$  and a drop in  $\phi_{\text{lift}}$  such that the lift force is approximately in-phase with the cylinder oscillation. The sharp jump in the lift properties has been observed in previous studies: Bishop & Hassan (1963), Sarpkaya (1995), Gopalkrishnan (1993) and Staubli (1993). As  $f_e/f_o$  increases further, the lift properties change gradually:  $C_L$  increases and  $\phi_{\text{lift}}$  decreases. The simultaneous jump in  $C_L$  and  $\phi_{\text{lift}}$  is indicative of significant changes in the cylinder wake. The sharp change in the lift properties is referred to herein as a transition from a low-frequency lift force to high-frequency lift force. The properties of the lift force can now be associated with either low frequencies before transition, or high frequencies after transition. Before transition,  $C_L$  is small and  $\phi_{\text{lift}}$  is large, while after transition  $C_L$  is large and  $\phi_{\text{lift}}$  is small, and generally negative.

The value of the lift phase indicates the direction of energy transfer between the cylinder and the fluid. When  $0 < \phi_{\text{lift}} < 180^\circ$ , there is positive energy transfer from the fluid to the cylinder. The oscillation of an elastically mounted cylinder requires positive energy transfer to the cylinder and therefore the lift phase is restricted to values  $0 \leq \phi_{\text{lift}} \leq 180^\circ$ . However, when the cylinder is forced to oscillate, all values of  $\phi_{\text{lift}}$  are physically possible. For the case presented here, the direction of energy transfer went from positive to negative as  $\phi_{\text{lift}}$  passed through  $0^\circ$ . Generally speaking, for forced oscillations, the value of  $\phi_{\text{lift}}$ , and therefore the direction of energy transfer, may also depend on  $Re$  and  $A/D$ .

We now consider transition in terms of the structure of the near-wake. The instantaneous vorticity fields in Figure 2(b, c) show the wake structure for values of  $f_e/f_o$  on either side of transition. The images, both acquired at the top of the cylinder's oscillation cycle, show two distinctly different wakes. Figure 2(b) is representative of the wake mode at low frequencies before transition, while Figure 2(c) is representative of the wake mode after transition. Comparing the two cases, we see that the vortex structures in the near-wake are of opposite sign. At  $f_e/f_o = 0.806$  a negative vortex structure is formed from the attached shear layer and a positive initial vortex forms close to the cylinder. After transition, at  $f_e/f_o = 0.869$ , the structure that is shed into the wake is positive and the initial vortex is negative. The change in sign of the vortex structures is consistent with the shift of approximately  $180^\circ$  in the lift phase. In the present investigation, a similar change in timing was also evident at lower amplitudes of oscillation; however, in these cases the formation of the 2P wake mode was not well defined. This finding is consistent with previous work at low amplitudes, including that of Gu *et al.* (1994) and will be reported in a forthcoming publication.

We now consider in more detail the wake modes on either side of the transition region. Figure 3 shows the time evolution of the vortex structures during the downwards stroke of the cylinder. At the top of the oscillation, the low-frequency wake ( $f_e/f_o = 0.806$ ) has a long negative vortex structure extending across the back of the cylinder and into the lower half of the wake. However, at the same phase of the oscillation cycle the attached negative vorticity in the high frequency wake ( $f_e/f_o = 0.869$ ) takes the form of a small concentrated structure at the back of the cylinder. As the cylinder moves downwards, the negative vorticity in the low-frequency wake is shed as two separate structures. The vorticity from the end of the attached shear layer is shed into the lower half of the wake and forms a counter-rotating pair with previously shed vorticity. The negative vorticity closer to the cylinder is shed into the upper wake, and eventually forms a second counter-rotating pair during the next half-cycle. Thus, the vorticity forms two counter-rotating pairs per cycle, which is commonly described as the 2P mode of shedding. However, the mode of vortex shedding in the high-frequency wake is clearly different. As the cylinder moves downwards, a single positive vortex is shed. In the next half-cycle, the shedding of a single negative vortex results in the classical Karman, or 2S, mode of shedding. At the transition from the low-frequency state to

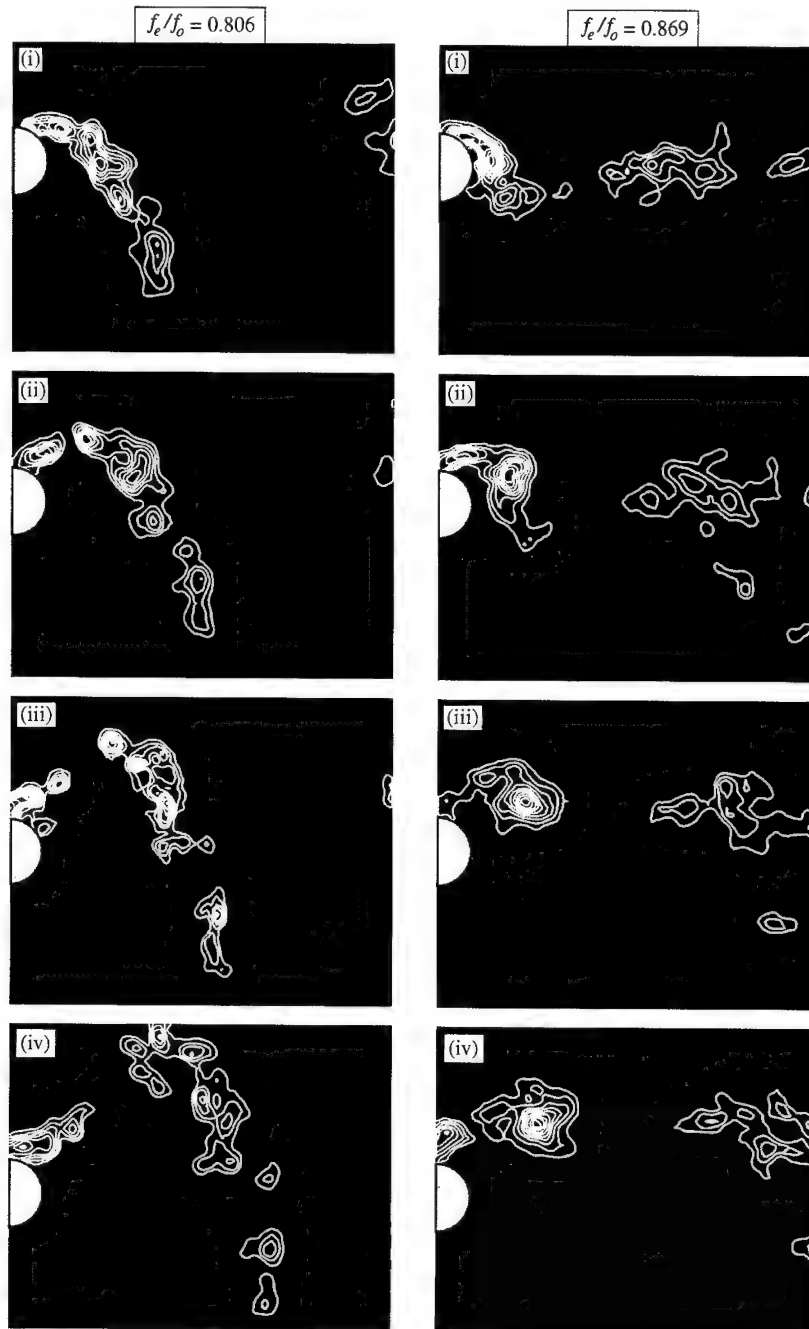


Figure 3. The evolution of vortex structures during the downward stroke of the cylinder. The left-hand side column shows the low-frequency wake mode before transition ( $f_e/f_o = 0.806$ ), while the high-frequency wake mode after transition ( $f_e/f_o = 0.869$ ) is on the right. The position of the cylinder for each image is shown in the displacement inserts beneath the fields.

the high-frequency state, we observed not only a change in the timing of vortex shedding, but also a change in the mode of vortex shedding.

The two modes of vortex shedding generate significantly different distributions of vorticity downstream of the cylinder. In the high-frequency wake, negative vorticity is found predominantly in the upper half of the wake, while the lower wake is dominated by positive vorticity. However, for the low-frequency wake, vorticity of both signs is found throughout the vertical extent of the wake.

The wake states either side of transition can now be described in terms of both the lift force and the structure of the near-wake. For the low-frequency wake state,  $C_L$  is small and  $\phi_{\text{lift}}$  is large, while the structure of the near wake is characterized by the wake shown in Figure 2(b), with a positive initial vortex. Whilst for the high-frequency wake state  $C_L$  is large,  $\phi_{\text{lift}}$  is small and the near-wake structure is characterized by the wake in Figure 2(c).

### 3.2. TRANSITION

In order to understand the nature of the transition between wake states we focused on frequencies close to transition. Representative images are shown in Figure 4. At each value of  $f_e/f_o$ , the wake state at  $t = 0$  is that of a stationary cylinder in a free stream. For  $t > 0$  the cylinder oscillates at a constant frequency and the oscillating wake appears to be fully established in less than 10 oscillations. For a narrow band of frequencies close to transition, after many oscillations, self-excited changes were observed in the lift properties. We will now show that these changes correspond to a self-excited transition from the low-frequency state to the high-frequency state.

The lift trace for a typical self-excited transition is shown in Figure 4(a). The corresponding instantaneous values of the amplitude and phase of the lift coefficient are shown in Figure 4(b). In this example, the transition begins after more than 150 oscillation cycles. For time less than 97 s the lift forces are consistent with the low-frequency state described previously: the lift coefficient is of small amplitude and the lift phase is large. Conversely, for times after 128 s the lift force is consistent with the high-frequency wake state. In-between these two states is a transient transition region where the lift force is not consistent with either state. The expanded time trace in Figure 4(c) shows the changing relationship between the lift and displacement within the transition region.

It is expected that the self-excited transition in the magnitude and phase of the lift coefficient corresponds to a change in the structure of the near-wake. The wake patterns in both Figures 4(d) and (e) were acquired at the top of the oscillation cycle, at the times indicated on the lift trace. These images are representative of the wake structures either side of the self-excited transition. Despite the fact that the oscillation frequency is constant, these wake states are clearly different. The wake structure shown in Figure 4(d) corresponds to values of lift magnitude and phase that are consistent with the low-frequency state. The wake is shedding in the 2P mode and is clearly consistent with the steady-state low-frequency state, described in conjunction with Figure 2(b). Similarly, Figure 4(e) correlates well with the steady-state high-frequency wake mode of Figure 2(c). Thus, the wake states either side of the self-excited transition are consistent with the wake states at much lower and higher frequencies.

For the self-excited transition, the instantaneous magnitude and phase of the lift coefficient change smoothly from their low-frequency values to high-frequency values. However, within this transition region we observe that the change in  $\phi_{\text{lift}}$  occurs slightly before the change in  $C_L$ . After transition, there is some variation in the magnitude and phase of the lift coefficient, which was not observed at higher values of  $f_e/f_o$ . During this variation, there is a clear inverse relationship between the instantaneous values of  $C_L$  and  $\phi_{\text{lift}}$ ; however, once

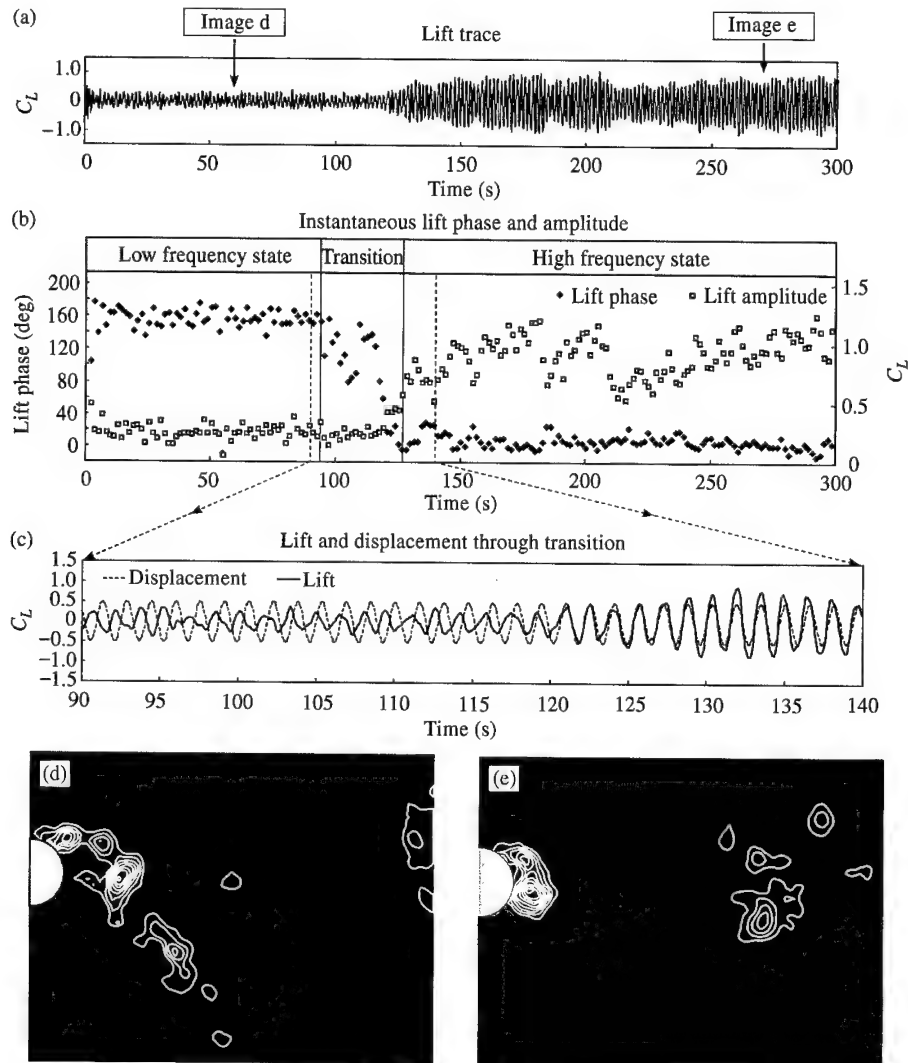


Figure 4. The lift time trace (a) shows a self-excited transition occurring after more than 150 oscillations cycles at a constant excitation frequency of  $f_e/f_o = 0.815$ . The corresponding variation in the instantaneous values of the lift phase and amplitude of the lift coefficient are shown in (b). The lift and displacement traces during the transition are shown in more detail in (c). The wake modes on either side of the self-excited transition are shown at  $t = 60$  s corresponding to image (d), and at  $t = 270$  s represented as image (e). Both images were acquired at the top of the oscillation cycle.

the high-frequency state was established by a self-excited transition, a return to the low-frequency state was never observed.

#### 4. CONCLUSIONS

In this paper we have described a transition between two wake states which exhibit distinctly different lift forces and wake modes. The interaction between the natural instability of the wake and the forced oscillation plays an important role and the flow properties depend strongly on  $f_e/f_o$ . At values of  $f_e/f_o$  close to unity the changing relationship between these instabilities results in an abrupt change in the wake state.

Our investigation showed that changes in the lift force are intrinsically related to changes in the structure of the near-wake. As  $f_e/f_o$  increased there was a transition from a small amplitude lift force, which was approximately out-of-phase with the cylinder oscillations, to a large amplitude in-phase lift force. Simultaneously, there was a change in the sign of the initial vortex and the mode of vortex shedding went from 2P to 2S. The change in the mode of vortex shedding appears to be related to the change in the timing of vortex formation, which is in turn related to the shift in the lift phase. For forced oscillations of the cylinder over a wide range of amplitudes, further consideration should be given to the occurrence of a change in timing of the initially shed vortex as a consistent requirement for the jump in the lift properties, as well as its relationship to the occurrence of, and transition between, the 2P and 2S modes.

For a narrow band of  $f_e/f_o$ , we observed a self-excited transition at a constant frequency of oscillation. Immediately following start-up, the lift force and wake mode conformed to the low-frequency wake state. After a number of oscillations, the lift force and wake mode changed smoothly until they were both consistent with the high-frequency wake state. The self-excited transition depends on the relative stability of three wake states: the low- and high-frequency wake states and also the wake state of the stationary cylinder before start-up. Therefore, the existence of this self-excited transition and the way in which it occurs may also depend on flow parameters such as  $A/D$  and  $Re$ .

#### ACKNOWLEDGEMENTS

Primary support for this research program was provided by the Office of Naval Research Grant N00014-94-1-0815, P0006, monitored by Dr Thomas Swean, and by the Australian Research Council through the ARC Large Grant A89702238. In addition, supplemental support was provided by NSF Grant CTS-9803734. Ms Carberry acknowledges support through an Australian Postgraduate Award. The authors gratefully acknowledge this financial support.

#### REFERENCES

- BISHOP, R. E. D. & HASSAN, A. Y. 1963 The lift and drag forces on a circular cylinder in a flowing fluid. *Proceedings of Royal Society (London) A* **277**, 32–50.
- BLACKBURN, H. M. & HENDERSON, R. D. 1999 A study of two-dimensional flow past an oscillating cylinder. *Journal of Fluid Mechanics* **385**, 255–286.
- BRIKA, D. & LANEVILLE, A. 1993 Vortex-induced vibrations of a long flexible circular cylinder. *Journal of Fluid Mechanics* **250**, 481–508.
- GOPALKRISHNAN R. 1993 Vortex induced forces on oscillating bluff cylinders. Ph.D. thesis, Massachusetts Institute of Technology, Cambridge, MA, U.S.A.
- GOVARDHAN, R. & WILLIAMSON, C. H. K. 2000 Modes of vortex formation and frequency response of a freely vibrating cylinder. *Journal of Fluid Mechanics* **420**, 85–130.
- GU, W., CHYU, C. & ROCKWELL, D. 1994 Timing of vortex formation from an oscillating cylinder. *Physics of Fluids* **6**, 3677–3682.
- KHALAK, A. & WILLIAMSON, C. H. K. 1999 Motions, forces and mode transitions in vortex-induced vibrations at low mass-damping. *Journal of Fluids and Structures* **13**, 813–851.
- LOTFY, A. & ROCKWELL, D. 1993 The near-wake of an oscillating trailing edge: mechanisms of periodic and periodic response. *Journal of Fluid Mechanics* **251**, 173–201.
- ONGOREN, A. & ROCKWELL, D. 1988 Flow structure from an oscillating cylinder Part1. Mechanisms of phase shift and recovery in the near wake. *Journal of Fluid Mechanics* **191**, 197–223.
- ROCKWELL, D., MAGNESS, C., TOWFIGHTI, J., AKIN, O. & CORCORAN, T. 1993 High image-density particle image velocimetry using laser scanning techniques. *Experiments in Fluids* **14**, 181–192.
- SARPKAYA, T. 1995 Hydrodynamic damping, flow-induced oscillations, and biharmonic response. *ASME Journal of Offshore Mechanics and Arctic Engineering* **117**, 232–238.

- STAUBLI, T. 1993 Untersuchung der oszillierenden Kräfte am querangeströmten, schwingenden Kreiszylinder. Dissertation ETH 7322.
- STAUBLI, T. & ROCKWELL, D. 1989 Pressure fluctuations on an oscillating trailing edge. *Journal of Fluid Mechanics* **203**, 307–346.
- WILLIAMSON, C. H. K. & ROSHKO, A. 1988 Vortex formation in the wake of an oscillating cylinder. *Journal of Fluids and Structures* **2**, 355–381.



## ON CIRCULAR CYLINDERS UNDERGOING TWO-DEGREE-OF-FREEDOM FORCED MOTIONS

D. JEON AND M. GHARIB

*Graduate Aeronautical Laboratories, California Institute of Technology  
Pasadena, CA 91125, U.S.A.*

(Received 15 August 2000, and in final form 15 November 2000)

Cylinders undergoing one- and two-degree-of-freedom (DoF) motions were studied. Since the forces on the cylinder fluctuate in both the streamwise and transverse direction, it is believed that such motions are more natural than transverse-only vibrations. A set of experiments was conducted in a water tunnel using both digital particle image velocimetry (DPIV) and force measurements. Several qualitative differences were noted, including a dramatic increase in phase coherence and the disappearance of the “2P” mode. It appears that the transverse motion sets the frequency of shedding, and the streamwise motion the relative phase therein.

© 2001 Academic Press

### 1. INTRODUCTION

ALTHOUGH THE PHENOMENON of vortex-induced vibration of bluff bodies has been studied extensively, the vast majority of these studies have concentrated solely on transverse vibrations. Works by Feng (1968), Sarpkaya (1979), Khalak & Williamson (1999), and Gharib (1999), among many others, have highlighted the behavior of an elastically mounted cylinder free to vibrate in the transverse direction. Various response curves have been measured showing the amplitude, frequency, and phase of cylinders undergoing vortex-induced vibration. The effects of damping and mass ratio and Reynolds number have also been scrutinized. However, since the fluctuating forces responsible for these oscillations have unsteadiness in both lift and drag, the role of streamwise vibrations cannot be ignored. Although the lift fluctuation is generally quite a bit larger than the drag fluctuation, the resultant streamwise vibration must have some effect upon the wake. Previous studies that have looked at two-degree-of-freedom (2-DoF) mechanical systems have indicated that while the behavior is qualitatively similar, some interesting differences exist. For example, Gharib (1999) found that his 2-DoF free vibration cases were much less likely to exhibit lock-in behavior (where the wake locks to the natural frequency of the structure for some range of parameters).

Forced vibration studies have been even more focused on 1-DoF vibrations. Two particular useful papers on 1-DoF forced motion are Bishop & Hassan (1964) and Williamson & Roshko (1988). Bishop & Hassan demonstrated that a phase shift in the lift force occurs near when the vibrations are on either side of the Strouhal frequency of the stationary cylinder. The wake seems to aid the motion of the cylinder at some frequencies and oppose it at others. Williamson & Roshko demonstrated a connection between the motions in this region of parameter space with a change in wake shedding patterns. The wake was shown to change from the so-called “2S” (two single vortices per cycle) to the “2P” (two opposite-signed pairs of vortices per cycle) mode near the Strouhal frequency. This change in mode was associated with the change in lift phase.

Using the results from previous 1-DoF forced vibration studies, a series of 2-DoF forced vibration cases was analyzed to better understand what differences result from the addition of streamwise motion. Since it is believed that nature prefers a figure-eight-type motion, this study was undertaken to discern the effects of the addition of streamwise motion, and to see which effects a transverse-only experiment would miss.

## 2. THEORY

Since the goal of this work was to study natural vibrations, motion parameters were chosen accordingly. Most researchers report typical free-vibration amplitudes slightly above 0.5 diameters — with cases of peak values in excess of 1 diameter being reported by some researchers — so, that value was chosen for the transverse vibration amplitude. Transverse frequencies were chosen from the Williamson & Roshko (1988) mode map, such that cases in the “2S” and “2P” regions were represented. (The corresponding positions on the 1-DoF parameter map are shown in Figure 1.) Streamwise frequency was fixed to be double the transverse frequency in order to generate the figure-eight patterns commonly observed. Streamwise amplitude was held at 0.1 diameters, or one-fifth of the transverse amplitude; this produced figure-eight patterns of approximately the correct aspect ratio.

This left one main parameter — the relative phase between the streamwise and transverse motion. The phase is defined relative to the transverse motion in the following manner: for a given transverse motion  $\sin(\omega t)$ , phase  $\phi$  is such that the streamwise motion is  $\sin(2\omega t + \phi)$ . The phase value tends to drift in free-vibration cases (along with frequency and amplitude), but is usually in the range of 0 to  $-45^\circ$ . Consequently, phases of 0 and  $-45^\circ$  were chosen for examination. (Negative 45 degrees of phase results in a figure-eight pattern with the lobes bent slightly downstream.)

It is worth noting that this represents a very small perturbation on the overall motion. As shown in Figure 2, if one were to plot the  $x$ - $y$  position of the cylinder through time, motions with and without the streamwise vibration are virtually identical. Since the cylinder moves about 5 diameters downstream per cycle, it is not surprising that a 0.1 diameter perturbation is nearly invisible on this plot. However, the effect on the wake is not so minuscule.

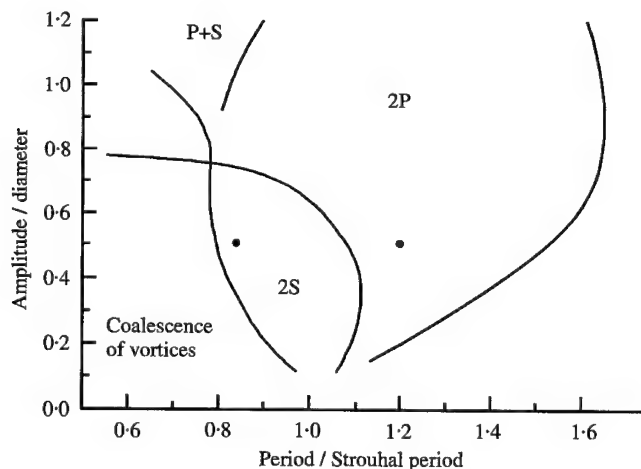


Figure 1. Transverse motion parameters plotted on the Williamson & Roshko (1988) mode map.

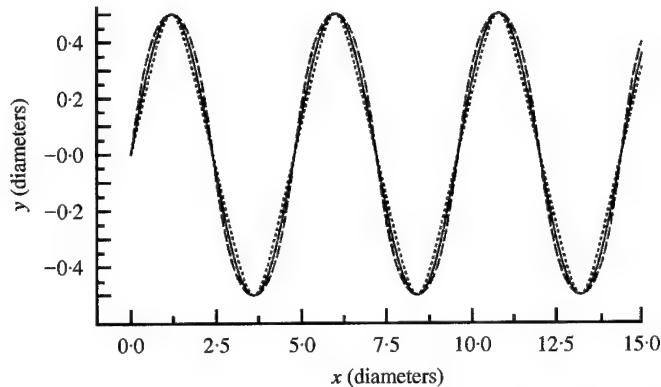


Figure 2. Trajectory of the cylinder in an  $X$ - $Y$  plane. Although the transverse scale is greatly exaggerated, the effect of the streamwise perturbation is barely visible.

### 3. EXPERIMENTAL SETUP

The experiments were conducted in a low-speed water tunnel located at Caltech. Above the test-section, a two-independent-axes traversing system was mounted, which permitted arbitrary motions in the streamwise and transverse directions. Glass cylinders between 2 and 2.5 cm were used; with a test-section approximately 45 cm wide and 58 cm deep, this gives about 5% blockage and an aspect ratio around 25:1. A schematic of this setup is shown in Figure 3.

Data were taken with a digital particle image velocimetry (DPIV) system and a strain gage force balance. The DPIV system used a pulsed laser to illuminate the region around the cylinder and a video camera looking from underneath. To minimize parallax effects (i.e., the bottom of the cylinder obstructing the view near the plane of interest), the camera was placed approximately 6 m from the imaging plane. The strain gage balance was located between the cylinder and traverse and was used to verify lift and drag forces computed from the flow data. In order to keep the flow velocities low enough for the traverse and the DPIV system, freestream velocities of the order of 4–6 cm/s were used. This results in very low force values; consequently, an alternative force deduction method was also employed (Noca *et al.* 1997, 1999).

### 4. RESULTS

To facilitate the comparative effects of streamwise motion, the phase-averaged nondimensional vorticity fields are plotted in Figures 4 and 5. (Vorticity is scaled by the freestream velocity and the cylinder diameter.) In each figure, the data is taken at the same relative transverse phase, so that the only differences should arise from differences in the cylinder motion. Each column represents data taken at the same transverse frequency and each row, data at the same class of streamwise motion. In particular, Figure 4 is taken when the cylinder is near the upper extrema of motion, and Figure 5, when the cylinder is near the middle, during a falling stroke. It is worth pointing out here that the familiar “2S” and “2P” modes are recovered when only transverse motions are used.

By plotting the various cases at constant phase, the apparent phase flipping of the wake is also quite evident. For example, in Figure 4, the vortex that is about to be shed is consistently negative (leeward) on the higher-frequency motions and consistently positive on the lower-frequency motions.

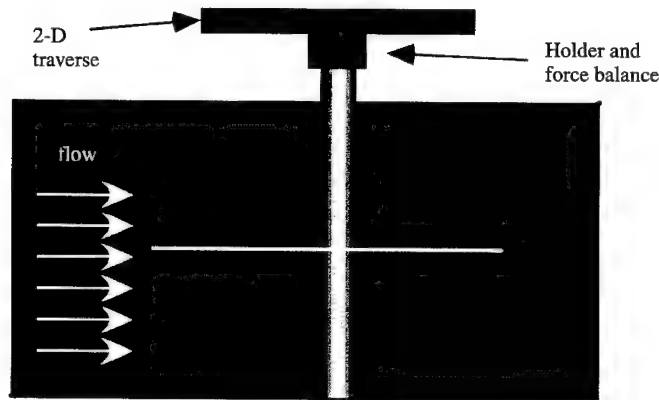


Figure 3. Schematic of the 2-DoF forced oscillation setup.

The computed lift forces are plotted in Figure 6. For comparison, lift is plotted both with and without the added mass term. In a sense, the “wake” component of the force (total lift – added mass) represents the work that the wake is doing on the cylinder. As expected from work like Bishop & Hassan’s (1964), the total lift forces are nearly  $180^\circ$  out-of-phase in the transverse-only case. However, the phase relationship is not so simple once the streamwise motions are added.

## 5. DISCUSSION

The effect of streamwise motion on the wake is quite noticeable. In the higher-frequency case (2S), there is a dramatic increase in phase coherence. The vorticity plots change from blobs of vorticity into compact circular vortices. This is most likely due to a regularization of the phase of the vortex shedding. In other words, the streamwise motion helps to control when, within the period, a vortex is shed. In the lower-frequency case (2P), an equally dramatic change occurs — the disappearance of the 2P mode. The pairing mode is quite evident in the 1-DoF case and the motion of the pair is easily tracked through time. However, with the addition of streamwise motion, the second vortex in the pair does not seem to form. It is believed that the primary vortex of the pair is produced in either case, but that the streamwise motion suppresses the formation of the secondary vortex.

On the other hand, the effect of relative phase is more subtle. Figure 5 shows how the phase of the wake can be directly altered by the phase of the streamwise motion. For example in the higher-frequency case, at the same point in phase, the shed vortex is displaced by nearly a diameter in the streamwise direction. This again suggests that streamwise vibration affects the phase of shedding. The phase change is also reflected in the lift curves. Compare either the two dotted or solid lines in the lower two panels of Figure 6. The advance of the lift force relative to the cylinder motion is quite evident, caused solely by the change in the relative phase of the streamwise motion. This can have a large effect on the energy balance of the system. For example, similarly to Blackburn & Henderson (1999), the lower-frequency case showed a net power transfer from the wake, while the higher-frequency case was the opposite. When the streamwise motion is added, the lower-frequency case actually changes sign (transfers to the wake) at  $0^\circ$  phase and has more than 50% higher power gain at  $-45^\circ$  phase. It would seem, then, that the large transverse motion sets the frequency of shedding, but the streamwise motion affects the relative phase therein, and that the effects of relative phase are significant.

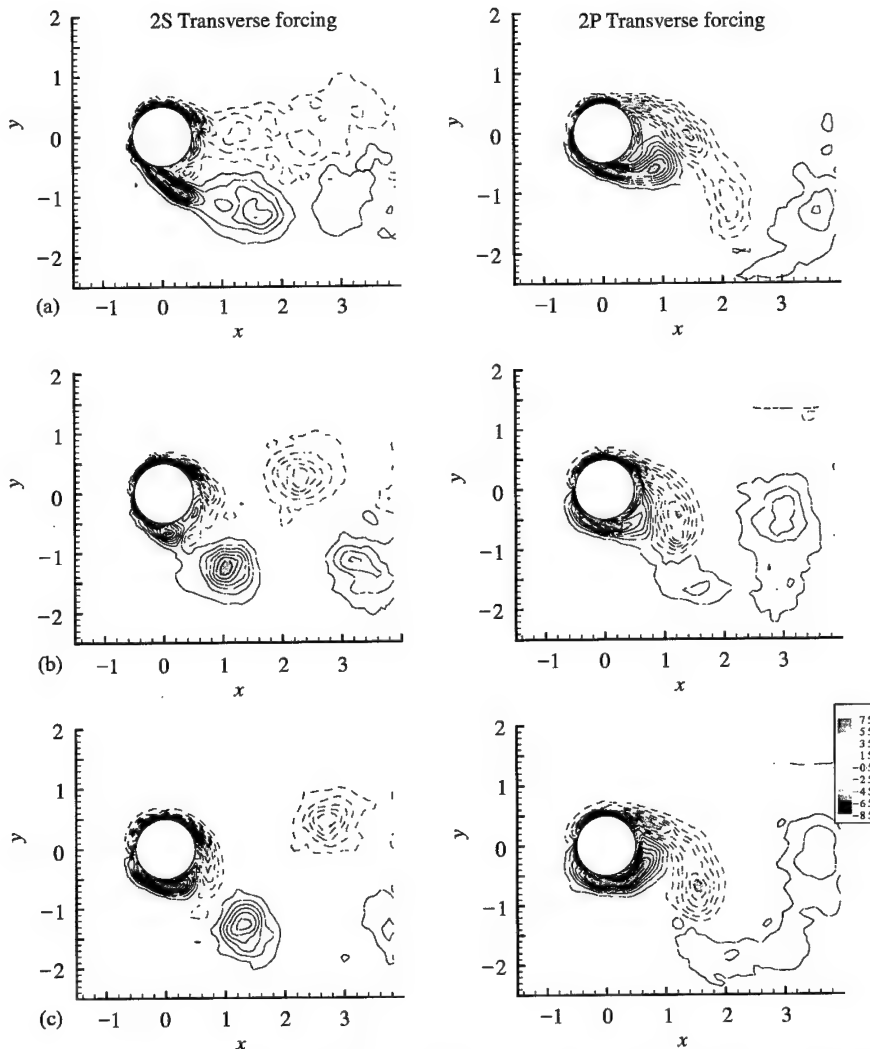


Figure 4. Comparison of the phase-averaged nondimensional vorticity in the wake of the oscillating cylinder. Cylinder approaching the upper extrema of motion (one-quarter period). Left column at higher frequency, right column at lower frequency (corresponding to the 2S/2P modes in the 1-DoF case). (a) No streamwise motion of the cylinder; (b) streamwise motion;  $\phi = 0$ ; (c) streamwise motion,  $\phi = -45^\circ$ .

Yet, it should not be surprising that streamwise motion of this magnitude should have a profound effect on the wake. If one looks at circulation production [see Morton (1984)], one sees that there are two primary sources of production for this class of problem: pressure gradients on the body and surface acceleration. Presuming the pressure gradients to change little between the various cases, one looks instead at the surface acceleration. Since the streamwise motion is at twice the frequency of the transverse motion, even though the motion amplitude is much smaller, the contribution to acceleration is quite comparable. Hence the contribution to circulation production from streamwise motion can be of the same order as that from transverse motion. This effect can be seen in the circulation of the shed vortices. For example, the 1-DoF cases resulted in vortices around 1.6 units of nondimensional circulation while their 2-DoF brethren were clustered around 2.1 units.

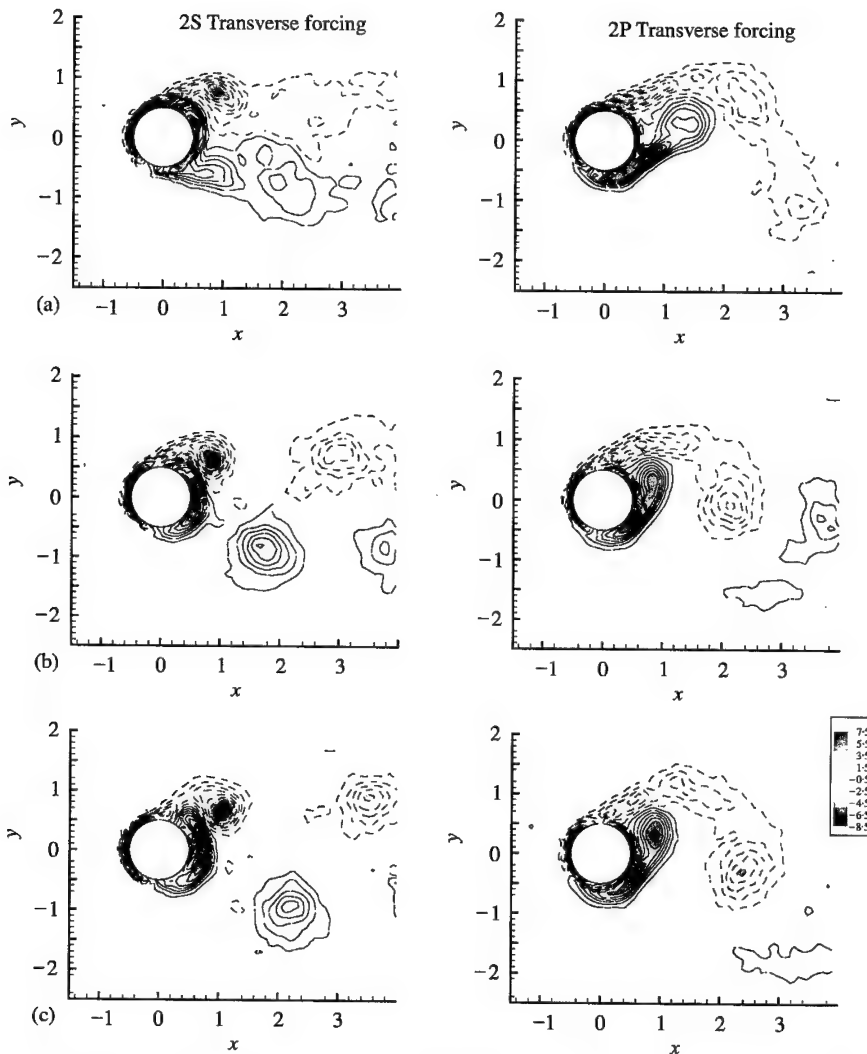


Figure 5. See Figure 4. Cylinder now near the mid-point, on the falling stroke (one-half period). (a) No streamwise motion of the cylinder; (b) streamwise motion;  $\phi = 0$ ; (c) streamwise motion,  $\phi = -45^\circ$ .

From a circulation production point of view, one cannot ignore the contribution from the streamwise motion.

At this point, it is worth considering Figure 7. Plotted here are the positions of the attached vortices as a function of phase. The origin is always centered on the cylinder, so the indicated positions are not in laboratory coordinates. Starting with the simplest case, consider first Figure 7(a), which corresponds to the high-frequency, no-streamwise-motion case. This results in the 2S wake mode, which can be easily seen in the vortex tracks. (One vortex trajectory from each side per cycle.) When the streamwise motion is added to this transverse motion [Figure 7(b, c)], the picture is qualitatively similar, although the vortices form and shed faster (formation/shedding time is indicated by the length of the track). Looking at motions at lower frequency [Figure 7(e, f)], one is first struck by the longer residence time of the vortices. Recall that in either case, only one vortex is formed and shed from each side in each cycle. Nevertheless, the residence time is nearly twice as long at lower

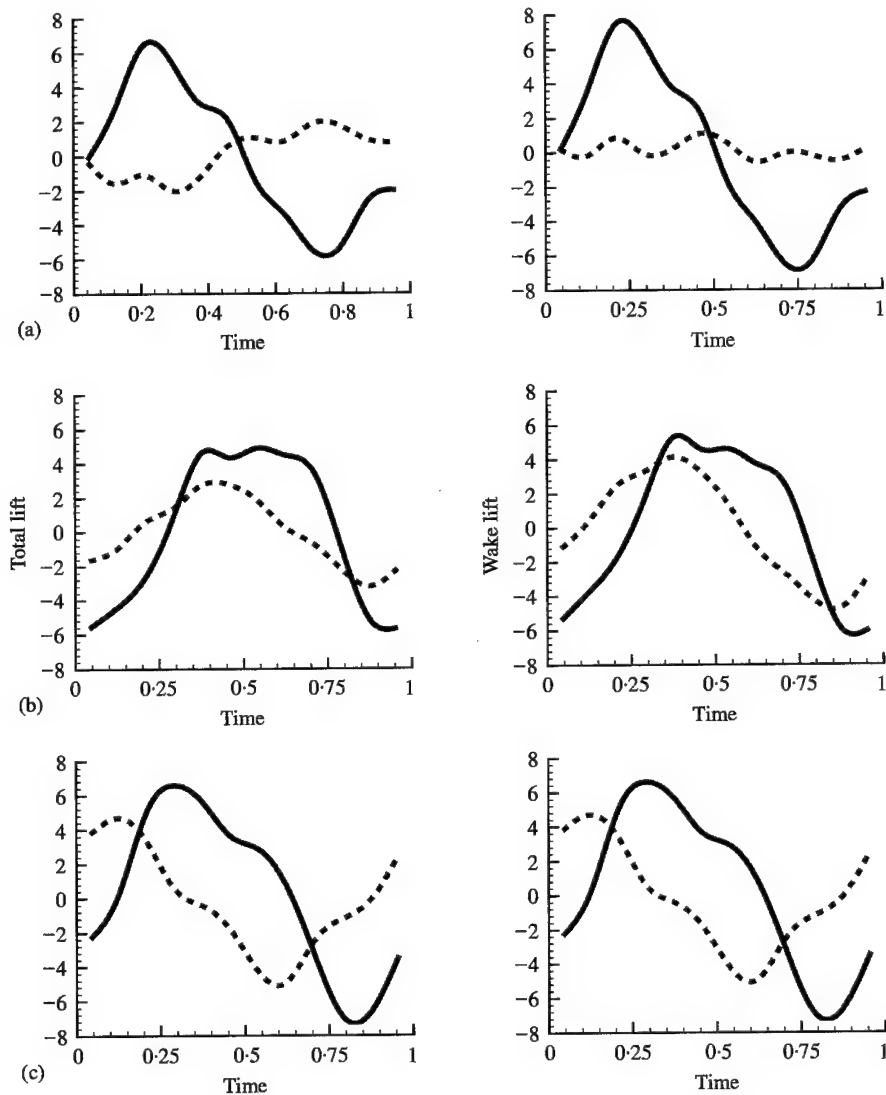


Figure 6. Deduced lift forces for the cases shown in Figures 4 and 5. Total lift on the left column and the wake component of lift on the right. ---, 2-transverse forcing, higher frequency; —, 2P transverse forcing, lower frequency. (a) No streamwise motion; (b) streamwise motion;  $\phi = 0$ ; (c) streamwise motion,  $\phi = -45^\circ$ .

frequency. Another interesting point is that formation happens on the opposite side of the cylinder. (A negative vortex resides on the upper side in the higher-frequency case and on the lower in the lower-frequency case.) This effect can be seen in either Figure 5 or 6 and is a result of the elongation of the vortical structure at lower frequency. The trajectory of the vortex pair in the 2P case is presented in Figure 7(d). The double tracks indicate the double vortices shed per cycle. It is worth pointing out that the first vortex formed on a given side appears to cross the axis and shed on the opposite side, pulling along the second vortex formed on the opposite side. This leads us to believe that the 2P mode is not so much a vortex pair (in the sense of a 2-D vortex ring) but more of a dominant primary vortex that pulls along the secondary vortex from the opposite side as it passes by.

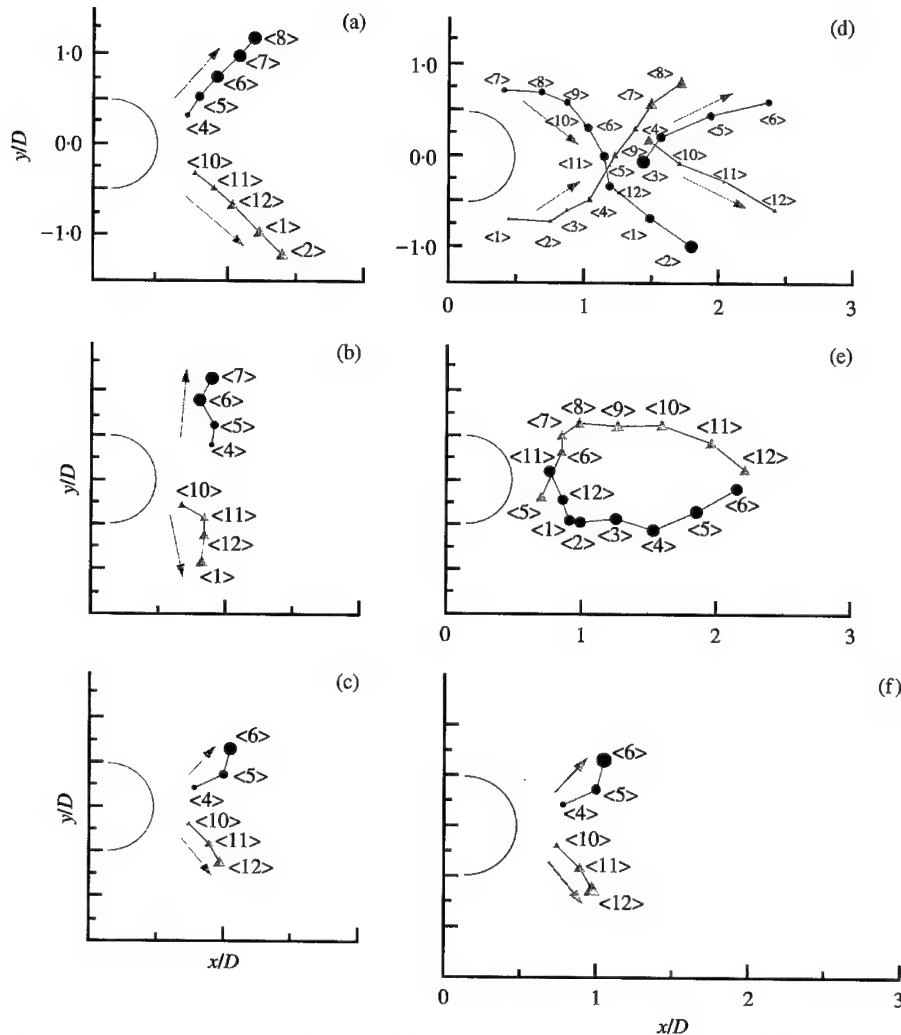


Figure 7(a-f). Trajectory of attached vortices in the wake of the cylinder: —●—, upper; —▲—, lower.

## 6. CONCLUSIONS

The importance of streamwise motion in forced vibration experiments has been presented here. The effect, seems primarily in the control of the phase of shedding. Changing the relative phase of shedding causes a corresponding change in the phase of the lift force. Since the energy transfer between the body and the wake is sensitive to the relative phase between the force and the body motion, the phase of the streamwise motion can control even the sign of energy transfer (wake driving the body or *vice versa*).

The addition of streamwise motion also resulted in qualitative changes in the wake. Perhaps the most dramatic is the disappearance of the pairing mode. When only a transverse vibration is used, the 2P mode is observed in our experiment; however, the wake reverts to shedding single vortices once this relatively small streamwise component is added. Since unconstrained systems will tend toward 2-DoF motions, it is hoped that this experiment has shed some light on the significance of streamwise vibration. It would seem that the effect is much more pronounced than the motion amplitude would imply.



## ACKNOWLEDGEMENT

The authors would like to thank the Office of Naval Research under grant ONR-N00014-94-1-0793 for their patience and generous support of this project.

## REFERENCES

- BISHOP, R. E. D. & HASSAN, A. Y. 1964 The lift and drag forces on a circular cylinder oscillating in a flowing fluid. *Proceedings of the Royal Society (London)* **A277**, 51–75.
- BLACKBURN, H. M. & HENDERSON, R. D. 1999 A study of two-dimensional flow past an oscillating cylinder. *Journal of Fluid Mechanics* **385**, 255–286.
- FENG, C. C. 1968 The measurement of vortex-induced effects in flow past a stationary and oscillating circular and D-section cylinders. M.A.Sc. thesis, University of British Columbia, Vancouver, BC, Canada. (As published in Parkinson, 1989.)
- GHARIB, M. R. 1999 Vortex-induced vibration, absence of lock-in and fluid force deduction. Ph.D. dissertation, GARCIT, California Institute of Technology, Pasadena, CA, U.S.A.
- JEON, D. S. 2000 On cylinders undergoing one- and two-degree-of-freedom forced vibrations in a steady flow. Ph.D. dissertation, GARCIT, California Institute of Technology, Pasadena, CA, U.S.A.
- KHALAK, A. & WILLIAMSON, C. H. K. 1999 Motions, forces and mode transitions in vortex-induced vibrations at low mass-damping. *Journal of Fluids and Structures* **13**, 813–851.
- MORTON, B. R. 1984 The generation and decay of vorticity. *Geophysical & Astrophysical Fluid Dynamics* **28**, 277–308.
- NOCA, F., SHIELS, D. & JEON, D. 1997 Measuring instantaneous fluid dynamic forces on bodies using only velocity fields and their derivatives. *Journal of Fluids and Structures* **11**, 345–350.
- NOCA, F., SHIELS, D. & JEON, D. 1999 A comparison of methods for evaluating time-dependent fluid dynamic forces on bodies, using only velocity fields and their derivatives. *Journal of Fluids and Structures* **13**, 551–578.
- PARKINSON, G. 1989 Phenomena and modeling of flow-induced vibrations of bluff bodies. *Progress in Aerospace Science* **26**, 169–224.
- SARPKAYA, T. 1979 Vortex-induced oscillations: a selective review. *Journal of Applied Mechanics* **46**, 241–258.
- WILLIAMSON, C. H. K. & ROSHKO, A. 1988 Vortex formation in the wake of an oscillating cylinder. *Journal of Fluids and Structures* **2**, 355–381.



## SPATIO-TEMPORAL RECONSTRUCTION OF VORTEX DYNAMICS IN AXISYMMETRIC WAKES

C. BRÜCKER

*Aerodynamisches Institut der RWTH Aachen  
Wüllnerstr. zw. 5 u. 7, D-52062 Aachen, Germany*

(Received 28 August 2000, and in final form 15 November 2000)

With time recording Digital-Particle-Image Velocimetry and spatio-temporal reconstruction technique, we obtained detailed quantitative results of the evolution of the velocity and vorticity field in the wake of axisymmetric bluff bodies—a sphere and an axially oriented cylinder with an elliptic nose and a blunt base. Experiments were carried out for Reynolds numbers of  $Re = 500, 700$  and  $1000$  in the transition range from “regular” to “irregular” shedding. DPIV-recordings in radial cross-sections at several distances downstream of the bodies allowed us to reconstruct the dynamics of the streamwise vorticity over a large number of shedding cycles. Our results prove that the wake in this regime consists of a double-sided chain of oppositely oriented hairpin vortices. In addition, the results show a well-defined low-frequency modulation of the vortex shedding, with a distinct peak in the frequency spectrum at a Strouhal number of about  $Sr \approx 0.05$  (in case of the sphere). The wake pattern in this “irregular” shedding regime typically exhibits periodic packets of 3–4 “regular” shedding cycles which are interrupted by phases with less action. The results indicate the coexistence of a long-wave instability of axisymmetric wakes against helical waves in addition to the primary instability causing the vortex shedding process.

© 2001 Academic Press

### 1. INTRODUCTION

THE PRESENT STUDY WAS UNDERTAKEN with the objective of a detailed quantitative analysis of the evolution of the flow field in the wake of axisymmetric bluff bodies like spheres and spheroids. While much experimental data exist for the wake of nominally two-dimensional bodies like the cylinder wake, considerably less has been reported on wake flows of axisymmetric bodies, although there is certainly the same strong physical and technical interest. Practical examples are the wake behind bubbles, drops and particles or projectiles and rockets. In comparison to the cylinder wake, the wake of axisymmetric bodies—from which the sphere wake is the most prominent—exhibits grave differences in the shape and dynamics of the vortices being shed. The wake structures are basically three dimensional and highly unsteady, which makes any measurements and interpretations difficult. To the best of the author's knowledge, any experiments which could provide detailed instantaneous flow field data in such type of wakes are still lacking. In addition, it is only recently that the progressively growing computing power has enabled the first numerical simulations of the unsteady wake flow of axisymmetric bodies (Johnson & Patel 1999; Mittal 1999; Lee 2000). Therefore, most of today's knowledge about the vortical structures contained in the wake is still based mainly on earlier flow visualisation studies (Magarvey & Bishop 1961; Achenbach 1974; Nakamura 1976; Sakamoto & Haniu 1990). For the sphere wake, these experiments revealed several stages in the transition of the wake from a steady axisymmetric wake to unsteady irregular vortex shedding. Up to Reynolds numbers of 130, the wake is stationary and forms an axisymmetric recirculating eddy. Beyond that, a weak

periodic wave-like wake with a long period was observed behind the axisymmetric eddy. In the range  $210 < Re < 270$ , the wake evolves into an attached hairpin-like vortex, with its legs forming a pair of streamwise vortex filaments pointing downstream. As this wake pattern appears, the wake still seems to be stationary as reported by Nakamura (1976). For higher Reynolds numbers, up to  $Re = 420$ , the flow visualisation experiments revealed a shedding of hairpin-like vortex structures. The wake appears as a chain of hairpin vortices with the heads pointing always to the same side in the same axial plane (Achenbach 1974). This pattern becomes irregular at increased Reynolds numbers.

Recent numerical simulations of the sphere wake flow by Johnson & Patel (1999) demonstrated that most of the flow visualisation experiments have overlooked vortex structures in the wake which are induced within the fluid and are not connected with the base of the bluff body. These occur as oppositely oriented hairpin vortices in-between the one-sided chain of hairpin vortices seen in the flow pictures from Nakamura (1976) and other authors. This discrepancy highlights that detailed chronological flow field measurements are necessary in order to provide the velocity and vorticity information for the entire wake. The objective of the present paper is to fill this gap in experimental knowledge by detailed analysis of the structure and dynamics of the vortices in the wake. Therefore, we applied chronological high-speed DPIV-technique to capture the temporal evolution of the flow field in radial cross-sections downstream of the axisymmetric bluff bodies. The time-series of DPIV results are used to analyze the vortex dynamics with the aid of spatio-temporal reconstruction method. The most relevant studies with respect to our work are the numerical simulations done by Tomboulides & Orszag (2000), Mittal (1999), Johnson & Patel (1999) and, most recently, the work from Lee (2000) which was published during the completion of this article. Of particular interest in Lee's paper is his observation of a low-frequency fluctuation, in addition to the primary vortex shedding which is one particular focus of our work.

## 2. EXPERIMENTAL METHODS AND ARRANGEMENT

The test-objects chosen in our study were a solid sphere and a cylindrical rod with an elliptical nose and a sharp trailing edge (Figure 1) which is aligned with its axis along the flow axis. In contrast to the sphere, the cylinder has a defined separation edge and the boundary layer thickness can be controlled by the length. This allows us to study the effect of boundary layer thickness on the stability of the wake. The experiments were carried out in a vertical water channel shown in Figure 1. The transparent test-section has a cross-section of  $10 \times 10 \text{ cm}^2$  and is 1.2 m high. The bluff bodies with a diameter of 3 cm were held by a thin hollow rod of 2 mm diameter in the centre of the channel. To reduce its effect on the flow around the body, we sucked the boundary layer fluid away through tiny holes along the rod. Small tracer particles (Vestosint, mean diameter of  $30 \mu\text{m}$ ,  $\rho = 1.02 \text{ g/cm}^3$ ) were added to the fluid upstream in the water basin and were mixed homogeneously.

The DPIV set-up was arranged to measure the velocity field in a horizontal cross-section, downstream of the body in order to obtain the distribution of streamwise vorticity in that plane. The beam of a continuous  $\text{Ar}^+$  laser was expanded with a rotating polygonal mirror to form an intense virtual light-sheet in a horizontal cross-section of the channel. A digital high-speed video camera (resolution:  $512 \times 512$  pixels; frame rate: 1000 Hz) was used to record the flow, synchronized with the polygonal mirror so that each frame corresponds to a single sweep of the laser beam. The recording rate was increased with the Reynolds number of the flow beginning from 60 Hz at  $Re = 300$ , 100 Hz at  $Re = 500$ , 200 Hz at  $Re = 700$  and 500 Hz at  $Re = 1000$ . Within the horizontal light-sheet plane ( $y$ - $z$  plane), the in-plane velocity components were obtained from cross-correlation of successive image

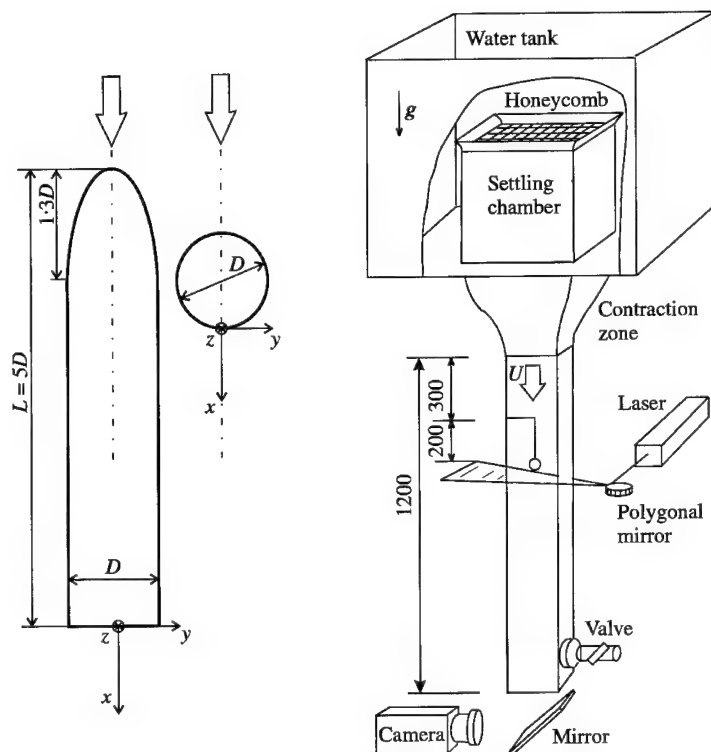


Figure 1. Experimental set-up and shape of the two axisymmetric bluff bodies used in this study.

pairs in small interrogation windows. The results represent a two-dimensional data set, in the form of velocity vectors on a grid with  $31 \times 31$  equidistant nodes over a square cross-section area of  $5 \times 5 \text{ cm}^2$ . The streamwise vorticity component was determined out of the velocity field by calculating the gradients in the  $3 \times 3$  neighbourhood of each node using central difference schemes.

In all experiments, the measurement plane was located at  $x = 3$  diameters downstream of the body base plane. At this position outside of the attached part of the wake, the vortex structures have not yet deformed by self-induction and are still mainly oriented in the streamwise direction while they are convected downstream; cf. the results from Tomboulides & Orszag (2000), Johnson & Patel (1999) and Mittal (1999). This enables to reconstruct the dominant part of the vortex structures by spatio-temporal display of the chronological DPIV results in the radial cross-sections.

### 3. RESULTS

Before we discuss the results by means of the spatio-temporal reconstruction images, an example of the dynamics of the bluff-body wake is first shown in a sequence of DPIV results in the following section.

#### 3.1. SPHERE WAKE AT $Re = 400$

Figure 2 gives an example of the instantaneous flow field in the radial cross-section at  $x = 3$  diameters downstream of the sphere for a Reynolds number of 400. The flow field shows

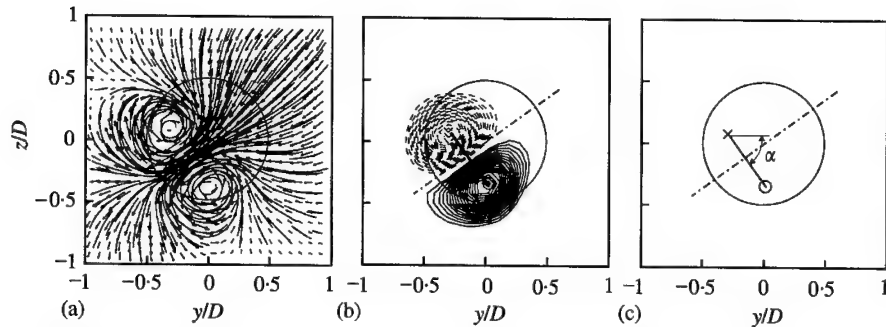


Figure 2. Example of DPIV results in the wake of a sphere ( $Re = 400$ ) in a cross-section at  $x/D = 3$ : (a) velocity field and sectional streamlines, integrated from the velocity field; (b) lines of constant streamwise vorticity with constant increment (continuous lines indicate positive rotation, dashed lines indicate negative rotation). (c) Definition of the angular orientation of the wake.

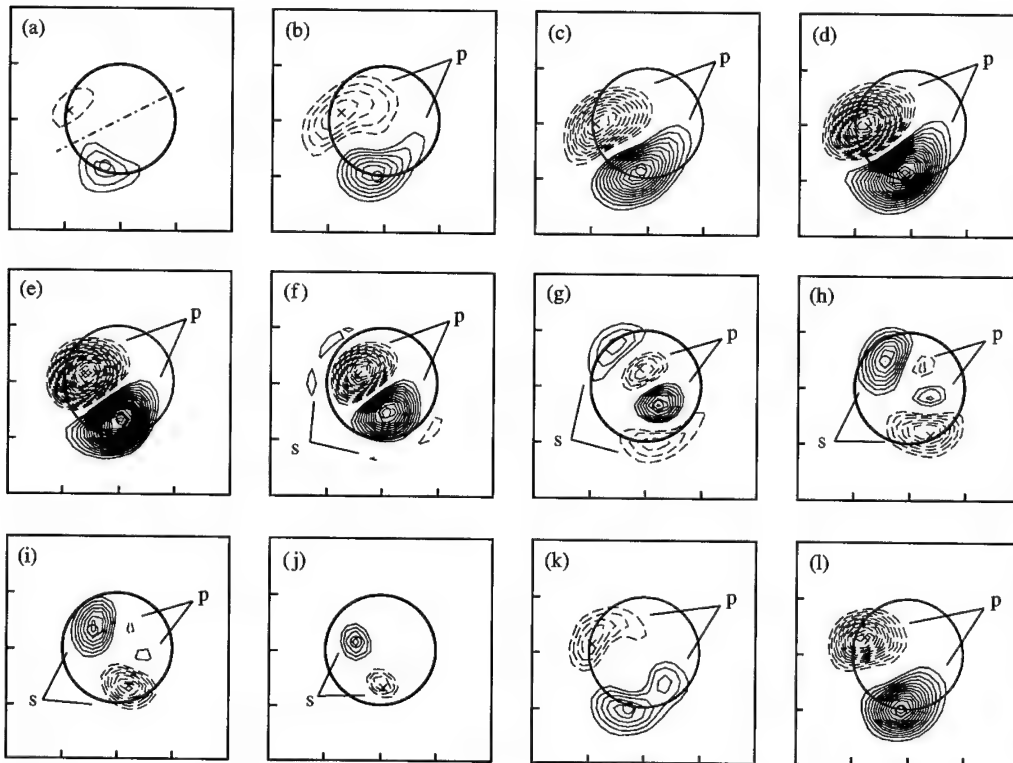


Figure 3. Evolution of the streamwise vorticity distribution in the wake of a sphere ( $Re = 400$ ) in a cross-section at  $x/D = 3$  over a complete shedding cycle; the mark "p" indicates the primary vortex pair, "s" the secondary pair.

a pair of streamwise vortices in the cross-section of the wake, which represent cuts through the legs of the vortex loop being shed into the wake. Note that the vortex pair is not located at the centre of the sphere-wake but offset to the lower left side. A strong radial cross-flow is induced between the vortices. The induced flow field exhibits a symmetry of the wake about a plane passing through the wake centreline, tilted about an angle of  $45^\circ$ ; the vortex centres

of the pair are mirror-symmetric to this plane. The orientation of the vortex pair (which is referred to as the "wake orientation") is defined by the angle  $\alpha$  of the connection line between the vortex centres, which we determine from the extrema of streamwise vorticity in our data. The temporal signal of this angle is used to display the angular stability of wake orientation in different stages of wake transition. In addition, the average value of positive streamwise vorticity and its variation over time is used as a first approximation of the variation of the strength of the vortices. An additional value of interest is the radial velocity component at the centreline.

The dynamics of the wake is shown in Figure 3 by a sequence of DPIV results over one single shedding cycle. During the cycle, the vortex pair (a "pair" is characterized by two regions with concentrated streamwise vorticity of opposite sign which are symmetrically positioned at opposite sides of the plane of symmetry) varies in strength and size and moves along the plane of symmetry. Both parts of the pair remain in their same angular relation and strength relative to each other, over the entire shedding cycle. Therefore, the angular orientation is maintained at a fixed plane of symmetry at all times during the shedding process, which is an intrinsic feature of the sphere wake at this range of Reynolds numbers. From Figure 3(a) to 3(d) the primary vortex pair, which is offset outside the centreline to one side of the sphere, grows in strength and size. Then the vortex pair starts to move towards the centreline, loses its strength, shrinks (both centres approach each other), until it has finally diminished in Figure 3(i). Meanwhile, one can see the generation of a secondary vorticity pair at the outer shoulders of the primary vortex pair with counter sign of rotation [Figures 3(f,g)]. This secondary pair shows the same trend over time as the primary pair, as it grows in strength [Figures 3(g,h)], starts to move towards the centre of the wake [Figures 3(h,i)], shrinks again and finally diminishes [Figures 3(j,k)]. Now the cycle is finished and the next one starts at Figure 3(k) with the appearance of a new primary vortex pair at the left side of the sphere, similar as in Figures 3(a,b).

The contours of regions of concentrated streamwise vorticity of the secondary vortex pair displayed in Figure 3 show that this pair never reaches the same size and strength compared to that of the primary pair. This, together with the observation that the secondary pair is generated at the outer shoulders of the primary vortex pair, suggests that the vorticity of the secondary pair is not being shed from the sphere but results from the roll-up of the shear layer between the outer flow and the strong swirling flow around the vortex tails of the primary vortex pair. Comparing our data with the results from Johnson & Patel (1999) let us conclude that the secondary pair reflects an induced hairpin vortex, while the primary pair reflects a shed hairpin vortex. The induced vortex structures—as they describe—are generated by the interaction of the near wake flow and the outer flow and are based on a different mechanism as the shed hairpin. Unfortunately, the limited information given in their paper does not allow a direct comparison of the streamwise vorticity distribution. Nevertheless, one can see from figure 29 in their article that the streamwise vorticity within the shed hairpin vortices is higher than in the induced hairpin vortices which agrees with our observation, too. Note also that the primary vortex pairs always evolves on the same side of the sphere, which means that the vortices shed only from one side in our experiments, as in the numerical results.

The spatio-temporal reconstruction of the vorticity field is in principle created from a time sequence as given in Figure 3, using the complete data set with a much higher temporal resolution and a total recording period of over several tens of shedding cycles. The vorticity values in the horizontal plane were taken from the results and stacked plane by plane vertically in a data cube over the complete sequence of DPIV results in the recorded period. The resulting data matrix can be displayed as an isosurface of constant streamwise vorticity which gives an image of the spatio-temporal evolution of the component of

streamwise vorticity at a stationary location within the wake. The following figures display the resulting images of the isosurfaces of streamwise vorticity from two orthogonal viewing sides (front view and side view, which allow recognition of the orientation of the vortex structures in the plane of symmetry) together with the temporal evolution of the radial velocity at the centreline, the phase angle  $\theta$ , the average value of positive axial vorticity and its power spectrum. The time unit is made dimensionless with the free-stream velocity and the diameter of the body.

### 3.2. CYLINDER WAKE AND SPHERE WAKE AT $Re = 500$

Figures 4 and 5 show the results for the cylinder and the sphere wake at a Reynolds number of 500. Note, that the isosurfaces are rotated such that the front view is along the plane of symmetry. The isosurfaces illustrate the periodic alternate downwash of oppositely oriented vortex pairs in the wake of the bodies over a period of about 14–15 cycles taking 80 time units. A comparison of the wake of the sphere (Figure 5) with the wake of the cylinder (Figure 4) shows that the boundary layer thickness has a strong influence on the stability and coherence of the vortex shedding. The sphere wake exhibits already the typical slight random variations of the orientation of the vortices and some “irregularity” in the shedding cycle. In comparison, the wake of the cylinder is approximately perfect periodic in time, with a stable orientation of the vortices (compare the phase angle plot in Figure 4). The strong coherence of the cycles in Figure 4 demonstrates the near periodic creation and discharge of the vortices which is similarly observed for the sphere wake at Reynolds numbers of less than about 420.

A typical pattern of a single cycle appears in the front view as a vertically stretched lambda-like vortex pair (the primary vortex pair marked “p”) with a second shorter vortex pair (the secondary vortex pair marked “s”) lying on top on its shoulders. Such a pattern would come out from spatio-temporal reconstruction of the cycle shown in Figure 3. The radial distance of the vortices of the primary pair decreases from bottom to top, giving the lambda-like shape. This corresponds—in the temporal evolution—to the convergence and shrinking of the vortex pair shown in Figures 3(d–h). As already concluded above from comparison of our results with the figures published by Johnson & Patel (1999) the vortex pairs represent parts of the actual three-dimensional hairpin-like vortices, namely the streamwise oriented legs.

Overall, our results clearly confirm a one-sided chain of the primary vortices in the wake which are interconnected with counter-oriented vortices of seemingly lower strength. The side views of the isosurfaces show that the induced hairpin vortices always point to the opposite side of the shed hairpin vortices and are of shorter vertical extension than the shed hairpin vortices. This is also well displayed in the evolution of the phase angle which we determined from the orientation of the dominant vortex pair. The moments at which the phase angle jumps about a value of  $\pi$  characterize the change of the dominant vortex pair in the cross-section from the shed hairpin vortex to the induced one and *vice versa*. The period in which the primary vortex pair dominates the flow in one cycle is considerably longer in the diagram of the phase angle than the period in which the secondary pair occurs. In addition, the evolution of the average value of positive streamwise vorticity—chosen as a first approximation to estimate the circulation of the hairpin-like vortices—shows that the vorticity in the phase of a primary vortex pair exceed that in the phase of a secondary vortex pair about a factor of 3–4 which indicates a low circulation of the induced hairpin vortices compared to the shed vortices.

An interesting feature can be deduced from the variation of the strength of the vortices over time (or the variation of the radial velocity at the centreline) in Figure 4. There is

a slight low-frequency modulation of the overall strength of the vortices which appears as a small peak in the spectrum at  $Sr = 0.015$ , in addition to the dominant peak at  $Sr = 0.168$  representing the “natural” vortex shedding. The effect of this modulation is however so small that it does not change the overall pattern of vortex dynamics. In the sphere wake, we can see a similar low-frequency modulation of the strength of the vortices (Figure 5). It can be recognized in the evolution of the vorticity and its power-spectrum but also in the spatio-temporal reconstruction image. The plot of streamwise vorticity clearly displays a sinusoidal low-frequency modulation of the strength of the vortices which show peak vorticity values at  $t \approx 10, 30, 50$  and  $70$ . The power spectrum shows a peak at a Strouhal-number of  $Sr = 0.05$  corresponding to this modulation. The second peak at  $Sr = 0.178$  belongs to the vortex shedding and falls well within the range of values reported by Sakamoto & Haniu (1990) and Tomboulides & Orszag (2000).

The variation of the strength of the vortices leads to a variation of the shedding period and the inclination angle of the loops against the vertical. The inclination of the vortex pair is strictly coupled to the strength of the loops since it is a result of the self-induction effect which scales with the circulation of the loops. It is well seen in the isosurfaces that in phases of high circulation of the loops, the vertical distances between successive vortex loops are shorter and the loops are more inclined against the vertical. In phases of less vorticity action the induced hairpin vortices reduce in size and strength in the same way as the shed hairpin vortices and sometimes even disappear. The mark “A” in Figure 5 indicates an interval  $40 < t < 45$  where shedding is completely suppressed. The isosurface displays a temporarily stable vortex pair, similar as it is observed in form of the “double-threaded” wake at  $Re < 290$ . As a result of the variation of the shedding period the power spectrum reveals a double-peak scenario; the peak at  $Sr = 0.225$  corresponds to the typical shedding period at high vorticity action around the times  $t \approx 10, 30, 50$  and  $70$ , while the peak at  $Sr = 0.178$  corresponds to the “natural” shedding phases in between.

### 3.3. CYLINDER WAKE AND SPHERE WAKE AT $Re = 700$

For the cylinder wake, the discovered low-frequency instability of the wake and the resulting effect on the vortex structures becomes dominant at  $Re = 700$ , shown in Figure 6. The vortices seem to be shed in “pockets” of 3–4 strong hairpin vortices, interrupted by shedding phases with weaker hairpin vortices. The strong phases are marked as “A”, “B” and “C” in Figure 6. The beginning of such a phase is coupled with a steep increase of the vorticity of the first hairpin and a flat decrease of the peak values for the following shedding cycles. The temporal profile of the mean vorticity shows a sawtooth-like envelope. The strength and size of the induced hairpin vortices are strictly coupled to that of the shed hairpin vortices, i.e., when the shed hairpin vortex is of higher circulation then it induces a stronger hairpin and vice versa. Similar to the sphere wake one can observe a faster shedding in phases of higher vorticity and a higher inclination of the loops to the vertical. The sawtooth-like envelope of variation of vorticity and the varying shedding frequency indicate a non-linear interaction of the low-frequency modulation and the “natural” shedding process.

The power-spectrum reveals—similarly as for the sphere—a double-peak scenario corresponding to the different phases of the shedding; the peak at  $Sr = 0.192$  corresponds to the typical shedding period with high vorticity action around the times  $t \approx 20, 50, 80$  in Figure 6, while the peak at  $Sr = 0.154$  corresponds to the “natural” shedding phases in-between. One additional important aspect of the results in Figure 6 is that the angular orientation of the wake seemingly remains stable (except for a very small rotational drift of the entire wake in one direction, which results in a total rotation of  $30^\circ$  over the complete process with 100



Figure 4. Dynamics of streamwise vorticity in the wake of the cylinder at  $Re = 500$ . The spatio-temporal behaviour of the streamwise vorticity component in the plane  $x/D = 3$  is illustrated as isosurfaces of positive and negative vorticity in front and side view. On the left-hand side from the top to the bottom are plotted for different quantities in the plane  $x/D = 3$  over the normalized time  $t$ : plot of the radial velocity at the centreline; plot of the phase angle; plot of the mean streamwise vorticity; power spectrum of the streamwise vorticity.

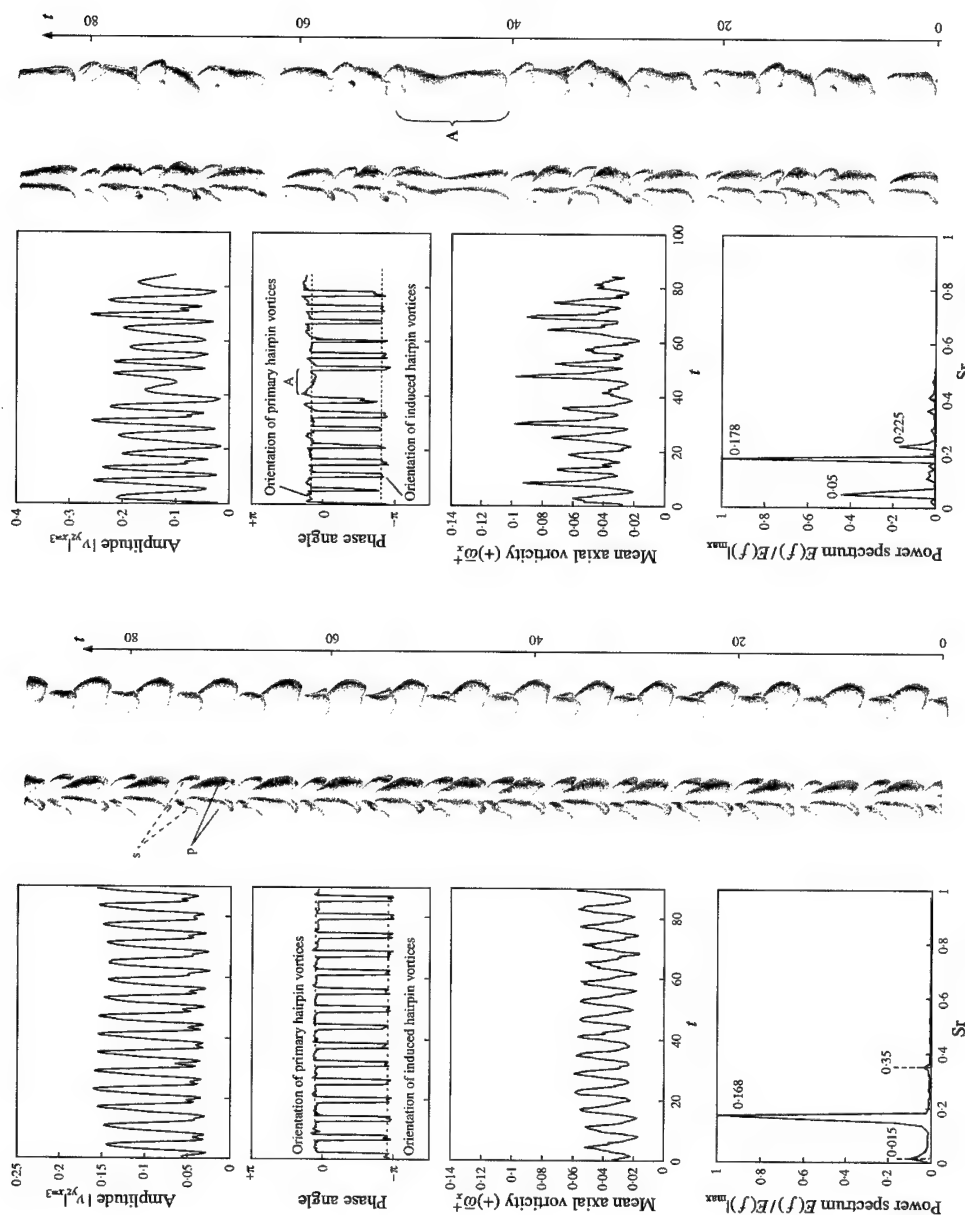


Figure 4

Figure 5. Same as Figure 4, but for the wake of the sphere at  $Re = 500$ .

Figure 5

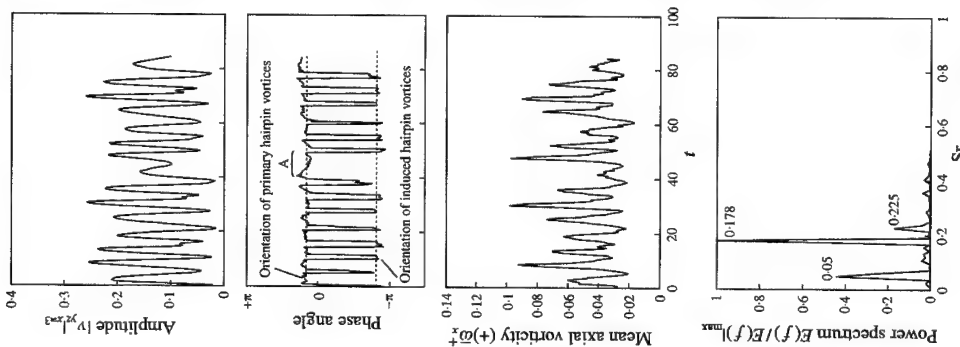
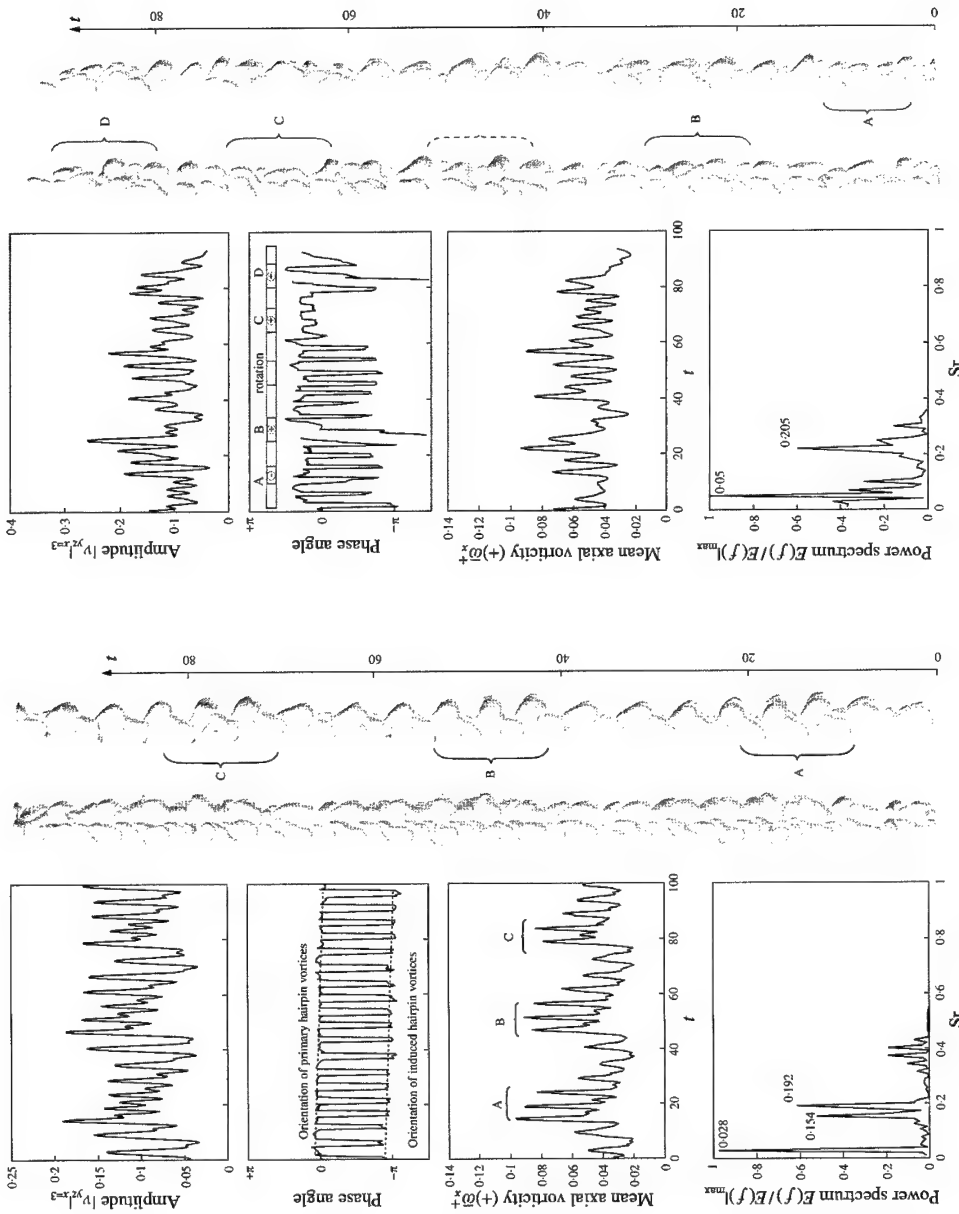


Figure 6. Same as Figure 4, but for the wake of the cylinder at  $Re = 700$ .

Figure 7. Same as Figure 4, but for the wake of the sphere at  $Re = 700$ .



time-units). The existence of the low-frequency fluctuation is therefore seemingly not necessarily coupled to a rotation of the detachment point of the vortex loop from the base of the body as speculated by Lee (2000). Rather, our results indicate that the low-frequency modulation is a generic instability of axisymmetric wakes to long-wavelength waves from which the helical-type waves are the most likely, according to the instability analysis by Natarjan & Acrivos (1993).

Figure 7 shows the results for the sphere wake at  $Re = 700$ . In comparison to the cylinder wake, the planar symmetry seems already to be lost and a more irregular pattern of vortex shedding is seen. The power spectrum of the vorticity shows the dominant peak at  $Sr = 0.05$  which proves that the low-frequency modulation is still present. The second peak at  $Sr = 0.205$  corresponds to the vortex shedding. One can best see, similarly to the cylinder wake, the low-frequency modulation from the vorticity and velocity profile. In phases with a more stable orientation of the wake, as for example in the period  $40 < t < 60$ , the isosurfaces show a similar pattern as in the cylinder wake at  $Re = 700$ . Between the stable phases one can observe a twisting or rotation of the whole wake structure, which we have marked with "A–D" in Figure 7. These phases seem to be coupled with a steep increase of the vorticity; the vorticity peak at  $t = 22$  initiates phase B, the peak at  $t = 58$  initiates phase C and the peak at  $t = 78$  initiates phase D. The peak at  $t = 40$  is the only one which does not immediately lead to a twisting of the wake. It lets us conclude that the sphere wake at higher Reynolds numbers reacts to the long-wavelength modulation with a rotation or twisting of the wake, unlike the cylinder wake which still remains stable at  $Re = 700$ . Note, that the vortex loops themselves are also twisted in phases A, B and D, which means that the rotation continues over the shedding process, sometimes even over periods of 2–3 cycles.

The power spectrum of the vorticity signal does not show anymore the typical double-peak scenario in the shedding regime but only a broader single peak at  $Sr = 0.205$ . However, one can still see a variation of the shedding frequency in the profile of the phase angle comparing the times at which the phase angle jumps about  $\pi$ . We believe that possibly the vorticity signal—especially during the wake rotation—does not reflect anymore a proper value to identify the shedding frequency; this might be the reason that an actual double-peak scenario has converged to a single broader peak in the power spectrum. A similar transition of the overall pattern as observed herein for the sphere at  $Re = 700$  is also observed for the cylinder wake at a higher Reynolds number of  $Re = 1000$ , for which results cannot be shown here due to space limits.

#### 4. DISCUSSION AND CONCLUSION

In general, the wake transition process shows similar patterns for the cylinder and the sphere wake, except the fact that, for the cylinder wake, the transition is shifted to higher Reynolds numbers. The planar symmetry of the sphere wake at  $Re = 400$  is lost at  $Re = 500$  in our experiments. For the cylinder wake this regime extends to at least  $Re = 500$ . First, slight fluctuations of the phase angle occur at  $Re = 700$ , which is comparable to the sphere wake at about  $Re = 500$ . This suggests that the boundary-layer thickness plays an additional role in the instability of axisymmetric wakes in the way that an increased boundary layer thickness seemingly stabilizes the wake orientation. DPIV measurements in the cross-section downstream of the sphere and the cylinder show that the overall shape of the generated vortices resembles hairpin-like structures. The legs are represented by the measured centres of streamwise vorticity in the cross-section. The reconstructed isosurfaces display a chain of hairpin vortices which consists of an alternate arrangement of a shed hairpin vortex followed by an induced, oppositely oriented hairpin vortex. A similar result is

documented in recent numerical results of sphere wake flow at  $Re = 300$  by Johnson & Patel (1999). A lower strength of the induced hairpins is observed here, too.

A possible explanation of the planar symmetry and its loss at higher Reynolds numbers will be discussed in the following from the interaction of helical waves in axisymmetric wakes. Natarajan & Acrivos (1993) found, via a global stability analysis, that axisymmetric wake flows are most unstable against helical waves. The first instability in the sphere wake appears for a nonfluctuating helical wave with an azimuthal wavenumber of  $k = 1$  (this means that the wavelength fits once within the circumference), i.e., the wake becomes asymmetric but remains steady. Beyond this first critical Reynolds number, the flow becomes unstable to fluctuating helical waves with  $k = 1$ , and the flow becomes unsteady. It is obvious from the planar symmetry of the wake in the range  $290 < Re < 420$  that two counter-rotating helical waves must exist simultaneously, which additionally must have the same amplitude and phase velocity. If so, the counter-rotating waves leads to a perfect planar oscillations of the wake which can be proved by simple additive superposition of both waves. However, if this system is destabilized, one of these helical waves would dominate, which would lead to a helical deformation of the wake. Our results suggest that this is what happens for higher Reynolds numbers, in which those phases with wake rotation are initiated by the low-frequency modulation of the wake as discussed in what follows.

Most interestingly in our experiments, we could identify a previously overlooked low-frequency modulation of the wake; the vortex patterns show a long-wavelength periodic variation of the circulation and shedding frequency of the hairpin vortices. The hairpin vortices with a higher circulation appear periodically in packets of 3–4 vortices which are more inclined against the vertical and shed more rapid in comparison to the phases of “natural” vortex shedding at frequencies which agree with those reported in earlier studies [see, e.g., Sakamoto & Haniu (1990)]. As a result, the shedding regime appears in the power spectrum of the vorticity signal as a double-peak scenario. In addition, a third peak indicates the low-frequency modulation at a Strouhal number of  $Sr = 0.05$  in the sphere wake and  $Sr = 0.03$  in the cylinder wake. It is assumed that the low-frequency modulation is again linked to helical-type waves with an azimuthal wave-number of  $k = 1$  according to the results from Natarajan & Acrivos (1993). This demonstrates that there is an interaction of instabilities at different characteristic frequencies which was not observed in experiments before.

While this low-frequency modulation seems to destabilize the planar symmetry of the sphere wake at  $Re = 500$ , it does not have a significant effect on the planar symmetry in the wake of the cylinder up to  $Re = 700$ . This suggests that the long-wave instability appears again as a pair of counter-rotating helical waves of the same amplitude and phase velocity. This instability exists over the entire transition range of the cylinder flow with a Strouhal number of  $Sr = 0.015$  at  $Re = 500$ ,  $Sr = 0.028$  at  $Re = 700$ , and  $Sr = 0.03$  at  $Re = 1000$ . At the higher Reynolds number, both the cylinder and the sphere wake show that the symmetry is not completely lost but reappears periodically in phases with regular shedding and a seemingly stable orientation, over 3–4 shedding cycles. This lets us conclude that the loss of planar symmetry in axisymmetric wakes is the primary consequence of the imbalance of the long-wave helical waves.

#### ACKNOWLEDGEMENTS

The author wishes to acknowledge support from the Deutsche Forschungsgemeinschaft DFG through the Habilitationsstipendium Br 1494 /2-1

## REFERENCES

- ACHENBACH, E. 1974 Vortex shedding from spheres. *Journal of Fluid Mechanics* **62**, 209–221.
- JOHNSON, T. A. & PATEL, V. C. 1999 Flow past a sphere up to a Reynolds Number of 300. *Journal of Fluid Mechanics* **378**, 19–70.
- LEE, S. 2000 A numerical study of the unsteady wake behind a sphere in uniform flow at moderate Reynolds-number. *Computers and Fluids* (to appear).
- MAGARVAY, R. H. & BISHOP, R. L. 1961 Transition ranges for three-dimensional wakes. *Canadian Journal of Physics* **39**, 1418–1422.
- MITTAL, R. 1999 Planar symmetry in the unsteady wake of a sphere. *AIAA Journal* **37**, 388–390.
- NAKAMURA, I. 1976 Steady wake behind a sphere. *Physics of Fluids* **19**, 5–8.
- NATARAJAN, R. & ACRIVOS, A. 1993 The instability of the steady flow past spheres and disks. *Journal of Fluid Mechanics* **254**, 323–344.
- SAKAMOTO, H. & HANIU, H. 1990 A study of vortex shedding from spheres in a uniform flow. *ASME Journal of Fluids Engineering* **112**, 386–392.
- TOMBOULIDES, A. G. & ORSZAG, S. A. 2000 Numerical investigation of transitional and weak turbulent flow past a sphere. *Journal of Fluid Mechanics* **416**, 45–73.



## MULTIPLE MODES OF VORTEX-INDUCED VIBRATION OF A SPHERE

N. JAUVTIS, R. GOVARDHAN AND C. H. K. WILLIAMSON

*Sibley School of Mechanical and Aerospace Engineering, Upson Hall  
Cornell University, Ithaca, NY 14853–7501, U.S.A.*

(Received 7 September 2000, and in final form 8 November 2000)

In this work, we discover the existence of multiple modes of vortex-induced vibration of a tethered sphere in a free stream. In addition to the first two modes, defined as Modes I and II, and found originally by Govardhan & Williamson (1997), we find the existence of an unexpected Mode III at much higher normalized velocities ( $U^*$ ). This third mode, involving large-amplitude and remarkably periodic vibrations, was discovered by changing our focus from “light”, or buoyant, tethered spheres in a water facility (where relative density,  $m^* < 1$ ), to “heavy” spheres in wind tunnel facilities (where  $m^* \gg 1$ ). In this manner, we are able to achieve a very wide range of normalized velocities,  $U^* = 0 - 300$ , and investigate a wide range of masses,  $m^* = 0.1 - 1000$ . The first two modes might be identified as analogies to the 2S and 2P modes for an excited cylinder (Williamson & Roshko 1988), and can be associated with a lock-in of the vortex formation frequency with the natural frequency. These modes of sphere dynamics occur within the velocity regime  $U^* \sim 5 - 10$ . However, our Mode III occurs over a broad range of high velocity ( $U^* \sim 20 - 40$ ), where the body dynamics cannot be synchronised with the principal vortex formation frequency. At extremely high velocities ( $U^* > 100$ ), we find yet another mode of vibration that persists to at least  $U^* > 300$ , which we define as Mode IV, but in this case the unsteady oscillations are characterized by intermittent bursts of vibration. Regarding the periodic Mode III, it cannot be explained by classical “lock-in” of the principal vortex shedding and body motion, and one is left with a tantalizing question: *What causes this unexpected periodic high-speed mode of vortex-induced vibration?*

© 2001 Academic Press

### 1. INTRODUCTION

THE CASE of a tethered sphere vibrating in a fluid flow is perhaps one of the most basic fluid-structure interactions that one can imagine. By a wide variation of the mass of the sphere, one can consider the case of an underwater tethered buoyant body, or indeed a “heavy” sphere in air flow, acting as a pendulum, as examples of essentially the same general problem. It is quite surprising that, despite the fact that tethered bodies are quite ubiquitous in engineering, very few investigations have shown whether a tethered sphere will oscillate in a steady fluid flow or current. It was demonstrated by Williamson & Govardhan (1997) and Govardhan & Williamson (1997), that such a structure will indeed vibrate vigorously at large amplitude, and these oscillations have a direct impact on the tether angle and drag coefficient. Gross errors in predictions of mean response of a tethered structure will ensue unless one takes account of their tendency to vibrate. Other studies in the literature are concerned with the action of surface waves on tethered buoyant structures, and they employ empirically-determined drag and inertia coefficients to predict sphere dynamics (Harleman & Shapiro 1961; Shi-Igai & Kono 1969; Ogihara 1980).

In this work, we define a sphere as either “light” or “heavy”, depending on the value of the relative density or mass ratio,  $m^*$  (where  $m^* = \text{mass of sphere}/\text{mass of displaced fluid}$ ):

“Light” sphere:  $m^* < 1$ ;

“Heavy” sphere:  $m^* > 1$ .

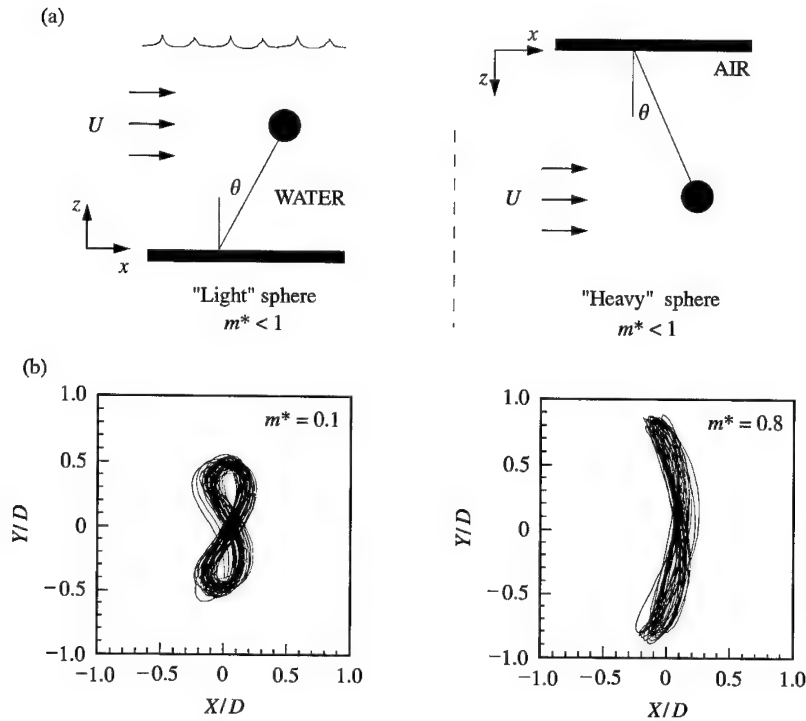


Figure 1. (a) Schematic of the experimental arrangement for the "light" and "heavy" tethered sphere. (b) Typical trajectories of sphere motion for "light" spheres.

Most of the studies in Govardhan & Williamson (1997) involved "light" spheres, where the tethered bodies in our Water Channel facility were buoyant, and typical trajectories were found to be of figure-of-eight or crescent topologies, as shown in Figure 1. The oscillation amplitudes transverse to the fluid flow ( $y$ -direction) are always found to be much larger than streamwise motions ( $x$ -direction), especially as the spheres become "heavy". It was shown in Williamson & Govardhan (1997) that the normalized amplitude ( $A^* = A/D = \text{amplitude/diameter}$ ) can be suitably collapsed using the normalized velocity  $U^* = U/f_N D$  (where  $U$  is the free-stream velocity,  $f_N$  the natural frequency in the fluid, and  $D$  the diameter), as could be expected on dimensional grounds. In the case of the vortex-induced vibration of a cylinder, such response plots show a resonance when the vortex shedding frequency  $f_V$  is close to the natural frequency of the structure  $f_N$ , which corresponds to a velocity  $U^* \sim 1/S \approx 5$ , where  $S$  is the Strouhal number. The response of the sphere, in Figure 2, shows just such a resonance at  $U^* \approx 6$ , which we define as the Mode I response, and this corresponds to the vortex formation frequency lying close to the (calculated) natural frequency of the tethered body.

At higher velocities ( $U^* > 8$ ), a Mode II periodic vibration appears, with large amplitudes close to one diameter, and in the case of the low mass,  $m^* = 0.8$ , the extent of the synchronization regime (the range in  $U^*$  over which large vibrations are observed) seems to persist to the limits of our facility, i.e. to at least  $U^* > 15$ . It is known that increasing the mass of a vibrating structure will decrease the synchronization regime; in the case of the vibrating cylinder, predictions of this effect can be made (Govardhan & Williamson 2000). In the case of sphere dynamics, by increasing the mass from  $m^* = 0.8$  to  $2.8$ , the end of the synchronization regime reduces to  $U^* = 11$ , as shown in Figure 2, and thus can be reached

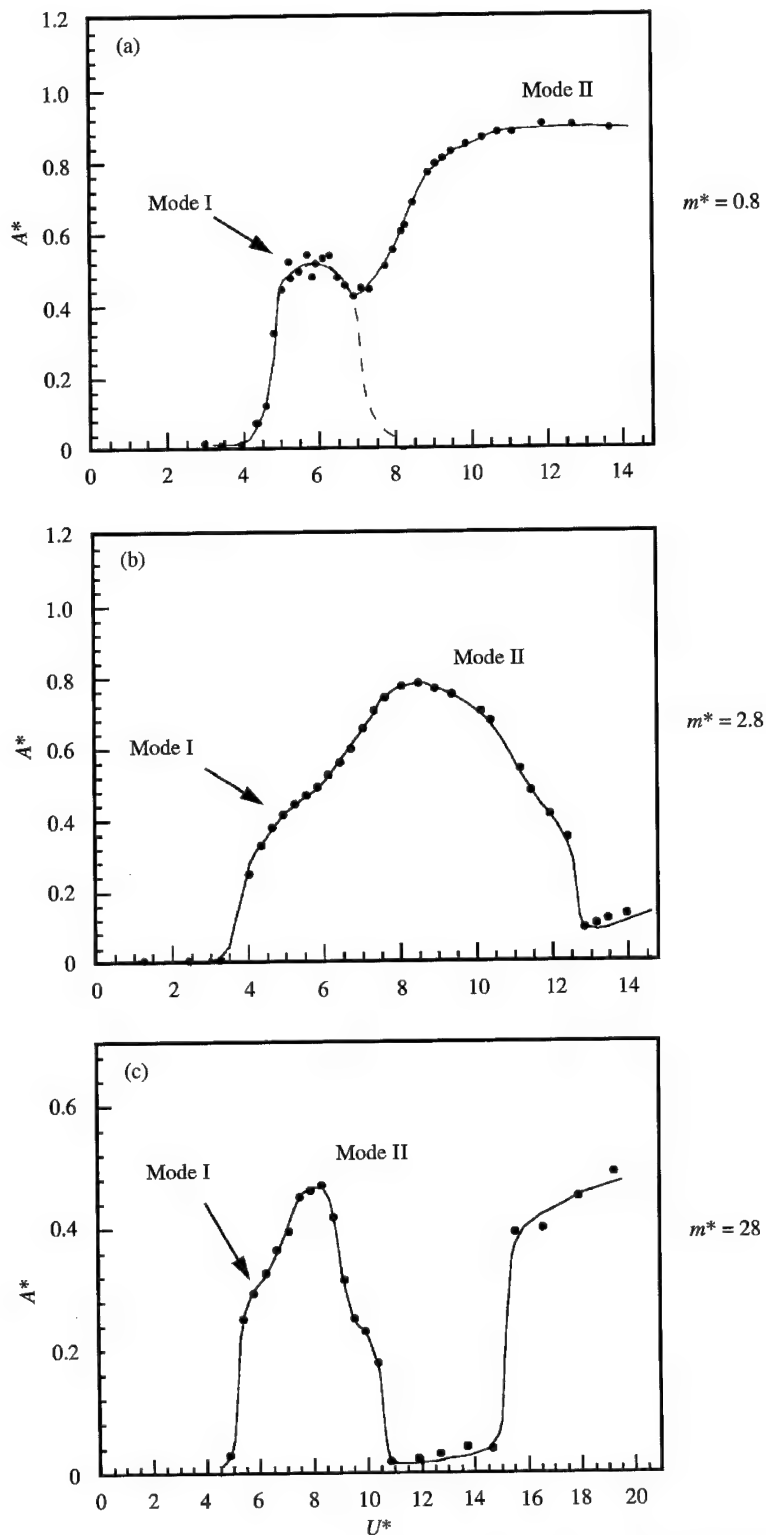


Figure 2. Amplitude response ( $A^*$ ) versus normalized flow velocity ( $U^*$ ), showing Modes I and II sphere oscillations: (a)  $m^* = 0.8$ , (b)  $m^* = 2.8$ , (c)  $m^* = 28$ .



within the flow speed limits of the water facility. It was naturally felt that any further increase in fluid velocity, beyond the limit of the Mode II regime (in the latter case, beyond  $U^* = 11$ ), would yield negligible amplitudes, and exhibit no further modes of response. However, one particular "strange" result from the Water Channel for  $m^* = 28$  showed an upsurge in the amplitude close to the limits of the facility flow speed, and beyond the Mode II regime, as shown in Figure 2. Our assumption for some months was that this was a problem with possible flow turbulence, as the channel was operating at "flat out" speed. In order to shed light on this problem, we decided to shift our efforts to wind tunnels, and purposely increase the mass ratio,  $m^*$ , beyond the maximum value possible in a water facility, and to enable much higher flow speeds to be studied, thereby permitting a much larger range of normalized velocities,  $U^*$ .

This paper presents the principal results from the research performed using the wind tunnels. We have been able to use large mass ratios, from  $m^* = 80$  up to 940, and we have achieved a very wide range of normalized velocity,  $U^* = 0-300$ . We shall see that not only was the upsurge in amplitude, mentioned above, a "real" effect, but that it is part of a wide regime of highly periodic large-amplitude vibrations. This is completely unexpected, because, at these high speeds, the vortex formation frequency is far above the vibration frequency, such that several cycles of vortex structures will be formed over a single period of body motion, and therefore the classical "lock-in" cannot occur. At higher velocities, beyond  $U^* = 100$ , we discover yet another mode of response, but in this case the oscillations are highly unsteady, and they occur in intermittent bursts.

## 2. EXPERIMENTAL DETAILS

The experiments described in the Introduction, which utilized the Cornell-ONR Water Channel, were conducted as part of Govardhan & Williamson (1997, 2000) and are described in detail therein. The wind tunnel experiments here involve the use of a 12 in  $\times$  12 in (test-section) wind tunnel, and an 18 in  $\times$  18 in tunnel (1 in = 25.4 mm). Typical spheres in this study had diameters of 6.9 and 7.6 cm, and had masses of 16.5 and 259.1 g, giving mass ratios of 80 and 940, and were tethered to the roof of the tunnel using fine polymer wires, of 0.001 in diameter. Displacement was measured using an optical biaxial displacement transducer, which was oriented upwards from beneath the wind tunnel lucite floor. We shall define the normalized amplitude of the transverse ( $y$ ) oscillations, unless otherwise noted, as  $A^* = \sqrt{2} y_{\text{rms}}/D$ , which, for purely sinusoidal oscillations, is simply  $A^* = A/D$ .

## 3. DISCOVERY OF MODE "III": A HIGH-VELOCITY RESPONSE MODE

By using the wind tunnels, we are able to explore the sphere dynamics at high normalized velocities, beyond the regimes of Modes I and II, using a sphere of mass,  $m^* = 80$ . We discover a new and unexpected mode of vibration, which we define as Mode III, and which is shown clearly in Figure 3, extending in a very broad regime of  $U^*$  from 20 to 40. This shows immediately that the upturn of data found in the Water Channel at the upper limit of flow speeds is in fact a real effect, and was a rather serendipitous signal of the beginnings of a significant regime of periodic vibrations, which we might otherwise have overlooked. However, suspicion remained that the results, though apparently real, could be related with the proximity of the sphere to the tunnel walls, or with the blockage of the sphere in the test section. For this reason, we relocated the complete experiment from the 12 in  $\times$  12 in tunnel to a larger tunnel of cross-section 18 in  $\times$  18 in, and found good agreement between the data

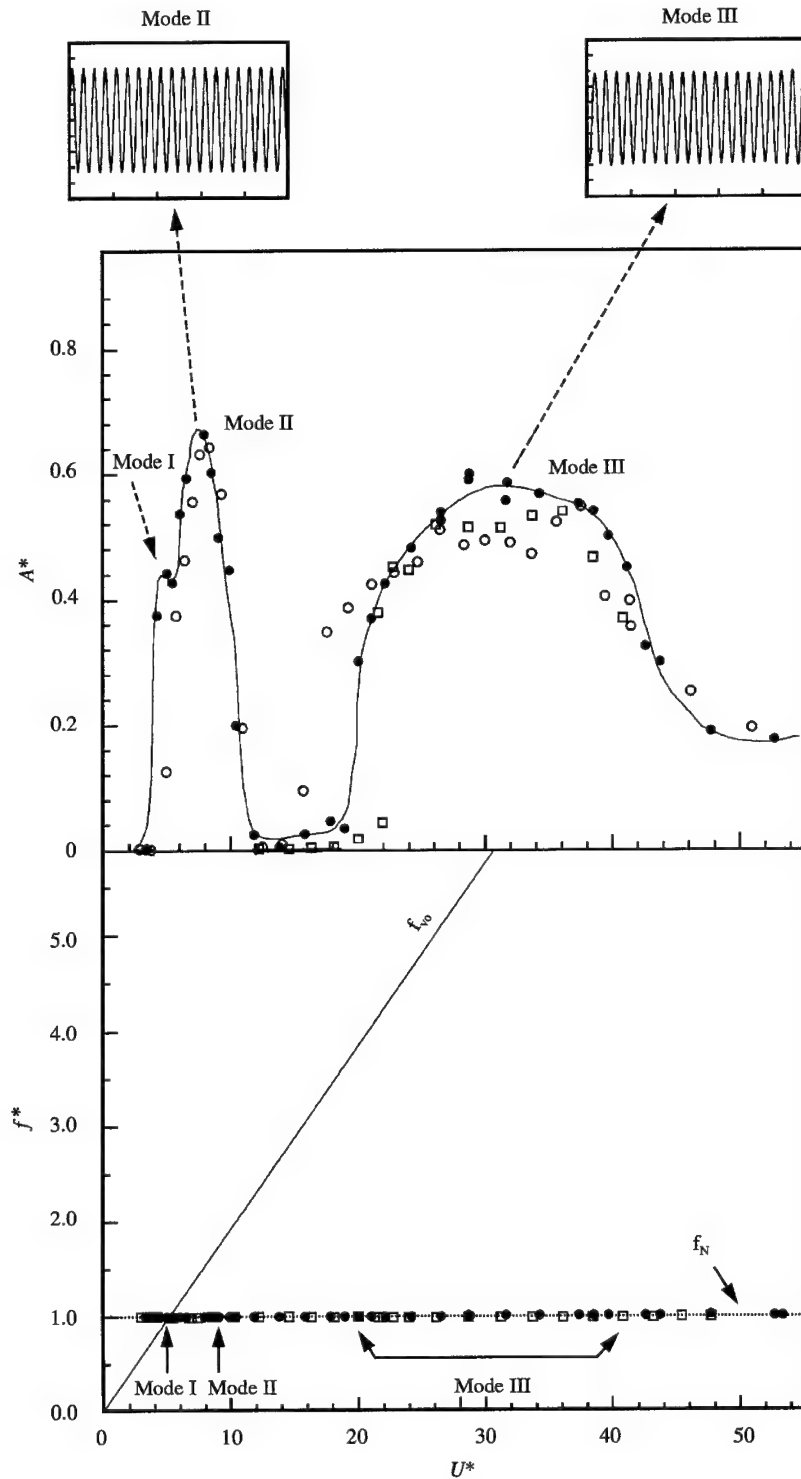


Figure 3. Amplitude ( $A^*$ ) and frequency ( $f^*$ ) response over a large range of  $U^*$ , showing the very broad regime of periodic Mode III oscillations ( $U^* = 20-40$ ). The oscillation frequency ( $f$ ) remains close to the natural frequency ( $f_N$ ) over the observed range of  $U^*$ ;  $f_{vo}$  is the non-oscillating shedding frequency.  $\bullet$ ,  $m^* = 80$  (12 in  $\times$  12 in wind tunnel);  $\circ$ ,  $m^* = 80$  (18 in  $\times$  18 in wind tunnel);  $\square$ ,  $m^* = 940$  (18 in  $\times$  18 in wind tunnel).

of the two tunnels. Finally, we studied the dynamics of a very heavy sphere of mass ratio,  $m^* = 940$ , in the larger tunnel, and found again the Mode III response regime, as shown in Figure 3. These experiments provide good evidence for the existence of this mode of vibration.

The sphere dynamics of Mode III are remarkably periodic, as indicated by the typical time traces of displacement in Figure 3. The oscillation frequency ( $f$ ) remains very close to the natural frequency ( $f_N$ ) of the tethered sphere (i.e.  $f^* = f/f_N \approx 1$ ), which is a consequence of the high mass of the spheres in this case. [Very low mass ratios yield oscillation frequencies which are higher than, and depart significantly from, the natural frequency, as shown in Govardhan & Williamson (1997)]. The existence of such a Mode III was completely unforeseen, because such a regime does not exist in the case of the cylinder free vibration, and also because it must reflect the presence of between 3 and 8 wavelengths of vortex formation, for each wavelength of body vibration. Therefore, this mode cannot be explained as a classical "lock-in" of the principal vortex shedding frequency with the body oscillation frequency.

For this high-speed mode of vibration to exist, there must be a net energy transfer from the fluid motions to the body motions, over each cycle of sphere oscillation. If one assumes that the transverse displacement ( $y$ ) and force ( $F$ ) are represented by the following functions:

$$y(t) = A \sin(\omega t),$$

$$F(t) = F_o \sin(\omega_o t + \phi)$$

and that the system damping and stiffness are linear, then one can simply show that the net energy transfer over a cycle of body oscillation ( $E_{in}$ ) is given by

$$E_{in} = (F_o A \omega) \sin \phi \int_0^T \cos(\omega t) \cos(\omega_o t) dt.$$

This integral is only nonzero if  $\omega = \omega_o$ . In other words, as one might expect, there is only energy transfer if there is a periodic component of the fluid force synchronized with the body oscillation frequency. The principal vortex structures are formed at a frequency much higher than the body oscillation frequency, and these cannot be expected to contribute to the body dynamics.

*However, there must exist vortex dynamics which are repeatable in each cycle, and which give rise to the fluid forcing component that is synchronized with the body motion.*

One should note that it is possible that the vortex shedding is modulated by the low-frequency body motion, such that self-excited motion will ensue. Although the existence of this Mode III is reported in this paper, the vorticity dynamics, which would explain its existence, will be explored in Govardhan & Williamson (2001), using the DPIV technique.

#### 4. MODE "IV": INTERMITTENT BURSTS OF LARGE AMPLITUDE VIBRATION

With further increase of normalized flow speed, beyond the regime for Mode III, one might finally expect negligible response amplitude, and this is the case until about  $U^* = 100$ . However, beyond this speed, we discovered yet another vibration mode, that grows in amplitude and persists to the limit in flow speed of our wind tunnel (in excess of  $U^* = 300$ ), as shown in Figure 4. (We must expect that the amplitude of this mode will ultimately saturate at sufficiently high velocity.) In this case, the sphere dynamics are not close to periodic, and are characterized by intermittent bursts of large-amplitude vibration, as may be seen in the typical displacement time traces in Figure 4, at  $U^* = 120$  and 220. These

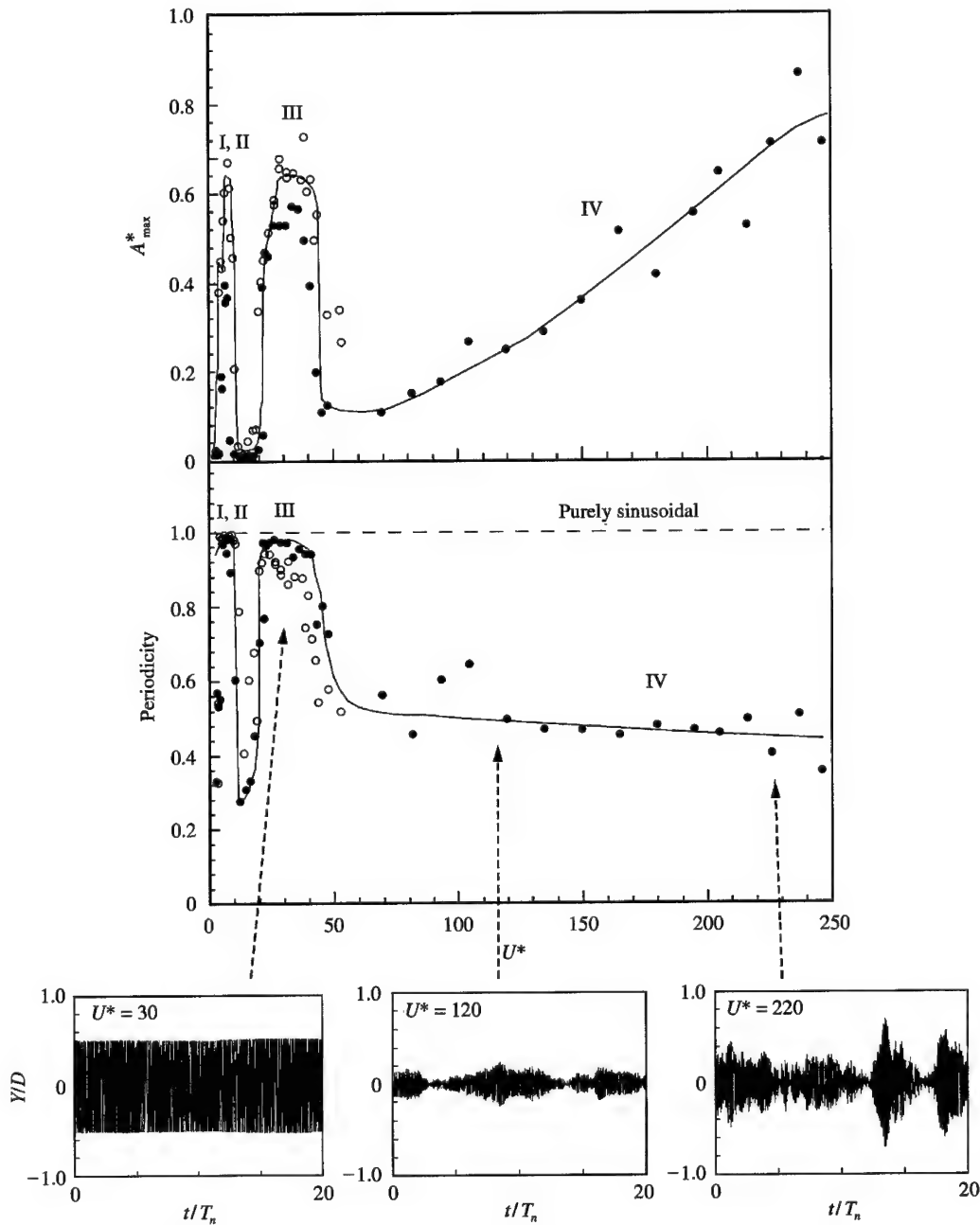


Figure 4. Amplitude response and "periodicity" ( $\sqrt{2}y_{\text{rms}}/y_{\text{max}}$ ) versus the normalized flow velocity ( $U^*$ ), showing that the Mode IV oscillations are not close to periodic. The "periodicity" is close to 1.0 for Modes I-III, indicating that these modes are quite sinusoidal.

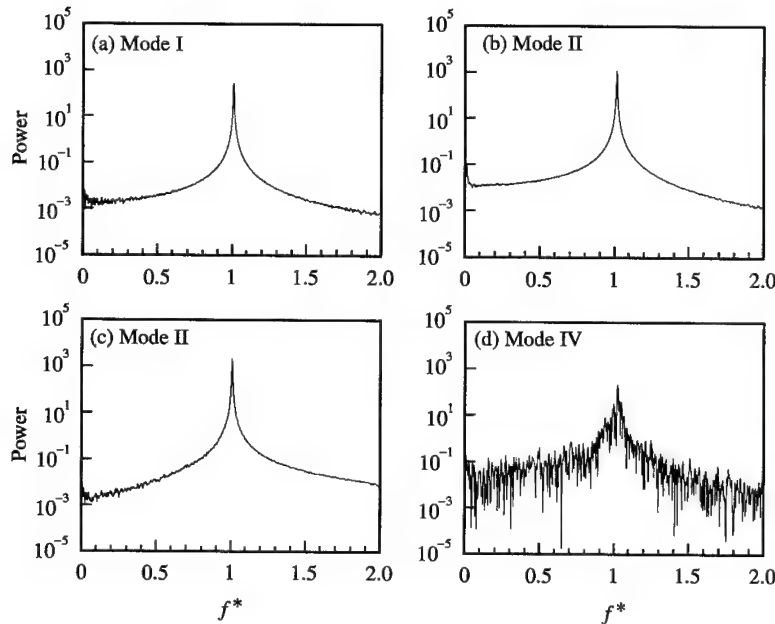


Figure 5. Position spectra in the different sphere oscillation modes for  $m^* = 940$ . Interestingly, although Mode IV has a low “periodicity”, the vibration frequency ( $f$ ) remains close to the natural frequency ( $f_N$ ) i.e.  $f^* = f/f_N \approx 1.0$ .

intermittent vibrations may be contrasted clearly with the periodic vibrations of Mode III, also shown in the figure, for  $U^* = 30$ .

A measure of the periodicity of the displacement may be given by plotting what we call the “periodicity”  $= (\sqrt{2} y_{\text{rms}}/y_{\text{max}})$ , as a function of velocity,  $U^*$ . A purely sinusoidal function has a value of “periodicity” equal to 1.0, and so the vibration Modes I, II and III are evidently strongly periodic, as also shown by the spectra in Figure 5. Mode IV, as expected has a low “periodicity”, but interestingly, despite the bursts of large-amplitude vibration for this mode, the vibration frequency remains very close to the natural frequency throughout the range of velocity up to at least  $U^* = 300$ , as shown by the typical spectrum in Figure 5. Clearly, the much higher principal vortex shedding frequency (around 40–50 times the vibration frequency) is not itself responsible for these large vibrations! The origin of these large transient bursts of vibration remains unknown.

## 5. CONCLUDING REMARKS

In this paper, we present evidence for the existence of an unforeseen, highly periodic mode of vortex-induced vibration for a tethered sphere, which occurs at speeds far above what might be expected, based on classical “lock-in”. The sphere appears to oscillate at large amplitudes, which can be up to one diameter for spheres of moderate mass ratio ( $m^* \sim 10$ ), over a broad range of normalized velocities,  $U^* = 20$ –40. Vibration modes of a tethered sphere, which might be explained in terms of classical lock-in of the vortex frequency with the body frequency, have been discovered in Govardhan & Williamson (1997, 2001), and defined there as Modes I and II.

However, for the present high-speed “Mode III”, the principal vortex shedding frequency is from 3 to 8 times the body oscillation frequency, and so the classical lock-in of frequencies cannot explain this vibration mode. Nevertheless, in order for these remarkably periodic

vibrations to occur, there must be a component of fluid force that is exciting the body at its oscillation frequency. One may suggest that the body vibration is causing some modulation to the vortex formation sufficient to provide a fluid force at the vibration frequency, and with the right phase (between force and displacement) to excite such vibration. Indications of this are suggested by further work using force, displacement and vorticity measurements in Govardhan & Williamson (2001). One might suggest that the high-speed Mode III vibrations are the result of a "movement-induced vibration" of the type classified in Naudascher & Rockwell (1993), such as flutter and galloping, where the body dynamics may be explained in terms of quasi-steady analysis. In our case, the body is spherically symmetric, so a direct link is not evident. A further unsteady mode of vibration (defined here as Mode IV), characterized by intermittent burst of large amplitude, is found for extremely high velocities beyond  $U^* = 100$ , and the origin of this mode remains unknown.

#### ACKNOWLEDGEMENTS

The support from the Ocean Engineering Division of O.N.R., monitored by Dr Tom Swean (O.N.R. Contract No. N00014-95-1-0332), and the Cornell Alumni Undergraduate Research Fund (in support of NJ) is gratefully acknowledged. We would like to acknowledge the ongoing enlightening discussions with Prof. Don Rockwell.

#### REFERENCES

- GOVARDHAN, R. & WILLIAMSON, C. H. K. 1997 Vortex induced motions of a tethered sphere. *Journal of Wind Engineering and Industrial Aerodynamics* **69–71**, 375–385.
- GOVARDHAN, R. & WILLIAMSON, C. H. K. 2000 Modes of vortex formation and frequency response for a freely vibrating cylinder. *Journal of Fluid Mechanics* **420**, 85–130.
- GOVARDHAN, R. & WILLIAMSON, C. H. K. 2001 Vortex-induced vibration of a sphere. Submitted to *Journal of Fluid Mechanics*.
- HARLEMAN, D. R. F. & SHAPIRO, W. C. 1961 The dynamics of a submerged moored sphere in oscillatory waves. *Coastal Engineering* **2**, 746–765.
- NAUDASCHER, E. & ROCKWELL, D. 1993 *Flow-Induced Vibrations: An Engineering Guide*. Rotterdam: A. A. Balkema.
- OGIHARA, K. 1980 Theoretical analysis on the transverse motion of a buoy by a surface wave. *Applied Ocean Research* **2**, 51–56.
- SHI-IGAL, H. & KONO, T. 1969 Study on vibration of submerged spheres caused by surface waves. *Coastal Engineering in Japan* **12**, 29–40.
- WILLIAMSON, C. H. K. & GOVARDHAN, R. 1997 Dynamics and forcing of a tethered body in a fluid flow. *Journal of Fluids and Structures* **11**, 293–305.
- WILLIAMSON, C. H. K. & ROSKO, A. 1988 Vortex formation in the wake of an oscillating cylinder. *Journal of Fluids and Structures* **2**, 355–381.



## PERIODIC WAKES OF LOW ASPECT RATIO CYLINDERS WITH FREE HEMISPHERICAL ENDS

L. SCHOUVEILER AND M. PROVANSAL

*Institut de Recherche sur les Phénomènes Hors Equilibre  
UMR 6594 CNRS/Universités Aix-Marseille I & II  
49, rue F. Joliot-Curie, B.P. 146, F-13884 Marseille Cedex 13, France*

(Received 21 September 2000, and in final form 10 November 2000)

The wakes of circular cylinders with free hemispherical ends and of different aspect ratios (length-to-diameter ratios) are experimentally studied for moderate Reynolds numbers. This investigation is restricted to cylinders with low aspect ratios, namely less than 5, and includes the case of the sphere. The transition to nonstationarity of the flow in these cylinder wakes is the main focus of this work: the results show that the stability of wakes is strongly dependent on aspect ratio and is also affected by the free-end conditions. We characterize the frequency, amplitude and phase as well as the critical Reynolds number of the periodic vortex shedding regime.

© 2001 Academic Press

### 1. INTRODUCTION

THE ALTERNATE VORTEX SHEDDING from the two sides of a cylinder, due to the Bénard–von Kármán instability, has received a great deal of attention in the past and these researches have been the object of extensive reviews [e.g., Williamson (1996)]. Although three-dimensional phenomena, such as oblique shedding, cellular structure and dislocations, are dominant for finite cylinders, even with large length-to-diameter ratios, the studies deal mainly with the two-dimensional parallel shedding. On the one hand, recent investigations have been in part devoted to experimentally promote parallel vortex shedding by manipulation of the end conditions [see, e.g., Williamson (1988), Eisenlohr & Eckelmann (1989), Hammache & Gharib (1989)] and, on the other hand, to model the three-dimensional structure of the cylinder wake. For example, Albarède & Monkewitz (1992) and Albarède & Provansal (1995) have shown the ability of the phenomenological Ginzburg–Landau model to describe the three-dimensional phenomena observed in the wake of a finite circular cylinder as a collective interaction of nonlinear oscillators.

For a finite cylinder with “natural” end conditions (i.e., without manipulation), namely with end plates parallel to the free stream or with free ends, experiments of Gerich & Eckelmann (1982) show a cellular structure for the periodic wake, with cells of lower frequency in the regions near the ends, for long enough cylinders [see also Williamson (1989)]. Free-end cylinder wakes have also been investigated numerically by Dauchy *et al.* (1997) and experimentally by Slaouti & Gerrard (1981); they report that the vortex shedding is diminished or suppressed near the free ends.

The sphere appears as the limiting case of the geometry of cylinders with two free hemispherical ends as considered in the present investigation. In contrast to the cylinder, for the sphere wake, the transition to a time-dependent (periodic) flow is preceded by a regular axisymmetry-breaking bifurcation giving rise to a wake with a plane symmetry, as described

e.g. in recent experimental (Sakamoto & Haniu 1995; Ormières 1999) or numerical (Johnson & Patel 1999; Tomboulides & Orszag 2000; Ghidersa & Dušek 2000) studies. Although this plane symmetry is maintained in the periodic regime resulting from this transition [Mittal (1999), and the previously cited references], the visualizations [see, e.g., Leweke *et al.* (1999)] of the sphere wake reveals a complex three-dimensional spatial structure with the periodic shedding of connected vortex loops.

Zdravkovich *et al.* (1989) have performed experiments for low aspect ratio free-end cylinders. In particular, using a oil-film visualization technique, they report a change of the symmetry of the surface pattern when the aspect ratio is reduced below 3.

In this paper, the wakes of circular cylinders with free hemispherical ends, including the sphere, are experimentally studied at moderate Reynolds number. The experimental set-up is presented in Section 2. Effects of aspect ratio and free ends on the onset of transition to the periodic wake are discussed in Section 3. The periodic state is characterized in Section 4 and the conclusion and the perspectives are given in Section 5.

## 2. EXPERIMENTAL DETAILS

The wake experiments were carried out in a square test-section ( $0.25 \times 0.25 \text{ m}^2$ ) of an open low-turbulence wind tunnel. Nine circular cylinders of same diameter  $D = 10 \text{ mm}$  and of different lengths  $L$  were used. To assure a “continuous” change of the body geometry from the cylinder to the sphere, hemispherical ends were used. The values of the aspect ratio  $L/D$  were 5, 4, 3, 2.6, 2.3, 2, 1.6, 1.3 and 1, respectively; the case  $L/D = 1$  corresponding to the sphere. The cylinders were mounted horizontally at the centre of the working section, with axis perpendicular to the free stream. They were held in their centre by a bent rigid thin rod, as shown in Figure 1, in such a way that their ends were free. The rod was upstream of the cylinders and inclined with the free stream of an angle  $\alpha$  of order  $10^\circ$ . One effect of this holding system was to induce a weak velocity gradient and thus to freeze the symmetry plane (see Section 1) of the sphere wake in the plane containing the rod (Sakamoto & Haniu 1995; Ormières & Provansal 1999). Ormières (1999) has shown that, for the sphere, the upstream bent rod introduces no change to the dynamics of the wake but can slightly vary its threshold of transition to nonstationarity.

The velocities were measured by laser Doppler anemometry with a mobile measurement point. The free-stream velocity  $U$  was measured  $6D$  upstream of the cylinders and corrections were applied for the blockage effect and for the growth of the boundary layers on the

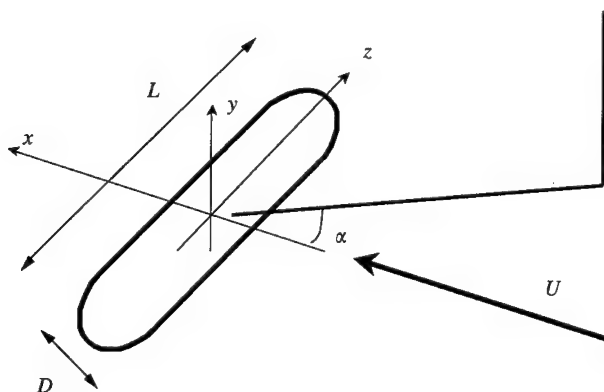


Figure 1. Experimental geometry and coordinate system.



tunnel walls. The temperature of the flow was measured with a thermocouple to calculate the kinematic viscosity  $\nu$  of air. Frequencies  $f$  and amplitudes of the vortex shedding modes were obtained by spectral analysis of the streamwise velocity measured in the wakes. For the phase measurements, a hot-wire anemometer was used. The hot-wire sensor was placed at a fixed position in the wake of the cylinders and the average phase difference relative to the signal of the mobile laser Doppler anemometer was deduced from the cross-correlation function.

For a given cylinder, the wake dynamics is controlled by the Reynolds number based on the cylinder diameter  $Re = UD/\nu$  which was varied between 50 and 400 during the present experiments. The shedding frequencies  $f$  are expressed in nondimensional form either with the Strouhal number  $St = fD/U$  or with the Roshko number  $Ro = fD^2/\nu$  which is based on the diffusion time. The interest in using  $Ro$  is to avoid the free-stream velocity  $U$  which has the highest associated uncertainty in the experiments. The estimated errors for the different quantities give a statistical error for  $Re$  and for  $Ro$  in the periodic regime of less than 2%.

For the following, we use the Cartesian coordinates  $(x, y, z)$  defined in Figure 1, with the origin at the centre of the cylinder.

### 3. TRANSITION TO NONSTATIONARITY

Increasing the Reynolds number, at a critical value  $Re_c$ , we observe a transition from a stationary state to a time-dependent regime for the flow in the wake of a cylinder. Figure 2 shows the evolution with the Reynolds number  $Re$  of the square of the amplitude of the streamwise velocity fluctuation  $u_x'$  measured for the sphere ( $L/D = 1$ ) at fixed positions ( $x/D = 6.5$ ,  $y/D = -0.5$ ,  $z/D = 0.5$ ) in the wake. At a well-defined value  $Re_c$  of  $Re$ , the fluctuation amplitude deviates from zero; this critical Reynolds number for the transition to the nonstationarity is then determined by extrapolation to zero amplitude of the linear behaviour of the  $u_x'^2(Re)$  relationship near the threshold  $Re_c$ . Such a linear behaviour is consistent with a Landau-Hopf bifurcation. The critical value  $Re_c$  for a given cylinder has been found to be independent of the location of the measurement point. These fluctuation amplitude measurements have been performed for both increasing and decreasing the Reynolds number and no evidence of a hysteretic cycle has been detected. Thus, the bifurcation associated with the appearance of the nonstationary wake flow appears supercritical for all the cylinders considered.

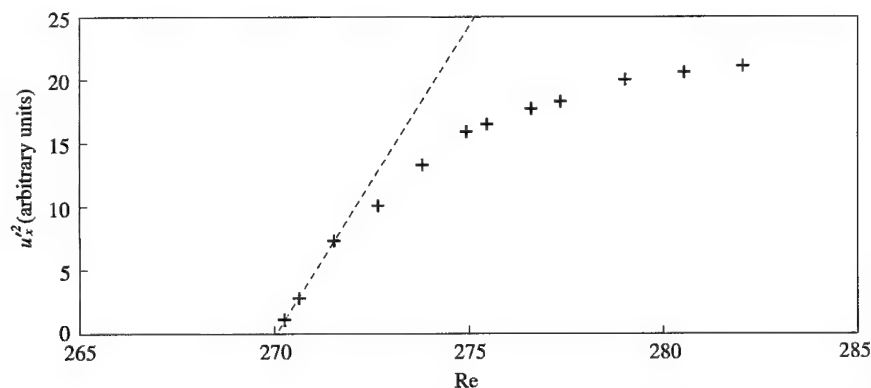


Figure 2. Square of the amplitude of the streamwise velocity fluctuation as a function of Reynolds number.  $L/D = 1$  (sphere),  $x/D = 6.5$ ,  $y/D = -0.5$ ,  $z/D = 0.5$ .

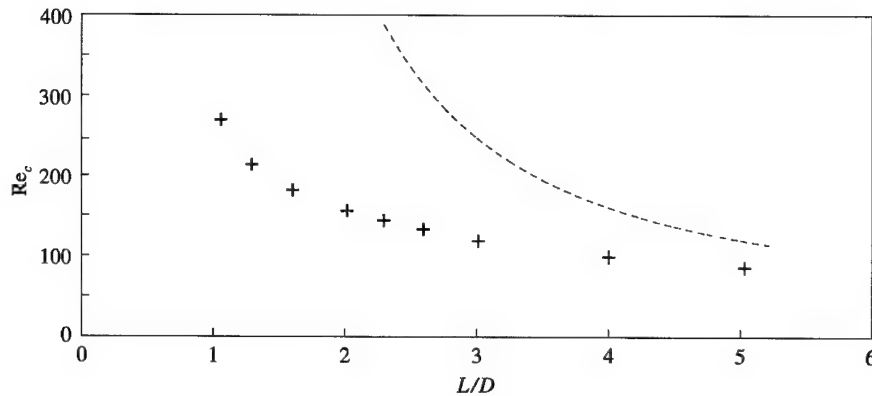


Figure 3. Critical Reynolds number as a function of aspect ratio; ---, cylinder confined between two end plates (Norberg 1994).

The critical values  $Re_c$  we have obtained for the different cylinders are displayed in Figure 3 as a function of the aspect ratio  $L/D$ . This diagram shows the strong influence of the aspect ratio on the stability of the wake flow: the smaller the  $L/D$ , the more stable is the stationary regime. In fact, the value of  $Re_c$  evolves from about 85 for  $L/D = 5$  to about 270 for  $L/D = 1$ . The critical Reynolds number we obtained for the sphere (of about 270) agrees with the values found in the recent numerical simulations of Johnson & Patel (1999), Tomboulides & Orszag (2000) and Ghidersa & Dušek (2000) which are between 270 and 280. The small difference with the critical value given in the experimental study of Ormières & Provansal (1999), between 275 and 285, can be explained by a few experimental details. In our case, the sphere, constructed from two hemispheres, presents a slight deviation from the perfect sphere used by Ormières & Provansal; moreover, the upstream rod tends to weakly decrease this value.

The stabilizing effect of the reduction of the aspect ratio has been also observed for cylinders confined between two end plates parallel with the free stream (Mathis *et al.* 1984; Lee & Budwig 1991; Norberg 1994). The results obtained by Norberg for aspect ratio larger than 2 are displayed in Figure 3. These observations agree, at least qualitatively, with the Ginzburg–Landau model which predicts that  $Re_c$  is given by the relation  $Re_c = Re_\infty + B(L/D)^{-2}$ , where  $Re_\infty$  is the critical Reynolds number for the parallel vortex shedding ( $L/D \rightarrow \infty$ ) which is known to be about 47; the constant  $B$  is proportional to the diffusive coupling constant  $\mu_r$  of the model [see, e.g., Albarède & Provansal (1995)].

Let us note that Albarède & Provansal (1995) have specified that the characteristic length to be considered in the model is not the geometrical one of the cylinder  $L$  but an effective length  $L'$  of the oscillating modes (see the next section). Finally, the comparison with the results of Norberg (1994) of the critical values  $Re_c$  (Figure 3) shows that the free-end conditions tend to decrease the stability of the cylinder wake. This could be explained by a smaller effective length due to the three-dimensional flow near the free ends.

#### 4. PERIODIC REGIME

For Reynolds numbers larger than the critical value  $Re_c$ , the spectrum of the streamwise velocity fluctuations measured in the wake, presents a well-defined peak at a frequency  $f$ , and eventually at its harmonics, characteristic of a periodic state. This single-frequency regime, corresponding to periodic vortex shedding, continues up to a second critical value

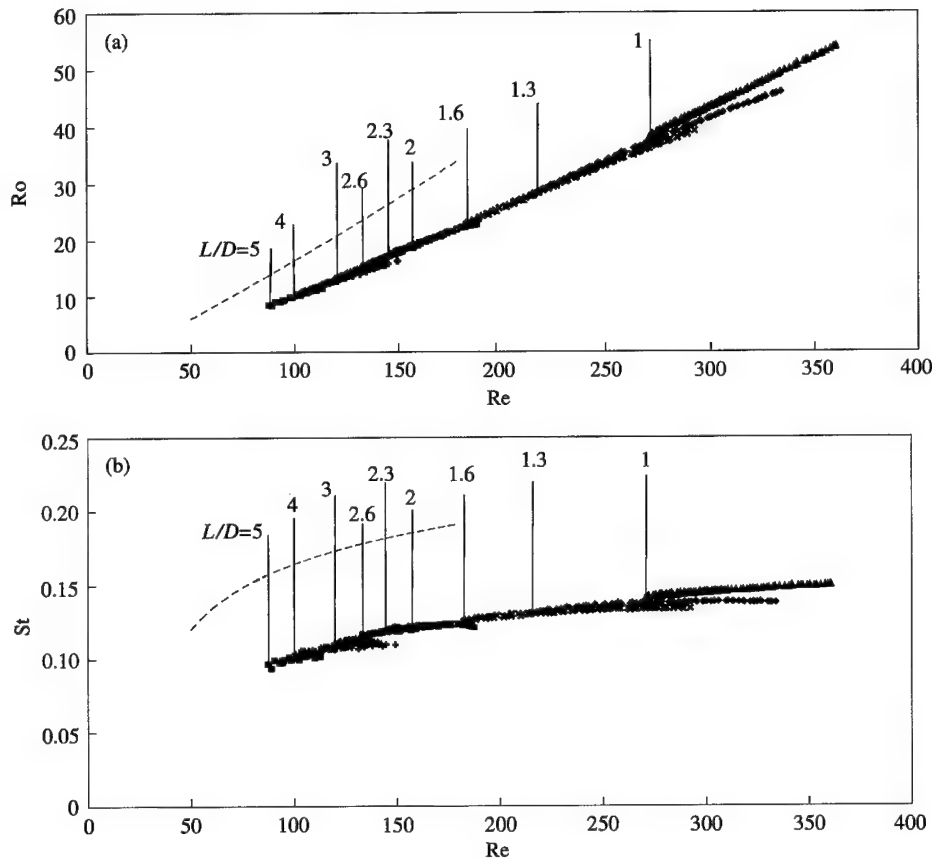


Figure 4. (a) Roshko number and (b) Strouhal number as functions of Reynolds number for the different aspect ratios; ---, parallel shedding (Lewke & Provansal 1995). The vertical lines mark the thresholds of transition to the periodic regime for the nine cylinders.

$Re_{c2}$  of the Reynolds number (also a function of aspect ratio) after which the velocity fluctuations appear less regular and their spectrum is characterized by the presence of a second peak at a lower frequency. When the Reynolds number is further increased, nonlinear interactions between modes contribute to the appearance of other peaks at frequencies equal to linear combinations of the two frequencies.

To characterize the periodic regime of cylinder wakes, the frequency of the vortex shedding has been determined. First, we can note that the same frequency has been found for different locations in the wake. In particular, no variation of the frequency along the span of the cylinder has been detected, meaning that the wake has a one-cell structure. This observation is consistent with the experimental results of Gerich & Eckelmann (1982), who report that the cellular structure of the wake disappears when the cylinder length is shorter than the dimension of the two end cells.

Figure 4(a,b) presents the dimensionless shedding frequency, expressed respectively, in terms of the Roshko number  $Ro$  and the Strouhal number  $St$ . The variation of  $Ro$  appears as an increasing function of the Reynolds number and is quite continuous for all the considered cylinders but with a slight change of the slope for the sphere ( $L/D = 1$ ). For the sphere wake at a Reynolds number of 300, the numerical studies of Johnson & Patel (1999), Tomboulides & Orszag (2000) and Ghidersa & Dušek (2000) furnish values for  $Ro$  between

40.5 and 41.1, which are slightly below the value of about 43.4 we found. According to the experimental study of Sakamoto & Haniu (1995) of a sphere in a uniform shear flow, this difference could be due to the velocity gradient induced by the upstream rod (see Section 2).

Although the upper limits  $Re_{c2}$  have not been precisely determined, we can also note the broadening of the Reynolds number range  $[Re_c, Re_{c2}]$  for the periodic regime when the aspect ratio is decreased. This stabilizing effect of the reduction of the aspect ratio upon the limit  $Re_{c2}$  is consistent with the evolution of the critical Reynolds number  $Re_c$ .

For comparison, we have displayed in Figure 4 the frequencies obtained by Leweke & Provansal (1995) for parallel shedding at Reynolds numbers between 47 and 180. We note that the shedding frequencies in the wake of low aspect ratio cylinders with free hemispherical ends are much smaller than the frequencies associated with the parallel shedding. In particular, in the whole Reynolds number range considered, the Strouhal number is less than the asymptotic value of 0.2 for parallel shedding. A similar observation has been reported by Gerich & Eckelmann (1982) for cylinders confined between two parallel end plates when the cylinder length is smaller than the dimension of the two lower frequency end cells. The difference of frequencies between oblique and parallel shedding has been explained by Williamson (1988) as a consequence of the inclination  $\theta$  of the vortex lines leading to a universal  $St(Re)$  curve after correction for the  $\cos \theta$  term. For example, at  $Re = 92$  (value corresponding to the measurements of Figure 5), we measure  $Ro \approx 8.9$  for the cylinder of aspect ratio  $L/D = 5$ , which is compared with the value of 14.7 deduced from the universal parallel shedding law giving an average inclination angle of about  $52^\circ$  ( $\cos \theta = 8.9/14.7$ ).

In Figure 5(a), we present an example (for  $L/D = 5$ ,  $Re = 92$ ) of the amplitude evolution of the streamwise velocity fluctuation with the spanwise position  $z$ . We can see that this amplitude is strongly diminished near the free ends of the cylinder as reported in the numerical work of Dauchy *et al.* (1997). We also note that, from flow visualizations, Slaouti & Gerrard (1981) state that the free-end effect is to suppress the vortex shedding in the vicinity of the ends.

Thus, one can observe a significant amplitude in the spanwise direction for  $z$  in the interval  $[-1D, +1D]$ . The effective length  $L'$  of the oscillating mode is then determined by intersecting the cosine law fit [dashed curve in Figure 5(a)], characteristic of a single-mode regime, with the  $z$ -axis. This length  $L'$  is much smaller than the geometric length  $L$  of the cylinder which extends from  $-2.5D$  to  $2.5D$ . The subcritical flow near the boundary region of the ends suppresses the instability and reduces the effective length  $L'$ . Spanwise evolution measurements of the fluctuation amplitude have been repeated for all the cylinders at different Reynolds number. The effective length  $L'$  appears to be function not only of the aspect ratio but also of the Reynolds number.

The isophase displayed in Figure 5(b) has been obtained under the same conditions ( $L/D = 5$  and  $Re = 92$ ) as the amplitude measurements [Figure 5(a)]. This curve is deduced from measurements of the spanwise and streamwise phase evolutions by neglecting the variation of the phase with the transverse coordinate  $y$ . The phase varies linearly in the streamwise direction with a spatial wavelength which evolves from  $5.7D$  to  $7.5D$  for cylinders of aspect ratio from 1 to 5, respectively. The isophase curve presents a flat hat shape. From this plot, the angle of inclination of the vortices linked to the strong variation at the sides would be about  $70^\circ$ , which is in agreement with the average value deduced from the frequency measurements.

The effective length  $L'$  has been determined for Reynolds numbers close to the threshold  $Re_c$  for the cylinders of aspect ratio 5, 4, 3 and 2. The corresponding values of  $Re_c$  are displayed in Figure 6 as function of  $(L'/D)^{-2}$  for comparison with the Ginzburg–Landau model.

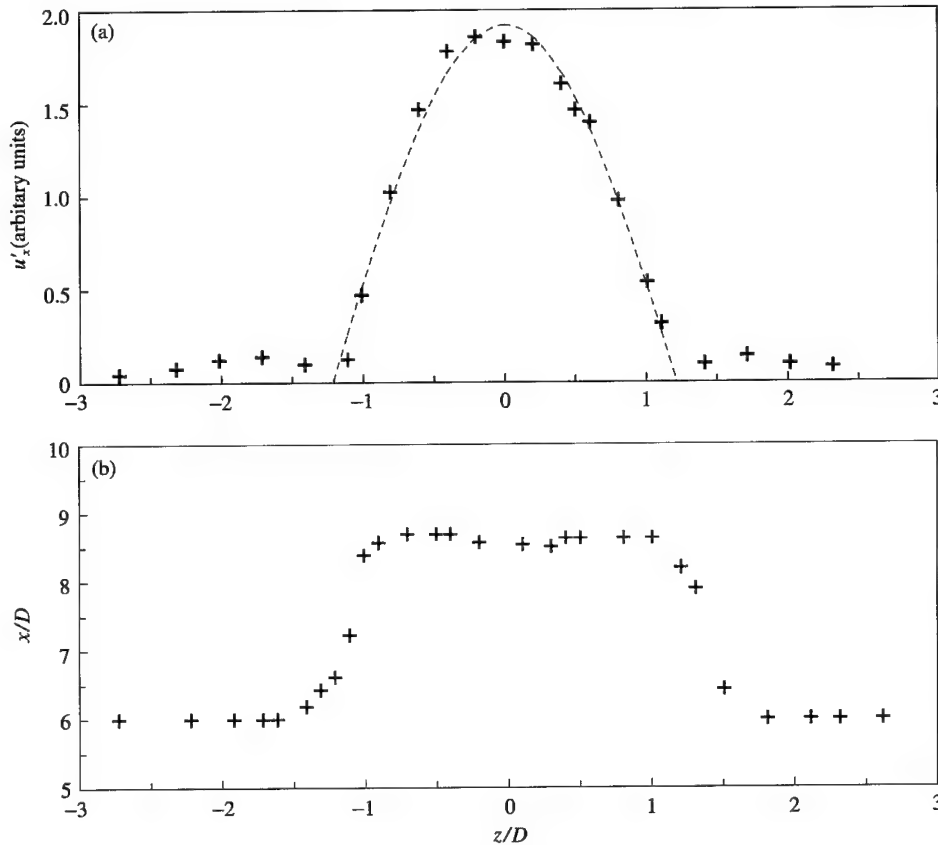


Figure 5. (a) Amplitude of the streamwise velocity fluctuation as a function of spanwise position; ---, fit with a cosine law ( $L/D = 5$ ,  $Re = 92$ ;  $x/D = 6$ ,  $y/D = -1.25$ ). (b) Isophase in the  $(x, z)$  plane  $y = -1.25D$  ( $L/D = 5$ ,  $Re = 92$ ).

According to this model, these data can be fitted with a law  $Re_c = A + B(L'/D)^{-2}$  having two adjustable parameters,  $A$  and  $B$ . The result of such a least-squares fit gives  $A \approx 46.1$  and  $B \approx 252.4$ . The value of 46.1 for  $A$  is very close to the known value, approximately 47, for the critical Reynolds number  $Re_\infty$  for the transition to parallel shedding ( $L'/D \rightarrow \infty$ ). From parameter  $B$ , we can evaluate the diffusive coupling constant  $\mu_r$  of the model to be approximately  $5.1\nu$  which is of the same order as the value  $\mu_r = 10(\pm 4)\nu$  obtained by Leweke & Provansal (1994). Let us note that, for this evaluation, we need the value of the linear growth rate  $\sigma_r = k(\nu/D^2)(Re - Re_\infty)$ . In the case of circular cylinders the value  $k = 0.2$  is valid for aspect ratio as low as 6, but differs to the one obtained for the sphere for which the measurements of Ormières (1999) give  $k \approx 1$ .

## 5. CONCLUSIONS AND PERSPECTIVES

The transition from steady to unsteady flow has been studied experimentally in the wake of nine bluff bodies from a circular cylinder to a sphere. The critical Reynolds numbers have been deduced from measurements of oscillation amplitude and have been shown to follow a Landau-type bifurcation in each case. The curves of variation of frequency with the Reynolds number follow a continuous envelope for all nine cylinders. Whereas the visualizations of Zdravkovich *et al.* (1989) show a symmetry change for an aspect ratio around 3,

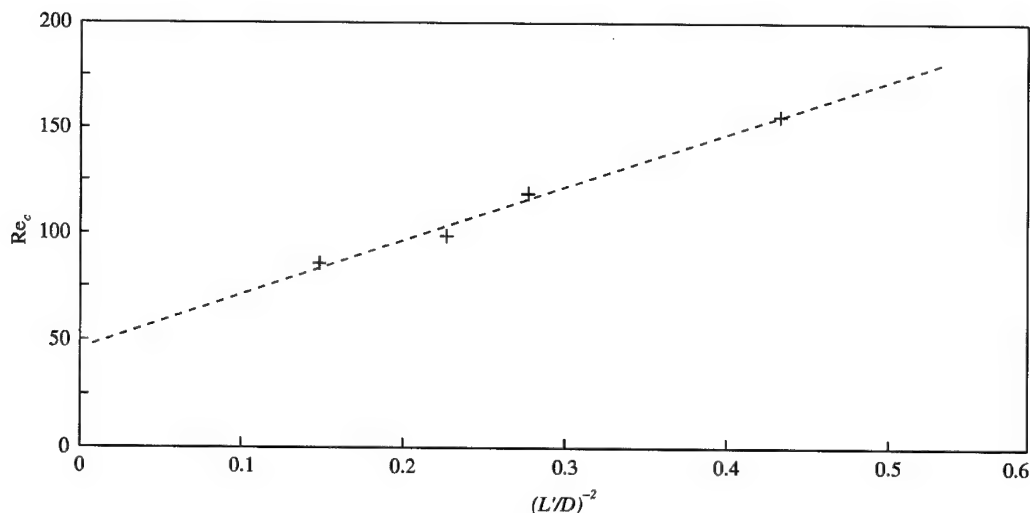


Figure 6. Critical Reynolds number as a function of  $(L'/D)^{-2}$ ,  $L'$  is the effective length of the oscillating mode as defined in the text; - - -, fit with the formula  $Re_c = A + B(L'/D)^{-2}$ .

such a behaviour is not observed in our quantitative results. Measurements of the amplitude evolution in the spanwise direction have been performed, allowing an effective length of the oscillating modes to be deduced, which is shorter than the geometric cylinder length. Finally, the critical Reynolds number has been plotted as a function of the effective aspect ratio in agreement with the prediction of the Ginzburg–Landau model.

Recently, Owen *et al.* (2000) have been able to suppress the von Kármán vortex shedding and to reduce the drag using a sinuous cylinder, namely a circular cylinder with a constant diameter and a sinuous axis. In such a configuration, the visualizations reveal vortical structures similar to the characteristic connected vortex loops observed behind a sphere or short free-end cylinders. Preliminary measurements have been undertaken with a sinuous cylinder with a spanwise wavelength of  $5.6D$  and a peak-to-peak amplitude of  $2D$ . A critical Reynolds number of 104 has been found. From the results of Figure 3, this value would correspond to a free-end cylinder of aspect ratio between 3 and 4. Moreover, the variation of the frequency measured in the wake of this sinuous cylinder fits perfectly to the continuous law (Figure 4) obtained in the present study, in this range of aspect ratio. In the future, our objective is to compare simultaneous measurements of amplitude, phase and frequency with the case of free-end cylinders. It would be worthwhile to check if a long sinuous cylinder behaves like a collection of free-end cylinder-type oscillators.

#### REFERENCES

- ALBARÈDE, P. & MONKEWITZ, P. A. 1992 A model for the formation of oblique shedding and 'chevron' patterns in cylinder wakes. *Physics of Fluids A* **4**, 744–756.
- ALBARÈDE, P. & PROVANSAL, M. 1995 Quasi-periodic cylinder wakes and the Ginzburg–Landau model. *Journal of Fluid Mechanics* **291**, 191–222.
- DAUCHY, C., DUŠEK, J. & FRAUNIE, P. 1997 Primary and secondary instabilities in the wake of a cylinder with free ends. *Journal of Fluid Mechanics* **332**, 295–339.
- EISENLOHR, H. & ECKELMANN, H. 1989 Vortex splitting and its consequences in the vortex street wake of cylinders at low Reynolds number. *Physics of Fluids A* **1**, 189–192.
- GERICH, D. & ECKELMANN, H. 1982 Influence of end plates and free ends on the shedding frequency of circular cylinders. *Journal of Fluid Mechanics* **122**, 109–121.

- GHIDERSA, B. & DUŠEK, J. 2000 Axisymmetry breaking and onset of instationarity in the sphere wake. *Journal of Fluid Mechanics* **423**, 33–69.
- HAMMACHE, M. & GHARIB, M. 1989 A novel method to promote parallel vortex shedding in the wake of circular cylinders. *Physics of Fluids A* **1**, 1611–1614.
- JOHNSON, T. A. & PATEL, V. C. 1999 Flow past a sphere up to a Reynolds number of 300. *Journal of Fluid Mechanics* **378**, 19–70.
- LEE, T. & BUDWIG, R. 1991 A study of the effect of aspect ratio on vortex shedding behind circular cylinders. *Physics of Fluids A* **3**, 309–315.
- LEWEKE, T. & PROVANSAL, M. 1994 Determination of the parameters of the Ginzburg–Landau wake model from experiments on a bluff ring. *Europhysics Letters* **27**, 655–660.
- LEWEKE, T. & PROVANSAL, M. 1995 The flow behind rings: bluff body without end effects. *Journal of Fluid Mechanics* **288**, 265–310.
- LEWEKE, T., PROVANSAL, M., ORMIÈRES, D. & LEBESCOND, R. 1999 Vortex dynamics in the wake of a sphere. *Physics of Fluids* **11**, S12.
- MATHIS, C., PROVANSAL, M. & BOYER, L. 1984 The Bénard–von Kármán instability: an experimental study near the threshold. *Journal de Physique – Lettres* **45**, 483–491.
- MITTAL, R. 1999 Planar symmetry in the unsteady wake of a sphere. *AIAA Journal* **37**, 388–391.
- NORBERG, C. 1994 An experimental investigation of the flow around a circular cylinder: influence of aspect ratio. *Journal of Fluid Mechanics* **258**, 287–316.
- ORMIÈRES, D. 1999 Etude expérimentale et modélisation du sillage d'une sphère à bas nombre de Reynolds. Ph.D. Dissertation, Université de Provence, Marseille, France.
- ORMIÈRES, D. & PROVANSAL, M. 1999 Transition to turbulence in the wake of a sphere. *Physical Review Letters* **83**, 80–83.
- OWEN, J. C., SZEWCZYK, A. A. & BEARMAN, P. W. 2000 Suppression of Kármán vortex shedding. *Physics of Fluids* **12**, Gallery of Fluid Motion S9.
- SAKAMOTO, H. & HANIU, H. 1995 The formation mechanism and shedding frequency of vortices from a sphere in a uniform shear flow. *Journal of Fluid Mechanics* **287**, 151–171.
- SLAOUTI, A. & GERRARD, J. H. 1981 An experimental investigation of the end effects on the wake of a circular cylinder towed through water at low Reynolds number. *Journal of Fluid Mechanics* **112**, 297–314.
- TOMBOULIDES, A. G. & ORSZAG, S. A. 2000 Numerical investigation of transitional and weak turbulent flow past a sphere. *Journal of Fluid Mechanics* **416**, 45–73.
- WILLIAMSON, C. H. K. 1988 Defining a universal and continuous Strouhal–Reynolds number relationship for the laminar vortex shedding of a circular cylinder. *Physics of Fluids* **31**, 2742–2745.
- WILLIAMSON, C. H. K. 1989 Oblique and parallel modes of vortex shedding in the wake of a circular cylinder at low Reynolds number. *Journal of Fluid Mechanics* **206**, 579–627.
- WILLIAMSON, C. H. K. 1996 Vortex dynamics in the cylinder wake. *Annual Review of Fluid Mechanics* **28**, 477–539.
- ZDRAVKOVICH, M. M., BRAND, V. P., MATHEW, G. & WESTON, A. 1989 Flow past short circular cylinders with two free ends. *Journal of Fluid Mechanics* **203**, 557–575.



## KINEMATICS AND DYNAMICS OF SPHERE WAKE TRANSITION

M. C. THOMPSON

*Department of Mechanical Engineering, Monash University  
Clayton, VIC 3800, Australia*

T. LEWEKE AND M. PROVANSAL

*Institut de Recherche sur les Phénomènes Hors Equilibre  
49, rue Frédéric Joliot-Curie, B.P. 146  
F-13384 Marseille Cedex 13, France*

(Received 15 September 2000, and in final form 22 November 2000)

The wake of a sphere undergoes a number of symmetry-breaking transitions as it changes from laminar to turbulent. This paper concentrates on the first two transitions. At  $Re = 212$  a *regular* transition occurs, when the wake develops a spectacular *two-tailed* structure consisting of two trailing streamwise vortices. During the second transition at  $Re = 272$  the flow undergoes a Hopf bifurcation. In this case there is a complex interaction between the trailing vortices leading to the periodic shedding of vortex loops. Both these transitions are shown to be supercritical (or nonhysteretic). Landau models are constructed for both transitions and the coefficients determined. The visual impression of an apparently sudden bifurcation to the two-tailed wake is shown to be due to the focal nature of the trailing vortices, which draws dye into the cores, even if their net circulation is small. A precursor to the second transition to the periodic wake is strong kinking of the trailing vortices about 1 diameter downstream from the back of the sphere. The vorticity structure of the two-tailed wake prior to transition is also quantified which may prove useful for development of models of the transition process.

© 2001 Academic Press

### 1. INTRODUCTION

AS THE REYNOLDS NUMBER is increased, the wake behind a sphere undergoes a series of well-defined transitions on its way to becoming fully turbulent. At low Reynolds number the separation bubble is axisymmetric. The attached separation bubble grows in length until the Reynolds number reaches approximately 210.

The first transition involves a (regular) symmetry-breaking topological change from a steady axisymmetric wake with an attached separation bubble to a steady nonaxisymmetric wake consisting of a shortened separation bubble with two trailing counter-rotating vortices. In experimental visualizations dye is trapped in the vortex cores and this leads to a dramatic two-threaded structure shown in Figure 1(a).

Johnson & Patel (1999) found numerically that this transition occurs at approximately  $Re_{c1} = 211$ . This value compares well to the value determined by Tomboulides *et al.* (1993) and Tomboulides & Orszag (2000) ( $Re = 212$ ) using a similar numerical formulation to that used to obtain the current results. These values are consistent with experimental predictions which tend to be lower, but have an upper limit close to the numerical estimates. This is



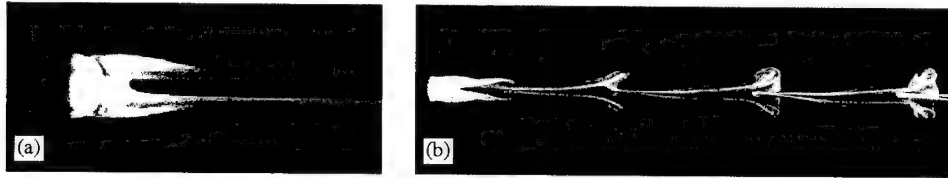


Figure 1. Dye visualizations of the sphere wake: (a) two-tailed stationary wake; (b) wake in the periodic regime.

probably because of perturbations introduced by the support structures. Magarvey & Bishop (1961*a, b*) found the *two-threaded* wake to exist in the range  $210 < Re < 270$ , Nakamura (1976) found the transition occurred at  $Re = 190$ , and Ormières (1999) and Ormières & Provansal (1999) observed the two threads between  $180 < Re < 280$ . In addition, the stability analysis of Natarajan & Acrivos (1993) revealed a *regular*, i.e., time-steady transition at  $Re = 210$ .

The second topological transition is from the steady two-threaded wake to a periodic wake in which the trailing vortices form kinks that develop into strongly skewed loops, and these move away downstream as shown in Figure 1(b).

Again, there have been various studies documenting and analysing this transition. The critical Reynolds number ( $Re_{c_2}$ ) has been determined experimentally to be: 280 (Ormières & Provansal 1999), 300 (Sakamoto & Haniu 1995), between 270 and 290 by Magarvey & Bishop (1961*a, b*), and in the range 200–300 in the older study by Taneda (1978). Numerical simulations predict values  $Re = 270$  (Johnson & Patel 1999), and in the range 250–280 (Tomboulides *et al.* 1993). In addition, the stability analysis of Natarajan & Acrivos (1993) found the transition to occur at  $Re = 277$ , although they based the stability analysis on an axisymmetric base flow.

The aim of the present study is to examine certain dynamical and topological features of the first two transitions, in particular, whether they are *subcritical* or *supercritical*, i.e., whether the transitions are hysteretic or not. The initial regular transition, in particular, shows a distinct (apparently discontinuous) change in flow topology and it is difficult to imagine *a priori* how the transition could take place smoothly.

The transitions for the circular cylinder wake are well modelled by the Landau equation; especially in the neighbourhood of the transitions. For example, Dušek *et al.* (1994) apply the model to the transition from steady two-dimensional flow to periodic two-dimensional flow, and Henderson (1997) uses it to describe the transition from two- to three-dimensional shedding. This theory can also be applied to the present system as has been done by Ormières & Provansal (1999), especially for the second transition. They find that the fluctuation energy varies linearly with  $(Re - Re_{c_2})$ , as expected for a supercritical transition obeying the Landau model.

## 2. NUMERICAL METHOD

A uniform flow with speed  $U_\infty = 1$  was directed along a positive  $z$ -axis past a sphere centred at  $(z, r, \theta) = (0, 0, 0)$  of radius  $R = 1$ . The Reynolds number is based on diameter ( $D$ ) and is defined as  $Re = U_\infty D/\nu$ , where  $\nu$  is the kinematic viscosity.

The current simulations employed a spectral/spectral-element method for axisymmetric geometries. A spectral-element discretization was used in the  $r$ - $z$  plane and a Galerkin-Fourier expansion in the  $\theta$ -direction. Typically, sixth-order tensor product Lagrangian polynomial expansions were used in each element and 24 Fourier planes in the  $\theta$ -direction. An initial study was performed to verify that the resolution was sufficient to resolve the

details of the flow, and selected higher-resolution simulations were used to verify the accuracy of the results. More details about the method can be found in Thompson *et al.* (1996).

### 3. RESULTS

#### 3.1. THE FIRST TRANSITION

Numerical simulations were performed at Reynolds numbers between 200 and 300. This covers the regular and periodic transitions. Typically, the initial velocity field for the next Reynolds number in the sequence is the asymptotic state of the previous Reynolds number solution examined.

We assume and verify that the initial transition behaves according to the Landau model:

$$\frac{dA}{dt} \approx \sigma A - lA^3, \quad (1)$$

where  $A$  represents the (global) perturbation amplitude of some quantity from the base flow. The right-hand side effectively represents the first two terms in a series expansion. The truncation is appropriate in the neighbourhood of the critical Reynolds number providing  $l$  is positive, otherwise higher-order terms determine saturation of the unstable mode. The coefficient  $\sigma$  is the growth rate coefficient in the linear regime. It changes from negative to positive through the transition and hence determines the stability of the system. The transition is supercritical if  $l$  is positive so that the first nonlinear term causes the initial linear growth of the instability to saturate. If  $l$  is negative then the next term in the series is required because that term (or higher-order terms) leads to the saturation of the transient growth. It can be shown (e.g., Dušek *et al.* 1994) that the energy in the mode ( $A^2$ ) varies as  $\sigma/l$ , which in turn is proportional to  $(\text{Re} - \text{Re}_{c_1})$ . Thus, the transition can be shown to be supercritical by examining the sign of  $l$  and the behaviour of the  $A^2$  away from the transition. (Note that because this transition is from one steady solution to another,  $A$  does not need to carry any phase information, so it is sufficient to take it to be real. For the second transition, a Hopf bifurcation, it is necessary to take  $A$  and the equation coefficients to be complex numbers.)

Two methods were used to determine the nature of the transition. The first involved recording the time-dependence of the velocity components during the transient evolution at a (mesh) point (4.3, 0, 0) downstream of the sphere. The azimuthal velocity component ( $w$ ) can be used to monitor the growth of the instability, since it is zero prior to criticality. Although the parameter  $l$  may vary in magnitude (because the saturation value of the velocity perturbation will vary from point to point), we expect the sign should be consistent throughout the wake. The linear growth rate ( $\sigma$ ) does not vary with position. Since the amplitude in the Landau model should be a global property of the wake, another method was used to verify the results obtained by this method. The second method was to define a global amplitude by

$$|A|^2 = \frac{1}{V_{\text{sphere}} U_{\infty}^2} \int_{\Omega} |(\mathbf{u}_{3D} - \mathbf{u}_{2D})|^2 dV, \quad (2)$$

where the integral is over  $\Omega$ , the volume of the domain (Henderson 1997). [The nondimensionalization by the volume of the sphere ( $V_{\text{sphere}}$ ) and the upstream speed ( $U_{\infty}$ ) is arbitrary.] This integral depends on the numerical domain size, which again means that  $l$  is not determined uniquely, but since we are mainly interested in the sign of the cubic term this is not a concern.

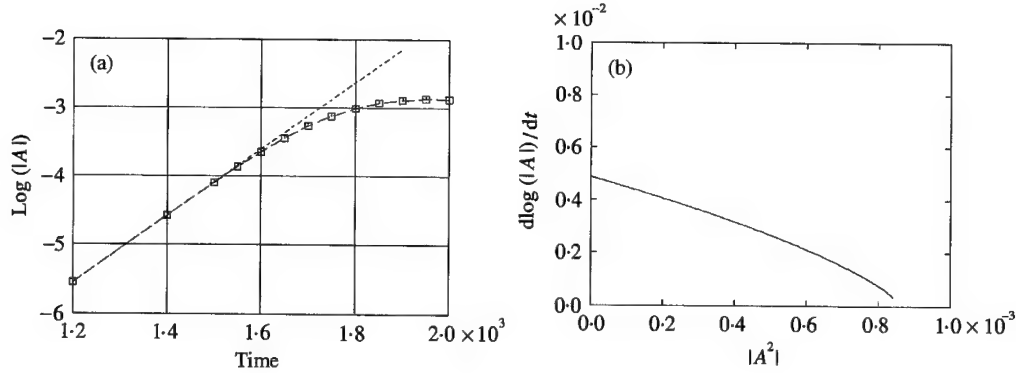


Figure 2. (a) The transition in terms of the global amplitude method. The dashed straight line shows the linear behaviour (for reference). The Reynolds number is 215. (b) Plot of  $d \log |A|/dt$  versus  $|A|^2$  during transition. The vertical intercept gives the growth rate ( $\sigma = 0.004868$ ) and the gradient is equal to  $l$  ( $= 3.78$ ). The linear behaviour near  $|A|^2 = 0$  also verifies that the first nonlinear term in the Landau model is a cubic term. The deviation from linearity for higher values indicates that higher-order terms become important close to saturation.

One determination of the critical Reynolds number is obtained from the behaviour of the linear growth rate ( $\sigma$ ) versus Reynolds number. Using a quadratic fit to the growth rate measured at  $Re = 205, 215$ , and  $220$ , it becomes positive at  $Re_{c1} = 212$ , close to predictions from other direct simulations and stability analysis.

The nature of the transition was determined by the sign of  $l$  for  $Re = 215$ ; just slightly in excess of the critical Reynolds number. Figure 2(a) shows the logarithm of the amplitude of global perturbation mode. The evolution using the point method (not shown) is consistent with this behaviour. This graph indicates the supercritical nature of the transition since the initial deviation from linearity is to *decrease* the growth rate.

The parameters  $\sigma$  and  $l$  can be determined accurately by plotting  $d \log |A|/dt$  versus  $|A|^2$ . For the point speed method this plot is shown in Figure 2(b). The  $y$ -intercept corresponds to  $\sigma$ , and the gradient gives  $l$ . The values are  $\sigma = 0.004868$  and  $l = 3.78$ . This growth rate agrees with the value obtained by the global mode method.

Note that the Landau model theory (and dimensional analysis) suggests that the growth rate depends on the diffusion timescale and the distance to the critical Reynolds number, i.e.,

$$\frac{1}{\sigma} \sim \frac{D^2}{\nu} (Re - Re_{c1})^{-1}. \quad (3)$$

For  $Re = 215$ , the right-hand side is 129, given  $(Re - Re_{c1}) \approx 3$ , while the actual growth rate timescale is  $1/0.00486 = 205$ .

The Landau model also predicts that the square of the amplitude of the perturbation should be proportional to  $(Re - Re_{c1})$  close to the transition. Figure 3 shows the behaviour of the *energy* in the saturated mode as a function of Reynolds number. A convenient measure of the energy is given by the azimuthal component, i.e.,

$$|A_\theta|^2 = \frac{1}{V_{\text{sphere}} U_\infty^2} \int_{\Omega} |w|^2 dV. \quad (4)$$

This is used because it does not require the calculation of the two-dimensional base flow (since the azimuthal velocity component is zero prior to transition).

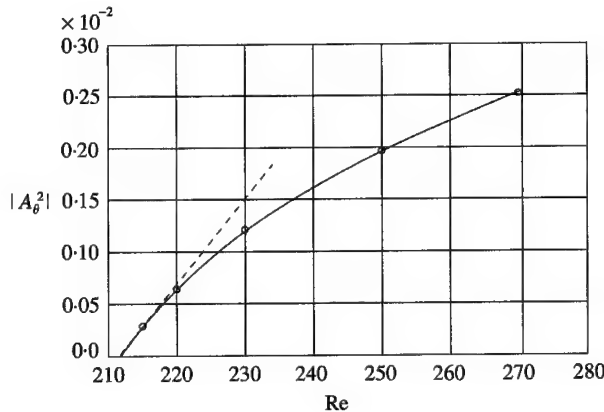


Figure 3. Plot of  $|A_\theta|^2$  against Reynolds number again confirming the transition is supercritical and well described by the Landau model.

### 3.2. THE TRANSITION PROCESS

There has been some discussion in the literature of the physical process leading to the transition and maintenance of the saturated state. For example, Johnson & Patel (1999) examine the process in terms of pressure, and Shirayama (1992) in terms of limiting surface streamlines. Some insight into the physical mechanism behind the bifurcation can be gained by examining the development of streamwise vorticity during the transition. Figure 4(a) shows streamwise vorticity isosurfaces corresponding to  $\omega_z = \pm 0.01$  at time 1400. Again the Reynolds number is 215. This is still in the linear growth regime. The initial development of streamwise vorticity apparently results from the tilting of azimuthal vorticity generated on the surface of the sphere. Below the transition point, rings of fluid which pass close to the surface of the sphere maintain their axes pointing along the  $z$ -axis. Above the critical point these rings become tilted, as can be verified by examining isosurfaces of stream-wise velocity component near the surface of the sphere. This tilting converts the azimuthal vorticity into streamwise vorticity — positive on one side of the sphere and negative on the opposite side, as is shown in Figure 4(a). After generation, the vorticity is carried away from the surface into the wake flow when the flow separates from the separation line at the back of the sphere. This process produces the double-threaded wake structure as seen in the experiments. The threads maintain considerable vorticity downstream as shown in Figure 4(b), which displays the wake structure at saturation. Johnson & Patel (1999) discuss the transition process in more detail and in particular demonstrate that the transition from axial to planar symmetry is associated with the out-of-symmetry-plane velocity component in the wake.

As commented previously, the experiments indicate that the two-threaded wake seems to appear quite suddenly once the critical Reynolds number is exceeded. Also note the apparently discontinuous change in wake topology, which seems to suggest that the transition might be subcritical. However, it is difficult for experiments to determine hysteresis directly. As shown in the previous section, the Landau model indicates the transition is not subcritical. The visualization of the developing streamwise vortex filaments shown in Figure 4(a) provide an explanation of why the dye filaments appear to occur discontinuously at transition. The visualization shows that there is a release of streamwise vorticity into the wake from distinct points on opposite sides of the attached separation

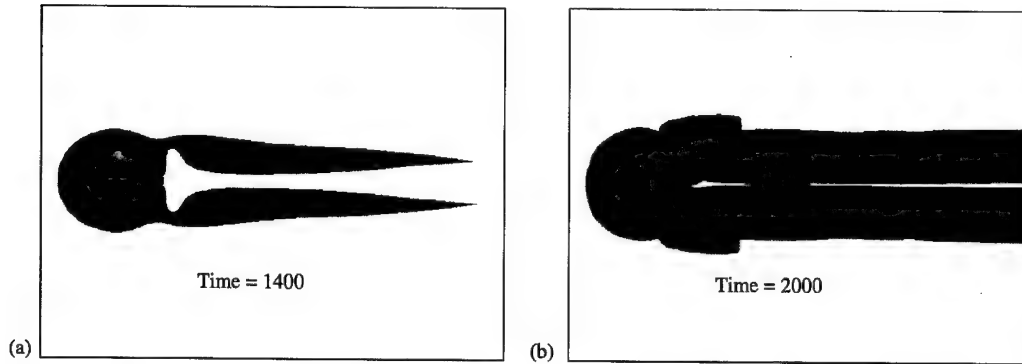


Figure 4. (a) Isosurfaces of positive and negative streamwise vorticity ( $\omega_z = \pm 0.01$ ) in the neighbourhood of the sphere during the transition to non-axisymmetric flow for  $Re = 215$ . (b) Isosurfaces at saturation for the same Reynolds number.

bubble. Note that this visualization shows the *shape* of linear instability mode structure. Importantly, the two trailing vortices do not migrate from the centreline as they grow in strength. Even very close to transition, although these structures possess little streamwise vorticity, they act as stable foci and hence draw dye into their cores. Thus, it is expected that there should be a sudden change to the wake at transition as monitored by dye visualizations.

### 3.3. WAKE DEVELOPMENT AFTER THE FIRST TRANSITION

The wake in this regime is characterized by counter-rotating vortex threads, usually observed in the experiments as two trailing dyelines. The counter-rotating vortices induce a velocity at the centreline of each other causing them to be convected away from the centreplane.

For  $Re = 250$ , the vortex thread structures are visualized in Figure 5. This figure shows a top and side view of the threads highlighted by plotting the 0.015-isosurface of the imaginary component of the eigenvalue of the velocity gradient tensor [e.g., Mittal (1999)].

The diffusion timescale  $D^2/\nu = Re D/U_\infty$  is approximately 500 for the dimensions used in the current simulations. Since the velocity in the wake is approximately the free-stream velocity, this means that diffusion is slow to cross-diffuse the two vortex threads, so they should preserve some strength for a considerable distance downstream even though they are close together.

Cross-sectional contour plots of the streamwise vorticity are shown in Figure 6 at  $z = 3R$  and  $12R$  downstream of the sphere. The contours deviate considerably from circularity even in the cores, presumably due to both cross-diffusion and the initial formation mechanism. Concerning the latter, Johnson & Patel (1999) have demonstrated that the tilting of vortex rings (as discussed above) in the initial formation region leads to streamwise vorticity being shed from a more downstream portion of the recirculation region. However, it is still possible to fit the profiles reasonably well using a combination of Gaussian vorticity distributions.

A least-squares fit of the actual vorticity distribution was computed for the following functional fit:

$$\begin{aligned} \bar{\omega}_z = & -S \exp[-(x - x_0)^2/a^2 - (y - y_0)^2/b^2] \\ & + S \exp[-(x + x_0)^2/a^2 - (y - y_0)^2/b^2] \end{aligned} \quad (5)$$

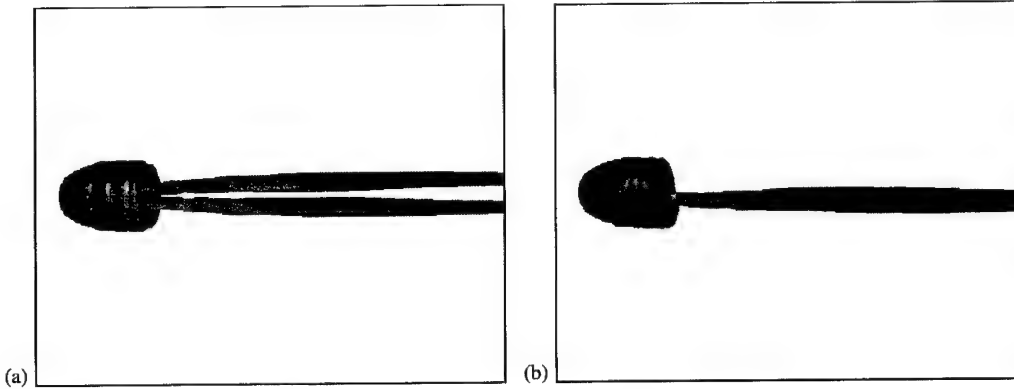


Figure 5. (a) Top and (b) side view of the trailing vortex threads for  $Re = 250$ . See text for details. The view of the sphere is obstructed by the isosurface. Note the irregularity of the structure covering the sphere is an artefact of the nonregular node-point distribution.

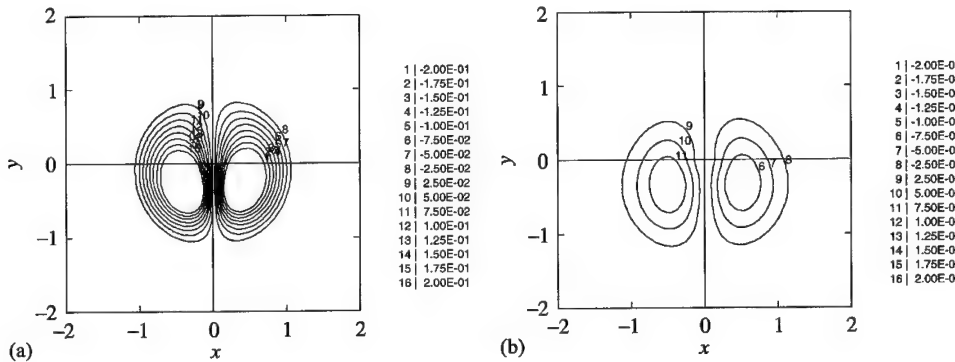


Figure 6. Streamwise vorticity contours for  $Re = 250$  at (a)  $z = 3R$  and (b)  $12R$ .

with  $z$  in the range  $[2R, 15R]$ . Here  $x$  and  $y$  are the Cartesian coordinates in the cross-planes. There are five fitting parameters:  $S$ ,  $a$ ,  $b$ ,  $x_0$  and  $y_0$ . The goodness of fit improves further downstream. A typical indication of the fit is shown in Figure 7 for  $Re = 250$  and  $z = 10R$ . Notice that the distribution in the  $y$ -direction is not symmetrical about the centre of each vortex; this is probably at least partially due to the induced velocity moving the vortices away from the centreplane.

The variation of the parameters as a function of distance and Reynolds number is shown in Figure 8. Interestingly, these figures show increased kinking of the trailing vortex filaments at 3 radii downstream from the sphere centre as the Reynolds number gets close to  $Re_{c_2}$ , especially noticeable in terms of the distance parameter  $x_0$ . The tails get closer together at this point, before moving apart again. Figure 9 is an isosurface plot of the tail structure at  $Re = 270$ , only slightly below the transition Reynolds number  $Re_{c_2}$ . This clearly shows the distortion. The kinking is considerably weaker at lower Reynolds numbers such as shown in Figure 5. It seems reasonable to speculate that this may be associated with the transition to the periodic wake. A typical post-transition visualization of the tail structure is shown in Figure 9(b) (see also Mittal 1999).

Figure 8(f) shows the variation of maximum vorticity in the threads as a function of downstream distance for  $Re = 250$ . This indicates the vorticity at the centre of the threads

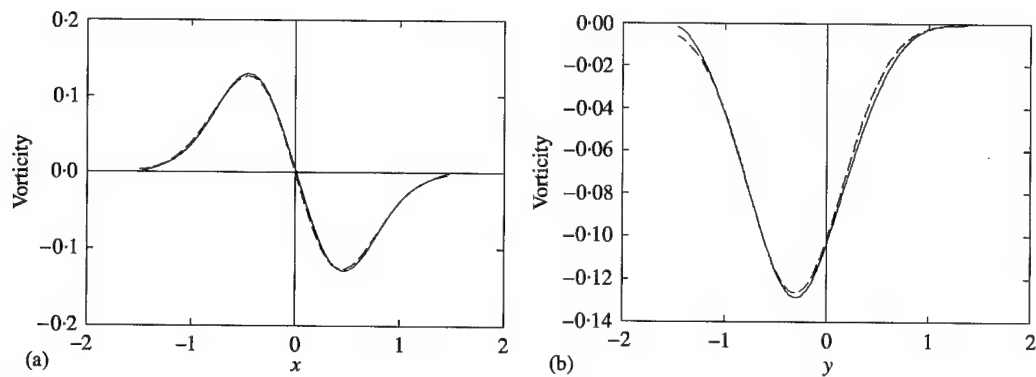


Figure 7. Variation of streamwise vorticity through the centres of the vortices in (a) the  $x$ -direction and (b) the  $y$ -direction. Solid lines show numerical predictions and dashed lines are least-squares fits;  $Re = 250$ ,  $z = 10R$ .

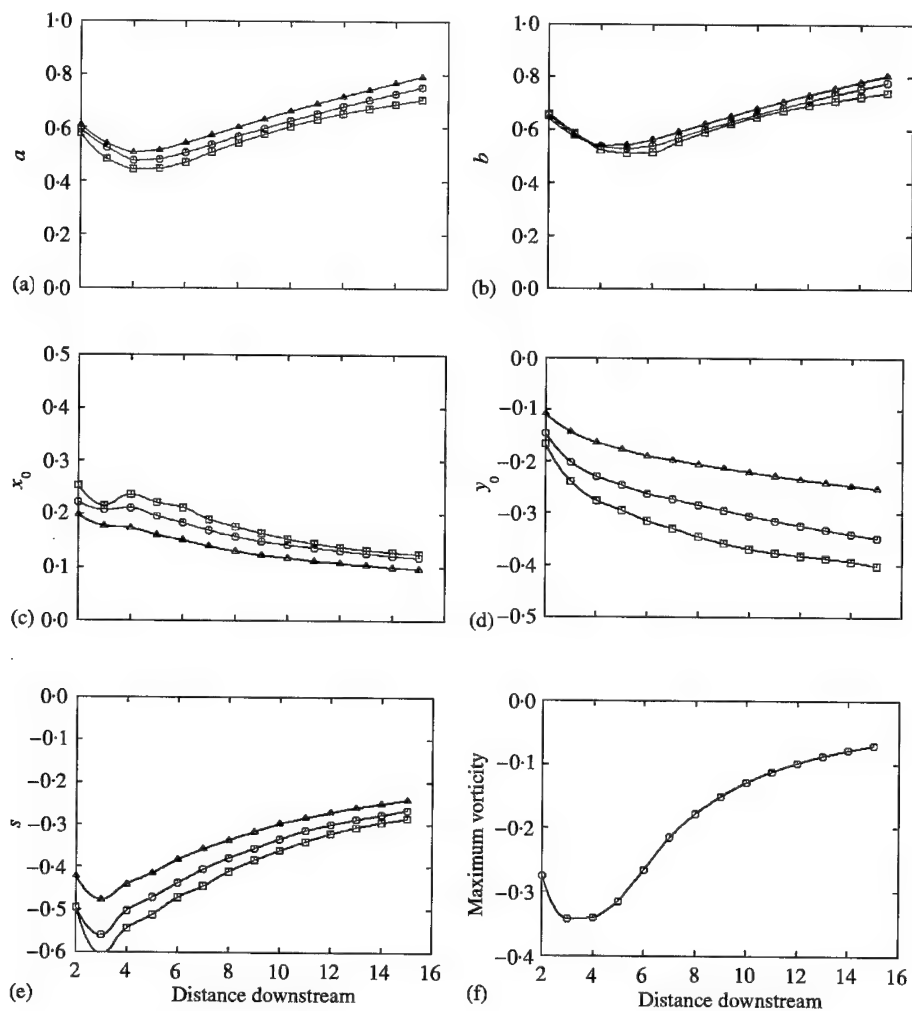


Figure 8. Size parameters (a)  $a$  and (b)  $b$ , position parameters (c)  $x_0$  and (d)  $y_0$ , and (e) strength parameter  $S$ ;  $\Delta$ ,  $Re = 230$ ;  $\circ$ ,  $Re = 250$ ;  $\square$ ,  $Re = 270$ . (f) Variation of maximum vorticity in the trailing vortex threads with downstream distance.

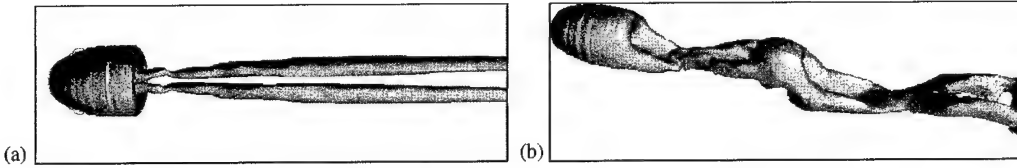


Figure 9. Isosurface plot of the vorticity structure. (a) Two-tailed wake at  $Re = 270$ , just below the transition to periodic wake flow. (b)  $Re = 290$  (side view).

decays (through diffusion and cross-annihilation) by a factor of about three over the first five diameters downstream of the sphere. The decay is much slower further down, and clearly the vortices maintain some strength for a considerable distance downstream.

### 3.4. THE SECOND TRANSITION

According to the current simulations, between  $Re = 270$  and  $280$  the transition from a stationary nonaxisymmetric wake to a periodic nonaxisymmetric wake takes place.

At  $Re = 270$  the growth rate for the development of the periodic mode is  $a_R = -0.00283$ , while at  $Re = 280$  the value is  $a_R = 0.015$ . Linear interpolation between these two values indicates that the transition occurs at about  $Re_{c_2} \approx 272$ . This is consistent with other numerical predictions described previously [e.g., Johnson & Patel (1999), Tomboulides *et al.* (1993), Tomboulides & Orszag (2000)] and slightly lower than the transition value of  $277$  predicted by the linear stability analysis of Natarajan & Acrivos (1993).

In this case, because phase information is required, the transition is modelled by the complex Landau equation

$$\frac{dA}{dt} = (a_R + ia_I)A - l_R(1 + ic)|A|^2 A. \quad (6)$$

By assuming a solution of the form  $A = \rho \exp[i\phi(t)]$ , this complex equation can be decomposed into an equation for the amplitude,  $\rho$ , and an equation for the phase,  $\phi(t)$ . The equation for the (real) amplitude is of the same form as before

$$\frac{d\rho}{dt} = a_R \rho - l_R \rho^3 \quad (7)$$

[see Le Gal *et al.* (2001), this issue, for more details]. As for the previous transition, the nature of the instability can be assessed by examining the sign of the (real) Landau coefficient ( $l_R$ ). Figure 10(a) shows the growth and saturation of the periodic wake. Initially, the flow receives a large jolt as the Reynolds number is increased from  $Re = 270$  to  $280$ . The transient dies away while the growth of the instability is still in the linear regime.

Numerical estimates of the coefficients in the Landau model can be obtained from Figure 10(b) which shows the variation of  $d \log |V_{amp}|/dt$  with  $|V_{amp}|^2$ , where  $|V_{amp}|$  is the amplitude of the velocity in the  $r-\theta$  plane at the sampling point  $(4.3, 0, 0)$ . This plot provides values of  $a_R = 0.015$  and  $l_R = 40.54$ , verifying the transition is supercritical. This finding is consistent with the experimental investigations of Ormières & Provansal (1999) who demonstrated supercriticality by showing the linear variation of perturbation energy with Reynolds number above the transition value. An attempt is currently being made to verify the conclusion of the point method by using the global amplitude method. The results will be reported elsewhere.



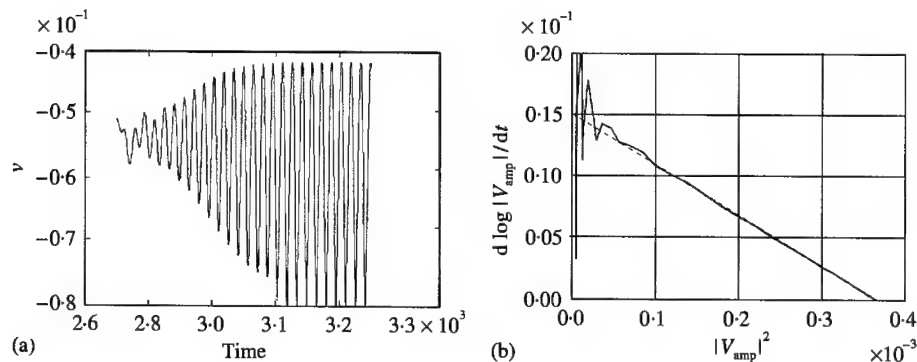


Figure 10. (a) Growth and saturation of the wake instability at  $Re = 280$  as measured by the vertical velocity component at a point in the wake. (b)  $d \log |V_{amp}| / dt$  versus  $|V_{amp}|^2$  used to determine the values of  $a_R$  and  $l_R$ . This indicates the transition is supercritical.

Simulations closer to the transition Reynolds number have also allowed an accurate determination of the Landau constant of  $c = -0.554$  at  $Re = 273$ . It is of interest that this is significantly smaller in magnitude than the corresponding value  $c \simeq -3$  for the Hopf bifurcation for a circular cylinder wake [e.g., Dušek *et al.* (1994), Le Gal *et al.* (2001)].

#### 4. CONCLUSIONS

This paper has examined the first two transitions in the wake of a sphere. Both the regular transition at  $Re = 212$  and the Hopf bifurcation at  $Re = 272$  are supercritical (or nonhysteretic), as determined from the evaluation of the cubic coefficients of the Landau model. The apparent sudden occurrence of the two-threaded wake structure observed in the experiments seems to be due to the release of streamwise vorticity into the wake from distinct points on opposite sides of the attached separation bubble. Even though these streamwise vortical structures possess little vorticity close to the transition Reynolds number, they act as stable foci and hence draw dye into their cores, leading to the possible misinterpretation of the transition as subcritical.

The vortical structure of the trailing threads has also been quantified and clearly shows kinking at about 3 radii downstream of the centre as the Reynolds number approaches the critical value. It may be possible to use this quantitative description of the wake to construct a simplified physical model of the transition process.

#### REFERENCES

- DUŠEK, J., LE GAL, P. & FRAUNIE, P. 1994 A numerical and theoretical study of the first Hopf bifurcation in a cylinder wake. *Journal of Fluid Mechanics* **264**, 59–80.
- HENDERSON, R. D. 1997 Nonlinear dynamics and pattern formation in turbulent wake transition. *Journal of Fluid Mechanics* **352**, 65–112.
- JOHNSON, T. A. & PATEL, V. C. 1999 Flow past a sphere up to a Reynolds number of 300. *Journal of Fluid Mechanics* **378**, 19–70.
- LE GAL, P., NADIM, A. & THOMPSON, M. 2001 Hysteresis in the forced Stuart–Landau equation: application to vortex shedding from an oscillating cylinder. *Journal of Fluids and Structures* **15**, 445–457.
- MAGARVEY, R. H. & BISHOP, R. L. 1961a Transition ranges for three-dimensional wakes. *Canadian Journal of Physics* **39**, 1418–1422.
- MAGARVEY, R. H. & BISHOP, R. L. 1961b Wakes in liquid–liquid systems. *Physics of Fluids* **4**, 800–805.
- MITTAL, R. 1999 Planar symmetry in the unsteady wake of a sphere. *AIAA Journal* **37**, 388–390.

- NAKAMURA, I. 1976 Steady wake behind a sphere. *Physics of Fluids* **19**, 1–18.
- NATARAJAN, R. & ACRIVOS, A. 1993 The instability of the steady flow past spheres and disks. *Journal of Fluid Mechanics* **254**, 323–344.
- ORMIÈRES, D. 1999 Etude expérimentale et modélisation du sillage d'une sphère à bas nombre de Reynolds. Ph.D. Dissertation, Université de Provence, Marseille, France.
- ORMIÈRES, D. & PROVANSAL, M. 1999 Transition to turbulence in the wake of a sphere. *Physical Review Letters* **83**, 80–83.
- SAKAMOTO, H. & HANU, H. 1995 The formation mechanism and shedding frequency of vortices from a sphere in a uniform shear flow. *Journal of Fluid Mechanics* **287**, 151–171.
- SHIRAYAMA, S. 1992 Flow past a sphere: topological transitions in the vorticity field. *AIAA Journal* **30**, 349–358.
- TANEDA, S. 1978 Visual observations of the flow past a sphere at Reynolds numbers between  $10^4$  and  $10^6$ . *Journal of Fluid Mechanics* **85**, 187–192.
- THOMPSON, M. C., HOURIGAN, K. & SHERIDAN, J. 1996 Three-dimensional instabilities in the wake of a circular cylinder. *Experimental Thermal and Fluid Science* **12**, 190–196.
- TOMBOULIDES, A. G. & ORSZAG, S. A. 2000 Numerical investigation of transitional and weak turbulent flow past a sphere. *Journal of Fluid Mechanics* **416**, 45–73.
- TOMBOULIDES, A. G., ORSZAG, S. A. & KARNIADAKIS, G. E. 1993 Direct and large eddy simulations of axisymmetric wakes. AIAA Paper 93-0546.
- WILLIAMSON, C. H. K. 1988 The existence of two stages in the transition to three-dimensionality of a cylinder wake. *Physics of Fluids* **31**, 3165–3168.



## FLOW PAST A BLUFF BODY WITH A WAVY STAGNATION FACE

R. M. DAREKAR AND S. J. SHERWIN

*Department of Aeronautics, Imperial College of Science, Technology and Medicine  
London, SW7 2BY, U.K.*

(Received 7 September 2000, and in final form 15 November 2000)

Numerical investigations have been performed to study the flow past square-section cylinders with a spanwise geometric deformation leading to a stagnation face with a sinusoidal waviness. The computations were performed using a spectral/*hp* element solver over a range of Reynolds numbers from 10 to 500. Starting from fully developed shedding past a straight cylinder at a Reynolds number of 100, a sufficiently high waviness is impulsively introduced resulting in the stabilization of the near-wake to a time-independent state. The steady nature of the near-wake is associated with a reduction in total drag of about 16% at a Reynolds number of 100 as compared with a straight, non-wavy cylinder. Further increases in the amplitude of the waviness lead to the emergence of hairpin vortices from the near-wake region, similar to the wake of a sphere at low Reynolds numbers. At higher Reynolds numbers, the drag reduction increases substantially, e.g. at a Reynolds number of 500 it is 34%, principally due to the increase in drag of the nonwavy cylinder. Alternative methods based on three-dimensional forms of bleed are investigated to suppress the von-Kármán vortex street of a straight, non-wavy cylinder.

© 2001 Academic Press

### 1. INTRODUCTION

TO REDUCE THE DRAG and weaken the vortex shedding of two-dimensional bluff bodies, three-dimensional disturbances can be introduced into the base geometry. Tanner (1972) introduced a broken separation line along the trailing edge of a blunt aerofoil. He applied a stepwise deformation to the trailing edge and observed that by increasing the depth of the steps, larger base drag reductions are obtained. The maximum drag reduction obtained using this method was 64%. The study of this drag reduction technique (segmented trailing edge) was then continued by Rodriguez (1991) and Petrusma & Gai (1994).

Bearman & Tombazis (1993) and Tombazis & Bearman (1997) investigated the three-dimensional features of the wake behind a blunt-based model with a wavy trailing edge at a Reynolds number of 40 000. They observed that the introduction of a spanwise waviness at the trailing edge fixed the positions of vortex dislocations along the span of the body. Increasing the wave steepness, defined as the ratio of peak-to-peak wave height divided by the wavelength, increased the base pressure which resulted in a drag reduction. The maximum drag reduction of 34% at a Reynolds number of 40 000 occurred for a wave steepness of 0.14. Based on these facts, they concluded that encouraging the formation of dislocations in the wake reduces the drag.

More recently Bearman & Owen (1998*a,b*) continued the above work by applying the waviness at the leading edge of a rectangular cross-section body. They observed that a mild disturbance (wave steepness of only 0.06–0.09) resulted in the complete suppression of

vortex shedding and substantial drag reduction of at least 30% at a Reynolds number of 40 000.

The aim of the current work is to carry out well-resolved numerical simulations of the flow past three-dimensional bluff bodies with a sinusoidal stagnation surface. The geometries used in this work have both sinusoidal front and rear faces. In the work of Bearman & Owen (1998*a, b*), only the front face was wavy for the rectangular cross-section bodies. However, in their experiments, similar results were also obtained with a flat plate which had both wavy front and rear faces. This latter result would suggest that the wavy trailing edge does not influence the qualitative observations made during the experiments of Bearman & Owen (1998*a, b*).

This paper is outlined as follows. Section 2 details the problem definition and introduces the nondimensional parameters as well as the numerical method. In Section 3, we present the main results of the effect of varying the Reynolds number for a cylinder with a constant amplitude of waviness. In addition, the effects of various forms of three-dimensional bleed on the wake topology of a straight, nonwavy cylinder are investigated.

## 2. PROBLEM DEFINITION AND SIMULATION METHOD

We are interested in the flow past a square-section cylinder with a waviness in both the front and rear faces as shown in Figure 1. The wavy cylinder is defined by the peak-to-peak wave height  $W$ , the wavelength  $\lambda$  and the base height  $D$ . The free-stream velocity  $U_\infty$  is aligned with the  $x$ -axis (streamwise direction), the span of the cylinder is aligned to the  $z$ -axis (spanwise or cross-flow direction) and finally the  $y$ -axis will be denoted as the vertical direction. We define the Reynolds number based on the base height  $D$  as  $Re = U_\infty D/\nu$ , where  $\nu$  is the kinematic viscosity of the fluid. The maximum denotes the most upstream cross-section (peak), while the minimum denotes the most downstream cross-section (valley). Furthermore, the waviness of the centreline (defined as a line going through the centroid of the body along the span) can be expressed mathematically in the following form:

$$\xi(z) = -\frac{W}{2} \cos(2\pi z/\lambda). \quad (1)$$

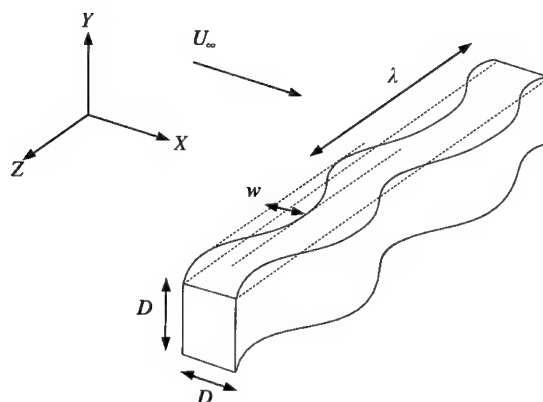


Figure 1. Schematic of the cylinder with the waviness at both the leading and trailing edge surfaces.

### 2.1. DIMENSIONLESS LENGTH SCALES

In contrast to the standard flow past a non-wavy cylinder, we have now introduced two extra length scales:  $W$  and  $\lambda$ . Whilst the non-wavy case can be completely characterized by the Reynolds number based upon the base height  $D$ , we now have a further two independent length parameters that we choose to define as  $W/\lambda$  and  $\lambda/D$ .

Differentiating equation (1) with respect to  $z$  gives an expression for the slope of the waviness  $d\xi/dz$ :

$$\frac{d\xi}{dz} = \pi \frac{W}{\lambda} \sin(2\pi z/\lambda) = A_s \sin(2\pi z/\lambda), \quad (2)$$

where  $A_s = \pi W/\lambda$  is the maximum magnitude of the slope and depends on  $W/\lambda$  which is defined as the wave steepness (Bearman & Owen 1998a, b). The slope of the waviness which is proportional to the wave steepness reaches a maximum value of  $A_s$  at the inflection points  $z = \lambda/4, 3\lambda/4$ .

### 2.2. SIMULATION METHOD

A parallel spectral element code *NEK5ar* (Sherwin & Karniadakis 1995) was employed to solve the three-dimensional incompressible Navier–Stokes equations. Spectral element methods have been widely used in the past for the prediction of bluff body flows due to their high spatial accuracy. Solution refinement can be obtained either by refining the mesh (*h*-refinement) or increasing the polynomial order  $P$  (*P*-refinement). To incorporate the wavy geometries, a geometric mapping is introduced as previously adopted by Newman (1996) and Evangelinos (1999). Application of the mapping to the Navier–Stokes equations leads to the modified set of equations:

$$\begin{aligned} \frac{\partial \mathbf{u}}{\partial t} + (\mathbf{u} \cdot \nabla) \mathbf{u} &= -\nabla p + \frac{1}{\text{Re}} \nabla^2 \mathbf{u} + \mathbf{A}(\mathbf{u}, p, \xi), \\ \nabla \cdot \mathbf{u} &= 0, \end{aligned} \quad (3)$$

where  $\mathbf{A}(\mathbf{u}, p, \xi) = [A_x, A_y, A_z]^T$  is the d'Alembert forcing term which as reported in Darekar & Sherwin (2001) has nonzero inviscid contributions of the form

$$A_z = \pi \frac{W}{\lambda} \sin(2\pi z/\lambda) \frac{\partial p}{\partial x}, \quad (4)$$

$$\begin{aligned} A_x &= \pi \frac{W}{\lambda} \sin(2\pi z/\lambda) \frac{\partial p}{\partial z} - \pi^2 \left( \frac{W}{\lambda} \right)^2 \sin^2(2\pi z/\lambda) \frac{\partial p}{\partial x} \\ &\quad - 2w^2 \pi^2 \frac{W}{\lambda^2} \cos(2\pi z/\lambda). \end{aligned} \quad (5)$$

## 3. RESULTS AND DISCUSSION

### 3.1. PARAMETER SPACE STUDY

In Darekar & Sherwin (2001), the wavelength  $\lambda$  and amplitude  $W$  of the waviness were varied at  $\text{Re} = 100$  introducing different degrees of geometric three dimensionality in the wake. From consideration of the wake topology in terms of the Jeong & Hussain (1995) identification criteria and force characteristics, the effect of introducing a wavy stagnation face was classified into five distinct regimes. A summary of the parameter space study is shown in Figure 2.

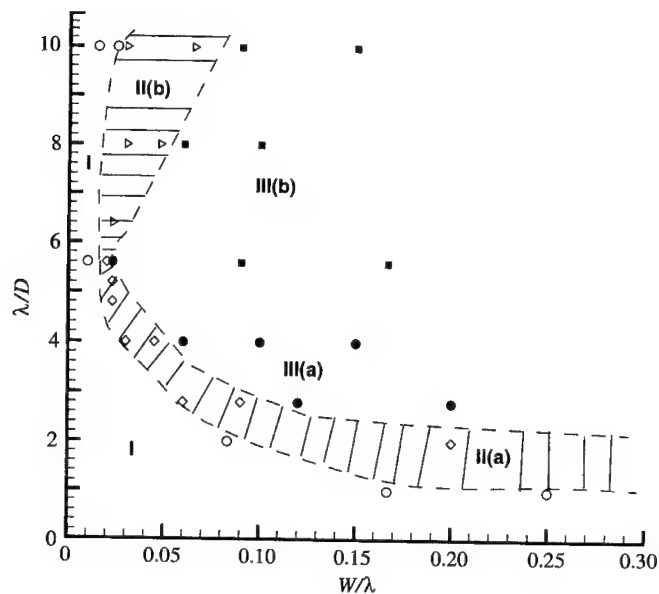


Figure 2. Summary of the parameter space study:  $\lambda/D$  versus  $W/\lambda$  at  $Re = 100$ .  $\circ$ , regime I;  $\diamond$ , regime II (type A);  $\triangleright$ , regime II (type B);  $\bullet$ , regime III (type A);  $\blacksquare$ , regime III (type B). From Darekar & Sherwin (2000).

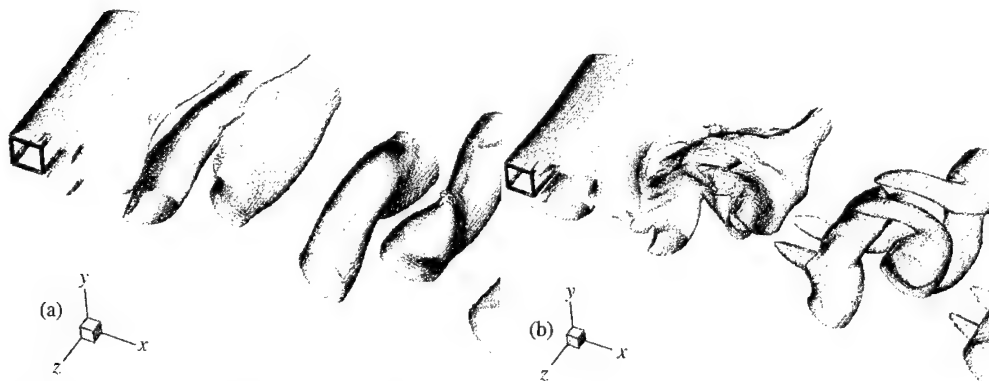


Figure 3. Perspective view from above showing the three-dimensional wake: (a) regime I; (b) regime II (type A).

For a mild geometric waviness we obtain regime I, where the formation of the wake at the base of the cylinder is mildly three dimensional and the force history is similar to the straight cylinder. However, as the wake evolves further downstream there is a discernible deformation of the spanwise Kármán vortices [see Figure 3(a)].

For a slightly higher level of waviness we obtain a transitional regime denoted as regime II. In this regime the effects of the geometric waviness in the formation region are more dominant. A large spanwise curvature appears in the top and bottom shear layers and an associated drop occurs in mean drag and the root-mean-square of the lift. Further downstream, we observe the formation of streamwise vortices associated with the sinusoidal spanwise deformation of the distorted Kármán vortices. Within this transitional regime II, we make a further distinction between normalized wavelengths above and below  $\lambda/D \approx 5.6$ .

For  $\lambda/D \leq 5.6$ , denoted as regime II (type A), we observe a time periodic state with a single frequency where streamwise vortices occur in the braids and connect adjacent Kármán vortices [see Figure 3(b)]. These streamwise vortices have some analogy with the streamwise structures of the mode A instability (see Williamson 1996). However, for  $\lambda/D > 5.6$ , denoted as regime II (type B), we observe a beating phenomenon where the wake topology alternates between a mildly three-dimensional state similar to regime I and a highly three-dimensional state similar to regime II (type A).

Finally, when the amplitude of the waviness is sufficiently large, we obtain a near-base region which is completely steady leading to a significant reduction in mean drag and the lift tending to zero. This region of maximal drag reduction is denoted by regime III and within this regime, there is no evidence of a Kármán vortex wake. Once again we can identify two sub-regimes. In the first case, regime III (type A), the flow is completely steady and has only been observed for  $\lambda/D \leq 5.6$ . It is in regime III (type A) that the most significant drag reduction occurs. The wake topology is similar to that shown in Figure 5(a). However, when  $\lambda/D > 5.6$ , hairpin vortices are shed periodically from the almost steady near-base region. In this regime, defined as regime III (type B), a small unsteadiness appears in the near-wake due to the shedding of these hairpin vortices. We note that the wake topology of the hairpin vortices in regime III (type B) resembles that of a sphere at low Reynolds numbers [see Figure 5(b)]. It was shown that the smallest wave steepness  $W/\lambda$  to force the flow into regime III (type A) occurs at around a value of  $\lambda/D \approx 5.6$ . This wavelength has a similar length scale as the mode A transition of the wake of a straight, nonwavy square section cylinder and the primary spacing of same-sign vortices in a Kármán vortex street.

### 3.2. REYNOLDS NUMBER EFFECT

The effect of the Reynolds number on the forces and wake topology of the wavy cylinder is investigated for the particular case of  $(\lambda/D, W/\lambda) = (5.6, 0.167)$ . The numerical simulations were performed over a range of Reynolds numbers from 10 to 500 and are compared with experimental data for the straight and wavy bodies up to a Reynolds number of 40 000. The results for the total drag coefficient against the Reynolds number are summarized in Figure 4.

For the straight cylinder, at low Reynolds numbers the flow is steady and a pair of symmetric vortices forms in the near-wake. In this regime, the drag is relatively high and has a strong component due to skin friction from the boundary layer. For example, at  $Re = 10$ , the total drag coefficient is 3.20, 32% of which is due to wall shear stresses. As the Reynolds number is increased, the shear stress component of the total drag coefficient decreases and the length of the closed recirculating region increases; e.g. at  $Re = 40$ , the total drag coefficient is reduced to 1.71 and only 16% is due to skin friction.

At a critical Reynolds number  $Re_1$ , the steady flow becomes unstable and bifurcates to a two-dimensional time-periodic flow, resulting in the well-known Kármán vortex street in the wake. This first transition, known as the primary instability, is the result of a Hopf bifurcation. For the square-section cylinder, the experimental value for  $Re_1$  reported in Sohankar *et al.* (1997) is  $Re_1 = 47 \pm 2$ , whereas previous numerical computations place the critical Reynolds number for the onset of vortex shedding near  $Re_1 = 51.2$  (Sohankar *et al.* 1998) and  $Re_1 = 53$  (Kelkar & Patankar 1992), respectively. Beyond this critical Reynolds number, the drag coefficient deviates from the steady and symmetric curve as shown in Figure 4. An interesting flow pattern then develops on the top and bottom surfaces with increasing Reynolds number as shown in the simulations of Robichaux *et al.* (1999). In this work, they show that at low Reynolds numbers, the shear layers remain attached on the top

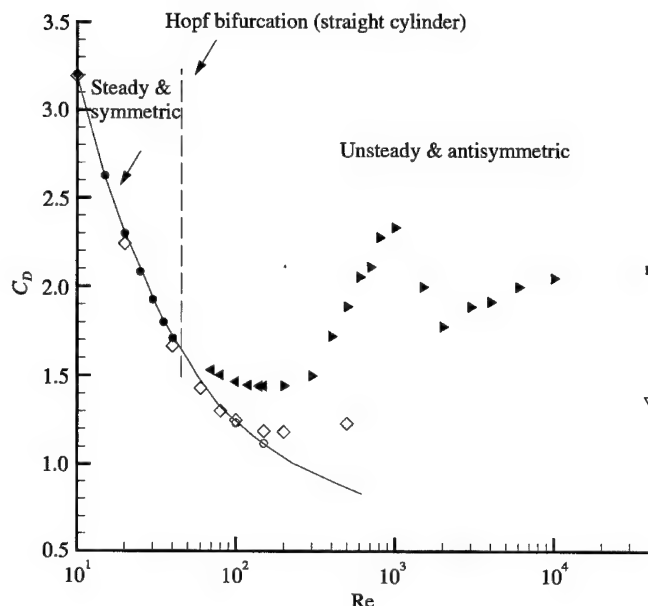


Figure 4. Drag coefficient against Reynolds number for the straight and wavy cylinders: ●, straight cylinder,  $Re = 10, 15, 20, 25, 30, 35$ , and  $40$  (steady flow); ▲, straight cylinder,  $Re = 70, 80, 100, 120, 140$ , and  $150$  (unsteady flow); ►, straight cylinder,  $Re = 200 - 10,000$  (experiments from Okajima 1995); ■, straight cylinder at  $Re = 40,000$  (experiments from Owen 1997); ○, straight cylinder with symmetry boundary condition on the wake centre line to promote steady flow at  $Re = 100, 150$ ; ◇, wavy cylinder,  $Re = 10, 20, 40, 60, 80, 100, 150, 200$ , and  $500$ ; ▽, wavy cylinder at  $Re = 40,000$  (experiments from Owen 1997).

and bottom surfaces. The shear layers then separate from the trailing edge, forming the von-Kármán vortex street in the wake. As the Reynolds number is increased to around  $Re = 120$ , the shear layers separate from the leading edge but reattach a short distance downstream, thus forming small unsteady recirculating cells on the top and bottom surfaces. Finally, at around a Reynolds number of  $150$ , the shear layers separate from the leading edge without reattachment. They also report that the two-dimensional wake becomes unstable to three-dimensional perturbations at around  $Re = 161$ , but the associated spanwise wavelength is not given. The onset of mode A for the square-section cylinder is given as  $Re = 162 \pm 12$ . The lower bound of the onset of three dimensionality seems to be very close to the Reynolds number at which the flow separates from the leading edge without reattachment. From the experimental data of Okajima (1995), the total drag coefficient increases sharply from  $Re \approx 200$ . It should be noted that this trend does not occur for the circular cylinder and is probably due to the fixed leading edge separation points. It is not yet clear why there is a large drop in the drag coefficient after  $Re = 1000$  but it would seem to be due to the shear-layer transition (Okajima 2000). Further increasing the Reynolds number leads to a monotonic increase in the drag coefficient.

For the wavy body, the transition process is distinctively different. In the low Reynolds number regime, the drag coefficient is similar to that of the straight cylinder (see Figure 4). For example, at  $Re = 10$ , the total drag coefficient is  $3.19$ ,  $32\%$  of which is due to viscous shear stresses and at  $Re = 40$ , the total drag coefficient is  $1.67$  where  $18\%$  is due to skin friction. The wake topology is steady and symmetric which results in a net zero lift force.



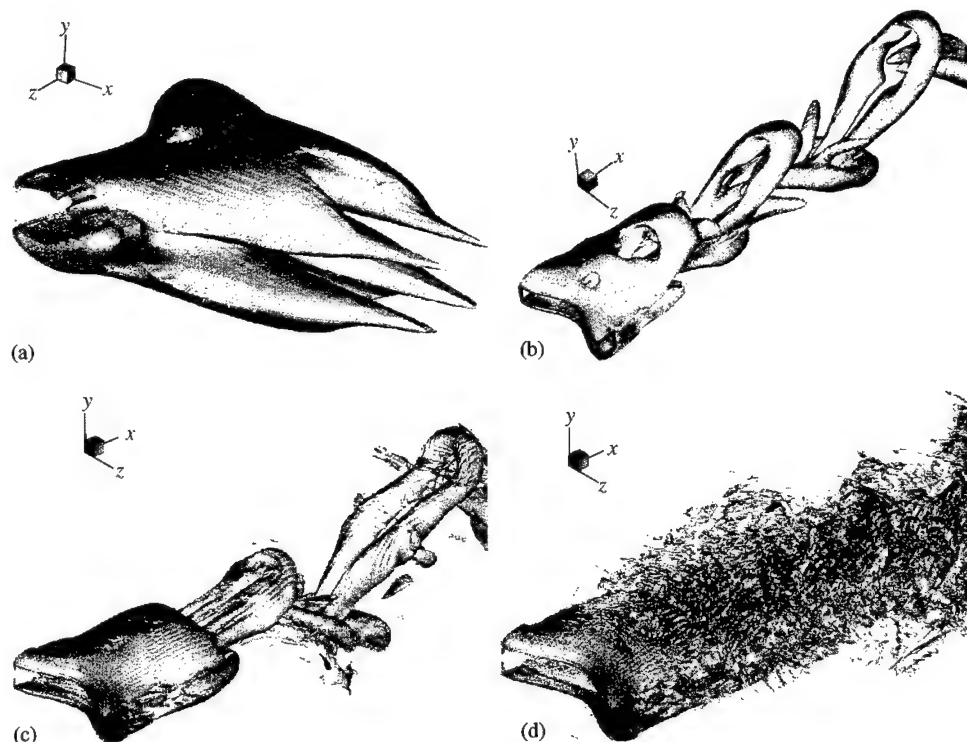


Figure 5. Perspective view showing the three-dimensional wake of the wavy cylinder ( $\lambda/D, W/\lambda$ ) = (5.6, 0.1667) at (a)  $Re = 80$ , (b)  $Re = 100$ , (c)  $Re = 200$ , and (d)  $Re = 500$ .

The drag coefficient follows the steady and symmetric curve shown in Figure 4. Beyond the critical Reynolds number for the onset of vortex shedding of the straight cylinder ( $Re_1 \approx 47$ ), the three-dimensional wake remains steady and symmetric. The topology of the wake at  $Re = 80$  is shown in Figure 5(a). The drag coefficient continues to follow the steady and symmetric curve until  $Re \approx 100$ . At around this critical Reynolds number, transition to unsteadiness occurs in the wake where the drag coefficient deviates from the steady and symmetric curve (see Figure 4). A staggered array of hairpin vortices emerge from the near-wake region as can be seen from Figure 5(b). The distinct structure of these hairpin vortices persists until  $Re = 200$ , after which smaller scale instabilities are induced as shown by Figure 5(d) at  $Re = 500$ . As can be seen, the wavy stagnation face has delayed the onset of unsteadiness to  $Re = 100$  and the antisymmetric mode has changed from a Kármán vortex street to a street composed of hairpin vortices, similar to the wake of a sphere at low Reynolds numbers.

Defining drag reduction with respect to the drag level of the straight cylinder, at  $Re = 80$  the drag reduction is about 13%, whereas at  $Re = 100, 200$  and  $500$ , it is 16, 20 and 34%, respectively. It can be appreciated that the drag reduction at  $Re = 500$  has substantially increased from that at  $Re = 100$  and is comparable to the experiments of Owen (1997) at  $Re = 40\,000$ . The increase in the drag reduction with increasing Reynolds number is principally due to the fact that for a straight, nonwavy cylinder, the shear layers separate from the leading edge from  $Re \approx 170$  whereas at  $Re = 100$  the shear layers remain attached until they separate from the trailing edge. Therefore, the leading edge separation leads to a higher drag for the straight, nonwavy cylinder. However, from the numerical simulation at higher Reynolds numbers, the asymptotic level of the drag coefficient of the wavy cylinder

does not change significantly from that at  $Re = 100$  (see Figure 4). Therefore, the higher drag reduction, at higher Reynolds numbers, is mainly due to the increase in the drag coefficient of the straight, nonwavy cylinder.

### 3.3. THREE-DIMENSIONAL BLEED

Considering Section 2.2, we can introduce an alternative interpretation of the waviness as the d'Alembert flow past a straight, nonwavy cylinder. The spanwise forcing term  $A_z$ , given by equation (4), depends on the streamwise pressure gradient and the  $z$ -derivative of the shape of the waviness. The streamwise pressure gradient  $\partial p/\partial x$  will be large near the stagnation face and will always be positive. The forcing term  $A_z$  will be positive between  $0 < z < \lambda/2$  and negative between  $\lambda/2 < z < \lambda$ . This forcing, therefore, sets up a spanwise or cross-flow velocity component,  $w$ , along the leading edge surface going from a position corresponding to the maximum towards a position corresponding to the minimum of the wavy cylinder. In Darekar & Sherwin (2001), it was shown that the streamwise forcing term  $A_x$ , given by equation (5), is mainly dominated by the term  $-\pi^2(W/\lambda)^2 \sin^2(2\pi z/\lambda)(1/\rho)(\partial p/\partial x)$ , which is negative along the leading edge and reaches a maximum in the region of the inflection points. The streamwise forcing term,  $A_x$ , will thus slow down the two-dimensional  $u$  component of the velocity more significantly close to the inflection points.

These observations motivated the interpretation of the wavy stagnation face as a combination of promoting a cross-flow at the stagnation face and slowing down the flow near to the inflection points. To simulate this effect, the influence on the unsteady wake of a straight cylinder due to various forms of surface bleed has been investigated at a spanlength of  $\lambda/D = 5.6$  at  $Re = 100$ . Two types of bleed were imposed as boundary conditions on the cylinder surface: (i) a cross-flow bleed on the stagnation face, and (ii) a vertical bleed on the top and bottom surfaces. The following mathematical formulations were used for each of the three-dimensional forms of bleed:

- (i) cross-flow bleed on the stagnation face,  $w_{cr} = 0.56 \sin(2\pi z/\lambda)(y - 0.5)(y + 0.5)$ ;
- (ii) bleed on the top and bottom surfaces,  $v_{tb} = \pm 0.01e^{-1000x^2}(1 + 200e^{-(z-2.8)^2})$ .

The cross-flow bleed was specified on the whole stagnation face of the straight, nonwavy cylinder. The bleed has a sinusoidal variation in the spanwise  $z$  direction and a parabolic variation in the  $y$  direction. It reaches a local maximum of 0.14, i.e. 14% of  $U_\infty$  at  $z = 1.4, 4.2$ . The results showed that the near-wake was stabilized to a time-independent state. The wake topology is shown in Figure 6(a) and has strong qualitative similarities with that of the wavy cylinder in the steady regime [see Figure 5(a)]. The stabilization of the near-wake resulted in a drag reduction of about 15% and in a zero lift force.

The bleed on the top and bottom surface was specified by modifying the velocity boundary conditions on the top and bottom surfaces to  $(u, v, w) = (0, \pm v_{tb}, 0)$ . The distribution is exponential in both the streamwise  $x$  and spanwise  $z$  directions. A maximum velocity of about 2 occurs at the midspan of the cylinder. The topology of the wake is shown in Figure 6(b) and has strong similarities to the unsteady flow past the wavy cylinder at  $Re = 100$  [see Figure 5(b)]. The lift force dropped to nearly zero and the drag reduction was equal to about 11%.

Current work is focusing on the minimum amount of bleed necessary to stabilize the near-wake. A comparison of this minimum amount of bleed will be done for the stagnation face cross-flow, the top and bottom surface bleed as well as the base bleed of the straight cylinder. It is anticipated that the stagnation face cross-flow will be the most effective means of stabilizing the near-wake as perturbations are introduced very early on in the shedding process and hence have a longer convective time to disrupt the shedding mechanism.

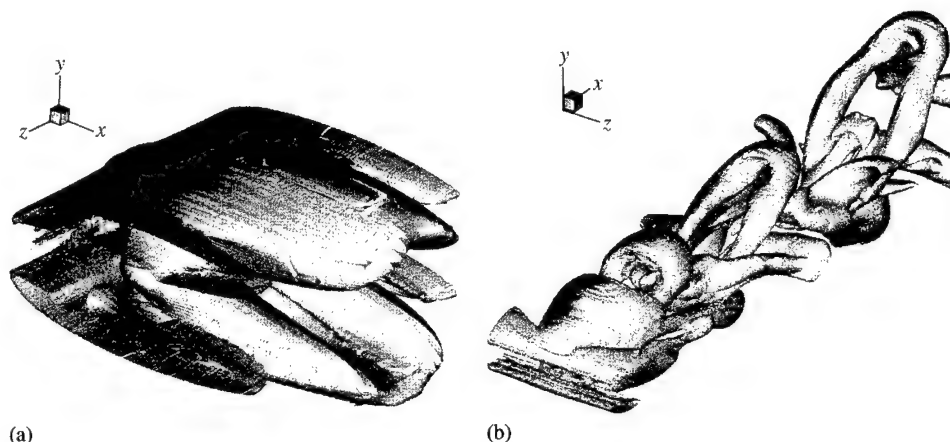


Figure 6. Perspective view showing the three-dimensional wake for the two forms of bleed: (a) on the stagnation face and (b) on the top and bottom surfaces.

#### 4. CONCLUSION

It was shown that the wavy stagnation face delayed the onset of unsteadiness to  $Re \approx 100$  for the particular case of  $(\lambda/D, W/\lambda) = (5.6, 0.167)$ . In contrast to the standard von-Kármán vortex street of a straight cylinder, the unsteady wake of the wavy cylinder is composed of a staggered array of hairpin vortices, which is similar to the wake of sphere at low Reynolds numbers. The drag was found to be substantially lower than that of a straight cylinder. This drag reduction increased with increasing Reynolds number. Alternative methods, based on three-dimensional forms of bleed, have been shown to suppress the von-Kármán vortex street of a straight, nonwavy cylinder, leading to similar wake structures to that found for the wavy cylinder.

#### ACKNOWLEDGEMENTS

The authors would like to acknowledge several inspiring discussions and critical feedback from J. C. Owen, Prof. P. W. Bearman and Dr D. Barkley. The first author is supported by the Edmund Davis Trust fund awarded by the University of London. Computational resources were provided by the Computer Services for Academic Research (CSAR) under the EPSRC Grant Number GR/M08424 and the Imperial College Parallel Computing Centre.

#### REFERENCES

- BEARMAN, P. W. & OWEN, J. C. 1998a Reduction of bluff-body drag and suppression of vortex shedding by the introduction of wavy separation lines. *Journal of Fluids and Structures* **12**, 123–130.
- BEARMAN, P. W. & OWEN, J. C. 1998b Suppressing vortex shedding from bluff bodies by the introduction of wavy separation lines. In *Proceedings of the 1998 Conference on Bluff-Body Wakes and Vortex-Induced Vibration* (eds P. W. Bearman & C. H. K. Williamson), Paper No. 45, Ithaca, NY: Cornell University.
- BEARMAN, P. W. & TOMBAZIS, N. 1993 The effect of three-dimensional imposed disturbances on bluff body near wake flows. *Journal of Wind Engineering & Industrial Aerodynamics* **49**, 339–350.

- DAREKAR, R. M. & SHERWIN, S. J. 2001 Flow past a square-section cylinder with a wavy stagnation face. *Journal of Fluid Mechanics* **426**, 263–295.
- EVANGELINOS, C. 1999 Parallel Spectral/hp Methods and Simulations of flow/structure Interactions. Ph.D. Thesis, Brown University, Providence, RI, U.S.A.
- JEONG, J. & HUSSAIN, F. 1995 On the identification of a vortex. *Journal of Fluid Mechanics* **285**, 69–94.
- KELKAR, K. M. & PATANKAR, S. V. 1992 Numerical prediction of vortex shedding behind a square cylinder. *International Journal for Numerical Methods in Fluids* **14**, 327–341.
- NEWMAN, D. 1996 A computational study of fluid/structure interactions: flow-induced vibrations of a flexible cable. Ph.D. Thesis, Princeton University, Princeton, NJ, U.S.A.
- OKAJIMA, A. 1995 Numerical analysis of the flow around an oscillating cylinder. In *Proceedings of the 6th International Conference on Flow-Induced Vibration*, pp. 159–166.
- OKAJIMA, A. 2000 Private communication.
- OWEN, J. C. 1997 The effect of three-dimensional disturbances on bluff body base drag. Final Year M. Eng. Project Report, Department of Aeronautics, Imperial College, London, U.K.
- PETRUSMA, M. S. & GAI, S. L. 1994 The effect of geometry on the base pressure recovery of the segmented blunt trailing edges. *The Aeronautical Journal* **98**, 267–274.
- ROBICHAUX, J., BALACHANDAR, S. & VANKA, S. P. 1999 Three-dimensional floquet instability of the wake of square cylinder. *Physics of Fluids* **11**, 560–578.
- RODRIGUEZ, O. 1991 Base drag reduction by control of the three-dimensional unsteady vortical structures. *Experiments in Fluids* **11**, 218–226.
- SHERWIN, S. J. & KARNIADAKIS, G. E. 1995 A triangular spectral element method: applications to the incompressible Navier–Stokes equations. *Computer Methods in Applied Mechanics and Engineering* **123**, 189–229.
- SOHANKAR, A., NORBERG, C. & DAVIDSON, L. 1997 Numerical simulation of unsteady low-Reynolds number flow around rectangular cylinders at incidence. *Journal of Wind Engineering & Industrial Aerodynamics* **69**, 189–201.
- SOHANKAR, A., NORBERG, C. & DAVIDSON, L. 1998 Low-Reynolds number flow around a square cylinder at incidence: study of blockage, onset of vortex shedding, and open boundary conditions. *International Journal for Numerical Methods in Fluids* **26**, 39–56.
- TANNER, M. 1972 A method of reducing the base drag of wings with blunt trailing edge. *Aeronautical Quarterly* **23**, 15–23.
- TOMBAZIS, N. & BEARMAN, P. W. 1997 A study of three-dimensional aspects of vortex shedding from a bluff body with a mild geometric disturbance. *Journal of Fluid Mechanics* **330**, 85–112.
- WILLIAMSON, C. H. K. 1996 Three-dimensional wake transition. *Journal of Fluid Mechanics* **328**, 345–407.

## PASSIVE CONTROL OF VIV WITH DRAG REDUCTION

J. C. OWEN, P. W. BEARMAN

*Department of Aeronautics, Imperial College of Science, Technology and Medicine  
London SW7 2BY, U.K.*

AND

A. A. SZEWCZYK

*Department of Aerospace and Mechanical Engineering, University of Notre Dame  
Notre Dame, IN 46556, U.S.A.*

(Received 13 September 2000, and in final form 9 November 2000)

An experimental investigation has been carried out to measure the drag and vortex-induced vibration amplitudes of a circular cylinder, a circular cross-sectional body with a sinuous axis and a circular cylinder with hemispherical bumps attached. A wide range of Reynolds number has been studied, up to a maximum value of  $10^5$ . Suppression of vortex shedding and drag reductions up to 47% have been observed for the body with a sinuous axis. Drag reductions of about 25% and suppression of vortex shedding have been recorded for the cylinder with bumps. VIV experiments over a range of the mass damping parameter from  $2 \times 10^{-2}$  to 5 have shown that amplitudes of oscillation for the wavy body and the cylinder with bumps still develop at low values of mass damping, even though shedding cannot be detected from the bodies when they are fixed. VIV can be suppressed at significantly lower values of mass-damping than required to stabilize a circular cylinder.

© 2001 Academic Press

### 1. INTRODUCTION

VORTEX SHEDDING FROM BLUFF BODIES is a challenging area of fluid dynamics and it continues to present problems to designers in a number of key industrial areas. For example, the large drag loads and possible vortex-induced vibration (VIV) of pipes and long slender tubular members are important design issues in the offshore industry. The widespread use of bluff sections has stimulated an interest in finding ways to weaken or even suppress vortex shedding. One avenue of research has been to take a nominally two-dimensional bluff body and to apply some form of three-dimensional geometric disturbance to the basic form. Naumann *et al.* (1966) varied the separation position along a circular cylinder by attaching short lengths of wire fixed alternately at two angular positions across the span. It is reported that this suppressed vortex shedding. Following this idea of breaking the separation line, a number of researchers, including Tanner (1972), Rodriguez (1991) and Petrusma & Gai (1994), have studied the reduction of the drag of blunt-trailing-edge wings by introducing a segmented trailing edge. Drag reductions up to 64% were found. The work reported here continues this theme but relates to bluff bodies where the geometry has some spanwise perturbation with a sinusoidal form.

In experiments carried out over the past few years it has been found that vortex shedding from bluff bodies can be weakened, and in some cases suppressed, when the flow separation

lines are forced to be sinuous. Three sets of experiments have been conducted: one using a blunt-based section with a wavy trailing edge (Tombazis & Bearman 1997), a second on rectangular cross-section bodies where the front face is wavy (Bearman & Owen 1998), and a third on bodies with a circular cross-section with constant diameter along the span and an axis that is sinuous (Owen *et al.* 1999). In all cases the introduction of the waviness is observed to reduce the drag and, for the rectangular and circular cross-sectional bodies, vortex shedding is suppressed if the ratio of peak-to-peak wave height,  $w$ , to wavelength,  $\lambda$ , of the sinuous form is above a critical value. The effectiveness of modifying the separation line appears to be greatest when the ratio  $\lambda/D$  of the wavelength to the body cross-flow width,  $D$ , is close to that of the mode A wavelength. This may or may not be a coincidence but it should be noted that vortex shedding can be suppressed across a wide range of Reynolds number, and not just in the regime normally associated with mode A. In the case of the wavy blunt-trailing-edge body, vortex shedding was not totally suppressed at the maximum wave steepness examined of 0.14, whereas for the other bodies von Kármán-type shedding disappeared for values of  $w/\lambda$  above about 0.1. Hence it might be deduced from this that the wavy front face also plays a role in vortex shedding suppression.

The experiments of Tombazis & Bearman (1997) were carried out to study three-dimensional features found in the wakes of nominally two-dimensional bluff bodies known as vortex dislocations. These are associated with spanwise changes in vortex shedding frequency and they provide a means by which vortices from adjacent cells, shedding at different frequencies, can join together. The occurrence of vortex dislocations was first investigated at low Reynolds numbers where the wake is unsteady but laminar [see for example, Williamson (1989)]. Bearman & Tombazis found that for a two-dimensional body at higher Reynolds numbers, dislocations appear apparently randomly in time and in spanwise position. In order to try to fix dislocation positions in the wake of a blunt-trailing-edge section they introduced a spanwise wavy trailing edge. It was found that the introduction of the waves fixed the dislocation positions but they also caused a further significant effect. It was observed that the base pressure increased as the wave steepness,  $w/\lambda$ , increased. Increasing base pressure is associated with drag reduction and hence it was deduced from these observations that encouraging the formation of dislocations reduces drag.

Bearman & Owen (1998) extended this work to rectangular cross-sectional cylinders with the front face normal to the flow. In order to generate a wavy separation line, the front face was machined into a sinusoidal form. For small values of  $w/\lambda$  similar vortex dislocation patterns and drag reduction to those for the wavy trailing edge body were observed. However, when  $w/\lambda$  was increased to 0.09, vortex shedding could not be detected. Drag reductions of over 30% were measured. Owen *et al.* (1999) took the research a stage further by studying how the flow around a circular cylinder changes if the axis is made sinusoidal. With the wavy axis in the plane of the flow they found similar features to those of the wavy rectangular sections, with vortex shedding suppression occurring for values of  $w/\lambda$  above 0.167. Distorting the axis of a circular cylinder may not necessarily generate wavy flow separation lines, but observations showed that the separation position did vary across the span. A common feature of the bodies where vortex-shedding suppression occurred is a wavy face onto which the free-stream flow impinges.

One of the aims of this paper is to attempt to explain why the introduction of relatively small degrees of spanwise waviness should have such a large effect on von Kármán vortex shedding. Also, it is of importance to know that waviness not only reduces drag but can also be used to reduce or even suppress VIV. One of the most widely used devices to suppress VIV, the helical strake, has the disadvantage that it increases drag. One obvious drawback of employing waviness is that it will be directionally sensitive, with perhaps little or no effect

when the body is orientated with the plane of the waves normal to the flow. It is proposed to show how some simple modifications to the geometry of a circular cylinder, based on ideas developed from studying wavy bluff bodies, may be used to reduce drag and to weaken and even suppress shedding.

## 2. EXPERIMENTAL ARRANGEMENT

Experiments have been carried out on slender bluff sections over a large range of Reynolds numbers from 10 to 340 000, using both air and water facilities. Insight into the structure of flows has been obtained from flow visualization studies at low Reynolds numbers in a towing tank 3 m long by 0.8 m wide and 0.6 m deep. Experiments at substantially higher Reynolds numbers in two low-speed wind tunnels with working sections 0.92 m by 0.92 m and 1.22 m by 1.37 m have shown that similar effects due to small spanwise waviness are present. Surface-pressure measurements and hot-wire anemometry studies were carried out in the smaller wind tunnel. The larger wind tunnel is equipped with a three-component balance and this was used for direct measurements of drag. PIV measurements of the wake structure of bluff bodies were also conducted in this tunnel.

Experiments to measure response amplitudes of bluff bodies due to VIV were conducted in a water channel with a test section 0.61 m wide and 0.69 m deep. The maximum flow speed in the channel is about 0.3 m/s. Two important structural parameters to consider are damping ratio,  $\zeta$ , and mass ratio,  $m^*$ , where  $m^* = m_{\text{sys}}/m_d$  and  $m_{\text{sys}}$  is the effective mass of the oscillating body and  $m_d$  is the mass of fluid it displaces. One of the advantages of working with water is that mass ratios can be kept low and in a similar range to that experienced by offshore structures. Low damping was achieved by mounting bodies from a double-pendulum suspension system situated above the test-section of the water channel. The pendulum, which is shown in Figure 1, was constructed using four arms with low-stiffness flexures at each end. The motion of an attached cylinder is predominantly in the horizontal plane and the vertical movement during a typical VIV experiment is extremely small. When discussing the parameters that control VIV, it is common to use the product of  $m^*$  and  $\zeta$  to form the single combined mass-damping parameter. However, care must be taken when  $m^*$  is small, because the magnitude of the fluid added mass becomes significant compared to  $m_{\text{sys}}$  and it can have a marked influence on the frequency at which the body oscillates. In the experiments,  $m^*\zeta$  was varied over the range  $2 \times 10^{-2}$  to 5 and the Reynolds number was varied between  $10^3$  and  $10^4$ . Full details of all the facilities and the experimental techniques used are described by Owen (2000).

## 3. EXPERIMENTAL RESULTS AND DISCUSSION

Low Reynolds number flow visualization results for a wavy circular cylinder, presented by Owen *et al.* (2000), show no evidence of regular Kármán vortex shedding above a value of  $w/\lambda$  of 0.167. Also, there is seen to be a periodic variation of the wake width across the span, with a wide wake behind the body where the axis is furthest downstream and a narrow wake where it is furthest upstream. In addition, there is evidence of longitudinal vortices in the wake which vary in sign in an alternate way across the span. Their senses of rotation are such as to induce the variation in wake width mentioned above. The origin of these vortices is thought to be in the skewed shear layers shed from the wavy body and the maximum strength of the longitudinal vorticity along the span is expected to be where the axis of the body is at the steepest angle to the free stream flow. This would provide a dependence of the flow on wave steepness,  $w/\lambda$ , which is what is observed. Cross-flows generated on the attached flow part of the bodies with a wavy front face must also play a role in weakening

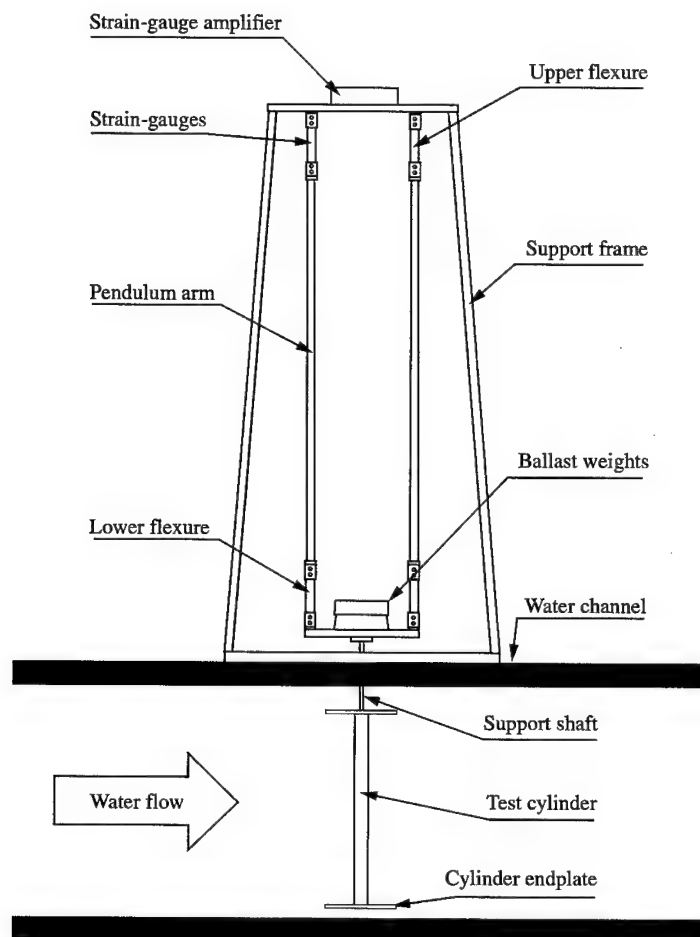


Figure 1. Schematic diagram of the double-pendulum system used for VIV experiments mounted above the water channel.

vortex shedding. The magnitude of these cross-flows would again be expected to depend on wave steepness. While the precise mechanism of how this flow stabilizes the near-wake and suppresses vortex shedding will probably only be revealed by hydrodynamic stability analysis, it seems clear that the longitudinal vortices play a dominant role.

Figure 2 shows the effect of wave steepness on the drag coefficient of a sinuous circular cylinder with a wavelength,  $\lambda$ , of  $7.5D$  and at a Reynolds number of  $3.3 \times 10^4$ . A large drag reduction of 47% is recorded when the wave steepness is just over 0.3, but even for  $w/\lambda$  of 0.1 the drag reduction is more than 30%. At the higher wave steepnesses hot-wire measurements revealed no discrete frequency at the expected vortex shedding periodicity. From results reported by Roshko (1954) on the effect of long splitter plates on circular cylinder flow, it is to be expected that drag reduction should accompany vortex shedding suppression. Changing the incidence of the flow approaching a wavy cylinder, the drag coefficient increases back to almost the same value as that for a straight cylinder when the incidence reaches  $90^\circ$ .

While there may be important applications for wavy cylinders when the flow is unidirectional, such as for cylinders in tidal flows or for heat exchanger tubes, there is also



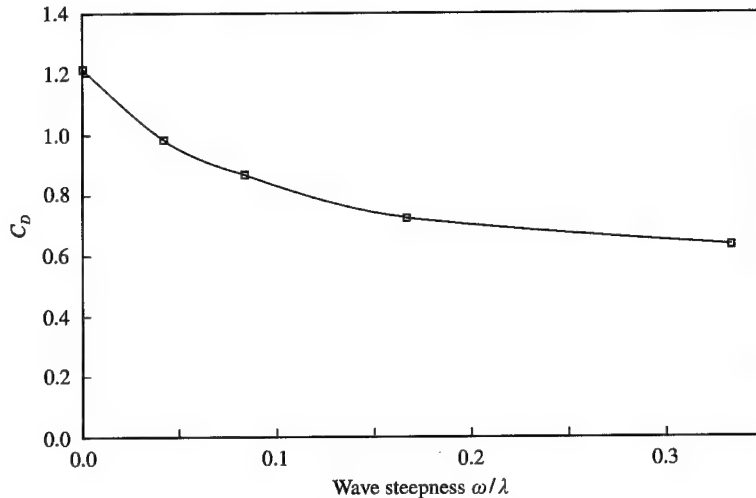


Figure 2. Measurements of drag coefficient versus wave steepness for a sinuous circular cylinder,  $\lambda/D = 7.5$ ,  $Re = 3.3 \times 10^4$ .

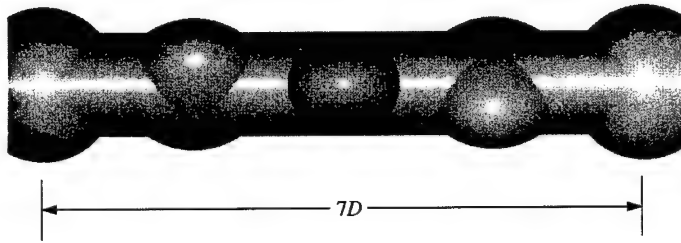


Figure 3. A view of a circular cylinder fitted with a spiralling arrangement of surface control bumps. Angular separation =  $45^\circ$ , longitudinal pitch of spiral =  $7D$ .

a requirement for VIV suppression and drag reduction of cylinders in multi-directional flows. Hence, how can the ideas discussed above be used to suppress VIV when the direction of the approach flow is unknown? In order to reproduce some of the effects of a wavy cylinder, hemispherical bumps or caps were attached to the forward-facing side of a straight cylinder at a similar spacing to the wave crests on the wavy cylinders. These were found to reduce the drag and to suppress vortex shedding but they are only effective for a relatively small range of flow incidence. The next step was to apply the bumps in a spiral pattern around the cylinder with a constant longitudinal spacing and an angular separation of  $45^\circ$ . A view of a typical arrangement of bumps is shown in Figure 3. Measurements of  $C_D$  for a body with a spacing between bumps of  $7D$ , versus incidence are shown in Figure 4 for a series of Reynolds numbers between  $2 \times 10^4$  and  $10^5$ . At  $0^\circ$  incidence a row of bumps is normal to the oncoming flow and since the bumps are distributed in a regular pattern it was only necessary to make measurements up to an incidence of up to  $22.5^\circ$ . It can be seen from Figure 4 that the addition of bumps reduced  $C_D$  by 25%, where  $C_D$  is based on the diameter of the plain cylinder.

Figure 5 shows three vorticity fields obtained from velocity measurements acquired using PIV at a Reynolds number of  $2.7 \times 10^4$ . One is for a spanwise position where the bumps are

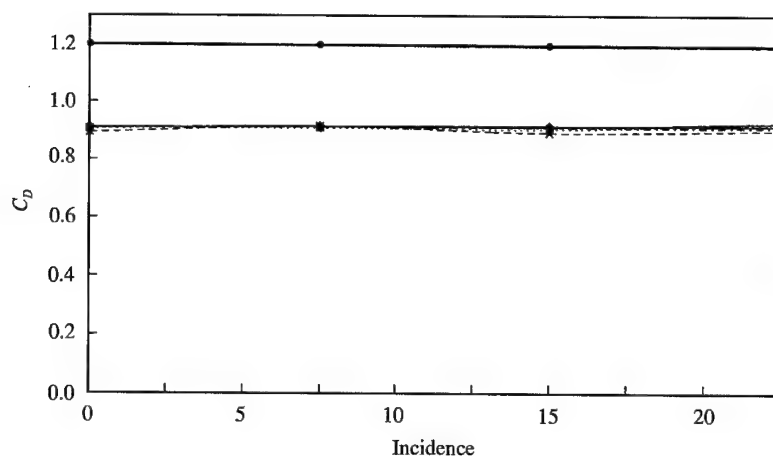


Figure 4. The effect of incidence on the drag of a circular cylinder fitted with a spiral arrangement of surface bumps: ●, circular cylinder; ×,  $Re = 2 \times 10^4$ ; □,  $Re = 4 \times 10^4$ ; △,  $Re = 6 \times 10^4$ ; ◇,  $Re = 2 \times 10^4$ ; +,  $Re = 10^5$ . Angular separation =  $45^\circ$ , longitudinal pitch of spiral =  $7D$ .

situated at  $\pm 90^\circ$ , another is for a position where bumps are at  $0^\circ$  and  $180^\circ$  and the third is for a plain cylinder. In both cases with bumps there is no evidence of Kármán-type vortex shedding and the flow has many similar features to that found around a wavy cylinder. Having demonstrated some drag reduction and suppression of vortex shedding the next stage in the investigation was to study how susceptible these cylinders are to VIV.

Maximum transverse response amplitude  $Y_{\max}$ , divided by  $D$ , is shown plotted in Figure 6 as a function of reduced velocity  $V_r$ , where  $V_r = nD/U$  and  $n$  is the oscillation frequency of the body in still water and  $U$  is the flow velocity. Two sets of results are plotted: one for a plain circular cylinder and the other for a cylinder with an array of bumps along the leading edge at a spacing of  $1.5D$ . The height of the bumps was equal to 25% of the diameter of the cylinder. The Reynolds number range was from 1650 to 7500 and  $m^*\zeta = 3.6 \times 10^{-2}$ . The plain cylinder results are similar to those found by other researchers and at first glance the results for the cylinder with bumps are disappointing. They indicate that when the body is flexibly mounted it is able to detect a very weak force fluctuation at a shedding frequency and that as it responds the excitation increases. The transverse oscillations of the cylinder with bumps developed extremely slowly compared to the plain cylinder and achieved a maximum amplitude about 25% lower. Hence it appears that with a relatively small amount of additional damping it may be possible to significantly reduce the response. This behaviour is similar to that found for cylinders with helical strakes which are effective at suppressing VIV for cylinders in air but still show a response at the lower mass damping parameters typical for water.

Figure 7 shows  $2Y_{\max}/D$  plotted against  $m^*\zeta$  for a series of body geometries.  $Y_{\max}$  is the maximum amplitude recorded over a range of reduced velocity that more than spans the expected lock-in regime. The Reynolds number for maximum response in all cases is about 4000 and  $m^*$  is held constant at 14.3. Results are shown for a plain cylinder, a wavy cylinder ( $w/\lambda = 0.167$ ) and cylinders with small, medium and large bumps. The heights of the three sets of bumps are, respectively, 25%, 33% and 50% of the diameter of the cylinder. The largest suppression of VIV is observed for the wavy cylinder, but the results for the cylinders with bumps are very close, with the cylinder having small bumps being almost as effective as

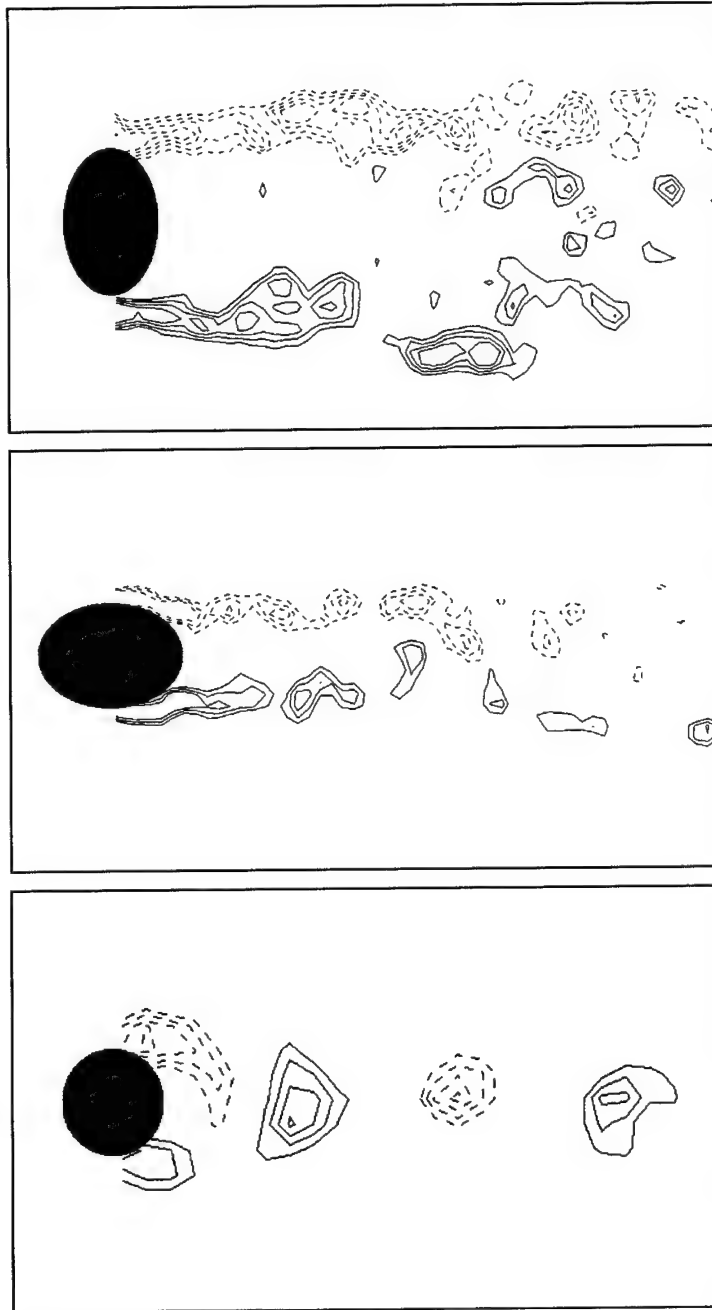


Figure 5. Nondimensional vorticity fields obtained using PIV in the wake of a circular cylinder fitted with surface bumps. The upper plot is from a spanwise position where the bumps are  $90^\circ$  to the flow, the middle plot is where the bumps are in-line with the flow and the lower plot is a plain circular cylinder. For bumps: angular separation =  $45^\circ$ , longitudinal pitch of spiral is equal to  $7D$ ,  $Re = 2.7 \times 10^4$ .

the cylinders with the two other sizes of bumps. It should be noted that no detailed attempt has been made to optimize the shape of the bumps, or their distribution, but the results demonstrate the potential for using this idea for suppressing VIV and reducing drag.

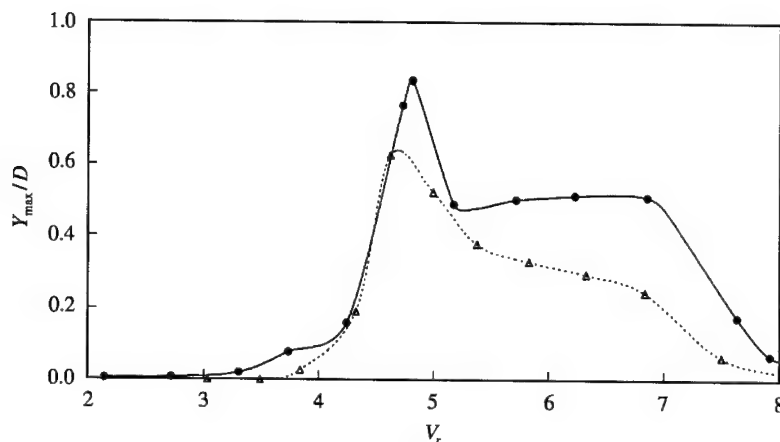


Figure 6. Maximum transverse response amplitude of an oscillating cylinder: ●, circular cylinder; △, cylinder with control bumps fitted to leading edge at a spacing of  $1.5D$ .  $m^*\zeta = 3.6 \times 10^{-2}$ ,  $Re = 1650-7500$ .

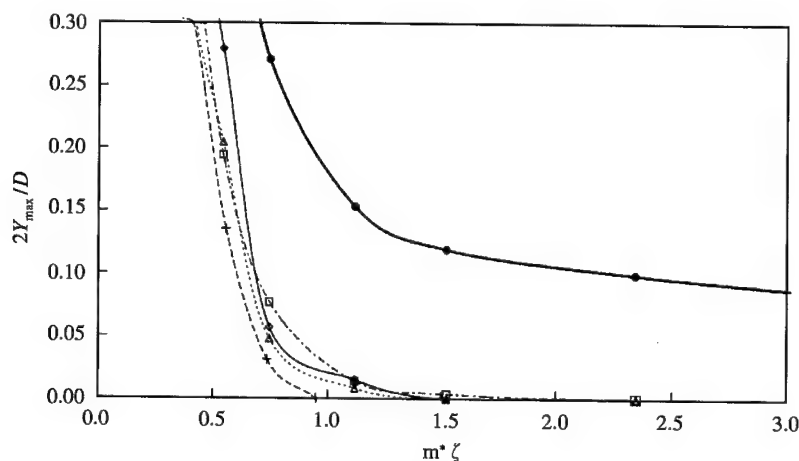


Figure 7. The effect of mass damping parameter ( $m^*\zeta$ ) on the maximum transverse response amplitude of various bodies: ●, circular cylinder; +, sinuous cylinder ( $w/\lambda = 0.167$ ); and cylinders fitted with increasingly large bumps to the leading edge: ◇,  $1.25D$ ; △,  $1.50D$ ; □,  $2.00D$ .  $m^* = 14.3$ .

#### 4. CONCLUSIONS

It is shown that sizeable reductions in drag can be achieved when the separation lines on a bluff body are forced to be sinuous. Drag reductions up to 47% are recorded for a circular cross-sectional body with a wavy axis. Above a certain value of wave steepness, regular vortex shedding can no longer be detected. The near-wake width is found to vary across the span in a sinusoidal way and longitudinal vorticity is introduced into the wake. Similar effects can be induced on a circular cylinder by attaching hemispherical bumps at regular intervals along the attachment line. Dependence on the angle of incidence can be removed by attaching the bumps in a spiral pattern. Measurements of VIV amplitudes show that a transverse response is recorded for the cylinder with bumps at low values of  $m^*\zeta$ , even though vortex shedding could not be detected for the same body when it was fixed.

However, the excitation is weakened and VIV can be totally suppressed for a cylinder with bumps at substantially lower values of  $m^*\zeta$  than for a circular cylinder.

### ACKNOWLEDGEMENTS

J. C. Owen was in receipt of a student bursary from EPSRC and A. A. Szewczyk acknowledges the support provided by ONR via Grant No. 0014-96-1-0756.

### REFERENCES

- BEARMAN, P. W. & OWEN, J. C. 1998 Reduction of bluff-body drag and suppression of vortex shedding by the introduction of wavy separation lines. *Journal of Fluids and Structures* **12**, 123–130.
- NAUMANN, A., MORSBACH, M. & KRAMER, C. 1966 The conditions of separation and vortex formation past cylinders. In *Separated Flow*, pp. 539–574; *NATO AGARD Conference Proceedings No. 4*.
- OWEN, J. C., SZEWCZYK, A. A. & BEARMAN, P. W. 1999 Suppressing Kármán vortex shedding by use of sinuous circular cylinders. *Bulletin of the American Physical Society* **44**, 124.
- OWEN, J. C., SZEWCZYK, A. A. & BEARMAN, P. W. 2000 Suppression of Kármán vortex shedding. Gallery of Fluid Motion. *Physics of Fluids* **12**, 1–13.
- OWEN, J. C. 2000 Passive control of vortex shedding in the wakes of bluff bodies. Ph.D. Dissertation, University of London, London, U.K.
- PETRUSMA, M. S. & GAI, S. L. 1994 The effect of geometry on the base pressure recovery of segmented blunt trailing edges. *Aeronautical Journal* **98**, 267–274.
- RODRIGUEZ, O. 1991 Base drag reduction by the control of three-dimensional unsteady vortical structures. *Experiments in Fluids* **11**, 218–226.
- ROSHKO, A. 1954 On the drag and shedding frequency of two-dimensional bluff bodies. NACA Technical Note 3169.
- TANNER, M. 1972 A method of reducing the base drag of wings with blunt trailing edges. *Aeronautical Quarterly* **23**, 15–23.
- TOMBAZIS, N. & BEARMAN, P. W. 1997 A study of three-dimensional aspects of vortex shedding from a bluff body with a mild geometric disturbance. *Journal of Fluid Mechanics* **330**, 85–112.
- WILLIAMSON, C. H. K. 1989 Oblique and parallel modes of vortex shedding in the wake of a circular cylinder at low Reynolds numbers. *Journal of Fluid Mechanics* **206**, 579–627.



## THE PHYSICAL MECHANISM OF TRANSITION IN BLUFF BODY WAKES

M. C. THOMPSON

*Department of Mechanical Engineering, Monash University  
Clayton, VIC 3800, Australia*

T. LEWEKE

*Institut de Recherche sur les Phénomènes Hors Equilibre  
49, rue Frédéric Joliot-Curie, B.P. 146, F-13384, Marseille Cedex 13, France*

AND

C. H. K. WILLIAMSON

*Sibley School of Mechanical & Aerospace Engineering, Cornell University  
Ithaca, NY 14853-7501, U.S.A.*

(Received 24 September 2000, and in final form 28 December 2000)

The physical nature of the initial transition to three-dimensionality of flow past a circular cylinder has been the subject of considerable debate in the literature. Of several proposed mechanisms, the possibility of classification as an elliptical instability is re-examined in this article. Detailed Floquet analysis of the transition shows clear evidence of the growth of an elliptic instability in the forming vortex cores followed by amplification by the strong strain field in the hyperbolic region between the forming and shed vortices. In fact, it appears that the wake immediately behind the cylinder shows distinct signs of a *cooperative elliptic instability* as found previously for interacting counter-rotating vortices. Further downstream, after the vortices have been shed into the wake, the instability again grows in the cores. Three-dimensional simulations provide a semi-quantitative estimate of the “elliptic content” of instability, and confirm that elliptic instability seems to be dominant in the initiation and maintenance of the 3-D perturbation.

© 2001 Academic Press

### 1. INTRODUCTION

THE TWO-DIMENSIONAL WAKE of a circular cylinder undergoes a hysteretic transition to three-dimensional flow at a Reynolds number  $Re = UD/\nu$  (where  $U$  is the free-stream velocity,  $D$  the cylinder diameter, and  $\nu$  the kinematic viscosity) of approximately 190. The initial instability causing this transition gives rise to the first of a sequence of two shedding modes, now generally referred to as modes A and B, which lead to the rapid evolution to fully turbulent flow [see, e.g., Williamson (1996a) and Henderson (1997)]. These modes have distinct unstable spanwise wavelength bands and different topologies. There are strong indications that the equivalent of mode A is the initial transition mode for a range of two-dimensional cylindrical bodies, from square cylinders (Robichaux *et al.* 1999) to long plates with aerodynamic noses (Hourigan *et al.* 2001). In addition, modes with the corresponding two distinct spatio-temporal symmetries have been observed in plane wakes both experimentally and numerically (Meiburg & Lasheras 1988). Figure 1 shows visualizations of modes A and B in the cylinder wake, obtained from direct numerical simulations (see Section 3.2).

Floquet stability analysis indicates that mode A first becomes unstable for a spanwise wavelength of  $\lambda = 4D$  at  $Re = 190$  (Barkley & Henderson 1996). This is consistent with experimental flow visualizations of Williamson (1988), which show the spanwise wavelength to be between 3 and  $4D$ . Interestingly, the unstable band of wavelengths becomes broad as the Reynolds number is increased, which may be the underlying cause of dislocations in wakes as observed by Williamson (1992, 1996*a, b*). At  $Re = 260$ , the Floquet analysis shows that the *two-dimensional* wake becomes unstable to a second shedding mode, mode B (Barkley & Henderson 1996). The critical wavelength in this case is about  $0.8D$ , again consistent with experimental observations of Williamson (1988). In a real flow, this transition occurs at a lower Reynolds number (Williamson 1988), because the development of mode A shedding substantially alters the assumed two-dimensional base flow, so that by  $Re = 230$ – $240$  the wake shows clear evidence of both modes, and of their non-linear interaction. Unlike mode A, mode B appears to remain unstable over a relatively small wavelength band, even at much higher Reynolds numbers. The remnants of mode B can be observed both visually and through spanwise cross-correlation measurements at  $Re = 1000$ , when the wake is certainly fully turbulent (Wu *et al.* 1996).

Despite the large number of experimental, theoretical and numerical studies of this 3-D transition, the precise physical nature of the secondary instabilities is not fully understood and has generated much debate. Several possible mechanisms have been proposed. Leweke & Provansal (1995) used a Ginzburg–Landau equation to model the wake as a collection of coupled oscillators. They proposed that the transition was due to a Benjamin–Feir instability found in such systems of oscillators. This was consistent with experiments into the dynamics of the wake; however, this instability has a vanishing spanwise wavenumber inconsistent with the observations of Williamson (1988), and numerical predictions of Barkley & Henderson (1996) of a finite wavenumber. Brede *et al.* (1996) suggested that the strong curvature of the streamlines in the near-wake, and especially of the braid regions between the rollers, was consistent with a centrifugal instability. However, no conclusive evidence was supplied to support this speculation. Karniadakis & Triantafyllou (1992) suggested that the route to turbulence was through period-doubling of the mode B instability. This conclusion was based on numerical computations on a narrow spanwise domain which suppresses mode A, whereas in a real flow its existence alters the evolution, leading to a faster (and different) route to turbulence (Hourigan *et al.* 1995).

Williamson (1996*b*) realized that the two distinct instabilities should be associated with two different length-scales of the two-dimensional wake flow. The two obvious wake length-scales are the core size of the Kármán vortices and the width of the braids between the rollers. He suggested that mode A instability was associated with an *elliptic* instability of the vortex cores, and that mode B instability was associated with an instability of the braid region (which includes the braid shear layer within the near-wake vortex formation region). Leweke & Williamson (1998*b*) showed that elliptic instability theory predicts the approximate spanwise wavelength of the mode A instability and is consistent with both the topology and the waviness of the core vortices. Henderson (1997) was critical of this proposed mechanism for two main reasons. The numerical simulation of the Floquet mode indicated that the instability is complex, showing strong growth both inside and outside the vortex cores, and hence it would not seem reasonable to classify it in terms of a simple instability of an idealized flow. The primary objection, however, was that the mode appears to have the largest amplitude outside the region in which elliptic instability theory indicates it should grow.

In this paper, we present further evidence that the principal physical origin of mode A instability can be attributed to an elliptic instability of the vortex cores.

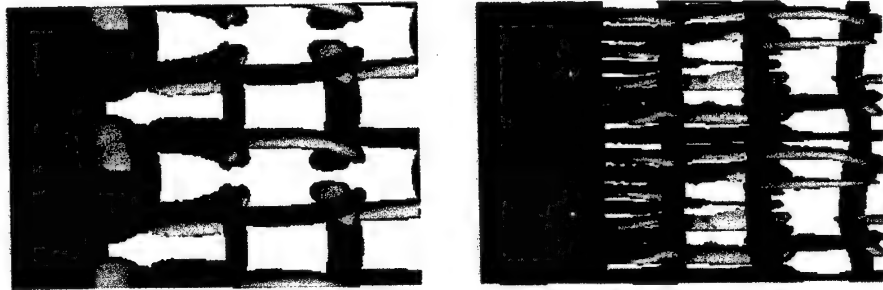


Figure 1. Visualizations of mode A (left,  $Re = 210$ ) and mode B (right,  $Re = 250$ ) shedding in the cylinder wake. The green and blue isosurfaces represent positive and negative streamwise vorticity. The flow is from left to right. The front of the circular cylinder is shown at the left of each plot.

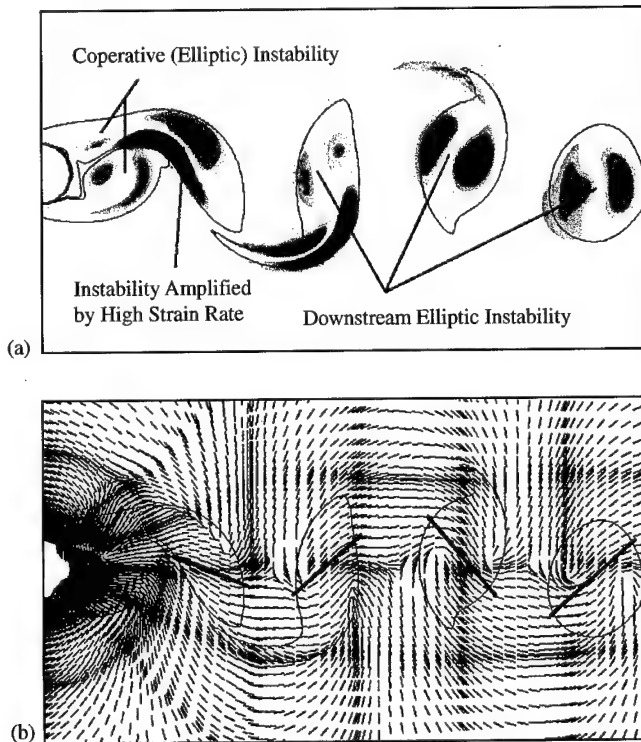


Figure 3. (a) Contour plot of the perturbation spanwise vorticity corresponding to the Floquet mode with spanwise wavelength of  $4D$  at  $Re = 190$ . (b) Stretching directions of the local strain. The heavy blue lines are indicative of the mean stretching direction through the vortex cores. In both plots, the positions of the wake vortices are indicated by the red lines marking vorticity levels of  $\pm 0.2U/D$ .



## 2. REVIEW OF THE ARGUMENTS

The theory of elliptic instability has been developed by Pierrehumbert (1986), Bayly (1986), Landman & Saffman (1987), Waleffe (1990) and others. In its basic form it considers the somewhat idealized case of two-dimensional flow with elliptic streamlines, which are generated by a superposition of a solid-body rotation with constant vorticity  $\omega$ , and plane strain of magnitude  $\varepsilon$ . The flow is (i.e., the streamlines are) elliptic if the eccentricity parameter  $\beta = 2\varepsilon/|\omega|$  is less than 1, and hyperbolic if  $\beta > 1$ .

It has been shown by various authors, that such unbounded linear flows are three-dimensionally unstable for all values of  $\beta$ , except  $\beta = 1$  (plane Couette flow), which is marginally stable. The mechanism of instability is an amplification of inertial waves in the rotating frame of reference of the base flow through a resonant interaction with the strain field. For inviscid flow, the growth rate  $\sigma_i$  of the most unstable perturbation is given by

$$\frac{\sigma_i}{\varepsilon} = \begin{cases} f(\beta) \approx \frac{9}{16}(1 - \beta^m)^n & \text{for } 0 < \beta < 1 \text{ (elliptic flow),} \\ = \sqrt{1 - \beta^{-2}} & \text{for } \beta > 1 \text{ (hyperbolic flow).} \end{cases} \quad (1)$$

The approximate expression for the elliptic growth rate, with  $m = 2.811$  and  $n = 0.3914$ , was computed by a least-squares fit of this functional form to the numerical result presented by Landman & Saffman (1987). The expression for the hyperbolic instability are given by Lagnado *et al.* (1984) and Lifshitz & Hamieri (1991). Importantly, although the growth rate depends on the orientation of the three-dimensional perturbation wave vector, it does not depend on its magnitude; i.e., all wavelengths  $\lambda$  are equally unstable. Also note that the growth rate is directly proportional to the magnitude of the strain.

Of course, the wake flow behind a circular cylinder is not an inviscid unbounded linear flow. As shown in Figure 2, the wake consists of finite regions of elliptic flow (primarily the Kármán vortices), and regions of hyperbolic flow (primarily the braid regions between the vortices). It is known, however, from studies by Waleffe (1990) and Leblanc & Godeferd (1998), that there exist localized modes of elliptic and hyperbolic instability that would fit into these regions and effectively "see" a uniform elliptic or hyperbolic flow. The finite core size of the Kármán wake vortices effectively imposes a length scale (the core diameter, which is of the order of  $D$ ) on the elliptic instability. This, in turn, leads to an effective upper limit on the spanwise wavelength because the length scales in the cross-stream plane and spanwise direction are coupled. [Recent comprehensive accounts on elliptic instability in finite-size vortices in a small strain, i.e. with  $\beta \ll 1$ , are given by Eloy & Le Dizés (1999, 2001).] In addition, the influence of viscosity imposes a lower limit on the allowable spanwise wavelengths. It was shown in Lewke & Williamson (1998*b*) that the expected spanwise wavelength of an elliptic instability of the Kármán vortices is  $\lambda \approx 3D$ , given estimates of the average value of  $\beta$  ( $\approx 0.6$ , which is relatively high), and estimates of the

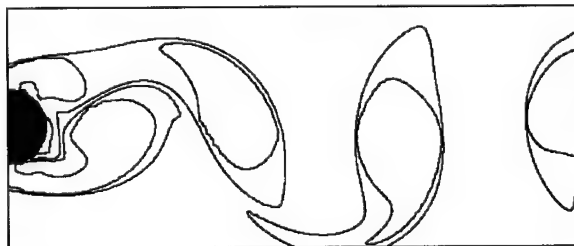


Figure 2. Relation of elliptical flow regions ( $\beta < 1$ , shown in grey) to the wake vortices (solid lines). The non-elliptic regions are hyperbolic regions (where the strain dominates).

vortex core diameter from direct numerical simulation of the two-dimensional flow. This is respectably in line with the observed experimental determination of  $\lambda = 3-4D$  and the Floquet analysis of Barkley & Henderson (1996) ( $\lambda = 4D$  at onset). The corresponding growth rate can also be evaluated, again using estimates from DNS of the various dependent parameters. In particular, the strain rate was measured to be  $\varepsilon D/U \approx 1$  at the center of the near-wake Kármán vortices. The estimated viscous growth rate of elliptic instability in the cylinder wake around  $Re = 200$  is  $\sigma D/U \approx 0.4$  [see Leweke & Williamson (1998b) for more details on these estimates].

Other strong supporting evidence is the apparent existence of invariant stream tubes as indicated by dye visualizations, surrounding the vortex cores, which remain unperturbed despite strong internal waviness of the cores (Leweke & Williamson 1998b). This peculiar spatial structure is a characteristic feature of the elliptic instability perturbation.

### 3. NEW RESULTS AND DISCUSSION

In this section, we shall present and interpret some new evidence on the nature of the initial instability from well-resolved Floquet stability analysis and direct numerical simulations of the transition.

#### 3.1. FLOQUET ANALYSIS OF MODE A TRANSITION

Floquet analysis determines three-dimensional stability of a periodic two-dimensional base flow by solving the linearized Navier–Stokes equations for the perturbation velocity and pressure fields. The present implementation is similar to that described in Barkley & Henderson (1996). The aim is to determine the growth of spanwise sinusoidal perturbations over one shedding period, as a function of Reynolds number and wavelength. The stability is determined by the Floquet multiplier, the multiplication factor connecting the amplitude of a given mode from one cycle to the next. When a multiplier exceeds unity, the corresponding mode becomes unstable. As determined by Barkley & Henderson (1996), the first Floquet multiplier becomes greater than 1 at the transition Reynolds number of 190, with a three-dimensional unstable mode of wavelength  $\lambda = 4D$ .

Figure 3(a) shows the Floquet instability mode at a certain time in the shedding cycle for  $Re = 190$  and for a Floquet wavelength of  $4D$ . For these parameters, the corresponding Floquet multiplier was determined to be approximately unity, consistent with the analysis of Barkley & Henderson (1996). It is this instability mode that is responsible for the transition to three-dimensional flow. In effect, the saturated Floquet mode corresponds to mode A.

The plot shows the perturbation spanwise vorticity. Several features of the flow have been marked. Immediately downstream of the cylinder, the wake shows local vorticity distributions reminiscent of the pattern characteristic of elliptic instability. The initial vortex structure in the lower half of the wake, shows the separation of positive and negative perturbation vorticity in the direction of the principal axis of strain [see Figure 3(b)], corresponding to a movement of the centre of the forming roller in the same direction, as is expected for elliptic instability. On the top half of the wake, there is another separation of positive and negative vorticity, again aligned with the strain field. The two localized perturbations together appear to be similar to the cooperative elliptic instability of two interacting counter-rotating vortices (Leweke & Williamson 1998a). In particular, they show the same topology and alignment with the local strain field. At this stage of vortex formation, both local perturbations are embedded in elliptic regions of the flow.

Figure 4(a) shows a greyscale plot of the local growth rate of the instability calculated using results from Landman & Saffman (1987). The vorticity and strain distributions are far from the constant values assumed in this study, nevertheless, the distribution is suggestive that the elliptical regions shown in Figure 3(a) are likely to be (elliptically) unstable.

The magnitude of the local strain is given in Figure 4(b). Interestingly, apart from the separating shear layers attached to the cylinder, the strain is large in the hyperbolic region between the two elliptic regions in the top half of the wake at the rear of the cylinder. This is important because the inviscid growth rate roughly scales with the strain rate, so high strain is an indication of high growth rates for both elliptic and hyperbolic instabilities.

Figure 5 shows a sequence of the images of the development of the spanwise vorticity perturbation close to the back of the cylinder. Initially, the perturbations develop in each elliptic region resulting in the generation of positive and negative perturbation vorticity on each side of the core centre. This is indicative of the movement of the core in the direction of principal strain as occurs for elliptical instability. For both the finite-size vortex examined by Waleffe (1990), and the cooperative elliptic instability studied by Leweke & Williamson (1998a), the perturbation growth (at least for a reasonable time) is limited to the elliptical regions of the flow. This is not true in this case. Here, although the initial development of the instability occurs in the forming vortex cores, the individual perturbations merge and grow strongly between the elliptical regions. This is not surprising as the region between the forming vortex structures, and especially towards the downstream limits of the structures, is strongly strained as can be seen from Figure 4(b). It appears that this high strain rate leads to strong amplification of the perturbation. As the merged perturbation is advected downstream, it appears to lag behind the advected vortex cores. This is probably due to a combination of two factors: (i) the mean wake velocity defect of the perturbation on the side of the cores closer to the wake centre line is advected downstream less quickly than the more off-centred parts or the cores themselves; (ii) the instability is preferentially amplified in the highly strained hyperbolic region *between* vortex structures from the same side of the wake. The end result is that, after the vortex has been shed into the wake, the maximum amplitude of the instability is in the braid regions rather than the vortex cores. This maximal amplitude occurring between the forming vortices and in the braid regions was noticed by Henderson (1997), and helped lead to the conclusion that the instability should not be classified as elliptic. It needs to be pointed out that unless resolution is adequate and the contour levels are chosen carefully, the initial development of the instability in the core regions can easily be overlooked.

As the vortices move further downstream, out of the formation region, they maintain their alignment and shape to a large extent and so are ideal candidates for a second elliptic instability. Initially, they are relatively perturbation-free, but the background perturbation

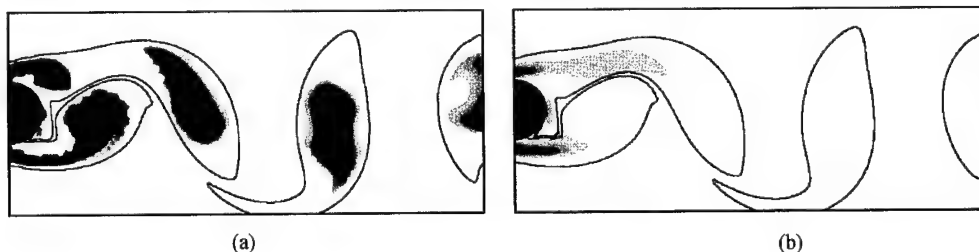


Figure 4. Contour plots of (a) the viscous growth rate predicted from elliptic instability theory (Landman & Saffman 1987), and (b) the strain magnitude showing that the strain maintains a high value in the hyperbolic region (between the two elliptic regions in the top half of the wake, immediately behind the cylinder).

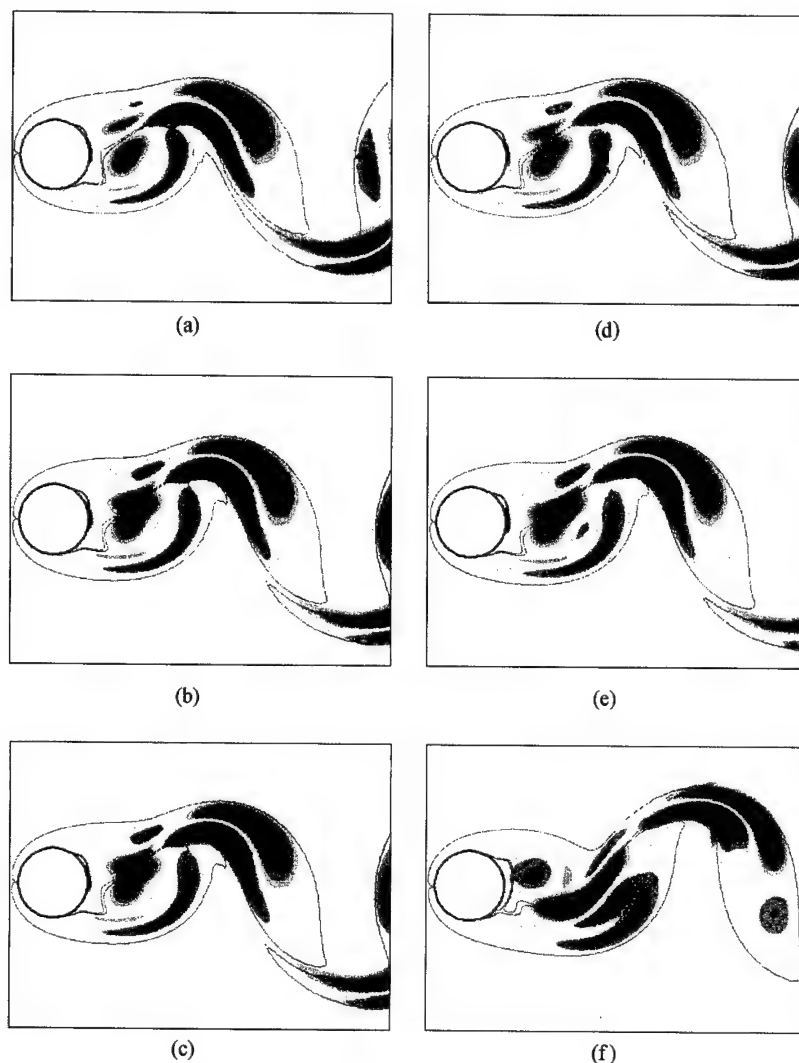


Figure 5. Development of the instability during the shedding process. Relative to the first (a), the subsequent images (b–f) are 0.04, 0.08, 0.12, 0.24 and 0.32 shedding periods later, respectively.

field leads to the rapid development of elliptic instability in the cores. Although the cores, by no means, have constant local vorticity and strain fields, they clearly show a perturbation field consistent with the vorticity distribution expected from elliptic instability. This rapid growth only occurs for a short time. Approximately one period further downstream, viscous growth rate calculations indicate that the instability is only marginally unstable. This is consistent with the observed development shown in Figure 3(b) (and further downstream).

It is possible to estimate the growth rates for the initial cooperative and the downstream elliptic instabilities from the simulations. This was done by measuring the rate of change of the circulation in each half of the bipolar spanwise perturbation vorticity of the cores over approximately one quarter of a shedding cycle. The line integral defining this circulation was evaluated numerically for at least five consecutive snapshots in time spaced 0.05 cycles apart. For the initial cooperative core instability, and downstream elliptic core instability, the growth rate was calculated to be  $\sigma D/U = 0.39$  and  $0.42$ , respectively. Although there is

some uncertainty in these estimates, they are in good agreement with the theoretical estimate  $\sigma D/U \approx 0.4$  given above.

In summary, an interpretation of the evidence is that there are two elliptic instabilities, contributing to the mode A transition. The first occurs immediately at the back of the cylinder as the Kármán vortices are forming, and the second further downstream as the vortices are shed into the wake. Although the first instability does not persist in the elliptic region, and appears to be amplified in the hyperbolic region, it seems likely that the spanwise wavelength is selected according to the scale of the Kármán vortices in line with elliptic instability theory. Both when the perturbation is initially forming in the core regions, and when it is undergoing amplification in the hyperbolic region, it appears that the growth is due to the action of the strain field. This is consistent with the physical mechanism responsible for both elliptic and hyperbolic instability.

### 3.2. THREE-DIMENSIONAL DIRECT NUMERICAL SIMULATION

As further support for the importance of the elliptical nature of the instability, direct numerical simulations were performed. The same three-dimensional spectral/spectral-element code used for previous wake transition simulations (Thompson *et al.* 1996) is used here. Spectral elements are used in the cross-stream planes and a Galerkin Fourier expansion in the spanwise direction. Care was taken to ensure adequate resolution and domain size to capture the essential physics of the mode A transition. However, due to space limitations, these validation studies are not described here. The spanwise domain size was chosen to be  $4D$  to approximately match the most unstable wavelength of the spanwise mode at transition. This limits the possible wavelengths represented by the Fourier expansion to be  $4D/n$  ( $n = 1, 2, \dots$ ). Of these wavelengths only  $\lambda = 4D$  is unstable at the Reynolds number of the simulations.

A three-dimensional simulation of mode A at  $Re = 200$  was started by extending the flow field from a previous two-dimensional simulation to the three-dimensional domain. To initiate the development of three-dimensionality, the field was perturbed by adding random noise at a relative level of  $10^{-4}$  to the velocity field. The flow was then evolved for sufficient time (approximately 10 shedding cycles), so that it effectively consisted of the two-dimensional base flow plus the most unstable Floquet mode. At this stage, the relative amplitude of perturbation field is still very small and the evolving flow is well within the linear regime where the growth is governed by the Floquet multiplier.

At this point in the temporal development of the mode A flow, the perturbation field was decomposed into two mutually exclusive components. The first perturbation field is only nonzero where the two-dimensional flow (shown in Figure 2) is elliptic ( $\beta < 1$ ), and the second where it is hyperbolic ( $\beta > 1$ ). From these two perturbation fields, two three-dimensional flow fields were constructed by adding the spanwise-averaged (two-dimensional) base flow to the *elliptic* and *hyperbolic* perturbation fields, respectively. Thus, the first flow field contains the elliptic part of the perturbation, while the second contains the hyperbolic part. This split-up was performed at a random time in the shedding cycle. The results that follow may, to a certain degree, depend on the choice of this time, a point which was not investigated further so far. (Formally, regions with  $\beta < 1$  may also develop instabilities linked to centrifugal effects. However, no attempt was made here to further isolate these effects from those of the elliptic instability.)

Using the two fields as initial conditions, the flow was evolved for several more shedding cycles. Figure 6(a,b) show isosurface visualizations of the perturbation spanwise vorticity after 2.4 shedding cycles, for the two initial fields. The isosurface level is the same in both cases. These visualizations show that the vorticity field that has evolved from the initially

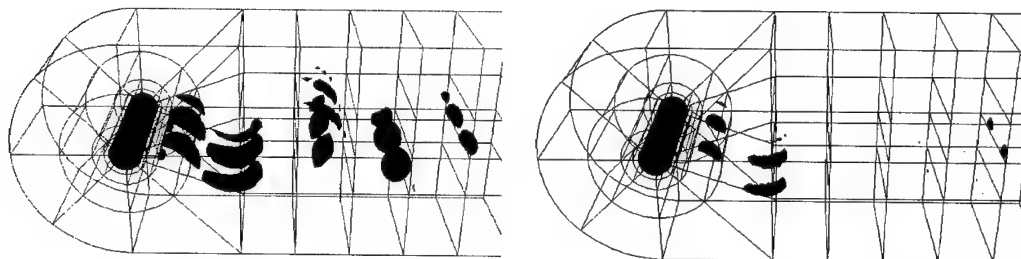


Figure 6. Isosurface visualization of the perturbation spanwise vorticity after removing (a) the hyperbolic or (b) the elliptic component of the Floquet mode and evolving the flow for 2.4 shedding periods.

elliptic field recovers towards the complete Floquet mode much more quickly than the initially hyperbolic one. In particular, starting from the “elliptic” conditions, the perturbation in the hyperbolic braids, initially set to zero, reappears very rapidly. On the contrary, with the “hyperbolic” initial field, i.e., in the absence of the elliptic core deformations, the perturbations in the braids actually *decrease* in the first few cycles of the simulation. Thus, it appears that the elliptic instability of the vortex cores in the wake formation zone has a dominant influence on the development of the instability.

The “degree of ellipticity” can be approximately quantified through the following argument. Let  $\Phi_0, \Phi_1, \Phi_2, \dots$  be the Floquet modes of the linearized Navier–Stokes equations, where the modes have been ordered according to magnitude of the eigenvalues (the Floquet multipliers) from largest to smallest. In particular,  $\Phi_0$  corresponds to the only growing mode, i.e., the one responsible for the mode A transition. To form the two initial fields, this Floquet mode is split into two mutually exclusive components  $\Phi_e$  (elliptic) and  $\Phi_h$  (hyperbolic):  $\Phi_0 = \Phi_e + \Phi_h$ . We can now expand these two components in terms of all the Floquet modes:

$$\Phi_e = \sum \alpha_i \Phi_i \quad \text{and} \quad \Phi_h = \sum \gamma_i \Phi_i. \quad (2)$$

From the definition of  $\Phi_e$  and  $\Phi_h$  the following relationships exist between the expansion coefficients:  $\alpha_0 + \gamma_0 = 1$  and  $\alpha_i + \gamma_i = 0$ , for  $i > 0$ . Effectively,  $\alpha_0/\gamma_0$  determines the ratio of elliptic to hyperbolic “contents” of the growing Floquet mode. After each shedding period, the amplitude of each Floquet mode is multiplied by its Floquet multiplier, i.e., after many shedding cycles the perturbation evolves towards  $\Phi_0$ , the multipliers of the other modes being less than 1. Thus, the ratio  $\alpha_0/\gamma_0$  is given by the ratio of the amplitudes of the two growing perturbations starting from the elliptic and hyperbolic conditions described above, after the same number of periods. In the present simulations, this ratio was measured eight shedding cycles after initialization, which is sufficient to damp out the contribution from the stable Floquet modes ( $\Phi_i, i > 0$ ), whose multipliers are all smaller than 0.2 at  $Re = 200$  (Barkley & Henderson 1996). The result is  $\alpha_0/\gamma_0 = 2.03$ . In this sense, the Floquet mode responsible for mode A transition may be characterized as being about two-thirds elliptic and one-third hyperbolic.

#### 4. CONCLUSIONS

It is useful, where possible, to attribute a flow transition to a simple physical mechanism applicable to idealized flows, because it aids with providing a physical understanding of the transition. This is valuable for interpreting other related (or unrelated) transitions. It is with this aim that we have attempted to interpret the transition to three-dimensionality for flow

past a circular cylinder. Importantly, there is now considerable evidence that the same transition scenario applies to a whole range of two-dimensional body geometries. Certainly, the transition is complex, the instability is not restricted to the forming vortices and the Kármán vortices in the wake, and even within the cores the ellipticity parameter is far from constant. In addition, linear stability analysis predicts that the unstable mode grows as a whole, rather than as a set of effectively decoupled regions with their own local physical instabilities triggering instabilities in other regions. Nevertheless, the evidence presented in this paper shows that the first instability to form as the fluid advects downstream past the cylinder occurs in the forming vortex cores, with a growth rate and spanwise wavelength close to those predicted by idealized elliptic instability theory. This initial instability shows distinct features similar to the cooperative elliptic instability found by Leweke & Williamson (1998a) for two counter-rotating vortices. Because of the complexity of the flow, it appears that the nascent perturbation is amplified in the highly strained hyperbolic region between forming vortices, leading to the observed high perturbation amplitudes in the braids. A second elliptic instability develops in the cores of the fully formed Kármán vortices further downstream. Direct numerical simulations, carried out to analyse the contributions of elliptic and hyperbolic flow regions to the three-dimensional transition, support the interpretation that the elliptic instability is dominant in the initiation and maintenance of the mode A perturbation.

## REFERENCES

- BARKLEY, D. & HENDERSON, R. D. 1996 Three-dimensional Floquet stability analysis of the wake of a circular cylinder. *Journal of Fluid Mechanics* **322**, 215–241.
- BAYLY, B. J. 1986 Three-dimensional instability of elliptical flow. *Physical Review Letters* **57**, 2160–2163.
- BREDE, M., ECKELMANN, H. & ROCKWELL, D. 1996 On secondary vortices in a cylinder wake. *Physics of Fluids* **8**, 2117–2124.
- ELOY, C. & LE DIZÈS, 1999 Three-dimensional instability of Burgers and Lamb–Oseen vortices in a strain field. *Journal of Fluid Mechanics* **378**, 145–166.
- ELOY, C. & LE DIZÈS, 2001 Stability of the Rankine vortex in a multipolar strain field. *Physics of Fluids* **13**, 660–676.
- HENDERSON, R. D. 1997 Nonlinear dynamics and pattern formation in turbulent wake transition. *Journal of Fluid Mechanics* **352**, 65–112.
- HOURLIGAN, K., THOMPSON, M. C. & SHERIDAN, J. 1995 The development of three-dimensionality in the wake of a circular cylinder. In *Advances in Turbulence V* (ed. R. Benzi), pp. 496–501. Dordrecht: Kluwer Academic.
- HOURLIGAN, K., THOMPSON, M. C. & TAN, B. T. 2001 Self-sustained oscillations in flows around long blunt plates. *Journal of Fluids and Structures* **15**, xxx–xxx (this issue).
- KARNIADAKIS, G. E. & TRIANTAFYLLOU, G. S. 1992 Three-dimensional dynamics and transition to turbulence in the wake of bluff objects. *Journal of Fluid Mechanics* **238**, 1–30.
- LAGNADO, R. R., PHAN-THIEN, N. & LEAL, L. G. 1984 The stability of two-dimensional linear flows. *Physics of Fluids*, **27**, 1094–1101.
- LANDMAN, M. J. & SAFFMAN, P. G. 1987 The three-dimensional instability of strained vortices in a viscous fluid. *Physics of Fluids* **30**, 2339–2342.
- LEBLANC, S. & GODEFERD, F. S. 1988 An illustration of the link between ribs and hyperbolic instability. *Physics of Fluids* **11**, 497–499.
- LEWEKE, T. & PROVANSAL, M. 1995 The flow behind rings: bluff body wakes without end effects. *Journal of Fluid Mechanics* **288**, 265–310.
- LEWEKE, T. & WILLIAMSON, C. H. K. 1998a Cooperative elliptic instability of a vortex pair. *Journal of Fluid Mechanics* **360**, 85–119.
- LEWEKE, T. & WILLIAMSON, C. H. K. 1998b Three-dimensional instabilities in wake transition. *European Journal of Mechanics B/Fluids* **17**, 571–586.
- LIFSCHITZ, A. & HAMEIRI, E. 1991 Local stability conditions in fluid dynamics. *Physics of Fluids A* **3**, 2644–2651.

- MEIBURG, E. & LASHERAS, J. C. 1988. Experimental and numerical investigation of the three-dimensional transition in plane wakes. *Journal of Fluid Mechanics* **190**, 1–37.
- PIERREHUMBERT, R. T. 1986 Universal short-wave instability of two-dimensional eddies in an inviscid fluid. *Physical Review Letters* **57**, 2157–2159.
- ROBICHAUX, J., BALACHANDAR, S. & VANKA, S. P. 1999 Three-dimensional Floquet instability of the wake of a square cylinder. *Physics of Fluids* **11**, 560–578.
- THOMPSON, M. C., HOURIGAN, K. & SHERIDAN, J. 1996 Three-dimensional instabilities in the wake of a circular cylinder. *Experimental Thermal and Fluid Science* **12**, 190–196.
- WALEFFE, F. 1990 On the three-dimensional instability of strained vortices. *Physics of Fluids A* **2**, 76–80.
- WILLIAMSON, C. H. K. 1988 The existence of two stages in the transition to three-dimensionality of a cylinder wake. *Physics of Fluids* **31**, 3165–3168.
- WILLIAMSON, C. H. K. 1992 The natural and forced formation of spot-like vortex dislocations in the transition of a wake. *Journal of Fluid Mechanics* **243**, 393–441.
- WILLIAMSON, C. H. K. 1996a Vortex dynamics in the cylinder wake. *Annual Review of Fluid Mechanics* **28**, 477–526.
- WILLIAMSON, C. H. K. 1996b Three-dimensional wake transition. *Journal of Fluid Mechanics* **328**, 345–407.
- WU, J., SHERIDAN, J., WELSH, M. C. & HOURIGAN, 1996 Three-dimensional vortex structures in a cylinder wake. *Journal of Fluid Mechanics* **312**, 201–222.



## THE SUPPRESSION OF LIFT ON A CIRCULAR CYLINDER DUE TO VORTEX SHEDDING AT MODERATE REYNOLDS NUMBERS

C. DALTON, Y. XU

*Mechanical Engineering Department, University of Houston  
Houston, TX 77204-4792, U.S.A.*

AND

J. C. OWEN

*Department of Aeronautics, Imperial College  
London, SW7 2BY, U.K.*

(Received 11 August 2000, and in final form 14 November 2000)

This paper discusses the effect of a small control cylinder on the transverse force (lift) on a large primary cylinder when the control cylinder is placed at select locations in the shear layer emanating from the primary cylinder. We have conducted both CFD and flow-visualization studies of this situation for Reynolds numbers of 100, 1000, and 3000. A 2-D Large Eddy Simulation was used in the CFD study to include the effects of wake turbulence. The CFD results show that the LES model predicts essentially an elimination of the transverse force on the primary cylinder for an appropriate placement of the control cylinder. The results also show that the drag on the primary cylinder is reduced. Our results, both from computation and flow visualization, indicate that the placement of a control cylinder has a noticeable influence on the drag and lift on the primary cylinder.

© 2001 Academic Press

### 1. INTRODUCTION

VORTEX SHEDDING from bluff bodies is a recognized phenomenon since the days of Leonardo da Vinci. One effect on, say, a circular cylinder is to cause the instantaneous force acting on the cylinder to vary, with time, which can cause vibration of the cylinder. This vortex-induced vibration (VIV) is the cause of at least three troublesome situations: fatigue of the cylinder due to sustained oscillations, possible impact with adjacent cylinders due to VIV, and possible extreme buffeting of trailing cylinders due to shed vortices from the upstream cylinder.

There are several ideas that have been pursued to influence, either to minimize or eliminate, vortex shedding and, thus, to control the effects of vortex shedding. These ideas fall into either of two categories: active control and passive control. We will discuss only the passive-control devices in this paper.

Zdravkovich (1997) presents a discussion of several of the passive control devices: the perforated shroud which has the effect of influencing the base pressure; a splitter plate which prevents communication between the opposing sides of the wake; and helical strakes which have the effect of destroying the longitudinal coherence in the vortex shedding.

A fourth passive control device is the placement of a second, and smaller, cylinder in the wake of a large cylinder, which will be the focus of this study. The smaller cylinder (the

control cylinder) has the effect of influencing the rollup of the shear layer from one side of the larger cylinder (the primary cylinder), i.e., the side of the primary cylinder near which the control cylinder is placed. Several authors have discussed this concept from both experimental and numerical points of view. Experimentally, this problem has been studied by Sakamoto *et al.* (1991), who used a square prism as the primary cylinder. They found that a close proximity configuration led to significant reductions of the fluctuating lift and drag on the primary cylinder. Igarishi & Tsutsui (1991) used a control cylinder to reduce the drag and lift on their primary cylinder. They explained their results by saying that the control cylinder provided a turbulent jet that attached itself to the near side of the wake of the primary cylinder and prevented the traditional vortex-shedding pattern from developing. Sakamoto & Hanui (1994) studied numerous different configurations of primary and control cylinders at a Reynolds number ( $Re$ ) of  $6.5 \times 10^4$ . Their experimental results showed that the maximum reduction of the drag and lift occurred when the control cylinder was placed at  $120^\circ$  from the stagnation point. Strykowski & Sreenivasan (1990) did both an experimental and numerical study of this same problem for  $Re = 100$ , which is in the range of a 2-D flow. They found that the control cylinder had a strong influence of the drag and lift on the primary cylinder. They attributed the drag and lift reductions to the control cylinder diffusing concentrated vorticity and a small amount of fluid into the wake of the primary cylinder where the flow was influenced by removing some of the unsteadiness from the wake.

## 2. ANALYSIS

We will treat the flow as 2-D and take the fluid to be incompressible. The governing equations will be expressed in general coordinates. We will spatially filter the governing equations to represent the problem by means of the Large Eddy Simulation (LES) method. Thus, the governing equations represent the 2-D resolved velocity field with the subgrid scale (SGS) effects represented by the Smagorinsky (1963) model. We use the LES method, which is normally used for 3-D representations of flow, in a 2-D simulation because of the complexities of representing two cylinders in the flow field. A full 3-D calculation would present computational requirements that would be insurmountable in terms of the facilities available to us for this study. We recognize that the 2-D calculations will not be truly representative of the actual flow at these Reynolds numbers, but the 2-D CFD analysis from this study will provide some insight not previously available. Because this is a 2-D study, we expect, based on our experience and that of others in related studies, that the calculated drag and lift coefficients will be slightly greater than the values that would have been obtained in a 3-D study.

We will use represent the problem in general coordinates and use the 3-D LES approach presented by Lu *et al.* (1997), although, in this case, we have a 2-D problem. The value for the Smagorinsky modeling constant for this problem is 0.1.

The boundary conditions to be applied are the typical no-slip and no-penetration conditions applied to the surface of the cylinders. The inflow boundary condition is that the incoming flow is uniform. The outflow boundary condition is that the flow crossing the outflow boundary is not affected by the presence of the boundary. This means that vortices approaching the outflow boundary cross the outflow boundary undisturbed by the presence of the boundary, i.e., the outflow vorticity gradients are set to zero.

## 3. REPRESENTATION OF A PAIR OF CYLINDERS

Representing a pair of cylinders in a flow field requires some special consideration of the geometry. Two cylinders present the problem of dealing with two branch cuts in

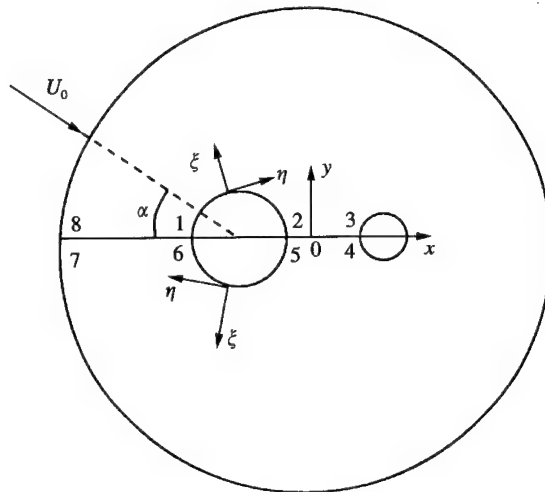


Figure 1. Schematic diagram of two cylinders.

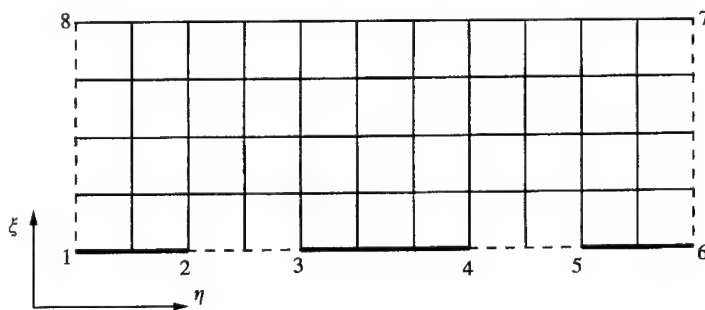


Figure 2. The two cylinders in the transformed plane.

the representation. Figure 1 shows the configuration of the cylinders in the physical plane. The branch cuts are along the lines 8-1 (or 7-6) and 2-3 (or 5-4). We need to transform the cylinders in the physical plane into a rectangular computational plane. To represent the computational plane, the region is opened as shown in Figure 2. Lines 1-2 and 5-6 represent the cylinder to the left while the cylinder to the right is represented by line 3-4. Thus, the computational grid is now rectangular which facilitates the solution of the problem. The no-slip boundary conditions for the surfaces of the cylinders are represented along the lines 1-2 and 5-6 for the left cylinder and along the line 3-4 for the right cylinder. The inflow boundary condition is represented on the ends of the line 7-8, while the outflow boundary conditions are represented toward the central part of line 7-8. The distinction between the two regions along line 7-8 cannot be specified in advance; it develops as a part of the solution. The lines 2-3 and 4-5 do not have boundary conditions specified, except to say that the values from 2-3 are the same as from 4-5. The same is said for lines 1-8 and 6-7.

#### 4. CYLINDERS OF UNEQUAL SIZE: SUPPRESSION OF VORTEX SHEDDING

We now examine the problem mentioned in the Introduction: a primary (larger) cylinder and a control (smaller) cylinder, configured so that the control cylinder is in the vicinity of

one of the separated shear layers from the primary cylinder. Our focus in this study is to examine the effect of the control cylinder on vortex shedding of the primary cylinder, i.e., under what circumstances, if any, is vortex shedding suppressed by the control cylinder? The primary cylinder is to have a diameter 10 times that of the control cylinder,  $D/d = 10$ , where  $D$  is the diameter of the primary cylinder and  $d$  is the diameter of the control cylinder. We treat this problem by placing both cylinders on the  $x$ -axis and changing the angle of attack of the flow, as shown in Figure 1. In this way, we can change the position of the control cylinder relative to the separated shear layer by changing the angle of attack. Results for three different Reynolds numbers will be presented. The reference velocity in the drag and lift coefficient definitions for the control cylinder is the approach velocity to the primary cylinder. The code used for the velocity and force calculations has been thoroughly tested for a large number of cases.

#### 4.1. $Re = 100$

This case is a physically 2-D, purely viscous flow calculation. The results for the drag and lift coefficients,  $C_D$  and  $C_L$ , on the primary cylinder are shown in Figure 3 for five different angles of attack at a gap distance of  $R/D = 1.4$ , where  $R$  is the center-to-center distance between the two cylinders. (The term "angle of attack" used herein means the angle above the rear centerline of the primary cylinder to the location of the control cylinder.) These results show that conventional vortex shedding is essentially suppressed at  $25^\circ$  and  $30^\circ$ , i.e., the lift coefficient on the primary cylinder has become virtually a constant (although nonzero) value. The explanation for the suppression of conventional vortex shedding is that the near wake has become fairly steady in its behavior as fluid from the control-cylinder-side shear layer is drawn steadily into the wake. There is still a conventional wake present, but it has been pushed much further downstream and does not seem to be affecting the near wake. For angles of attack greater than about  $30^\circ$ , the control cylinder is essentially out of the wake of the primary cylinder and its effect is still present, but is lessened. The lift coefficient is oscillating with a nonzero mean value, which indicates that vortex shedding is occurring, but in a different manner than for a single cylinder. The nonzero mean value of

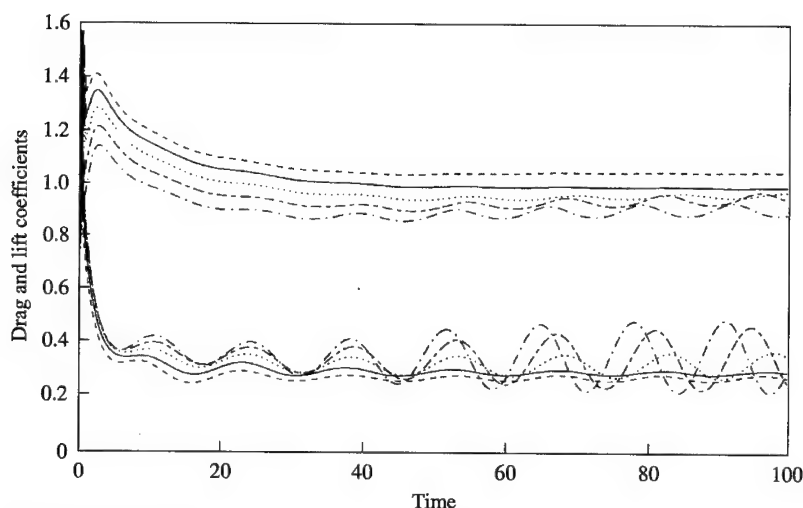


Figure 3. Drag and lift coefficients for the primary cylinder at  $Re = 100$  and  $R/D = 1.4$ : ---,  $\alpha = 25^\circ$ ; —,  $\alpha = 30^\circ$ ; ···,  $\alpha = 35^\circ$ ; - · -,  $\alpha = 40^\circ$ ; - - -,  $\alpha = 45^\circ$ .

the lift coefficient is because the mean flow field is no longer symmetric due to the presence of the control cylinder.

Suppression of conventional vortex shedding has also affected the drag coefficient, which is seen to have a fairly flat value at 25 and 30°. The drag coefficient for a single cylinder at this Reynolds number is approximately 1.5, so not only has the lift become a constant value, the drag has also decreased in value by about 33%. Virtually no difference is observed in the drag coefficient, while the lift coefficient has decreased in value very slightly when the gap spacing is changed from 1.4 to 1.6 (results not shown).

A reason for this suppression of vortex shedding was offered by Strykowski & Sreenivasan (1990) who suggested that the "secondary (control) cylinder has the effect of altering the local stability of the flow by smearing and diffusing concentrated vorticity in the shear layers behind the body". They also noted that the control cylinder diverted a small amount of fluid into the wake of the primary cylinder. Both of these effects are seen in Figure 4 which is a plot of the vorticity field at 30° and a gap spacing of 1.4D. The control cylinder is quite clearly deflecting fluid into the wake of the primary cylinder. The far wake of the pair of cylinders consists of elongated and attached vortices with a much less pronounced waviness between the sides of opposing vorticity than is seen in a comparable flow without the control cylinder. The wake of the control cylinder is behaving in the same way as the wake of the primary cylinder in that there is no vortex formation and shedding occurring.

Figure 5 shows a flow visualization comparison between the cases of a control cylinder and no control cylinder at  $Re = 100$ . The control cylinder is at 30° and a gap spacing of 1.4. The near-wake behind the primary cylinder in the presence of a control cylinder is very steady compared to the case of no control cylinder. The unsteady wake seems to have been pushed farther downstream when the control cylinder is present. The steady near-wake is consistent with the calculated result of small, but steady, lift coefficient. The flow visualization technique is "laser-induced fluorescence", in which a laser sheet is used to illuminate a fluorescent dye that is washed from the front face of the cylinder as it is towed at constant velocity through water.

#### 4.2. $Re = 1000$

As stated earlier, the LES calculations for the turbulent wake cases will be 2-D because of the computational requirements to do the full 3-D two-cylinder case. We recognize the limitation of this approach, but we still feel that the results will be of practical use in examining the effects of the control cylinder. We do anticipate that the 2-D calculations will produce drag and lift coefficient values, which will be approximately 5–10% higher than would be obtained from a full 3-D simulation or from experimental results.

Figure 6 shows the drag and lift coefficient behavior for the primary cylinder for several cases. We note first that the results at  $Re = 1000$  are noticeably more sensitive to both angle of attack of the configuration and the gap spacing. There is very little difference in both drag and lift when the angle is changed from 25 to 28°. However, when the gap spacing is increased from 1.2 to 1.6 at an angle of 25°, a conventional vortex-shedding-type behavior is present. This is explained by the control cylinder having moved to the outer portion of the shear layer where its position seems to be much less influential on the vorticity field. At an angle of 30° and a gap spacing of 1.3, the drag has decreased very slightly compared to the 25°–1.2 case, and the lift has increased very slightly with a small oscillation now present. This indicates the return of a vortex-shedding-type behavior, although it clearly is not the conventional vortex-shedding behavior expected for a single cylinder. We also note in Figure 6 that the drag coefficients at a gap spacing of 1.2 have essentially a constant value of

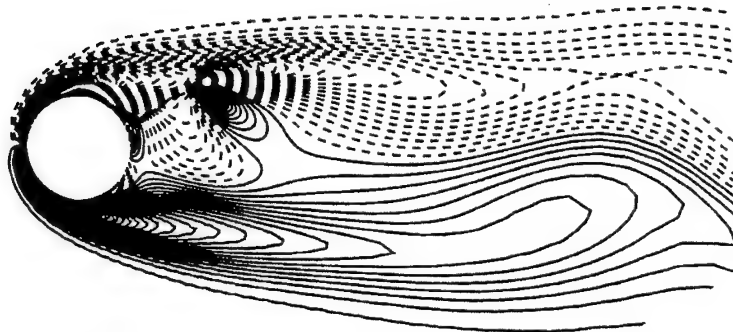


Figure 4. Axial vorticity field at  $Re = 100$ ,  $R/D = 1.4$ , and  $\alpha = 30^\circ$ .



Figure 5. Flow visualization comparison at  $Re = 100$ ,  $\alpha = 30^\circ$ , and  $R/D = 1.4$ .

about 0.8 while the single-cylinder experimental value at  $Re = 1000$  is about 1.0. The lift coefficient on the primary cylinder for the gap spacing of 1.2 has decreased to an almost constant value of 0.1. The lift coefficient has a nonzero mean value because the presence of

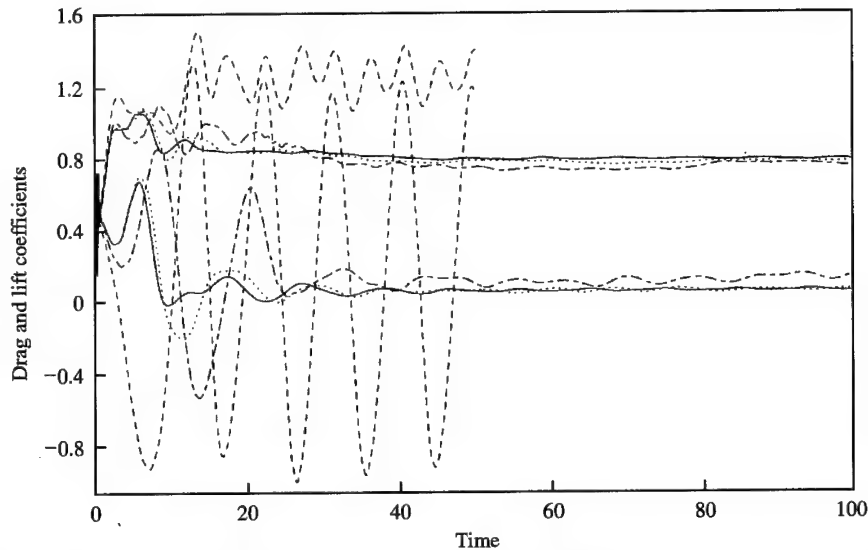


Figure 6. Drag and lift coefficients for the primary cylinder at  $Re = 1000$  for several conditions: —,  $\alpha = 25^\circ$ ;  $R/D = 1.2$ ; ---,  $\alpha = 25^\circ$ ;  $R/D = 1.6$ ; ···,  $\alpha = 28^\circ$ ;  $R/D = 1.2$ ; - · - ·,  $\alpha = 30^\circ$ ;  $R/D = 1.3$ .

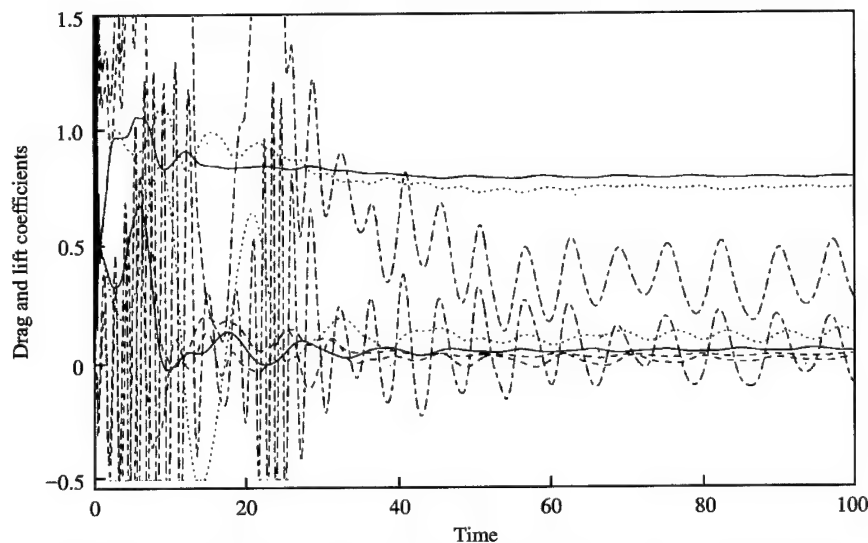


Figure 7. Drag and lift coefficients for both cylinders at  $Re = 1000$ ,  $R/D = 1.2$ , and  $\alpha = 25^\circ, 30^\circ$ . For  $\alpha = 25^\circ$ ; —, primary; ---, control. For  $\alpha = 30^\circ$ ; ···, primary; - · - ·, control.

the control cylinder, although suppressing conventional vortex shedding, is still creating an asymmetry in the flow field.

Figure 7 shows the drag and lift coefficients for both cylinders at a gap spacing of 1.2 and two different angles of attack: 25 and 30°. The drag coefficient traces for the primary cylinder are reasonably flat at both angles, with the 30° result, at a fairly steady value of 0.8, being very slightly lower than the 25° result. Also for the primary cylinder, the lift coefficient for the 25° angle, with a steady value of about 0.1, is slightly less than the average value at 30° which also has some small-amplitude oscillatory behavior. For the control cylinder at

25°, both the drag and lift coefficients have a similar behavior; they both oscillate between 0 and 0.1. At 30°, the control cylinder has a drag coefficient with a value of about  $0.35 \pm 0.2$  while its lift coefficient is about  $0.1 \pm 0.2$ . Based on the values of the lift and drag coefficients on the primary cylinder, these results indicate that the angle of attack position of 25° is only slightly better than the one at 30°.

The differences in drag and lift behavior noted in Figure 7 can be explained by noting the difference in wake vorticity behavior at the time the attached vortex on the primary cylinder extends farthest downstream. The vorticity plot for an angle of attack at 25° and a gap spacing of 1.2 is shown in the top part of Figure 8. First, we note that the primary cylinder wake is elongated over the wake for an isolated single cylinder. The slight oscillatory lift behavior shown in Figure 7 at an angle of attack of 25° is explained by noting, in Figure 8, the far wake of the configuration. There is a distinct Karman vortex street forming as the vortices move away from the vicinity of the cylinder pair. The near-wake at 25° shows the wake of the control cylinder is deflected down into the core of the primary cylinder wake. For the conditions shown in Figure 7, the control-cylinder wake acts as a jet-like stream that seems to steady the wake of the primary cylinder. The bottom part of Figure 8 shows the result of the same calculation for an angle of attack of 30°. The jet-like behavior seems less intense in this case. The drag and lift traces on the control cylinder at 30° show that there is time dependence in the wake behavior that is not present for the 25° case. Also, the length of the primary cylinder large vortex is greater in the 25° case which pushes whatever unsteadiness is present farther away from the near-wake. This greater wake length has the effect of steadying the near-wake and suppressing conventional vortex shedding.

Figure 9 shows a sequence of flow visualization pictures at  $Re = 1000$ , with and without the control cylinder, at the same relative time in the shedding cycle of the primary cylinder alone. The control cylinder is at 25° and a gap spacing of 1.2. In this case, the physical wake behind the primary cylinder is 3-D and turbulent which means that the flow structure from flow visualization is not nearly as vivid as at  $Re = 100$ . However, the difference in the two wake structures is still obvious. The case on the left, with no control cylinder, shows the roll-up of the vortex sheets emanating from the separation points and the alternate and

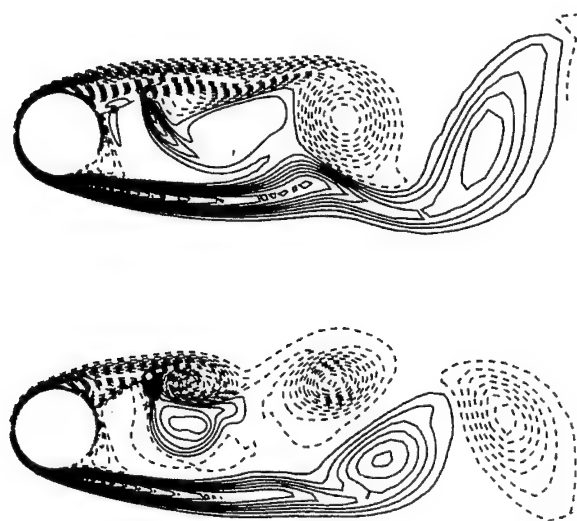


Figure 8. Axial vorticity field at  $Re = 1000$ ,  $R/D = 1.2$ , and  $\alpha = 25^\circ$  (top). Axial vorticity field at  $Re = 1000$ ,  $R/D = 1.2$ , and  $\alpha = 30^\circ$  (bottom).



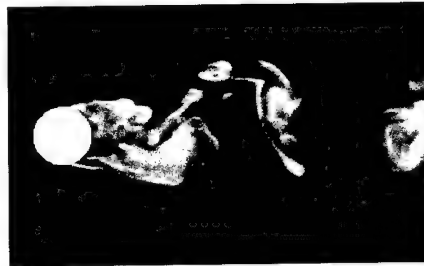
Cylinder

Control cylinder

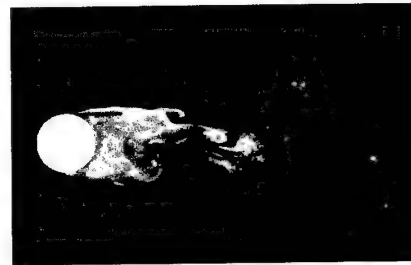
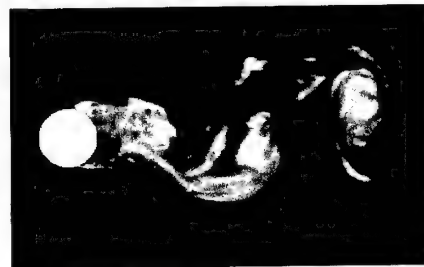
$t = 0.00$



$t = 0.33$



$t = 0.66$



$t = 1.00$



Figure 9. Flow visualization comparison at  $Re = 1000$ ,  $\alpha = 25^\circ$ , and  $R/D = 1.2$ .

periodic shedding of vortices, all of which is predictable and expected. However, the case on the right, with the control cylinder present, has a distinctly different structure. There is a shedding-like behavior, but it is less wavy and occurs slightly farther downstream. The near-wake seems to be less time-dependent. This, however, is a qualitative judgement since the turbulence in the wake distorts the mean flow structure that is present. Nevertheless, the near-wake with a control cylinder present is clearly less time-dependent which helps to explain the small, yet constant, value of the lift coefficient.

#### 4.3. $Re = 3000$

Again, this flow is at a Reynolds number at which the wake has an established turbulent behavior. However, we continue with our 2-D representation due to the computational requirements necessary to do the full 3-D two-cylinder case, fully recognizing the limitations of the 2-D results. Due to the 2-D restriction, flow (including turbulence) in the axial direction of the cylinder is suppressed.

Figure 10 shows the drag and lift coefficients on the primary cylinder at  $Re = 3000$ , a gap spacing of 1.2, and three angles of attack: 15, 20, and 25°. At 20°, the lift coefficient on the primary cylinder is relatively flat, especially when compared to its behavior at the other two angles, and has a value just slightly greater than zero. At 15 and 25°, the lift coefficient has fairly irregular oscillations about a mean of slightly greater than zero. These results show that the configuration at 20° has the best behavior regarding lift reduction; vortex shedding from the primary cylinder is virtually suppressed due to the presence of the control cylinder. The time-averaged drag coefficient, also seen in Figure 10, for each of the three angles is about the same. At 15 and 25°, the instantaneous drag coefficient is somewhat irregular with a mean value of about 0.8. At 20°, the instantaneous drag coefficient is fairly flat with an average value of about 0.8. The average value for a single, isolated cylinder is about 0.95 at  $Re = 3000$ . These results indicate that the presence of the control cylinder has a drag-reducing influence on the primary cylinder, with the best results obtained for 20°.

At  $Re = 3000$ , the same behavior as at  $Re = 1000$  is noted regarding the wake length (although not shown). At the two angular placements (15 and 20°) of the control cylinder for which calculations were done, the 20° placement had the longer, hence steadier, wake which caused the lift coefficient to lessen and be reasonably steady. This is exactly the same behavior noted in Figures 8 and 9 for the  $Re = 1000$  case. At 20°, the wake extends farther downstream than at 15°. The wake at 20° shows a region of recirculation region in the center of the near-wake. The base pressure is affected by this recirculation in such a way that the drag and lift on the primary cylinder are both decreased with the lift having decreased significantly and with virtually no oscillation. The region of recirculation in the 20° wake plays the same role as a flexible splitter plate. In the 15° wake, there is no evidence of an organized recirculation and, consequently, the lift and drag both have an unsteadiness, albeit small, in this case not found in the 20° case.

Figure 11 shows the drag and lift coefficients for both cylinders at a gap spacing of 1.2 and two different angles of attack, 20 and 25°. As stated earlier, the control cylinder, being in the wake of the primary cylinder, does not see a steady approach velocity. The control cylinder, on the lower side of the upper shear layer, sees an irregular approach flow. The drag coefficient trace for the primary cylinder is reasonably flat at 20° with a value of about 0.75, while at 25° it has a small amplitude oscillation with approximately the same mean value. The value of 0.75 is a reduction from the single cylinder value of about 1.0 at  $Re = 3000$ . The lift coefficient on the primary cylinder at 20° has a slight oscillation with a mean value of approximately 0.05 as compared to a single-cylinder value of  $\pm 0.35$  with a zero mean value. At 25°, the lift coefficient on the primary cylinder has an irregular behavior, with

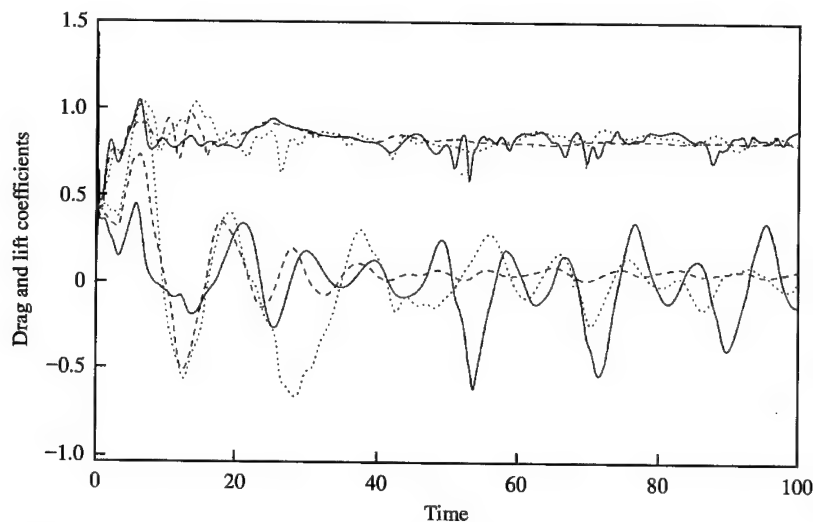


Figure 10. Drag and lift coefficients for the primary cylinder at  $Re = 3000$  and  $R/D = 1.2$ : —,  $\alpha = 15^\circ$ ; ---,  $\alpha = 20^\circ$ ; ···,  $\alpha = 25^\circ$ .

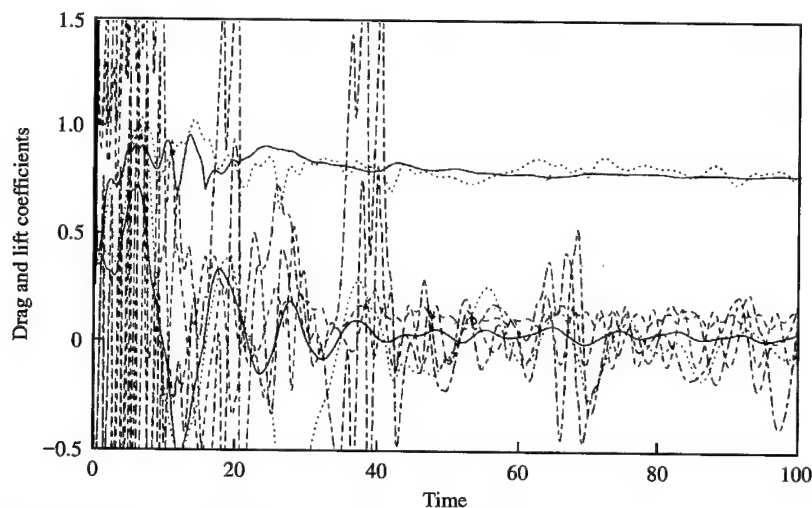


Figure 11. Drag and lift coefficients for both cylinders at  $Re = 3000$ ,  $R/D = 1.2$ , and  $\alpha = 20^\circ, 25^\circ$ . For  $\alpha = 20^\circ$ : —, primary; ---, control. For  $\alpha = 25^\circ$ : ···, primary; -.-, control.

evidence of an unidentified higher harmonic present in the signal, with a mean of approximately zero. The control cylinder at  $20^\circ$  has both drag and lift coefficients oscillating at small amplitude with approximately zero mean values while, at  $25^\circ$ , the lift and drag on the control cylinder each have a very irregular pattern with alternating regions of high and low amplitude behavior.

Figure 12 shows the contrast in the wake structures at  $Re = 3000$ , with and without the control cylinder in place, similar to Figure 9 for  $Re = 1000$ . For the  $Re = 3000$  case, the control cylinder is at  $20^\circ$  and the gap spacing is 1.2. Again, the physical wake is 3-D and turbulent, making the flow visualization much less vivid than for a laminar flow case. However, the difference in the two wake structures is quite distinct. The pictures on the left,

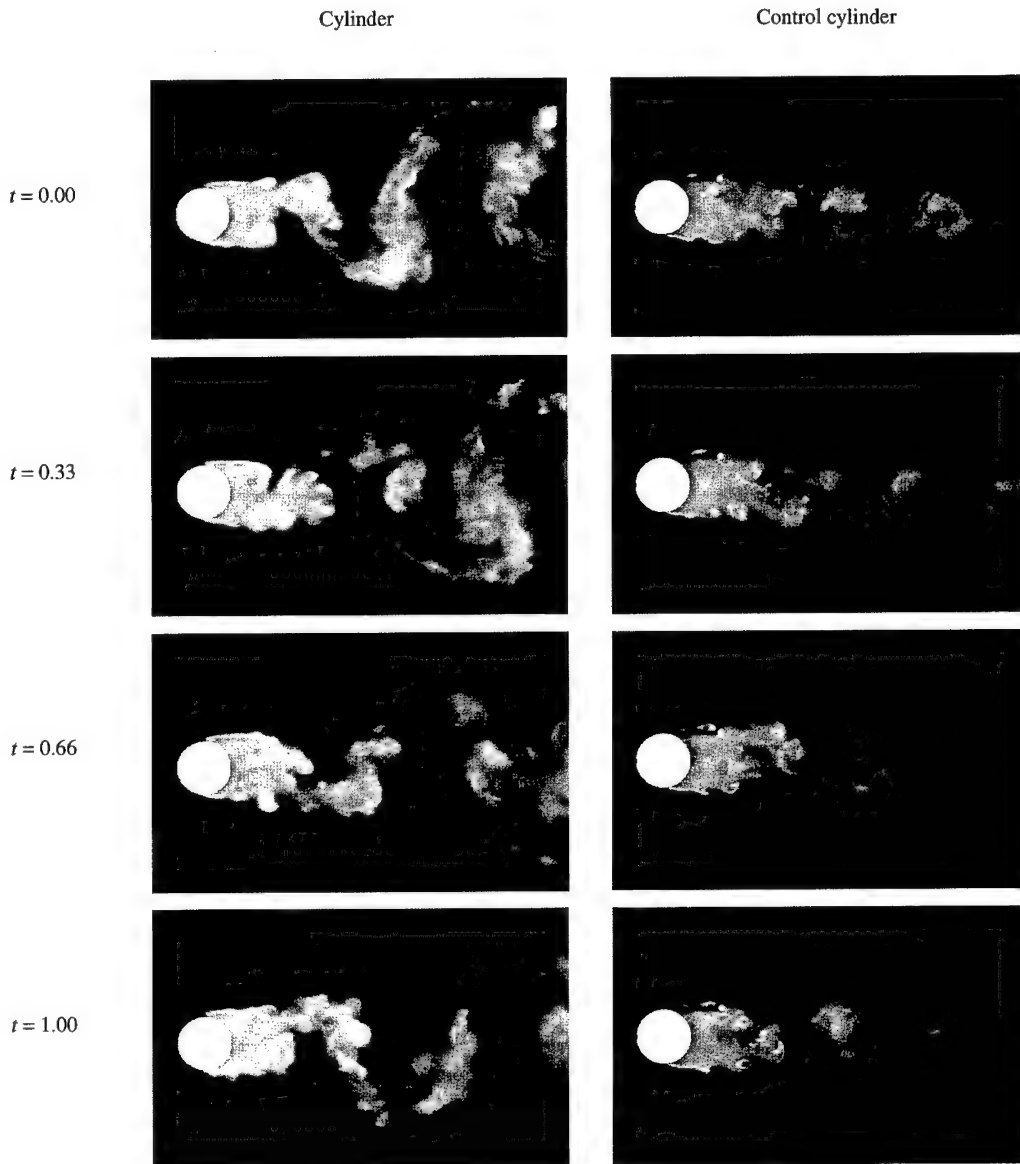


Figure 12. Flow visualization comparison at  $Re = 3000$ ,  $\alpha = 20^\circ$ , and  $R/D = 1.2$ .

without the control cylinder in place, show the classical alternate and periodic shedding of vortices, with the wake widening as the vortices move downstream. The pictures on the right, with the control cylinder in place, show a much narrower wake and a less pronounced vortex structure in the wake. The near-wake again seems to be less time-dependent, which is a result consistent with the calculated results.

## 5. CONCLUSIONS

We have shown that the presence of a properly placed small control cylinder in the wake of a primary cylinder can significantly reduce the possibility of vortex-induced vibration by

essentially eliminating conventional vortex shedding from the primary cylinder for  $Re \leq 3000$ . The suppression of conventional vortex shedding was found to be sensitive to both the angle of attack of the approach flow and the gap distance separating the centers of the two cylinders. The minimum values of both lift and drag on the primary cylinder were found to depend on both angle of attack and the gap distance. A physical application of this concept would have to be a flow which kept the same orientation to the primary and control cylinder, such as a flow past a pipeline spanning a river.

### ACKNOWLEDGEMENTS

The authors are grateful to the University of Houston for the computer time used in these calculations. The second author is grateful to the State of Texas for his graduate support from the Advanced Technology Program on Grant no. 003652-019. The third author acknowledges EPSRC for his graduate support.

### REFERENCES

- IGARISHI, T. & TSUTSUI, T. 1991 Flow control around a circular cylinder by a new method (Third Report: Properties of the reattachment jet). *Proceedings JSME* **57**, 8–13 (in Japanese).
- LU, X., DALTON, C. & ZHANG, J. 1997 Application of Large Eddy Simulation to flow past a circular cylinder. *ASME Journal of Offshore Mechanics and Arctic Engineering* **119**, 219–225.
- SAKAMOTO, H., TAN, K., & HANUI, H. 1991 An optimum suppression of fluid forces by controlling a shear layer separated from a square prism. *ASME Journal of Fluids Engineering* **113**, 183–189.
- SAKAMOTO, H. & HANUI, H. 1994 Optimum suppression of fluid forces acting on a circular cylinder. *ASME Journal of Fluids Engineering* **116**, 221–227.
- SMAGORINSKY, J. 1963 General circulation experiments with the primitive equations. I. Basic experiments. *Monthly Weather Review* **91**, 99–164.
- STRYKOWSKI, P. J. & SREENIVASAN, K. R. 1990 On the formation and suppression of vortex shedding at low Reynolds numbers. *Journal of Fluid Mechanics* **218**, 71–107.
- ZDRAVKOVICH, M. M. 1997 *Flow Around Circular Cylinders. Volume I: Fundamentals*. Oxford: Oxford University Press.



## ENERGY HARVESTING EEL

J. J. ALLEN AND A. J. SMITS

*Department of Mechanical and Aerospace Engineering, Princeton University  
Princeton, NJ 08543, U.S.A*

(Received 1 September 2000, and in final form 16 November 2000)

The current study examines the feasibility of placing a piezoelectric membrane or “eel” in the wake of a bluff body and using the von Kármán vortex street forming behind the bluff body to induce oscillations in the membrane. The oscillations result in a capacitive buildup in the membrane that provides a voltage source that can be used, for example, to trickle-charge a battery in a remote location. The aim of the hydrodynamic testing is to maximize the strain energy and mechanical power by coupling the unsteady flow field with the vibration of the membrane. The requirement of optimal coupling is best defined as a resonance condition where the membrane has a negligible damping effect on the original von Kármán vortex street.

© 2001 Academic Press

### 1. INTRODUCTION

LITERATURE RELATED TO THE CHARACTERISTICS of bluff body wakes is extensive and there is also considerable literature related to the problem of flutter and the response of flexible structures placed in a cross-flow. The response of a flexible membrane may be considered to demonstrate aspects of these phenomena. Flows behind bluff bodies in the Reynolds number range  $10^3$ – $10^5$  are characterized by the formation of a vortex street of reasonably constant Strouhal number with respect to Reynolds number. The vortex streets in this range have a strongly three-dimensional character. Huerre & Monkewitz (1990) provide a description and review the formation of the von Kármán street in terms of being the result of a local absolute instability growing into a global linear instability, and arguing against the mechanism if the vortex street formation does not involve details of flow separation. The presence of a rigid splitter plate behind a bluff body can have dramatic effects in terms of reducing and suppressing vortex street formation and therefore the stability characteristics of the flow, e.g., Roshko (1954), Gerrard (1966). These studies highlighted the way the presence of a splitter plate of increasing length can delay and eventually prevent the formation of oscillations in the wake. The effect of splitter plates is relevant in the current study as in some flow configurations the membrane is stiff enough to have the effect of a rigid splitter plate. If the membrane has small inertia and is flexible enough to be able to respond rapidly to the unsteady pressure field set up by the vortex shedding, one may expect that the membrane may oscillate with a wavelength and frequency similar to that observed in the unobstructed wake. This results in a coupled fluid/structure problem.

The study of oscillating structures excited by flow fields is often described in terms of free and forced vibration. If one considers a simplified description of the displacement of the structure in the spanwise direction,  $y(x, t)$ , as a mechanical system of mass  $m$  subject to an external force field, then

$$m\ddot{y}(t, x) + H(\dot{y}, y, x, t) = f_1 + f_2. \quad (1)$$

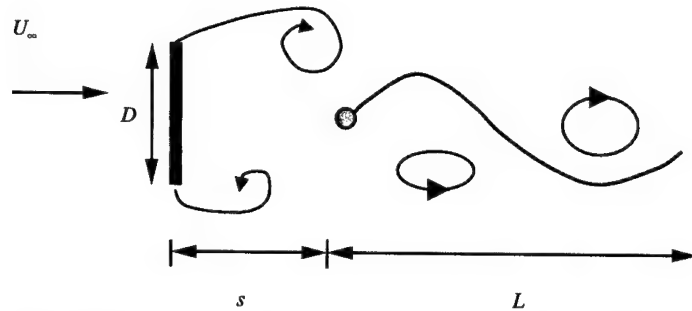


Figure 1. Geometry of oscillating membrane behind a flat plate.

The function  $H$  represents internal restoring forces related to the body stiffness and damping properties. The forcing function on the right-hand side, which is the result of the external flow field, is often expressed as the sum of two parts. The first term  $f_1$  is the free vibration forcing field and represents the self-induced effects of the unsteady wake, generated by vortex shedding. This type of excitation has been classified as movement-induced excitation (MIE); see, e.g., Naudascher & Rockwell (1994), Khalak & Williamson (1999). This type of forcing is the mechanism responsible for wing flutter.

The second term,  $f_2$ , represents the effect of an external forcing field that has its source remote from the body being excited. This type of forcing is classified as extraneously induced excitation (EIE) and is a feature of "gusting". Paidoussis (1966a) developed relationships for the stability of a long flexible slender cylinder, orientated parallel with the free stream. He developed an approximation for the unsteady pressure field acting on the cylinder by using small-amplitude assumptions and an approximation for the added mass of the cylinder when oscillating in the free stream. Using this expression for the pressure differential based on the shape and velocity of the cylinder, the conditions of stability for the successive modal shapes based on cylinder properties and flow conditions were calculated. The flow-induced oscillations were self-excited and the experiments of Paidoussis (1966b) showed oscillation dominated by single modes. In contrast, we are interested in the excitation of a membrane produced by the vortex shedding of the bluff body.

## 2. EXPERIMENTS

A number of different membranes were tested in a water channel running at speeds of 0.05–0.8 m/s. Two different bluff body widths were used, 5.08 and 3.81 cm, resulting in a Reynolds number range,  $Re_D = U_\infty D/\nu$ , of  $5 \times 10^3$ – $4 \times 10^4$ . The aspect ratios of the bluff bodies were 6 and 10, respectively.

Figure 1 shows the important experimental parameters involved in describing the behavior of the undulating eel,  $D$  is the width of the bluff body,  $s$  is the distance downstream of the bluff body where the head of the eel is placed, and  $U_\infty$  is the free-stream velocity. The physical properties of the eel are described in terms of its stiffness  $E$ , length  $L$ , thickness  $h$ , width  $W$  and mass per unit length  $\rho_{eel}$ . Figure 1 also shows an interpretation of the type of vortical structures forming over the membrane.

Experiments were conducted in a recirculating water channel 18 in wide and 5 in deep (1 in = 25.4 mm). The ratio of gap width  $S$  to bluff body size  $D$  was equal to unity in the current experiments and not varied. Flow visualization using fluorescent dye and particle image velocimetry (PIV) experiments both used a laser sheet generated from a continuous 7 W argon-ion laser to image a cross-section through a horizontal plane of the flow.

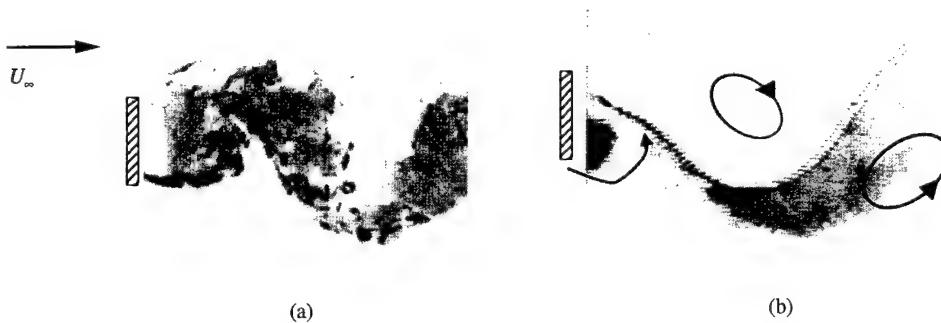


Figure 2. (a) Formation of von Kármán vortex street without membrane and (b) the formation of a coherent wake behind the bluff body with a flexible membrane present.

Figure 2(a, b) shows dye visualization images behind a 5.08 cm bluff body with and without an eel present at  $Re_D = 10\,000$ . At this Reynolds number, the vortex shedding behind the plate, although coherent, is strongly turbulent and three dimensional. The membrane in this case is executing large forced oscillations, and the conjectured vortical structures are highlighted in Figure 2(b). The spacing of vortical structures in both cases is of the order  $1.9D$ . Although the flow visualizations in Figure 2 show a somewhat similar spacing of structures, the overall topologies of the two flows must be different, as the membrane acts as a streamline to prevent communication between the separating shear layers.

The PIV system consists of an externally triggered Cohu 6600–3000 series full frame transfer camera,  $659 \times 496$  pixels, with 10-bit resolution. The acquisition timing sequence is as follows. The first frame is triggered for a short electronic exposure, of the order of 1 ms in the current experiments. The transfer time for the first frame is 17 ms. While the data for the first image are being transferred, the camera is triggered for a second exposure. The exposure period for the second image is set electronically for 17 ms, the maximum time exposure for a single frame. However, rather than expose the CCD array to the laser light for this period, the light source is interrupted mechanically in order to have an equivalent exposure time in the second frame as in the first. This system allows an effective time delay between images of the order 0.5 ms if required and an image pair acquisition rate up to 30 Hz. It is critical for the electronic exposure period in the second image to be 17 ms, as this prevents corruption of the data transfer of the first image, i.e., all the data from the first image have been transferred before the second image data transfer begins.

To generate information on the unsteady shape of the eel, a series of images were grabbed to PC RAM at a rate of 60 Hz. Figure 3(a) shows superimposed images of the oscillating eel over a full cycle, which is used to define a maximum amplitude. The instantaneous membrane images were interrogated with edge detection software to extract information about the instantaneous position of the membrane. Figure 3(b) shows a sequence of membrane shapes after edge processing, superimposed on the one plot.

In the Reynolds number range 5000–40 000 the Strouhal number,  $St$ , behind the 1.5 in bluff body was equal to  $0.155 \pm 0.002$ , and for the 2 in bluff body it was  $0.160 \pm 0.002$ . This slight variation is a function of increased tunnel blockage. The Strouhal number was essentially invariant over the range of Reynolds numbers being investigated. Four membranes were tested. The first two were 18 in and 24 in long, made from polyvinylidene fluoride (PVDF), which is a piezoelectric material that when strained generates a voltage potential in capacitor-like polymers. A third membrane was made primarily from polyurethane (PU), with two thin outer layers of PVDF attached to the polyurethane. The





Figure 3. (a) Superposition of membrane shapes and (b) a sequence of individual membrane shapes.

TABLE 1  
Properties of membranes tested

	Thickness, $t$ (mm)	Length, $L$ (m)	Mass, $m$ (g)	$EI/\rho_{eel}$ ( $\text{m}^4 \text{s}^{-2}$ )	$L/D$ (—)
18 in PVDF eel	0.7	0.457	38	0.0028	12, 18
24 in PVDF eel	0.7	0.076	53	0.0028	12
18 in PU eel	0.6	0.457	34	0.00062	12
18 in Plastic eel	0.1	0.457	7	0.0021	12

fourth membrane was made from plastic shim stock, selected so as to have similar natural frequencies to the 18 in PVDF membrane but with a much smaller mass per unit length. The width of all membranes,  $W$ , was 0.0762 m.

The properties of the eels tested are listed in Table 1. Here  $I$  is the 2nd moment of area and  $\rho_{eel}$  is the mass per unit length of the eel. The term  $EI/\rho_{eel}$  represents the effective stiffness of the eel in response to bending, and its value was determined directly from a deflection test. This term is somewhat similar to the spring-mass ratio which is used to describe the undamped natural frequency of a spring-mass system.

The internal damping of the shim-stock eel is a factor of approximately two smaller than the PVDF and PU, as estimated from a free vibration experiment in air. Values of length of the eel to the bluff body size,  $L/D$ , are also shown. To assess the behavior of this range of eels, measurements were made of the frequency of oscillation and amplitude, as defined in Figure 3(a). Figure 4(a) shows the ratio of the response frequency  $f_{eel}$  to the natural frequency  $f_{nat}$  with increasing  $Re_D$ , and Figure 4(b) shows the ratio of eel amplitude to bluff body with increasing  $Re_D$  for the PU membrane.

At Reynolds number of order 1000, the amplitude of oscillation of the membrane is small and the ratio of frequencies is about 0.5. The oscillation in this case is infrequent. In this mode, the behavior of the eel can be interpreted as being similar to that of a rigid splitter plate. At Reynolds numbers less than 500, the eels appear to be causing the separated shear layers from the bluff body to reattach on the eel surface and form an essentially closed recirculation bubble on the eel, as shown in the dye visualization image in Figure 5.

At a Reynolds number of order 10000, the membrane begins to oscillate at a fairly constant frequency. An image of the membrane flapping in this mode is shown in Figure 6(a). Although the membrane appears to be oscillating with an apparently traveling waveform, it is not well coupled to the flow, as indicated by the fairly low value of  $f_{eel}/f_{nat} \approx 0.6-0.8$ , indicating that the membrane exerts a damping effect on the flow. As the Reynolds number is further increased, the eels effective length gradually shortens. This

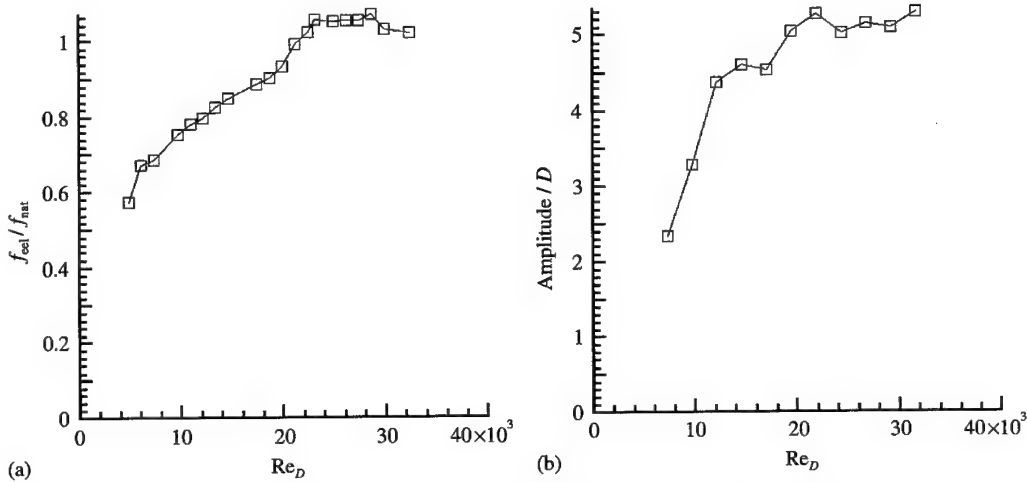


Figure 4. (a) Plot of frequency response and (b) amplitude of the PU membrane versus Reynolds number.

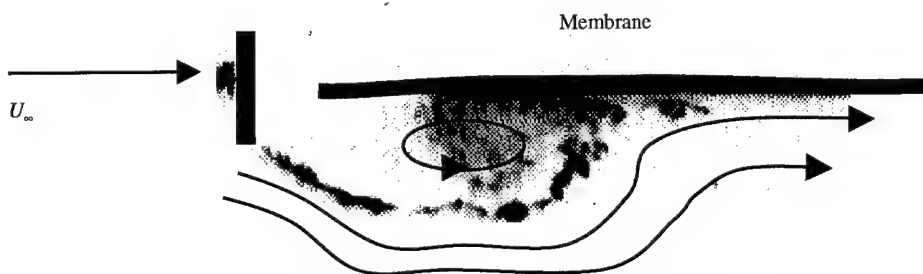


Figure 5. Flow visualization of PU membrane at  $Re_D = 1000$ .

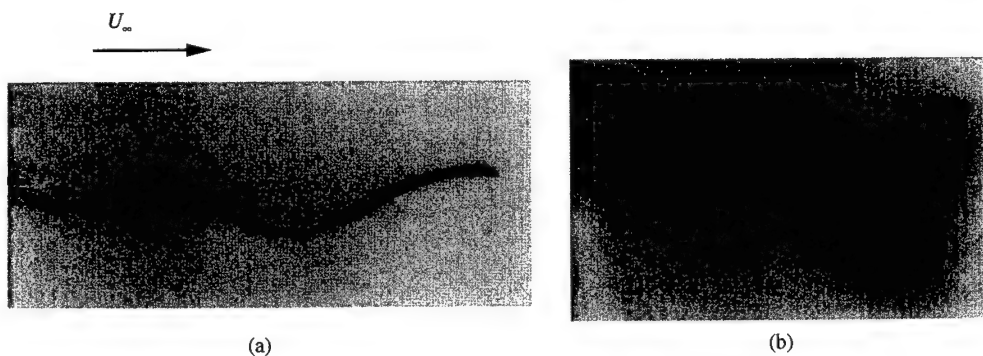


Figure 6. Membrane oscillation: (a)  $Re_D = 10000$ ; (b)  $Re_D = 20000$ .

results in a decrease in wavelength and an increase in amplitude of oscillation. As this occurs, there is also a trend for the frequency ratio to approach unity, indicating that the eel is well coupled to the flow. The wavelength of the membrane shortens to a point where it appears that it closely resembles the wavelength of the coherent structures in the wake of

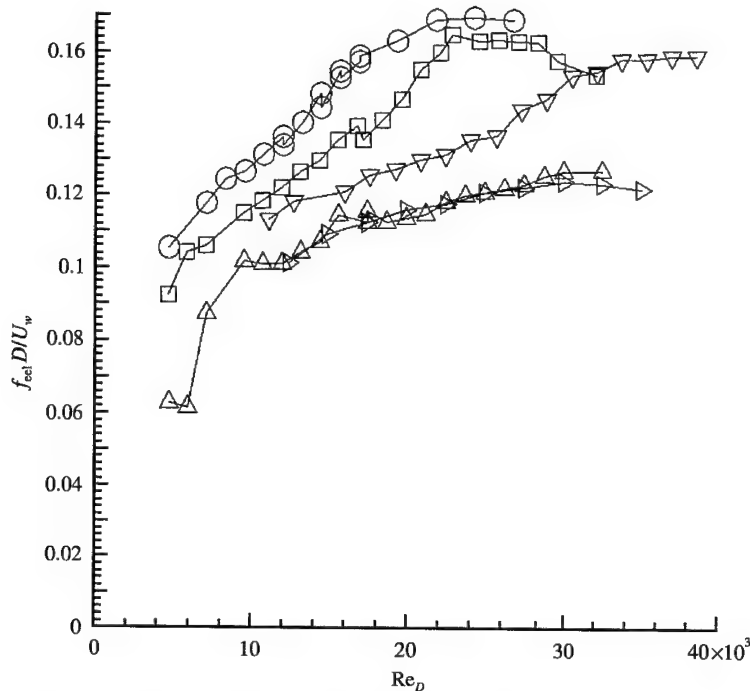


Figure 7. Scaling of Strouhal number versus Reynolds number for a range of membranes:  $\square$ ,  $\rho U$ ;  $\triangle$ , 18 in PVDF,  $D = 1.5$  in;  $\nabla$ , 24 in PVDF,  $D = 2.0$  in;  $\triangleright$ , 24 in PVDF,  $D = 1.5$  in;  $\circ$ , 101  $\mu$ m shim stock.

a plate without a membrane being present, as shown in Figure 6(b). The amplitude of oscillation of the membrane in Figure 6(b) appears to be similar or larger than the width of the wake when the membrane is not present. This would imply an increased momentum deficit caused by the motion of the membrane.

As the Reynolds number increases beyond 20 000 for the membrane shown in Figure 6 we see relatively constant amplitude of oscillation and a linear increase of frequency of oscillation with flow velocity. The concatenation of the wavelength of the eel translates directly into an increase of amplitude, which seems to indicate the length of the eel is essentially constant. The amplitude of response and the frequency ratio  $f_{eel}/f_{nat}$  appear to be directly related, as the amplitude plots versus  $Re_D$  show similar trends. Note that when the eel reaches the optimal coupling condition and its effective wavelength is fixed, and if it is not being stretched, the amplitude will remain constant. This apparent length preserving aspect of eel behavior also suggests that tension is not an important factor when considering the dynamics of the eel. It also implies that the phase speed of structures convecting along the eel surface is approximately constant for a fixed flow velocity, regardless of the ability of the eel to couple to the flow. The phase speed is defined as  $U_{phase} = \lambda f_{eel}$ , where  $\lambda$  is the membrane wavelength. The fact that the eel amplitude appears to reach a maximum may indicate the effect of the free stream or internal damping. The membrane appears to be able to oscillate with a maximum amplitude that is similar to the natural wake width, but does not exceed it, despite being forced close to its natural frequency.

Figure 7 shows the response of the range of eels tested, plotted with respect to their nondimensional frequency,  $f_{eel}D/U_\infty$  and bluff body Reynolds number,  $Re_D$ .

The various data sets show that, as the Reynolds number increases, the trend of the membrane behavior is towards optimal flow coupling, defined by  $f_{eel}D/U_\infty \approx 0.16$ , which is

equivalent to  $f_{\text{eel}}/f_{\text{nat}} \approx 1$ . This trend can be seen in all the data sets as the flow speed increases, suggesting that there may be a similarity scaling to describe the membrane behavior. However, the different membranes approach  $f_{\text{eel}}/f_{\text{nat}} \approx 1$  at different rates when scaled with respect to Reynolds number. This can be explained by the fact that the Reynolds number does not take into account any material properties of the eel, which obviously have a significant effect on the membrane response. Important aspects of the above data sets are that the frequency response of the 24 in and 18 in eel behind the 1.5 in plate are identical, suggesting that the membrane response does not depend critically on the length of the membrane, at least for the relatively large  $L/D$  ratios we are considering here. The 24 in eel displays a marked improvement in response behind the 2 in bluff body, compared to the 18 in eel placed behind the 1.5 in bluff body, indicating a significant response sensitivity to the bluff body size. The shim-stock eel, which has almost the same natural frequencies as the 18 in PVDF eel displays far superior coupling to the flow, suggesting that an inertial or internal damping factor is important to describe the membrane behavior. The data sets show a leveling out of the nondimensional frequency, indicating that the oscillation appears to have an upper bound of frequency as determined by the bluff body size and flow speed. This would also seem to indicate that the observed phenomenon is not a self-excited, but is critically dependent on the presence of the bluff body.

### 3. NONDIMENSIONAL DESCRIPTION OF MEMBRANE BEHAVIOR

A simplified description of the motion of the membrane, defined by  $y(x, t)$ , is given by the Euler–Bernoulli beam equation where the forcing function  $f(x, t)$  is the effect of the fluid on the membrane:

$$\frac{d^2 y}{dt^2} + \frac{\zeta}{\rho_{\text{eel}}} \frac{dy}{dt} + \frac{EI}{\rho_{\text{eel}}} \frac{d^4 y}{dx^4} - T \frac{d^2 y}{dx^2} = f(x, t). \quad (2)$$

The solution for the displacement of the membrane can be represented as  $y(x, t) = \sum_{n=1}^{\infty} \Phi_n(x) A_n(t)$ , where  $\Phi_n(x)$  represent an orthogonal set of eigenfunctions. These eigenmodes were used by Paidoussis (1966a) to describe the dynamics of a flexible cylinder, pinned at both ends, in a stream. For the case of the cylinder pinned at one end and free at the other Paidoussis (1966a) used a power-series expansion for the shape of the cylinder. Wu (1961), in contrast, used traveling waves to describe the motion of a swimming plate through water. The choice of the orthogonal basis functions in the current study is based on the approximation of the membrane with an Euler–Bernoulli beam and provides a compact, though not necessarily unique way to describe the membrane motion. If we neglect the effects of tension and damping, this equation also yields information on the natural frequencies of these modes, which may be expressed as  $\omega_n = (\beta_n^2/l^2) \sqrt{EI/\rho_{\text{eel}}}$ , where  $\beta_n$  represent the eigenvalues corresponding to  $\Phi_n(x)$ , which depend on the boundary conditions of the membrane. If single-mode excitation were to be possible, it would imply that the membrane is oscillating as a standing wave. This would mean a significant departure of the flow field topology from the natural von Kármán street, which seems unlikely as the mass ratio is small,  $\rho_{\text{eel}}/\rho \approx 1.3$ , and hence, we expect a broadband response of the membrane. If the membrane is to follow closely the forcing of the von Kármán street, as experiments show, then the forcing is essentially a traveling pressure wave. Since the membrane is fixed at a pivot point, the only way its response can resemble a traveling wave is if there are significant contributions to the eel shape from more than one mode.

Data sets for the shape of the eel have been projected onto the eigenmodes to evaluate the contribution of each mode to the shape of the eel. Figure 8(a) shows the relative modal contributions  $A_n(t)$ , for modes 0–5 for the PU eel operating at 0.36 m/s behind a 1.5 in bluff

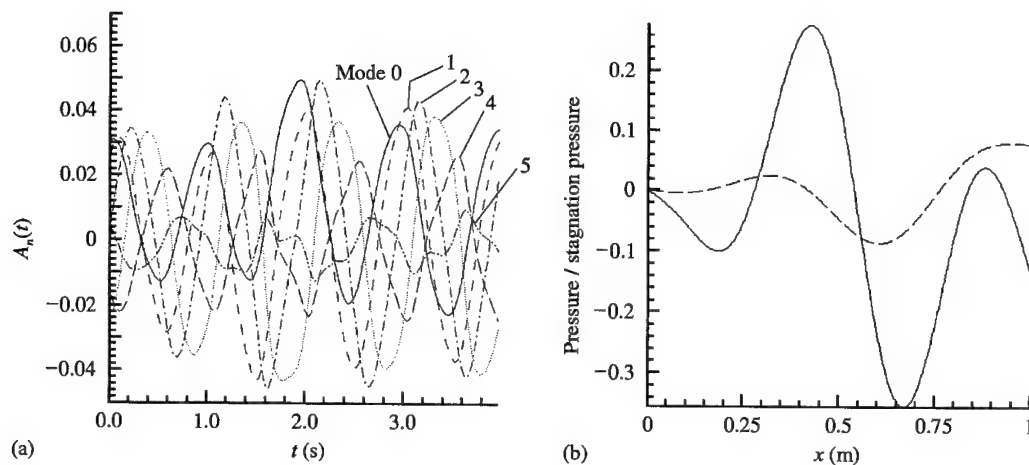


Figure 8. (a) Modal contributions to shape of membrane —, mode 0; --, mode 1; —·—, mode 2; ·····, mode 3; — — —, mode 4; - - - - -, mode 5 and (b) pressure differential acting across membrane. In (b): —, pressure/stagnation pressure; --, eel.

body. The modal contributions start to decay significantly past mode 4 and hence we have a fairly compact data set to describe the eel motion. The functions  $A_n(t)$  oscillate at the same frequency and display significant phase differences between successive modes. The fact that there are multiple modes present rather than a dominant single mode, coupled with the earlier observation that the peak frequency ratio  $f_{eel}/f_{nat} \approx 1$  seems to be linked directly to the size of the bluff body, would seem to indicate that the motion of the membrane is not self-excited. Substituting the experimental data for  $y(x, t)$  into the linearized equation of motion [equation (2)] and neglecting the effects of damping and tension, yields an expression for the pressure field acting on the eel. Figure 8(b) shows a plot of the pressure differential, normalized with respect to the stagnation pressure,  $\frac{1}{2} U_\infty^2 \rho$ , acting across the eel. The pressure differential is a small fraction of the stagnation pressure, which seems to indicate that the reduced differential equation description of the system is reasonable. An accurate test of this conclusion would be from a PIV measurement of the velocity differential across the membrane. The pressure differential at the tail of the eel indicates that a velocity difference exists at this point and hence the possibility exists of measuring vortex shedding into the wake. Figure 8(b) indicates that the wavelength of the forcing function is similar in shape to the eel and hence similar in shape to the pressure field set up by a traveling vortex street. This suggests that the forcing is related in frequency to the size of the bluff body, and hence the Strouhal number. An example of the reconstructed shape of the membrane using the first 5 modes is also shown in Figure 8(b).

If the form of the forcing function is modeled as a traveling wave, it may be approximated by  $P(x) \sin(2\pi/\lambda(x - ct))$  where  $\lambda$  is the wavelength of the disturbance given by the von Kármán vortex street; so that  $c \approx \lambda U_\infty St/D$ . The magnitude of the forcing will be a fraction of the stagnation pressure. From experimental data this function is of the order of  $P(x) \approx 0.1 \rho D U_\infty^2 W / \rho_{eel}$ . Projection of the eigenmodes onto this forcing function results in a time-varying function  $\xi_n(t) = \int_0^L \Phi_n P(x) \sin(2\pi/\lambda(x - ct)) dx$ . Results obtained by integrating for the first four modes are shown in Figure 9.

The integration of the traveling wave forcing function results in oscillating functions that vary successively in phase. This is a possible explanation for the phase shifts in the response functions shown in Figure 8(a). Modes 2 and 3 have the largest amplitude as their wavelengths are closest to that of the selected traveling wave. Using the description of the

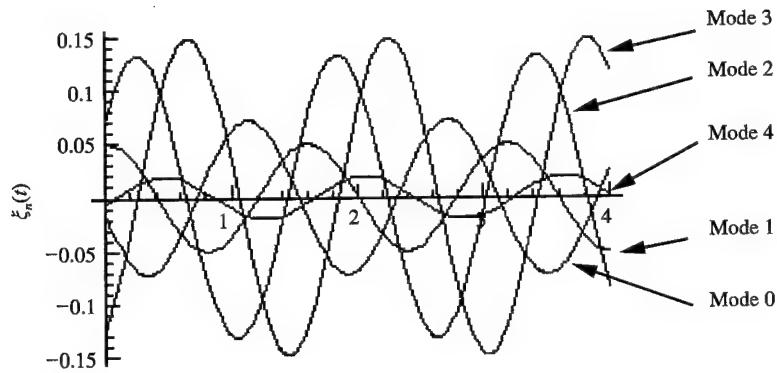


Figure 9. Integration of eigenmodes  $\Phi_n(x)$  with  $P(x) \sin(2\pi/\lambda(x - ct))$ .

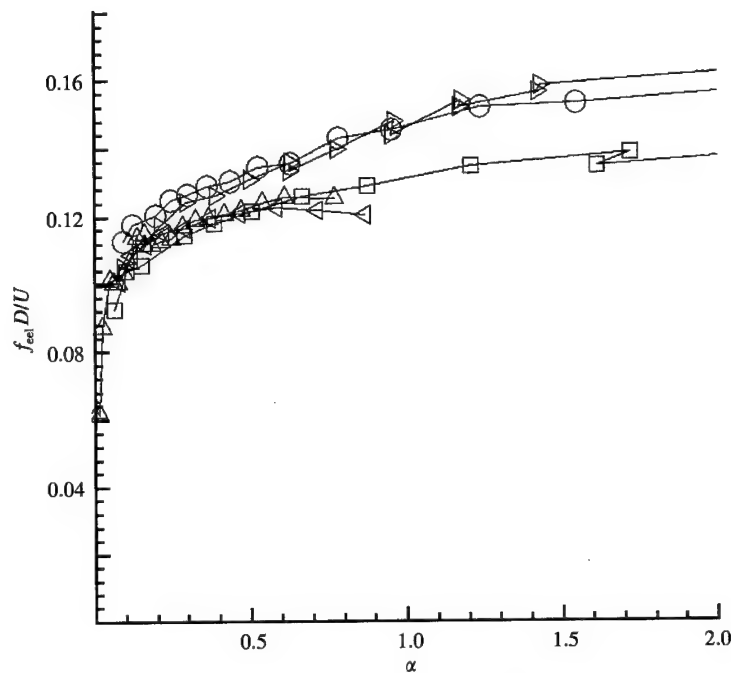


Figure 10. Reduced frequency  $f_{eel} D/U_\infty$  versus  $\alpha$ :  $\Delta$ , 18 in PVDF;  $\triangleright$ , 101  $\mu$  in shim stock;  $\triangleleft$ , 24 in PVDF eel, 1.5 in bluff body;  $\circ$ , 24 in PVDF, 2 in bluff body;  $\square$ , map 5.

response of the membrane as  $y(x, t) = \sum_{n=1}^{\infty} \Phi_n(x) A_n(t)$ , the result of projecting the eigenmodes onto a reduced description of the system gives a system of ordinary differential equations for the time-varying functions  $A_n(t)$  as

$$\ddot{A}_n(t) + \omega_n^2 A_n(t) = 0.2 U_\infty^2 \rho W / \rho_{eel} \xi_n(t). \quad (3)$$

Solution of these equations for  $A_n(t)$  gives similar results to the experimental value of the modal functions. This simplified analysis suggests that the amplitudes of response of the respective modes,  $\bar{A}_n$ , are of order  $0.2 \xi_n U_\infty^2 \rho W / (\rho_{eel} (-\omega_{eel}^2 + \omega_n^2))$ , where  $\omega_{eel}$  is the oscillating frequency of the membrane and fluid, and  $\xi_n$  is the amplitude of the modal function  $\xi_n(t)$ . This expression for the modal amplitude term incorporates the effect of the

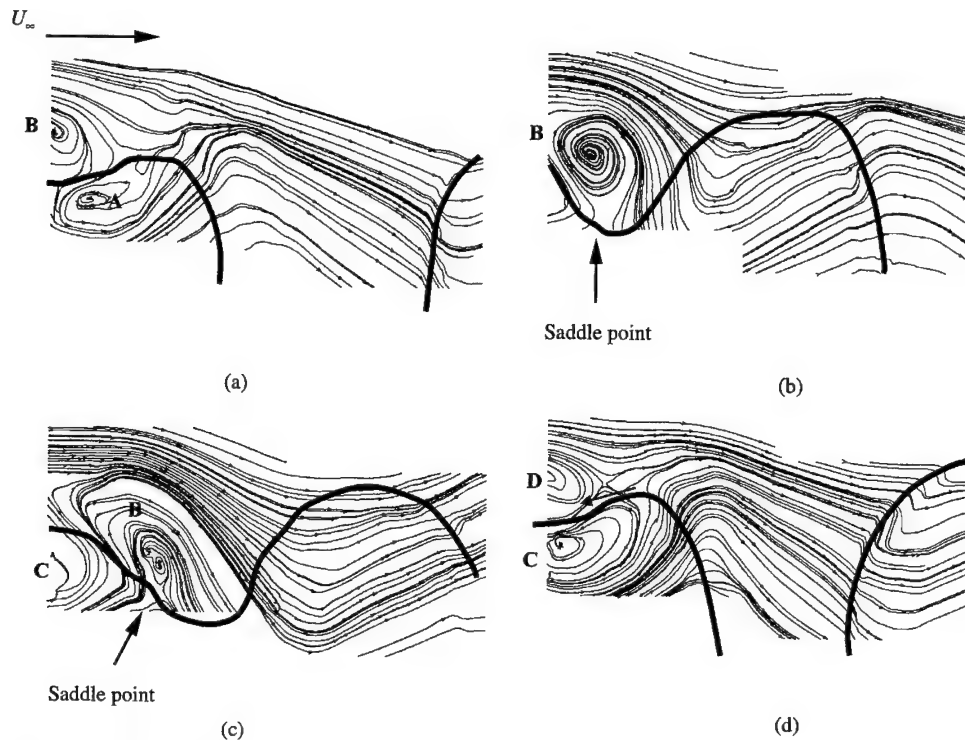


Figure 11. Streamline patterns showing vortex shedding cycle in stationary frame of reference.

magnitude of the fluid forcing,  $\rho U_\infty^2$ , the forcing frequency  $\omega_{eel}$ , the mass of the eel,  $\rho_{eel}$ , the stiffness of the eel via  $\omega_n$  and the wavelength of forcing,  $\xi_n$ . We expect that for the eel to be well coupled to the flow, this amplitude should be of the order of the bluff body width; hence, we suggest that when  $\alpha = \bar{A}_n/D \approx 1$  the eel should be well coupled to the flow. Figure 10 shows a plot of the response of the nondimensional membrane frequency  $f_{eel}D/U_\infty$  as a function of  $\alpha$ . The modal function,  $\xi_n$ , was selected as the function that has the closest wavelength to the structures in the flow. If  $\alpha \ll 1$  we expect the membrane to be acting essentially as a long splitter plate and hence poor coupling would be expected, as indicated by a low Strouhal number for  $\alpha \approx 0.1$ . The plot shows that for  $\alpha > 1.5$  the eel appears to be well coupled, as would be expected if the amplitude of oscillation is larger than the bluff body width. The effect of internal damping and the free stream would be to limit the amplitude of response; these effects are not accounted for in this simplified model of response. The definition of  $\alpha$  as the system description parameter follows a similar derivation to the “effective stiffness” parameter defined by Leonard & Roshko (2001).

#### 4. PIV RESULTS

Figure 11 shows the streamline pattern developing around the membrane during one oscillation cycle. The region shown represents about 3/4 of the membrane wavelength. Figure 11(a) shows the presence of two coherent vortical structures, vortex A and B, adjacent to the membrane. Vortex A is starting to convect along the underside of the membrane, while vortex B is beginning to impinge on the top surface of the membrane. Both structures show that reversed flow exists on the surface of the membrane close to the pivot point. Hence, secondary vorticity, of opposite sign to the impinging structures, is

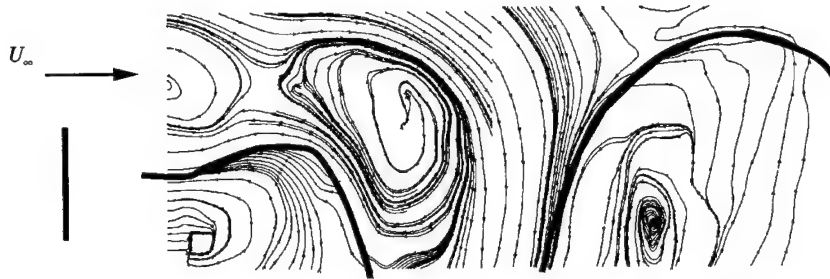


Figure 12. Streamline pattern when moving with bias velocity of  $0.65U_\infty$ .

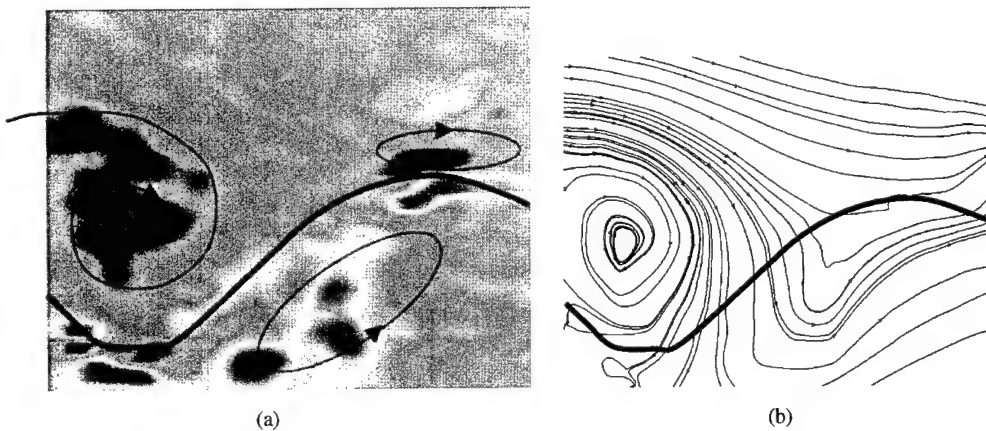


Figure 13. (a) Vorticity field and (b) streamline pattern at the same phase point in shedding cycle.

being generated on the membrane surface under these structures. Figure 11(b) shows that the membrane appears to be deforming significantly in response to the impingement of vortex B. The presence of vortex A is no longer evident, although there is significant deformation of the streamline pattern in the region into which it was convecting. In Figure 11(c), vortex B appears to be significantly deforming in response to the membrane, which is now moving upwards as a result of pressure from a newly impinging vortex, vortex C. An interesting feature of Figure 11(c) is the appearance of a saddle point in the flow below the core of vortex B, indicating that two streamlines terminating at the eel surface have joined and bifurcated away from the surface. Figure 11(d), the final phase in the shedding cycle, shows vortex C beginning to convect along the surface and the appearance of a saddle point in the free stream separating the like signed vortical structures, vortex B and D. There is reversed flow under this saddle point and hence a communication of material from vortex B to D. This communication of material has also been observed in flow visualization experiments. The reversed flow is highlighted in Figure 11(d).

Figure 12 shows the streamline pattern for a section of Figure 11(d) when a bias velocity of the order 0.65 of the free-stream velocity has been applied. This velocity bias results in the membrane appearing as a streamline in the flow and also shows the presence of structures along the length of the membrane for the full field of view. This indicates that the vortical structures impinge on the membrane head with significant reversed flow, and then accelerate downstream along the membrane surface. Figure 13 shows a comparison of a vorticity



and streamline field corresponding to the point in the oscillation cycle when an impinging vortex is fully formed and the membrane is at maximum deflection in response to this impinging structure. Vorticity from the previous half of the shedding cycle can be seen on the underside of the membrane.

## 5. CONCLUSIONS

The response of a flexible membrane or "eel" to external forcing due to the vortex shedding downstream from a bluff body has been examined using frequency response measurements and PIV. Data show that the membranes are able to exhibit lock-in behavior to the bluff body shedding. Lock-in is defined to occur when the membranes oscillate at the same frequency as the undisturbed wake behind the bluff body. When the membrane reaches this condition, its wavelength and amplitude are also similar to the undisturbed vortex street. The amplitude of oscillation appears to be confined to within an envelope that is similar in width to the wake that forms behind the bluff body when no membrane is present. A condition for lock in has been suggested as occurring when  $0.2\xi_n U_\infty^2 \rho W / (\rho_{eel}(-\omega_{eel}^2 + \omega_n^2)D) > 1$ . This relationship is derived from a simplified description of the oscillating system as an Euler-Bernoulli beam and fits the data reasonably well. PIV data sets indicate the presence of vortical structures convecting along the length of the eel in synchronization with the eel distortion. These structures correspond to the alternating vortices that are formed and shed from the edges of the bluff body.

## ACKNOWLEDGEMENT

This work is supported by Ocean Power Technologies Inc., Office of Naval Research and DARPA.

## REFERENCES

- GERRARD, J. H. 1966 The mechanics of the formation region of vortices behind bluff bodies. *Journal of Fluid Mechanics* **25**, 401–413.
- HUERRE, P. & MONKEWITZ, P. A. 1990 Local and global instabilities in spatially developing flows. *Annual Review of Fluid Mechanics* **22**, 473–537.
- KHALAK, A. & WILLIAMSON, C. H. K. 1999 Motions, forces and mode transitions in vortex-induced vibrations at low mass-damping. *Journal of Fluids and Structures* **19**, 813–851.
- LEONARD, A. & ROSHKO, A. 2001 Aspects of flow-induced vibrations. *Journal of Fluids and Structures* **15**, 415–425.
- NAUDASCHER, E. & ROCKWELL, D. 1994 *Flow-Induced Vibrations — An Engineering Guide*. Brookfield, VT: A. A. Balkema.
- PAIDOUSSIS, M. P. 1966a Dynamics of flexible cylinders in axial flow. Part 1. Theory. *Journal of Fluid Mechanics* **26**, 717–736.
- PAIDOUSSIS, M. P. 1966b Dynamics of flexible cylinders in axial flow. Part 2. Experiments. *Journal of Fluid Mechanics* **26**, 737–752.
- ROSHKO, A. 1954 On the drag and shedding frequency of two-dimensional bluff bodies. NACA Technical Note No. 3169.
- WU, T. Y. 1961 Swimming of a waving plate. *Journal of Fluid Mechanics* **10**, 321–344.

## VORTEX DISLOCATIONS AND FORCE DISTRIBUTION OF LONG FLEXIBLE CYLINDERS SUBJECTED TO SHEARED FLOWS

D. LUCOR, L. IMAS AND G. E. KARNIADAKIS

*Center for Fluid Mechanics, Division of Applied Mathematics  
Brown University, Providence, RI 02912, U.S.A.*

(Received 29 August 2000, and in final form 14 November 2000)

We present DNS results of vortex-induced vibrations (VIV) of flexible cylinders with aspect ratio greater than 500, subjected to linear and exponential sheared flows. The maximum Reynolds number is  $Re_m = 1000$  resulting in a turbulent near-wake. The first case corresponds to lock-in of the third mode ( $n = 3$ ), while the second case is a multi-mode response with excited modes as high as  $n = 12$  and 14. We observed vortex dislocations similar to the structures visualized in experiments for stationary cylinders, and obtained corresponding force distributions. Strong vortex dislocations can result in substantial modulation of the forces on the body, and such effects have to be taken into account when constructing low-dimensional predictive models.

© 2001 Academic Press

### 1. INTRODUCTION

PREVIOUS EXPERIMENTAL STUDIES of vibrating cylinders subjected to sheared flows have shown the existence of cellular shedding patterns (Stansby 1976; Woo *et al.* 1981; Peltzer & Rooney 1985). The size and stability of such cells have some subtle differences with similar structures encountered in stationary cylinders, as synchronization (lock-in) and multi-mode response compete directly with frequency mismatching along the span. The latter is the primary reason for the cell formation in either sheared flow or uniform flow past tapered cylinders (Maull & Young 1973; Noack *et al.* 1991; Williamson 1992). The results from the experimental work suggest that the size of the cells is proportional to the amplitude of vibration and inversely proportional to the shear parameter  $\beta$ . This parameter is defined as  $\beta = (d/U)(\partial u/\partial z)$ , where  $z$  denotes the spanwise (cylinder axis) direction,  $d$  is the cylinder diameter, and  $U$  the span-averaged free-stream velocity. It is possible, therefore, to find cells of constant shedding frequency of 40 diameters or more unlike the stationary cylinder where such cells are not longer than approximately 10 diameters (Peltzer & Rooney 1985).

The experimental work has primarily focused on frequency and point-measurements. However, measurements of forces on the cylinders are needed to establish the effect of vortex dislocations. Such data are currently missing with the exception of recent work by Triantafyllou and collaborators who investigated the effect of vortex splits (Hover *et al.* 1998). In numerical work, the first three-dimensional simulations of VIV of flexible cylinders subjected to sheared flow has been reported in Newman & Karniadakis (1997). Follow-up work including a detailed force distribution for *uniform inflow* was reported in Evangelinos *et al.* (2000). In that work, the difference between a traveling and a standing wave response was examined, and a new empirical model was proposed for predicting the average drag force.

TABLE 1

FLOW	Linear shear inflow	Exponential shear inflow
Reynolds number (max ~ min)	Re = 1000 ~ 607	Re = 1000 ~ 300
Re = $Ud/\nu$	Turbulent regime	Turbulent/transition regime
Inflow profile	Linear	Gaussian
STRUCTURE	Beam	Beam/cable
Boundary conditions	Pinned and hinged ends	
Constraints	No streamwise motion (x-direction)	
	Free transverse motion (y-direction)	
Aspect ratio, $L/d$	$L/d = 567$	$L/d = 914$
Mass ratio, $m$	$m = 2$	$m = 2$
Cable phase velocity, $c$	$c = 0.0$	$c = 25.8$
Beam phase velocity, $\gamma$	$\gamma = 4487.92$	$\gamma = 345.248$
Damping, $R$	$R = 0.0$	$R = 0.1$

In the current work, we investigate numerically VIV of flexible cylinders subjected to shear flows. We only consider crossflow motion which is described by

$$\frac{\partial^2 Y}{\partial t^2} = c^2 \frac{\partial^2 Y}{\partial z^2} - \gamma^2 \frac{\partial^4 Y}{\partial z^4} - \frac{R}{m} \frac{\partial Y}{\partial t} + \frac{1}{m} F(z, t), \quad (1)$$

where we denote by  $Y(z, t)$  the crossflow displacement and by  $F(z, t)$  the total lift force, i.e., including both pressure and viscous contributions. Also,  $m$  is the mass ratio,  $R$  is the damping coefficient, and  $c = \sqrt{T/m}$ ;  $\gamma = \sqrt{EI/m}$ , where  $T$  is the tension and  $EI$  the bending stiffness. The lift force is obtained by DNS using the spectral/hp element method (Karniadakis & Sherwin 1999), implemented in the parallel code  $\mathcal{N}\varepsilon\kappa\mathcal{T}\alpha r$ .

In Table 1, we list the values of the parameters in equation (1) for the two main cases we consider in this paper. The first case corresponds to inflow with *linear shear* while the second case corresponds to *exponential shear* described by a Gaussian distribution. The maximum Reynolds number is  $Re_m = 1000$  in both cases and thus a turbulent near-wake is developed. These two cases represent realistic situations corresponding to experimental and field conditions [see references in Furnes (1998) and Allen (1995)]. In equation (1), we refer to the type of structure as a *beam* if  $\gamma \neq 0$  and as a *cable* if  $c \neq 0$ . For the linear shear we examine a beam, and for the exponential shear a mixed beam–cable structure. We also note that unlike most of the previous studies where the aspect ratio of the cylinder was of the order of 100 or less (typically 20–50), here we consider a very large value of aspect ratio ( $\geq 500$ , see Table 1).

The numerical simulation and mesh is similar to the one used in Evangelinos & Karniadakis (1999) with 64 points placed along the span, which is sufficient to capture the larger structures only. In order to process spectral information, 64 history points were placed in the near-wake of the cylinder. They are located equidistantly along the span, at the centerline and at  $x/d = 3$  in the streamwise direction. Values of velocity and pressure fields are sampled at these history points. Handling such large computational domains requires a great amount of computational resources, especially long-time integration to achieve stationarity of the flow. The only other DNS we are aware of is the work of Vanka and collaborators (Mukhopadhyay *et al.* 1999), who study the laminar wake of a stationary cylinder at an aspect ratio of 24 using a finite volume method.

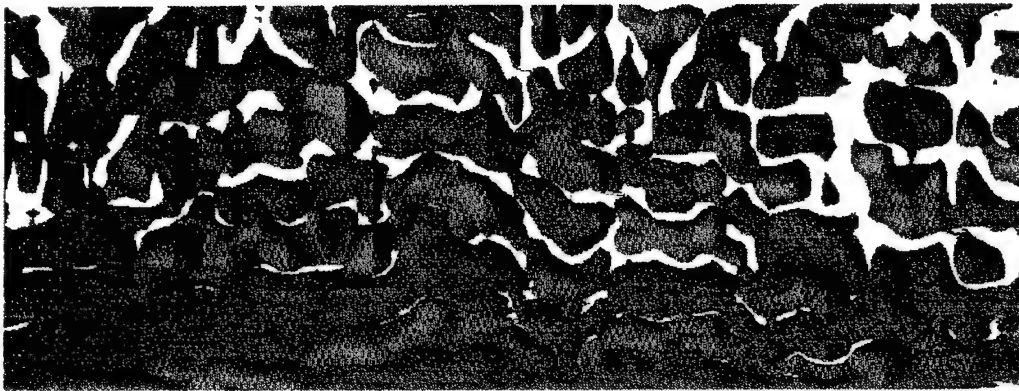


Figure 1. Linear shear case. Iso-contours of crossflow velocity at  $Re_m = 1000$ . Only the part corresponding to the large inflow is shown. Dark color:  $v = -0.2$ ; light color:  $v = 0.2$ . View normal to the  $(x, z)$  horizontal plane, where  $80 \leq z/d \leq 400$  and  $0 \leq x/d \leq 12.5$ ; flow is upward.

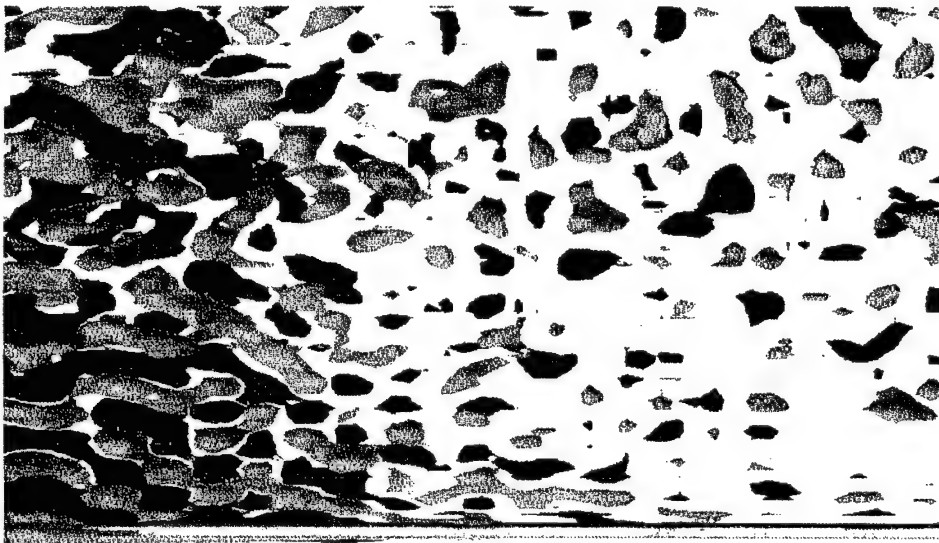


Figure 2. Exponential shear case. Iso-contours of crossflow velocity at  $Re_m = 1000$ . Dark color:  $v = -0.2$ ; light color:  $v = 0.2$ . View normal to the  $(x, z)$  horizontal plane, where  $0 \leq z/d \leq 400$  and  $0 \leq x/d \leq 35$ ; flow is upward.

---

7.

---

### 1.1. VISUALIZATION OF VORTEX DISLOCATIONS

The most prominent feature observed in shear flow over a bluff body is the shedding of vortices in cells of constant frequency. Because of the mismatch in frequency, vortex dislocations are generated between these cells. The presence of these vortex dislocations in wakes contributes to the transition to turbulence. Vortex dislocations are encountered in transitional and turbulent wakes as well as in laminar wakes, but in a more ordered fashion.

Visualization of vortex dislocations is more clear at low Reynolds number. To this end, we first simulated shear flow past a flexible beam subject to forced and free vibrations for a pinned cylinder of aspect ratio  $L/d = 567$  with a mean Reynolds number  $\overline{Re} = 80.35$  and a shear parameter  $\beta \approx 8.8 \times 10^{-4}$ ; these results and corresponding visualizations were first reported in Lucor *et al.* (2000). The frequency reduces as the *cosine* of the shedding angle (this angle gets steeper as the inflow velocity decreases); similar results were reported for a stationary cylinder in Mukhopadhyay *et al.* (1999). A localized lock-in of the left part of the beam, which corresponds to the side experiencing the large inflow, is obtained. This is similar to the lock-in cell observed in the experiments of Peltzer & Rooney (1985) which extended over 44 cylinder diameters in a cylinder with aspect ratio 107. Here the size of the first cell is larger than that, as both the amplitude of the vibration is larger and the shear parameter is smaller than the experiment [see also Peltzer & Rooney (1985)]. In addition, a significant increase of drag and lift forces was observed in this region of the structure.

The structure, size and dynamics of the dislocations in the case of uniform inflow past a *stationary* cylinder have also been described by Williamson in more recent experimental work (Williamson 1992). He obtained a relationship between the different vortex structures across the boundary between two cells, and explained the interactions between these structures. He also established, in the case of transitional wakes, that the beating frequency of the dislocation between a cell of frequency  $f_1$  and a cell of frequency  $f_2$  is  $f_D = f_1 - f_2$ . This has successfully been verified in our simulation for a *moving cylinder*, suggesting a universality of vortex dislocations. As regards the fluctuation of cell boundaries, our results confirm the experimental results of Stansby (1976) and Peltzer & Rooney (1985) that vibrations have a stabilizing effect.

Similar visualizations were obtained for a freely moving cylinder. At higher Reynolds number, however, it is more difficult to discern such a clear pattern although a similar picture emerges. For example, for the linear shear flow at  $Re_m = 1000$  we use the crossflow velocity to qualitatively capture instantaneous vortex dislocations in Figure 1. In Figure 2, we plot the crossflow velocity contours in the near-wake for the exponential shear case. We observe a structure much more complex than the linear shear case but with distinct pockets of vortex dislocations, qualitatively similar to the structures we observed in laminar wakes and in linear shear. It is also clear from this plot that the flow does not correlate well along the span of the cylinder, and this invalidates the assumption of full-span correlation employed in the semi-empirical models such as SHEAR7 (Vandiver & Li 1994).

## 2. VIV FOR LINEAR SHEAR INFLOW

For this simulation the cylinder-to-fluid mass ratio is 2, the structural damping is set to 0.0 in order to obtain a maximum response, and the beam phase speed is set to  $\gamma = 4487.92$  for lock-in; this corresponds to a natural nondimensional frequency for the beam of 0.1973. For this *linear* shear inflow, the *maximum* Reynolds number (at  $z/d = 0.0$ ) and *minimum* Reynolds number (at  $z/d = 567$ ) are 1000 and 607, respectively, with a mean value of 803.5. The shear parameter is  $\beta \approx 8.8 \times 10^{-4}$ , smaller than most of the values used in previous experiments, where  $\beta \geq 0.005$  [see e.g., Peltzer & Rooney (1985)]. These values are close to

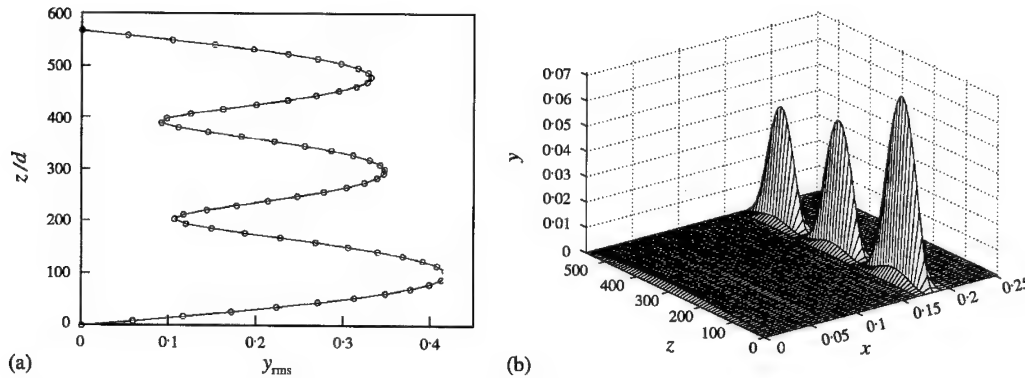


Figure 3. Left: crossflow-displacement (r.m.s. values — horizontal axis) of the beam along the span normalized with the cylinder diameter. Right: corresponding power spectral density (x-axis: frequency nondimensionalized with maximum velocity; y-axis: power spectral density; z-axis: span of the cylinder).

those used in the experiments reported in Furnes (1998) with the exception of Reynolds number, which is lower in the current simulations.

## 2.1. DISPLACEMENT AND FORCE DISTRIBUTION

In Lucor *et al.* (2000), we first reported results for this case; a standing wave response was obtained with the *third mode* excited. The location of the nodes, however, moves somewhat in time, which explains the small but nonzero r.m.s. values of the crossflow displacement. Specifically, a slight shift of these nodes towards the side of the low inflow in the shear inflow case compared to the uniform inflow cases is observed (Evangelinos *et al.* 2000). The standing wave partitions the span of the cylinder in three different cells. The maximum structural response of the beam is reached on the side of the high inflow. Figure 3 displays the standard deviation or r.m.s. values of the vertical displacement of the beam,  $(Y(z)/d)_{\text{rms}}$ , (normalized by the cylinder diameter), and the spectrum of  $(Y(z)/d)_{\text{rms}}$ . The maximum r.m.s. value of the crossflow displacement of the beam occurs within the first cell. The r.m.s. structural responses obtained in the second and the third cell are equal even though the beam experiences different inflow velocity. These amplitudes are about 20% lower than the maximum amplitude of the first cell.

The natural frequency of the beam was set to 0.1973, which is the frequency response of a rigid cylinder subject to VIV at a Reynolds number of 1000 (Evangelinos & Karniadakis 1999). If we represent the crossflow motion in the spectral space, we see that only one mode is excited. The structure frequency response is 0.183 (see Figure 3, right). The spectral density is maximum in each cell between the nodes. The wake frequency based on the Reynolds number associated with the mean inflow velocity from the shear inflow for a stationary cylinder is around 0.21 (Fey *et al.* 1998). Therefore, the coupled flow-structure system has a frequency response that deviates towards a smaller value from the imposed frequency, here  $f = 0.197$ , [see also Evangelinos & Karniadakis (1999)].

In Figure 4, we plot the mean values of the drag coefficient,  $(C_d(z))_{\text{mean}}$ , and r.m.s. values of the lift coefficient along the span of the cylinder. The lift and drag coefficients represented along the span are normalized by the *local* inflow velocity. Due to the shear inflow the local Reynolds number along the span varies from 1000 to 607. The mean value of  $C_d(z)$  is about 1.66. The maximum value of  $C_d(z)$  takes place at the midspan and its value is 13% larger than the maximum  $C_d(z)$  in the case of the uniform inflow [2.1 versus 1.82; see Evangelinos *et al.* (2000)] and 29% larger than the  $C_d(z)$  at the same location in the case of the uniform

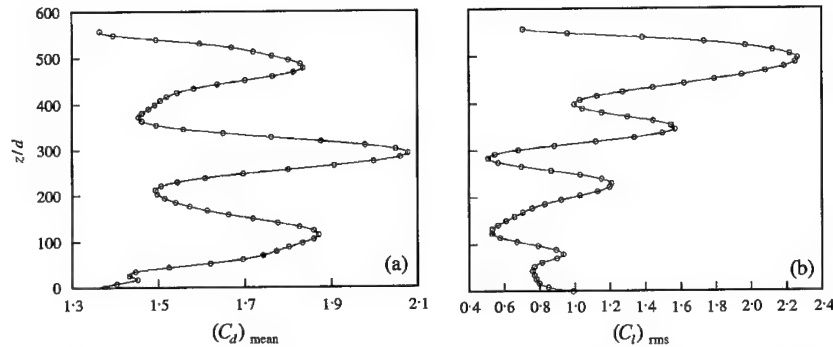


Figure 4. (a) Distribution of  $(C_d)_{\text{mean}}$  along the span. (b) Distribution of  $(C_l)_{\text{rms}}$  along the span. The local inflow velocity is used in the normalization.

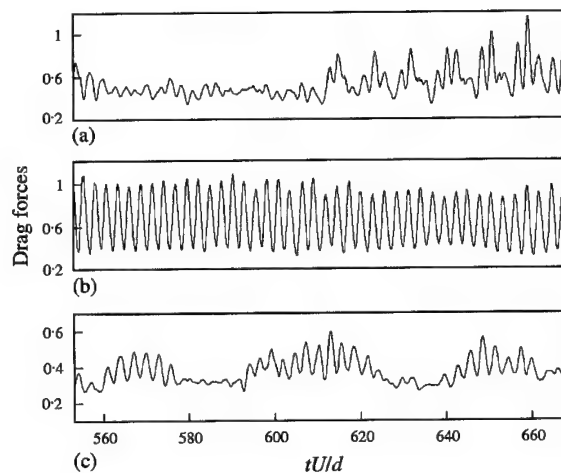


Figure 5. Comparison of time-histories of drag force at different locations along the span: (a)  $z/d = 248.06$ ; (b)  $283.5$ ; (c)  $416.39$ .

inflow [2.1 versus 1.55; see Evangelinos *et al.* (2000)]. The local minimum values of the  $C_d(z)$  are located at the nodes, in agreement with the uniform inflow results (Evangelinos *et al.* 2000).

The plot of  $(C_l(z))_{\text{rms}}$  exhibits a large value in the third cell and a small value in the first cell. The response in the central cell is more intriguing and is split into two zones. The overall  $(C_l(z))_{\text{rms}}$  along the span has a mean value of 1.12. A maximum value of 2.22 is reached at  $z/d = 505$  and a minimum value of 0.35 is achieved at the midspan.

The plot of the lift coefficient can be related to the crossflow motion. The apparent inconsistency between the plots above could be explained by a phase analysis. The spectral density plot (not shown here) of the  $C_l$  signal as a function of the frequency shows that only two frequencies are primarily excited. The first one corresponds to the frequency of the beam oscillation ( $f = 0.183$ , see also Figure 3), while the second one is an incommensurate higher frequency ( $f = 0.296$ ), which we have not been able to relate to other frequencies. Clearly, the dominant frequency of  $C_l$  along the cylinder is  $f = 0.183$ , especially within the third cell where large spectral densities are obtained. We have observed that the  $C_l$  signal is in-phase with the beam motion in this cell. This might also explain why the displacement in



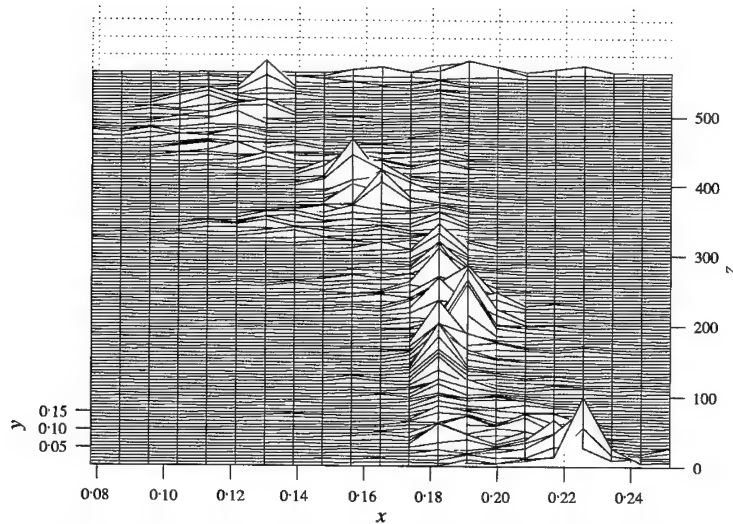


Figure 6. Spanwise ( $z$ ) power spectral density of the  $v$ -component of the velocity field ( $x$ -axis denotes frequency nondimensionalized with maximum velocity;  $y$ -axis denotes power spectral density,  $z$ -axis denotes the span of the cylinder).

the third cell is comparable to the displacement of the second cell even though they experience different inflows.

Finally, in Figure 5 we plot the time histories of the drag force at three different locations along the beam. These positions have been identified after a spectrum analysis of the crossflow  $v$ -velocity and streamwise  $u$ -velocity (not shown here) in order to locate the positions of the main vortex dislocations. The first plot shows the drag force at  $z/d = 248.06$ , which is the location of the main vortex dislocation of this flow. The second graph is used as a reference and does not reside within a vortex dislocation. Finally, the third graph shows values of drag forces at another vortex dislocation of smaller intensity. There exists a significant *low-frequency modulation* at the first and the third locations compared to the second one. These low frequencies are the same as the leading frequencies of the streamwise  $u$ -velocity at these positions.

## 2.2. FREQUENCY RESPONSE

In Figure 6, we plot frequency spectra of the crossflow velocity along the beam. These frequencies can be interpreted as Strouhal numbers based on the *maximum* inflow velocity of the flow ( $U_m = 1.0$ ). The most distinguishing feature observed in Figure 6 is the shedding of vortices at constant frequencies. It can be shown that all these peak frequencies are, in fact, linear combinations of the harmonics of  $f_1 = 0.1996$  with the harmonics of  $f_2 = 0.2082$ , and they can be written in this case as

$$[m - 3(n - 1)]f_1 + [4(n - 1) - m]f_2, \quad (2)$$

where  $n = 2$  and  $m = 1, 2, \dots, 16$ . It is interesting to note that  $f_1$  is very close to the natural frequency for the beam ( $f = 0.1973$ ) and  $f_2$  corresponds to the Strouhal number of the flow past a stationary circular cylinder at Reynolds number of 620 (Fey *et al.* 1998). We recall that 607 is the Reynolds number that corresponds to the *minimum* inflow velocity of our shear inflow.

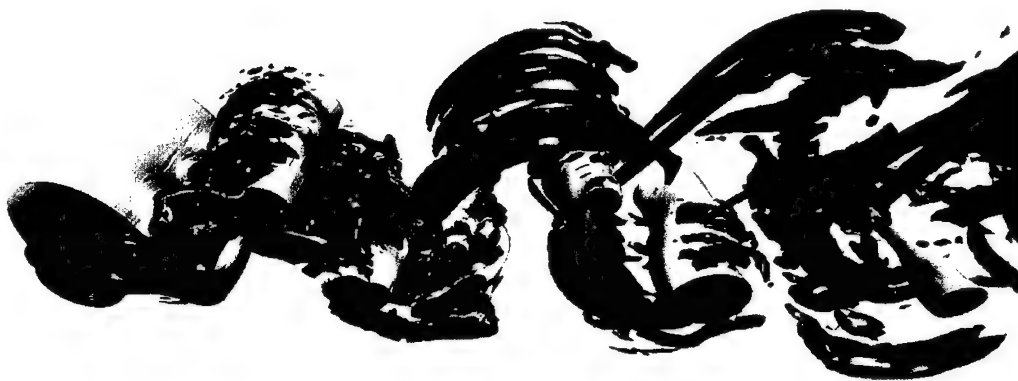


Figure 7. Instantaneous isosurfaces of pressure (predominant alignment spanwise) and streamwise vorticity (predominantly streamwise) from three-dimensional simulation. The cylinder is upstream at left.

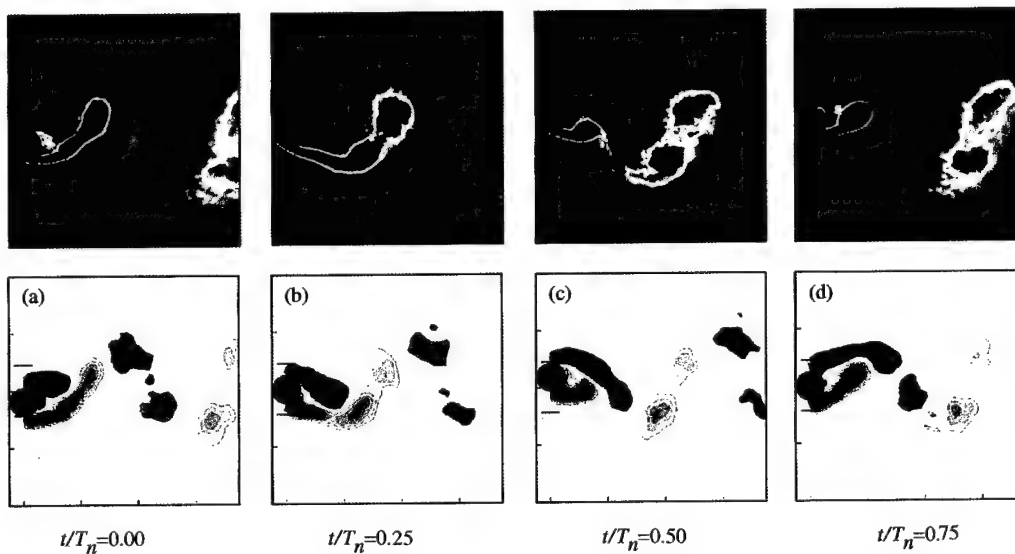


Figure 8. Phase and spanwise average contours of spanwise vorticity for four phases of the cylinder motion cycle (upper plots), compared to (lower) similar (two-dimensional) phase averages from experiments at a somewhat higher Reynolds number (Govardhan & Williamson 2000).

Barring end-effects that may be induced by possible numerical artifacts, we can distinguish several different frequency cells or frequency ranges. These cells do not match the cells defined by the beam displacement (see Figure 3). The length of these cells is approximately as follows. There is a large first cell from  $z/d = 50$  to 250 with a frequency of  $f = 0.183$ , which is the frequency of the crossflow motion of the beam. Then, the second cell lies between  $z/d = 250$  and 370 with two frequencies  $f = 0.183$  and  $0.165$ . A third large cell is between  $z/d = 370$  and 425, and the last cell fills the gap between  $z/d = 430$  to the end of the beam span. In this case, the spectrum is not very sharp, and it is therefore more difficult to identify the characteristic frequency. Between the cells we notice buffer zones with small spectral density, low energy, e.g. at the midspan, or total energy distributed over a larger number of modes, e.g. at the second-node zone. Clearly, these cells are much larger than the cells encountered in stationary cylinders but this is expected for vibrating cylinders, especially since the shear parameter is very small in our case, and the aspect ratio is very large. The current results are certainly consistent with the experimental results and conclusions reported in Peltzer & Rooney (1985).

### 3. VIV FOR EXPONENTIAL SHEAR INFLOW

In inflows with large shear the possibility exists for excitation of high modes and of a multi-mode response (Kim *et al.* 1985; Vandiver 1991). This is evident in the case we consider here that corresponds to  $\gamma = 345.248$  and  $c = 25.8$  (see Table 1). The corresponding eigenspectrum of a beam-cable structure pinned at both ends is determined by

$$\omega^2 = \gamma^2 k^4 \left[ 1 + \frac{c^2}{\gamma^2 k^2} \right], \quad k = \frac{n\pi}{(L/d)}, \quad (3)$$

where  $n$  is the mode number. Substituting the parameters of Table 1 we obtain a non-dimensional frequency of 0.193 for mode  $n = 12$ . Given that the Strouhal number at  $Re \sim \mathcal{O}(1000)$  is about  $St \approx 0.2$ , we verify that indeed the possibility exists for such high modes to be locked-in to the wake.

The specific form of shear profile imposed at the inlet in this case is described by

$$U(z) = (1 - U_f) e^{-a(z/d)^2} + U_f, \quad U_f = 0.3, \quad a = 5.0 \times 10^{-5} \quad (4)$$

with the high inflow velocity located at  $z/d = 0$ . The shear parameter in this case is  $\beta \approx 0.005$ .

#### 3.1. DISPLACEMENT AND FORCE DISTRIBUTION

In Figure 7, we plot the time-history of the crossflow displacement along the spanwise direction. We see that a mixed response is established, which can be characterized as hybrid between a standing wave and a traveling wave, unlike the linear shear case where a lock-in standing wave pattern was obtained. The r.m.s. values of the crossflow displacement along the span of the cylinder are plotted in Figure 8 (left) along with the corresponding spectrum (right) showing a multi-mode frequency response. Unlike the linear shear case, here the structure oscillates at low frequencies. To investigate further this multi-mode response we obtained the excited modes by analyzing two different instantaneous responses in wavenumber space (plot not shown here). The highest contributing modes are  $n = 14-16$  which agree with the results of Triantafyllou *et al.* (1994), a code based on empirical modeling of the flow and eigenfrequency analysis for the structure. The span-averaged value of the crossflow displacement predicted by the current simulation is 0.22 compared to 0.243

obtained by Triantafyllou *et al.* (1994). Also, comparison of the instantaneous response profiles with field measurements (performed on a drilling riser with similar geometric properties and responding to a current with similar shear parameter) between the locations  $27 \leq z/d \leq 55$ , is very good (Allen 1995). An important difference, already mentioned, between the linear shear response and the exponential shear response is that in the former a standing wave pattern is observed, whereas in the latter a hybrid standing-traveling wave pattern prevails.

### 3.2. FREQUENCY RESPONSE

We have already seen that the beam-cable structure oscillates at a low frequency. This frequency is approximately the same as the low frequency in the wake (plot not shown here) on the low inflow side. In contrast, the lift follows a response similar to the wake on the side of the high-velocity inflow. Therefore, unlike the linear shear case where the frequency response of lift, the wake, and the structure are the same, in the case of exponential shear the lift and the beam-cable response are not the same.

## 4. SUMMARY AND DISCUSSION

In this paper, we have addressed the effects of linear and exponential shear profiles in VIV of very long flexible cylinders using spectral DNS. The main difference between the two cases is that in linear shear the structural response resembles a standing wave pattern, whereas in the exponential shear case it resembles a mixed standing-traveling wave pattern. For the parameters considered here, the linear shear led to a low-mode (mode 3) response while the exponential shear led to a multi-mode response with modes as high as 12 and 14 participating.

More quantitatively, the difference in the two cases can be summarized in the plots of Figure 9, which include the frequency response of the wake and the structure as well as the natural frequency of the structure. The crossflow velocity at points  $(x/d = 3, y/d = 0, z/d)$  is analyzed to obtain the shedding frequency. The most distinguishing feature in these plots is the shedding of vortices at constant frequencies, as it is evident by the values of the Strouhal number which are on parallel lines. This is more pronounced for the linear shear case, for which we also observe that the beam locks on to a wake frequency which dominates on the side of the high inflow. This frequency is lower than the natural frequency of the beam for mode  $n = 3$ . On the other hand, for the exponential shear we need to consider different modes because of the multi-mode response of the structure. The structure response (non-dimensional) frequency varies from about 0.05 to just above 0.23 with corresponding excited natural modes from  $n = 3$  to 12.

We have found that the nodes of the structure are not always located exactly at a boundary between two cells. We also obtained cells of constant shedding frequency, which are much longer than the cells in stationary cylinders reported in experimental work. However, their size is consistent with the experimental results and corresponding conclusions reached in the works of Stansby (1976) and Peltzer & Rooney (1985). It was reported in these works that the size of the cells scales proportionally to the amplitude of crossflow displacement and inversely proportional to the shear parameter. Moreover, we have seen in our simulations that the larger aspect ratio of the flexible cylinder allows for larger cellular patterns. This too is consistent with the experimental results of Peltzer (1982) if we extrapolate from his range of aspect ratio ( $L/d \sim 20-100$ ) to our values ( $L/d \sim 567-914$ ).

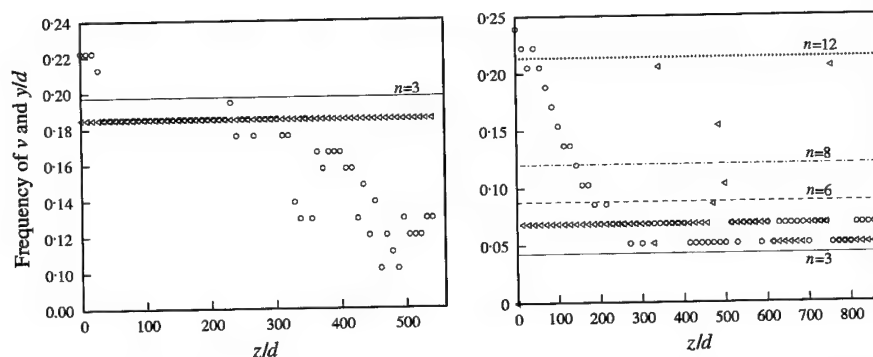


Figure 9. Frequency distribution of wake and structure along the span showing cellular shedding and multi-mode response. (a) linear shear; (b) exponential shear. Circles denote dominant frequency of crossflow velocity and triangles dominant frequency of the structure response. The maximum inflow velocity is used in the normalization of the frequency.

With regards to force distribution on the structure, we have found that vortex dislocations have a significant effect on the *instantaneous* force distributions along the span of the cylinder. The location of vortex dislocations in the wake can best be obtained by searching for energetic low frequencies of the streamwise velocity component (plot not shown here). We have observed that there exists a significant modulation of the forces on the body by these low frequencies at the spanwise locations corresponding to the vortex dislocations. This demonstrates that strong vortex dislocations can have a substantial effect on the forces acting on the body, and such effects have to be taken into account when constructing low-dimensional predictive models.

#### ACKNOWLEDGEMENTS

This work was supported by the Office of Naval Research, the Department of Energy, and the National Science Foundation. Computations were performed on the NAVO T3E, on the MHPCC SP2, and on the SP Power 3 computer of Brown's Center for Scientific Computing & Visualization. We would like to thank Dr Gunnar Furnes of Norsk Hydro and Dr Owen Oakley of Chevron for useful discussions. We would also like to thank R. M. Kirby and C. Evangelinos for their help with the  $\mathcal{N}_{EK}\mathcal{T}ar$  code.

#### REFERENCES

- ALLEN, D. 1995 Vortex induced vibration analysis of the auger TLP production and steel catenary export risers. In *Proceedings Conference on Offshore Technology*, Houston, TX, Paper No. 7821.
- EVANGELINOS, C. & KARNIAKAKIS, G. E. 1999 Dynamics and flow structures in the turbulent wake of rigid and flexible cylinders subject to vortex-induced vibrations. *Journal of Fluid Mechanics* **400**, 91–124.
- EVANGELINOS, C., LUCOR, D. & KARNIAKAKIS, G. E. 2000 DNS-derived force distribution on flexible cylinders subject to VIV. *Journal of Fluids and Structures* **14**, 429–440.
- FEY, U., KÖNIG, M. & ECKELMANN, H. 1998 A new Strouhal-Reynolds-number relationship for the circular cylinder in the range  $47 < Re < 2 \times 10^5$ . *Physics of Fluids* **10**, 1547–1549.
- FURNES, G. 1998 On marine riser responses in time and depth dependent flows. Technical Report, Norsk Hydro, Bergen, Norway.
- HOVER, F. S., TECHET, A. H. & TRIANTAFYLLOU, M. S. 1998 Forces on oscillating uniform and tapered cylinders in crossflow. *Journal of Fluid Mechanics* **363**, 97–114.
- KARNIAKAKIS, G. & SHERWIN, S. 1999 *Spectral/hp Element Methods in CFD*. New York: Oxford University Press.

- KIM, Y.-H., VANDIVER, J. & HOLLER, R. 1985 Vortex-induced vibration and drag coefficients of long cables subjected to sheared flows. In *Proceedings Fourth International Offshore Mechanics and Arctic Engineering Symposium*, New York: ASME.
- LUCOR, D., EVANGELINOS, C. & KARNIADAKIS, G. 2000 DNS-derived force distribution on flexible cylinders subject to VIV with shear inflow. In *Proceedings Flow Induced Vibration* (eds S. Ziada & T. Staubli). Rotterdam: A.A. Balkema.
- MAULL, D. J. & YOUNG, R. A. 1973 Vortex shedding from bluff bodies in shear flow. *Journal of Fluid Mechanics* **60**, 401–409.
- MUKHOPADHYAY, A., VENUGOPAL, P. & VANKA, S. P. 1999 Numerical study of vortex shedding from a circular cylinder in linear shear flow. *Journal of Fluids Engineering* **121**, 460–468.
- NEWMAN, D. J. & KARNIADAKIS, G. E. 1997 Simulations of flow past a freely vibrating cable. *Journal of Fluid Mechanics* **344**, 95–136.
- NOACK, B. R., OHLE, F. & ECKELMANN, H. 1991 On cell formation in vortex streets. *Journal of Fluid Mechanics* **227**, 293–308.
- PELTZER, R. 1982 Vortex shedding from a vibrating cylinder with attached spherical bodies in linear shear flow. Report 4940, Naval Research Laboratory, Washington, DC, U.S.A.
- PELTZER, R. & ROONEY, D. 1985 Vortex shedding in a linear shear flow from a vibrating marine cable with attached bluff bodies. *ASME Journal of Fluids Engineering* **107**, 61.
- STANSBY, P. K. 1976 The locking-on of vortex shedding due to cross stream vibration of circular cylinders in uniform and shear flows. *Journal of Fluid Mechanics* **74**, 641–665.
- TRIANTAFYLLOU, M., GOPALKRISHNAN, R. & GROSENBAUGH, M. 1994 Vortex-induced vibrations in a sheared inflow: A new predictive method. In *Hydroelasticity in Marine Technology* (eds O. Faltinsen *et al.*). Rotterdam: A. A. Balkema.
- VANDIVER, J. 1991 Dimensionless parameters important to the prediction of vortex-induced vibrations of long, flexible cylinders in ocean currents. MIT Sea Grant Report No. MITSG 91-93, Massachusetts Institute of Technology, Cambridge, MA, U.S.A.
- VANDIVER, J. & LI, L. 1994 SHEAR7 Program Theoretical Manual. Technical Report, Department of Ocean Engineering, Massachusetts Institute of Technology, Cambridge, MA, U.S.A.
- WILLIAMSON, C. H. K. 1992 The natural and forced formation of spot-like 'vortex dislocations' in the transition of a wake. *Journal of Fluid Mechanics* **243**, 393–441.
- WOO, H., CERMAK, J. & PETERKA, J. 1981 Experiments on vortex shedding from stationary and oscillating cables in a linear shear flow. Report No. N68305-78-C0055, Naval Civil Engineering Laboratory, Colorado State University, Fort Collins, CO, U.S.A.



## VORTEX-INDUCED VIBRATION OF A FLEXIBLE CANTILEVER

A. L. C. FUJARRA

*Naval Architecture and Ocean Engineering, Escola Politécnica  
University of São Paulo, SP - 05508-900, Brazil*

C. P. PESCE

*Mechanical Engineering, Escola Politécnica, University of São Paulo  
SP - 05508-900, Brazil*

AND

F. FLEMMING AND C. H. K. WILLIAMSON

*Sibley School of Mechanical and Aerospace Engineering  
Upson Hall Cornell University, Ithaca, NY 14853-7501, U.S.A.*

(Received 22 September 2000, and in final form 17 December 2000)

This study is concerned with the vortex-induced vibrations of a flexible cantilever in a fluid flow. Our cantilever comprises a leaf spring encased within a rubber flexible cylinder, restricting the vibrations of the body in a water channel flow to principally transverse motion. It is found that the transverse amplitude response of the cantilever has a marked similarity with transverse vibrations of an elastically mounted rigid cylinder, in that there is a clear initial branch extending to high amplitudes, with a jump to a lower branch response, as normalized velocity is increased. The continuous initial branch suggests that a distinct upper branch does not exist for the cantilever, as is found for a rigid cylinder under similar conditions of low mass and damping. Good agreement is found between the response amplitude and frequency for two “identical” cantilevers, one set up by Pesce and Fuarra, where strain is measured to infer the body dynamics, and the other arrangement by Flemming and Williamson, where the tip motion is measured using optical techniques. An interesting large-amplitude response mode is found at higher normalized velocities ( $U^* > 12$ ) outside the principal synchronization regime (typically  $U^* = 4-8$ ), which is observed for an increasing velocity, or may be triggered by manual streamwise disturbances of the body. This vibration mode is due to a coupled streamwise-transverse motion, where the streamwise amplitude becomes non-negligible, and may be related to a further vibration mode at high normalized speed, found for a vibrating pivoted rod, by Kitagawa *et al.* (1999).

© 2001 Academic Press

### 1. INTRODUCTION

IN THIS WORK, we are concerned with the vortex-induced vibrations of a flexible cantilever in a fluid flow. This configuration, of some practical significance, has received only little attention in the literature to date. The early studies of Vickery & Watkins (1964) and King (1974) demonstrated large-amplitude tip vibration of around 1.5–1.6 diameters, while recent related studies of cantilever dynamics have been undertaken at São Paulo (Fuarra *et al.* 1998; Pesce & Fuarra 2000), showing comparable tip amplitudes of around 1.7 diameters. The relation between the dynamics of such cantilevers and elastically mounted rigid cylinders has been briefly addressed in Pesce & Fuarra (2000), and it is apparent that the

amplitude variation, as one increases flow velocity, exhibits a similar discontinuity between two response branches to what is found in elastically mounted rigid cylinder studies. A comparison between the peak amplitudes for cantilevers and rigid cylinders was undertaken by Griffin & Skop (1976). In that study, they attempted to collapse the peak amplitudes versus a mass-damping parameter in what we call a "Griffin plot" (Khalak & Williamson, 1999), although even using an "eigenmode factor",  $\gamma$  (where  $\gamma = 1.305$ ), to normalize the cantilever amplitude, the peak values do not collapse well. In a further relevant study, the dynamics of pivoted rods has been investigated by Kitagawa *et al.* (1999), who observe a vibration mode at high speed, outside the principal synchronization regime, which they attribute to the influence of an end cell of lower frequency vortex shedding near the tip of the rod. A more recent study of vibration of pivoted rods has been presented in a seminar by Atsavapranee & Wei (1999), who find large-amplitude oscillations comparable to the present cantilever dynamics.

In the present investigation, the cylindrical cantilever is constructed of an elastomeric material, but within this structure is a thin flexible aluminium plate, allowing much more flexibility in the transverse direction to the fluid flow, than exists in the streamwise direction. In the case of a cantilever whose flexibility is the same in the transverse and streamwise directions (Pesce & Fujarra 2000), there are distinct similarities of the response with the elastically mounted rigid cylinder case (Khalak & Williamson 1997a), as shown in Figure 1. The cantilever study was chosen to have a similar mass ( $m^*$ ) and damping ( $\zeta$ ) to the rigid cylinder arrangement [ $m^* = (\text{oscillating mass})/(\text{displaced fluid mass}) = 2.4$ ; leading to a mass-damping parameter  $m^*\zeta = 0.016$ , where  $\zeta = \text{structural damping ratio}$ ]. Although the rigid cylinder studies of Khalak & Williamson (1996, 1997b, 1999) show clearly a three-branch type of response, comprising an initial, upper, and lower branch of amplitude response, it appears that the response of the cantilever in Figure 1 exhibits a single "initial" branch, which then drops to a lower branch; in essence showing only a two-branch type of response, despite the very low mass and damping. The case of the flexible cantilever cannot be considered equivalent to the elastically restrained rigid cylinder, because the amplitude varies along the span in the case of the cantilever. Nevertheless, the response amplitude plots in Figure 1 are surprisingly similar in overall shape, especially along the lower segment of the initial response branch, and along the lower branch. This agreement is markedly improved, as in Figure 1, if one dispenses with the classical use of the "eigenmode factor", mentioned above, which has been employed in past work to normalize cantilever amplitudes.

An interesting point in the cantilever studies of Pesce & Fujarra (2000) is the existence, at the highest oscillation amplitudes (at the top of the left-hand response branch in Figure 1), of coupled streamwise-transverse oscillations. It was felt that by using a leaf spring in the present investigation, these stream-wise oscillations and their coupling with the transverse vibrations, could be largely prohibited. While this might be true for the principal synchronization regime ( $U^* = 4-12$ ), where the streamwise oscillations are negligible, we find instead that such a coupling can still exist at higher speeds. For the present cantilever, the stiffness and natural frequency are greater in the streamwise direction, which therefore shifts the regime of coupling to higher normalized flow speeds. What might be found surprising is the large magnitude of the oscillation amplitudes due to this coupling, and these are discussed later, with reference to Figure 4.

## 2. EXPERIMENTAL DETAILS

The cantilever in the present work is constructed of rubber, but within this cylindrical material is a thin flexible aluminium plate, as discussed earlier. The diameter of the cylinder



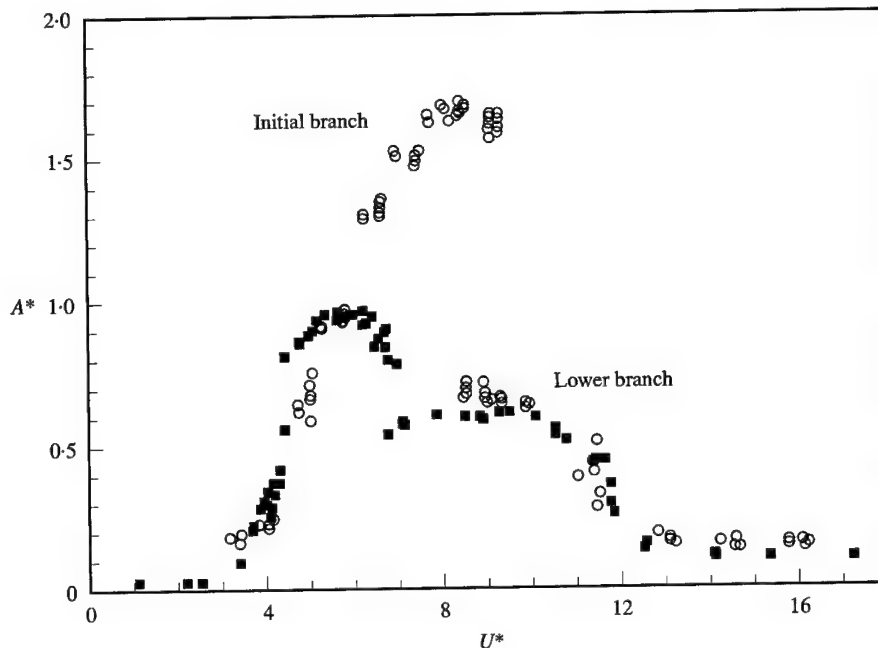


Figure 1. Comparison between amplitude response ( $A^*$ ) for a flexible cantilever and an elastically mounted rigid cylinder, as a function of normalized velocity,  $U^*$ . The cantilever in this case has the same stiffness in the streamwise and transverse directions.  $\circ$  Flexible cantilever;  $\blacksquare$  Rigid cylinder.

is 10 mm, giving an immersed length–diameter ratio of 41. Two “twin” cantilevers have been constructed expertly at University of São Paulo, and subsequently placed in two different water channel facilities, one in São Paulo (and at University of Michigan during the sabbatical of CPP and ALCF in 1999), and one at Cornell. The ratio of stiffness between the streamwise–transverse oscillations is 18.9. Both of the cylinders have a mass ratio,  $m^* = 1.3$  and a mass-damping  $(m^* + C_A)\zeta = 0.185$  and are identically clamped. The blockage ratios are 2.6% (Cornell) and 1% (Michigan). The free-stream turbulence is less than 0.9% in both facilities. Over the range of Reynolds numbers,  $Re = 1000$ –2500, we take the Strouhal number as 0.208. The “Brazilian” cantilever is arranged with strain gauges, to infer the tip amplitudes. The tip amplitudes for the “Cornell” cantilever are measured directly using an optical bi-axial displacement transducer. In both arrangements, the initially vertical cantilever is clamped just above the water surface, and the gap between the cantilever tip and a false end plate within the channel, is kept close to 1 mm.

### 3. DYNAMICS OF THE FLEXIBLE CANTILEVER

Corresponding with the recent work in Pesce & Fuarra (2000), the response amplitude ( $A^* = A/D$ ), as a function of normalized velocity ( $U^*$ ) seems to exhibit two distinct branches, labelled here as the “initial” branch and the “lower” branch, and shown in Figure 2. (We define the normalized velocity by  $U^* = U/f_n D$ , with  $U$  = free-stream velocity,  $f_n$  = the natural frequency in water,  $D$  = diameter). Comparisons between techniques to measure amplitude response (computing the tip amplitude from strain data, versus using direct measurement of the tip deflections using optical methods) are quite reasonable, as shown in Figure 2. Despite the differences in the amplitudes of the lower branch, the oscillation frequencies match very well, and show similar behaviour to what is found for

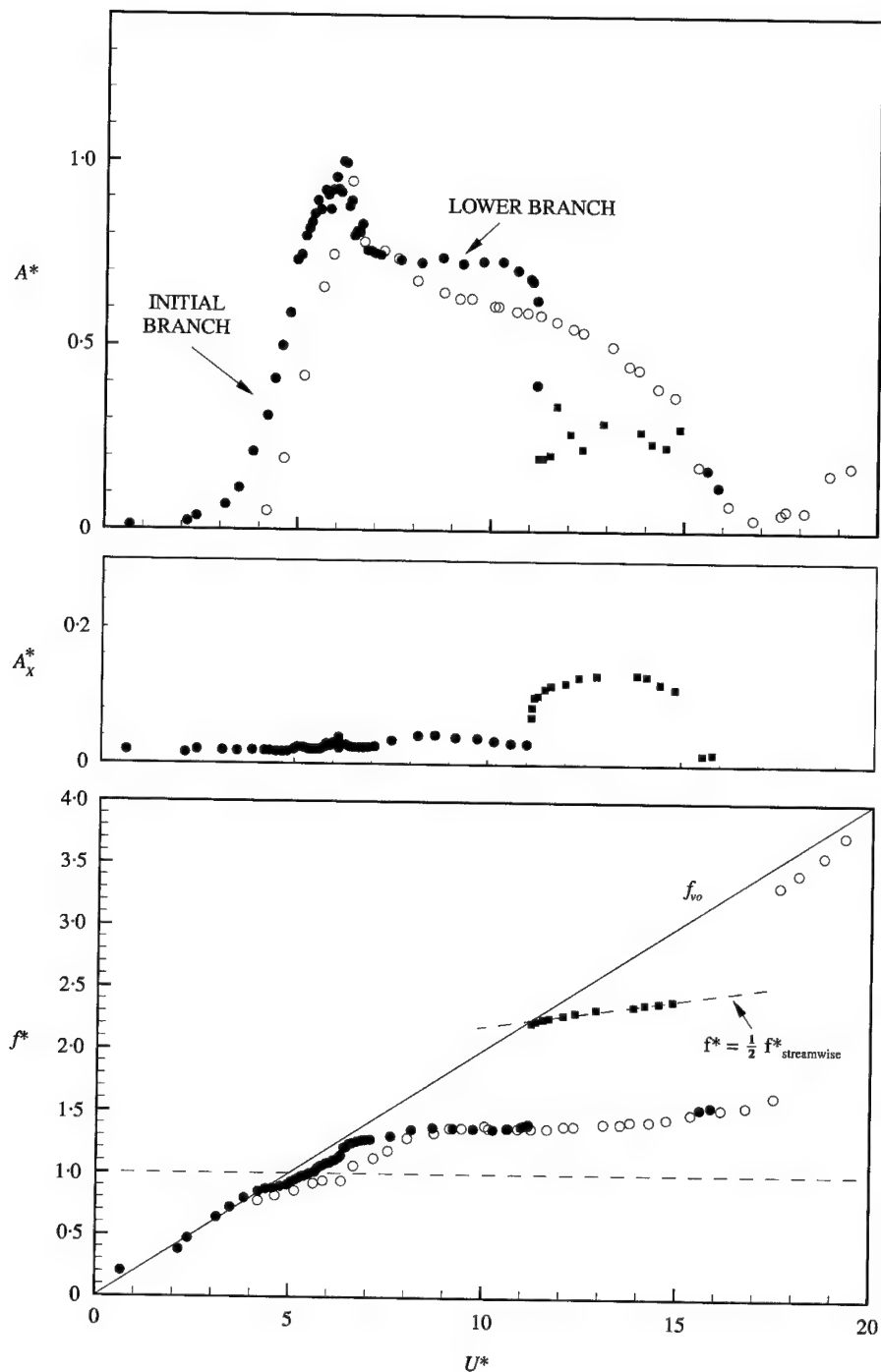


Figure 2. Amplitude response in the transverse direction ( $A^*$ ) and in the streamwise direction ( $A_x^*$ ), and frequency response ( $f^*$  = oscillation frequency/natural frequency), versus normalized velocity,  $U^*$ . The streamwise amplitudes were measured simultaneous with transverse vibrations, using an optical transducer (in the case of the solid symbols).  $\circ$ , cantilever (strain);  $\bullet$ , cantilever (optical);  $\blacksquare$ , cantilever (optical) where comparable streamwise oscillations exist.

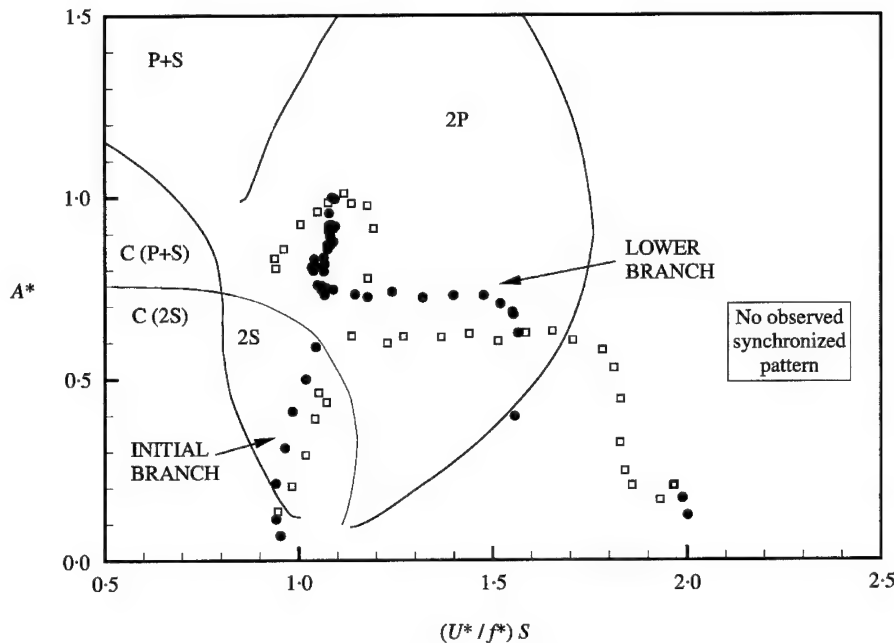


Figure 3. Comparison of cantilever amplitude response (●) with the response of an elastically-mounted rigid cylinder (□) at similar mass ratios ( $m^* = 1.3$  and  $1.2$ , respectively), using the “true normalized velocity”,  $(U^*/f^*)S$ . These amplitudes are superposed onto a map of vortex formation modes (2S, 2P, etc) as defined in Williamson & Roshko (1988).

rigid-cylinder vibrations. They lie well above the natural frequency (for  $U^* > 6$ ), and this is a characteristic of low mass ratio vortex-induced vibrations, as shown for example in Khalak & Williamson (1997b) and Gharib *et al.* (1998). In the presentation of Figure 2, the “initial” branch appears to be a single continuous branch.

It has recently been clarified by Govardhan & Williamson (2000) that elastically mounted rigid cylinders exhibit a three-mode response (initial-upper-lower branches) for low mass-damping ( $m^*\zeta$ ), and a two-mode response (only initial-lower branches) for high mass-damping. If we now directly compare the cantilever data, in Figure 3, with free vibrations of a rigid cylinder (Govardhan & Williamson 2000), at similar mass ratios ( $m^* = 1.3$  and  $1.2$ , respectively), they both exhibit an initial branch and a lower branch. However, the rigid cylinder case exhibits the three-mode type of response, and it is known that the data above  $A^* = 0.6$  corresponds to a separate “upper” branch, with a distinct vortex formation mode. The data in Figure 3 indicate that possibly the cantilever also has an “upper” branch, although to prove this point one would need to demonstrate a discontinuity in the initial response branch. Such a discontinuity is quite clear in the case of the rigid cylinder. In the case of the cantilever, it is possible that two vortex formation modes, defined as 2P and 2S mode (Williamson & Roshko 1988) exist simultaneously along the span, as suggested by the mode boundaries in Figure 3. Such a “hybrid” mode was found by Techet *et al.* (1998) for an oscillating tapered cylinder. Further understanding of this point would be forthcoming with the implementation of the PIV technique on this problem, and such experiments are presently planned.

A further interesting result for the cantilever is the large-amplitude transverse vibration response for high speeds,  $U^* > 12$ , in Figure 4. (These results are from the cantilever fitted with strain gauges, and comprise a separate set of experiments to those in Figure 2. We also

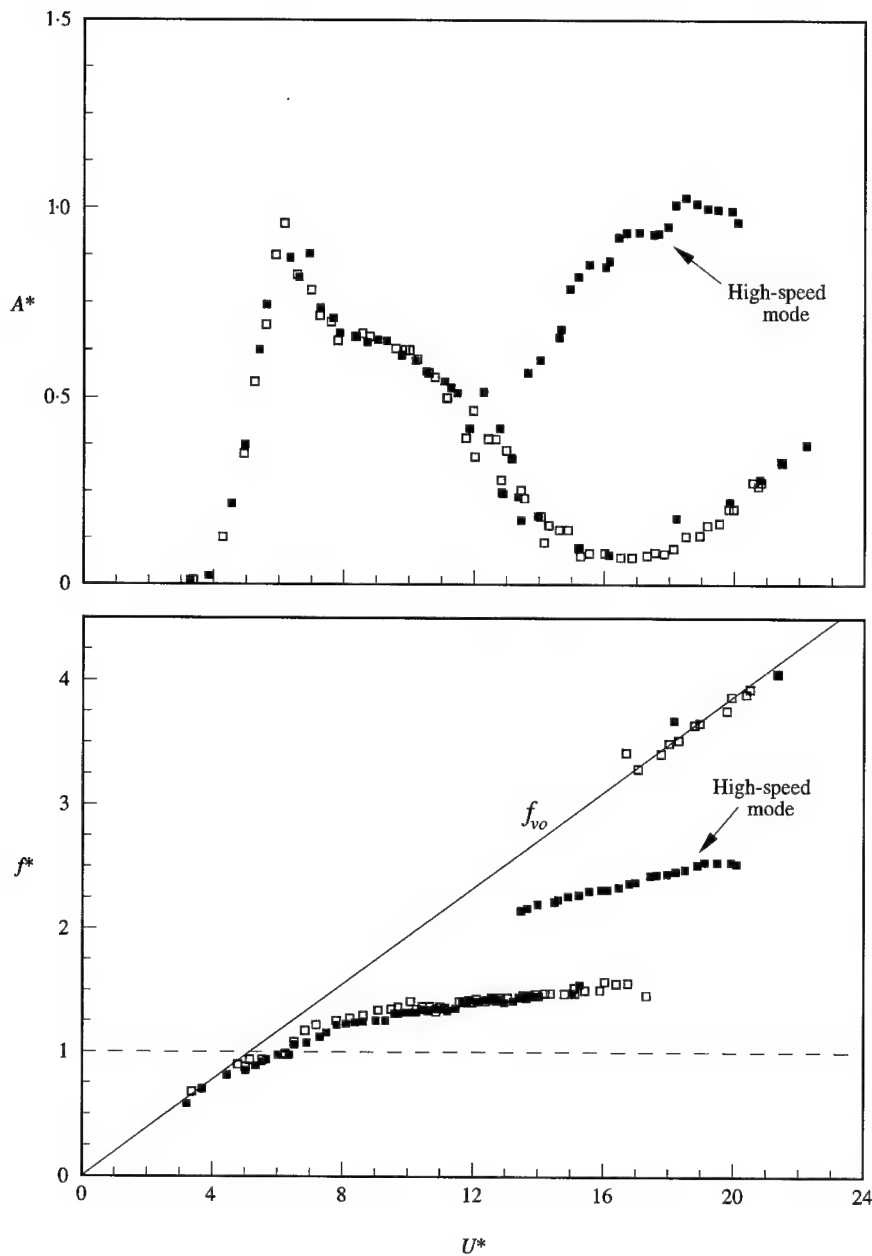


Figure 4. Tip amplitude and frequency response versus normalized velocity, as measured from the cantilever instrumented with strain gauges: ■, increasing velocity; □, decreasing velocity.

include here the upper amplitudes for  $U^* > 12$ , which were omitted from Figure 2, for clarity.) These data, along the high-amplitude branch for  $U^* > 12$ , are for increasing velocity, though evidence that the high-amplitude branch can be reached for decreasing velocities will be shown in a further more comprehensive study (Fujarra *et al.* 2001). The cause of this mode is apparently related to the simultaneous presence of streamwise and transverse vibrations. (This might be expected, because the natural frequency in the streamwise direction is roughly 4 times that for the transverse direction, yielding an

expected streamwise response at around  $U^* \sim 20$ .) In the other set of experiments (using optical diagnostics), shown in Figure 2, the square symbols for  $U^* > 12$  at amplitudes  $A^* \sim 0.25$ , correspond to conditions where the streamwise and transverse vibrations are comparable. There is evidently a strong correlation between the streamwise and transverse vibrations, as we find that the frequency of transverse vibration (square symbols in Figure 2) is exactly half the frequency for the streamwise oscillations, as measured using the optical technique. One may deduce that the frequency of the high-speed response of Figure 4 also reflects a streamwise-transverse coupling, and in fact this is clear from visual observation in the experiments, where the cantilever tip follows a figure-of-eight trajectory.

A similar response mode has been found by Kitagawa *et al.* (1999), at high normalized velocities,  $U^* = 14$ – $17$ , which they attribute to the influence of forcing from a vortex shedding cell of low frequency adjacent to the tip of their pivoted rod. It is conceivable that their response mode could also be associated with a coupled streamwise-transverse motion as found in the present work, although their oscillation amplitudes are far smaller,  $A^* \approx 0.05$ , and no streamwise amplitudes were measured to investigate this point.

#### 4. CONCLUSIONS

In summary, vortex-induced vibrations of a cantilever exhibit distinctly similar response modes as found for the elastically restrained rigid cylinder, despite the fact that the cantilever oscillation amplitude varies along the span. As velocity is increased, it appears that there are two branches of response in the case of the cantilever; whereas in the case of the elastically mounted rigid cylinder, three response branches are found, at comparable values of low mass and damping. Evidence for the existence of three response branches for the cantilever (not only an initial and lower branch, but also a separate upper branch) would require demonstration of a discontinuity in the initial response branch. It is planned to investigate the wake vortex dynamics at different points along the span, using the DPIV technique to determine wake vorticity.

A high-speed mode of large-amplitude response has been found, which is outside the principal synchronization regime, and which is associated with a streamwise-transverse vibration coupling. The natural frequency of the cantilever is higher in the streamwise direction (it has been made stiffer in that direction by enclosing a leaf spring within the rubber cantilever), and so the streamwise oscillations are excited at higher speeds. When streamwise vibrations are stimulated, the transverse frequency of this high-speed mode corresponds to precisely half the streamwise vibration frequency. Although the high-speed vibration mode of a pivoted rod, investigated by Kitagawa *et al.* (1999), yields much smaller amplitudes, it is conceivable that their vibrations may be related to coupled streamwise-transverse oscillations of the type observed here, since they also used a leaf spring as their pivot, restricting most of the motion to the transverse direction.

#### ACKNOWLEDGEMENTS

The authors particularly thank Prof. Noel Perkins (Michigan) and Prof. Julio Meneghini for enlightening discussions, and Professors Bernitsas, Troesch and Cohen, all at Michigan. The authors (Pesce and Fuarra) acknowledge the support of CNPq, Brazilian NRC, No. 304062-EM, and FAPESP, São Paulo Research Foundation, No. 98/00271-02, while the authors (Flemming and Williamson) acknowledge the support of the US Office of Naval Research, Ocean Engineering Division, monitored by Dr Tom Swean (ONR Contract No. N00014-95-1-0332). The authors acknowledge the superb help in the preparation of the manuscript by Dr Raghu Govardhan at Cornell.

## REFERENCES

- ATSAVAPRANEE, P. & WEI, T. 1999 DPIV and hot film measurements in the wake of an oscillating cylinder. *Bulletin of the American Physical Society* **42**, 2170.
- FUJARRA, A. L. C., PESCE, C. P. & PARRA, P. H. C. C. 1998 Vortex-induced vibrations experiments on a flexible cylinder. *Proceedings of the Eighth International Offshore and Polar Engineering Conference*, Vol. 3, pp. 393–399, Golden, CO: ISOPE.
- FUJARRA, A. L. C., PESCE, C. P., FLEMMING, F. & WILLIAMSON, C. H. K. 2001 Vibrations of a flexible cantilever in a fluid flow. In preparation.
- GHARIB, M. R., LEONARD, A., GHARIB, M. & ROSHKO, A. 1998 The absence of lock-in and the role of mass ratio. In *Proceedings of the 1998 Conference on Bluff-Body Wakes and Vortex-Induced Vibration* (eds P. W. Bearman & C. H. K. Williamson), Paper No. 24, Ithaca, NY: Cornell University.
- GOVARDHAN, R. & WILLIAMSON, C. H. K. 2000 Modes of vortex formation and frequency response for a freely vibrating cylinder. *Journal of Fluid Mechanics* **420**, 85–130.
- GRIFFIN, O. M. & SKOP, R. A. 1976 Vortex-Induced oscillations of structures. *Journal of Sound and Vibration* **44**, 303–305.
- KHALAK, A. & WILLIAMSON, C. H. K. 1996 Dynamics of a hydroelastic cylinder with very low mass and damping. *Journal of Fluids and Structures* **10**, 455–472.
- KHALAK, A. & WILLIAMSON, C. H. K. 1997a Investigation of the relative effects of mass and damping in vortex-induced vibration of a circular cylinder. *Journal of Wind Engineering and Industrial Aerodynamics* **69–71**, 341–350.
- KHALAK, A. & WILLIAMSON, C. H. K. 1997b Fluid forces and dynamics of a hydroelastic structure with very low mass and damping. *Journal of Fluids and Structures* **11**, 973–982.
- KHALAK, A. & WILLIAMSON, C. H. K. 1999 Motions, forces and mode transitions in vortex-induced vibrations at low mass-damping. *Journal of Fluids and Structures* **13**, 813–851.
- KING, R. 1974 Vortex-excited structural oscillations of a circular cylinder in flowing water. Ph.D. dissertation, Loughborough University of Technology, Loughborough, U.K.
- KITAGAWA, T., FUJINO, Y. & KIMURA, K. 1999 Effects of free end condition on end-cell induced vibration. *Journal of Fluids and Structures* **13**, 499–518.
- PESCE, C. P. & FUJARRA, A. L. C. 2000 Vortex-induced vibrations and jumping phenomenon: An experimental investigation with a clamped flexible cylinder in water. *International Journal of Offshore and Polar Engineering* **420**, 26–33.
- TECHET, A. H., HOVER, F. S. & TRIANTAFYLLOU, M. S. 1998 Vortical patterns behind a tapered cylinder oscillating transversely to a uniform flow. *Journal of Fluid Mechanics* **363**, 79–96.
- VICKERY, B. J. & WATKINS, R. D. 1964 Flow-induced vibrations of cylindrical structures. In *Proceedings of the First Australian Conference on Hydraulics and Fluid Mechanics* (ed. R. Silvester), pp. 213–241, New York: Pergamon Press.
- WILLIAMSON, C. H. K. & ROSHKO, A. 1988 Vortex formation in the wake of an oscillating cylinder. *Journal of Fluids and Structures* **2**, 355–381.



## NUMERICAL PREDICTION OF VIV ON LONG FLEXIBLE CIRCULAR CYLINDERS

R. H. J. WILLDEN AND J. M. R. GRAHAM

*Department of Aeronautics, Imperial College of Science, Technology and Medicine  
London, SW7 2BY, U.K.*

(Received 5 September 2000, and in final form 14 December 2000)

Two-dimensional and quasi-three-dimensional numerical methods have been employed to simulate the vortex-induced vibrations of a circular cylinder. A low Reynolds number two-dimensional study at low mass ratio and zero damping revealed lock-in across a large range of reduced velocities. For the low mass ratio cylinder simulated, the oscillatory frequency was found to be controlled by the fluid via its added mass. Oscillations far from the body's natural frequency were observed. The shear stress contributions to the transverse force acting on the body were very significant and play an important role in the dynamics of low Reynolds number vortex-induced vibrations. The quasi-three-dimensional method was employed to simulate the flow past a long stationary cylinder in shear flow. Cellular shedding was observed in its wake. The free transverse flexible vibrations of the same body exhibited significant spanwise correlation over a large length of the body despite the sheared inflow.

© 2001 Academic Press

### 1. INTRODUCTION

RISER PIPES ARE LONG FLEXIBLE, substantially vertical, circular cylinders used in the offshore industry to convey fluids from the sea bed to sea level and *vice-versa*. For exploration in ultra deep waters, risers of up to 2000 m length, yielding aspect ratios of order  $10^3$ , have been proposed. The Reynolds number associated with these flows is typically of order  $10^5$ .

Flexibly supported cylinders may undergo vortex-induced vibrations, through which the vortex-shedding frequency may lock on to a frequency of vibration of the structure. The range over which lock-in occurs depends on the vibration amplitude and on the mass and damping ratios. Flow-induced vibrations are a multiple-degree-of-freedom problem, in which coupling exists between motions in-line with and transverse to the stream. The amplitude of transverse oscillations can be of the order of one diameter and therefore present a potent source of fatigue as well as the possibility of clashing in multiple-cylinder assemblies.

Risers can be subject to currents with significant shear profiles, giving rise to large variations in the vortex-shedding frequency with depth. At any one depth the mode of vibration closest in frequency to the local natural vortex shedding frequency is the most likely to be excited. However, the influence of other modes of vibration excited by the current at other depths may result in constructive or destructive interference.

The vortex-induced vibrations of rigid cylinders have recently received renewed attention. In particular the multiple branching behaviour and hysteresis effects observed for the amplitude of free transverse vibrations of a circular cylinder at low mass and damping ratios have been the focus of many works (Brika & Laneville, 1995; Khalak & Williamson, 1999; Newman & Karniadakis, 1995). Due to the high aspect ratios of riser pipes, three-dimensional flow simulations at realistic Reynolds numbers are still considered infeasible. Lucor

*et al.* (2000) have simulated the flow over a flexible cable of aspect ratio 567, subject to a sheared current with a peak Reynolds number of 1000, a long way short of the values required for full riser computations.

Consequently, approximate techniques such as strip theory (Herfjord *et al.* 1999) have been used to simulate riser response. The technique employed in the present work is a quasi-three-dimensional extension of strip theory. A two-dimensional hybrid Eulerian/Lagrangian Navier–Stokes code (Graham 1988) is used to simulate the flow around several spanwise sections of the riser. These are linked hydrodynamically through a three-dimensional large-scale vortex lattice representation of the wake (Giannakidis & Graham 1997). A three-dimensional structural dynamics model is coupled to the fluid solver so as to predict the response.

The work presented here focuses on the flow-induced transverse vibrations of a rigid two-dimensional low mass cylinder, elastically mounted with zero damping, so as to excite a large response, and on the transverse vibrations of a long flexible cylinder in sheared flow.

## 2. SIMULATION METHOD

The two-dimensional Navier–Stokes solver and its quasi-three-dimensional extension are briefly described below along with the structural dynamics models and the fluid–structure interaction procedure. For a more detailed account see Willden & Graham (2000).

### 2.1. FLUID DYNAMICS MODELS

A first-order simulation is used to solve the two-dimensional incompressible Navier–Stokes equations in their velocity–vorticity formulation:

$$\frac{\partial \omega_z}{\partial t} + (\mathbf{u} \cdot \nabla) \omega_z = \nu \nabla^2 \omega_z, \quad (1)$$

where  $\omega_z$  is the spanwise vorticity component. A time-split approach is followed, whereby the diffusion of vorticity is treated in an Eulerian fashion by modelling the flow variables using linear finite element approximations on an unstructured mesh, and the convection is handled using a Lagrangian approach that employs discrete point vortices. The velocity field is evaluated through the finite element solution of the two-dimensional derivative of the Poisson equation relating velocity and vorticity:

$$\nabla^2 \mathbf{u} = -\nabla \wedge \boldsymbol{\omega}. \quad (2)$$

The Poisson equation relating pressure to velocity (divergence of the momentum equations), is solved using the finite element method to yield the pressure components of the body forces. Those due to viscous shear stresses at the wall,  $\tau_w$ , are computed from the vorticity at the wall, according to  $\tau_w(s) = -\mu \omega_z(s)$ , where  $s$  defines the tangent to the wall.

In three dimensions, multiple two-dimensional computational planes are placed along the cylinder span. These are linked hydrodynamically using an inviscid unsteady three-dimensional vortex lattice. The lattice is constructed so as to represent the three-dimensional vorticity field. This is done by updating its spanwise vorticity content from the underlying two-dimensional vorticity fields. The remaining vorticity components are deduced by constructing the lattice so as to be divergence free. The lattice is allowed to self-convect over the step. Once a part of the lattice passes the downstream extremities of the computational planes it can no longer be up-dated and is allowed to self-convect and distort into the far wake. The Biot–Savart law is used to retrieve velocity information from



the lattice, including  $\partial w / \partial z$ , the spanwise derivative of the spanwise velocity component. This provides a source term in the sectional solution of equation (2), which allows mass conservation in three dimensions to be retained. The far-field velocity boundary conditions of the computational planes are modified to include the velocities induced by the lattice.

## 2.2. STRUCTURAL DYNAMICS MODELS

A spring-mass-damper model is used to simulate the single-degree-of-freedom transverse vibration of a two-dimensional cylinder. The equation of motion for the cylinder displacement,  $y$ , in response to fluid loading, represented by the lift coefficient  $C_L$ , is given by

$$m \frac{d^2 y}{dt^2} + 2\beta m (2\pi f_n) \frac{dy}{dt} + m (2\pi f_n)^2 y = C_L(t) \frac{\rho U^2}{2} D, \quad (3)$$

where  $m$ ,  $f_n$  and  $\beta$  are the mass of the cylinder per unit length, the natural frequency of cylinder vibration and the fraction of critical viscous damping respectively;  $U$ ,  $\rho$  and  $D$  are the upstream velocity, the density of the fluid and the cylinder diameter, respectively.

The three-dimensional flexible cylinder is modelled as a bending beam under pre-tension using a linear finite element implementation of the Bernoulli-Euler beam equations. The model permits three degrees of freedom at each of the finite element nodes, axial and transverse displacements and a rotation about an axis normal to the plane of the displacements. The model incorporates tension, buoyancy and gravity but neglects structural damping.

The response of the cylinder to the fluid loading is calculated explicitly by both structural dynamics models. The fluid dynamics is subsequently solved implicitly.

## 3. RESULTS & DISCUSSION

### 3.1. TWO-DIMENSIONAL FREE TRANSVERSE VIBRATIONS OF A FLEXIBLY MOUNTED CYLINDER

The response of a circular cylinder free to vibrate in the transverse direction has been computed over a range of reduced velocities,  $V_r = U/f_n D$ , from 2.5 to 16. The simulations were performed on a continuous basis by incrementing the Reynolds number in small positive steps, starting with the cylinder at rest at  $Re = 50$  ( $V_r = 2.5$ ) and terminating at  $Re = 320$  ( $V_r = 16$ ). The purpose of this was to ensure that the simulations incorporated any fluid memory effects that may be seen experimentally with increasing flow speed. The mass and damping ratios,  $m^* = 2m/\rho D^2$  and  $\beta$ , of the cylinder are 1 and 0 respectively.

The nondimensional response amplitude,  $A/D$ , is shown in Figure 1 over the range of  $V_r$  simulated. The response amplitude at the start of the simulation,  $V_r = 2.5$ , is  $0.02D$ . Relatively small amplitude oscillations are maintained until  $V_r = 3.1$ , after which the response increases markedly with  $V_r$ . The increasing response amplitude starts to saturate at  $V_r = 4.7$  at an amplitude of  $0.47D$ . It is not until  $V_r = 6.1$  that the response peaks at  $0.50D$ . This amplitude is approximately maintained until the end of the simulation at  $V_r = 16$ . Although the flow past a circular cylinder is considered to be three-dimensional past a Reynolds number of approximately 190, the simulation was continued past this point,  $V_r = 9.5$ , on the premise that lock-in has two-dimensionalizing effects.

The oscillatory and vortex-shedding frequencies are defined as  $f_o$  and  $f_v$  respectively, with  $f_o = f_v$  at lock-in. It is apparent that at this low mass ratio the oscillatory and vortex-shedding frequencies remain locked-in to one another throughout the  $V_r$  range simulated.  $f_o/f_n$  (Figure 1) does not display the step at  $f_o/f_n \approx 1$  that characterizes lock-in for moderate to high mass ratios. Instead, the variation in  $f_o$  is close to linear and varies from  $0.29f_n$  at the

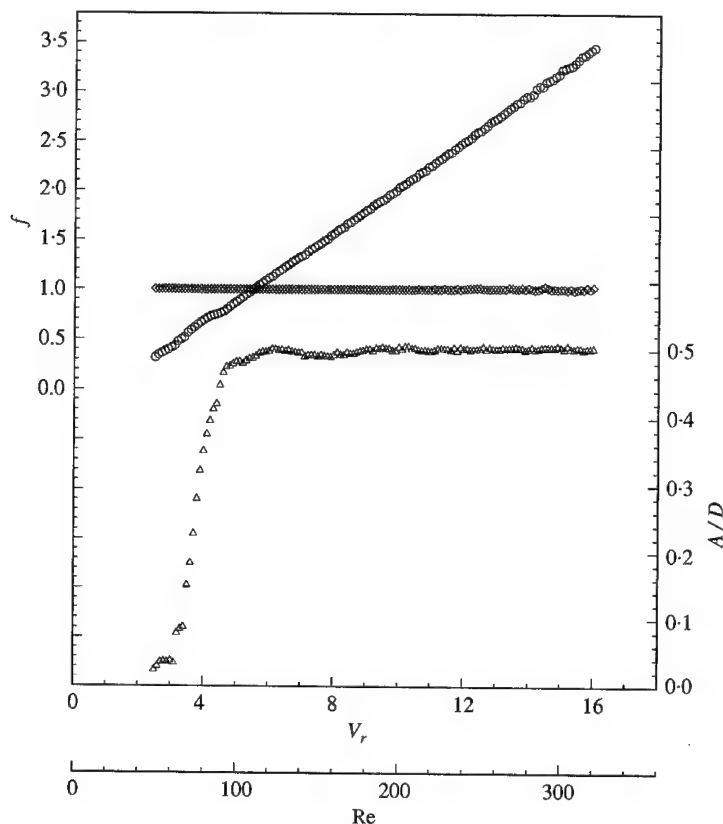


Figure 1. Amplitude and frequencies of a circular cylinder vibrating freely in the transverse direction for  $m^* = 1$ ,  $\beta = 0$ :  $\triangle$ ,  $A/D$ ;  $\circ$ ,  $f_o/f_n$ ;  $\diamond$ ,  $f_o/f_N$ .

start of the simulation to  $3.45f_n$  at its end. This infers that for this very low mass ratio, the fluid is dominant over the structure in controlling the oscillatory frequency throughout lock-in. The reverse of this is true where the lock-in step is observed.

The ability of the structure to oscillate far from its natural frequency is better understood by considering the role of the added mass,  $m_a = \hat{L}/A(2\pi f_o)^2$ , where  $\hat{L}$  is the amplitude of the component of the fluctuating lift force in phase with body displacement. Zero structural damping infers that  $\hat{L}$  is necessarily the amplitude of the total fluctuating lift force; hence,  $L(t) = \hat{L} \sin(2\pi f_o t)$ . This definition of  $m_a$  allows equation (3), in the absence of damping,  $\beta = 0$ , and for the case of lock-in,  $f_o = f_v$ , to be written as

$$(m + m_a) \frac{d^2 y}{dt^2} + m(2\pi f_n)^2 y = 0, \quad (4)$$

where  $y(t) = A \sin(2\pi f_o t)$ . An effective natural frequency of the combined fluid and structure system,  $f_N$ , may be defined according to  $f_N^2 = f_n^2/(1 + m_a/m)$ . Non-dimensionalizing  $f_o$  by  $f_N$  reveals that the body oscillates at or very close to  $f_N$  throughout lock-in (Figure 1).

The ratio  $m_a/m$  describes the relative magnitudes of the fluid and body inertia forces. At high values of this ratio the body behaves as if it is controlled by a forced motion at the vortex-shedding frequency. At low values the body oscillates near its natural frequency. Figure 2 displays  $m_a/m$  against  $f_o/f_n$  for the simulated data. At the start of the simulation

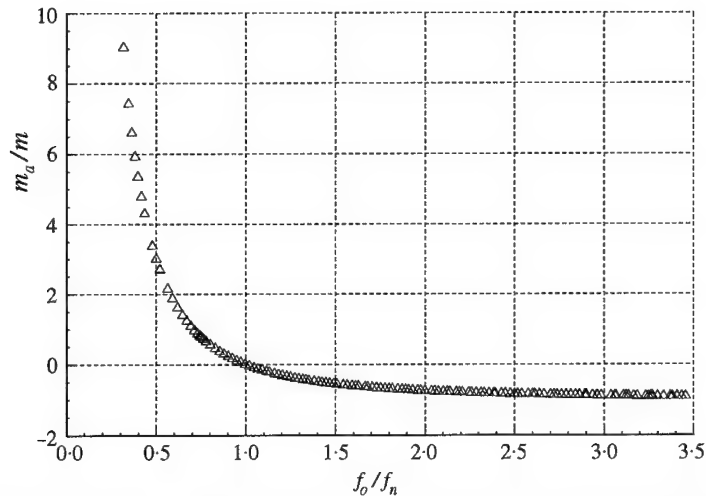


Figure 2. The added mass,  $m_a$ , of a circular cylinder vibrating freely in the transverse direction for  $m^* = 1$ ,  $\beta = 0$ .

$m_a/m$  peaks at 9.03. The added mass rapidly decreases with increasing  $V_r$  until it reaches zero, somewhere between  $V_r = 5.5$  and  $5.6$ , at which point the body is free to oscillate at its natural frequency,  $f_o/f_n = 1$ . Past this point, the added mass becomes negative as the lift force moves out of phase with the displacement. As  $V_r$  is increased still further,  $m_a/m$  asymptotes to a value close to  $-1$ ; the minimum value achieved is  $-0.91$  at  $V_r = 16$ .

Figure 3 depicts a selection of vortex particle images of the wake of the oscillating cylinder along with corresponding time traces of response, lift and drag coefficients,  $y/D$ ,  $C_L$  and  $C_D$ , respectively. Also shown are time traces, over different time periods for clarity, of the contributions to  $C_L$  by pressure forces and shear stresses,  $C_{Lp}$  and  $C_{Lf}$  respectively.

This figure depicts simulations at  $V_r = 3.9$ , where  $C_L(t)$  is in phase with  $y(t)$ , at  $V_r = 5.5$ , approximately at the phase change, and at  $V_r = 10.0$ , where  $C_L(t)$  is in anti-phase with  $y(t)$ . The shedding in all cases is of the 2S type. The increasing oscillatory amplitude with  $V_r$  is responsible for a breakdown in the stability of the von Kármán street due to larger transverse separations between vortices. Consequently the staggered vortex wake has to readjust itself in the middle-wake region, by rolling up and coalescing like signed pairs of vortices to form larger vortex structures, as depicted in the wake images for  $V_r = 5.5$  and  $10.0$ . The time traces for these two cases show slight modulations for which the frequencies are given by the differences in the frequencies of the near- and far-wake vortex structures.

The in-phase and anti-phase nature of  $y/D$  and  $C_L$  are best observed for cases  $V_r = 3.9$  and  $10.0$ , respectively. Less clear is the relative phase of the traces for  $V_r = 5.5$  which is made more complex by higher frequencies. A small phase difference between the pressure and shear stress contributions to  $C_L$  can be observed for  $V_r = 3.9$ . Both are approximately in phase with  $y/D$ . For the case just prior to the phase change,  $V_r = 5.5$ , there is a phase difference of approximately  $180^\circ$  between  $C_{Lp}$  and  $C_{Lf}$ ;  $C_{Lp}$  is in anti-phase with the displacement whilst  $C_{Lf}$  remains in phase. This phase difference between  $C_{Lp}$  and  $C_{Lf}$  persists until the end of the simulation at  $V_r = 16$ , as shown in the traces for  $V_r = 10.0$ .

Much of this information is summarized by Figure 4. The high relative magnitude of  $C_{Lf}$  with respect to  $C_{Lp}$ , in particular before the phase change ( $f_o = f_n$ ), is evident. The pressure contribution on its own changes phase with respect to the response between  $V_r = 4.8$  and  $4.9$ . The peak in the overall lift coefficient occurs at  $V_r = 3.9$  some way short of

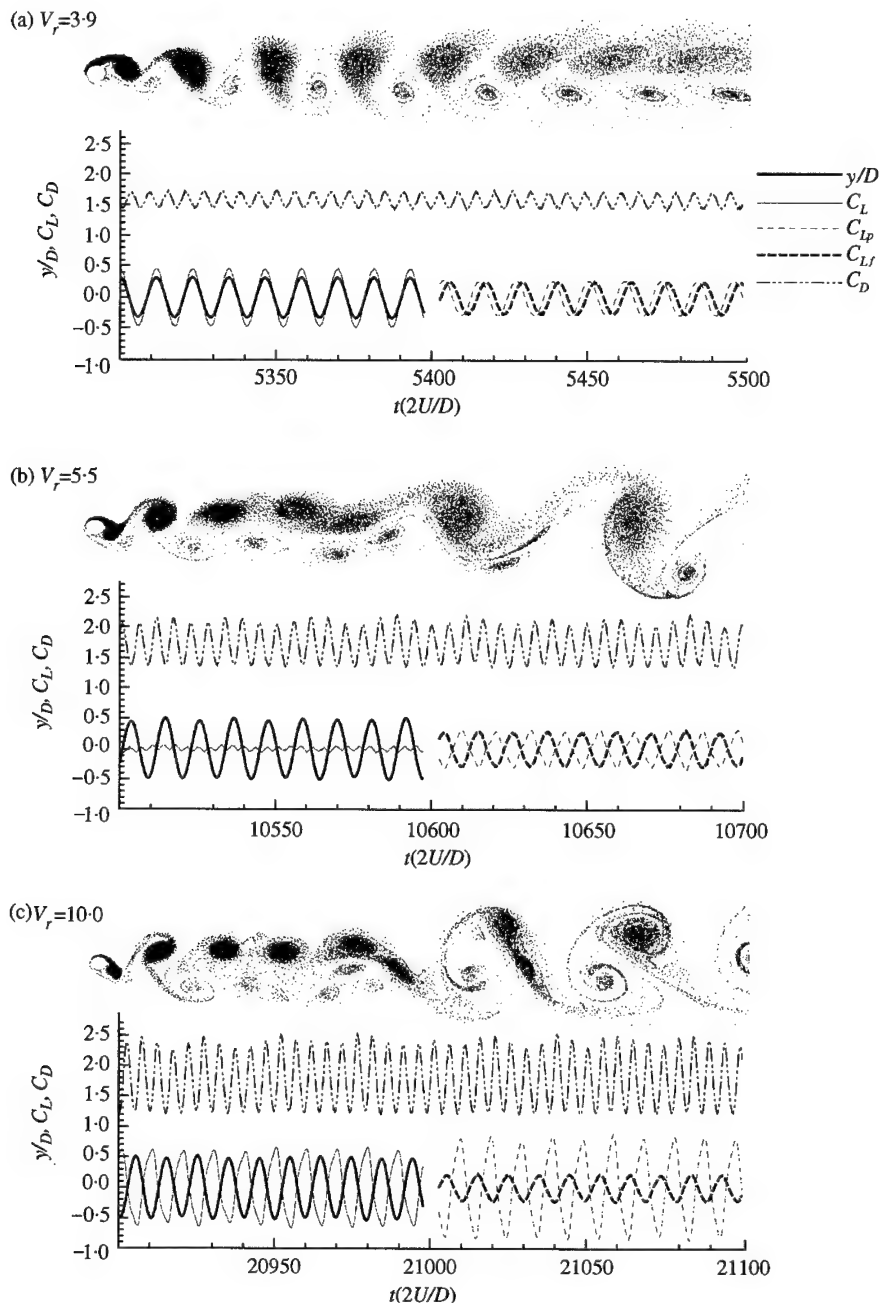


Figure 3. Particle images of the wake, response, lift and drag coefficient ( $y/D$ ,  $C_L$  and  $C_D$ ) histories of a circular cylinder vibrating freely in the transverse direction;  $m^* = 1$ ,  $\beta = 0$ , at reduced velocities, (a, b, c)  $V_r = 3.9$ ,  $5.5$  and  $10.0$ .

the  $V_r$  of the maximum response amplitude. This is in contrast to the higher Reynolds number observations of Khalak & Williamson (1999) who observed a peak in  $C_{L\text{rms}}$  just prior to the maximum response. The high relative magnitude of  $C_{Lf}$  at these low Reynolds numbers undoubtedly plays a role in these discrepancies.

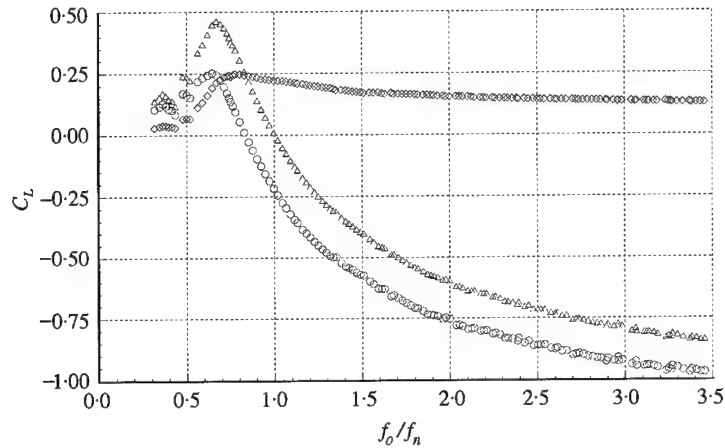


Figure 4. Variation of the component of the lift coefficient, in phase with body displacement, and its constituent parts with oscillatory frequency, for a circular cylinder vibrating freely in the transverse direction,  $m^* = 1$ ,  $\beta = 0$ :  $\Delta$ ,  $C_L$ ;  $\circ$ ,  $C_{Lp}$ ;  $\diamond$ ,  $C_{Lf}$ .

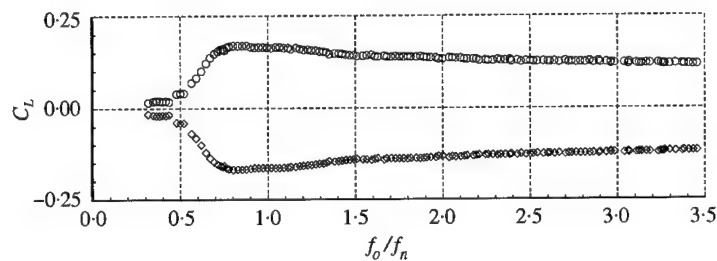


Figure 5. Variation of the constituent parts of the component of the lift coefficient in phase with body velocity with oscillatory frequency for a circular cylinder vibrating freely in the transverse direction,  $m^* = 1$ ,  $\beta = 0$ :  $\circ$ ,  $C_{Lp}$ ;  $\diamond$ ,  $C_{Lf}$ .

Although  $C_L$  must remain entirely in phase or out of phase with  $y/D$  since  $\beta = 0$ , the contributions to  $C_L$  from  $C_{Lp}$  and  $C_{Lf}$  may have components, of equal and opposite sign, in phase with the body velocity (Figure 5). The component of  $C_{Lp}$  in phase with velocity provides an excitation force as it remains positive throughout. This is balanced by the equivalent component of  $C_{Lf}$  which acts as hydrodynamic damping. The magnitudes of these components are not insignificant in comparison to  $C_L$ . The extraordinarily large shear force would appear to be constraining the motion that would otherwise be excited by the considerable component of  $C_{Lp}$  in phase with the body velocity.

### 3.2. FREE TRANSVERSE VIBRATIONS OF A THREE-DIMENSIONAL FLEXIBLE CYLINDER

The quasi-three-dimensional solver has been used to simulate the flow past a rigid cylinder, length 25 m and aspect ratio 100, subject to a sheared inflow. The inflow Reynolds number is linearly sheared from 200 at its top end to 100 at its bottom end. A particle and lattice image of the wake is shown in Figure 6. Although this figure yields limited insight into the structure of the wake, it demonstrates how the computational method works. Nine equally spaced computational planes are depicted in this figure, each separated by  $10D$ .

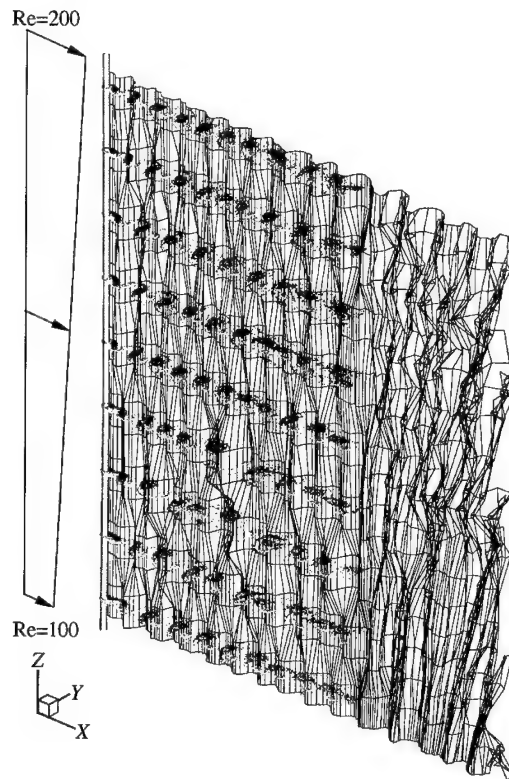


Figure 6. Particle and lattice visualisation of the flow behind a circular cylinder subjected to a sheared onset flow.

Figure 7 displays the spanwise Strouhal number variation as well as the time evolution of the lift coefficient acting on the cylinder. The Strouhal number varies from 0.156 at the low Reynolds number end to 0.185 at the upper end. The time evolution of  $C_L$  shows signs of cellular shedding, as has been widely reported for sheared flow. However, one must be cautious in identifying dislocations between such cells, given the coarse nature of the spanwise resolution.

The cylinder was then released and allowed to oscillate freely in the transverse direction, with its ends pinned. The stiffness and applied axial tension are  $19.8 \text{ MN m}^2$  and  $14.8 \text{ MN}$ , respectively. The tension was set deliberately high in order that the fundamental mode be excited. Buoyancy and gravity forces are ignored, and structural damping is set to zero. The mass ratio,  $m^* = 2m/\rho D^2$ , is 4.26, where  $m$  is the mass per unit length of the body.

The response (Figure 8) is close to that of the fundamental mode, except that the peak displacement,  $0.36D$ , is found towards the lower Reynolds number end at  $z/D = 44$ . The frequency of oscillation,  $f_o$ , is  $1.05f_n$ , where  $f_n$  is the frequency of the fundamental mode in a vacuum. In contrast with the lower mass ratio case simulated in two dimensions, the structure is dominant in modifying the shedding frequency towards the natural frequency. As indicated by Figure 9, the shedding frequencies at the end points remain relatively unperturbed by the oscillation, whereas those in between are significantly modified.

The lift coefficient evolution (Figure 9) shows significant spanwise correlation between  $z/D = 25$  and  $75$ , over which the shedding and oscillatory frequencies remain locked. At the location of the peak response,  $z/D = 44$ , the  $C_L$  evolution shows an abrupt phase change.

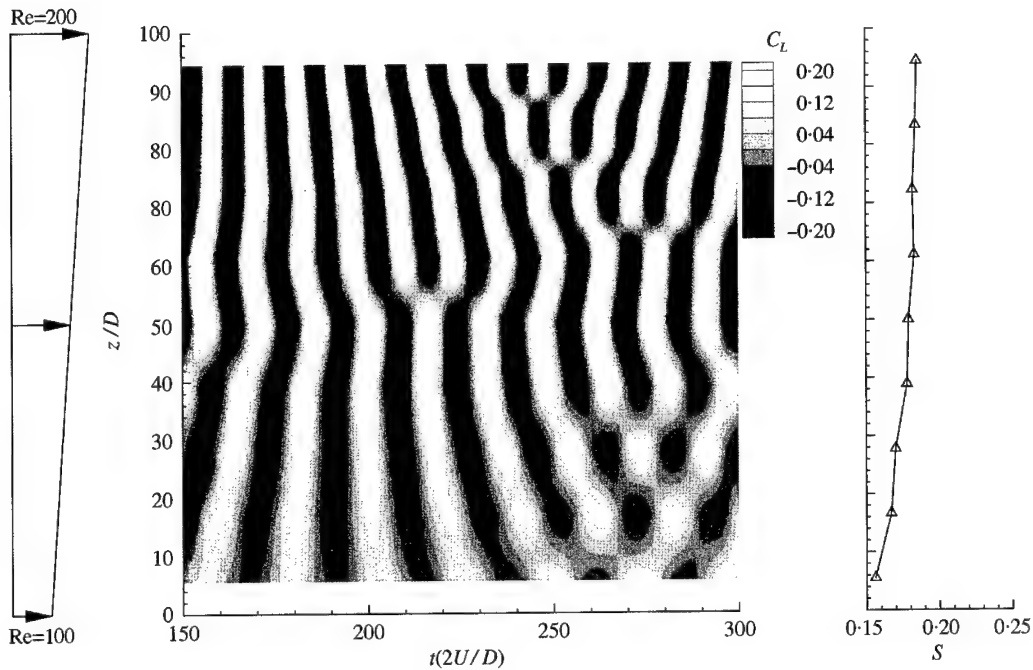


Figure 7. Spanwise Strouhal number,  $S$ , variation and time evolution of the lift coefficient,  $C_L$ , acting on a stationary circular cylinder subjected to a sheared onset flow.

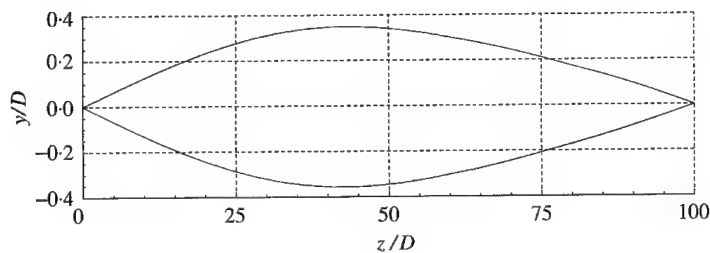


Figure 8. Response envelope of a circular cylinder subjected to a sheared onset flow, vibrating freely in the transverse direction.

On the lower  $V_r$  side,  $z/D < 44$ ,  $C_L$  and  $y/D$  remain in phase; towards the higher  $V_r$  end,  $z/D > 44$ ,  $C_L$  and  $y/D$  are in anti-phase. This phase change is not altogether unsurprising as to some degree it mimics the changes one would expect from a variable reduced velocity.

#### 4. CONCLUSIONS

The low Reynolds number two-dimensional simulations exhibited lock-in throughout. The ability of the fluid at low mass ratios to dominate over the structure in oscillating the body far from its natural frequency was observed. This was facilitated by considerable changes to the added mass. Very high shear stress contributions to the lift force were observed, which

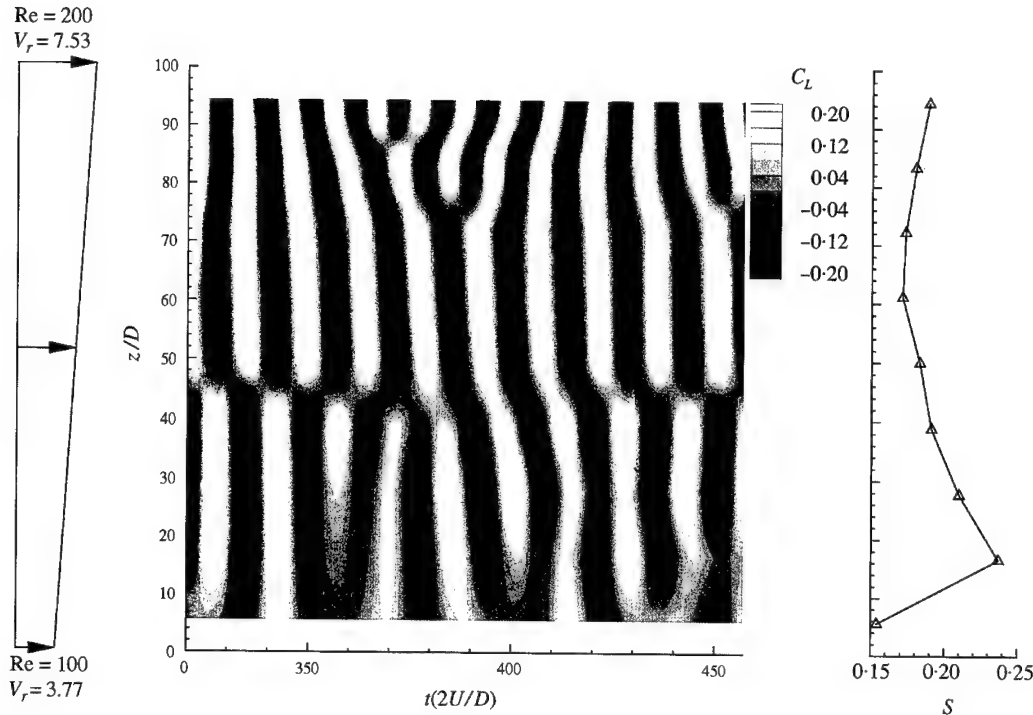


Figure 9. Spanwise Strouhal number,  $S$ , variation and time evolution of the lift coefficient,  $C_L$ , acting on a transversely oscillating flexible circular cylinder subjected to a sheared onset flow.

undoubtedly play a significant role in the dynamics of the vortex excited cylinder at low Reynolds numbers.

Cellular shedding in the wake of the three-dimensional circular cylinder, when subject to a sheared onset flow, was observed. Despite the shear, the transverse vibrations of the cylinder were seen to correlate the vortex shedding over a substantial proportion of the body's length whilst towards its ends little synchronization was observed.

#### ACKNOWLEDGEMENTS

The financial support of BP and of the U.K. EPSRC is acknowledged for this work.

#### REFERENCES

- BRIKA, D. & LANEVILLE, A. 1995 The hysteresis and bifurcation phenomena in the aeolian vibrations of a circular cylinder. In *Flow-Induced Vibration* (ed. P. W. Bearman), pp. 27–38, Rotterdam: A. A. Balkema.
- GIANNAKIDIS, G. & GRAHAM, J. M. R. 1997 Prediction of the loading on a HAWT rotor including effects of stall. In *EWEC97* (ed. R. Watson), pp. 434–439, Dublin: IWEA.
- GRAHAM, J. M. R. 1988 Computation of viscous separated flow using a particle method. In *Numerical Methods for Fluid Dynamics III*, IMA Conference Series 17, 310–317.
- HERFJORD, K., LARSEN, C. M., FURNES, G., HOLMÅS, T. & RANDA, K. 1999 FSI-simulation of vortex-induced vibrations of offshore structures. In *Computational Methods for Fluid-Structure Interaction* (eds T. Kvamsdal *et al.*), pp. 283–303, Trondheim: Tapir.
- KHALAK, A. & WILLIAMSON, C. H. K. 1999 Motions, Forces and Mode Transitions in Vortex-Induced Vibrations at Low Mass-Damping. *Journal of Fluids and Structures* **13**, 813–851.



- LUCOR, D., EVANGELINOS, C. & KARNIADAKIS, G. E. 2000 DNS-derived force distribution on flexible cylinders subject to VIV with shear flow. In *Flow-Induced Vibration* (eds S. Ziada & T. Staubli), pp. 281–287, Rotterdam: A. A. Balkema.
- NEWMAN, D. & KARNIADAKIS, G. E. 1995 Direct numerical simulations of flow over a flexible cable. In *Flow-Induced Vibration* (ed. P. W. Bearman), pp. 193–203, Rotterdam: A. A. Balkema.
- WILLDEN, R. H. J. & GRAHAM, J. M. R. 2000 Vortex induced vibration of deep water risers. In *Flow-Induced Vibration* (eds S. Ziada & T. Staubli), pp. 29–36, Rotterdam: A. A. Balkema.

## NOTICE

Under the terms of the U.S. copyright law effective January, 1, 1978, and the copyright laws of many other countries, journal publishers are required to obtain written confirmation from authors to acquire copyright rights for papers published in their journals. We ask your cooperation because it is of vital importance for the widest possible dissemination of your paper. We must have your written confirmation to authorize libraries and other information centers to use this material and to perform other appropriate publishing functions. We are therefore asking you to sign and return the applicable section of the form enclosed with this notice. **PLEASE SIGN ONLY THE APPLICABLE SECTION.**

**Which section of the form should you sign?** If you and your co-authors, if any, own rights in your paper as individuals (for example, you are working at a university or research institute, even if you are supported by a government grant), please sign **Section A** of the attached form. If you work for a corporation that owns the rights in the paper, please have an authorized officer of the corporation sign **Section B**. If the paper is in the public domain because you and all your co-authors created it within the scope of your employment with the U.S. government, please sign **Section C**. If the paper is subject to Crown copyright because you and all your co-authors are employees of the British or Canadian government, please sign **Section C**. If not all authors are government employees, then the nongovernment author should sign Section A. If any governmental entity other than the U.S., British, or Canadian government owns copyright, please call Academic Press at the number below. No manuscript will be processed until the appropriate form has been returned.

If your manuscript is not published within a reasonable period of time after acceptance, upon written request, AP will promptly return the rights to the manuscript to the author(s).

### General Terms of Publication in Academic Press Journals

#### 1. Author Warranties

- 1.1 The work submitted for review is new and has been written by the stated authors and has not been published elsewhere.
- 1.2 The work submitted is not currently under review for another journal and will not be submitted to another journal while under review for the present journal.
- 1.3 Submission of the work has been approved by all the authors and by the institutions where the work was carried out. Written authorization may be required at the Editor's discretion. For works with multiple authors, all the authors participated meaningfully in the work and agree on the submitted version of the work.
- 1.4 Any person cited in the work as a source of personal communications has approved such citation.
- 1.5 Submitted paper and electronic versions of the work are identical, except for elements that cannot be represented on paper.
- 1.6 All necessary permissions for the reproduction or excerpting of the work of others have been obtained.

#### 2. Understandings

- 2.1 All works submitted to Academic Press journals are subject to peer review, a process that is the responsibility of the Editors.
- 2.2 The authors agree that, if the work is accepted for publication, they will transfer the copyright in it exclusively to Academic Press, including the right of reproduction in all forms and media, whether now known or hereafter developed, and the right to include it in collections and databases.

#### 3. Personal Servers

- 3.1 Upon submitting an article to an Academic Press journal for review and possible publication, the authors are requested to add the following notice to the first screen of any posted electronic preprint versions of the paper: *This work has been submitted to Academic Press for possible publication. Copyright may be transferred without notice, after which this version may no longer be accessible.* Authors should note that posting the entire work may be regarded as prior publication by some journal editors (see Information for Authors of the specific journal).
- 3.2 When an Academic Press journal accepts the work for publication, the authors may post it, in its final accepted form, on their personal servers (but not on any organized preprint server) with a notice *Accepted for publication in <name of journal> as of <date>*, until it is published by Academic Press in print or electronic form.
- 3.3 After publication, authors may post their Academic Press copyrighted material on their own servers without permission, provided that the server displays as the first line of the HTML page the following notice alerting readers to their obligations with respect to copyrighted material: *This material has been published in <name of journal, issue number and date, page number>, the only definitive repository of the content that has been certified and accepted after peer review. Copyright and all rights therein are retained by Academic Press. This material may not be copied or reposted without explicit permission.* The posted work must also include the Academic Press copyright notice (Copyright © 200x by Academic Press) and a link to IDEAL (International Digital Electronic Access Library) at <http://www.idealibrary.com>.

**IMPORTANT:** Note that Academic Press may choose to publish an abstract or portions of the paper prior to publishing the paper in the journal. Please contact Academic Press immediately if you would like Academic Press to refrain from such prior publication for any reason, including disclosure of a patentable invention.

If you have any questions about the procedures, please call Academic Press at +1 (619)699-6413.

Please **return the form** to *Journal of Fluids and Structures*, Academic Press, 32 Jamestown Road, London NW1 7BY, UK.

Thank you.

## Copyright Transfer Agreement

Journal: \_\_\_\_\_

Tentative Manuscript Title: \_\_\_\_\_

Authors: \_\_\_\_\_

**A. University/research institute employees and others who own rights as individuals.** You hereby confirm the assignment to Academic Press (AP) of the entire copyright in and to the manuscript named above (the Work) throughout the world in all forms and media, whether now known or hereafter developed, and in all languages effective if and when it is accepted for publication by AP. You agree to abide by the terms of publication stated on the accompanying notice. You also warrant that the Work has not been published before and contains no materials the publication of which would violate any copyright or other personal or proprietary right of any person or entity, and you acknowledge that AP is relying on this document in publishing this Work. Notwithstanding the assignment of copyright to AP, you:

1. Retain patent rights, if any.
2. May make photocopies of all or part of the Work for use in your classroom teaching.
3. May use your original figures/tables/illustrations/photographs from the Work in future works of your own.
4. May include the Work as part of your dissertation, for noncommercial distribution only.

You agree that all copies and inclusions made under the above conditions will carry a notice of copyright and a citation to the journal article.

To be signed by all the authors (or by an author who has obtained the written assent of the nonsigning authors).

Signed: \_\_\_\_\_ Date: \_\_\_\_\_

**B. Corporate employees.** The Work was written as part of the duties of the author as an employee of the company signing below or otherwise as a "work made for hire" (as defined in the relevant copyright law) for such company. As the authorized representative of such company, you hereby confirm the assignment to AP of the entire copyright in and to the Work throughout the world in all forms and media, whether now known or hereafter developed, and in all languages effective if and when it is accepted for publication by AP. You agree to abide by the terms of publication stated on the accompanying notice. You also warrant that the Work has not been published before and contains no materials the publication of which would violate any copyright or other personal or proprietary right of any person or entity, and you acknowledge that AP is relying on this document in publishing this Work. Notwithstanding the assignment of copyright to AP, you:

1. Retain patent rights, if any.
2. May prepare derivative works based on the Work, with proper acknowledgment.
3. May reproduce the Work in reasonable quantities for internal use, with proper acknowledgment. However, copies of the Work may not be used for resale or in any way that implies that AP, the journal, or the editorial board endorses any procedures or products of your company.

Signed: \_\_\_\_\_ Date: \_\_\_\_\_

Title: \_\_\_\_\_

**C. Government employees.** You certify that the Work has been written as part of your official duties either as (a) an employee of the U.S. government or another government whose works are not subject to copyright protection, and as such there is no copyright to transfer, or as (b) an employee of the British, Canadian, or other government whose works are subject to Crown copyright, and via the authorized signature of the relevant government entity below, AP is hereby obtaining a nonexclusive license to publish (and to authorize others to publish) the Work in all forms and media, whether now known or hereafter developed, and in all languages effective if and when it is accepted for publication. If not all of the authors are government employees, one of the nongovernment employees should sign Section A. You also warrant that the Work has not been published before and contains no materials the publication of which would violate any copyright or other personal or proprietary right of any person or entity, and you acknowledge that AP is relying on this document in publishing this Work.

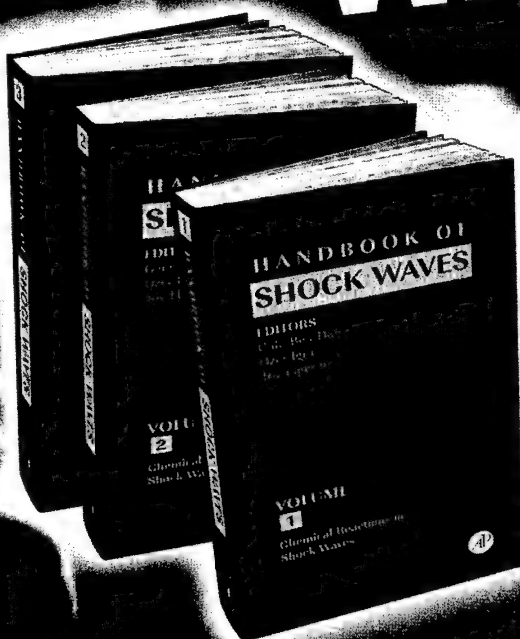
To be signed by all the authors (or by an author who has obtained the written assent of the nonsigning authors).

Signed: \_\_\_\_\_ Date: \_\_\_\_\_

Government authorization (if needed): \_\_\_\_\_ Date: \_\_\_\_\_

# HANDBOOK OF SHOCK WAVES

**First Handbook Ever  
To Include Under One  
Separate Cover:  
Experimental, Theoretical,  
And Numerical Results**



*Edited By*

**Gabi Ben-Dor**

Ben-Gurion University of the Negev,  
Beer-Sheva, Israel

**Ozer Igra**

Ben-Gurion University of the Negev,  
Beer-Sheva, Israel

**Tov Elperin**

Ben-Gurion University of the Negev,  
Beer-Sheva, Israel

*Guest Editor*

**Assa Lifshitz**

The Hebrew University of Jerusalem,  
Jerusalem, Israel

ISBN: 0-12-086430-4

Fall 2000, Casebound, Three-Volume Set

List Price: \$1,500.00/£1,000.00

## RELATED TITLES

These and an extensive list of other related titles can be found at  
[www.academicpress.com/physics](http://www.academicpress.com/physics) and [www.academicpress.com/engineering](http://www.academicpress.com/engineering)

**Handbook of Infrared and Raman  
Spectra of Inorganic Compounds and  
Organic Salts, Four-Volume Set**

Richard A. Nyquist, Ronald O. Kagel

1996, \$1,213.00/ISBN: 0-12-523444-9

**Fluid Mechanics**

Pijush K. Kundu

1990, \$69.95/ISBN: 0-12-428770-0

[www.academicpress.com/shockwaves](http://www.academicpress.com/shockwaves)

Order from your local bookseller or directly from:

### ACADEMIC PRESS

Order Fulfillment Dept. DM27098

6277 Sea Harbor Drive, Orlando FL 32887

Call Toll Free: 1-800-321-5068

Fax: 1-800-874-6418

E-mail: [ap@acad.com](mailto:ap@acad.com)

### HARCOURT, INC.

Customer Service Department

Foots Cray High Street, Sidcup, Kent DA14 5HP, UK

Tel: 44 208 308 5700

Fax: 44 208 308 5702

E-mail: [cservice@harcourt.com](mailto:cservice@harcourt.com)



**ACADEMIC  
PRESS**

A Harcourt Science and  
Technology Company

Secure online ordering: [www.academicpress.com](http://www.academicpress.com) or [www.harcourt-international.com](http://www.harcourt-international.com)

Prices and publication dates subject to change without notice. ©2001 by Academic Press. All Rights Reserved. LN/SLR/PECS—16011-D 1/01

[www.academicpress.com/elasticproperties](http://www.academicpress.com/elasticproperties)

# Handbook of Elastic Properties of Solids, Liquids, and Gases

## Volume 1

Dynamic Methods for Measuring the Elastic Properties of Solids

## Volume 2

Elastic Properties of Solids: Theory, Elements and Compounds, Novel Materials, Technological Materials, Alloys, Building Materials

## Volume 3

Elastic Properties of Solids: Biological and Organic Materials, Earth and Marine Sciences

## Volume 4

Elastic Properties of Fluids: Liquids and Gases

Edited By

**Moises Levy**

University of Wisconsin at Milwaukee

**Henry Bass**

University of Mississippi

**Richard Stern**

Pennsylvania State University

Supervising Editor

**Veerle Keppens**

University of Mississippi

### RELATED TITLES

FOURIER ACOUSTICS

Earl Williams

ISBN: 0-12-753960-3

FOUNDATIONS OF ENGINEERING ACOUSTICS

Frank J. Fahy

ISBN: 0-12-247665-4

ACOUSTIC AND ELECTROMAGNETIC SCATTERING ANALYSIS

Adrian Doicu, Yuri A. Eremin, Thomas Wriedt

ISBN: 0-12-219740-2

For more information visit:

[www.academicpress.com/acousticsandvibrations](http://www.academicpress.com/acousticsandvibrations)

and [www.academicpress.com/materials](http://www.academicpress.com/materials)

### RELATED JOURNALS

Journal of Sound and Vibration

[www.academicpress.com/jsc](http://www.academicpress.com/jsc)

Journal of Fluids and Structure

[www.academicpress.com/jfs](http://www.academicpress.com/jfs)

Mechanical Systems and Signal Processing

[www.academicpress.com/mssp](http://www.academicpress.com/mssp)

October 2000, Four-Volume Set,

ISBN: 0-12-445760-6

List Price: \$1,500.00 / £1000.00



**ACADEMIC PRESS**

A Harcourt Science and Technology Company

Order from your local bookseller or directly from:

#### ACADEMIC PRESS

Order Fulfillment Dept. DM27098

6277 Sea Harbor Drive

Orlando FL 32887

Call Toll Free: 1-800-321-5068

Fax: 1-800-874-6418

E-mail: [ap@acad.com](mailto:ap@acad.com)

#### HARCOURT, INC.

Customer Service Department

Foots Cray High Street

Sidcup, Kent DA14 5HP, UK

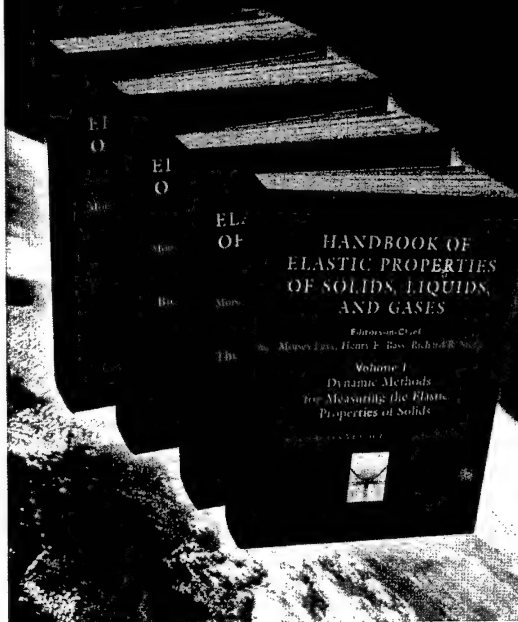
Tel: 44 208 308 5700

Fax: 44 208 308 5702

E-mail: [cservice@harcourt.com](mailto:cservice@harcourt.com)

Secure online ordering: [www.academicpress.com](http://www.academicpress.com)  
or [www.harcourt-international.com](http://www.harcourt-international.com)

Prices and publication dates subject to change without notice. ©2001 by Academic Press. All Rights Reserved. LN/SLR/PECS—20120 1/01



## CONTENTS

INTRODUCTION . . . . .	375
HOURIGAN, K., THOMPSON, M. C. AND TAN, B. T. Self-Sustained Oscillations in Flows Around Long Blunt Plates . . . . .	387
KIYA, M., MOCHIZUKI, O. AND ISHIKAWA, H. Interaction Between Vortex Rings and A Separated Shear Layer: Towards Active Control of Separation Zones . . . . .	399
LEONARD, A. AND ROSHKO, A. Aspects of Flow-Induced Vibration . . . . .	415
ROCKWELL, D., LIN, J.-C., CETINER, O., DOWNES, K. AND YANG, Y. Quantitative Imaging of The Wake of a Cylinder In a Steady Current and Free-Surface Waves . . . . .	427
LE GAL, P., NADIM A. AND THOMPSON, M. Hysteresis in the Forced Stuart-Landau Equation: Application to Vortex Shedding from an Oscillating Cylinder . . . . .	445
NORBERG, C. Flow Around a Circular Cylinder: Aspects of Fluctuating Lift . . . . .	459
PIER, B. AND HUERRE, P. Nonlinear Synchronization in Open Flows . . . . .	471
BLACKBURN, H. M., GOVARDHAN, R. N. AND WILLIAMSON, C. H. K. A Complementary Numerical and Physical Investigation of Vortex-Induced Vibration . . . . .	481
GOVARDHAN, R. AND WILLIAMSON C. H. K. Mean and Fluctuating Velocity Fields in The Wake of a Freely-Vibrating Cylinder . . . . .	489
HOVER, F. S. AND TRAIANTAFYLLOU, M. S. Galloping Response of a Cylinder with Upstream Wake Interference. . . . .	503
STANSBY, P. K. AND RAINEY, R. C. T. A CFD Study of The Dynamic Response of a Rotating Cylinder in a Current . . . . .	513
CARBERRY, J., SHERIDAN, J. AND ROCKWELL, D. Forces and Wake Modes of an Oscillating Cylinder . . . . .	523
JEON, D. AND GHARIB, M. On Circular Cylinders Undergoing Two-Degree-of-Freedom Forced Motions . . . . .	533
BRÜCKER, C. Spatio-Temporal Reconstruction of Vortex Dynamics in Axisymmetric Wakes . . . . .	543
JAUVTIS, N., GOVARDHAN, R. AND WILLIAMSON, C. H. K. Multiple Modes of Vortex-Induced Vibration of a Sphere. . . . .	555
SCHOUVEILLER, L. AND PROVANSAL, M. Periodic Wakes of Low Aspect Ratio Cylinders with Free Hemispherical Ends. . . . .	565
THOMPSON, M. C., LEWEKE, T. AND PROVANSAL, M. Kinematics and Dynamics of Sphere Wake Transition . . . . .	575
DAREKAR, R. M. AND SHERWIN, S. J. Flow Past a Bluff Body with a Wavy Stagnation Face . . . . .	587

OWEN, J. C., BEARMAN, P. W. AND SZEWCZYK, A. A. Passive Control of VIV with Drag Reduction . . . . .	597
THOMPSON, M. C., LEWEKE, T. AND WILLIAMSON C. H. K. The Physical Mechanism of Transition in Bluff Body Wakes . . . . .	607
DALTON, C., XU, Y. AND OWEN, J. C. The Suppression of Lift on a Circular Cylinder Due To Vortex Shedding at Moderate Reynolds Numbers . . . . .	617
ALLEN, J. J. AND SMITS, A. J. Energy Harvesting Eel . . . . .	629
LUCOR, D., IMAS, L. AND KARNIADAKIS, G. E. Vortex Dislocations and Force Distribution of Long Flexible Cylinders Subjected to Sheared Flows . . . . .	641
FUJARRA, A. L. C., PESCE, C. P., FLEMMING, F. AND WILLIAMSON, C. H. K. Vortex-Induced Vibration of a Flexible Cantilever . . . . .	651
WILLDEN, R. H. J. AND GRAHAM, J. M. R. Numerical Prediction of VIV on Long Flexible Circular Cylinders. . . . .	659

## Aim and Scope

The *Journal of Fluids and Structures* serves as a focal point and a forum for the exchange of ideas, for the many kinds of specialists and practitioners concerned with fluid-structure interactions and the dynamics of systems related thereto, in any field. One of its aims is to foster the cross-fertilization of ideas, methods and techniques in the various disciplines involved.

The Journal publishes original full-length papers and brief communications on (a) fundamental aspects of excitation mechanisms and fluid-structure interaction processes, flow- and flow-acoustic excited phenomena, independent of any concrete application or area of specialization; (b) application-oriented or -inspired papers dealing with fluid-structure interactions, flow-induced excitation, flow-induced instability and vibration of structures in various fields—involving “internal flows”, e.g. in piping, turbomachinery, heat exchangers or physiological systems; or “external flows”, e.g. in aeroelasticity and other relevant aeronautical applications, offshore and marine problems, and wind-induced phenomena; (a) appropriate topics in unsteady fluid dynamics. Theoretical, analysis or computational, and experimental research papers in any of the foregoing areas are of interest, as well as review articles.

Important new findings, new ideas and breakthroughs in the field may be published on a priority basis, extra fast, as a brief *special Letters to the Editor*.

## Submission of Manuscripts

Papers may be submitted to the Editor or to one of the Associate Editors (see inside front cover for names and addresses) whose area of specialization is closest to the subject matter of the paper. Each paper is subject to review and criticism by independent referees: the authors are provided with copies of their comments, so that appropriate revisions may be effected prior to publication. The Editor together with the Editorial Board are responsible for Journal policy. The Journal is published in the English language.

Comments on previously published work and brief preliminary reports on new work, should be submitted as Brief Notes or Letters to the Editor. Breakthrough-type Letters should be submitted by fax.

Announcements of, and brief reports on, relevant meetings or discussions may be submitted for publication. Books may be submitted for review, and advertisements may be accepted.

For any item to be published in a given issue of the Journal, the *final* manuscript must reach the Editor at least 14 weeks before the publication date.

Manuscripts of papers should be submitted in quadruplicate. Careful preparation will aid publication: carelessness will cause delay.

When supplying your final article please include, where possible, a disc of your manuscript prepared on PC-compatible or Apple Macintosh computers, **along with the hard copy print-out**. 5¼" or 3½" sized discs and most word processing packages are acceptable, although any version of WordPerfect or Microsoft Word are preferred.

## Preparation of Manuscripts

Detailed **Information for Authors** is printed in the last pages of some issues of the Journal. This includes information regarding **Preparation of Manuscripts**, which should be adhered to as closely as possible.



Special Issue on  
Bluff Body Wakes and Vortex - Induced Vibrations  
edited by  
T. Leweke, P. W. Bearman and C. H. K. Williamson

For Contents see inside back pages.

Journal title is covered in *Applied Mechanics Reviews*; *Bioengineering Abstracts*; *Current Contents/Engineering, Computing and Technology*; *Engineered Materials Abstracts*; *Fluid Abstracts (Civil Engineering)*; *Fluid Abstracts (Process Engineering)*; *FLUIDEX*; *Geo Abstracts (Geobase)*; *HTFS Digest*; *International Aerospace Abstracts*; *Mechanics*; *MSCI*; *Research Alert*; *Science Citation Index*

The home page for the *Journal of Fluids and Structures* can be found at  
<http://www.academicpress.com/jfs>

IDEAL, Academic Press' online scientific journal library, where guest users can freely search and browse journal abstracts, can be found at:  
<http://www.idealibrary.com>

The main Academic Press home page is at <http://www.academicpress.com/> where you will find general information about Academic Press and the AP Online Book Catalog.



0889-9746 (200104/05) 15:3/4;1-X